esa

SP-406
March 1997

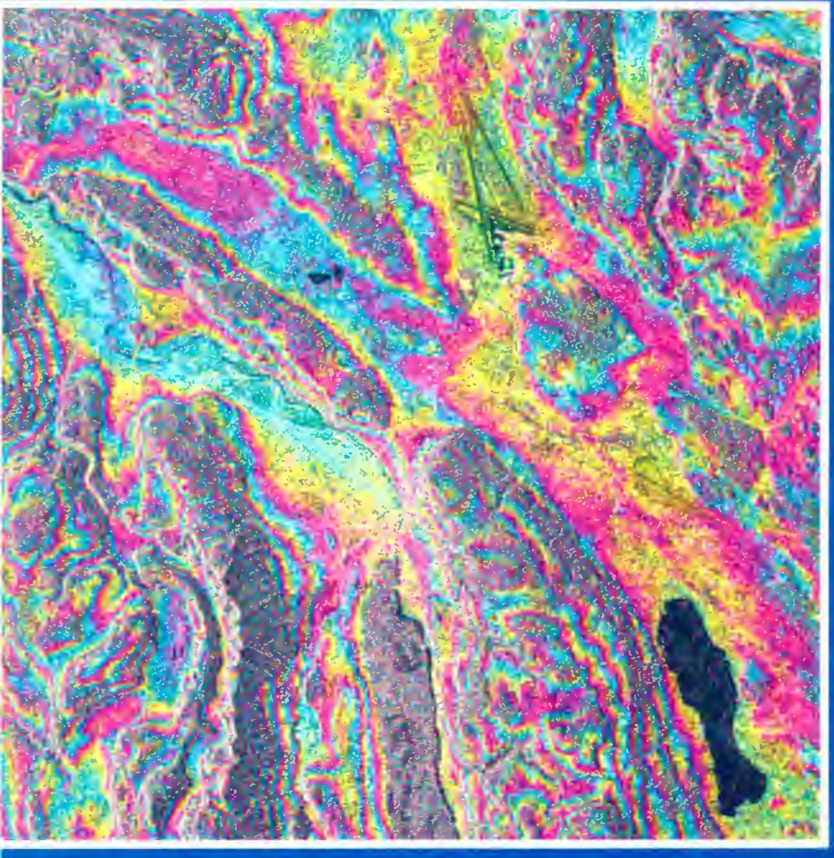

Fringe 96 Workshop

ERS SAR Interferometry

Zurich, Switzerland
30 September - 2 October 1996

European Space Agency
Agence spatiale européenne

SP-406
March 1997
ISBN 92-9092-307-5

'Fringe 96' Workshop

ERS SAR
Interferometry

Zurich, Switzerland
30 September – 2 October 1996

European Space Agency
Agence spatiale européenne

ESA SP-406: *Proceedings of the 'Fringe 96' Workshop on ERS SAR Interferometry*

Published by:	ESA Publications Division ESTEC, Noordwijk, The Netherlands
Compiled by:	T.-D. Guyenne & D. Danesy
Price Code:	80 Dfl.

ISBN 92-9092-307-5	Printed in The Netherlands

Cover design: *An interferogram of Zurich city and its immediate surroundings processed by Remote Sensing Laboratory, University of Zurich from ERS-1 & 2 Tandem SAR data acquired at Fucino station, Italy, on 4 and 5 November 1995 (22.33 local time).*

This image is a combination of radar backscatter intensity (grey scale) and interferometric phase fringes (colour cycle magenta-cyan-yellow). The fringes correspond to height contours and follow closely the local topography, e.g. the flat region around the airport (in the upper centre of the image) and the hills on either side of Lake Zurich (bottom-middle of the image). The small dark feature towards the bottom right of the image is Lake Greifensee; this appears much darker than Lake Zurich probably because the water surface of the latter was rough due to wind effects in the central valley.

As expected with the Tandem mission, one-day interferogram shows an overall improvement in the quality of the fringes (i.e. coherence) when compared to a similar 35-day example.

CONTENTS

Session 3 - Forest & Landcover Applications

Chairman: M. Borgeaud

Session 4 - Processors & Products

Chairman: J-P. Guignard

Session 5 - Algorithms & Techniques

Chairman: E. Attema

Session 6 - Validation

Chairman: G. Solaas

Session 7 - Ice & Glaciers

Chairman: Y-L. Desnos

WORKSHOP PROGRAMME

Abstracts and Papers

Monday, 30 September

Opening Session
Chair: Nuesch D, Kohlhammer G

14.00	Welcome address by Haefner H (Dean of Faculty of Science), Berthet S (Member of the Swiss ESA Delegation) and Emiliani L (Director of Observation of the Earth and its Environment)
14.40	Rocca F: Keynote: SAR Interferometry
15.00	Rott H: SAR Interferometry: Latest Status as presented during the PIERS Conference
15.20	Duchossois G (Head Earth Observation Mission Management Office, ESA): ERS Tandem Mission: Current Status and Future Plans
15.40-16.00	Coffee Break
16.00	Coulson S: Overview of ESA activities with SAR interferometry
16.30	Guerre L F: The Digital Elevation Model market: Current situation and perspectives
16.50	Baltuck M: Overview of NASA activities in SAR Interferometry
17.10	Farr T: The Shuttle Radar Topography Mission
17.30	Hermann J: Study on dedicated SAR Interferometry Mission
18.00	Reception

Tuesday, 1 October

Session 1: Geology/Hazards Applications
Chair: Laur H

08.40	Carnec C: SAR Interferometry for monitoring land subsidence: application to areas of underground earth resources mapping
09.00	Farr T: Topographic Signatures in Geology
09.20	Timmen L: Monitoring of small motions in mining areas by SAR interferometry
09.40	Stow R: Application of SAR interferometry to the imaging and measurement of neotectonic movement applied to mining and other subsidence/downwarp modelling
10.00	Rudant J-P: SAR Interferometry: potential and limits for mining subsidence detection, with examples in the Mulhouse area (eastern France)
10.20-10.40	Coffee Break
10.40	Peltzer G: Crustal deformation studies in southern California using SAR interferometry
11.00	Capes R: CivInSAR (TM) Quake Assessment: An integration of differential SAR Interferometry into a GIS to assist in earthquake risk management
11.20	De Chabalier J-B: The 1995 Grevena (Northern Greece) earthquake:fault model constrained with tectonic observations and SAR interferometry
11.40	Fruneau B: Observation and modelling of the Saint-Etienne-de-Tine landslide using SAR interferometry

Session 2: DEM Applications
Chair: Coulson S

08.40	Carron B: INSAR Quantative Evaluation
09.00	Moccia A: DEM generation by using ERS tandem data
09.20	Dammert P: Accuracy of INSAR DEM measurements in forested areas
09.40	Wehr A: The effects of different landcover on the accuracy of the interferometric DEMS
10.00	Kenyi L: Accuracy assessment of interferometrically derived DTMs
10.20-10.40	Coffee Break
10.40	Muller J-P: Accuracy assessment of DEMs derived from ERS tandem interferometry comparison with SPOT-stereo
11.00	Small D: Validation of height models from ERS Interferometry
11.20	Archambault F: SAR Interferometric DEM Quality Assessment
11.40	Luca D: Multi-resolution analysis of DEMs: error and artifact characterization

Session 3: Forest/Landcover Applications
Chair: Borgeaud M

13.00	Solaas G: Initial testing of tandem quality for INSAR applications. Examples from Taiwan, Madagascar, Zaire, Mali, Ivory Coast and Greenland
13.20	Borgeaud M: On the use of SAR Interferometry for the retrieval of geo- and bio-physical information
13.40	Askne J: Forest INSAR decorrelation and classification properties
14.00	Beaudoin A: Forest monitoring over hilly terrain using ERS INSAR data
14.20	Floury N: Interferometry for Forest Studies
14.40	Stebler O: Analysis of ERS-SAR tandem time series using coherence and backscattering coefficient
15.00-15.20	Coffee Break
15.20	Reich M: The use of interferometric results with other remote sensing data in the EMAP project
15.40	Muller J-P: Assessment of land cover effects in Africa using tandem ERS interferometry
16.00	Morley J G: Wetland monitoring in Mali using SAR interferometry
16.20	Rudant J-P: Phase shift interpretation on ERS-1 interferograms and laboratory measurements
16.40	Derauw D: Preliminary results of Tandem SAR interferometry and differential interferometry over the Dead Sea area
17.00	Wegmuller U: Land applications using ERS1/2 Tandem data

Session 4: Processors/Products
Chair: Guignard JP

13.00	Carrasco D: The developing of a wide area interferometric processor
13.20	Adragna F: Description of the DIAPASON software developed by CNES: Current and Future Applications
13.40	Herland E: Operational use of SAR interferometry for DEM generation and land use mapping
14.00	Eineder M: GEMSAR: DLR'S system for the generation of global digital elevation models from SAR
14.20	Prati C: An interferometric quick look processor
14.40-15.20	Coffee Break
15.20	Tannous I: An integrated methodology for DEM computation through fusion of interferometric, radargrammetric and photogrammetric data
15.40	Upton M: The UCL 3D Image Maker system for automated differential SAR interferometry
16.00	Van Der Kooij M: A workstation for spaceborne interferometric SAR data
16.20	Marzo C: ERS Interferometric Products Development at ASI Space Geodesy Centre

Wednesday, 2 October

Session 5: Algorithms/Techniques
Chair: Attema E

08.40	Ferretti A: Multi-baseline interferometric techniques and applications
09.00	Werner C: Comparison of repeat track interferometric correlation signatures from ERS-1, ERS tandem, SIR-C and JERS-1
09.20	Muller J-P: The potential of ERS tandem for global 100m topography by the year 2000
09.40	Kraemer R: Presentation of an improved phase unwrapping algorithm based on Kalman-Filters combined with local slope estimation
10.00-10.20	Coffee Break
10.20	Costantini M: A phase unwrapping method based on network programming
10.40	Datcu M: The multiresolution approach in SAR interferometry
11.00	Taravre H: New methods of phase unwrapping and baseline adjustments in SAR interferometry
11.20	Hanssen R: A first quantitative evaluation of atmospheric effects on SAR interferometry
11.40	Taravre H: Atmospheric artifacts on interferograms
12.00	Arndt C: Estimating the derivative of modulo-mapped phases

Session 6: Validation
Chair: Solaas G

08.40	Gens R: Comparison of several multi-look processing procedures in INSAR processing for ERS-1&2; tandem mode
09.00	Barmettler A: Cross-compatibility of ERS-SLC products
09.20	Timmen L: Impact of Precise Orbits on SAR Interferometry
09.40	Reigber A: On the interferometric coherence: A Multi-frequency, multi-temporal analysis
10.00	Gens R: An approach to Error Propagation Modeling of SAR interferometric data
10.20-10.40	Coffee Break

Session 7: Ice/Glaciers
Chair: Desnos Y-L

10.40	Doake C: SAR Interferometry over Rutford Ice Stream and Carlson Inlet, Antarctica
11.00	Eldhuset K: First results of ERS tandem INSAR processing on Svalbard
11.20	Fatland R: INSAR at ASF: Analysis of the 1993 Bering Glacier Surge
11.40	Mohr J: Multi-pass interferometry for studies of glacier dynamics
12.00	Wu X: The use of Tandem data in the Antarctic area
12.20	Rott H: Glaciological studies in the Alps and in Antarctica using ERS interferometric SAR

Conclusion/Plenary Session
Chairs: Marelli L, Duchossois G

Session 1

Geology & Hazards Applications

Chairman: H. Laur

SAR Interferometry for monitoring land subsidence: Application to areas of underground earth resources mapping

Claudie Carnec, Christine King — BRGM, Research Division, Geophysics and Geological Imagery, 3 Ave. C., Guillemin, B.P.6009, 45060 Orleans Cedex 2, France
carnec@dr.brgm.fr

Didier Massonnet — CNES, Satellite Image Quality and Processing Division, Dept. Performance of radar systems, 18, Ave. Edouard belin, 31055 Toulouse, France.

Thierry Rabaute — SCOT Conseil, 1 Rue Hermes, Parc Technologique du Canal, 31526 Ramonville Cedex, France

Abstract

Numerous studies carried out within the framework of natural hazards research programs have enabled to test the contribution of SAR remote sensing. The assessment of the interferometry possibilities with the first European Remote Sensing Satellite has been done for sites already known for their instability, involving landslides and subsidence.

Differential interferograms were generated using ERS RAW data recorded either during a 35 days or a 3-days cycle and combined with a DEM covering an underground coal mining in the south of France. The time series of results show good correlations (1) between the geographic location of fringes and the exploitation schedule of the coal deposit that has been mined on the dates the images were taken and (2) between the fringe patterns and the intensity of the ocal subsidence measured along the benchmark network. Therefore those results provide a good way for mapping evolutive surface deformations in a semi-industrial area and for testing the quality of theoretical models of subsidence.

Keywords:

Carnec, C. , Massonnet, D., Villain, J.P., King, C., 1994:
Potential application of differential SAR interferometry for monitoring impact of underground mining. *First Workshop on SAR Interferometry, Tokyo, Japan*, pp. 41-45.

Carnec, C. ,King, C., Massonnet, D., 1995:
Measurement of land subsidence by means of differential SAR interferometry. *Fifth International Symposium on Land Subsidence (FISOLS 95), Barends et al., ed. Balkema. (Rotterdam)* , pp. 139-148.

Carnec, C. , Massonnet, D.,King, C., 1995:
Potentiel d'Application de l'Interferometrie SAR a la detection et a la caracterisation de mouvements de terrain. *Int. Symp "Extraction de parametres bio-geophysiques a partir de donnees RSO pour les applications terrestres, CNES/IEEE, Toulouse, France*, pp. 639-648.

Carnec, C., 1996:
Interferometrie SAR Differentielle : application a la detection et au suivi de mouvements de terrain. *these de 3e cyle Univ.Paris 7, document BRGM.*

Topographic Signatures in Geology

T.G. Farr, D.L. Evans Jet Propulsion Laboratory, California Institute of Technology, Pasadena, CA USA
tom.farr@jpl.nasa.gov

Abstract

Topographic information is required for many Earth Science investigations. For example, topography is an important element in regional and global geomorphic studies because it reflects the interplay between the climate-driven processes of erosion and the tectonic processes of uplift. A number of techniques have been developed to analyze digital topographic data, including Fourier texture analysis. A Fourier transform of the topography of an area allows the spatial frequency content of the topography to be analyzed. Band-pass filtering of the transform produces images representing the amplitude of different spatial wavelengths. These are then used in a multi-band classification to map units based on their spatial frequency content. Results using a radar image instead of digital topography showed good correspondence to a geologic map, however brightness variations in the image unrelated to topography caused errors. An additional benefit to the use of Fourier band-pass images for the classification is that the textural signatures of the units are quantitative measures of the spatial characteristics of the units that may be used to map similar units in similar environments. * Work performed under contract to NASA.

Keywords: Topography, Geology, Texture, Fourier analysis

The Shuttle Radar Topography Mapper

T.G. Farr, M. Kobrick Jet Propulsion Laboratory, California Institute of Technology, Pasadena, CA USA
tom.farr@jpl.nasa.gov

Abstract

The Shuttle Radar Topography Mapper (SRTM), is a cooperative project between NASA and the Defense Mapping Agency of the U.S. Department of Defense. A formal memorandum of understanding to develop and conduct the mission was finalized on July 8. The mission is designed to use a single-pass radar interferometer to produce a digital elevation model of the Earth's land surface between about 60 degrees north and south latitude. The DEM will have 30 m horizontal resolution and about 10 m vertical errors. SRTM will use the same radar instrument that comprised the Spaceborne Imaging Radar-C (SIR-C) that flew twice on the Shuttle Endeavour in 1994. To collect the interferometric data, a 60 m mast, additional C-band imaging antenna, and improved tracking and navigation devices will be added. A second X-band antenna is also planned to be added, which will produce higher resolution topographic measurements in strips nested within the C-band coverage. * Work performed under contract to NASA.

Keywords: Shuttle Radar Topography Mapper, Interferometry, Global DEM

SAR Interferometry: potential and limits for mining subsidence detection, with examples in the Mulhouse area (eastern France)

Daniel Raymond, Jean-Paul Rudant
U.R.A. C.N.R.S 1759, Dépt Géotectonique, Case 129, T26 E1, Université P & M Curie, 4, Place Jussieu, 75252 Paris Cedex 05, France

Abstract

Purpose: Detection of subsidence due to mining in the Mulhouse potassic mining district (eastern France), by means of SAR interferograms.

Thematic context: In the Mulhouse potassic mining district, to the North of Mulhouse, the subterranean working involves subsidence at the surface. This subsidence is increasing during 12 - 15 months after the caving processes, with a maximum vertical movement of 10 mm/day. Subsidence areas are at the most 0.5 km2, and are asymmetrical saucer-shaped, with an active slope moving in the same direction as the mining. Moving in the active areas is followed by the mining Society.

Data: Three interferograms (10.09.92/26.03.93, 11.06.93/16.07.93, 24.09.93/29.10.93) have been established by the French Centre National d'Etudes Spatiales (C.N.E.S) in the area studied. The topographic effects have not been corrected, because the area is an alluvial plain with very little relief.

Results: On the latter interferogram, subsidence effects have been identified. Nevertheless; the active slopes (50m wide, or one pixel) are not visible, the subsidence rate is too rapid with respect to the resolution of the interferogram (interval; 35 days). An interval of three days would be necessary for an effective survey of the subsidence.

Crustal deformation studies using synthetic aperture radar (SAR) interferometry

G. Peltzer, P. Rosen, F. Rogez, C. Werner, E. Fieldings JPL/Caltech,Pasadena, CA, USA
gilles@altyn.jpl.nasa.gov

K. Hudnut USGS, Pasadena, CA, USA

Abstract

Crustal deformation produces a wide variety of landforms at the surface of the Earth and their size depends on the duration of the process involved in their formation. Co- and post-seismic deformations take place over periods of a few seconds to several days, and produce fault scarps and surface displacement ranging from a few centimeters to several meters in magnitude. Over longer periods of time (10 Kyr - 1 Myr), the cumulative effect of earthquakes displaces Quaternary surfaces and geomorphic features by tens to hundreds of meters, producing landforms of greater spatial wavelengths. Over millions of years, such processes build mountain ranges. With the advent of spaceborne radar systems (ERS-1/2, JERS-1, SIR-C, RADARSAT), SAR interferometry is becoming a new tool for active tectonics by providing both surface change maps spanning periods of days to years, for measuring co- and inter-seismic deformations, and accurate, high resolution topographic maps for measuring crustal strain accumulated over longer periods of time. The talk will illustrate both applications of this technique with examples taken along seismic faults in the western US and western China.

Co-seismic surface change maps generated for recent earthquakes in the western US revealed details of the displacement field inaccessible to conventional geodetic techniques. Slow deformation processes such as post-seismic deformation subsequent to large earthquakes or creep events along active faults have also been detected using SAR interferometry. Along the Altyn Tagh fault in western China, radar derived, high resolution topographic maps allowed us to estimate cumulative offsets recorded by displaced geomorphic features over 10,000 to 100,000 years.

Proceedings of the 'Fringe 96' Workshop on ERS SAR Interferometry, *Zurich, 30 September - 2 October 1996* (ESA SP-406, March 1997)

CivInSAR(TM) Quake Assessment: An integration of differential SAR interferometry into a GIS to assist in earthquake risk managment

R. Capes, M. Haynes — The NPA Group

G. Lawrence — TREICoL

A. Smith — Phoenix Systems

J.P. Muller — UCL

B. Parsons, P. England, P. Clarke — Oxford University

Abstract

Differential SAR interferometry has the capability to provide inexpensive, holistic and timely maps of seismic displacements that can be used to assess actual and potential economic risk. Though the science is proven, the methods of communicating the advantages from the complexity of SAR interferometry are still immature. To make such information useful to non-specialist decision makers requires novel techniques in visualisation that can be supported by Geographic Information Systems (GIS). The CivInSAR(TM) Quake Assessment product is a GIS that relates and integrates results from differential SAR interferometry with other satellite and ground data to provide a classified risk map that may be used by the non-specialist on-site. The aim is to place such systems into earthquake prone regions to assist in the management of associated risks. The GIS demonstrated is based upon the Greneva region of Northern Greece where a M=6.6 earthquake occurred on May 13th 1995.

Keywords: interferometry, earthquake, GIS

The 1995 Grevena (Northern Greece) Earthquake: Fault model constrained with tectonic observations and SAR interferometry

B. Meyer (1), R. Armijo (1), D.Massonnet (2), J.B. de Chabalier (1), C. Delacourt (1), J.C. Ruegg (1) and D. Papanastassiou (3)

(1) Institut de Physique du Globe, 4, Place Jussieu, 75252 Paris Cedex 05, France(2) Centre National d'Etude Spatial, Toulouse, France(3) National Observatory, Athens, Greece
dechabal@ipgp.jussieu.fr

Abstract

After the 1995 Grevena Ms=6.6 event in northern Greece, we mapped the earthquake fault break in detail. The surface break is small (8-12 km long, 4 cm slip) compared to the moment release of the event. However, the morphologic and tectonic study of the active faults, in the field and using the SPOT satellite imagery, suggests that the earthquake ruptured part of a much larger fault system including interconnecting segments. We used SAR interferometry with ERS1 satellite images to characterize the coseismic displacement field. This shows a kidney-shaped zone of subsidence reaching 34 cm flanked by an uplift zone reaching 6 cm. We reproduce this field using dislocations in a halfspace consistent with our observations of the fault system. This requires 1 m slip from 4 to 15 km depth on a main normal fault segment dipping NNW. Our preliminary model include significant NE dipping tear faulting at the eastern end of the rupture, clearly seen in the interferograms.

Keywords: earthquake, active faults, SAR interferogramm, modeling

Observation and modelling of the Saint-Etienne-de-Tinée landslide using SAR interferometry

Fruneau Bénédicte

Institut de Physique du Globe

Département Etudes Spatiales

4 place Jussieu 75252 Paris Cedex 05, France

fruneau@ipgp.jussieu.fr

http://www.ipgp.jussieu.fr

Delacourt Christophe

Institut de Physique du Globe

Département Etudes Spatiales

4 place Jussieu 75252 Paris Cedex 05, France delac@ipgp.jussieu.fr

http://www.ipgp.jussieu.fr

Achache José

BRGM, Direction de la Recherche
3 av. C. Guillemin, BP 6009
45060 Orléans Cedex 2, France

j.achache@dr.brgm.fr

Abstract

SAR interferometry has been shown to lead to accurate large-scale surface displacements mapping. The study of the "La Clapière" landslide, located in Southern France on the left bank of the Tinée river, was carried out in order to demonstrate the capability of interferometry to monitor displacements of small spatial extension. In a first study, six different interferograms have been derived from ERS-1 SAR images acquired during the Commissioning Phase. The coherence of the associated images was shown to remain significant over most of the surface of the landslide during the two weeks of the survey. The interferograms, generated on a massively parallel computer, clearly evidenced deformation fringes associated with the landslide. They were remarkably similar, and indicated steady-state displacements over at least 12 days. The displacement field derived from the interferograms was modeled and shown to be characterized by a non-uniform displacement gradient from the top to the bottom. It also revealed a significantly faster motion of the western part of the landslide. The amplitude of the motion was shown to be in good agreement with ground measurements. Furthermore, the interferograms allowed us to evidence a small-scale instability which could not be observed with discrete ground measurements. Finally, we present preliminary results obtained on the same site with images acquired during the second Tandem mission. It provided the opportunity to extend the study of the landslide, which displacements are too high to be observed with images acquired on the standard orbital cycles of 35 days.

Keywords: SAR differential interferometry - Deformation field - Saint-Etienne-de-Tinée landslide - Massively parallel processing - Tandem.

Introduction

Landslides can be a major threat to populations in mountainous areas. Even when they occur away from inhabited areas, they can be a significant hazard and have a serious economic impact by blocking roads and rivers. The "La Clapière" landslide is a good example. It is located near Nice, in Southern France, on the left bank of the Tinée river. This landslide, which extends over a few km^2 between 1100 m and 1700 m, is bounded at the top by a high lobate scarp (fig.1). It is also characterized by an active scree slope on the NW part. A competent layer, known as the barre d'Iglière, produces a sub-horizontal mechanical discontinuity at mid-level in the landslide.

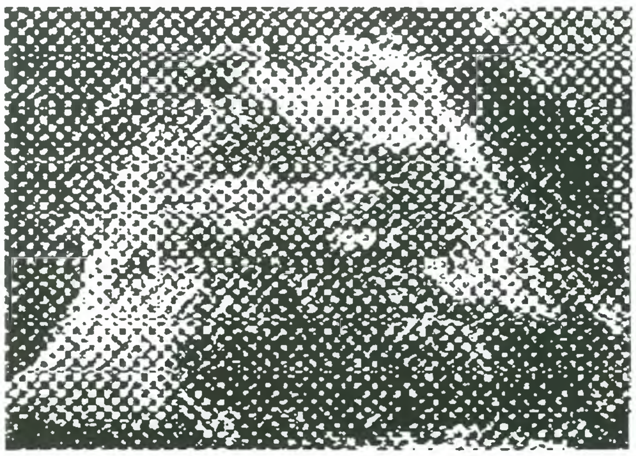

***Figure 1**: The "La Clapière" landslide*

It threatens to obstruct the valley, and then may lead to an overflow of the upstream village of Saint-Etienne-de-Tinée. This hazard has been mitigated with significant road and tunnel construction. It has also been monitored by laser-ranging since 1982. Such a permanent monitoring requires the deployment and servicing of several tens of laser reflectors as well as daily measurement operations. We propose in this paper to apply the technique of SAR interferometry (Zebker et Goldstein, 1986 ; Gabriel *et al.*, 1988) to this landslide, in order to demonstrate its capability for studying small scale deformations. In particular, we compare the characteristics of SAR monitoring derived from this analysis to those of ground measurements

Interferometry

In a first study, we constructed six interferograms with images acquired by ERS-1 with a 3-days repeat cycle, on descending orbits, on August 20, 23, 26, 29 and September 4, 1991.The interferograms are generated on a massively parallel computer (Connection Machine 5). The effect of topography in each interferogram is removed using a 5 m x 5 m Digital Elevation Model (DEM) of the site provided by Institut Géographique National of France (Massonnet *et al.*, 1993 and 1995). The resulting differential interferograms are then projected from SAR geometry to DEM geometry. They correspond to a contour map of the component of the surface displacement field in the direction of the line of sight of the satellite. Significant phase variations associated with the landslide can be detected on these interferograms.

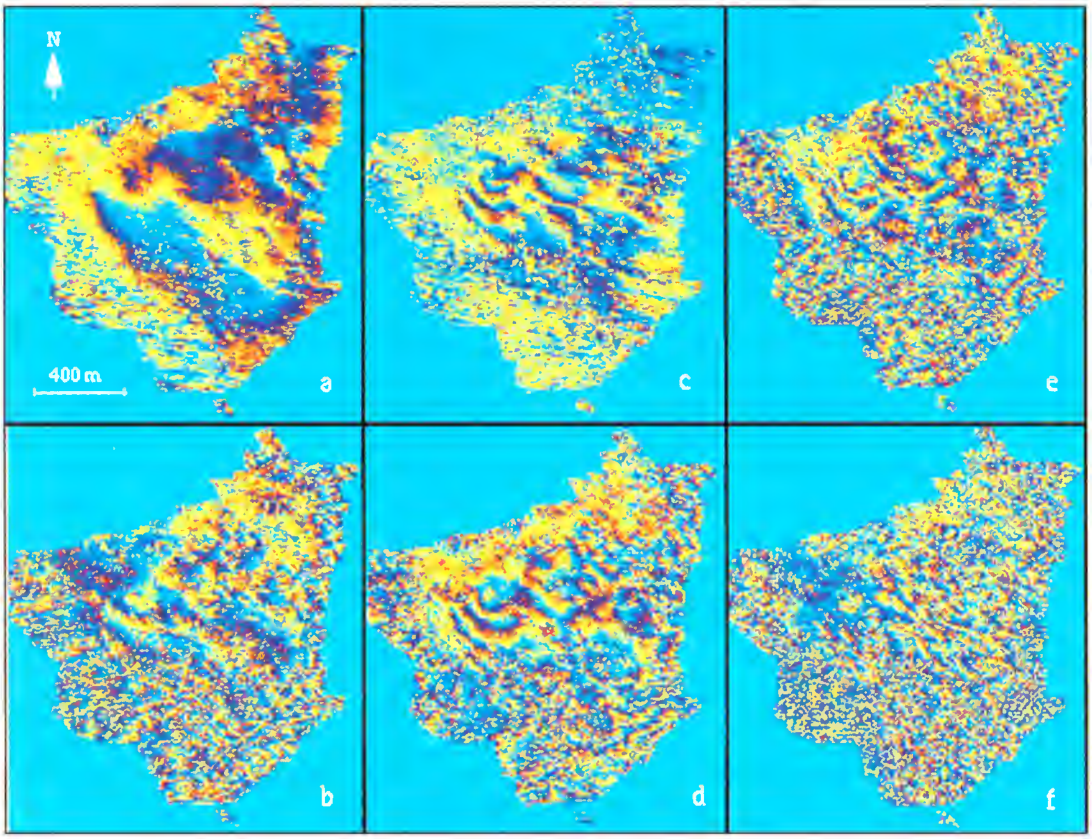

Figure 2: Geocoded differential interferograms. (a) 23-26 pair (3 days). Bperp= 43 m. (b) 26-04 pair (6 days). Bperp= -298 m. (c) 20-29 pair (9 days). Bperp= -4 m. (d) 26-04 pair (9 days). Bperp= 248 m. (e) 23-04 pair. Bperp= 291 m. (f) 20-04 pair. Bperp= -301 m

Figure 2 shows the 6 interferograms. The 3-days interferogram (fig.2a) provides the clearest picture of the landslide, due to its small baseline and a very short time interval. Its boundaries are well described, especially the northwestern part and the 2 lobes at the top. The others present fringes with a lower SNR, because of larger baselines and larger time intervals. All computed interferograms are shown to be similar. The number of fringes increases linearly with the elapsed time between the various image acquisitions, while their overall geometry remains the same. This suggests that the observed landslide motion is stationary over the period surveyed. On all six interferograms, NW-SE trending fringes attest of a downhill movement characterized by a gradient of displacement from the top to the bottom of the landslide, the motion decreasing towards the bottom. A full phase rotation is equivalent to a displacement gradient of 3.9 cm along the landslide average steepest slope. The fringe intervals are not constant over the landslide, suggesting both downhill and lateral variations of the displacement gradient. This gradient changes from top-to-bottom, especially in the SE part: the gradient is very low between the intermediate scarp and the "barre d'Iglière" and seems to increase below this layer. This is consistent with the hypothesis that this layer behaves as a competent layer that blocks the movement and maintains some coherence in the upper part of the massif. From the active scree slope towards the SE, i.e. towards the right side, one observes a progressive increase of the fringe separation, indicating a decrease of the displacement gradient. This variation occurs near the N20° faults that cut the landslide.

Modelling

Since interferograms measure only one component of the displacement (its projection on the slant-range), recovering the 3 components of the displacement field requires some a priori hypotheses on the mechanical behaviour of the landslide. Synthetic interferograms have been computed for two different sliding models which represent the most important types of slope failure: rotational and translational slips (Bromhead, 1986 ; Giani, 1992). In rotational slip, the sliding surface has a spoon shape, and can be approximated by a circle in vertical cross-section. With translational slip, the failure surface tends to be planar and roughly parallel to the slope.

Rotational model

The surface displacements associated with this model are similar to the simple tilt of a rigid block. As already shown by Peltzer *et al.* (1994), we observe that the fringe separation. is not sensitive to the curvature of the sliding surface and only depends on the rotation of the block. With such a model, the interferogram analysis appears therefore not to be efficient to estimate the depth of the sliding surface, a parameter which controls the behaviour of the landslide and the related hazard. In any case, this type of model does not seem to describe the St-Etienne-de-Tinée landslide since it shows fringes with a regular spacing interval and cannot account for the observed non-uniform gradients displayed by the interferograms.

Planar model

A preliminary model based on the 20-29 interferogram was proposed in a previous study (Fruneau et Achache, 1995). In this model, elastic deformation along 3 major discontinuities (faults trending N20°) was superimposed on a uniform gradient of displacement from top-to-bottom. A rigid block of a few hundred meters was also included in the eastern part, between the "barre d'Iglière" and the intermediate scarp. However, when the amplitude of the displacements is rescaled assuming a constant velocity field, this model cannot account for the fringes observed on the new 3, 6 and 12 days interferograms derived in the present paper.

Using these additional interferograms, we derived a new model in which elastic deformation along the major structural discontinuities is modelled by progressive lateral decrease of the top-to-bottom displacement gradient (Fruneau *et al.*, 1995b; Fruneau, 1995). Figure 3a displays synthetic fringes produced by such a displacement field with a gradient ranging from 1.5 cm/100 m in the west of the slide to 0.5 cm/100 m in the east above the barre d'Iglière and 1 cm/100 m below the barre. This variation of the gradient of displacement from the top to the bottom was introduced to further improve the fit between observed and synthetic fringes in the eastern part of the landslide. It may be associated with a swelling of the topography above the "barre d'Iglière" and is consistent with the mechanical behaviour of this layer which holds back the upper part of the landslide. This interferogram (figure 3a) can be compared with the 23-26 interferogram (figure 2a). The displacement field of figure 3a can, then, be rescaled by factors 2, 3 and 4 and the resulting fringes (figure 3b, c and d) can be readily compared with the 6, 9 and 12 days interferograms of figure 2b, c and e, showing a satisfactory agreement. Furthermore, this modelling confirms the stationarity of the displacements.

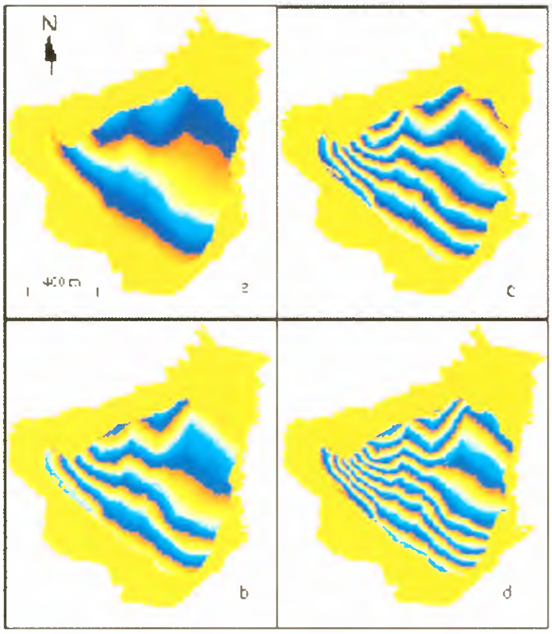

***Figure 3**: **(a)**-Synthetic interferogram. A top-to-bottom gradient of displacement is gradually decreased across the landslide from 1.5 cm/100 m in the NW to 0.5 cm/100 m in the SE. This interferogram should be compared with the 3 days interferogram of figure 2a. **(b)**-The displacement field is increased be a factor 2 with respect to figure 3a. To be compared with the 6 days interferogram of figure 2b. **(c)**-The displacement field is increased by a factor 3 with respect to figure 3a. To be compared to the 9 days interferograms of figure 2c and d. **(d)**-The displacement field is increased by a factor 4 with respect to figure 3a. To be compared to the 12 days interferogram of figure 2e.*

Figure 4 displays the difference between modelled and observed fringes of the 23-26 pair. We observe a nearly uniform phase value over the area of the landslide, indicating a good agreement between the two interferograms over most of the sliding zone. At the eastern top of the slide, figure 4 displays significant phase variations over a small area. This evidences a small unit in the landslide which movement is rapid, and which has not been taken into account by the uniform translational model.

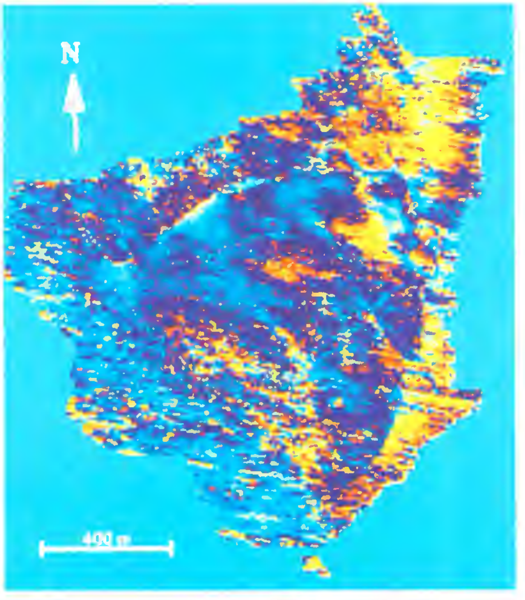

***Figure 4**: Difference between the real and the modeled interferogram.*

Comparison between SAR and ground measurements

The interferometric analysis provides accurate estimates of the displacement gradients in close agreement with existing ground measurements. Figure 5 shows displacement vectors monitored on ground superimposed on displacement vectors derived from our model (which gives a smoother representation that the noisy real interferograms).

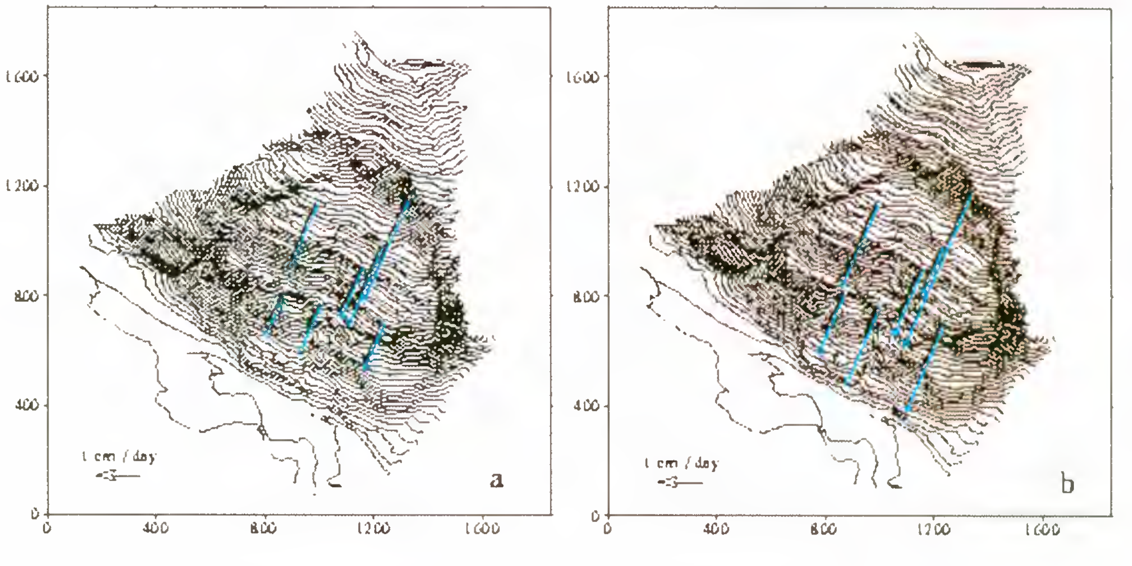

***Figure 5**: **(a)**-Displacement vector measured on ground by laser telemetry (bleu arrows) and computed from the model (black arrows) for the 26-04 period. **(b)**-Same as figure 5a for the 23-26 period.*

Some discrepancies are observed on figure 5b near the bottom of the slide. This can be explained by the fact that interferometry provides only the gradients of displacement. Then only relative displacements can be evaluated because of the discontinuity of the movements between the landslide and the steady massif and ground reference points are necessary to determine absolute displacements. A constant displacement corresponding to the bottom displacement should be added to our model. In the present case, ground measurements by laser telemetry reveal a systematic offset with the average displacement recorded by SAR interferometry. This offset varies from 2 to 7 mm / day over the duration of the survey and provides an estimate of the absolute displacement at the bottom of the landslide.

This shows the complementarity of ground and SAR measurements.

Tandem mission

The tandem mission allowed us to circumvent the incompatibility between the amplitude of the movements and the repeat period of the standard ERS orbit (35 days). It offered the opportunity to carry-on our study of the Saint-Etienne-de-Tinée landslide.

Two interferograms calculated with images from the second Tandem mission give interessant preliminary results. On the 13-14 august 1995 interferogram (fig.6a), we observe a nearly uniform phase change over the area of the landslide, with respect to the bulbe of the landslide. The phase change is also observed on the second couple (10-11 march 1996)(fig.6b), but is less uniform, and clearly evidences the small block on the upper right part of the landslide, which was already detected on the previous interferograms of the previous study. It confirms the high value of displacement of this block, and then emphasizes its instability.

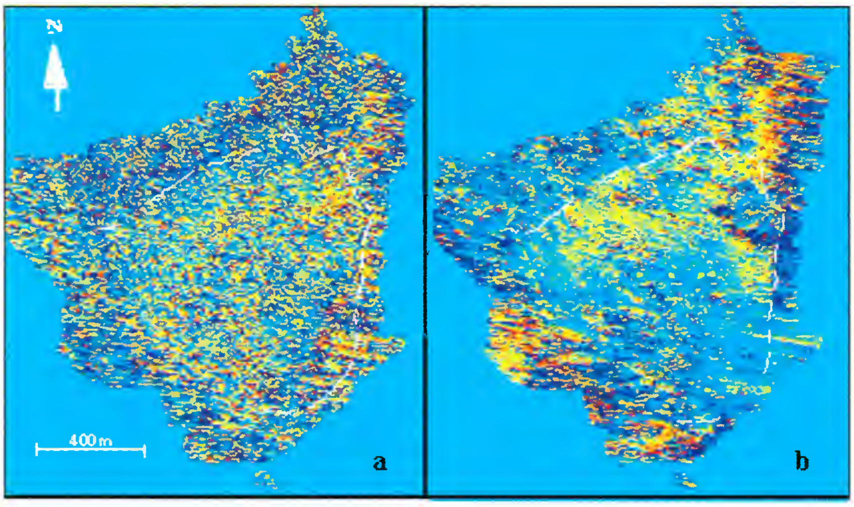

***Figure 6**: Geocoded interferograms calculated with ERS-1 / ERS-2 tandem images. **(a)**-13-14 august 1995 interferogram. Bperp= 50m. **(b)**-10-11 march 1996 interferogram. Bperp= 17 m.*

SAR interferometry versus ground monitoring

A higher density of "measurements" can be achieved with SAR interferometry: SAR monitoring provides a continuous displacement field in comparison with discrete ground measurements. It allows, in particular, to delineate the limits between the different units of the landslide. It also allows to detect local instabilities (in this study we detect a small block at the upper east part) which may not be disclosed by ground measurements if it has not been anticipated, so that laser targets can be installed on this particular block (Achache et al., 1995). Furthermore, ground measurements suffer from the problem of representativeness of the global motion by some targets deployed on the site. Ground measurements are very sensitive to local heterogeneities.

The major limitation of SAR interferometry is the loss of coherence between the 2 images due either to changes in the orbital geometry of the two acquisitions, to ground surface changes, or to a too high gradient of deformation. The two orbital tracks have to be within a few hundred meters to preserve the coherence . This limits the number of interferograms which can be produced from satellite images (among the 10 interferograms which could be generated with the 5 ERS-1 images of 1991, only 6 have good coherence). Ground-surface changes also affect directly the contribution of individual ground targets to the phase. Coherence loss then occurs often in the presence of vegetation or surface water. We note that the active scree

Ground-surface changes also affect directly the contribution of individual ground targets to the phase. Coherence loss then occurs often in the presence of vegetation or surface water. We note that the active scree slope where there is little vegetation remains the most coherent part. Displacements with high values of gradient, such as those associated with the landslide, lead also to incoherence since phase variation across a pixel exceeds one cycle. Orbit cycles of a few days as well as Tandem configuration allows the user to
Of course, interferometry is limited by its "mono-component vector" evaluation, and by the ambiguous nature of the signal, which is known within one half of the wavelength only. Furthermore, it provides only the gradient of displacements, and hence relative displacements can only be evaluated by remote sensing. Reference points are necessary to determine absolute displacements.

Conclusion

This investigation demonstrates the capability of SAR interferometry to monitor surface displacements at the scale required for landslide monitoring. The constraints of this kind of study are totally different from the ones associated with earthquakes, due to small spatial extension and often the high topography encountered. SAR interferometry demonstrated its capability for studying the deformation over small areas. We were able to construct several interferograms on which the landslide is clearly evidenced. These interferograms show an organized fringe system for an elapsed time as large as 12 days, allowing us to construct a steady-state model of surface displacements valid for the whole period of observation. A simple model of translational slide satisfactorily accounts for the observed interferogram, and suggests the existence of a significant plastic deformation in the vicinity of the N20° structural discontinuities cutting the slide. The influence of the major heterogeneities of the landslide ("barre d'Iglière", intermediate scarp) on its mechanical behaviour can also be constrained by the interferometric analysis. It also provides accurate estimates of the displacement gradients in agreement with ground measurements and even allows us to detect small blocks with enhanced displacement which may represent a potential hazard.

References

Achache, J., Fruneau, B., and Delacourt, C., 1995:
Applicability of SAR interferometry for operational monitoring of landslides, *Proceedings of the Second ERS Applications Workshop*, London, 6-8 December 1995, p.165-168.

Fruneau, B., 1995:
Interférométrie différentielle d'images SAR. Application au glissement de terrain de la Clapière, Thèse d'université, Paris 7, 200p.

Fruneau, B., et Achache, J., 1995:
Détection du glissement de terrain de Saint-Etienne-de-Tinée par interférométrie SAR et modélisation, *C.R. Acad. Sci. Paris*, t.320, Série IIa, p. 809-816.

Fruneau, B., Achache, J., et Delacourt, C., 1995:
Observation and modelling of the Saint-Etienne-de-Tinée landslide using SAR interferometry, accepted in *Tectonophysics*.

Gabriel, A.K., Goldstein, R.M., et Zebker, H.A., 1988:
Mapping small elevation changes over large areas: differential radar interferometry, *J. Geophys. Res.*, **94**, p. 9183-9191.

Massonnet, D., Rossi, M., Carmona, C., Adragna, F., Peltzer, G., Feigl, K., et Rabaute, T., 1993:
The displacement field of the Landers earthquake mapped by radar interferometry, *Nature*, **364**, p. 138-142.

Massonnet, D., Briole, and Arnaud, A., 1995:
Deflation of Mount Etna monitored by spaceborne radar interferometry, *Nature*, **375**, p. 567-570.

Zebker, H.A., et Goldstein, R.M., 1986:
Topographic mapping from interferometric Synthetic Aperture Radar observations, *J. Geophys. Res.*, **91**, p. 4993-4999.

Session 2

DEM Applications

Chairman: S. Coulson

INSAR Quantitative Evaluation

B. Carron
Laboratoire de Traitement des Images et du Signal, MATRA CAP SYSTEMES, BP 14, 6 rue Dewoitine, 78142 VELIZY VILLACOUBLAY
e-mail: Bruno.Carron@matra-ms2i.fr

Abstract

We will present the INSAR Quantitative Evaluation Study, conducted for ESA/ESRIN. The INSAR consortium coordinated by Matra Cap Systèmes gathers 9 European partners to validate interferometry for 5 applications over more than 15 test sites, from Antarctica to northern Norway Islands. The INSAR project aims to evaluate and quantify interferometric SAR approach towards conventional measurements, with ground truth reference data, in the field of the following applications : digital elevation model (DEM) production ; hydrology ; forestry ; earth science (earthquake and volcanoes monitoring) and glaciology (ice monitoring).

Keywords:quantitative evaluation, applications, interferometry, INSAR project

INSAR Consortium partners are 10 industrial and academic organizations working on SAR images in different fields :

- CNES, Toulouse, France. (interferometry expert)
- Chalmers University of Technology, Göteborg, Sweden. (forestry)
- GRGS, Toulouse, France. (earthquake monitoring)
- Institut für Navigation, Stuttgart, Germany. (glaciology in antarctic)
- Institut de Physique du Globe de Paris, Paris, France. (volcanoes survey)
- ISTAR, Sophia Antipolis, France. (DEM production)
- Norsk Polarinstitutt, Oslo, Norway. (glaciology in arctic)
- Remote Sensing Laboratories, Zurich, Switzerland. (DEM production & forestry)
- Synoptics, Wageningen, the Netherlands. (hydrology)
- MCS, Vélizy-Villacoublay, France. (DEM production)

Management of the INSAR project is performed by MCS. Technical reporting is performed by ESA experts. We will focus our presentation on the three scientific tasks in which MCS is involved: Project organisation, DEM production, INSAR processor system specification, and WWW demonstrator

Introduction

INSAR project is conducting for ESA/ESRIN by MATRA CAP SYSTEMES, leading to a quantitative evaluation of the INSAR technique towards several applications and their conventional measurement techniques. The project has begun in march 1995, and will end before the end of the year. An European Consortium has been constituted, composed of the industrials and academic organizations detailed on figure 1. All the members of the INSAR Consortium have an expertise in their application area, and the applications are covering a large spectrum :

DEM production : three techniques are evaluated : ISTAR, RSL (Small 1996)and MCS ;

Hydrology : interferometric DEM are compared with SPOT DEM and GPS measurements, and coherence is used in hydrological models (SYNOPTICS) ;

Forestry : interferometry can detect with forest changes, and gives an estimation of the forest parameters (Chalmers University of Technology Dammert 1996 & Askne 1996 and RSL) ;

Glaciology : at Norsk Polarinstitut (Lefauconnier 1996)and Institut für Navigation (Rott 1996) ice movements and quality are to be measured in arctic and antarctic;

Earth sciences : both earthquakes (Feigl 1996)and volcanoes monitoring (Briole 1996) applications are studied.

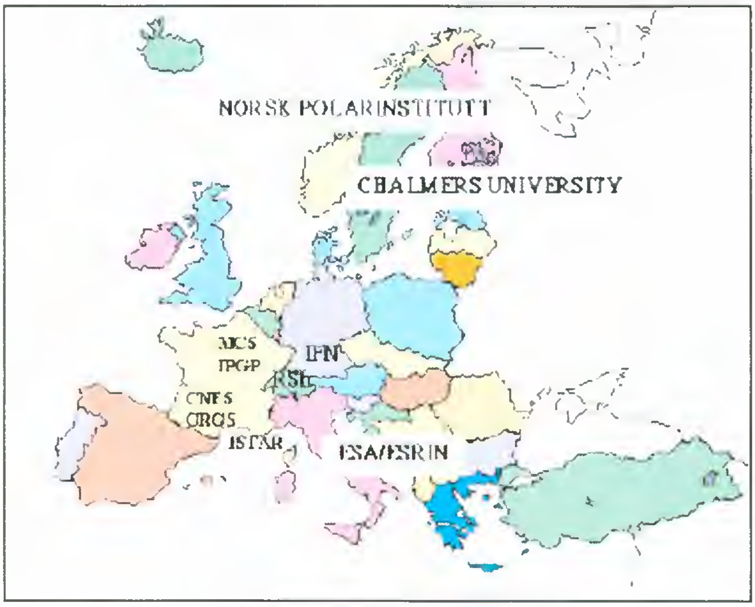

Figure 1: Composition of the Consortium

Several test sites have been chosen by the members of the Consortium all over the world. Following figure gives examples of the test sites locations.

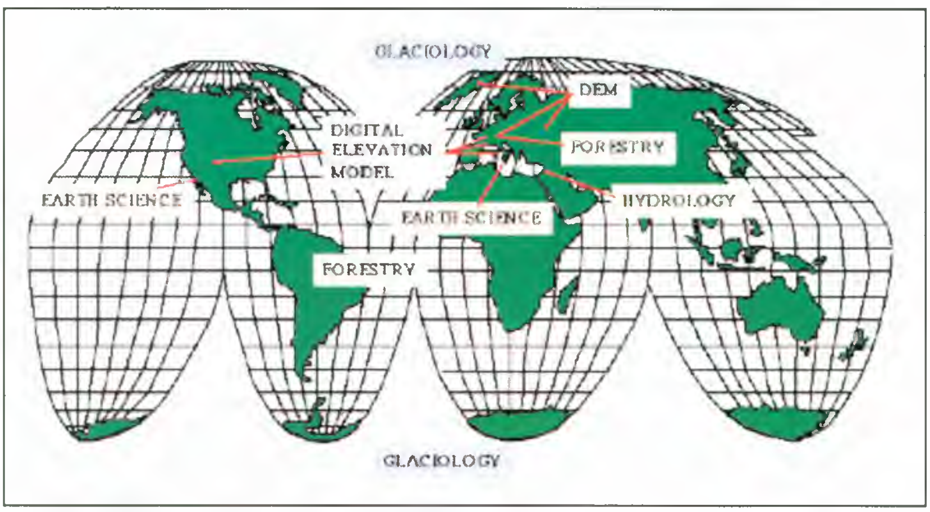

Figure 2: Some of the test sites

The INSAR project

The INSAR project includes the following parts :

Management of the Consortium

- a common evaluation methodology is needed from all the members of the Consortium ;
- Scientific work
- application evaluation (all members of the Consortium, see other publications)
- DEM study
- INSAR processor system specification

- WWW demonstrator

ESA role

ESA has delivered an important number of images in the INSAR study. so that each member of the Consortium may process interferograms. and evaluate its method towards its application extensively.

ESA is also the technical expert for all the application evaluation.

Evaluation methodology

In order to get all the quantitative results available in a common form, a generic evaluation method is to be used by all the members of the INSAR Consortium. For example, for each application, the following items are needed :

An overview of the application is performed

- what is the context of the application area
- what are the common sources of data for that application
- a connection with radar interferometry is to be added
- The conventional measurement techniques are described
- what are the problems or drawbacks of these methods
- what is new with interferometry
- Specific works include
- test sites description
- problems addressed in the evaluation
- detailed results over each test site
- Some of the members of the INSAR Consortium will present their results at FRINGE 96, and the hole package will be available at ESA at the end of the project.

DEM study

H. Tarayre has developed during her PhD-thesis at MCS (Tarayre, 1996 a) a software to produce DEM with interferometry. Production of Digital Elevation Models (DEM) from SAR images through INSAR, seems now possible by using semi automatic phase unwrapping algorithms. This approach will provide a third method to evaluate the DEM production techniques with interferometry (ISTAR, RSL and MCS).

The following example has been used for the algorithmic validation, in France, over Vosges. First image is the DEM produced and second one a combination of the orthorectified amplitude and coherence images.

(click on the images)

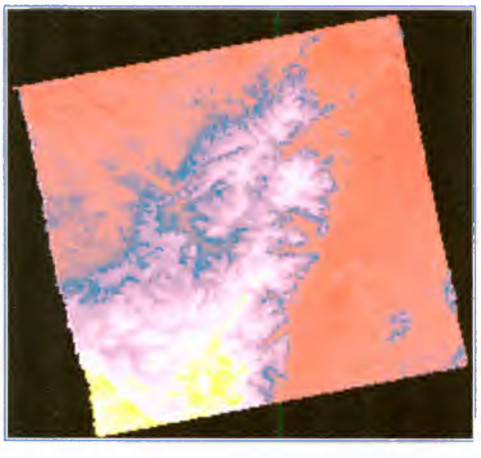

Figure 3: DEM of the Vosges

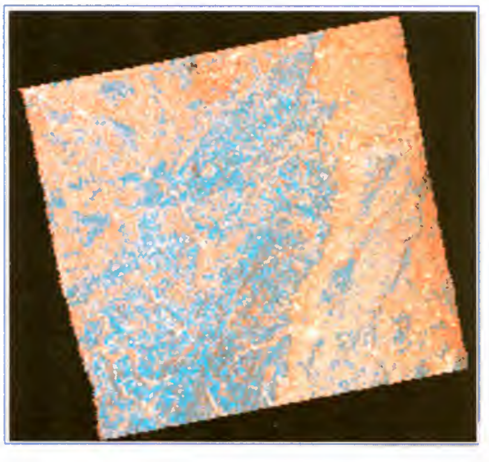

Figure 4: Amplitude and coherence of the Vosges

A validation based on ground control points coming from 1/25000 scale maps (Tarayre 1996 b) give a rms error of 15 meter for a hilly terrain, and 35 meters on stronger relief area, to be compared to the theoritical error from 10 to 14 meters.

Another test site has been choosen over Marseille, with TANDEM images. MCS will unwrap the fringes, and produce the DEM, and the final validation is to be performed by ISTAR, using the ISTAR DEM Marseille database as a reference.

INSAR processor system specification

Based on CNES expertise (Massonnet 1996) an INSAR processor system has been specified by MCS, designed to be able to produce high level interferograms. Main steps of the INSAR processor system are :

- correlation of the two input images, and interferogram computation ;
- DEM ingestion and simulation over the input DEM (suppression of the fringes from the known terrain), then filtering of the histogram ;
- optimisation of the phase function.
- An interferometric quicklook facility is foreseen in a massive interferometric production system, at least in order to choose quickly correct interferometric couples (based on coherence criteria).

WWW demonstrator

At the end of the whole project, a WWW demonstrator will gather the quantitative evaluations of every applications, in order to be accessed by the scientific community, either specialist or non-specialist of the considered applications.

The following figure is the home page of the WWW demonstrator. The whole demonstrator could be available at ESRIN near the end of the year.

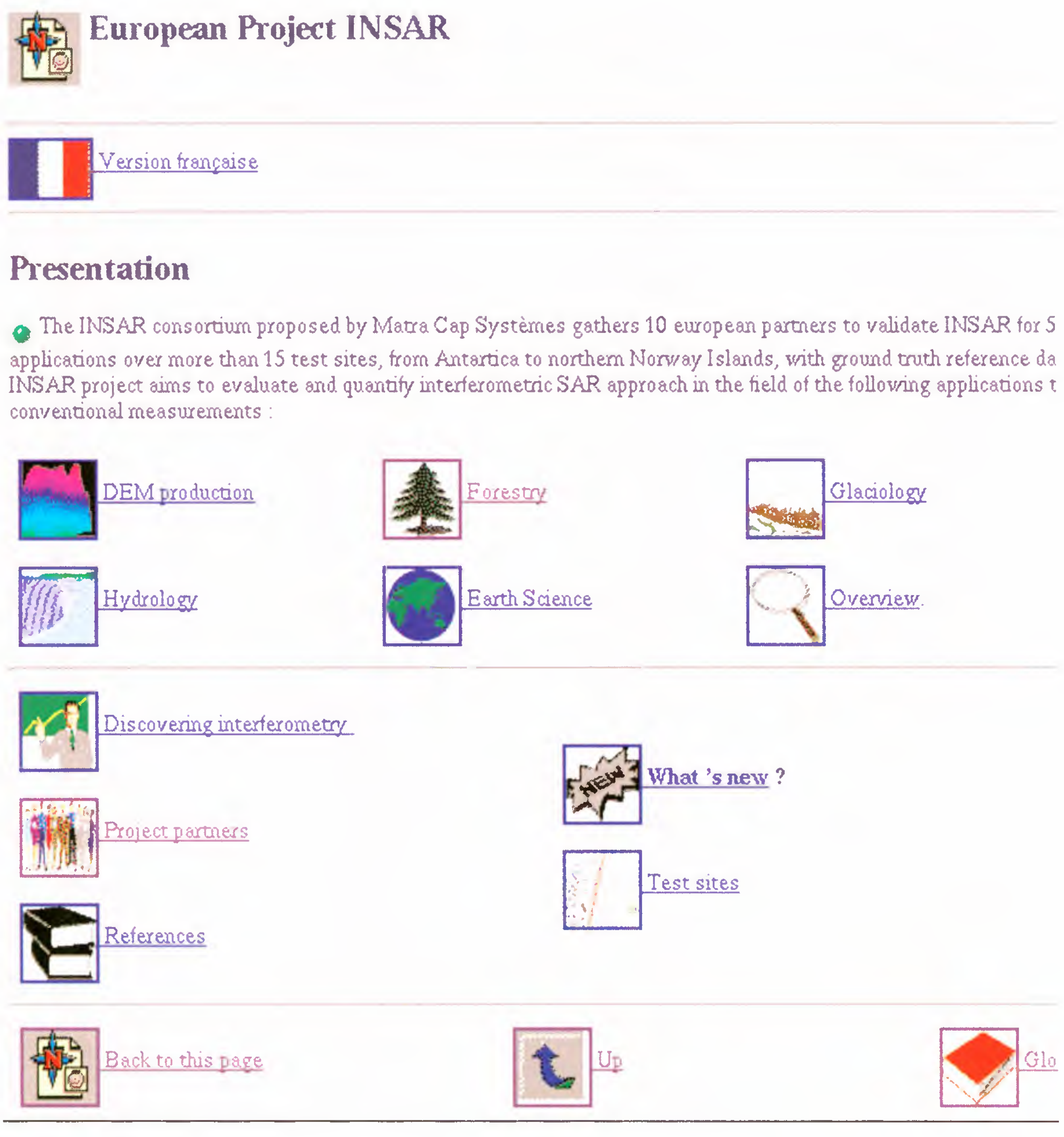

Figure 5: Home page of the WWW demonstrator

Conclusion

The INSAR study is currently ending, and will propose the first quantitative evaluation of the INSAR techniques towards the conventionnal measurement ones for the 5 considered applications. It is a necessary step for understanding the interferometric market.

References

Tarayre Hélène, 1996 a:

Extraction de modèles numériques de terrain par interférométrie radar satellitaire, algorithmie et artéfacts atmosphériques. *PhD Thesis, MCS 1996.*

Tarayre Hélène, 1996 b:

New methods of phase unwrapping and baseline adjustments in SAR interferometry & Atmospheric artifacts on interferograms *FRINGE 96.*

Massonnet Didier, 1996:

Description of the DIAPASON software developed by CNES:Current and Future Applications.

FRINGE 96.

Lefauconnier Bernard, 1995:
Glacier flow measurements in Spitsbergern, Svalbard, from differential interferometry *FRINGE 96.*

Askne Jan., 1996:
Forest INSAR decorrelation and classification properties. *FRINGE 96.*

Dammert Patrick, 1996:
Accuracy of INSAR DEM measurements in forested areas. *FRINGE 96.*

Small David, 1996:
Validation of height models from ERS Interferometry *FRINGE 1996.*

Rott H, 1996:
Glaciological studies in the Alps and in Antarctica using ERS interferometric SAR *FRINGE 1996.*

Briole Pierre, Massonnet Didier, Delacourt C., 1996:
Post eruptive deformation associated with the 1989 lava flow of Etna detected by radar interferometry. To be submitted in: *Geophysical Research Letters, August 1996.*

Feigl Kurt L., Dupré Emmeline, 1995:
RNGCHN: a programm to calculate displacement components from dislocations in an elastic half space. To be submitted in: *Computers and Geosciences, September 1995.*

Accuracy of INSAR Measurements in Forested Areas

Patrik B.G. Dammert Department of Radio and Space Science
Chalmers University of Technology
S-412 96 GOTHENBURG, Sweden
dammert@rss.chalmers.se
http://www.rss.chalmers.se

Abstract

A large part of world is covered by boreal forest. As forest usually have low coherence, it is interesting to see how accurate INSAR-derived DEMs can be in forested areas. Both to see how the low coherence increases the noise in the DEM and to see how the forest will contribute to the DEM height. Different coherence measures are reviewed and DEM compensated coherence is found to the best. It has the lowest bias and standard deviation. Whenever a DEM is not available any knowledge of the topography improves the coherence estimation. However, without a DEM, coherence can both be underestimated and overestimated. For good land cover classification from coherence maps and analysis of INSAR-derived DEMs, a high-quality DEM from another source is preferred. An INSAR-derived DEM from an area in Sweden covered partly with boreal forest, has a total height RMS error for a 100x100 meter grid of around 5 meters. Of course, local RMS errors can be much higher depending on the local coherence. The three main problems in this case are height outliers over open water lakes, frozen lakes (ice-covered) can be on any level and the height bias caused by forests (in this case up to around 8 meters). Problems can partly be solved by averaging several interferometric DEMs, outliers will decrease or fully disappear. Unfortunately, the height bias over forests will only stabilize to a certain value, in this case to around 4 meters. For a five-pair interferometric DEM the total RMS error for a 100x100 meter grid was around 3.5 meters with maximum height errors up to 21 meters.

Keywords: SAR interferometry, DEM accuracy, coherence estimation, estimation bias

Introduction

C-band repeat-pass interferometric measurements from the satellites ERS-1 and ERS-2 have produced several interesting applications, *e.g.* DEM production, tree height measurements, glacier movements and earthquake measurements (see for example Goldstein et al. 1993, Massonnet et al. 1993, Zebker et al. 1994). Particularly DEM production is considered with high interest since a large part of the world does not have good and accurate DEMs and the interferometric SAR technique is very promising to overcome this lack of DEMs. Unfortunately, in the repeat-pass case the imaged ground has to be very stable between acquisitions to preserve the coherence in the image and that is almost only found in areas with dry rock and ground, *e.g.* deserts. The interferometric coherence is an important parameter determining how accurate the interferometric measurements are. For example, over forested terrain in Sweden (Ulander et al. 1993, Dammert et al. 1995, Hagberg et al. 1995) the coherence is usually very low but it is still possible to make measurements. Over forested terrain it is also important to investigate how the trees will contribute to the phase measurements. Measurements have earlier shown that the phase bias caused by forests is a complex function of tree and ground coherence, density of the trees and the tree height itself (Askne et al. 1995).

As a large part of the northern hemisphere is covered with boreal forest, it is interesting to see how good an INSAR-derived DEM corresponds to the real terrain height in such areas. It is also interesting to see how the accuracy of an INSAR-derived DEM corresponds with RMS errors predicted to be around 5 meters by (Zebker et al. 1994) and 1.7 meters by (Hagberg and Ulander 1993) (the difference in predictions are due to the different methods deployed in the articles). Large areas in Sweden are covered with forests which makes the problem more difficult since forests usually give rise to low coherence. In order to assess a INSAR-derived DEM, a good estimate of the coherence must first be determined. High coherence is easy to estimate but for low coherence the estimate is contaminated with a bias. This paper is divided into two main sections, one dealing with coherence estimation and the other with accuracy of INSAR-derived DEMs.

Interferometric data model

The two interferometric signals, $g1$ and $g2$, can be considered determined from

$$\begin{cases} g_1 = a + b \\ g_2 = ae^{j\phi} + c \end{cases} \tag{1}$$

where a, b and c are independent circular complex Gaussian random variables distributed as ~ $CN\left(0, \sigma^2_{a,b,c}\right)$ and ϕ is the phase related to ground topography in the scene. The interferometric coherence is then defined as (Born and Wolf 1980)

$$\gamma = \frac{E\{g_1 g_2^*\}}{\sqrt{E\{|g_1|^2\}E\{|g_2|^2\}}} \tag{2}$$

where $E\{\ \}$ denotes expectation value. As coherence is an important parameter in interferometric SAR, it has to be estimated correctly.

Maximum likelihood coherence estimation

The maximum-likelihood, ML, estimator of the coherence for the model in Equation 1, with no ground induced phase, can be shown to be (Seymour and Cumming 1995)

$$\hat{\gamma} = \frac{\left|\sum_{i=1}^{N} g_{1,i} g_{2,i}^*\right|}{\sqrt{\sum_{i=1}^{N} |g_{1,i}|^2 \sum_{i=1}^{N} |g_{2,i}|^2}} \tag{3}$$

where N is the number of pixels. The estimate is only unbiased for asymptotically large datasets. However, the estimator's statistical properties are known (Tough et al. 1995, Touzi et al. 1996). Using the scheme in (Touzi et al. 1996) it is possible, given the mean of several coherence estimates, to retrieve the true coherence.

Equation 2 is, however, not valid when we have a topography-induced phase in the data, which is normally the case for INSAR images. The coherence ML estimator is then slightly revised as

$$\hat{\gamma} = \frac{\left|\sum_{i=1}^{N} g_{1,i} g_{2,i}^* e^{-j\phi_i}\right|}{\sqrt{\sum_{i=1}^{N} |g_{1,i}|^2 \sum_{i=1}^{N} |g_{2,i}|^2}} \tag{4}$$

where $e^{-j\phi_i}$ is a ground topography correction factor. In other words, ML estimation requires that the topography-induced phase is removed. Note that the fully topography-phase corrected coherence estimator (above) has exactly the same statistics as the estimator in Equation 3.

Insar coherence estimation

Using a DEM from another source is common for topography-correction of normal SAR intensity images and can also be used for coherence estimation as the topography-correction for the interferometric data. This leaves the interferometric coherence estimation as described in Equation 4 above.

On the other hand, if a DEM of the ground is not available, which normally is the case we must make an assumption about the ground topography. The topography-induced phase can be assumed to be constant, linear, quadratic or higher-order function over the estimation window. If the topography-induced phase is assumed to be constant over the whole estimation window, the estimator above will in practise look as the one in Equation 2. Note that the statistics of this estimator (let us call this estimator $\hat{\gamma}_0$) are not the same as those of the estimator in Equation 3, unless the true topography is constant over the estimation window.

If ground topography is assumed to change linearly over the estimation window, the coherence estimator corrects for a ground plane in the interferometric data as

$$\hat{\gamma}_1 = \frac{\max\limits_{w.r.t.\ \nu} \left| \sum_{i=1}^{N} g_{1,i} g_{2,i}^* e^{-j\nu i} \right|}{\sqrt{\sum_{i=1}^{N} |g_{1,i}|^2 \sum_{i=1}^{N} |g_{2,i}|^2}} \tag{5}$$

where $e^{-j\nu i}$ denotes the ground topography correction factor and it can also be seen as a Fourier kernel. The coherence is found locating the highest peak in the spectral domain. This procedure will give a higher bias as it reduces the variance and independent number of samples in the data and it will find the wrong values for low coherence values (the spectrum will be whiter as the coherence drops). However, a sufficiently large number of samples in the estimate will make it possible to measure low coherences.

For small estimation windows, the phase can in practise always be assumed to be linear. For larger estimation windows or steep terrain, it may on the other hand be necessary to correct for quadratic phase values, *i.e.*

$$\hat{\gamma}_2 = \frac{\max\limits_{w.r.t.\ \nu\ \text{and}\ \mu} \left| \sum_{i=1}^{N} g_{1,i} g_{2,i}^* e^{-j\nu i - j\mu i^2} \right|}{\sqrt{\sum_{i=1}^{N} |g_{1,i}|^2 \sum_{i=1}^{N} |g_{2,i}|^2}} \tag{6}$$

or even cubic phase values in the data. Of course, higher-order corrections will reduce the dataset variance more and the bias of the estimator will not decrease leaving low coherence measurements still biased.

Some basic knowledge about the topography in the imaged scene will improve the assumptions. Very little and slowly varying topography, use linear phase correction. Steep and very varying topography, use parabolic phase correction or decrease the estimation window. For practical reasons although, phase is usually considered linear as this makes it possible to estimate the coherence by a Fourier transform, see Equation 5 above.

Using an imperfect assumption of the ground topography or a too large estimation window will result in a lower estimated coherence. Unresolved topographic variations, if they are assumed to be Gaussian, will lower the estimate as

$$\hat{\gamma} \propto \exp\left(-\frac{1}{2} \left(\frac{4\pi b_n}{\lambda R \sin\theta} \sigma_h \right)^2 \right) \tag{7}$$

where σ_h denotes unresolved topographic RMS variations. Equation 7 is also valid for evaluating topographic variations inside a resolution cell. As illustrated in Figure 1, the effect is small for short baselines. Figure 1 also illustrates the fact that for long baselines and large topographic variations the estimated coherence will be practically zero while the coherence using topography-correction could actually be one. In steep terrain this can be true, on the other hand steep terrain is often related to other problems such as layover and shadow effects.

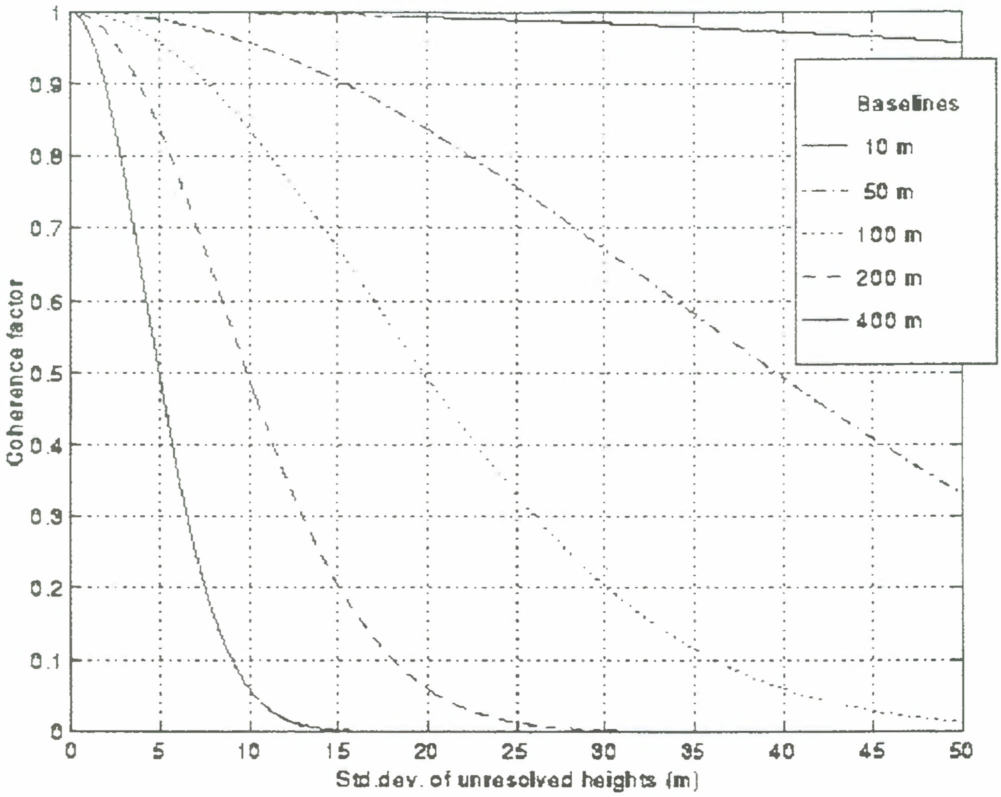

Figure 1. Coherence factor due to unresolved topographic variations. ERS-1 system parameters are used.

Other coherence estimators

A simple case occurs when the power is known *a priori* in the interferometric dataset. In this case, it leaves the coherence ML estimation as

$$\hat{\gamma}_3 = \frac{1}{\sigma_{g1}\sigma_{g2}N}\left|\sum_{i=1}^{N} g_{1i}g_{2i}^*\right| \tag{8}$$

where σ_{g1} and σ_{g2} are the powers of the two signals respectively. As the estimate includes only the magnitude this will lead to a biased estimator. Following the p.d.f. in (Lee et al. 1994) and the integral tables in (Gradshteyn and Ryzhik 1994) it is possible to calculate the expected value of this estimator as

$$E\{\hat{\gamma}_3\} = \frac{\sqrt{\pi}\left(1-\gamma^2\right)^{N+1}\Gamma(N+1/2)}{2\Gamma(N)} F\left(\frac{3}{2}, N+\frac{1}{2}; 1; \gamma^2\right) \tag{9}$$

where $\Gamma()$ is the Gamma function and $F(,;;)$ is the hypergeometric function. Comparison between the above estimator and the ML estimator (Equation 3) yields that the above estimator is slightly better for low coherence. Moreover, information about image statistics *a priori* is not very likely, but determining power from a large homogenous area in the image will yield a good estimate with a small confidence interval. This will leave a coherence estimation with information nearly *a priori*. This procedure can be exploited for real interferograms but with the problem of how to determine homogeneous areas.

A "quick-and-dirty" coherence estimator has been derived by the group at POLIMI in Italy (Gatelli et al. 1996). It is intended for selection of interferometric pairs with good coherence as its implementation is quick. This estimator is included in this study for interest only and is described as

$$\hat{\gamma}_4 = \begin{cases} \sqrt{2\hat{\rho}-1} & \hat{\rho} > \frac{1}{2} \\ 0 & \hat{\rho} \leq \frac{1}{2} \end{cases} \tag{10}$$

where
$$\hat{\rho} = \frac{\sum_{i=1}^{N} |g_{1,i}|^2 |g_{2,i}|^2}{\sqrt{\sum_{i=1}^{N} |g_{1,i}|^4 \sum_{i=1}^{N} |g_{2,i}|^4}}$$

Note that the phase is not used in this estimator. As this coherence estimator can be derived from the higher-order moments of the combined p.d.f. of the interferometric dataset, the variance of this higher-order moment estimator is larger than the best moment estimator which is the same as the above ML estimator (see Equation 3).

Spectral whiteness

The spectral whiteness of a signal is defined as (Markel and Gray Jr 1976)

$$\Theta_x = \frac{\exp\left\{ \int_{-1/2}^{1/2} \ln S_x(\upsilon) d\upsilon \right\}}{\int_{-1/2}^{1/2} S_x(\upsilon) d\upsilon} \tag{11}$$

where Θ_x is the spectral whiteness and S_x is the spectrum for the stochastic signal X. The spectral whiteness will be unity for totally white signals and between zero and unity for more colored signals. As discussed above (under the assumption of a linear phase in the data), a low coherence dataset will have a white spectrum while higher coherence datasets will have more sharp peaks in their spectra (*i.e.* more colored spectra). Ideally, zero-coherence datasets should have unity spectral whiteness. Therefore it is interesting to see how the spectral whiteness varies with the coherence in the dataset.

Simulations

An evaluation of the different estimators was carried out through simulations using the interferometric model in Equation 1. The number of independent samples was chosen to be 50, which corresponds to approximately 5x25 pixels (=100x100 square meters on ground) for an ERS-1 interferogram. Two simulations were carried out, one simulation with the topography-induced phase set to zero and one with a real DEM-modulated phase.

The first simulation (without a topography-induced phase) shows, as expected, that higher-order functions fitted to the phase increase the bias of the coherence estimates. Results are illustrated in Figure 2. However, the most interesting simulation is when the true coherence is zero as illustrated in Table 1. Simulations also validated the known statistics for the normal ML estimator (see Equation 3) as well as for the estimator with power *a priori* (see Equation 8). Note that the DEM-compensated estimator loses its relevance in this case.

The power *a priori* coherence estimator performs slightly better than the normal ML estimator, however, the difference is almost negligible. It is more critical that this estimator performs very poor for high coherence, *e.g.* large standard deviations and giving estimates larger than one. The POLIMI estimator performs poorly for low coherence, a high bias and a large standard deviation, while the high coherence estimates are accurate. This is expected as the purpose of this estimator is only selection of good interferometric pairs. It also shows that higher-order moment estimators for coherence is not the route to good low-coherence estimators.

Simulations for the spectral whiteness show a small variation depending on coherence. The zero coherence simulation which should have produced a spectral whiteness of unity, does instead produce a measure 0.5734. An explanation is that the dataset is finite, for an infinite dataset, the spectral whiteness would be unity. However, increasing the estimation window will reduce resolution and perhaps violate the linear-phase assumption. More or less, the simulations show that spectral whiteness is not a good discriminator for different coherence values.

Table 1 Performance of coherence estimates with true coherence set to zero. 10000 simulations.

Coherence estimator	Mean of simulation result	Std.dev. of simulations result	Mean - Std.dev.	Mean + Std.dev.
γ_0	0.1238	0.0640	0.0598	0.1878
γ_1	0.3191	0.0383	0.2808	0.3574
γ_2	0.4182	0.0322	0.3860	0.4504
γ_3	0.1232	0.0650	0.0582	0.1882
γ_4	0.2035	0.2068	~0	0.4103
Θ_x	0.5734	0.0447	0.5287	0.6181

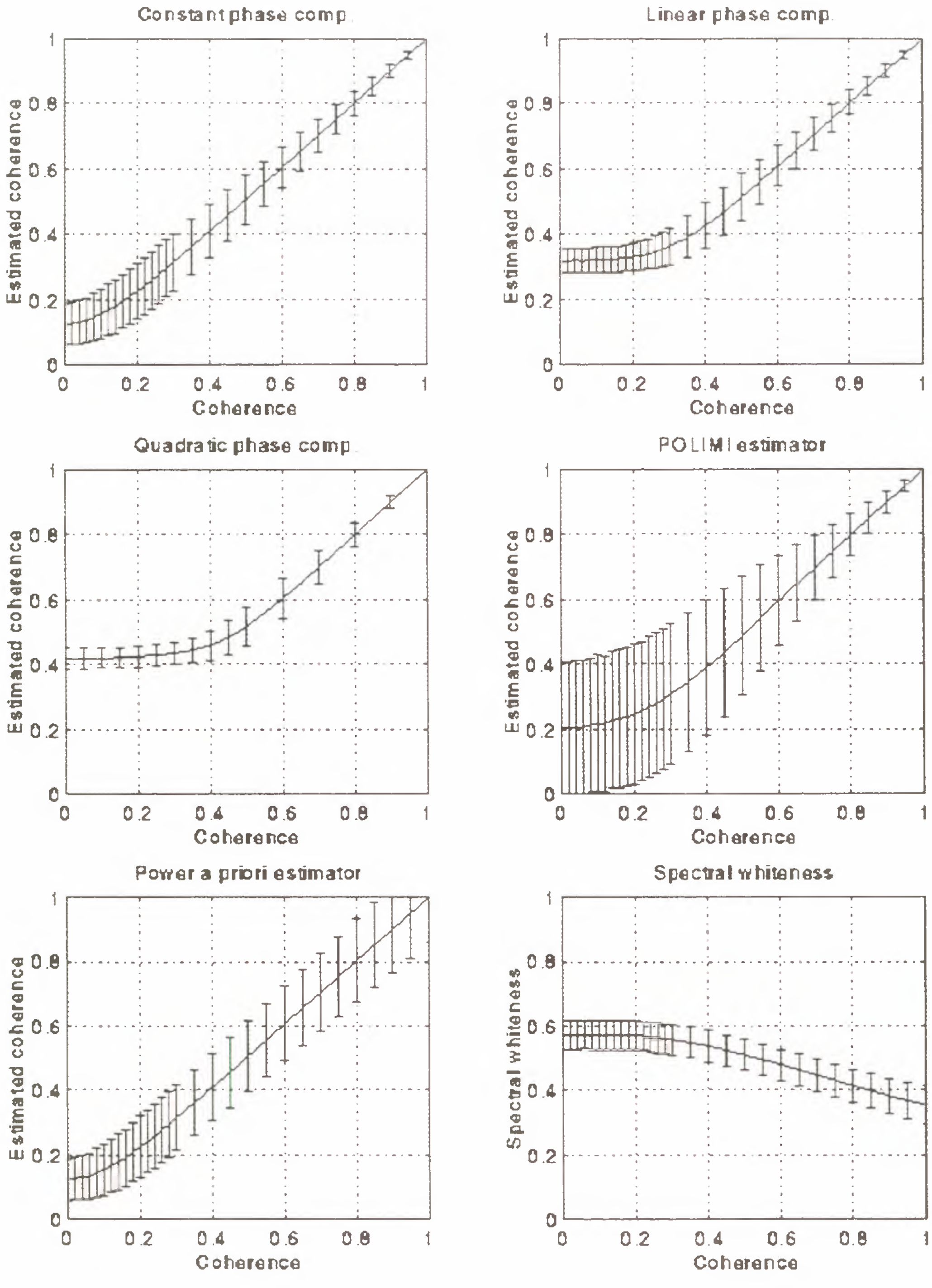

Figure 2. Simulations of the six coherence measures. The bars denote the standard deviations. Number of simulations 10000.

The simulations with a DEM-modulated phase show other interesting artefacts. The chosen DEM describes a rather flat coastland with some farmland scattered around but the main part of it is more hilly forested terrain. Highest mountain is around 200 meters high and maximum slope is never over 15 degrees. The interferometric phase is calculated with parameters equal to ERS-1 geometry and the true coherence is set to unity.

Results are found in Table 2. Simulations show that the power *a priori* coherence estimator performs very poor, it has a large standard deviation and can even give values above one. The spectral whiteness measure also seems to have a large estimation interval. Moreover, as expected the POLIMI estimator and the DEM corrected estimator performed best in this simulation. The other coherence estimators which give values below one is merely because there is unresolved topographic variations in the estimation window, *cf.* Equation 7 and Figure 1. It is also obvious why the linear-phase compensation performed better than the constant-phase compensation.

Table 2 Performance of coherence estimates with a topographic phase.

Coherence estimator	Mean of simulation result	Std.dev. of simulations result	Max. of simulation	Min. of simulation
γ_0	0.9937	0.0136	1	0.7958
γ_1	0.9971	0.0037	1	0.9738
γ_3	0.9944	0.0903	1.4325	0.6942
γ_4	1	0	1	1
DEM-corrected coherence	1	0	1	1
Θ_χ	0.3460	0.0328	0.2234	0.5670

Coherence measurements from real images

For practical reasons, the constant- and linear-phase assumption coherence estimators together with the POLIMI estimator are often used because of the simple implementations, although for different purposes. Using a DEM as a phase correction is also straightforward, whenever such is available. Figure 3 illustrates the difference between the linear-phase assumption and with a DEM available for an existing interferometric pair. As the DEM corrected coherence estimates are believed to be best, the fitted line shows that the linear-phase assumption overestimates low coherence and underestimates high coherence. The overestimates for low coherence is explained by the definition and simulations (see sections above). However, the linear-phase compensated coherence estimator can always underestimate coherence, the effect is here clearly seen for high coherence. For low coherence, there can be both over- and underestimation of the coherence using the linear-phase compensation. The underestimates is an outcome of unresolved topographic variations in the estimation window which, of course, is there for both low and high coherence (*cf.* Equation 7). As the DEM-compensated coherence estimator performs better at all coherence values, reliable coherence measurements should be done with a DEM compensation. Moreover, looking at DEM compensated coherence maps, lakes are easier discriminated than in linear-phase compensated coherence maps.

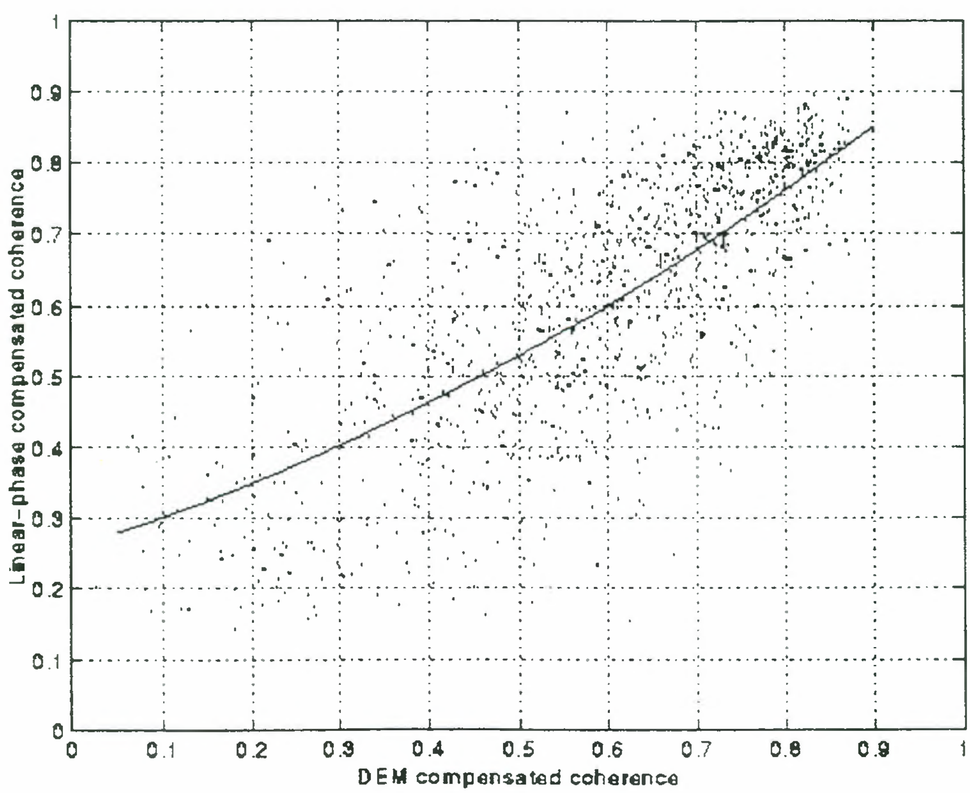

Figure 3 DEM compensated vs. linear-phase compensated coherence estimates, a line is fitted for visual aid. Part of the image pair no. 1 in Table 4.

Unfortunately, there is a problem over forested areas. The scattering centre in a forest is not at ground level (Ulander et al. 1993, Dammert et al. 1995, Hagberg et al. 1995, Small et al. 1995), so the DEM compensation is actually wrong over any kind of forest. The effect will be an underestimated coherence (as above), but the effect can be negligible if the RMS of the scattering centre height is small, *c.f.* Equation 7 and Figure 1. For our baselines and rather homogenous forests, the effect is therefore considered negligible in this paper.

Phase estimation

A reliable coherence measure is extremely important for evaluating the interferometric phase accuracy, *i.e.* the accuracy of an INSAR derived DEM. Given the interferometric model in Equation 1, the maximum-likelihood phase estimate is (Seymour and Cumming 1995)

$$\hat{\phi} = \arg\left(\sum_{j=1}^{N} g_{1,j} g_{2,j}^{*}\right) \tag{12}$$

which can be seen merely as the phase of the ML complex coherence estimator. The variance of this estimator is given by (see for example Lee et al. 1994)

$$\begin{aligned}\sigma_{\hat{\phi}}^2 = & \frac{\Gamma(N+1/2)(1-\gamma^2)^N \gamma}{2\sqrt{\pi}\Gamma(N)} \int_{-\pi}^{\pi} \frac{\phi^2 \cos\phi}{(1-\gamma^2\cos^2\phi)^{N+1/2}} d\phi + \\ & + \frac{(1-\gamma^2)^N}{2\pi} \int_{-\pi}^{\pi} \phi^2 F(N,1;1/2;\gamma^2\cos^2\phi) d\phi\end{aligned} \tag{13}$$

where $\Gamma()$ is the Gamma function and $F(,;;)$ is the hypergeometric function. Knowing the true coherence in an area, it is possible to calculate the variance of the phase estimate and thus the variance of the height measurement, *i.e.* the interferometric DEM. Of course, the accuracy of the topographic height also depends on the accuracy of system parameters (for example such as interferometric baseline, incidence angle etc.), but they are believed to be negligible compared with the phase noise.

Accuracy of interferometric dems

A total of five interferometric pairs is included in the analysis, the pairs are described in Table 4. To assess the accuracy for an interferometric DEM over an area in northern Sweden covered partly with boreal forest, a comparison with a real DEM was made. However, to circumvent the difficult problem of phase unwrapping in low-coherence areas and exact geocoding of the interferogram, "synthetic" interferograms were simulated from the real DEM. By looking at the phase difference between the real and synthetic interferograms, it is possible to determine the accuracy of the interferometric DEM.

Table 4 Interferometric pairs used in this study.

Pair number	Acq. date 1	Acq. date 2	Normal baseline (m)
1	94-02-24	94-02-27	204
2	94-02-06	94-02-15	295
3	94-03-11	94-03-23	203
4	94-03-14	94-03-23	182
5	94-03-17	94-03-23	177

One-pair interferometric DEM

This analysis includes interferometric pair no. 1. Figure 4 illustrates the local RMS error of the interferometric DEM together with a predicted RMS error map derived according to Equation 13. The fact that the heavy multi-looked data display higher height differences than the theoretical values for a given coherence is probably caused by uncertainty of system parameters. As illustrated in Table 5, the accuracy of the interferometric DEM is quite bad for the 1-look, 5-look and 20-look cases. Only the 125-look case seems to give reasonable vertical resolution. However, looking at Figure 4 it is true that the worst values are around the same, but these values occur for low coherence. For high coherence values the vertical resolution improves. In other words, multi-looked interferometric DEMs improve the accuracy at high coherence but for low coherence the accuracy is approximately the same. The multi-look interferometric DEM is more accurate as expected, but horizontal resolution is traded off for improvement of vertical resolution.

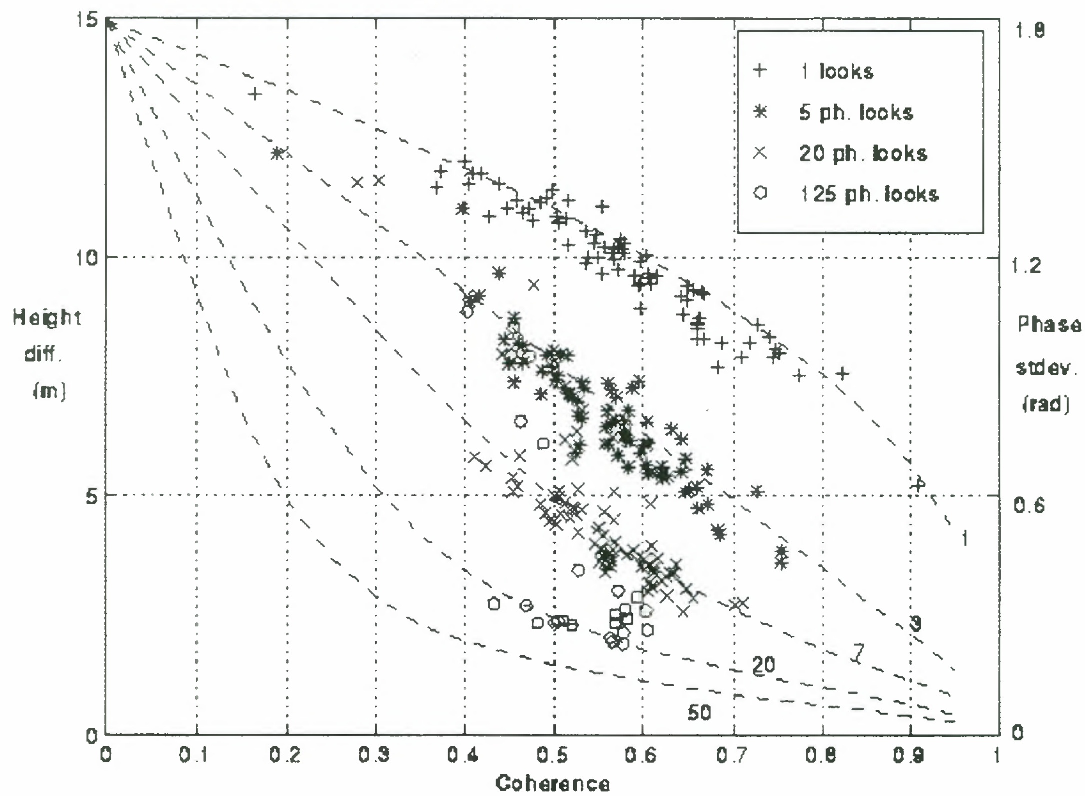

Figure 4 Local RMS error of the interferometric DEM. Dashed lines are the theoretical values given by Equation 13 for a certain number of independent looks (number of looks placed right of the lines). Right-hand y-axis displays the phase while the left-hand y-axis displays the corresponding heights. Note also the difference between independent and physical number of looks.

Table 5 Phase and height differences compared with different horizontal resolution.

No. of physical looks	Approx. ground area (m2)	Approx. no. of independent looks	Max. local RMS phase difference (rad)	Max local RMS height difference (m)
1	20 x 4	1	1.80	14.9
5	20 x 20	3	1.79	14.8
20	40 x 40	8	1.56	12.9
125	100 x 100	50	1.08	8.86

For the single pair DEM, one of the largest problem is the outliers caused by lakes and sea. For open water coherence is zero and the phase can thus take on any value. In this case with partly frozen lakes, another problem has occurred. The ice cover has moved coherently between acquisitions giving rise to a phase shift. For DEM production it means that the height of the lake can be on any level.

As pointed out in several papers (Ulander et al. 1993, Dammert et al. 1995, Hagberg et al. 1995, Small et al. 1995), a forest will cause a height bias in the interferometric DEM. Depending on circumstances and bole volume of a forest, the bias will be different. In this area, the interferometric height of a certain large homogeneous forest has been measured to 2.2 meters for this pair but can be higher for other pairs, see Table 6. Of course, the low coherence over forests gives rise to large height standard deviations as well. More multilooking will decrease the height standard deviation (*i.e.* decrease the phase noise).

A large part of this area is covered by forests, so an additional error caused by the trees is expected in the interferometric DEM. Part of the RMS error in the above interferometric DEM can thus be explained by forests in the scene.

Table 6 Measured forest heights for the image pairs (Askne et al. 1996).

Pair number	Forest mean height (m)	Forest std. dev. (m)
1	2.2	11.9
2	1.1	8.5
3	5.3	N/A
4	7.3	12.8
5	2.7	N/A

Multiple pair interferometric DEM

An average of the five interferometric DEMs, derived from the pairs in Table 4, was performed to decrease height errors. The errors should decrease as $1/\sqrt{M}$, where M is the number of independent measurements. As the interferometric forest height varies in different interferograms (*c.f.* Table 6), an average of several interferometric DEMs will also stabilize the height bias caused by forests. Nevertheless, a high RMS error will always exist over a forested area because of the low coherence. The result is illustrated in Table 7.

Table 7 Accuracy of one INSAR-pair DEM and a multiple INSAR-pair DEM.

		DEM derived from one pair		DEM derived from five pairs	
Number of physical looks	Approx. ground area (m2)	Total RMS height error (m)	Maximum height error (m)	Total RMS height error (m)	Maximum height error (m)
5	20 x 20	8.02	25.88	4.70	22.46
20	40 x 40	6.15	25.88	4.23	21.76
80	80 x 80	5.19	25.77	3.65	22.26
125	100 x 100	4.98	25.87	3.49	21.03

The maximum errors for the one-pair DEM corresponds actually to $\pm\pi$ radians in that interferogram, *i.e.* the maximum phase value in the interferograms. In the five-pair DEM RMS errors are decreased as expected, but more important is that outliers, seen in the one-pair DEM, seem to fully disappear. Moreover, the interferometric heights of frozen lakes are better than for the one-pair case. The error caused by a certain forest for this particular five-pair DEM is easily evaluated from measurements and is approx. 3.7 meters for this forest, see Table 6. Other forests are expected to have similar values, of course depending on forest density, actual tree height and other circumstances.

Conclusions

As already well known, coherence estimates are biased for low coherence measurements. Decreasing horizontal resolution will decrease the estimate's bias. As low coherence means a noisy signal, more data has to be averaged to get good measurements. Simulations show that DEM corrected coherence estimates outperforms those of any other estimator, both for low and high coherence. Simulations also show that even for quite moderate topography, the other estimates will be good, although for larger topography coherence will always be underestimated. To have a reliable coherence measure is important both for DEM production and land cover classification by coherence. Estimation with a DEM is therefore always preferred. Nevertheless, for DEM production there may not be a *a priori* DEM and in this case any basic knowledge about the topography will improve the coherence estimates. Furthermore, it is very hard to distinguish low coherence areas in this case.

The DEMs derived in this study, have generally rather low RMS height errors. However, they are worse than those predicted in (Hagberg and Ulander 1993, Zebker et al. 1994) which were 5 and 1.7 meters respectively. Of course, the RMS errors in this study include very low coherence values which could affect RMS errors in a negative way. For the single pair DEM, the largest problem is the outliers caused by lakes and sea. In this case with partly frozen lakes, another problem has occurred. The ice cover has moved coherently between acquisitions giving rise to a phase shift. For DEM production it means that the height of the lake can be on any level. With forests in the scene, there can be an additional height bias up to around 8 meters.

The multiple pair DEM shows a better RMS height error as expected. However, most noteworthy is that outliers over open water lakes have disappeared and the height bias caused by a certain forest is decreased to around 4 meters. Other forests are believed to cause similar height biases. Errors caused by coherent movements of ice in lakes are of course also decreased. The multiple pair DEM is much smoother than the one pair DEM.

Multiple pair DEMs will thus decrease errors caused by unfrozen lakes, frozen lakes and forests. The benefit going from one pair to several pairs is thus obvious. For DEM production, more than one pair is therefore needed, preferably a series of SAR images.

Future work should include areas with greater topography, perhaps even with layover and shadow effects, to see where the actual limit is for INSAR derived DEMs. As different interferometric DEMs have different SNRs (*i.e.* coherence) a minimum variance DEM average can be performed to decrease height errors even further. This should also be studied for future work. Of course, a good and stable phase unwrapping technique for low coherence areas also has to be developed.

Acknowledgements

I would like to acknowledge insights and valuable discussions with Prof. Jan Askne, at Chalmers, together with the new and good ideas and problem clarifications by Dr. Lars Ulander at FOA, Sweden. Ideas and help from Gary Smith and Prof. D. Rosenholm are also acknowledged. LMV, Sweden, is acknowledged for the DEM.

The research in this study is financed by a grant from the Swedish National Space Board.

References

Askne, J., Dammert, P. B. G., Fransson, J., Israelsson, H. and Ulander, L. M. H., 1995, Retrieval of forest parameters using intensity and repeat-pass interferometric SAR information, *Proceedings of Retrieval of Bio and Geophysical Parameters from SAR Data for Land Applications held in Toulouse, 10-13 October 1995*, ,

Askne, J., Dammert, P. B. G. and Smith, G., 1996, INSAR Application Evaluation Report: INSAR for Forest Mapping, Department of Radio and Space Science, Chalmers University of Technology, Gothenburg, Sweden.

Born, M. and Wolf, E., 1980, *Principles of Optics* (Pergamon Press).

Dammert, P. B. G., Ulander, L. M. H. and Askne, J., 1995, SAR Interferometry for Detecting Forest Stands and Tree Heights, *Proceedings of European Symposium on Satellite Remote Sensing II held in Paris, France, 25-28 September 1995*, ,

Gatelli, F., Monti Guarnieri, A., Prati, C. and Rocca, F., 1996, Medium Resolution Efficient Phase Preserving Focusing for Interferometry, *Proceedings of IGARSS'96 held in Lincoln, 27-31 May 1996*, ,

Goldstein, R. M., Engelhardt, H., Kamb, B. and Frolich, R. M., 1993, Satellite radar interferometry for monitoring ice sheet motion: application to an Antarctic ice stream, *Science*, **262,** 1525-1530.

Gradshteyn, I. S. and Ryzhik, I. M., 1994, *Table of Integrals, Series and Products* (Boston: Academic Press Inc.).

Hagberg, J. O. and Ulander, L. M. H., 1993, On the Optimization of Interferometric SAR for Topographic Mapping, *IEEE Transactions on Geoscience and Remote Sensing*, **31,** 303-306.

Hagberg, J. O., Ulander, L. M. H. and Askne, J., 1995, Repeat-Pass SAR Interferometry over Forested Terrain, *IEEE Transactions on Geoscience and Remote Sensing*, **33,** 331-340.

Lee, J., Hoppel, K. W., Mango, S. A. and Miller, A. R., 1994, Intensity and Phase Statistics of Mulitlook Polarimetric and Interferometric SAR Imagery, *IEEE Transactions on Geoscience and Remote Sensing*, **32,** 1017-1028.

Markel, J. D. and Gray Jr, A. H., 1976, *Linear Prediction of Speech* (New York: Springer Verlag).

Massonnet, D., Rossi, M., Carmona, C., Adragna, F., Peltzer, G., Feigl, K. and Rabaute, T., 1993, The Displacement Field of the Landers Earthquake Mapped by Radar Interferometry, *Nature*, **364,** 138-142.

Seymour, M. and Cumming, I., 1995, Maximum Likelihood Estimation and Cramer-Rao Bounds for SAR Interferometry, Department of Electrical Engineering, University of British Columbia, Vancouver.

Small, D., Holecz, F. and Nüesch, D., 1995, Combination of Ascending / Descending ERS-1 INSAR Data for Calibration and Validation, *Proceedings of IGARSS'95 held in Firenze, 10-14 July 1995*, ,

Tough, R. J. A., Blacknell, D. and Quegan, S., 1995, A Statistical Description of Polarimetric and Interferometric Synthetic Aperture Radar Data, *Proceedings of the Royal Society, London*, **449,** 567-589.

Touzi, R., Lopes, A. and Vachon, P. W., 1996, Estimation of Coherence Functions for Interferometric SAR Applications, *Proceedings of EUSAR'96, 26-28 March 1996 held in Königswinter*, ,

Ulander, L. M. H., Hagberg, J. O. and Askne, J., 1993, ERS-1 SAR Interferometry over Forested Terrain, *Proceedings of Second ERS-1 Symposium Space at the Service of Our Environment held in Hamburg, 11-14 October 1993*, ,

Zebker, H. A., Werner, C. L., Rosen, P. A. and Hensley, S., 1994, Accuracy of Topographic Maps Derived from ERS-1 Interferometric Radar, IEEE Transactions on Geoscience and Remote Sensing, **32**, 823-836.

Accuracy assessment of DEMs derived from ERS tandem interferometry and comparison with SPOT-stereo

J.-P. Muller, A. Mandanayake, M. Upton University College London
jpmuller@ps.ucl.ac.uk

Abstract

Accurate digital terrain model are essential to a number of scientific and commercial applications, in particular natural resources, utilities and mobile communication systems.

SAR Interferometry presents an important new tool for the production of accurate digital terrain models comparable to optical based systems such as SPOT.

The method of creating a DEM is discussed in a companion paper "The UCL 3D Image Maker system for DEM generation from SAR interferometry" (IFSAR-3DIM) by Muller, Mandanayake, Upton in this workshop.

This paper presents an accuracy assessment of DEMs derived from ERS tandem interferometry, including a detailed description and results of the IFSAR-3DIM process over 2 study sites: Montagne Saint Victoire and Mt Etna as well as a quantitative comparison with SPOT-stereo using panchromatic SPOT data.

Accuracy assessment of interferometrically derived DTMs

Lado KENYI and Hannes RAGGAM

Institute for Digital Image Processing, Joanneum Research, Wastiangasse 6, A-8010 Graz, AUSTRIA.

e-mail:lado@pdib40.joanneum.ac.at / raggam@pdib40.joanneum.ac.at

Abstract

In this paper results of a quantitative analysis of interferometrically derived digital terrain models (DTMs) and topographic maps digitised DTMs of two different test sites are presented. Two INSAR derived DTMs from ERS-1 phase D SLC data of the area around the city of Dortmund in Germany and an ERS-1/2 tandem phase SLC image pair of the area around the city of Graz in Austria were assessed. For the comparison of the results, difference DTMs were computed from the INSAR derived DTMs and the topographic maps digitised DTMs. Although good rms height error were achieved for the ground control points used in the DTM generation, the standard deviation of the difference DTMs on average was about 18 m for the Dortmund test data and 29 m for the Graz test area. The horizontal accuracy, i.e. residuals of the Easting and Northing of the ground control points, on average was within half a pixel and a pixel in the North and East directions respectively. Obviously, a need for the use of more ground control points and the 100 points state vector orbit restitution has been identified in this work. With the use of these extra data, the vertical and horizontal accuracy of INSAR generated DTM can be significantly improved even in SLC image pairs of relatively smaller baselines.

1. Introduction

Before the launch of ERS-2, ERS INSAR data have been acquired by ERS-1 in time intervals of 3 or 35 days - or multiples therefrom - between the image pairs. However, recently a combination of an ERS-1 and an ERS-2 SLC scene being acquired during the ERS Tandem mission. This mission was specifically designed for the acquisition of appropriate SLC image pairs within a period of typically one day, which is the repeat orbit interval between the two satellites.

Although satisfactory results concerning the validation of interferometrically derived digital terrain models have been reported in the literature, a comprehensive analysis of the results especially the reproduction of the results from the same test area with different data sets have not been performed. Therefore, in this paper results of a comprehensive analysis of interferometrically derived DTMs and topographic maps digitised DTMs of two different test sites are presented. The work includes the assessment of two INSAR derived DTMs from ERS-1 phase D SLC data of the area around the city of Dortmund in Germany and an ERS-1/2 tandem phase SLC image pair of the area around the city of Graz in Austria. The reference digital terrain models were resampled to cell sizes of 40m x 40m for matters of comparison with the interferometric products.

2. Test Area and SLC Data

In general, experiments made over two different test sites are presented in this paper. These are:

Test area "Dortmund":

For an area south-west of the city of Dortmund in Germany, the following ERS-1 SLC image pairs were processed:

Orbits: 12864 & 12907 (Dortmund-1);

Proceedings of the 'Fringe 96' Workshop on ERS SAR Interferometry, *Zurich, 30 September - 2 October 1996* (ESA SP-406, March 1997)

13896 & 13939 (Dortmund-2).

Dates: 31-12-1993 & 03-01-1994;

13-03-1994 & 16-03-1994.

Baselines: 63 & -74 meters.

Test area "Graz":

This test site covers the city of Graz as well as the south-western areas. An ERS Tandem SLC image pair was used for this area with acquisition dates as follows:

Orbits: 21338 (ERS-1) & 1665 (ERS-2).

Dates: 14-08-1995 & 15-08-1995.

Baseline: 56 meters.

3. Data Processing

The above selected data sets were interferometrically processed by an in-house built INSAR software tool. The tool typically consist of all the interferometric chain, i.e. coregistration, spectral filtering, flat terrain phase removal, fringe generation and smoothing, phase unwrapping and the conversion of the unwrapped phase into terrain height information. Here only the last step which is the derivation of the terrain heights will be described. For the description of the other processing steps the reader is referred to references [1] - [6] and [10].

4. DTM Generation Procedure

The geometric imaging disposition for interferometric data is shown in figure 1. Various approaches may be used to convert the unwrapped phase values pixel-by-pixel to corresponding ground points. The procedure which has been implemented in our software is briefly described in the following.

First, the slant range difference δ_i is calculated for each pixel from the individual phase values Φ_i:

$$\delta_i = -\frac{\lambda}{4\pi} \cdot (\Phi_i + \Phi_c)$$

Usually, Φ_c is a constant phase offset. In our approach, however, linear terms in range and azimuth are additionally considered in order to compensate for converging or diverging orbits and similar effects because of erroneous a-priori information. The terms of this phase offset „function" are determined in advance by using a sufficient number of ground control points with respective reference values for δ_i and Φ_i.

Besides, the slant range distance R_1, which corresponds to the length of vector $\vec{r}_1$, is determined from the SAR range pixel coordinate. Then, the slant range distance R_2 and the baselength B can be calculated in a next step as follows:

$$R_2 = |\vec{r}_2| = R_1 + \delta$$

$$B = |\vec{s}_2 - \vec{s}_1|$$

These entities are used to determine the angle α between baseline vector $\vec{B}$ and pointing vector $\vec{r}_1$ in sensor position $\vec{s}_1$ by the equation:

$$\cos\alpha = \frac{R_2^2 + B^2 - R_1^2}{2 \cdot B \cdot R_1}$$

Using $\vec{s}_1$, $\vec{B}$, α, R_1 as well as 3D vector relations, the pointing vector $\vec{r}_1$ and the ground point $\vec{p}$ are finally calculated.

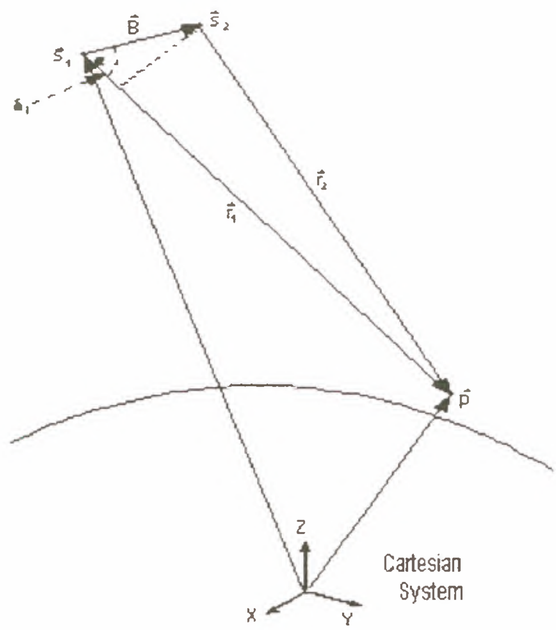

Figure 1: Geometric INSAR imaging disposition.

5. Analysis of Results

In the following, analysis of the results achieved for the individual test areas with regard to the production of digital terrain models and their comparison to the reference DTMs is given.

Test area "Dortmund"

For this test area good quality interferograms could be generated from the ERS SLC data. Practically, all over the quarter scene the achieved coherency was very high, above 0.75, except of the water bodies and some forested areas. Based on ground control points measured in a 1 : 50000 topographic maps, two DTMs were generated from the unwrapped phase data. These DTMs are shown in figures 2 and 3, while in figure 4 the reference DTM is presented, both being illustrated in height colour coding. Only from a comparison of the difference DTMs generated by subtraction of the reference DTM from the INSAR ones, the differences between these DTMs become obvious. Whereas, the pure gray value coded shapes of the terrain correspond almost perfectly, especially at the hilly part of the area.

Cross checking verification activities on a number of points in the image have shown a good height correspondence for most parts of the INSAR generated DTM, with some exceptions in the hilly terrain areas. In general, it can be stated that because of the small baseline the orbits reconstruction during the DTM generation might become unstable and could lead to such local errors. Also other parameters, such as weather information, need to be investigated in order to conclude on some of these variations that have been observed in the INSAR DTM, especially in the flat terrain part of the image (upper left side). The statistical errors achieved for the ground control points and the difference DTMs for this test area are shown in tables 1 and 2 respectively.

Test area "Graz"

Relatively good quality interferograms were generated from some parts of this ERS-1/2 tandem data set of this test area, but the coherency in some parts of the quarter scene was very low and on average it was around 0.45. This in particular applies to the forested areas, which by experience are rather critical for the interferometric data processing. Generally, a DTM was successfully generated from the unwrapped phase data which is shown in figure 5, while in figure 6 a reference DTM derived from topographic maps of the test area is presented. It can be noted that the INSAR derived DTM, as shown in figure 5, accurately reflect the shape of the topography of the area. This can simply be deduced from the visual comparison with the map derived reference DTM in figure 6. From the cross checking of some points in the INSAR DTM with the reference one, it was observed that large deviations (about 50 m) could be found especially in the hilly regions. As mentioned before, the small baselines could be of influence in the stability of the orbits reconstruction. A comprehensive analysis, which deals with INSAR DTMs of different baselines could, in our opinion, lead to good qualitative and quantitative analysis of this test area. The statistical errors obtained for this test area are presented in tables 1 and 2, respectively for the GCPs and difference DTMs.

Table 1: Residuals of GCPs coordinates.

Test Area	East	North	Height
Dortmund - 1	53 m	32 m	14 m
Dortmund - 2	51 m	33 m	15 m
Graz	50 m	34 m	12 m

Table 2: Residuals of difference DTMs.

Test Area	Mean	Std. Deviation
Dortmund-1	12 m	18 m
Dortmund-2	14 m	19 m
Graz	23 m	29 m

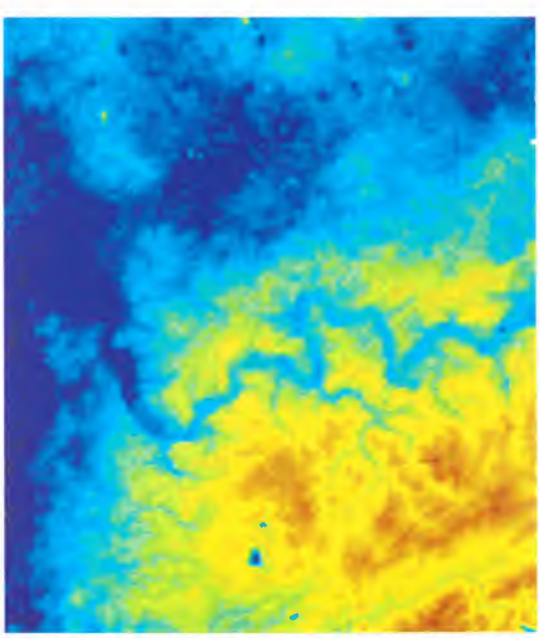

Figure 2: INSAR derived DTM from "Dortmund-1" test data.

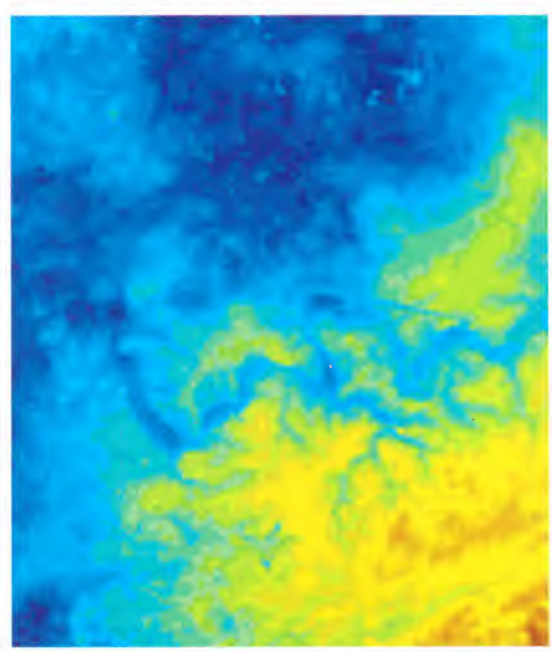

Figure 3: INSAR DTM derived from "Dortmund-2" test data.

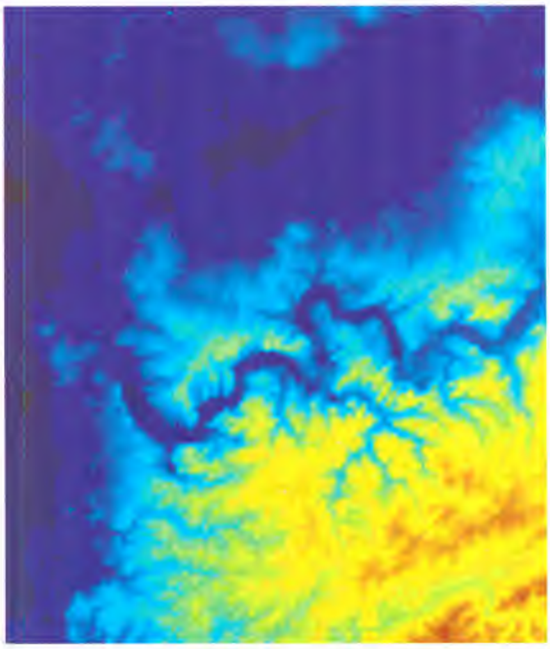

Figure 4: Reference DTM for "Dortmund" test area.

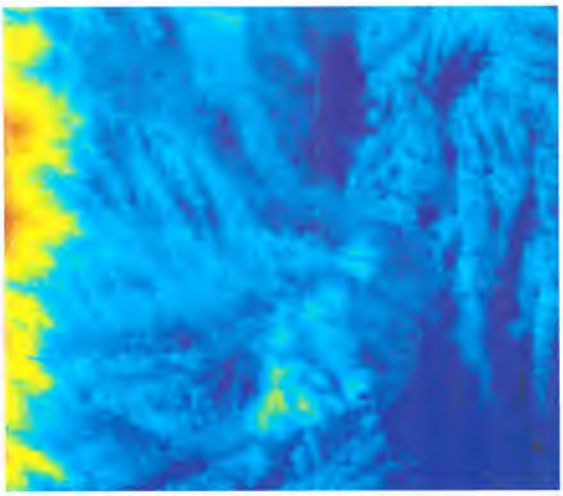

Figure 5: INSAR derived DTM from the "Graz" test data.

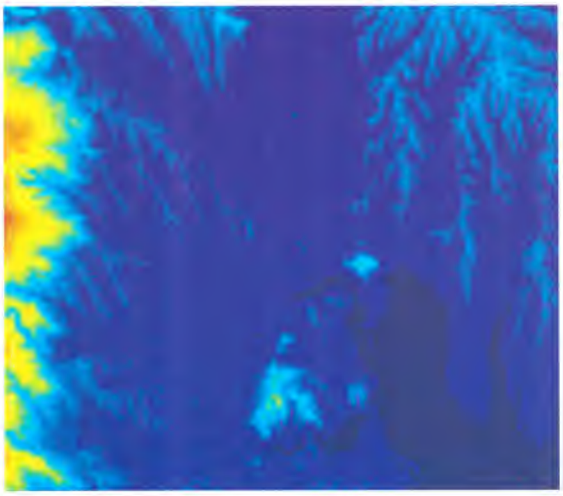

Figure 6: Reference DTM for "Graz" test area.

6. Conclusions

Generally, it can be concluded that even at relatively small baselines INSAR derived DTMs give height information with acceptable errors. The rms errors for the Dortmund test area were quite good, whereas those for the Graz test site were poor. However, enough care must be exercised due to the fact that atmospheric turbulence can introduce errors of large magnitude in the INSAR height measurements. But to come to qualitative and quantitative conclusions on the INSAR derived DTMs, further work still needs to be performed for the validation of INSAR derived DTMs. These could typically consist of SLC data sets of different baselines and from various terrain topography, use of the precision orbit information, and adequate selection of control points for the DTM generation process.

Acknowledgement

The reference DEM of the Dortmund test area has been provided by the Deutsche Forschungsanstalt für Luft- und Raumfahrt (DLR) for comparative analyses. Assistance in the control point measurement was provided by our colleagues A. Almer and S. Teufel. We thankfully acknowledge these contributions.

References

1. Gabriel A., Goldstein R., and Zebker H. (1989): Mapping Small Elevation Changes Over Large Areas: Differential Radar Interferometry. J. Geophysical Research, Vol. 94, No. B7, pp. 9183- 9191, July 10, 1989.
2. Geudtner D., Schwäbish M., and Winter R. (1994): SAR-Interferometry with ERS-1 Data. Proceedings of PIERS'94 Symposium, Noordwijk, The Netherlands, 11-15 July 1994.
3. Goldstein R., Zebker H., and Werner C. (1988): Satellite Radar Interferometry: Two-Dimensional Phase Unwrapping. Radioscience, Vol. 23, No. 4, pp. 713 - 720, July-August, 1988.
4. Kenyi L. W., Raggam H., and Kubista E. (1996): Feasibility of Atmospheric Effect on Interferometric Data and Its Interpretation. DIBAG Report 64, ESA Contract No. 9949/92/NL/PB, JOANNEUM RESEARCH, Institute for Digital Image Processing, April 1996.
5. Massonnet D., Rossi M., Carmona C., Peltzer G., Feigl K., and Rabaute T. (1993): The Displacement of Field of the Landers Earthquake Mapped by Radar Interferometry. Nature, Vol 364, No. 6433, pp. 138 - 142, 1993.
6. Prati C., Rocca F., and Monti-Guarnieri A. (1992): SAR Interferometry Experiments with ERS-1. In Proceedings of 1st ERS-1 Symposium, Cannes, France, pp. 211 - 218, November 1992.
7. Raggam H. (1990a): Interpolative Map-to-image Coordinate Transformation for Spaceborne Imagery. In Proceedings. of 10'th Annual IGARSS Symposium: Remote Sensing - Science for the Nineties, Vol. II, pp. 1423-1426, Washington D.C., U.S.A, May 20-24 1990.
8. Raggam H. (1990b): Analytical Simulation for Quality Control of Geocoded SAR Images. Technical Note made under contract for the German PAF for ERS-1., JOANNEUM RESEARCH, Institute for Digital Image Processing, July 1990.
9. Zebker H., Rosen P., Goldstein R., Gabriel A., and Werner C. (1994a): On the Derivation of Coseismic Displacement Fields Using Differential Radar Interferometry: The Landers Earthquake. J. Geophysical Research, Vol. 99, No. B10, pp. 19617- 19634, 10 October 1994.
    1. Zebker H., Werner C., Rosen P., and Hensley S. (1994b): Accuracy of Topographic Maps Derived from ERS-1 Interferometric Radar. IEEE Trans. Geoscience and Remote Sensing, Vol. 32, No. 4, pp. 823 - 836, 10 October 1994.

SAR Interferometric DEM quality assessment

Laurent Polidori — Aérospatiale Espace & Défence, Cannes (France)

Francois-X. Archambault — Ecole Supérieure des Géomètres et Topographes, Evry (France)

Michel Kasser — Institut Géographique National, Saint-Mandé (France)

Abstract

The aptitude of SAR interferometric acquisition for relief mapping has been demonstrated, and illustrated on a few test sites. Unfortunately, the validation of this mapping technique is still very limited, for three main reasons :

First, the quality assessment of each interferometric DEM is generally performed using questionable data sets, i.e. either a small number of ground control points with limited statistical representativity, or a so-called reference DEM (obtained from a SPOT stereo pair or from an official data base) which is often less accurate than the interferometric DEM itself.

Second, very few experiments have been carried out completely, i.e. including height computation and DEM geocoding. Therefore, it is difficult to predict the performances of SAR interferometry in general terms without taking into account the influence of a particular landscape (vegetation, atmosphere, slope...) or particular acquisition conditions (sensor parameters, baseline...).

Third, DEM quality assessment is often limited to a single criterion, namely, elevation standard deviation, which is very easy to evaluate. This criterion is very relevant for orthorectification but not for most DEM applications, in particular geoscientific applications. Therefore, user needs have to be expressed more clearly before a user-oriented quality assessment can be undertaken.

These limitations will be analysed in our presentation. We will propose solutions for overcoming them, based on a simulation-based concept already published (Polidori & Armand 1995) and we will present some preliminary results.

Keywords: SAR, interferometry, DEM, quality, errors

To overcome this problem, we have developed a validation environment dedicated to testing new algorithms or new SAR systems and to quantitatively evaluate the aptitude of existing interferometric processing chains to map relevant topographic parameters (altitude but also slope or terrain motion). The approach we use is based on artifact modelling and image simulation. Indeed, studies performed by Aerospatiale and ESGT have shown that SAR image simulation is a powerful tool for the validation of relief mapping techniques such as SAR interferometry, stereo-radargrammetry or shape- from-shading (Polidori & Armand 1995).

We have also successfully used this approach to validate other cartographic applications, e.g. change detection in radar images, building extraction from optical stereo images or spectral sensing from future MERIS data.

Simulation-based validation of radar interferometric processing (illustrated on Figure 1) has three main advantages : * it allows a great variety of situations, i.e. a variety of both SAR systems and landscapes, so that a new algorithm can be tested in many cases and not only on a particular data set ; * it can be handled in a parametric way so that the impact of any parameter on the resulting accuracy can be evaluated (by parameter we refer to both imaging parameters related to sensor, SAR processing or acquisition conditions - and landscape parameters such as slope, roughness, moisture but also atmospheric refraction index) ; * it relies on an input landscape which can be considered as an exact and dense ground truth, required to derive error maps and therefore to analyse the relationship between the behaviour of an algorithm and local terrain characteristics.

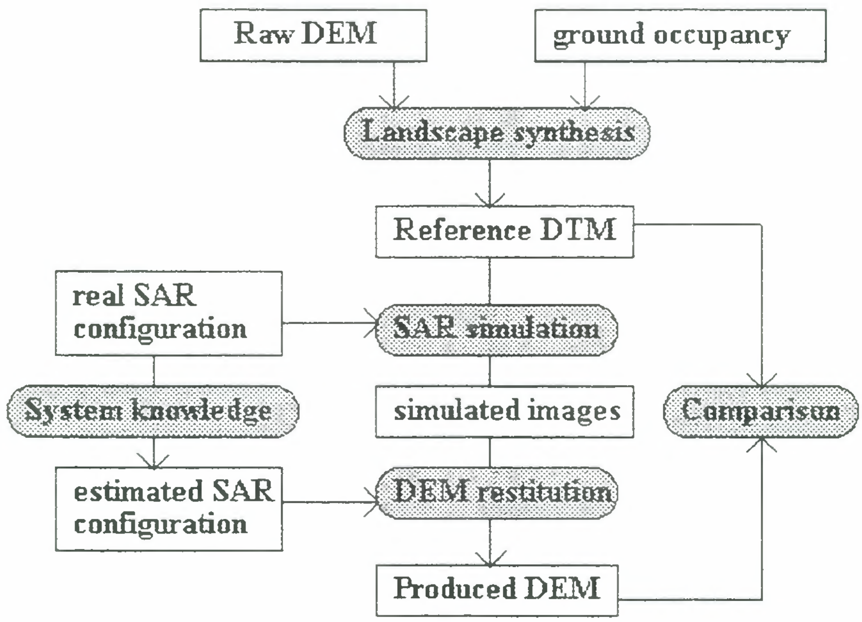

Fig. 1 : Simulation-based validation environment for radar interferometric processing.

In the case of SAR interferometry, the simulation procedure must be designed in such a way that all phase effects can be taken into account, namely : - orbit ; - platform stability ; - clock ; - atmosphere and ionosphere ; - raw signal compression and decompression ; - SAR processing ; - terrain elevation ; - terrain slope and curvature ; - roughness (i.e. spatial organization of scatterers) ; - volumetric scattering ; - subsurface penetration ; - temporal variation of ground parameters.

Since it would be very time consuming to consider all these effects in a rigorous raw signal simulator, we have implemented a simplified simulator, fully dedicated to interferometry, in which the SAR impulse response is modelled in a separate simulator.

Some results are presented in fig.2 A reference map is presented in fig.2a, based on a digital elevation model and a synthetic, manually drawn land use map. Sensor parameters corresponding to the ERS case have been used. Fig.2b represents the raw interferogram obtained with a 64 meter baseline. Phase unwrapping, elevation computation and finally geocoding have led to the output map presented in fig.2c. A visual comparison of the input map and the output map is not very relevant since the data are very similar. Reversely, computing elevation differences leads to a very interesting error map (fig.2d), on which the local behaviour of our algorithms can be revealed. Error histograms can be computed, even over restricted areas, which would not be possible when validating with few unaccurate ground control points.

Fig.3 shows similar results obtained with a greater baseline (138 m). The effect of the baseline can be evaluated not only in average but also locally.

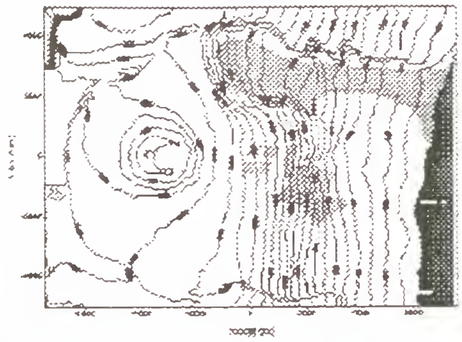

Fig.2a : input map

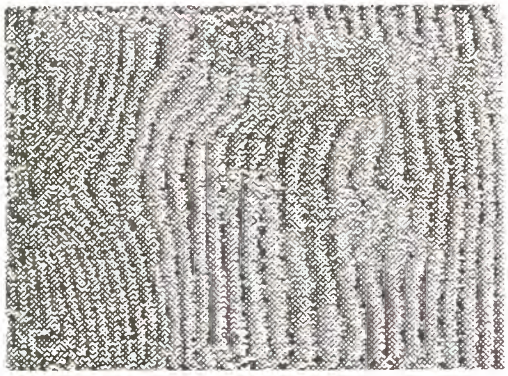

Fig.2b : raw interferogram

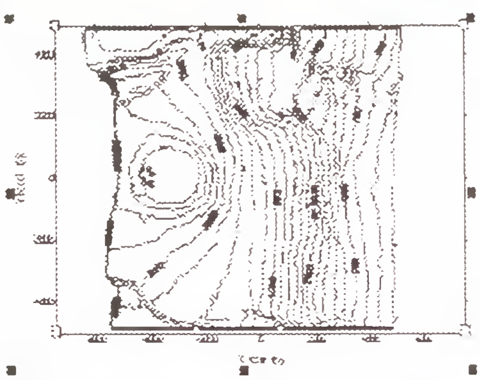

Fig.2c : output map

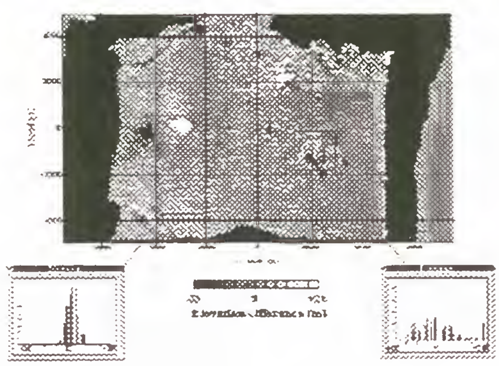

Fig.2d : error map

Fig. 2 : Results obtained for baseline = 64 m

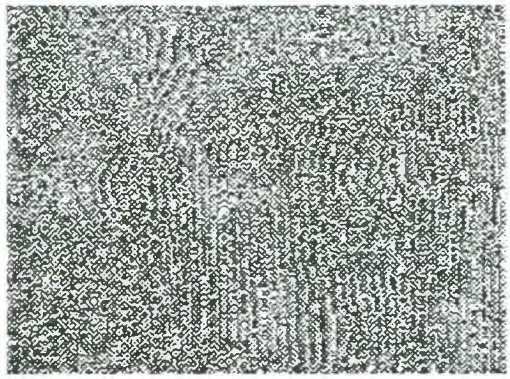

Fig.3a : raw interferogram

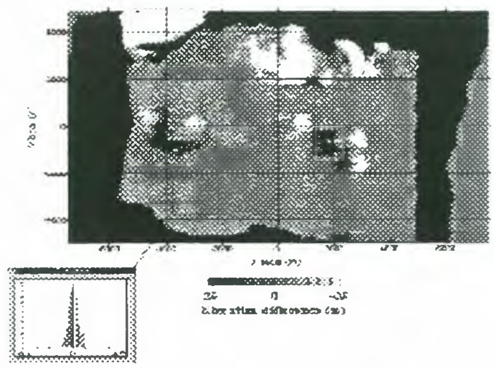

Fig.3b : error map

Fig. 3 : Results obtained with baseline = 138 m

In conclusion, a validation tool based on a dedicated image simulator is available. We use it to evaluate and improve our own interferometric processing chain, but we can propose it to other research groups who wish to evaluate the performances of their algorithms or test them in very special conditions, for instance for sensors that have not been launched yet. In a very near future, we are planning to use the same approach to validate slope mapping algorithms in the frame of the ERS tandem mission.

Reference

Polidori L. & Armand P. 1995:
On the use of SAR image simulation for the validation of topographic mapping techniques. *EARSEL, Advances in Remote Sensing*, **Vol 4, No 2**, pp. 40-48.

Multiresolution Analysis of DEMs: Error and Artifact Characterization

Dragos Luca Image Science Division, Communication Technology Laboratory, ETHZ, Gloriastr. 35, CH-8092 Zürich, Switzerland
dluca@vision.ee.ethz.ch
http://www.vision.ee.ethz.ch/

Mihai Datcu Deutsche Forschungsanstalt für Luft und Raumfahrt e.V., Deutsches Fernerkundungsdatenzentrum, D-82234 Wessling, Germany
datcu@dfd.dlr.de
http://www.dfd.dlr.de/

Klaus Seidel Image Science Division, Communication Technology Laboratory, ETHZ, Gloriastr. 35, CH-8092 Zuerich, Switzerland
seidel@vision.ee.ethz.ch
http://www.vision.ee.ethz.ch/

Abstract

Digital elevation data is often affected by errors due to excessive interpolation or to interferometric artifacts. The local analysis of the DEM roughness allows both the detection of these errors and the segmentation of the elevation data for a better understanding of the existing geological structures. This analysis can be performed by means of fractal dimension estimators. We compare several fractal estimation methods and show that those based on the multiresolution (wavelet) data analysis yield the best results from the point of view of their segmentation capabilities. This is a natural conclusion considering that fractals and wavelets rely on many common concepts. As an example we show an application in which SAR intereferometric artifacts are revealed and the elevation data is separated in different roughness classes using fractal dimension measurements and an unsupervised clustering algorithm.

Keywords: DEM, fractals, wavelets, multiresolution, artifacts, segmentation

1 Introduction

Digital Elevation Models (DEMs) have become an important tool in many remote sensing applications like e.g. SAR simulators, orthorectification of satellite and airborne images, classification of ground cover types, Geographic Information Systems, etc. Still in most of the cases, the resolution of the DEMs derived from digitized topographic maps is unsufficient for the requirements of the corresponding applications. SAR interferometry allows the achievement of much better resolutions, however this technique is not yet available on a large scale and the resulting surface is affected by typical artifacts. The detection of the artifacts is an important task, especially in remote areas where no other digital elevation data is available for comparison.

Relying on the observation that relief conserves the same statistical characteristics over a wide range of scales, some DEM characterization techniques have been developed that perform a multiresolution analysis of the elevation data. These techniques use fractal models to measure the local roughness of the DEM and extract derived information. In this way, better interpolation methods for higher resolution elevation data sets have been developed (Yokoya and Yamamoto 1989, Polidori *et. al.* 1991, Franceschetti *et. al.* 1994) and a better understanding of the geological and geomorphic processes has been achieved (Huang and Turcotte 1990,Clarke and Schweizer 1991,Clarke 1988).

This work investigates the use of multiresolution techniques for the characterization of DEM roughness and points out a method for the detection of errors and artifacts in intereferometric elevation models. The roughness of a DEM is estimated locally by measuring the fractal dimension of the underlying model. Two fractal dimension estimators are compared: the power spectrum estimator and the wavelet-based estimator. The power spectrum method was selected as a reference since it has often been designated to be the algorithm which achieves the best performance (Stewart *et. al.* 1993, Schepers *et. al.* 1992). Our approach concentrates on the wavelet-based method and is motivated by the fact that wavelets and fractals are closely related by the concept of scale and share many common properties (Akujuobi and Baraniecki 1994). We compare the two methods both on synthetic and on real elevation data. The result of this comparison shows that the wavelet-based estimator achieves a better reliability of the measurements in terms of their standard deviation and is better suited for the segmentation of fractal images.

The paper is organized as follows. Section 2 gives an overwiev of the fractal and wavelet theory emphasizing the common concept of scale. Section 3 presents the results of a comparison between the spectral and the wavelet-based fractal estimators based on synthetic images. This comparison is performed in terms of image segmentation capabilities, i.e. the algorithms are applied to image windows of small size and the obtained set of measurements is analysed statistically. In the last section we discuss some examples in which the fractal analysis of DEMs reveals artifacts in the computation of elevation data and allows the separation of different roughness classes.

2 Elements of Fractal and Wavelet Theory

Fractals are mathematical objects that show the same structure when examined at all possible scales (Mandelbrot 1982). Although more formal definitions can be given, this qualitative characterization expresses the very essence of the fractal phenomenon and at the same time represents the basis for all fractal analysis algorithms: the algorithms check for fractal behaviour simply by examining the object at several scales (resolutions). The basic parameter characterizing a fractal object is its dimension: while non-fractal objects have dimensions given by integers (1 for curves, 2 for surfaces, etc.), fractals will have fractional dimensions since they represent transition structures between curves and surfaces, surfaces and solid bodies, etc.

The statistics of roughness measurements has been shown to agree - in a limited resolution range - with that of specific fractal models and several attempts have been made to characterize DEMs by means of the fractal theory. The most popular model used in this respect is the *fractional Brownian motion (fBm)* model (Voss 1988). This model describes a signal $B(t)$ characterized by the fact that its increments between two moments of time $t1$ and $t2$ have a variance proportional to a power $2H$ of the time lag $|t2-t1|$. The parameter H is called "Hurst exponent" ($0<H<1$) and is related to the dimension D of the corresponding fractal by (Voss 1988) $D = n + 1 - H$, n being the topological dimension of the space in which the fractal object is represented (n=1 for *fBm* time-functions, n=2 for *fBm* surfaces, etc.). D will typically measure the "roughness" of the signal and most fractal analysis algorithms concentrate on an accurate estimation of D. Note that *fBm* signals are nonstationary; this makes their analysis both from the theoretic and from the practical point of view quite difficult. Several methods have been developed that try to cope with these difficulties.

A classical algorithm for the estimation of D is based on the computation of the time (space) averaged power spectrum of the signal. This power spectrum is represented in a log-log plot vs. frequency. It can be shown (Voss 1988, Saupe 1988) that if the signal is a *fBm* the points of the plot will align along a straight line. The slope of this line is directly related to the dimension D of the fractal and is usually estimated via a regression technique. This method of fractal dimension estimation is called the *power spectrum method* and has been shown to yield very accurate estimation values (Stewart *et. al.* 1993).

But other methods exist as well and deserve increasing attention since they present some very useful features for different applications. Our research focuses on an alternative way for the estimation of D based on the wavelet decomposition of *fBm* signals. Just like fractals, wavelets heavily rely on the scale concept, i.e. on the analysis of the data at several resolutions (Mallat 1989, Wornell 1993). Given a signal $x(t)$, a sequence $A[m]x(t)$ of approximations to $x(t)$ is constructed, each $A[m]x(t)$ representing the signal approximation at a given resolution (scale) m. If we define $D[m]x(t)$ the detail signal at resolution m to be the difference between the two succesive approximations $A[m+1]x(t)$ and $A[m]x(t)$, then this detail signal can be written as an orthogonal expansion of the signal $x(t)$ using some special basis functions that are called "wavelets". The wavelet transform represents thus a way of quantifying signal changes from one scale to another. The wavelets themselves are obtained using the concept of scale: they are all dilations and translations of a single function called "mother wavelet".

The similar fundamental concepts of the fractal and wavelet theory have stimulated several researchers to investigate this relation in more detail. The main result in this field is due to G. W. Wornell who showed that the wavelet transform applied to a *fBm* signal whitens the signal, i.e. the transformed-domain samples at a given resolution *m* (the detail signal samples) become stationary and weakly correlated and both the theoretic and the numeric analysis are much easier to perform. The direct estimation of the fractal dimension relies in this case on the the computation of the detail signal variances at different scales. A maximum likelihood estimation algorithm (Wornell and Oppenheim 1992) can be used to estimate from several variance measurements the fractal dimension *D*.

3 Comparisons of Fractal Models

In order to compare the performance of the methods presented in the previous section, a set of 256-by-256 spatially isotropic *fBm* surfaces ranging from dimension 2.0 to dimension 3.0 was generated. In each image, the dimension was estimated locally in a sliding window of size 32-by-32 pixels with the spectral and the wavelet-based algorithm (using Daubechies wavelets with 4 filter coefficients).

The comparison of the different estimation algorithms is performed mainly by means of two parameters: the "mean of measurements" and the "uniformity of measurements". These parameters are plotted vs. the real dimension of the fractal surface in figure 1. The mean of the measurements represents the mean value of the fractal dimension estimations for all the positions of the sliding window. For a uniform surface of fractal dimension *D*, this mean should yield exactly the value *D*, i.e. the ideal shape of the mean plot is that of the diagonal line. The uniformity of measurements is defined as the standard deviation of the measurements about the measured mean. The uniformity plot should thus be flat and of minimal value to characterize a reliable estimation method.

The results of this analysis show that although the spectral method has a better performance in terms of measurement accuracy, the wavelet-based method has a substantially better uniformity. A good uniformity is in our opinion more important for image segmentation than the exact estimation of the numeric values for the fractal dimension, provided that the relation mean vs. *D* remains monotonic. This is the case for the wavelet-based method, where the mean vs. *D* plot can be used as a LUT for the correction of estimated values.

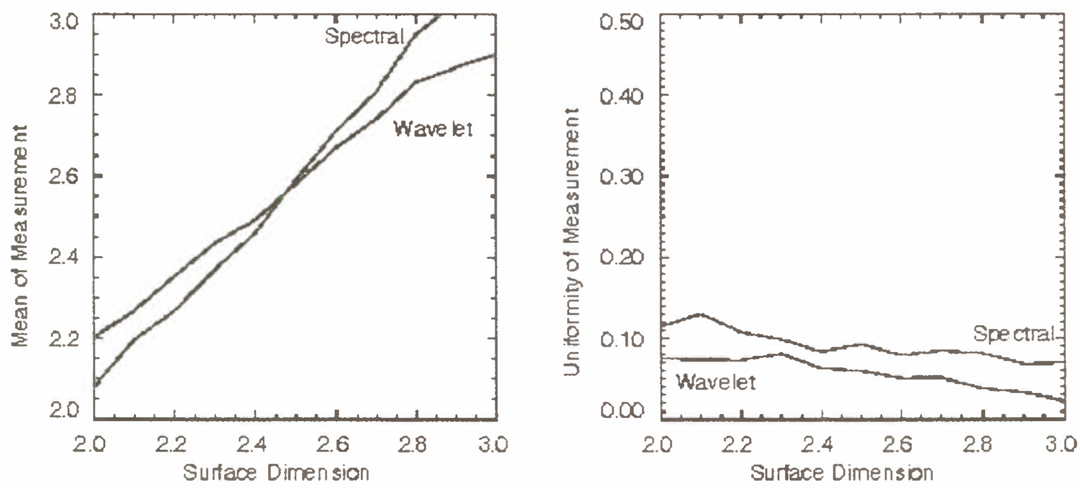

Figure 1: Mean and uniformity of fractal dimension measurements for synthetic surfaces. Window size is 32 x 32 = 1024 pixels

These results can be visualized by means of an example. Figure 2a shows a synthetic DEM (shown as a shaded relief) consisting of a central square of fractal dimension *D*=2.8 surrounded by a rectangular border of fractal dimension *D*=2.2. Figures 2b and c show the estimation results for *D* (i.e. for the roughness of the relief) using the spectral and the wavelet-based algorithms respectively in a sliding window of size 32 x 32 pixels. The estimated numeric values are scaled linearly from [2.0, 3.0] to [0, 255] and are presented as gray scale images. White corresponds to a high fractal dimension ("rough") and black to a low fractal dimension ("smooth"). To avoid problems generated by discontinuities on the borders of the image, we did not compute the fractal dimension in a swath of 16 pixels on each image side. This swath is shown here in black.

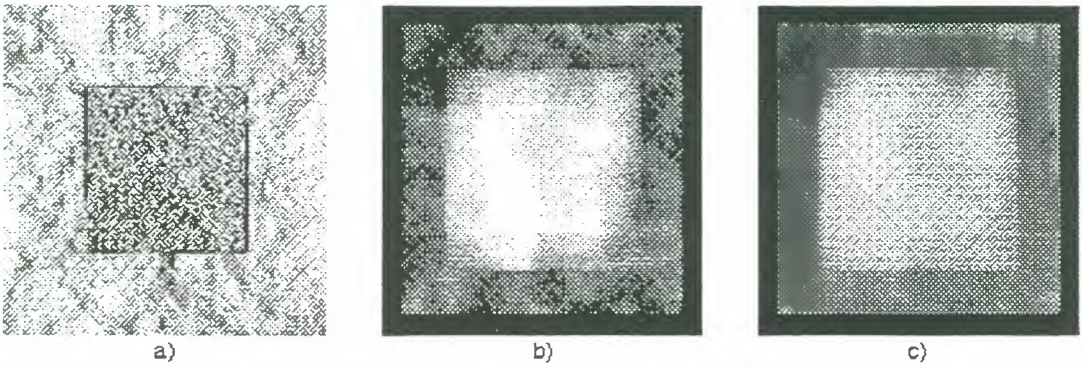

Figure 2: Segmentation example for synthetic DEM consisting of a central square of fractal dimension D=2.8 surrounded by a border of fractal dimension D=2.2. The dimension is estimated in a sliding window of size 32 x 32 pixels. a) Original image, b) Fractal dimension estimated with the spectral algorithm, c) Fractal dimension estimated with the wavelet-based algorithm

Figure 2 confirms the conclusions of the mean and uniformity plots. Due to the better uniformity of the wavelet-based estimation algorithm the fractal dimension map in figure 2b appears less noisy than the one computed with the spectral method (figure 2c). This leads to a better visual appearance and to an easier thresholding for segmentation.

4 Application to Digital Elevation Models

The algorithms described in the previous section have been tested on two elevation data sets that present different characteristics and allow us to consider different aspects of the fractal estimation process.

The first data set consists of three DEMs of the region of Davos, Switzerland at resolutions of 50m, 25m and 10m respectively (figure 3a). The DEMs were obtained by digitization of elevation data from maps of different resolution. For each of the DEMs the fractal dimension was computed in a sliding window of a size selected roughly proportional to the dimensions of the DEM (16 x 16 pixels for the 50m DEM, 32 x 32 pixels for the 25m DEM and 64 x 64 pixels for the 10m DEM).

Figure 3b shows the histograms of the estimated values for D obtained using the wavelet-based method. First note that all the histograms show a single peak. This fact means either that the whole considered area has a single fractal dimension or that it consists of several areas with very close fractal dimensions which cannot be differentiated by this method. Note also that the peak is at about the same position for all three histograms, i.e. the structure of the terrain is invariant to scale. Since the data of the three DEMs was obtained by independent processes and not by interpolation of one set to another, this example proves that the terrain shows indeed a fractal structure. The dimension of this fractal lies in the range of D=2.1 to D=2.2. Similar fractal dimension values have been reported for DEMs of other areas as well (Polidori *et. al.* 1991, Clarke and Schweizer 1991).

Figure 3c shows the histogram of the estimated values for D using the spectral method. The variance of the measurements is higher and the estimation of D is less reliable. This result confirms the simulations described in the previous section.

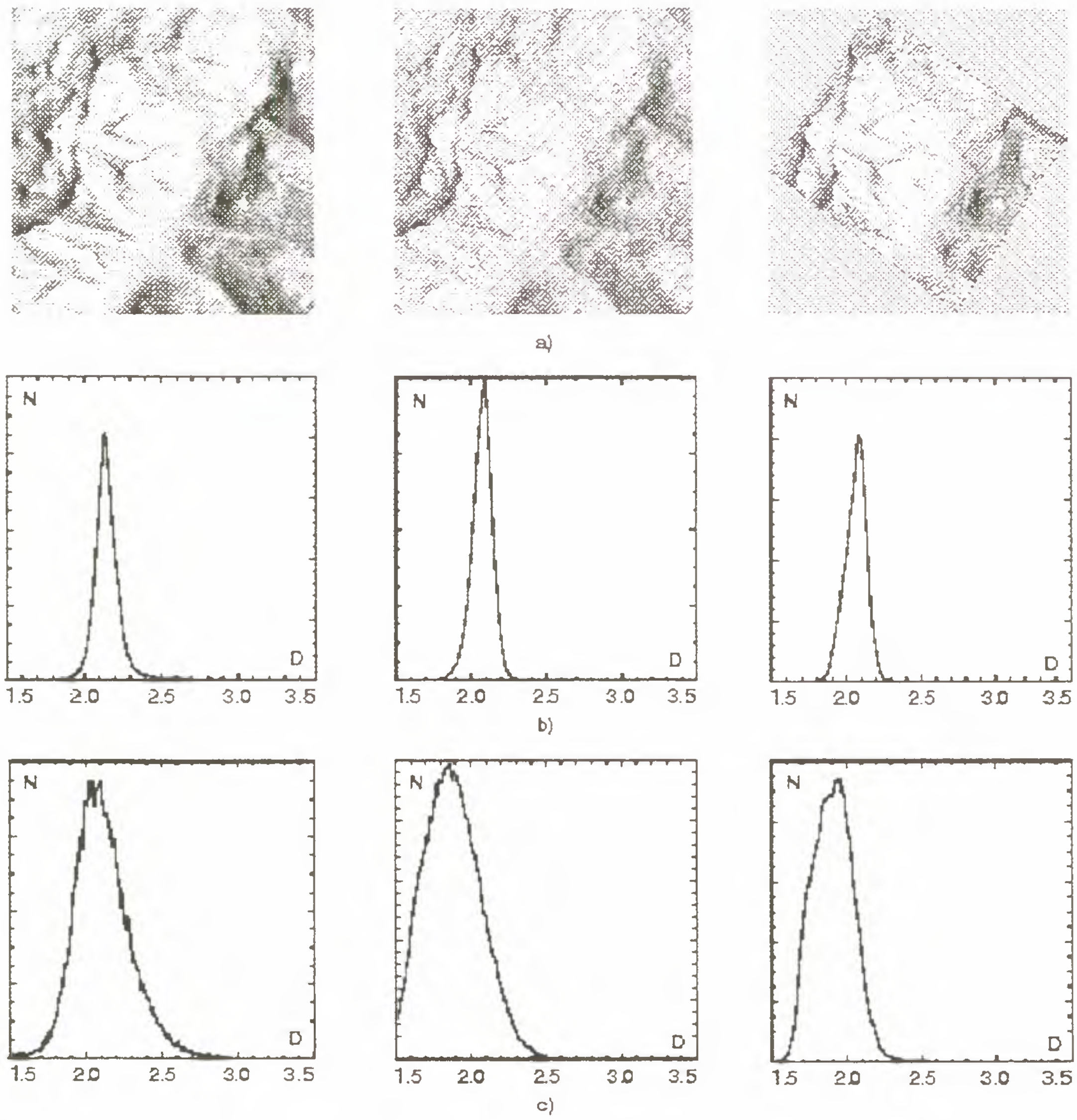

Figure 3: Fractal dimension measurements for three DEMs of different spatial resolution of the Davos area. a) DEMs presented as a shaded relief: left to right 50m, 25m, 10m; b) Histograms of fractal dimension measurements for the DEMs in figure a) using the wavelet-based method? c) Histograms of fractal dimension measurements for the DEMs in figure a) using the spectral method

Our second example shows the possibility to use the estimation of fractal dimensions to detect artifacts in elevation data. The data consists of two DEMs of an area along the river Rhine in Germany. The first DEM (figure 4a) was obtained from digitized cartographic information and has a resolution of 25m, while the second one (figure 4b) was obtained by SAR interferometry and has a resolution of about 20m. Note also that the topographic DEM is represented in geographical coordinates and the interferometric DEM is shown in range/azimuth coordinates which are slightly rotated with respect to the geographical ones. In spite of these differences the data was not preprocessed (e.g. reinterpolated and rotated) since that would have affected the fractal structure of the images.

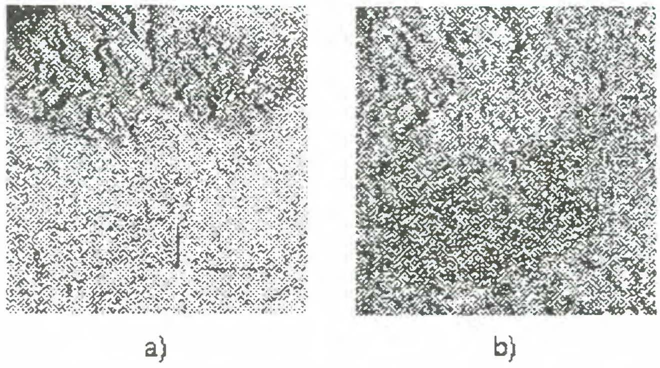

Figure 4: a) Topographic DEM of an area along the river Rhine; b) Interferometric DEM of approximately the same area

The topographic and the interferometric DEM are analysed by computing the fractal dimension in a sliding window of size 32 x 32 pixels. The histograms of the values for D obtained with the wavelet method are shown in figure 5a and b respectively. While for the topographic DEM, *D* lies in the range 2.0 ... 2.4 (the "usual" values for the fractal dimension of terrain structures), the interferometric data has much higher fractal dimensions, ranging from 2.4 to 2.8. These values indicate that the interferometric method induces some artifacts leading to an unusually high roughness of the elevation data. The estimation of the fractal dimensions provides thus a good method to detect the artifacts in an automatic way.

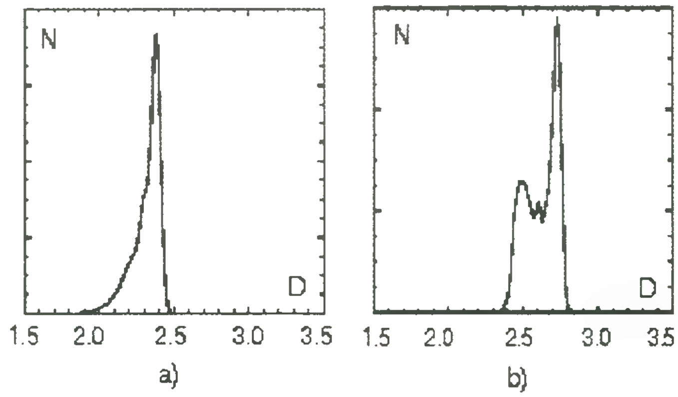

Figure 5: a) Histogram of fractal dimension measurements for the topographic DEM; b) Histogram of fractal dimension measurements for the interferometric DEM

Additionally, the histograms of *D* allow the segmentation of the DEMs according to their roughness. An unsupervised classification algorithm developed by Narendra and Goldberg (Narendra and Goldberg 1977) looks first for the dominant *modi* of the image histogram, then clusters the pixels around these *modi*, setting thresholds in the valleys between them. The algorithm was applied for the histograms in figure 5 and resulted in the classification map of figure 6. As expected, for both the topographic and the interferometric DEM, the clustering algorithms detected 2 classes of roughness: the first one corresponds to the mountain area, the second one to the plain area. These classes are presented here in pseudocolors to allow for a better visual separation.

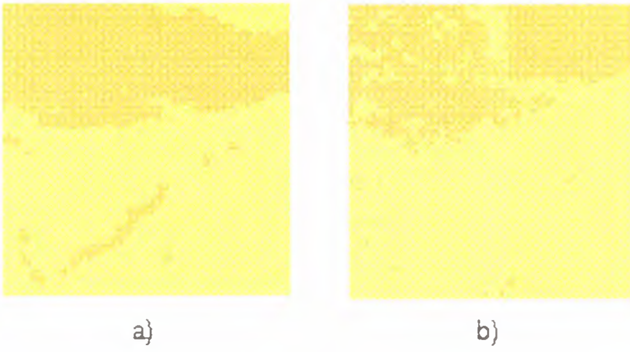

Figure 6: a) Unsupervised classification of the topographic DEM according to its roughness, b) Unsupervised classification of the interferometric DEM according to its roughness

As a final experiment, another roughness measure, the standard deviation of the elevation values in an image window is computed for the topographic and the interferometric DEMs and compared to the fractal dimension. The result of this comparison is shown as a scatterogram of the values of the standard deviation vs. D (figure 7). Little correlation can be seen between the two roughness measures, especially in the case of the interferometric DEM where the points are scattered all over the plane. Obviously, the fractal dimension characterizes the roughness of the relief in a different way than the standard deviation of the elevation values. While the standard variation is a parameter that assumes a Gaussian distribution, D relies on a fractional Brownian motion model which is non-Gaussian. The appropriateness of one of these measures is related to the assumptions that can be made on the statistics of the image. Usually these statistics are not checked and an *a priori* assumption is made, based on some physical and/or empiric considerations. We feel that in this context a more rigorous approach is necessary, implying some better mathematical modeling. This approach is the object of further study and research to be reported soon.

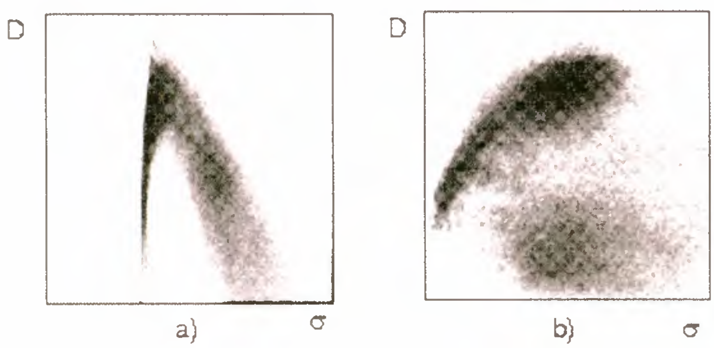

Figure 7: Scatterogram of the standard deviation of elevation data vs. fractal dimension for the topographic DEM b) Scatterogram of the standard deviation of elevation data vs. fractal dimension for the interferometric DEM

5 Conclusions

The present paper presents an automatic method for the detection of errors and artifacts in the generation of interferometric DEMs. The detection is based on the estimation of terrain roughness and uses the observation that zones where interferometric artifacts appear have a higher roughness than "normal" terrain.

The roughness is measured assuming a fractal model for the elevation data and is expressed by the fractal dimension, estimated locally in a small sized window. Several estimation methods are compared from the point of view of their segmentation capabilities. Based on important conceptual similarities between fractals and wavelets, we make the hypothesis that wavelets are a very appropriate analysis tools for fractal images. This assumption is confirmed by experiments both on simulated and on real elevation data: wavelet-based fractal dimension estimators show the highest reliability in terms of measurement variances and are thus better suited for DEM characterization than other methods.

Acknowledgements

We would like to acknowledge the German Remote Sensing Data Center (DFD) at DLR, Wessling, Germany for providing us the DEMs of the Rhine valley and the Remote Sensing Laboratories of the University of Zürich, Switzerland for providing us the 10m resolution DEM of the Davos area. Special thanks also to Dr. Marcus Schwäbisch from DLR for the derivation of the interferometric SAR DEM.

References

Akujuobi, C. M. and Baraniecki, A. Z. (1994).
A Comparative analysis of wavelets and fractals. In Leondes, C. T., editor, *Digital Image Processing: Techniques and Applications*, volume 67 of *Control and dynamic systems*, pages 143-197. Academic Press, Inc.

Clarke, K. C. (1988).
Scale-based simulation of topographic relief. *The American Cartographer*, **15**(2):173-181.

Clarke, K. C. and Schweizer, D. M. (1991).
Measuring the fractal dimension of natural surfaces using a robust fractal estimator. *Cartography and Geographic Information Systems*, **18**(1):37-47.

Franceschetti, G., Mihliaccio, M. and Riccio, D. (1994).
SAR simulation of natural landscapes. In stein, T. I., editor, *Surface and Atmospheric Remote Sensing: Technologies, Data Analysis and Interpretation, IGARSS'94, Pasadena*, pages 1181-1183.

Huang, J. and Turcotte, D. L. (1990).
Fractal image analysis: application to the topography of Oregon and synthetic images. *J. Opt. Soc. Am. A*, **7**(6):1124-1130.

Mallat, S. G. (1989).
A theory for multiresolution signal decomposition: The wavelet representation. *IEEE Trans. on PAMI*, **11**(7):674-693.

Mandelbrot, B. B. (1982).
The Fractal Geometry of Nature. Freeman, CA.

Narendra, P. M. and Goldberg, M. (1977).
A non-parametric clustering scheme for Landsat. *Pattern Recognition*, **9**:207-215.

Polidori, L., Chorowicz, J. and Guillande, R. (1991).
Description of terrain as a fractal surface and application to digital elevation model quality assessment. *Photogrammetric Engineering and Remote Sensing*, **57**(10):1329-1332.

Saupe, D. (1988).
Algorithms for random fractals. In H.-O. Peitgen and D. Saupe, editors, *The Science of Fractal Images*, chapter 2, pages 71-120. Springer-Verlag.

Schepers, H. E., van Beek, J. H. G. M. and Bassingtwaighte, J. B. (1992).
Four methods to estimate the fractal dimension from self-affine signals. *IEEE Engineering in Medicine and Biology*, pages 57-71.

Stewart, C. V., Moghaddam, B., Hintz, K. J. and Novak, L. M. (1993).
Fractional Brownian motion models for synthetic aperture radar imagery scene segmentation. *Proceedings of the IEEE*, **81**(10):1511-1521.

Voss, R. F. (1988).
Fractals in nature: From characterization to simulation. In H.-O. Peitgen and D. Saupe, editors, *The Science of Fractal Images*, chapter 1, pages 21-70. Springer-Verlag.

Wornell, G. W. (1993).
Wavelet-based representations for the $1/f$ family of fractal processes. *Proceedings of the IEEE*, **81**(10):1428-1450.

Wornell, G. W. and Oppenheim, A. V. (1992).
Estimation of fractal signals from noisy measurements using wavelets. *IEEE Trans. on Signal Processing*, **40**(3):611-623.

Yokoya, N. and Yamamoto, K. (1989).
Fractal-based analysis and interpolation of 3D natural surface shapes and their application to terrain modeling. *Computer Vision, Graphics and Image Processing*, **46**:284-302.

GEMSAR: DLR's project for the generation of global digital elevation models

Wolfgang Noack, Richard Bamler, Michael Eineder, Achim Roth, Hartmut Runge

Deutsche Forschungsanstalt fuer Luft- und Raumfahrt Oberpfaffenhofen, Deutsches Fernerkundungsdatenzentrum, D-82234 Wessling, Phone: +49-8153-28-1390, Fax: +49-28-1446
noack@dfd.dlr.de
http://dfd.dlr.de

Abstract

Exact knowledge of terrain height is an indespensable prerequisite of remote sensing applications e.g. for the interpretation of SAR data from mountaineous and hilly terrain. The usage of currently available digital elevation models (DEMs) is handicapped by a number of reasons: they are not global, not homogeneous, the resolution is not adequate and they are expensive.

The conventional approach for generating DEM's is to use stereo cameras or digitized maps. For the past ten years techniques applying interferometric SARs (INSAR) have been developed, e.g. the ERS tandem data are a new and operational source for the generation of DEM's.

DLR has been receiving ERS tandem data at its Neustrelitz receiving station. However, the most important source of interferometric SAR data in the future will be the SRTM (Shuttle Radar Topography Mission) carrying a modified SIR-C? X-SAR instrument used as a single pass interferometer: the SIR-C C-band SCANSAR will deliver a global and homogeneous DEM of all landmasses between 60 deg. north and 60 deg. south, and in parallel X-SAR will deliver regional DEMs of high resolution. SRTM will be launched in May 2000 on a two-week shuttle mission.

Therefore, within the GEMSAR (Global Elevation Models from SAR) project algorithms will be developed for the generation of interferograms from ERS tandem, X-SAR and SIR-C data, including automatic phase unwrapping and mosaicking of continent wide DEMs. The systems to be built up comprise SAR processors, interferogram generators and DEM generators.

The DEMs will be archived in a growing DEM data base and will be made available through a user interface which allows for the specification of arbitrarily shaped areas, resolutions and cartographic representations. This data base will be capable of storing DEMs from different sensors, including optical sensors.

Keywords: SAR, INSAR, DEM, GEMSAR, SRTM, X-SAR

The Digital Elevation Model market: current situation and perspectives

L.-F. Guerre, A. Hirschfeld, L. Demargne — Spot Image
Louis-Francois.Guerre@spotimage.fr

C. Foucher — Institut d'Economie Industrielle de Toulouse

Abstract

The description of the current market for Digital Elevation Models as well as its potential development has been studied by Spot Image at the request of ESA. Forecasting a boost in Digital Elevation Model offer induced by the ERS tandem mission, an assessment of the market for DEM is particularly relevant. Although, DEMs (from airborne, spaceborne, digitized maps) have been produced and used for many years now, no comprehensive studies of this market are available. Indeed, it is very surprising to find that few assessments of this market have been made.

This study aimed to describe the offer and the demand for DEMs. This involved: identifying the structure of the market, the different uses and applications, as well as the suitability of the current offer to the user needs. The market for DEMs was analysed both qualitatively and quantitatively. The information was gathered with questionnaires, direct interviews, and from existing surveys.

There is a real current market for DEMs of various sources such as digitised topographic maps, airborne or spaceborne stereoscopic imagery, with accuracies ranging from 1 m to 100m. There is already an existing archive of a few tens of millions of km2 and an annual production of several millions km2. There are a few number of large producers in the world and many small producers. However, the offer of DEM is not very visible and the market not yet well structured or organised. The price depends on the type of DEM and the service associated and can vary from 0.1 to 150 US $ per km2. End users requiring a product that is adequate to their needs are ready to pay several $ per km2 for spaceborne DEMs.

There is an important latent commercial demand which can not be served by the current offer of DEMs. This demand is stronger for high-resolution DEMs (height accuracy better than 5m), but the market for DEMs with lower accuracy is still significant. This later market can be addressed by ERS SAR interferometry. Among the main commercial applications of DEMs are: telecommunications, defence, thematic mapping and GIS.

The perspectives of the potential market for DEMs are important thanks to the potential of market development of the most promising applications using DEMs. However, the market can develop only with a strong increase in the worldwide availability of the DEMs for the users, and a development of the distribution and marketing of DEMs products.

Proceedings of the 'Fringe 96' Workshop on ERS SAR Interferometry, *Zurich, 30 September - 2 October 1996* (ESA SP-406, March 1997)

Assessment of interferometric SAR DEM for UK National mapping

Jan-Peter Muller

Dept. of Photogrammetry and Surveying, University College London,
Gower Street, London WC1E 6BT
United Kingdom
jpmuller@ps.ucl.ac.uk
http://www.ps.ucl.ac.uk

Athula Mandanayake

Dept. of Photogrammetry and Surveying, University College London,
Gower Street, London WC1E 6BT
United Kingdom
athula@ps.ucl.ac.uk
http://www.ps.ucl.ac.uk

K. Murray

Ordnance Survey
Romsey Road
Southampton SO16 4GU
United Kingdom
kmurray@ordsvy.gov.uk

D Holland

Ordnance Survey
Romsey Road
Southampton SO16 4GU
United Kingdom
dholland@ordsvy.gov.uk

Abstract

High resolution DEMs at 10m and 30m have been created from SAR interferometric tandem pairs over 3 areas in the UK to assess the potential of this technology for UK National Mapping as part of an Applications Demonstration Programme (ADP) funded by the Ordnance Survey R (OS) and the BNSC. The UCL 3D Image Maker (IfSAR) for DEM generation has been employed (described by Muller, Mandanayake, Upton) and OS National Mapping products have been used to provide a quantitative assessment of accuracy as well as for phase flattening.
The 3 areas include the city of St Albans, Herts and the M25/M1 motorway junctions; Mablethorpe, Lincolnshire and an area within the Lake District. These areas have been selected for studying the effects of urban buildings and topography (St Albans); for assessment of the potential of IfSAR-DEMs for coastal flat regions (Mablethorpe); for studying the effects of topography (Lake District) and for studying the potential of IfSAR-DEMs to measure topography over narrow cuttings associated with new road developments. System effects studied include the effect of winter vs summer; day vs night; atmospheric effects as well as baseline (Bperp) separation. Results of the quantitative assessment for St Albans are presented here.

Keywords: SAR Interferometry, DEM, UK National mapping

Introduction

The UK is one, if not the most, well mapped countries in the world with primary digital mapping coverage from maps of scale 1:1250 up to 1:10 000 including a National Height dataset based on photogrammetric contour surveys of the underlying terrain surface with 5m and 10m contour interval and a derived gridpoint interpolated 10m DEM both known as the Land-Form PROFILE (TM) data-set. PROFILE (TM) contours are at 10m intervals in mountainous areas and 5m in all other areas.

Murray et al., 1996 recently described a number of studies which are being conducted as part of a BNSC Application Demonstrator Programme under OS and BNSC sponsorship at UCL and for land use only at the University of Southampton. The LANDMASS project is evaluating remote sensing data sources for applications in topographic mapping, Digital Elevation Models, Building and 3D Urban modelling and land use.

Specifically for DEMs, the ERS tandem IfSAR data is being evaluated as part of the following investigations:

automatic detection of changes in the terrain surface
remodelling the surface following major engineering works (e.g. highways)
improving the surface elevation resolution where 5m and 10m contours are inappropriate, especially flat regions which may be sensitive to flooding

Existing topographic data (50m OS Land-Form PANORAMA (TM)) is used in order to phase flatten the ERS interferograms and so concentrate on evaluating where and why there are differences between the IfSAR-DEM and existing OS DEM products derived from the digitised 1:10 000 map contours.

In order to extend this study to a general study of DEM densification, a 100m degraded version of the 50m DEM has also been used for phase flattening in an attempt to evaluate what the effect of using medium scale resolution grids such as those used by the US National Intelligence Mapping Agency (NIMA, part of which was formerly known as the Defence Mapping Agency) for DTED DMA, 1990 could have on automating higher resolution DEM production using ERS tandem interferometry if and when these data may become available globally (see Muller, this workshop).

SAR interferometry is now gaining increasing acceptance as a spaceborne technique for rapid and potentially accurate determination of topographic information. As the use of such SAR sensors increases and systems to extract If SAR-DEMs become more automated and reliable, it is likely that their use will become more widespread.

Therefore, it is important to evaluate such systems and understand their limitations and strengths in order to get the best final DEM product quality. In this paper, we make a quantitative quality assessment of the accuracy which can be achieved by terrain densification using IfSAR pairs from the ERS tandem mission. Qualitative remarks will also be made concerning the potential use of ERS SAR from detecting narrow cutting and it 's use for updating existing low resolution DEM to produce high resolution DEMs.

Methods

Muller, Mandanayake, Upton (this workshop) describe the UCL- 3DIM (IfSAR) processing system developed at UCL. IfSAR-DEMs can be produced using either the WGS84 ellipsoid, a coarse DEM or a fine DEM resampled all of which can be resampled to the spacing required for the final output IfSAR-DEM. Currently, nearest neighbour interpolation is used for terrain densification which can cause small artifacts.

All phase unwrapping (loc.cit.) and phase-to-height conversion operations are done in ground range which is considerably different to previous approaches. Precision state vectors from the German D-PAF have been used to provide accurate planimetric geocoding whose accuracy from our experiments appears to be well within the final 30m DEM spacing.

The final IfSAR-DEM produced at either 10m or 30m grid-spacing is compared statistically at each and every elevation gridpoint with the OS 10m grid using the techniques described in Day and Muller, 1989 . A example of the phase coherence is shown and statistics are given.

Data set description

The SAR data used in this study are all night-time passes of two ERS1/2 tandem and two ERS2 35-day repeat passes over St Albans. The location of the frames are shown in Figure 1 over a coarser DEM and basic parameters given for each data-set are shown in Table 1. This test area covers a part of the M25 motorway and large parts of the built-up area in St Albans and North London.

Accurate determination of the SAR acquisition geometry is required for several of the interferometric processing steps of the UCL-3DIM (IfSAR) such as phase flattening using coarser DEM and geocoding. Precision state orbital vectors from the D-PAF were used for geocoding and phase flattening.

Phase flattening for each image pair was done using three different resolution coarser DEMs (based on the supplied 50m OS DEM) to produce higher resolution IfSAR DEMs. Resolution of the coarser DEMs used are:

50m OS dem resampled to 1/10000 deg (~10m) to produce IfSAR DEM at 1/10 000 deg
50m OS dem resampled to 1 arc-second (~30m) to produce IfSAR DEM at 1 second
50m OS degraded resampled to 3 arc-seconds (~100m)

Satellite	Orbit of	Frame	Date	Latitude extent/deg	Longitude extent/deg	Bperp/m	Day/Night	MODE
ERS1	23006	1035	08/12/95	51.30 - 52.38	-1.56 - 0.16	217	Night	Tandem
ERS2	3333	1035	09/12/95	51.30 - 52.38	-1.56 - 0.16	217	Night	Tandem
ERS1	22505	1035	03/11/95	51.30 - 52.38	-1.56 - 0.16	-141	Night	Tandem
ERS2	2832	1035	04/11/95	51.30 - 52.38	-1.56 - 0.16	-141	Night	Tandem
ERS2	2832	1035	04/11/95	51.30 - 52.38	-1.56 - 0.16	206	Night	35 day
ERS2	3333	1035	09/12/95	51.30 - 52.38	-1.56 - 0.16	206	Night	35 day

*Table 1. ERS Image details**Figure 2. St Albans, SAR Geocoded Amplitude images*
Four tiled image, DEM used to geocode is OS 50m at 1/10000 deg grid Top Left: ERS1 Orbit:22505 Date: 03/11/95 time: NightTop Right: ERS1 Orbit:23006 Date: 08/11/95 time: NightBottom Left: ERS2 Orbit:2832 Date: 04/11/95 time: NightBottom Right: ERS2 Orbit:3333 Date: 09/11/95 time: Night

Figure 3(a-d). St Albans, Input DEMs for phase flattening and DEM comparison (a) 10m OS DEM (used for comparison) (b) 50m OS DEM 10m gird(used for flattening)(c) 50m OS DEM 30m gird(used for flattening)(d) 100m OS DEM 30m gird (used for flattening)

Results

Figure 2 shows 4 SAR amplitude images for 2 of the ERS tandem pairs. Notice the distinct dark linear feature associated with the M25 motorway in this figure which goes from West to East and the bright urban ribbon development along the M1 from South to North.

The ground truth OS DEMs are shown in Figure 3. The reduction in resolution between the 10m Land-Form PROFILE and 50m Land- Form PANORAMA products is easily visible as are the artifacts associated with grid-point interpolation of contours.

Figure 4a shows the flattened interferometric phase, Figure 4b the phase coherence and Figure 4c the unwrapped phase for the tandem image pair (orbits 23006 and 3333) using the UCL-3DIM (IfSAR) system. Figure 4c also includes the digital map vector data taken from the 1:1250 map scale series which clearly shows the motorway features as well as the built-up areas. The 50m DEM interpolated to 10m was used to flatten the interferogram. Figures 4a-4c all clearly shows the M25 Motorway Junction with the M1 as bright features as well as the underpass. Neither of these features in visible in any of the OS DEMs (see Figure 3). Pixels that cannot be unwrapped or have too low a phase coherence are shown in black (figure 4b) and are not used in the unwrapped phase to DEM transformation. They are filled by the input 10m (derived from 50m interpolated) DEM although the 10m DEM could have been used instead.

Figure 5a shows the 10m IfSAR DEM that was produced from the ground-range unflattened interferogram. It should be closely compared with the OS 10m DEM (Figure 3a). The overall morphological structure is maintained but there are a great deal more details present aside from the aforementioned roads. Some of these details may be the result of phase noise.

Three IfSAR DEM were produced for this tandem image pair and compared against the 10m OS DEM and their statistics are shown in tables 2-3 with a histogram plot comparison of elevations in Graph 1.

Table 4 shows the elevation difference statistics for all 9 DEMs created from the 3 pairs. Notice how the error sharply goes up for the second pair (23006/3333) when degraded 100m DEMs are used for phase flattening and the much poorer accuracy and coverage of the 35-day repeat ERS-2 derived IfSAR-DEM (2832/3333). However, even for the 35-day repeat the overall elevation rms is around 12m which is comparable to SPOT (Muller, Mandanayake, Upton) for a vegetated area.

Figure 5b shows an example DEM elevation difference image between the IfSAR-DEM and the OS 10m DEMs. Note the apparent tilt across the data-set. This may be due to residual errors in the orbital state vectors. It may be possible to reduce these systematic errors in future through the use of Ground Control Points. Differences in elevation may be due to buildings, deciduous tree-trunks and coniferous tree canopies (the DEMs were produced from late Autumn data, see Table 1).

DEM	Number of Points	Min.	Mean	Max.	RMS	SD
OS 10m	260000	57.890	85.258	136.580	86.516	14.697
OS 50m in 10m grid	260000	58.000	85.158	134.000	86.429	14.768
OS 50m in 30m grid	29078	58.000	85.221	134.000	86.464	14.608
OS 100m in 30m grid	29078	58.000	85.080	134.000	86.342	14.707

Table 2. St Albans, OS DEM Elevation statistics coarse DEMs and 10m DEM

Input DEM Resolution/m	Output DEM DEM Resolution/m	Number of Points	Min.	Mean	Max.	RMS	SD
50	10	260000	-12.030	0.100	7.710	1.806	1.804
50	30	29078	-25.950	0.087	29.800	6.098	6.097
100	30	29078	-24.950	0.227	39.590	6.301	6.297

Table 3. St Albans, Input DEM - 10M OS DEM Elevation difference statistics for coarser DEM used for phase flattening

Image Pair	Flatten DEM / output DEM Resolution/m	Number of Points	Min.	Mean	Max.	RMS	SD
22505/2832	50m/10m	260000	27.085	72.848	161.638	74.857	17.224
22505/2832	50m/30m	29078	28.638	72.896	163.362	74.918	17.288
22505/2832	100m/30m	29078	26.723	73.055	163.362	75.044	17.167
23006/3333	50m/10m	260000	36.392	81.501	153.155	82.521	12.934
23006/3333	50m/30m	29078	36.392	80.916	142.155	81.925	12.817
23006/3333	100m/30m	29078	36.297	86.985	151.182	88.130	14.162
2832/3333	50m/10m	260000	35.845	80.889	156.608	82.706	17.237
2832/3333	50m/30m	29078	35.845	80.812	156.608	82.577	16.982
2832/3333	100m/30m	29078	35.845	81.104	156.155	82.779	16.570

Table 4. St Albans, IfSAR DEM Elevation statistics

Image Pair	Flatten DEM / output DEM Resolution/m	Number of Points	Min.	Mean	Max.	RMS	SD	% of points filled
22505/2832	50m/10m	255133	-24.267	-0.639	49.628	7.192	7.164	1.87
22505/2832	50m/10m	28516	-33.302	-0.661	56.832	8.687	8.662	1.93
22505/2832	100m/30m	27801	-57.527	-0.831	56.832	8.454	8.414	4.39
23006/3333	50m/10m	257802	-23.295	-0.786	31.223	5.759	5.705	0.85
23006/3333	50m/30m	28794	-46.548	-1.436	42.073	7.812	7.679	0.98
23006/3333	100m/30m	28225	-57.223	4.745	39.635	10.036	8.843	2.93
2832/3333	50m/10m	223789	-24.108	-0.050	32.941	10.617	10.617	13.93
2832.3333	50m/30m	25021	-45.599	-0.206	49.505	12.153	12.152	13.95
2832/3333	100m/30m	20911	-54.047	-0.763	45.423	11.859	11.835	28.09

Table 5. St Albans, IfSAR - OS 10M DEM Elevation difference statistics

Image Pair	Number of Points	Min.	Mean	Max.	RMS	SD
22505/2832	260000	0.00	54.37	94.00	56.80	16.45
23006/3333	260000	0.00	44.99	92.00	47.07	13.85
2832/3333	260000	0.00	33.25	93.00	37.27	16.85

Table 6. St Albans, Phase coherence statistics

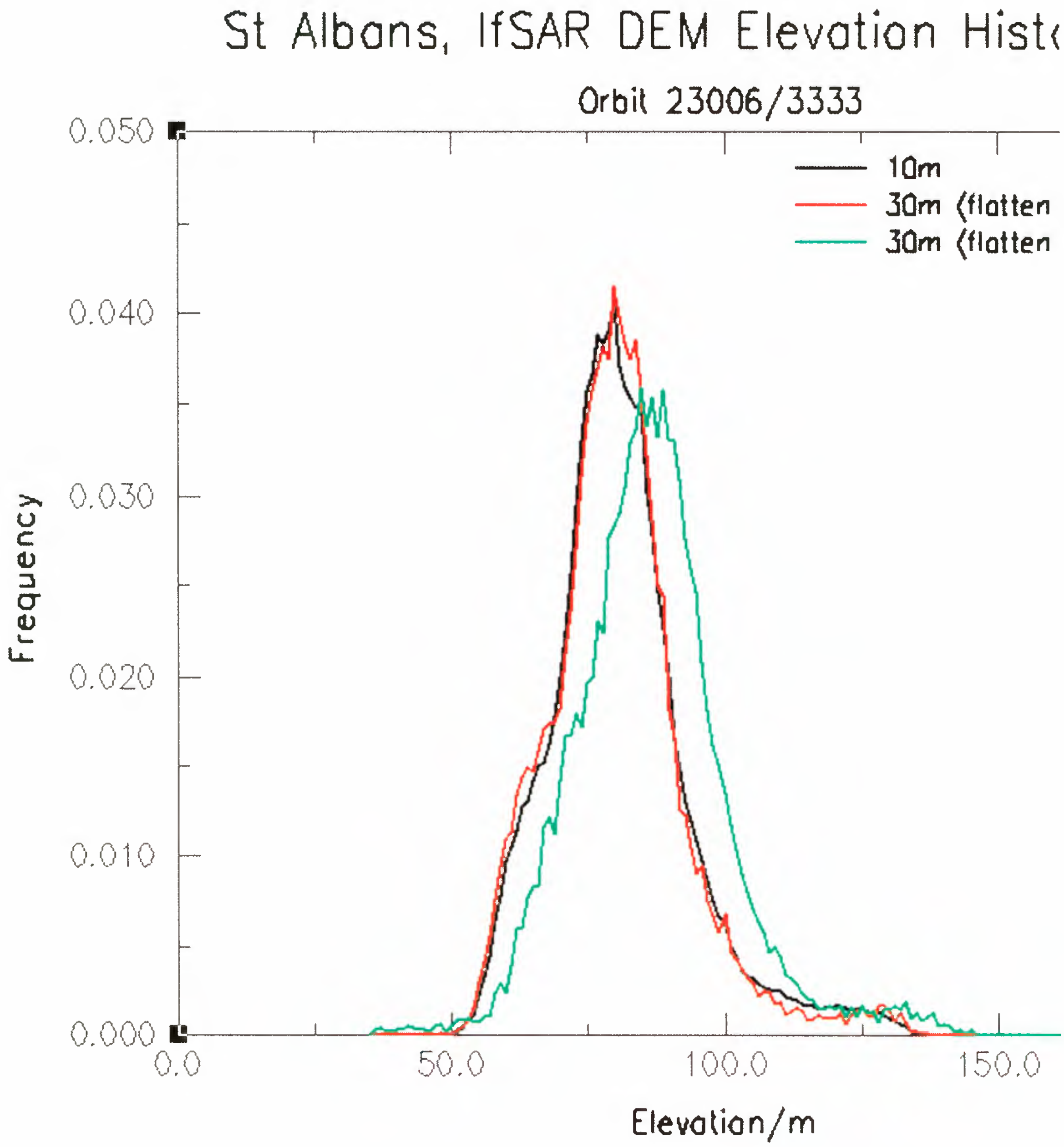

1. St Albans, DEM Elevation Histogram for Orbit 23006/3333

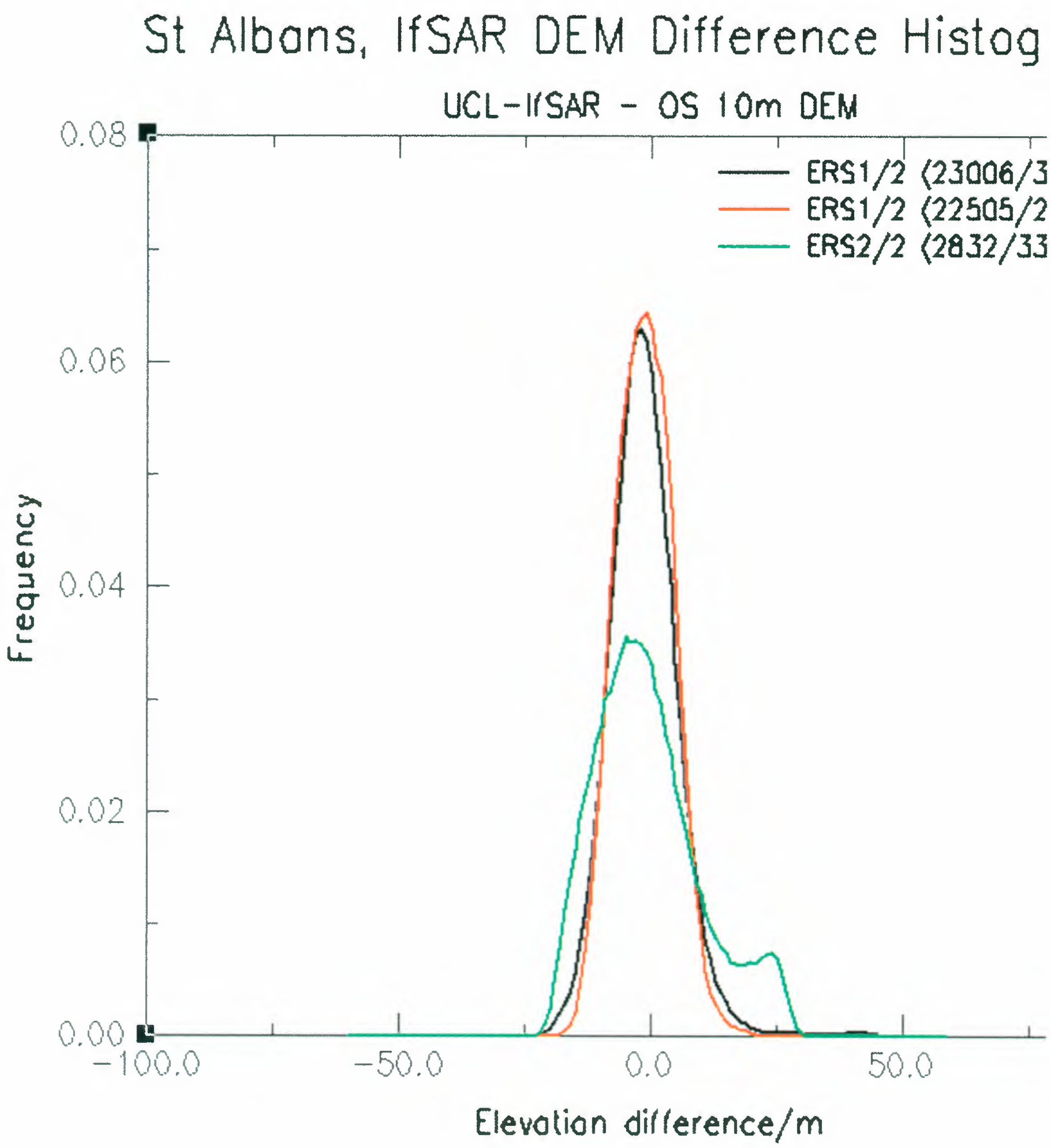

Graph 2. St Albans, 10m DEM Elevation difference Histogram Orbit 23006/3333,22505/2832 and 2832/3333

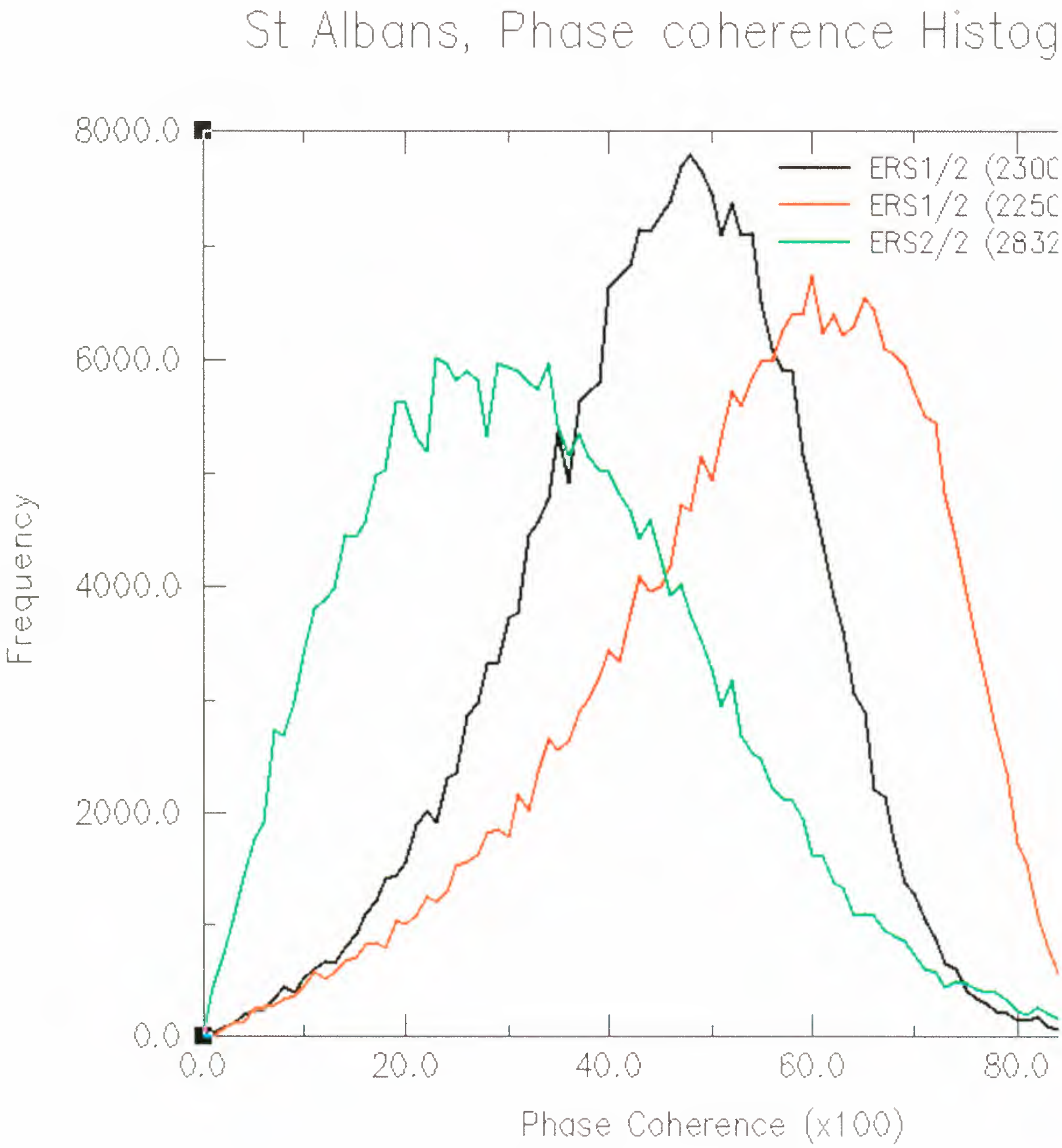

Graph 3. St Albans, Phase coherence Histogram

Conclusions and Future work

IfSAR-DEMs using densification of existing UK National Mapping data have been shown to produce DEMs of elevation accuracy between 7 and 12 m rms which is comparable to SPOT.

It was possible to detect in the IfSAR-DEM, a narrow cutting of the M25 motorway which is not present in the highest resolution OS product. It was also possible to produce DEMs over a highly vegetated and cluttered scene with even a 35-day repeat. No atmospheric effects were detected and no detectable difference in accuracy even with Bperps differing by one-third.

Further work is required to look at the effects of different baselines and to try to understand what the elevation differences refer to, particularly regarding detailed land cover. Processing is being extended to the other 2 regions currently and results will be reported in the upcoming Florence Symposium.

Acknowledgements

UCL would like to acknowledge financial support from the OS and BNSC for the research described here. The UCL-3DIM (IfSAR) system was developed under NERC grant reference GR3/09745 whilst the phase unwrapping portions (used with permission) were developed at UCL under support from Logica Space Systems. The authors would like to thank Alessandro Ferretti of Milan Polytechnic who has been visiting UCL for the last 2 months for use of his prototype SLC-to-interferogram generation software.

Ordnance Survey

Copyright

References

Day, T., and J.-P. Muller, Digital Elevation Model Production By Stereo-matching Spot Image-pairs: A comparison Of Algorithms, Image And Vision Computing, 7 (2), 95 - 101, 1989.

DMA, Digitising the Future, Defence Mapping Agency (USA), 1990.

Murray, K.J., A.J. Davey, and G.M. Tait, Ordnance Survey: Imagery applications in support of a National Geospatial data infrastructure., in Int. Arch. of Photo. & Rem. Sens., pp. 99-106, ISPRS, Vienna, Austria, 1996.

Session 3

Forest & Landcover Applications

Chairman: M. Borgeaud

On the Use of ERS SAR Interferometry for the Retrieval of Geo- and Bio-Physical Information

Maurice Borgeaud

European Space Agency
ESTEC-XEP
P.O. Box 299
2200 AG Noordwijk
The Netherlands
Tel: +31-71-565-4830
Fax: +31-71-565-4999
Email: maurice@xe.estec.esa.nl
http://www.estec.esa.nl

Urs Wegmueller

GAMMA Remote Sensing AG
Thunstrasse 130
3074 Muri BE
Switzerland
Tel: +41-31-951-7005
Fax: +41-31-951-7008
E-mail: gamma_rs@pingnet.ch
http://www.primenet.com/~gamma/gamma.html

Abstract

At the present time, most of the research activity in SAR interferometry is directed towards development and improvement of SAR interferometric techniques, mapping of scene topography (DEM), and displacement mapping with differential interferometry. Recently, it has been however shown that SAR interferometry has also a large potential for the retrieval algorithms for bio- and geophysical parameters.
Using only the coherence information derived from the complex correlation of two co-registered ERS SAR images, it is possible to retrieve additional information complementary to information contained in the amplitude value of the backscattering coefficient. Phase-unwrapping, one of the most critical steps of the interferometric processing chain, is not required for this type of analysis.
Applications of SAR interferometry for forest mapping, forest type discrimination, freezing, land-use classification, soil moisture monitoring, crop classification, crop density, crop growth and field development monitoring, monitoring of open water surfaces, and erosion are discussed. Examples from four different test sites (Bern, Flevoland, Middle Zeeland, and Death Valley) are shown using ERS-1 data collected during 3-day and 35-day repeat orbits as well as ERS-1/2 tandem data.
Keywords: SAR, interferometry, ERS, coherence, forest, land-use, crop, erosion

Introduction

In the last few years, SAR interferometry has become a very attractive technique to obtain extra information from SAR images. Not only the amplitude of the signal is considered, but its phase as well. In order to use this technique, two SAR images of the same region, acquired with slightly different sensor positions, are coherently combined together. SAR interferometry can be performed either using data collected by repeat-pass or single-pass sensors. The former implies the same antenna is used twice while the latter requires two distinct antennas to be flown aboard the aircraft or satellite.

This paper deals with repeat-pass SAR data acquired by ERS-1 during the 3-day (1991 and 1994) and 35-day repeat periods as well as during the ERS-1/2 tandem mission (1995). ERS-1, a satellite carrying a spaceborne C-band SAR, was built by ESA and launched in July 1991 while ERS-2 was launched in April 1995. Both satellites are identical (from the SAR point of view) and acquire data over the Earth with incidence angles varying between 19 deg and 26 deg with slant-range pixel spacing set to 7.9 m (for the single look complex SLC product generated by ESA).

A promising applications of SAR interferometry is to generate digital elevation maps (DEM) owing to the fact that the height information can be related to the phase difference between two SAR images. However, other applications of are emerging and this paper describes some of those for the retrieval of geo- and bio-physical information.

After a brief description on how the SAR data are processed, the paper lists the test sites which used for the study and then describes the potential of ERS SAR interferometry for several applications including forestry, agriculture, land-use classification, soil moisture monitoring, freezing, and erosion.

Processing of the SAR data

Interferometric processing of complex SAR data combines two single look complex (SLC) images into an interferogram. In a first step the two images are co-registered at sub-pixel accuracy. In the same step common band filtering of the azimuth and range spectra can be conducted, in order to include only those parts of the spectra which are common to the two images, and thereby optimizing the interferometric correlation and minimizing the effects of the baseline geometry on the interferometric correlation. Then the two images are cross correlated, i.e. the normalized complex interferogram is computed. The azimuth and range phase trends expected for a flat Earth are then removed from the interferogram. From this "flattened " interferogram and the two registered intensity images the multi-look interferometric correlation and backscatter intensities are estimated. The backscatter intensity and interferometric correlation estimators have to include a sufficiently large number of looks in order to reduce speckle noise and biased correlation estimation at low correlation levels. To optimize the trade off between spatial resolution and estimation accuracy estimators with adaptive window sizes were used. Notice that no phase unwrapping step if necessary for the estimation of the backscatter intensities and the interferometric correlation.

Test sites and data description

Several test sites have been used to investigate the potential of SAR interferometry for retrieving geo- and bio-physical information. Each of them is listed in Table 1 as well as the ERS data used and the bio/geo-physical parameter investigated.

Test site	Data	Season	Parameter retrieval
Bern (CH)	ERS-1	Nov. 91	Forest types, freezing
Bern (CH)	ERS-1/2 tandem	July 95	Forest/non-forest, forest types, land-use classification
Middle Zeeland (NL)	ERS-1	Jan.-Apr. 1994	Soil moisture, freezing
Flevoland (NL)	ERS-1	Sep.-Nov. 1991	Crop type, crop growth, field development
Flevoland (NL)	ERS-1/2 tandem	1995	Crop type, crop growth, field development
Death Valley USA)	ERS-1	Jan.-May 1993	Vegetation density, geometric change (erosion), mapping of surface types

Table 1: Test sites investigated

Applications of SAR interferometry

Some of the potential applications of SAR interferometry for the retrieval of bio- and geo-physical information, including forestry, agriculture, land-use classification, soil moisture monitoring, freezing, and erosion, are examined and examples are given in this section.

Forestry

It is difficult to identify forested areas using only single-frequency and single-polarization C-band amplitude SAR data as shown in Figure 1 . The city of Bern can be recognized at the bottom of the image while the lake of Bienne and Morat are displayed on the left of the image. However, it is almost impossible to differentiate forested from non-forested areas.

Figure 1: Part of the ERS-1 image (SLC format) over the Bern test site acquired on 24 November 1991 (full size image)

Using the coherence information between two ERS-1 images acquired 3 days apart (in this case: 24 and 27 November 1991), one can derive the so-called ``RGB" image to get a visual impression of the additional information that the coherence carries (Wegmueller 1995a, Wegmueller 1995b) . The red channel is proportional to the coherence, the green with the mean amplitude image, and the blue with the amplitude difference between the two images. Figure 2 shows the corresponding RGB image for the Bern test site.

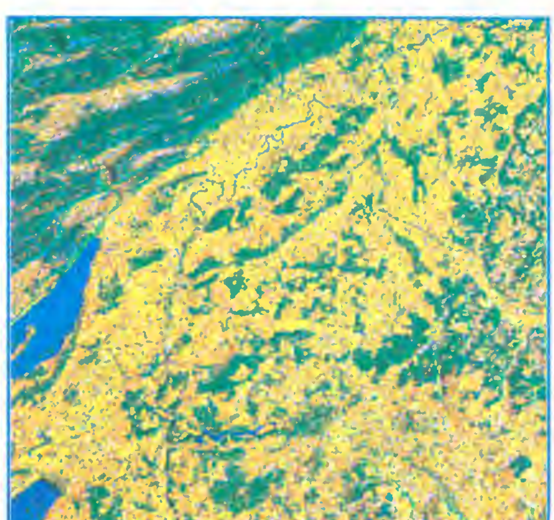

Figure 2: RGB interferometric image over the Bern test site (full size image)

During the winter season. the coherence is quite high for agricultural fields (mainly bare soils) while forests exhibits a low coherence due to a three-day temporal decorrelation. Figure 3 shows the variation of backscattering coefficient as a function of the interferometric coherence. derived from ERS 3-day repeat-pass interferometry for different types of land surfaces.

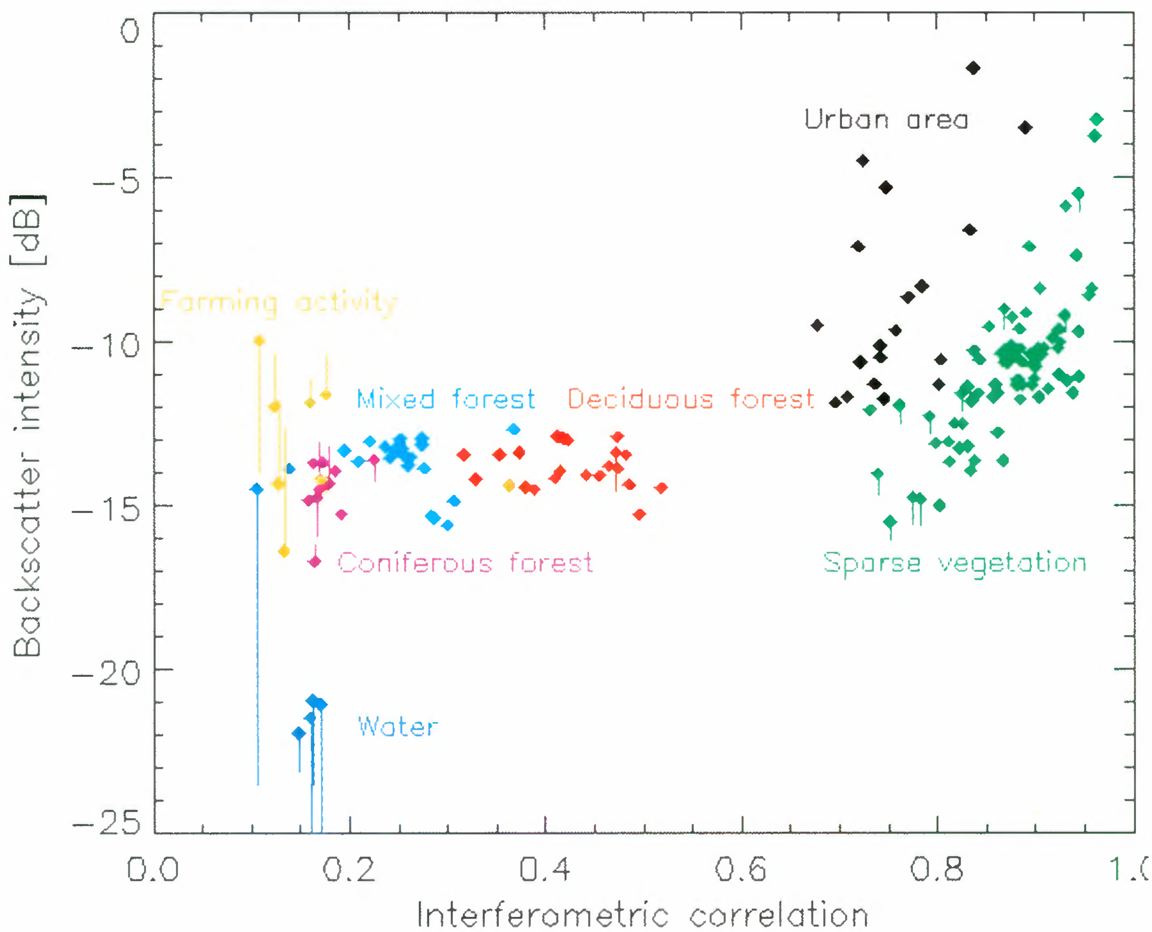

Figure 3: Variation of backscattering coefficient as a function of the interferometric coherence for different types of land surface

It can be observed that both urban areas and sparse vegetation have a high backscattering coefficient and a high correlation. However. forested areas, while having a similar relatively high backscattering coefficient value. are described by a much lower coherence. Taking these differences into account. forested areas can easily be identified in green on Figure 2 using the RGB color scheme.

More recently. it was shown (Wegmueller 1996a) that it might also be possible to separate deciduous from coniferous trees using ERS SAR interferometry. From Figure 3 . it can be noted that the interferometric correlation is higher for deciduous trees than for coniferous while having an approximate constant backscattering coefficient. One should however not forget that this result is true only for winter time when deciduous trees have lost their leaves and hence are less sensitive to wind effects and is based on 3-day repeat-pass interferometry. In order to generalize this result. the different seasonal development of the two forest types (deciduous vs coniferous) was used. Deciduous forest sheds its leaves in fall, coniferous not. For the deciduous forest stands this results in increased interferometric correlation during winter time because the scatter contribution of more stable structures such as branches. stronger twigs and the soil is increased. The classification shown in Figure 4 was based on the interferometric correlation of the June 95. November 95 and April 96 ERS-1/2 tandem pairs over the Bern test site.

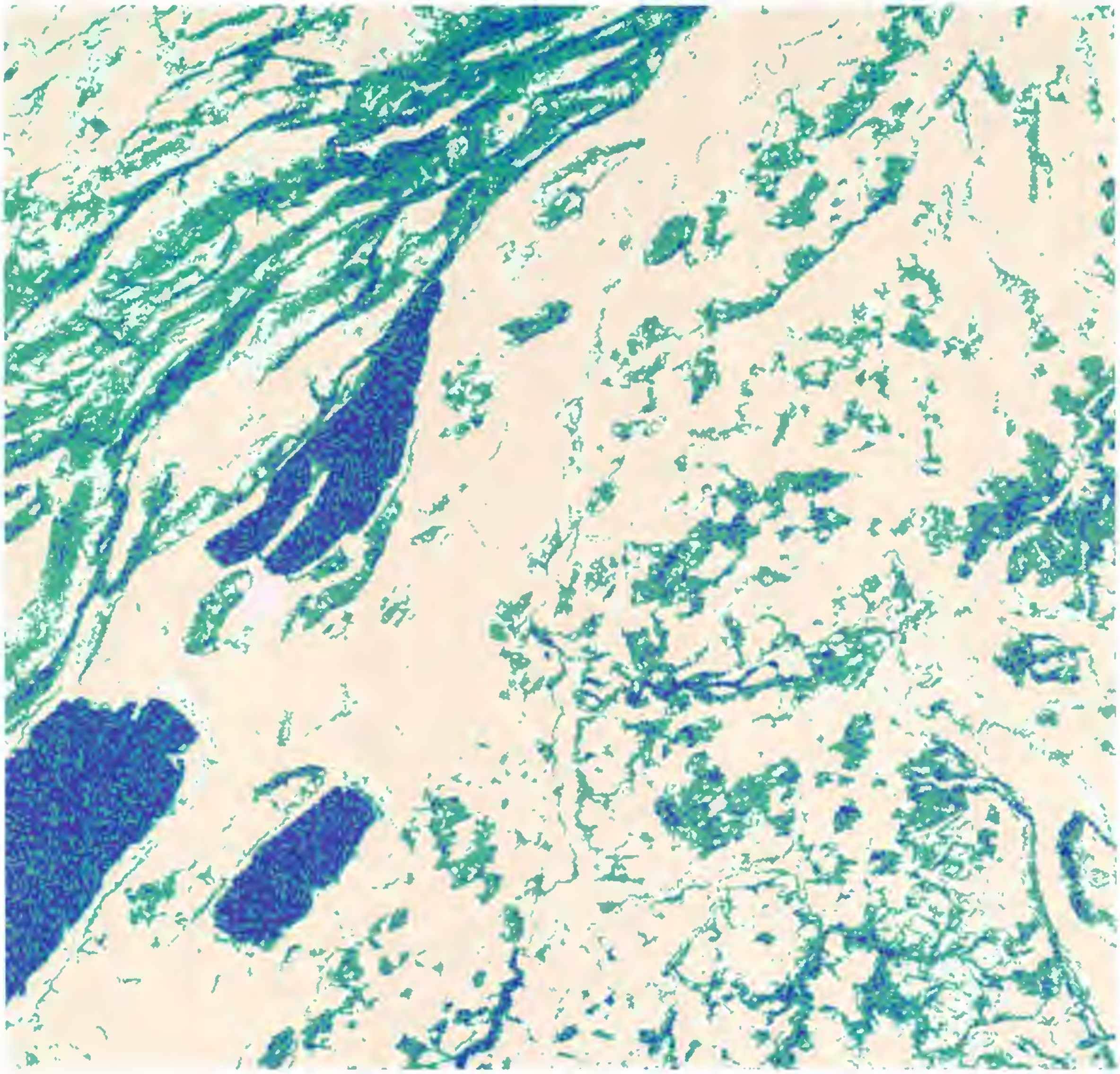

Figure 4: Forest type classification based on multi-temporal interferometric correlation for Bern test site. June 1995, Nov. 1995 and April 1996 ERS-1/2 tandem pairs were used for the classification.

The dark green areas correspond predominantly to coniferous forest, the bright green areas to deciduous forest. Blue corresponds to permanently very low correlation like water and lay-over. Grey-brown corresponds to higher correlation, i.e. urban areas and agricultural fields. The result was only validated for a few known forest stands. More quantitative validation is planned.

Agriculture

It has been recognized that ERS-SAR data can be very valuable for agricultural applications (Wooding 1995), not only because of the all-day capability of microwave vs optical data, but also due to the fact that SAR data are very sensitive to moisture, soil roughness, and vegetation structure.

Additional, and most of time complementary, information can be derived from SAR interferometry. Several crops where observed during the Fall 1991 over the Flevoland test site by ERS-1. The temporal variation of the backscattering coefficient as well as the interferometric coherence is shown in Figure 5.

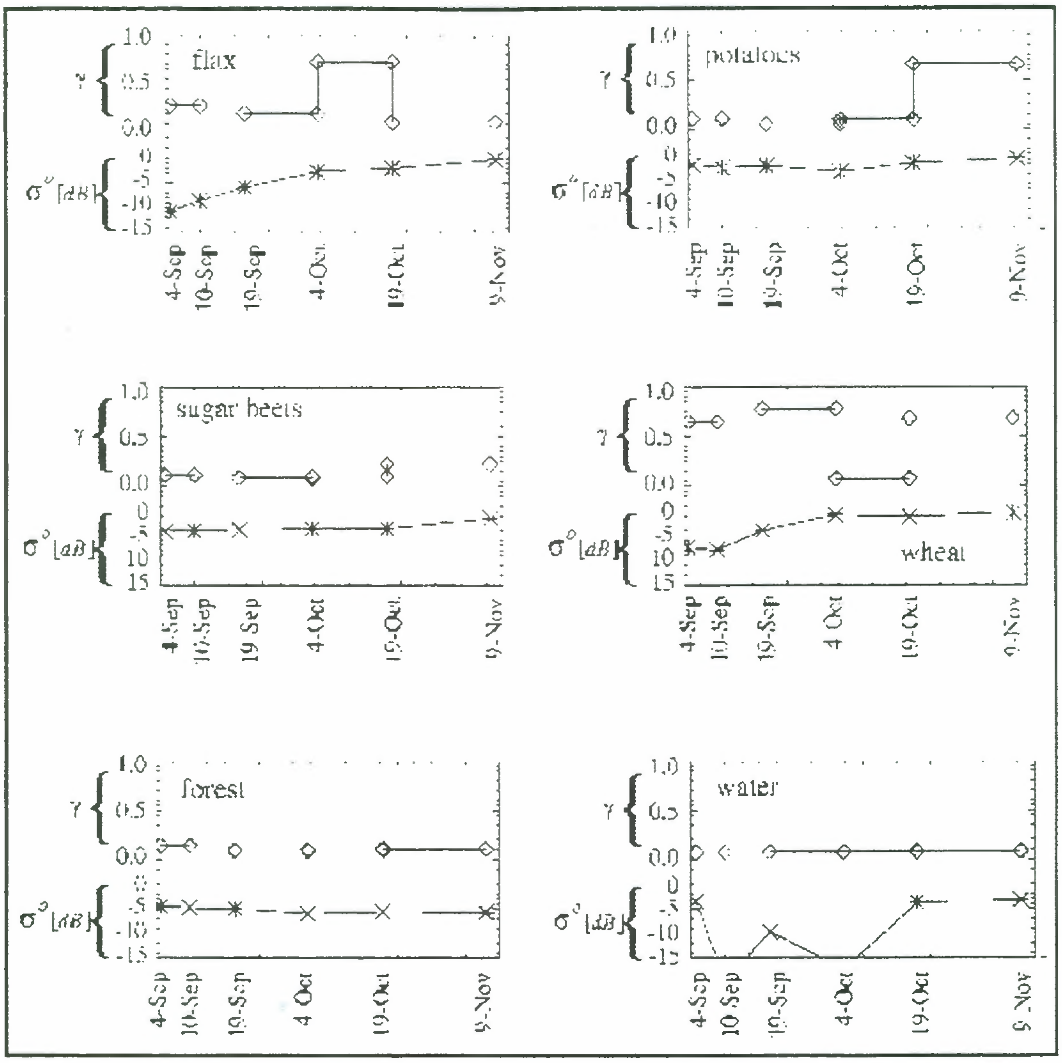

Figure 5: Temporal signatures of interferometric correlation and backscattering coefficient for several crops over Flevoland (full size image)

It can be seen that abrupt changes in the coherence for potatoes and wheat are not observed in the backscattering coefficient values. These losses of coherence can be attributed either to harvesting or mechanical preparations of the fields (e.g. ploughing).
In addition to the extraction of the signatures for selected fields, multi-temporal composites were generated. Figure 6 shows the multi-temporal image of the interferometric correlation combining the correlation of the 19 Sep. & 4 Oct. (red channel), 4 Oct. & 19 Oct. (green channel), and 19 Oct. & 9 Nov. (blue channel) interferograms. The fields appear in different colors according to its vegetation cover and farming activity occurring.

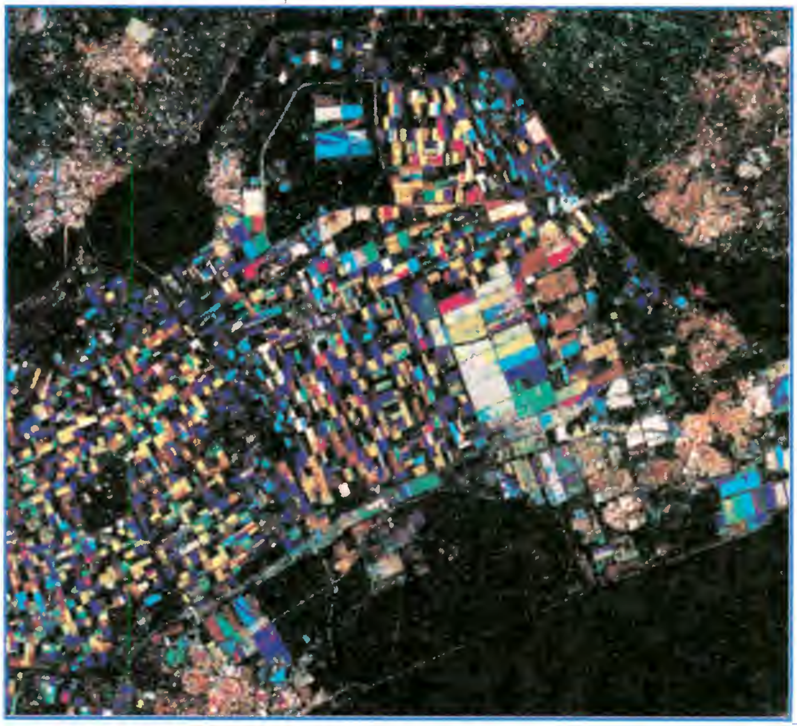

Figure 6: Multi-temporal coherence image over Flevoland in the Fall 1991 (full size image)

Using this technique, the area can also be classified in eight different classes depending on the value of the coherence between two dates. If the coherence is higher than 0.5, one assumes that no change has taken place during the time interval. On the other hand, if it is lower than 0.5, one assumes that some kind of "change" has occurred such as harvesting or mechanical preparations of the fields. Using the color table definition described in Table 2 , the classification of the Flevoland test site in eight different classes can be derived and is shown in Figure 7. Forest, water areas always exhibit change of correlation. therefore these areas are shown in black while bare soil fields (or spare vegetation covered fields) which are not mechanically cultivated during the whole period are displayed in white.

19 Sep. & 4 Oct.	4 Oct. & 19 Oct.	19 Oct. & 9 Nov.	Code	Color
change	change	change	000	Black
change	change	no change	001	Blue
change	no change	change	010	Green
change	no change	no change	011	Turquoise
no change	change	change	100	Red
no change	change	no change	101	Pink
no change	no change	change	110	Yellow
no change	no change	no change	111	White

Table 2: Color table definition according to a coherence greater (no change) or smaller (change) than 0.5 between two dates

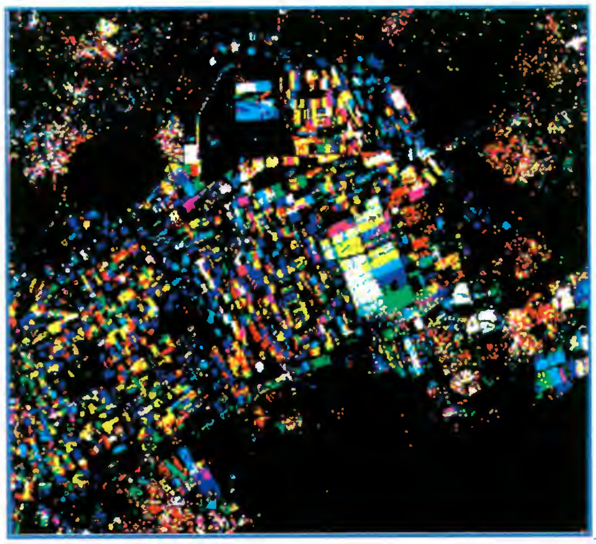

Figure 7: Map of multi-temporal change over Flevoland in the Fall 1991 (full size image)

The temporal monitoring of the coherence may also give some information about the status of a crop. As shown in Figure 8 for the case of rapeseed (two different fields located in the Flevoland test site) during the growing season 1991-1992, the coherence decreases as the soil cover fraction increases. This can easily be explained due to the fact that as the vegetation increase, the coherence (measured by repeat-pass interferometry) decreases. With knowledge of the farming calendar, such information would allow the identification of the crop. For the specific case of the rape seed, it is possible to identify it as early as November 1991

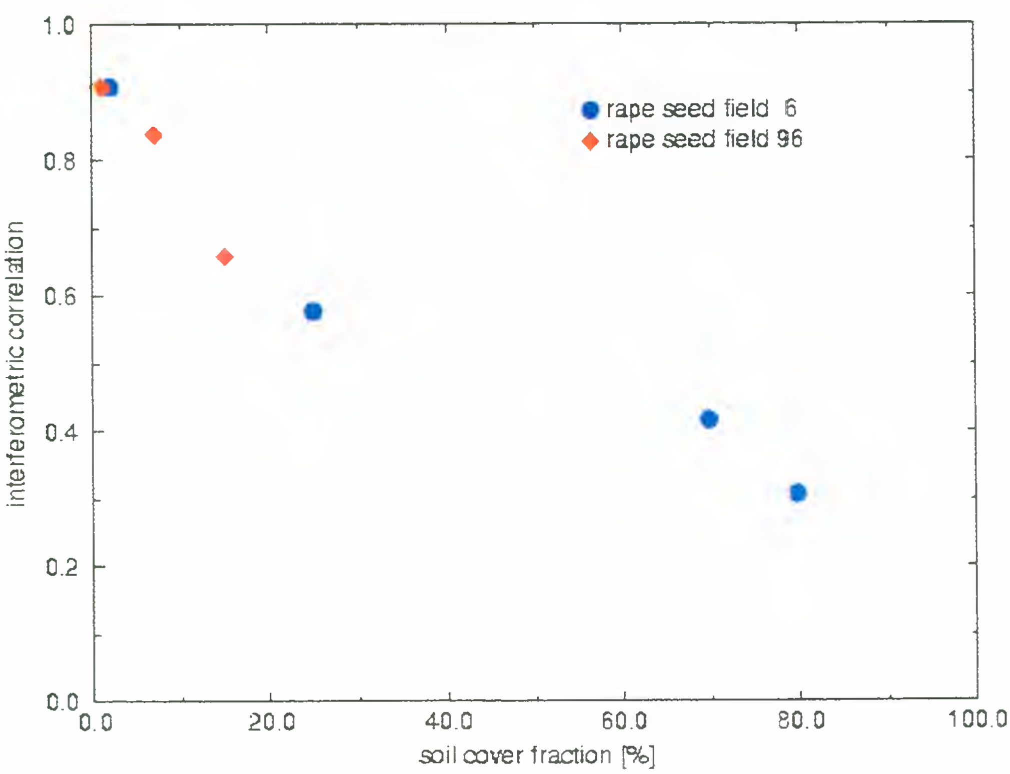

Figure 8: Interferometric correlation as a function of rape seed soil cover fraction over the Flevoland test site

A promising approach would be to couple this information linked to the biomass content with crop growth models to predict the crop yield (Van Leeuwen, 1996) .

Land-use classification

Using SAR interferometry and combining coherently the data acquired on 24 November 1991 by data measured three days later (i.e. 27 November 1991), it is now possible (Wegmueller, 1996a) to derive land-use maps, as illustrated in Figure 9. Land classes such as lakes, urban, forest, agriculture can be identified with a classification accuracy of 90%. Furthermore, lay-over areas are shown in yellow. The color table used is displayed in Figure 10. This classification was made possible by combining the mean amplitude and differences between the data as well as the coherency image acquired on both days.

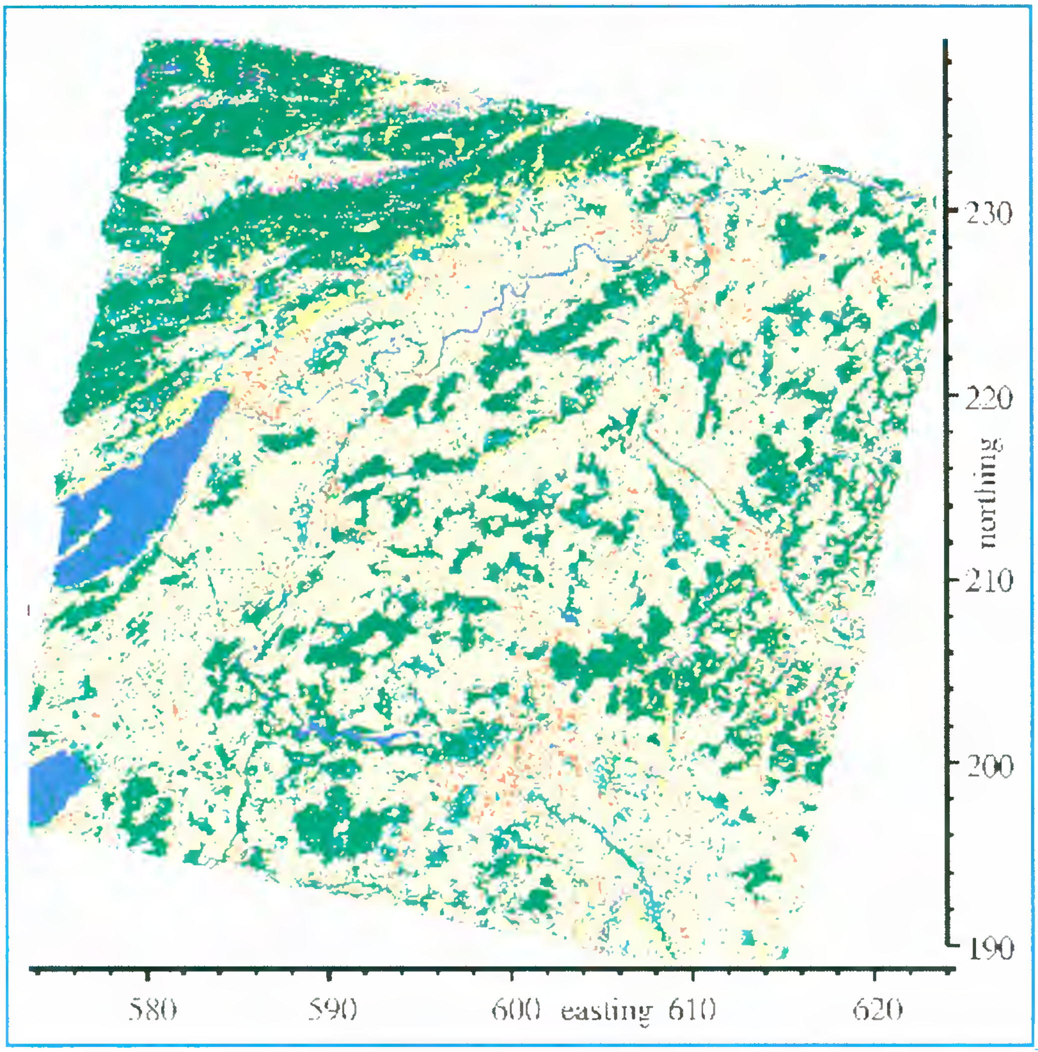

Figure 9: Landuse map using SAR interferometry technique with ERS-1 data acquired on 24 and 27 November 1991 over the Bern test site. Water (blue), urban (red), forest (dark green), agriculture (light green), and lay-over (yellow) are shown. (full size image)

Color coding used:

- water
- urban area
- forest 1 (dense/coniferous)
- forest 2 (open/deciduous)
- sparse vegetation
- moisture change / freezing
- mechanical cultivation
- layover area

Figure 10: Color table for Figure 9

Soil moisture monitoring

The scattering properties of a soil surface are dominated by its geometry and its permittivity or dielectric constant. The permittivity itself depends strongly on the soil moisture content because of the very high permittivity of liquid water. The main limitation in soil moisture retrieval is that the geometry of the soil as well as vegetation cover influence the backscattering coefficient, too. SAR interferometry can help to resolve the effects of the soil moisture, the soil roughness and the vegetation cover, which are very difficult to separate, otherwise (Wegmueller 1996b) . As discussed above vegetation can be identified by its lower interferometric correlation. This allows to identify bare and sparsely covered fields. In addition, high interferometric correlation indicates that no geometric change, that means also no surface roughness change, occurred between the acquisition of the image pair. Even if the surface roughness remains unknown, the fact that surface roughness change may be excluded allows to monitor soil moisture change more reliable. Of course, these ideas improve the situation primarily for those fields which are bare and without geometric change. Using a similar technique as described in Table 2 (setting a change/no change threshold for the coherence to 0.5), a multi-temporal image of the change of the interferometric correlation over the Middle Zeeland test site Figure 11 shows that such fields exist in relatively high number (identifiable by a white color), confirming that the presented ideas are be applicable in practise. The color table is the same as described in Table 2 , however different dates are used.

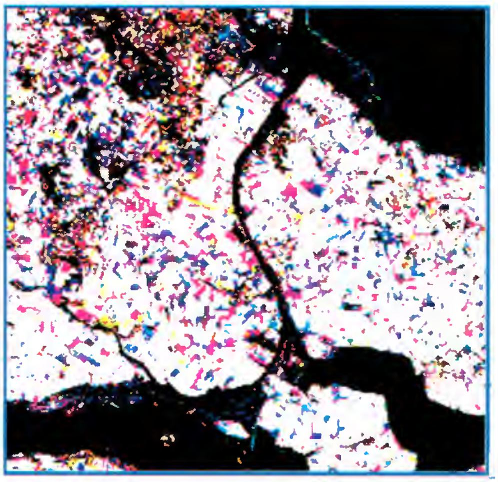

Figure 11: Map of multi-temporal change over Middle Zeeland in the winter 1994 (full size image)

Under the assumption of constant surface roughness, quite reliable soil moisture estimates may be obtained from the microwave backscattering coefficient as was shown in the past (Borgeaud, 1995) . The backscatter intensities of fields of high interferometric correlation allow to monitor near-surface soil moisture. Additional advantages of SAR interferometry with respect to soil moisture monitoring are the possibility to use the interferometric phase to retrieve topographic information. and to carry out geometric- and radiometric calibration of the data.

Freezing

The most drastic cases of permittivity change are freezing and thawing events. The liquid water content changes between almost zero for the frozen case to the usually very high values near saturation which are typically observed during winter season. As illustrated in Table 3 , the interferometric correlation (cc) and the backscatter change (delta sigma) in [dB] between the first and the second acquisition were extracted for three fields over the Middle Zeeland test site. The drastic decrease in the backscattering of more than 4 dB between 11 and 14 Feb at a high interferometric correlation (> 0.70) clearly indicates the freezing event.

Dates	Baseline [m]	Time interval [day]	In-situ info	Field 4 [cc]	Field 4 [delta sigma, dB]	Field 5 [cc]	Field 5 [delta sigma, dB]	Field 6 [cc]	Field 6 [delta sigma, dB]
5 & 11 Feb. 1994	30.1	6	not frozen	0.96	-0.8	0.97	-1.4	0.97	-0.4
11 & 14 Feb. 1994	136.8	3	frozen on 14 Feb.	0.76	-4.3	0.78	-4.7	0.73	-5.1
14 & 17 Feb. 1994	112.9	3	frozen both days	0.81	-0.2	0.80	+0.8	0.76	+0.5

Table 3: Coherence [cc] and change in backscattering coefficients [delta sigma] for three fields over the Middle Zeeland test site during the period 5-17 February 1994.

Vegetation density and erosion

Over semi-arid to arid sites such as the Death Valley and Amargosa Desert the interferometric correlation is high even after 35 days or longer. Besides radar system and processing related effects, decorrelation occurs from geometric change. In such areas mainly two sources of geometric change occur: changing vegetation (motion, growth, etc.) and erosion. Wind and rain change the shape of unstable sandy surfaces. As a result such surfaces can be distinguished from more stable surfaces with larger rocks. Figure 12 shows the interferometric correlation (color scale from 0.1 to 1.0). The plains of the Amargosa Desert are relatively unstable and affected by wind and rain erosion. On the other hand larger rocks are typically found in dry River beds and on the alluvial fans of the Panamint Range, Amargosa Range, and Yucca Mountain. An extreme example for erosion with very low correlation after 35 days are sand dunes as for example the Big Dune in the Amargosa Valley.

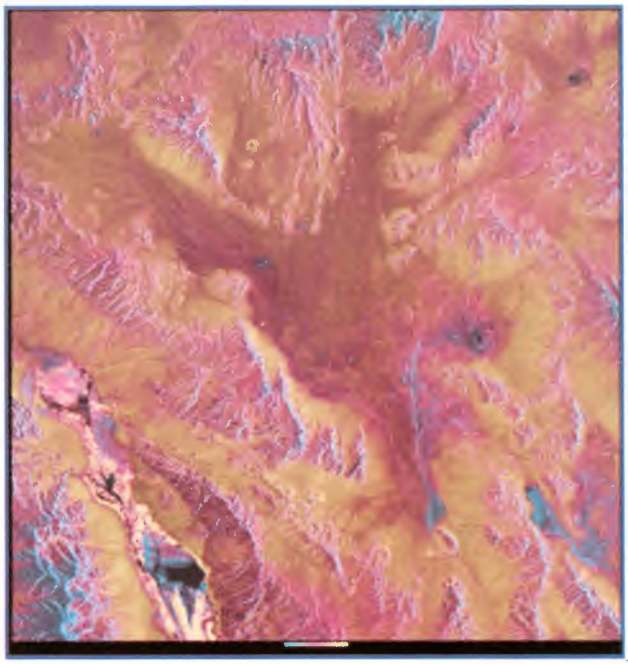

Figure 12: ERS repeat-pass ERS interferometry (35-day) over Death Valley (29 January & 5 March 1993)
(full size image)

Conclusions

In this paper, techniques using SAR interferometry have been presented to retrieve several bio- and geo-physical parameters. Using only the coherence information derived from the complex correlation of two co-registered ERS SAR images, it is possible to retrieve additional information complementary to information contained in the amplitude value of the backscattering coefficient. Applications of SAR interferometry for forest mapping, forest type discrimination, freezing, land-use classification, soil moisture monitoring, crop classification, crop density, crop growth and field development monitoring, monitoring of open water surfaces, and erosion have been clearly demonstrated.

References

Borgeaud, Attema, Salgado-Gispert, Bellini, Noll, 1995:
Analysis of Bare Soil Surface Roughness Parameters with ERS-1 SAR Data, *Symposium on Retrieval of Bio- and Geophysical Parameters from SAR Data for Land Applications* , Toulouse, France, 10-13 October 1995.

Van Leeuwen, Bakker, van den Broek, Rijckenberg, Bouman, Clevers, 1996
Vegetation retrieval by combined microwave and optical remote sensing, *ESA contract 11154/94* , Noordwijk, The Netherlands.

Wegmueller, Werner, Nuesch, Borgeaud, 1995a:
Forest Mapping Using ERS-1 SAR Interferometry, *ESA Earth Observation Quarterly* , No. 49.

Wegmueller, Werner, Nuesch, Borgeaud, 1995b:
Land-Surface Analysis Using ERS-1 SAR Interferometry, *ESA Bulletin* , No. 81, pp. 30-37.

Wegmueller, Werner, 1995c:
SAR interferometric signatures of forest, *IEEE Transactions on Geoscience and Remote Sensing* , Vol 33, No 5, pp 1153-1161.

Wegmueller, Urs, 1996a:
ERS SAR interferometry for land applications, *ESA contract 11740/96* , in progress, Noordwijk, The Netherlands.

Wegmueller, Urs, 1996b:
The potential of ERS SAR interferometry for hydrology, *Environmental Remote Sensing and Applications* , Parlow (ed.), Balkema, Rotterdam, (ISBN 90 54 10 5984), pp. 319-324, in progress.

Wooding, Attema, Aschbacher, Borgeaud, Cordey, de Groof, Harms, Lichtenegger, Nieuwenhuis, Schmullius, Zumda, 1995
Satellite Radar in Agriculture: Experience with ERS-1, *ESA SP-1185 Publication* , Noordwijk

Forest INSAR decorrelation and classification properties

J. Askne
Chalmers University of Technology,
Dep. of Radio and Space Science,
S-41296, Göteborg, Sweden
askne@rss.chalmers.se
http://www.rss.chalmers.se

G. Smith
Chalmers University of Technology
Dep. of Radio and Space Science
S-41296, Göteborg, Sweden
smith@rss.chalmers.se
http://www.rss.chalmers.se

Abstract

Large areas are covered by forest and the decorrelation properties of the forest are important to understand in order to use INSAR for deriving forest properties and determine the potential for DEM production. From the 3-day repeat cycle of ERS-1 in 1994 we have determined interferograms of forested areas in northern Sweden. Variations of coherence with time and stem volume have been determined. Discrimination between forest and clear cuts has been characterised. A model for the coherence variation is discussed and critical parameters for further studies identified.
Keywords:. Coherence analysis, forestry, land classification

Introduction

Estimation of forest biomass is important on a global scale as an input parameter to environmental models and on a local scale for assessment of forest properties. It is of great economical value for forestry companies to improve forest inventory methods.

A large number of observations of boreal forest properties have been performed based on the radar backscatter, e.g. using the ERS-1 satellite C-band SAR. A conclusion is that the radar backscatter at C-band saturates for relatively small values of the stem volume or biomass, see e.g. (Israelsson and Askne, 1994). However, the information content from the ERS satellites is increased by using interferometric repeat pass INSAR observations. From these we can derive the interferometric effective height of the forest layer and the coherence, see e.g. (Dammert et al., 1995; Hagberg et al., 1995). These properties have been found to vary with forest parameters and there is a need for analysis of the potential of interferometric measurements and to understand the basic phenomena related to the interferometric imaging of forest.

The most significant aspect of INSAR observations of forest areas is the typically low coherence. This complicates the analysis as the phase variations are then hard to estimate. But the low coherence of forests also makes it possible to use coherence to discriminate forest and non-forest, and we will also study some clear cuts and open fields.

In this presentation we will report on ERS-1 INSAR observations and extend the previous model approaches to understand the signal dependence on different parameters (Askne et al., 1995; Hagberg et al., 1995; Askne et al.. to be publ.). An aim is also to identify those properties we need to investigate further in order to improve our modelling of the INSAR response of vegetation.

Observations

Field site

The test areas are centred around Hökmark (lat. 64 25'. long. 21 15') in northern Sweden characterised by boreal forest. The most dominant species are conifers (Norway spruce and Scotch pine). A typical value of the stem volume in this part of Sweden is 100 m^3/ha. An illustration of the forest at one of the test sites is given in Figure 1, and for a fairly typical clear cut with regrowth in Figure 2.

Figure 1. Illustrating an area with a stem volume estimated to 240 m^3/ha. Note the gaps in the vegetation canopy.

Figure 2. Illustrating a clear-cut in the area.

Data set

Repeat-pass interferometry is dependent on the time interval between the acquisitions as temporal changes decrease the coherence. For this reason we have concentrated on observations during the 3-day repeat pass period of ERS-1 in February - March 1994. We have studied 55 interferogram pairs based on 11 SAR images. For 13 interferograms the baseline was too long, while 27 were characterised by too low coherence. Of the 15 remaining interferograms we have here concentrated on four interferograms with coherence values for the forests above the coherence bias (see below). These interferograms are based on six SAR images

INSAR measurements

In Figure 3 we have illustrated for five forest areas and six clear cuts of varying age. The values have been determined from ERS-1 SLC images and are estimated to have an accuracy of about 0.5 dB. The variation in illustrated by Figure 3 are partly related to temperatures changing from above zero to -15C. These variations are larger for the forest due to the dielectric constant changes than for the fields which are assumed to be frozen for the entire observation period.

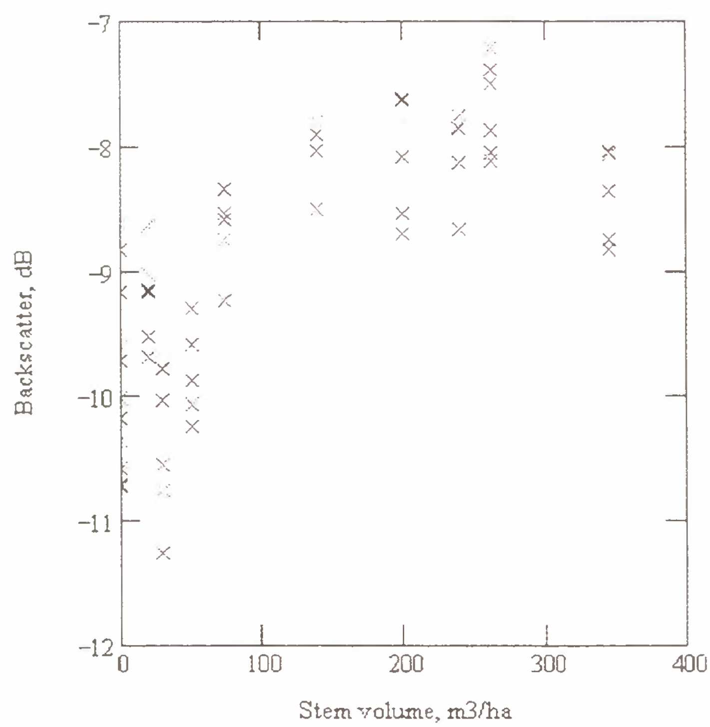

Figure 3. Illustration of for five forest areas and six clear cuts of varying age (note stem volumes for clear cuts are preliminary estimates).

Coherence is defined by

$$\gamma = \frac{E\{g_1 g_2^*\}}{\sqrt{E\{|g_1|^2\}E\{|g_2|^2\}}}$$

g_1 and g_2 denote pixel values in each of the two images respectively and $E\{\}$ denotes expectation value.

Observations of the coherence as function of stem volume is illustrated in Figure 4. The accuracy of the coherence measurements is determined by the averaging area, in our case 10^4 m^2 = 1 ha. Only values above 0.3 have been illustrated as the coherence estimator is biased for lower values. As coherence is dependent on the baseline, B_n, we have divided the figure for two cases with B_n = 21 and 30 m and B_n = 175 and 203 m

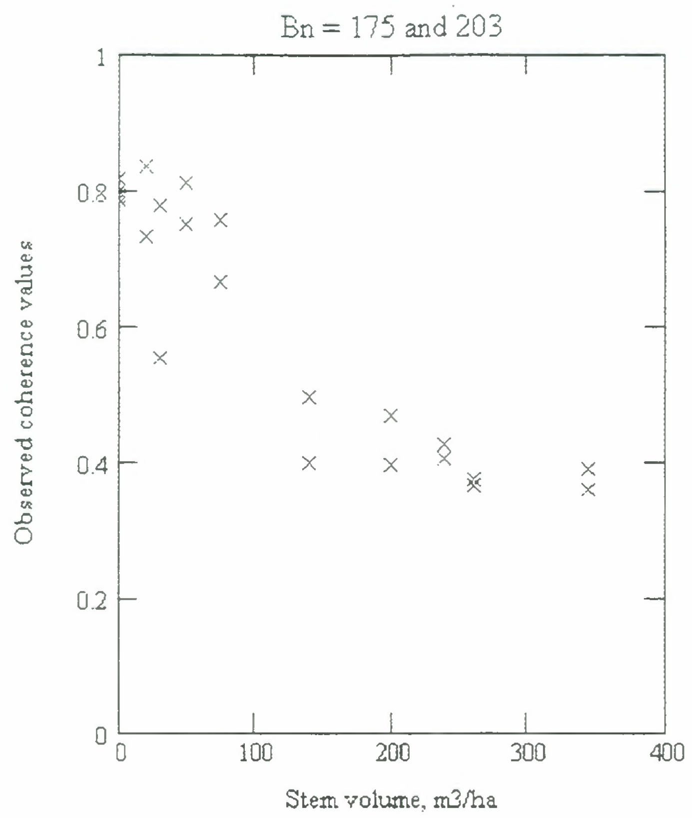

Figure 4. Illustrating coherence variations with stem volume, V. a) small baselines, b) medium baselines.

An interferometric phase shift relative surrounding open fields can be observed over forested areas. By comparison with the open field phase values or a DEM over the forested area an interferometric forest height can be determined. Results have been reported in (Askne et al., to be publ.). This information is as important as the coherence for classification of the forest properties. However, in this presentation we will concentrate on the variation of coherence as function of stem volume.

Interpretation of observations

INSAR system model

The interferometric SAR observations are dependent on system parameters (e.g. system noise and baseline), on processing steps (e.g. resampling), and medium (forest) properties. Assuming the processing of the images to affect the coherence negligible we obtain (Ulander and Hagberg, 1995)

$$|\gamma| = |\gamma|_{noise} \cdot |\gamma|_{spatial} \cdot |\gamma|_{temporal}$$

For reasonably high signal levels the noise part is also negligible. The spatial part includes decorrelation due to the surface and volume scattering. Of these the surface related part, the baseline decorrelation, can be corrected for by the technique in (Gatelli et al., 1994). All coherence values reported here have been corrected for baseline with local slopes determined by FFT analysis. The accuracy of the coherence measure is dependent on the resampling procedure, on the estimator properties, on correction for local topography etc. Further aspects are reported by Dammert in this conference. We will here concentrate on the variation of the volume and temporal decorrelation and investigate the coherence variations with stem volume.

INSAR scattering model

Models to determine the backscatter from forested areas have reached a maturity with the introduction of programs like MIMICS, (Ulaby et al., 1990a), and other similar approaches. Such models are useful for the forward model, but due to the number of included parameters the inverse model has to be based on observations from multi frequency, multi polarisation measurements. Including phase dependent interactions necessitates still further complex modelling and to obtain a more conceptual feeling for the influences of various factors we will return to a more basic and simple description of the radar backscatter model. the so called water cloud model. (Attema and Ulaby. 1978).Then the forest layer is described simply by a homogenous layer of scattering particles. The basic parameters in the model are the radar cross section and total attenuation cross section of each scattering "particle" in combination with the ground parameters. N is the number of particles per unit volume (here assumed proportional to the stem volume V).

However. in particular for sparse forests like boreal forests. radar scattering is obtained not only due to the radar wave penetrating the forest layer. but also through gaps in the vegetation (McDonald and Ulaby. 193). The water cloud model has been generalised to take this into account (Askne et al., 1995; Askne et al.. to be publ.).

The decorrelation due to changes in the scattering is the most complex aspect of repeat pass interferometry. Aspects of interferometric decorrelation have been described in e.g. (Zebker and Villasenor. 1992). Very little is known about actual mechanisms. In the forest case we anticipate there are decorrelation phenomena on various time scales. On the short time scale we have the effect of wind moving the scatterers in a random manner. in a relatively short time scale we can have dielectric constant changes e.g. due to rain and temperature transitions around the ice/water transition point. On the longer time scales we have e.g. the growth of the vegetation. man made changes. storm damages and fires. The temporal decorrelation affects the ground surface and the forest layer differently. For some of the effects meteorological information can help in the interpretation. and this is important for the future development of the technique.

Our model assumptions are suffering from lack of observations or accurate observations of some parameter values. The aim of the model is therefore not to make a detailed analysis in order to support the measurements. but to test what properties are important for understanding the measurements by comparing the model with measurements. By including a large number of parameters in a model observations can be adjusted to fit any observations. Instead we try to use as few as possible and limit these to such which are reasonably easy to estimate and observe independently. This also means that each parameter is a complex function of many important phenomena in a more detailed future model.

Forest parameters

For simplicity we will describe the forest by means of the stem volume. This is a parameter which can with high correlation be related to many other basic properties such as biomass. basal area. height. and age. In particular the relation to the forest height is important in an interferometric model.

In the water cloud model the forest properties are described in a statistical manner as a continuous layer of properties. This is in contrast to the clumping of properties of an actual forest. In our case we have included an area fill parameter to characterise the leakage of electromagnetic energy through small gaps in the canopy layer down to the ground level. The area fill factor is estimated in a few cases from site inspections and photographs. see Figure 1. We have also used results reported by (Pulliainen et al., 1994) where their transmissivity is interpreted as a combination of attenuation through the vegetation layer and the leakage through vegetation gaps. The area fill factor can be assumed to be climatologically dependent and smaller in northern parts of Sweden than in southern parts.

Decorrelation properties

For short baselines the temporal decorrelation dominates over volume decorrelation. We find forest coherence values between 0.30 and 0.45 over time intervals up to nine days. For middle range baselines (170 - 300 m) the coherence values are of the same order and we have found coherence values above 0.3 for time intervals up to 15 days. This make us believe that the temporal decorrelation dominates over volume decorrelation.

Of the various decorrelation phenomena we believe the wind decorrelation is most important. acting on time scales of minutes and shorter. The important aspect is the stability of those scatterers causing the major part of the coherent backscatter. which is believed to be branches in the upper part of the canopy. As the wind is affecting the top of the trees most in a forest. and the lower part of the stems very little. we model the decorrelation as a function increasing from the top downwards.

Long term changes have not been dealt with specifically in the model. However observations show that the coherence change with time and the backscatter difference between the image pairs increase with time. Such changes may be related to local storms combined with precipitation and also to temperature changes. These effects may also cause irreversible changes resulting in very low coherence in image pairs acquired on each side of such an occasion.

Attenuation through vegetation layer

To measure the attenuation of a vegetation layer is very complex due to the variability of the vegetation and due to speckle effect. Very few observations are known to the authors and we estimated the attenuation based on results from (Ulaby et al., 1990b; Fleischman et al., 1992; Seifert et al., 1995) and some MIMICS simulations.

Model properties

By testing the sensitivity of the model results to variations of the various parameters it is possible to estimate the importance of each parameter and then the importance of increasing our knowledge of each of these "effective" parameters. Model assumptions are illustrated in Figure 5, and will be further discussed in future papers, see also (Askne et al., to be publ.). Each one of the illustrated parameters needs to be further observed in the future.

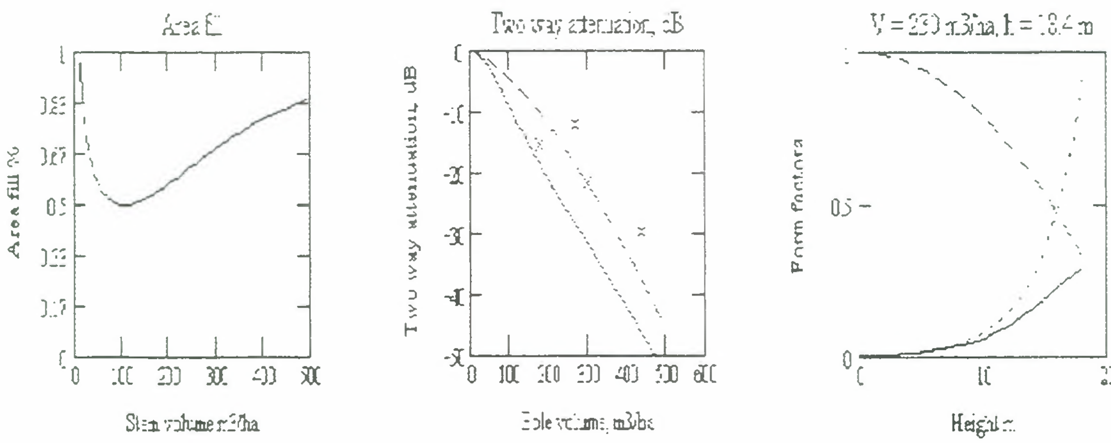

Figure 5 (a) area fill factor; (b) two way attenuation through the homogeneous vegetation layer, dotted line, and corrected for the denser vegetation by the area fill factor, solid line, x marks estimates from literature; (c) assumed temporal decorrelation factor due to wind (dash line), attenuation in a forest with a stem volume of 230 m^3·ha (dotted line), and the resulting effective layer (the product of the two previous factors) giving rise to the coherent scattering (solid line).

Results of model calculations and comparison with observations

Some results of the model calculations are given in Figure 6. The coherence is determined by a combination of the ground layer coherence (as observed by open fields in the forest) and a lower coherence for a dense vegetation layer. The vegetation coherence is determined by the temporal decorrelation effect and by volume decorrelation. Local topography is not taken into account but can also contribute. The relative importance of the ground component and the vegetation component is determined by the attenuation through the vegetation layer and the gaps in the vegetation layer. The coherence is typically decreasing with stem volume but may oscillate due to the interference between the two contributing factors.

The interferometric effective height is similarly determined by the interference of the scattering from the ground and from the vegetation layer. The effective height of the forest is typically increasing with the true volume, but the difference between the true height and the interferometric effective height can be quite large as function of stem volume and then coherence. The coherence values are obtained as a combination of the vegetation and ground part with a phase difference related to the interferometric phase. As this phase is very sensitive to actual conditions we have also illustrated the case with the two coherence parts combine constructively and destructively. This represents some upper and lower bounds on the coherence values. As seen in Figure 7 the observations fall within these bounds.

Feasibility of ERS-1/2 Interferometry for Forest Inventory

Juha Hyyppä	Helsinki University of Technology, Laboratory of Space Technology, Otakaari 5 A, FIN-02150 Espoo, Finland, hyyppa@ava.hut.fi
Marcus Engdahl	engdahlava.hut.fi o
Jarkko Koskinen	koskinenava.hut.fi
Mikko Inkinen	mjiavasun.hut.fi
Hannu Hyyppä	hyyppahava.hut.fi
Martti Hallikainen	hallikainenava.hut.fi

Abstract

The feasibility and usefulness of ERS-1/2 SAR repeat-pass interferometry for estimating forest resources is studied by applying the following strategy: a) interferometric SAR data (coherence and interferograms) are compared with field inventory data and HUTSCAT-derived stand profiles (tree height profiles) to evaluate what forest parameters can be estimated using SAR interferometry alone; b) interferometric SAR data (including interferometric correlation, backscatter intensity and backscatter intensity change) are combined with other potential satellite (Landsat, SPOT, RADARSAT and JERS-1) and airborne data (aerial photographs, image produced by a imaging spectrometer AISA and a 94-GHz imaging radiometer and forest stand profiles produced by a ranging scatterometer HUTSCAT) to test whether interferometric SAR data include additional explanatory power in developing remote sensing-based forest inventory methods.

Keywords: interferometry, ERS-1/2, forest inventory, multi-source.

Introduction

Forest inventory

Traditional forest inventory is both expensive and time-consuming. In theory, remote sensing methods offer a good alternative and/or a supporting method for traditional forest inventory and, therefore, the utilization of remote sensing techniques has been subject of intensive investigations during the past few years. Most of the developed satellite methods are based on the use of data obtained at visible, near-infrared or infrared bands. Poor availability of such data - due to the limited penetration capability (e.g. through clouds) at these wavelengths - hinders utilization of these methods. This has stimulated research towards the use of radar-based methods, especially since the launch of remote sensing satellites equipped with a synthetic aperture radar (ERS-1, ERS-2, JERS-1, RADARSAT). However, the reported accuracy of satellite-based methods for standwise stem volume estimates has been worse than 40 % irrespective of the spectral band used, Table 1. Hence, airborne measurements have been recognized as a potential tool for small-area inventories, while the aim of satellite-aided studies is mainly concentrated on large-area monitoring. For operational standwise inventory, even single-source airborne data may not be accurate enough. In order to meet the accuracy requirements (typically 15 %) of standwise forest inventory, data fusion, combining several remote sensing data sources, is suggested.

Table 1. Comparison of various methods for standwise forest inventory.

Method/Instrument	RMSE	Coefficient of variation
Ocular field inventory (Päivinen et al., 1993)	30 m^3/ha	16 %
Radar-derived stand profiles combined with aerial photography (Inkinen and Hyyppä, 1995)	29.4 m^3/ha	21.7 %
Radar-derived stand profile (Hyyppä, 1993)	31 m^3/ha	26.5 %
Imaging Spectrometer AISA (Mäkisara and Tomppo, 1996)	42.4 m^3/ha	29.8 %
Aerial photography (Päivinen et al., 1993)	55.6 m^3/ha	29.4 %
Landsat TM (Päivinen et al.,1993)	84.2 m^3/ha	44.5 %
ERS-1 SAR (Tomppo et al., 1995)	90 m^3/ha	58.4 %

SAR interferometry and forests

Recent advances in SAR interferometry include detecting subtle changes in the Earth's land and ice surfaces over periods of days to years with a global scale, millimeters accuracy and all-weather capability that are unprecedented. Recent examples illustrate how SAR interferometry can be applied to study glaciers (Goldstein et al. 1993), earthquakes (Massonnet et al. 1993), and volcanoes (Massonnet et al. 1995). SAR interferometry can be used to generate very-high-resolution topographic maps.

Gray and Farris-Manning (1993) reported a loss of coherence at both C- and X-band for forested areas under light to moderate winds (using airborne interferometric SAR) implying a degradation of performance with ERS-1 3-day orbit. Hagberg et al. (1995) found out that coherence was found to be sensitive to temperature changes around 0°C but surprisingly insensitive to wind speed. Hagberg et al. (1995) suggested also that tree height and density of forests can be estimated with interferometric phase information. There are three major phenomena that determine the effective volume scattering distribution of the forests (Hagberg et al., 1995): 1) attenuation of the canopy, which is assumed to be high for boreal forest at C-band, 2) the movements of the scatterers, which are assumed to be largest in the upper part of the trees, and 3) proportion of the area that are filled with trees.

The ranges of backscatter intensities over forests and agricultural fields overlap strongly. Therefore, it is difficult to distinguish between and within these two classes based exclusively on the backscattering intensity at C-band. The interferometric correlation, together with the backscatter intensity and the backscatter intensity change, has proved to a useful tool for the classification of the land-surface classes (Wegmüller et al. 1995).

A laser altimeter is a possible complement to any space-based SAR system. Combined laser or radar altimetry and SAR interferometry can show areas of clear-cutting as well as estimates of the rates of regrowth where extensive logging has occurred. This was the recommendation of 39 scientists gathered in Boulder, Colorado, on February 3-4, 1994, for the SAR Interferometry and Surface Change Detection (RSMAS Technical Report).

Objective

The main objective of the on-going project is to evaluate the feasibility and usefulness of ERS-1/2 SAR repeat-pass interferometry for estimating forest resources. The strategy is as follows:

a) interferometric SAR data (backscatter amplitude and its change, coherence and interferograms) are compared with field inventory data and HUTSCAT-derived stand profiles (tree height profiles) to evaluate what forest parameters can be estimated using SAR interferometry alone. The combination of ranging radar together with interferometric SAR images, as suggested in Boulder workshop, are studied for the first time. With this manner the idea proposed by Hagberg et al. (1995) can be verified.

b) interferometric SAR data (including interferometric correlation, backscatter intensity and backscatter intensity change) is combined with other potential multi-temporal satellite data (Landsat, SPOT, RADARSAT and JERS-1) and airborne data (aerial photographs, image produced by a imaging spectrometer AISA and a 94-GHz imaging radiometer and forest stand profiles produced by a ranging scatterometer HUTSCAT) to test whether interferometric SAR data includes additional explanatory power in developing remote sensing-based forest inventory methods.

Seasonal effects, optimum data combinations and interferometric SAR parameters are studied.

Special emphasis is in the evaluation of accuracy and cost-benefit analysis of interferometric SAR techniques compared to the present methods.

Material

Three test sites locate in southern Finland, Teijo (130 km west of Helsinki), Porvoo (30 km east of Helsinki) and Kalkkinen (130 km north of Helsinki) representing a variety of different forest types and covering about 10 000 hectares of forest land. Kalkkinen is the main area of activities with a large multi-source, multi-temporal remote sensing data set.

From the 5000-ha test site Kalkkinen the following information is collected:

- field inventory data (ground truth)
- remote sensing data
- GIS information

Field inventory data

Field inventory data is collected by Uudenmaa-Häme Forestry Center in summer 1996. About 100 parameters describing stand characteristics such as stem volume per hectare, basal area per hectare, mean tree height and tree species are measured for each stand (homogeneous forest areas of about one hectare in size). In order to evaluate the accuracy of field inventory, 40 stands were extremely carefully checked by sample plot measurements. The average value of the stem volume per hectare of the Kalkkinen test site is 141 m^3/ha.

Remote sensing data

The remote sensing data set includes satellite data from SPOT, Landsat, ERS-1/2 (Table 1), JERS-1 and Radarsat (SAR) and airborne data from imaging spectrometer AISA, airborne ranging radar (HUTSCAT), 94 GHz airborne imaging radiometer and digitized aerial photographs. The area was successfully measured by SPOT and Landsat satellites in the late August. Color-infrared photographs in a scale of 1:5000, 1:10000, and 1:20000 and imaging spectrometer measurements were conducted from Kalkkinen at the beginning of June. The remote sensing data will be collected by the end of October, with an exception of 94 GHz radiometer measurement, which is scheduled for early spring 1997 under wet snow conditions. The ranging radar HUTSCAT is capable to probe the canopy from the top to the bottom with range resolution of 65 cm. The HUTSCAT profiles are available in all three test sites. The tree-height-determining capability of HUTSCAT is used as a ground truth information for interferograms.

Table 1. ERS-1/2 product specifications

Sat	Quadr	Track	Orbit no	Frame	Date	SAR product type
ERS-1	3	408	20937	2367	17.7.1995	both SLC and PRI
ERS-2	3	408	01264	2367	18.7.1995	SLC
ERS-1	3	408	21438	2367	21.8.1995	both SLC and PRI
ERS-2	3	408	01765	2367	22.8.1995	SLC
ERS-1	3	408	21939	2367	25.9.1995	both SLC and PRI
ERS-2	3	408	02266	2367	26.9.1995	SLC
ERS-1	3	408	22440	2367	30.10.1995	both SLC and PRI
ERS-2	3	408	02767	2367	31.10.1995	SLC
ERS-1	3	408	23442	2367	8.1.1996	both SLC and PRI
ERS-2	3	408	03769	2367	9.1.1996	SLC
ERS-1	3	179	24215	2367	2.3.1996	both SLC and PRI
ERS-2	3	179	04542	2367	3.3.1996	SLC

GIS information

Additional information includes digital elevation model (DEM), digital land-use map and base map 1:20000. Air/soil/vegetation temperature and precipitation monitoring statistics in selected areas is also gathered.

Methods

After preprocessing (e.g. radiometric correction, geometric correction, geocorrection and orthorectification), the multi-source, multi-temporal remote sensing data is combined with GIS and ground truth data in ARC/INFO system. Standwise predictor variables are calculated using intensity, texture, band ratio transformations, and image processing techniques. Multivariate data analysis techniques are applied to develop models to estimate stand characteristics and biodiversity information.

Schedule

The project schedule is the following:

Preparatory work (January-May 1996)

- detailed experimental plan
- request for satellite images
- coordination of activities with Finnish Forest Research Institute and Forestry Centre Tapio (Uudenmaa-Häme Forestry Centre)

Data acquisition (June - October 1996)

- airborne measurements (HUTSCAT),
- airborne spectrometer measurement (AISA),
- aerial photographs

- acquisition of needed satellite images.
- collection of ground truth information

Preprocessing (September- December 1996)

- preprocessing of remote sensing data
- preprocessing of ground truth data
- production of interferograms and coherence images
- integration of data into database management GIS

Data analysis (January -October 1997)

- analysis based on interferometric data only
- combining interferometric fringes with radar profiles
- combination of optical and microwave satellite methods
- other development of methods and inversion algorithms
- cost-benefit analysis
- preliminary results reported

Reporting (September - December 1997)

- final report (ESA, Technology Development Centre, Academy of Finland)
    - papers submitted for several international journals

Anticipated results

The following results are anticipated from this project:

a) The HUTSCAT feature to produce tree height maps with an accuracy of 1.5 metres is used to evaluate the capability and accuracy of ERS-1/2 Tandem interferometric fringes to estimate tree height and density of forests, the idea proposed by Hagberg et al. (1995). As ground truth information, over 300 km of high-accuracy tree height maps are available.

b) Feasibility of a combined set of radar profilometry (HUTSCAT) and SAR interferometry to monitor areas of clear-cuttings, deforestation and defoliation as well as estimate rates of regrowth.

c) Feasibility of combined set of SAR interferometry, optical satellite images (SPOT and Landsat), radar satellite images (JERS-1 and Radarsat) and airborne images to estimates forest stand characteristics?

d) Estimation corcerning the smallest area for which the estimates can be computed reliably; examples are 1) the whole country or a part of the country (order of magnitude 10 million hectares), b) a forestry board district (0.5-1 million hectares), c) a municipality (50 000 hectares), d) forest holding.

e) Optimum interferometric parameters for forest inventory.

f) Suggestion of instruments needed for a forest inventory satellite mission.

g) Costs and benefits of the proposed methods.

References

Goldstein, R., Engelhardt, H., Kamb, B. and Frolich, R., 1993:
Satellite radar interferometry for monitoring ice sheet motion: application to an Antarctic ice stream. *Science*, **262**, pp. 1525-1530.
Gray, A.L. and Farris-Manning, P., 1993:
Repeat-Pass interferometry with airborne synthetic aperture radar. *IEEE Transactions on Geoscience and Remote Sensing*, **31**, pp. 180-191.
Hagberg, J., Ulander, L. and Askne, J., 1995:
Repeat-pass SAR interferometry over forested terrain. *IEEE Transactions on Geoscience and Remote Sensing*, **33**, pp. 331-340.

Hyyppä, J., 1993:
Development and feasibility of airborne ranging radar for forest assessment. Doctor of Technology thesis, Laboratory of Space Technology, Helsinki University of Technology, Espoo, Finland, 112 p.

Inkinen, M., and Hyyppä, J., 1995:
A forest inventory method by combining radar-derived stand profiles and aerial photography. *IEEE Transactions on Geoscience and Remote Sensing,* 10-14 July 1995, Firenze, Italy, pp. 1909-1911.

Massonet, D., Rossi, M., Carmona, C., Adragna, F., Peltzer, G., Feigl, K. and Rabaute, T., 1993:
The displacement field of the Landers earthquake mapped by radar interferometry. *Nature*, **364**, pp. 138-142.

Massonet, D., Briole, P. and Arnaud, A., 1995:
New insights on Mount Etna from 18 months of radar interferometric monitoring. *Nature* (in press).

Mäkisara, K., and Tomppo, E., 1996:

Airborne imaging spectrometry in national forest inventory. *Proceedings of IGARSS'96 Conference*, 27-31 May, 1996, Lincoln, Nebraska.

Päivinen, R., Pussinen, A., and Tomppo, E., 1993:
Assessment of boreal forest stands using field assessment and remote sensing. *Proceedings of Earsel 1993 Conference*, 19-23 April, 1993, ITC Enshedene, The Netherlands, 8p.

RSMAS Technical Report, 1995:
SAR interferometry and Surface change detection. Report of a Workshop held in Boulder, Colorado, February 3-4, 1994.

Tomppo, E., Mikkelä, P., Veijanen, A., Mäkisara, K., Henttonen, H., Katila, M., Pulliainen, J., Hallikainen, M., and Hyyppä, J., 1995:
Application of ERS-1 SAR data in large area forest inventory. *Proceedings of the Second ERS Applications Workshop*, 6-8 December, 1995, London, UK.

Wegmüller, U., Werner, C., Nüesch, D. and Borgeaud, 1995:
Land-surface analysis using ERS-1 SAR interferometry. *ESA Bulletin*, **81**, pp. 30-37.

The use of interferometric results with other remote sensing data in the EMAP-project

Manfred Reich — Universität Stuttgart Institut für Navigation Keplerstr. 11 70174 Stuttgart Germany
reich@nav.uni-stuttgart.de

Alois Wehr — Universität Stuttgart Institut für Navigation Keplerstr. 11 70174 Stuttgart Germany
wehr@nav.uni-stuttgart.de

Abstract

The purpose of the project EMAP (ERS-1/ERS-2 SAR DATA FOR MONITORING AGRICULTURAL LAND USE AS A LONG-TERM PROJECT) is to analyze ERS-1/-2 SAR data as a tool for agricultural crop monitoring. The focus is to apply the data for crop identification. This analysis is supported by combining ERS SAR data with optical satellite images and non remote sensing data in a Geographical Information System. The investigations are carried out in 4 different test sites in Germany, where we have intensive agricultural land use but different characteristics in land use. The aim is to detect parameters which significantly support the crop identification and classification process and to integrate these together in an expert system consisting of remote sensing data (optical and SAR) and GIS-information. The information extracted from interferometric processing of the SAR-data are the coherence properties as a function of seasonal changes in land use and the monitoring of agricultural land management activities by differential interferometry. Therefore the interferometric processing of ERS-1/ERS-2 SAR.SLC data can improve the quality of multi-sensoral / multi-temporal classification.

The EMAP-project started in April 1996. First results concerning the detection of changes in agricultural land use are presented. Our first results show that interferometric processing of ERS-1/ERS-2 SAR data and analysis of the resulting coherence images is an important step for the monitoring of the agricultural land use by remote sensing methods: No other remote sensing data can display the farming activities in a similar way. Also coherence information can improve classification accuracy especially in all cases where no data from optical sensors are available.

Keywords: crop classification, land use, coherence, GIS, detection of land-management activites

Introduction

The project EMAP (ERS-1/-2 SAR DATA FOR MONITORING AGRICULTURAL LAND USE AS A LONG- TERM PROJECT) is a ERS-1 project, which had been accepted by ESA and is financed by Deutsche Agentur für Raumfahrtangelegenheiten (DARA) and Bundesministerium für Ernährung, Landwirtschaft und Forsten (BML).

Principal Investigator of the EMAP-project is Prof. Kühbauch of the Institut für Pflanzenbau, University of Bonn. Project partners are the Institute of Navigation (INS), University of Stuttgart, the research centre for environment and health (GSF-PUC) Oberschleißheim and the Jena-Optronic GmbH (DJO) at Jena.

The purpose of this project is to analyze ERS-1/-2 SAR data as a tool for agricultural crop monitoring. The ERS-1 /ERS-2 satellites allow a continuous multitemporal monitoring of cultivated crop species. Within this project ERS-1/ERS-2 SAR.SLC data acquired in 35 days intervals at four important agricultural sites in Germany are used to identify crops and analyze crop cultivation practices, crop rotation and biomass development. These four sites represent areas with intensive agricultural land use but with different characteristics. For improving crop identification with ERS-1 /-2 radar image data it is necessary to decouple short-term effects on the radar backscattering resulting from non-crop parameters like rainfall, soil moisture or wind from those of the crops itself. For this reason the project is separated into short term and long term multitemporal investigations, which cover the development of a Geographical Information System (GIS) for the four test sites. The analysis is supported by combining SAR-data with optical satellite images and non remote sensing data contained in the GIS. The complementary use of ERS-1 SAR data, optical data and GIS information improves the reliability of the classification with exclusive optical data or only radar data. This is due to the fact that radar data are statistically independent from optical data. The interaction between incoming energy and scattered / backscattered electromagnetic waves by vegetation canopies and soil surface is quite different in the microwave and optical frequencies: Microwave backscattering is dominated by physical ground parameters like geometrical structure, water content, dielectric constants, polarisation etc. Scattering of optical waves is dominated by biochemical effects like photosynthesis. For this reason a combined classification should provide more accurate results with a better separation of different types of land use. The objective of our method for classification is to use only one optical scene per year combined with a multitemporal set of SAR scenes, which can be acquired independent from weather conditions and sun illumination. The high repetition rate of SAR image acquisition improves multitemporal data analysis and investigations.

Interferometric processing of the SAR-data is an important point in the EMAP conception: the main objective is to characterize coherence properties as a function of seasonal changes in land use of the cultivated areas. Tandem-pair scenes acquired at different dates are studied in terms of their coherence properties, which are related to their biophysical variations. Coherence images again provide information, which is independent from the information contained in the intensity images. They are therefore complementary to both radar intensity and optical intensity images. It could be shown that the interferometric results also allow the monitoring of agricultural land management activities. The various types of land management and the timing of the work on the soil is of particular interest for the expert system, which has to be developped by integrating radar and optical remote sensing data and ancillary data in a GIS.

Testsites

The investigations are performed at four different regions in Germany, which are characterized by intensive agricultural land use with significant different site characteristics:

1. Test site „Weilerswist" Lat: 50°39' - 50°48' North Lon: 6°45' - 6°55' East. The test site is located near Bonn/Germany. Very flat area with field sizes between 1 - 45 ha.(Test site of Institut für Pflanzenbau)
2. Test site „Ostalb" Lat: 48°30' - 49°02' North Lon: 10°09' - 10°30' East. The test site is located in Baden-Württemberg/Germany. It consists of different landscapes (hilly and flat).The field sizes are very small between 0.5 - 2 ha. The test site is characteristic for Baden-Württemberg. (Test site of INS)
3. Test site „Scheyern" Lat: 48°24' - 48°36' North Lon: 11°20' - 11°40' East. The test site is located in Bavaria / Germany between Munich and the Danube river. The size of the farm „Scheyern" is 150 ha. The farm is located within the center of a very hilly area. (Test site of GSF-PUC).
4. Test site „Buttelstedt" Lat: 51°01' - 51°07' North Lon: 11°16' - 11°' East. The test site is located in Thuringia / Germany. It is characterized by large field sizes.(Test site of DJO)

Each of the four test sites is surveyed by one of the EMAP-project partners as indicated above.

Ground Truth and Geographical Information System (GIS)

A crop survey has been performed on the basis of a 1:5000 scaled map, where the exact boundaries of each field were digitized and with the present crop type had been entered into polygon attribut table of GIS. Extra information as crop damage, soil erosion and other pecularities have also been identified parcelwise. In the case of test site „Ostalb" for example 2030 parcels with a total area of 3200 ha have been surveyed.

For 24 selected fields (6 fields for each of the four main crop types: winter wheat, winter barley, winter rape and corn) besides the above mentioned parameters other relevant parameters are registered and digitized to obtain a complete knowledge about these polygons for further investigations. These parameters can be devided in three groups:

1. Data registered at each acquisition date: growth stage of plants (phenology, ear angle), plant height, fresh and dry biomass of plants and crop products, soil moisture, leaf area index, moisture on leaf surface.
2. Data collected through farmer interview: sowing date ,sowing density, row direction, interrow distance,

number of plants per squaremeter, pecularites of cultivations (e.g. deseases, soil compaction) practice and dates for tillage, spraying pestizides fertilizing, rotation scheme, yield.
3. Ancillary information: official digital cadastral map (ALK = Automatisierte Liegenschaftskarte), official soil map (soil classification), meteorological data, digital terrain model.

Additional ground truth data acquisitions in between two consecutive ERS-1 acquisitions have been foreseen during the period of May and July, where we have very rapid changes in the vegetation state.

Most of these data have been entered in the polygon attribut table of GIS. The GIS had been adapted to the regional needs for a sucessful crop monitoring for each of the four testsites separately. Further input parameters are boarders of countries and municipality, official digital topographic information (ATKIS = Amtliches topographisch kartographisches Informationssystem), phenological data of the main crops, meteorological an agro-ecological data.

These data are used for spatial intersection within GIS and satellite imagery for further analysis.

ERS-1 / ERS-2 data selection and pre-processing

ERS-1 / ERS-2 tandem data and ERS-2 data have been ordered in 35-days intervals as SAR.SLC scenes for all 4 test sites between April and November 1996. Similar data requests are planned for 1997 and 1998. (ERS-1 data have only be made available until 3rd of June 1996). Additional SAR-Images already acquired between 1991 and 1994 are available at INS for the test sites „Weilerswist" and „Ostalb". These provide information about crop species cultivated on the same fields in the past years. This is important because the current agricultural management practices use a specific sequence (crop rotation), which could be analyzed using these data.

Several filter methods have been tested to reduce the speckle effect in the SAR-intensity images. A modified GMAP filter (Lopes et. al, 1993) has been selected for final filtering with a filter size of 7 x 7 pixels. The geocoding of the SAR.SLC data as well as for the interferometric image products using digital terrain models of the test site areas is performed by DJO for all EMAP-project partners.

ERS-1 radar intensity signatures and their influences on land use classification

To analyze the radar signatures of agricultural fields in ERS-1 SAR images the mean grey values of more than 560 test fields were analyzed in the case of „Ostalb" test site. Ground truth information about the field area and vegetation type of these fields were taken from the GIS. A mean value of all pixels was calculated for each of these fields, where pixels containing the field edge were eliminated.

The analysis showed large variations of mean grey values of fields belonging to the same vegetation type. Variations in mean grey values of fields belonging to the same vegetation type are due to differences in the biophysical parameters, responsible for the radar response of an agricultural field. These could be differences in soil moisture content and soil roughness, where the vegetation canopy is not dense enough to block contributions of the soil surface to the backscattering characterics of the field. Other biophysical parameters of the vegetation canopy are volumetric density of plant, water content, size and density of the individual scatterers and the height of the vegetation canopy. These parameters change the radar response throughout the development stages of the vegetation. There are of course field to field variations of these parameters because of different growing conditions.

To get a better understanding we used radar backscatter models to simulate the different influences. One important result of these studies was: Due to the very steep incidence angle of the ERS-1 the vegetation canopy of agricultural fields can only block the contribution of the underlying soil, when the vegetation cover is dense enough and not dry.

Obviously this is only the case during a short period before the plants get ripe and dry. Only then the vegetation dominates the intensity of the radar return. However besides these, there are other influences on the radar backscatter intensity:

1. the influence of the field orientation towards the SAR sensor, i.e. the actual fluctuation of sensor look angle due to the topography. Field slopes reach values up to +/- 6 degrees from the horizontal plain. This could lead to backscatter intensity variations of up to 5 db. Corresponding fluctuations in mean

grey values had to be analyzed and corrected.

2. the influence of the orientation of plant rows relative to the SAR-sensor. In the early development stage of the plants significant variations in grey values could be observed (Müller et. al., 1993) depending on the row direction of the plants, which resulted in higher grey values if the row direction is parallel to the ERS-1 flight path and in lower grey-values for row directions perpendicular to the flight path.

Conventional Maximum Likelihood Classification (ML) has been tested using multitemporal radar data together with one optical scene for validation areas (see Fig. 1) in the southern part of the „Ostalb" test site (Hartl et. al., 1995). The non agricultural areas (red = urban, dark green = forest, light green = grassland) have been masked and the corresponding pixels were not used for the classification.

A separation between the vegetation types is not possible, if only multitemporal ERS-1.SAR images are used for classification.This is the case although the filtered radar intensity images (combined to a multitemporal colour composite) show some structural information about the land use (Fig. 2). We could only separate with an accuracy of about 80 % between two groups: one group consists of winter wheat, summer barley and oat and the other one of winter barley, rape and corn.

However, if one optical scene (Fig. 3) is used together with the 3 multitemporal SAR images shown in Fig 2 in a combined classification, the separation of the six main crop types was possible with limited accuracy. However the accuracy is better than with the optical data alone. A 10 % average increase of separation accuracy for the most important crop types was achieved in comparison to optical classification. Tab. 1 shows the confusion matrix of the results achieved with the combined classification.

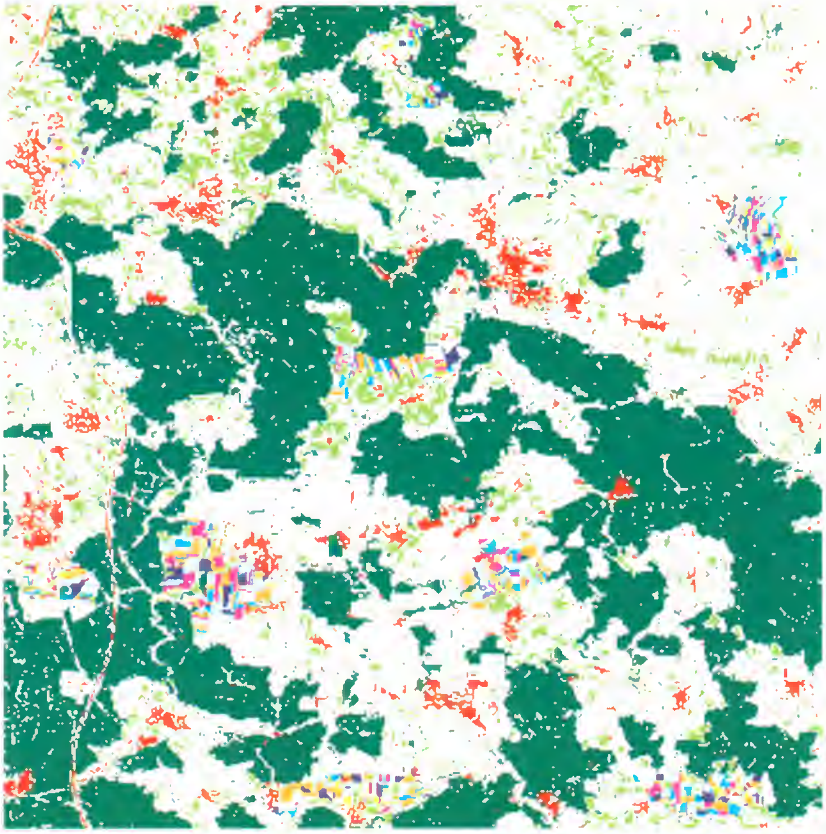

Fig 1: Test site „Ostalb": Detailed ground truth derived from inspection and implemented in the GIS is available in several test areas. Sealed areas (red), forest (dark green) and grassland (light green) has been separated by masking.

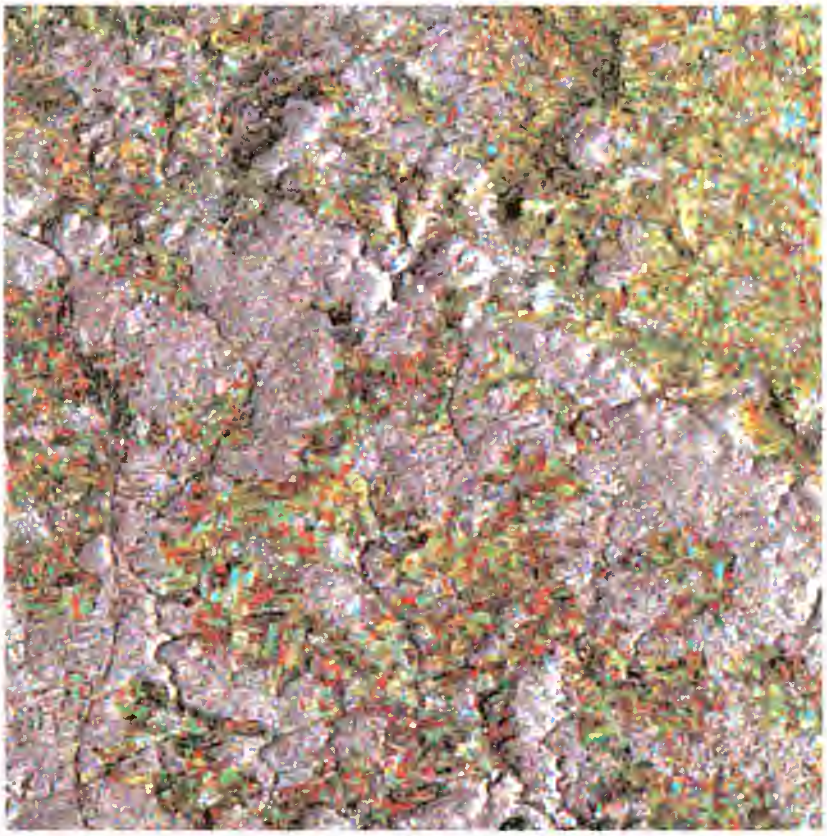

Fig. 2: Multitemporal colour composite of the 3 SAR-images used for classification

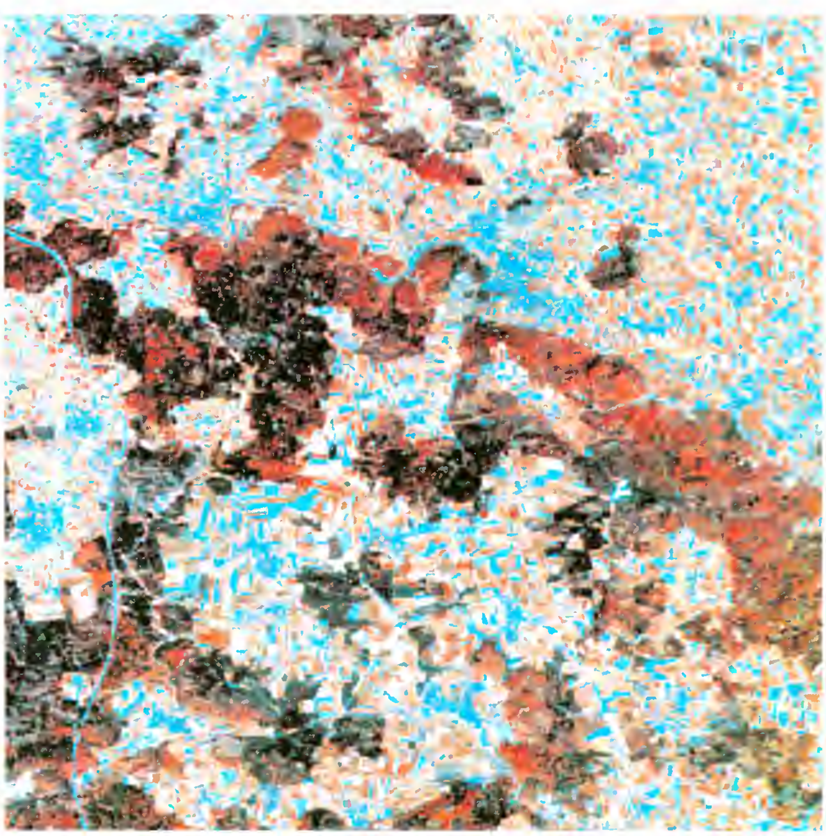

Fig. 3: Optical image of „Ostalb" test site

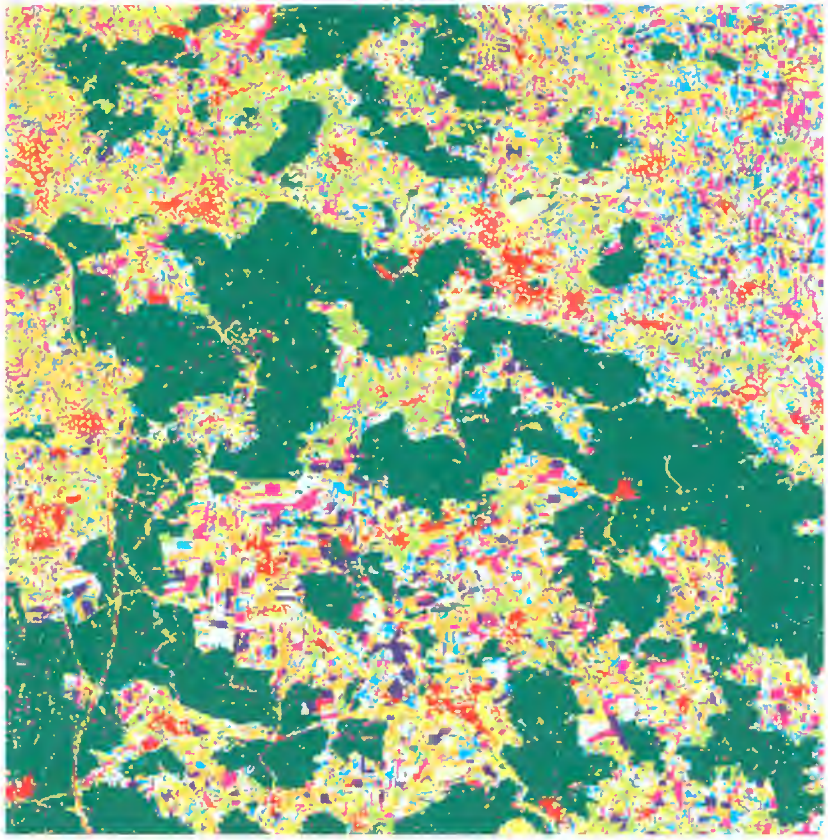

Fig. 4: Result of Maximum Likelihood classification

Tab. 1: Result of Maximum Likelihood classsification for validation areas

vegetation type	pixels class.as:	WW %	WB %	SB %	OAT %	RAPE %	CORN %
winter wheat	51477	**56.08**	11.30	11.37	18.62	0.77	1.79
winter barley	24015	15.09	**57.21**	11.29	12.71	1.81	1.82
summer barley	37727	3.87	6.52	**67.77**	17.15	2.66	1.98
oat	9327	20.75	10.39	26.60	**34.75**	1.01	6.43
rape	19802	0.30	1.06	6.16	7.17	**84.55**	0.72
corn	25484	0.45	0.62	2.39	12.78	0.88	**82.48**
sum	167832	36062	23356	38442	27028	18895	23870

average accuracy: 63.81%
overall accuracy: 65.05%
Kappa coefficient: 57.32%

The classification results are shown in Fig. 4. The results suffered from the extremely small field sizes in some parts of the test site. Other classification methods using neural network classifiers (Benedictsson et. al., 1990),(Foody et. al., 1995) have been tested for the same data. However no significant improvements were detected. Better results could be achieved with all classifiers, if only field sizes of more than 1 ha and 50 m width are taken into account.

It could be shown that post-classification with majority filter based on known geometry of agricultural fields in the validation areas increases the overall classification accuracy about 20 %. Nevertheless the achieved accuracy is disappointing, but having in mind the above mentioned results of the radar backscatter analysis one can understand that the classification accuracy, which can be achieved with multitemporal ERS-1 / ERS-2 intensity must be limited. For that reason the phase information contained in the ERS-1/ ERS-2 images, which could be extracted by interferometric processing of the SAR-data, should be used to improve these results.

Interferometry

Interferometric processing of the SAR-SLC data has been foreseen to analyze the coherence properties as a function of seasonal changes in the land use of cultivated areas in all four test sites. Especially TANDEM-data with only 1 day interval between the acquisitions have been selected for this purpose, because decorrelation due to vegetation changes have often been the reason for poor results in the past. The data of all 4 test sites are processed at INS making use of the INS-ANTIS (Schmidt, 1995) interferometry system, which is based on PCI-EASI-PACE image processing system software. The interferometric processing is an important part of the EMAP-project because of the additional statistically independent information about land use and because farmers activities can be extracted from coherence and relative phase images. To demonstrate these capabilites, a series of 10 consecutive ERS-1.SAR.SLC images of the Bonn test-site, taken during the second ice-phase has been analyzed by INS. These images were sampled in 3 days intervals. We have therefore good coherence between two consecutive images. Coherence images have been produced for the following pairs with acquisition dates:

TAB 2: ERS-1 image pairs used for generation of coherence images

SAR-IMAGE 1 DATE	SAR-IMAGE 2 DATE	COHERENCE IMAGE NR
01.03.1994	04.03.1994	COHERENCE IMAGE 1
04.03.1994	07.03.1994	COHERENCE IMAGE 2
07.03.1994	10.03.1994	COHERENCE IMAGE 3
10.03.1994	13.03.1994	COHERENCE IMAGE 4
13.03.1994	16.03.1994	COHERENCE IMAGE 5
16.03.1994	19.03.1994	COHERENCE IMAGE 6
19.03.1994	22.03.1994	COHERENCE IMAGE 7
22.03.1994	25.03.1994	COHERENCE IMAGE 8
25.03.1994	28.03.1994	COHERENCE IMAGE 9

The nine coherence images generated with each of these pairs are quite similar to one another. They show the following general effects:

Forest areas and highways show up as dark areas, i.e. as areas with low coherence. For forest areas thisis quite clear due to decorrelation effects caused by the vegetation. For the highways, no coherence could be detected, because the amplitude of the reflected signal is too low. Agricultural fields appear in general quite bright, but in all images there are always some fields which appear dark, i. e. with low coherence. These are the fields, where we expected that coherence was lost due to farmers activities during the time between the two datatakes of each pair. An interrogation of farmes about their farming activities on the fields which showed low coherence gave us the confirmation: In all cases the reason for the loss of coherency could be identified as some kind of farming activities as ploughing the fields in the time gap between the 3 days interval of the two ERS-1 acquisition of the corresponding image pair.

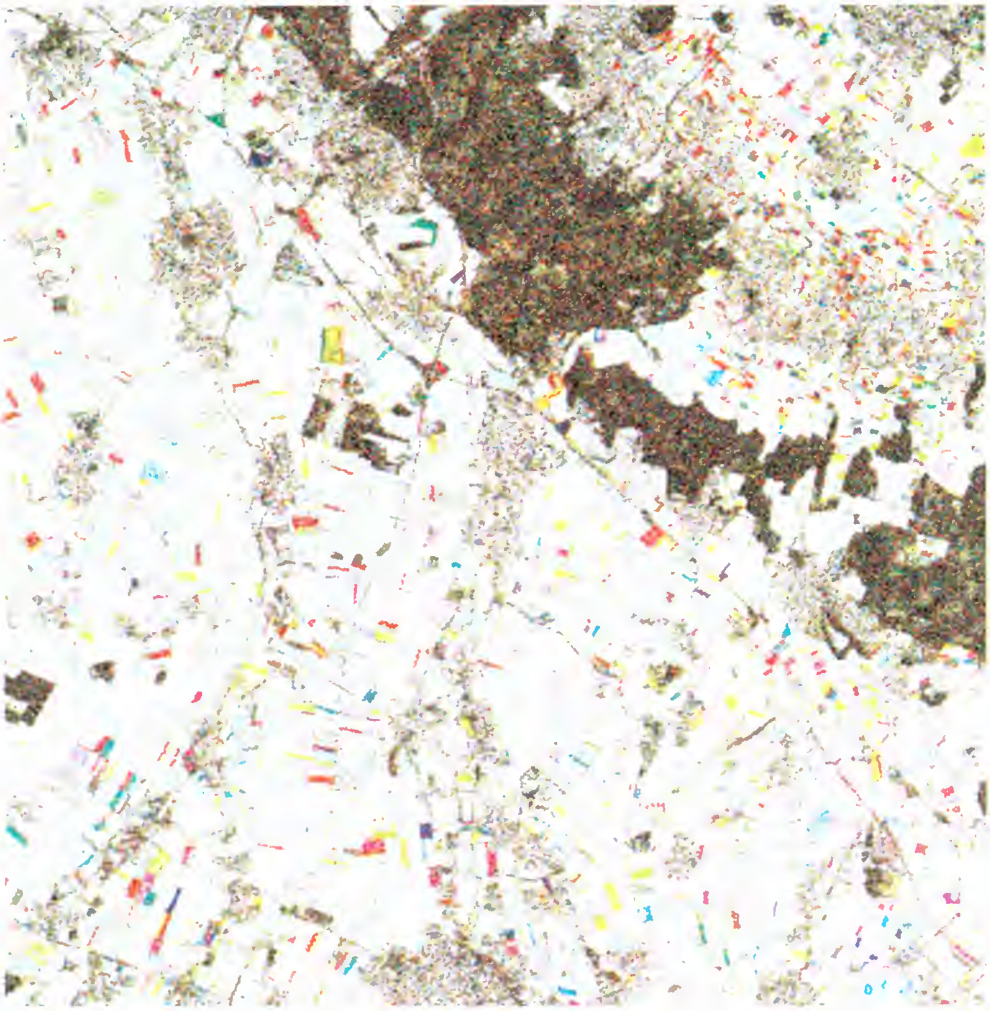

Fig. 5: Coulor composite of 3 coherence images of the „Weilerswist" test site
red = coherence image 3 (07.03.1994 ÷ 10.03.1994)
green = coherence image 4 (10.03.1994 ÷ 13.03.1994)
blue = coherence image 5 (13.03.1994 ÷ 16.03.1994)

To show up the farmers activities in a very condensed way over a longer period we produced a multitemporal colour composite image of 3 of our 9 coherence images, where the coherence of the pair taken on 07.03.1994 + 10.03.1994 is shown in red, the pair 10.03.1994 + 13.03.1994 in green and the pair 13.03.1994 + 16.03.1994 in blue colour. The result is given in Fig.5. All fields with similar coherence grey-values in all three channels, i. e. with no change in coherency over the whole period from 07.03.1994 to 16.03.1993 appear as non coloured black and white pixels. The different coloured fields of Fig. 5 result from different grey values in the 3 channels. The red have low coherence in the green and blue channel, i. e. the farming activities must have taken place between 13.03.1993 and 16.03.1993 and between 16.03.1993 and 19.03.1993. Yellow fields are the fields with no coherence in the blue channel, i. e. farming activities in this case have taken place after 13.03.1994.

Not only farmers activities, but also meteorological effects or changes in the vegetation can be the reason for decorrelation. However these effects must have been neglectable in our case, because the vegetation canopies in March are still very low and we had a short time interval between two ERS-1 datatakes.

Fig. 6 to 8 show three coherence images of the „Ostalb" test site, where a series of 3 ERS-1/ERS-2 tandem-pairs have been used. Fig. 6 is quite similar to the series of nine coherence images of the „Weilerswist" test site. Agricultural fields appear quite bright, since only few vegatation is present at that timeof the year. Also only very few fields can be detected as fields with farming activities. Fig.7 and even more Fig.8 show a more datailed structure of the agricultural fields with all levels of coherence values between 0.1 and 0.7-0.8. Fig. 8 shows a field structure pattern similar to an optical remote sensing image. In this case the low coherence values for many of the fields are due to the vegetation canopy and not due to the farmers activities.

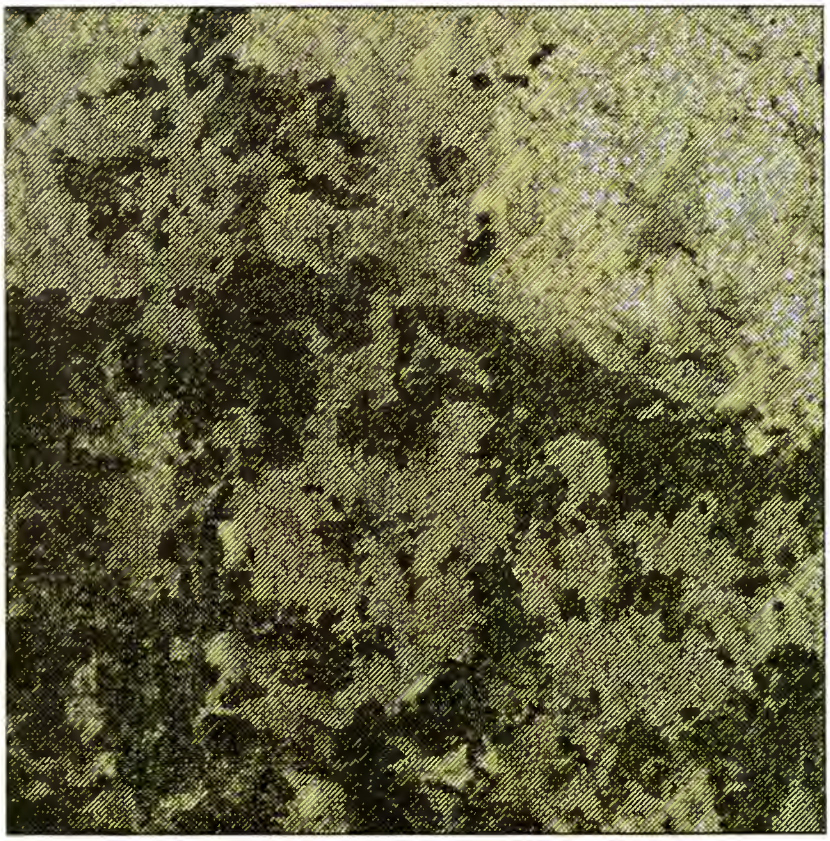

Fig. 6: Coherence image ERS-1 23.03.96 / ERS-2 24.03.96
Test site „Ostalb"

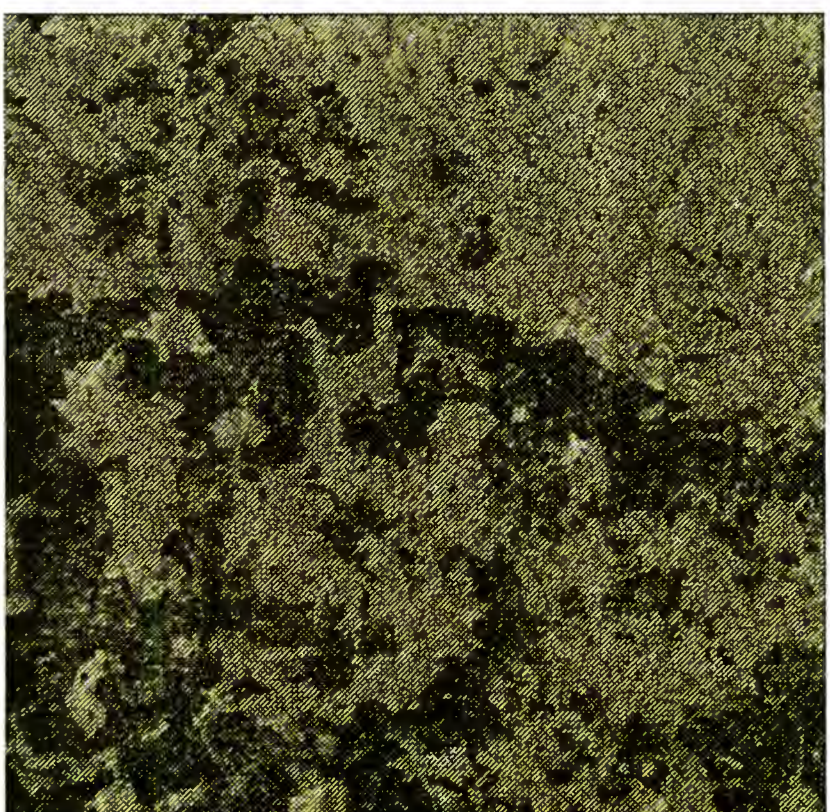

Fig. 7: Coherence image ERS-1 27.04.96 / ERS-2 28.04.96
Test site „Ostalb"

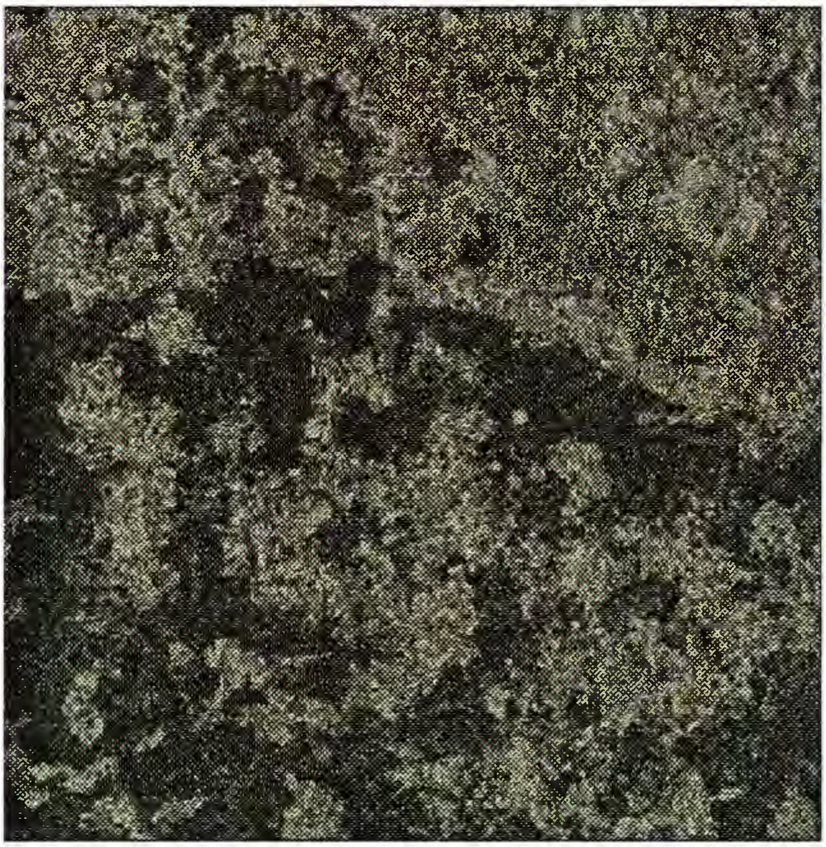

Fig. 8: Coherence image ERS-1 01.06.96 / ERS-2 02.06.96
Test site „Ostalb"

Conclusion

The additional information extracted from coherence images can further improve the accuracy of land use classification using multitemporal ERS-1/ERS-2 data together with one optical scene. In general coherence is one additional channel in feature space, statistically independent from optical and radar intensity channels. The degree of coherence, if not degraded by systematic effects (large baselines, different zero doppler frequencies in processing the data) is sensitive to the vegetation. High coherence values indicate that no decorrelation due to the vegetation canopy had taken place. This is the case for bare soil conditions and for thin and/or dry vegetation canopies, where the vegetation has only little influence on the radar backscatter. On the other hand low coherence values are not always the result of a dense or wet vegetation canopy, which is blocking the radar returns from the ground. Also farmers activities on bare soil, if they took place between the acquisitions of the corresponding image pair can result in a full decorrelation. One has to be careful when applying coherence images as additional channels for conventional classification methods. Fields, where the low coherence is due to farming activities have to be excluded from the automatic classification using coherence information. However these fields can easily be identified. Also the detection of farmers activities can be helpful for classification, because the knowledge of field activities at a certain time of the year allow the agricultural experts to extract information about the type of vegetation. However to make use of this information a more sophisticated system is necessary rather than conventional ML- or NN- classification methods.

Nevertheless our first results show that interferometric processing of ERS-1/ERS-2 SAR data and analysis of the resulting coherence images are an important step for monitoring of agricultural land use by remote sensing methods: No other remote sensing data can display the farming activities in a similar way. Also coherence information can improve classification accuracy especially in all cases where no data from optical sensors are available. It seems that coherence information extracted from a tandem.SAR acquisition taken in the middle of the vegetation period can substitute the information containecd in an optical remote sensing image.

References

BENEDIKTSSON J.A., SWAIN P.H., and ERSOY O.K.: Neural network approaches versus statistical methods in classification of multisource remote sensing data. IEEE Transactions on Geoscience and Remote Sensing, 28, 540-551, 1990.

FOODY G.M., MCCULLOCH M.B., YATES W.B.: Classification of remotely sensed data by an artificial neural network: issues related to training data characteristics. Photogrammetric Engineering and Remote Sensing, 61(4), 391-401, 1995.

HARTL PH., GÜTH S., KLAEDTKE H.-G., PALUBINSKAS G., REICH M., WÖRZ K.: Land use classification of agricultural fields with multitemporal ERS-1 SAR data and optical remote sensing data. Proceedings of the second ERS Applications Workshop, London U.K. 6 - 8 December 1995, ESA SP-383.

LOPES A., NEZRY E., TOUZI R., LAUR H.: Structure detection and statistical adaptive speckle filtering in SAR image. International Journal of Remote Sensing, 14(9), 1735 - 1758, 1993.

MÜLLER U., LÖCHERBACH TH., KÜHBAUCH W., FÖRSTNER W.: Suitability of ERS-1 SAR PRI-Data for multitemporal agricultural land -use mapping. Proceedings of the second ERS-1 Symposium, Hamburg Germany, 1993, ESA SP-361.

SCHMIDT J.: Antarktisches Interferometrie System ANTIS Benutzerhandbuch Version 1.0, Internal Report of the Institute of Navigation, University of Stuttgart, Stuttgart,111 pages, 1995.

Assessment of land cover mapping potential in Africa using tandem ERS interferometry

B. Mumford, J-P Muller, A. Mandanayake,
Department of Photogrammetry & Surveying, University College London, Gower Street, London. WC1E 6BT, U.K.

Abstract

Accurate mapping of land cover types is essential to a number of scientific disciplines, in particular environmental monitoring. This goal relies on accurately calculating the extent of changes in surface cover such as forest. Recent research shows that ERS tandem interferometry products, especially phase coherence may be related to land cover type.

Traditional ground based methods of land cover mapping are prohibitively expensive due to the large areas involved. Optical satellite remote sensing methods are more appropriate but require cloud-free conditions for data to be useful. In tropical areas cloud free acquisitions can be rare reducing these sensors' applicability to such studies. ERS interferometry data can be acquired day and night irrespective of weather conditions and the introduction of ERS-2 means tandem scenes are imaged just 24 hours apart. These factors coupled with the wide coverage available means that ERS tandem interferometry offers an exciting alternative to optical sensors for land cover mapping.

In this study ERS tandem data are acquired and processed over the HAPEX-SAHEL area in Niger to which SPOT XS, Landsat TM and ATSR2 data are also available. The geocoded coherence maps are compared to land cover maps produced from the above sensors and a classified image produced. A quantitative analysis of the land cover maps shows high correlation between the vegetated classes. This analysis demonstrates clearly the viability of using tandem interferometry data in the evaluation of land cover types.

The study shows the huge potential of ERS tandem interferometry not only as a source of topographical information but also as a way of accurately monitoring changes in surface cover.

Keywords: tandem interferometry, phase coherence, land cover, optical methods

Introduction

The production of land cover maps from remotely-sensed images has always been perceived as one of the greatest contributions which satellite earth observations could make to both scientific and commercial exploitation of these data.

Since the launch in 1972 of the US ERTS-1 (renamed LANDSAT) programme, scientists have been using optical and near-infrared data to obtain 30m-100m resolution land cover maps. More recently from the LANDSAT-TM and SPOT-XS sensors.

The objectives here are to assess the potential of ERS tandem interferometry to provide an alternative source of land cover information for a semi-arid environment. Existing optical-NIR have poor land cover mapping quality in these environments due to their inability to deal with low Leaf Area Index areas (LAI<2). The clear advantage of this approach is it could permit land cover maps to be produced at anytime of year irrespective of cloud cover which is very high particularly during the rainy season when the Inter-Tropical Convergence Zone is present. It may also be used to validate land cover maps produced using coarse resolution sensors such as AVHRR [*Loveland et al.*, 1991] and ATSR-2 [*Higgins*, 1995] as well as exploring scaling and generalisation issues [*Barnsley et al.*, 1995]

Results are presented of a quantitative comparison between a land cover map derived using SPOT-XS, LANDSAT-TM and ERS SAR interferometric results. The method used to obtain the SAR interferometric results is briefly described together with an analysis of the results.

Data-Set Description

Both the SPOT-XS and LANDSAT-TM scenes were acquired on 25 September 1992. Details of these scenes as well as the HAPEX-SAHEL experiment can be obtained from *Prince et al.,* 1995. Unfortunately, due to the limited availability of ERS tandem data from the Libreville, Gabon Receiving Station, only a dry season data-set was acquired which would have much greater amounts of bare earth present (see later). The location of the HAPEX-SAHEL test site is shown below (Figure 1) as well as a close up showing the processed area and the location of the anciliary data (Figure 2).

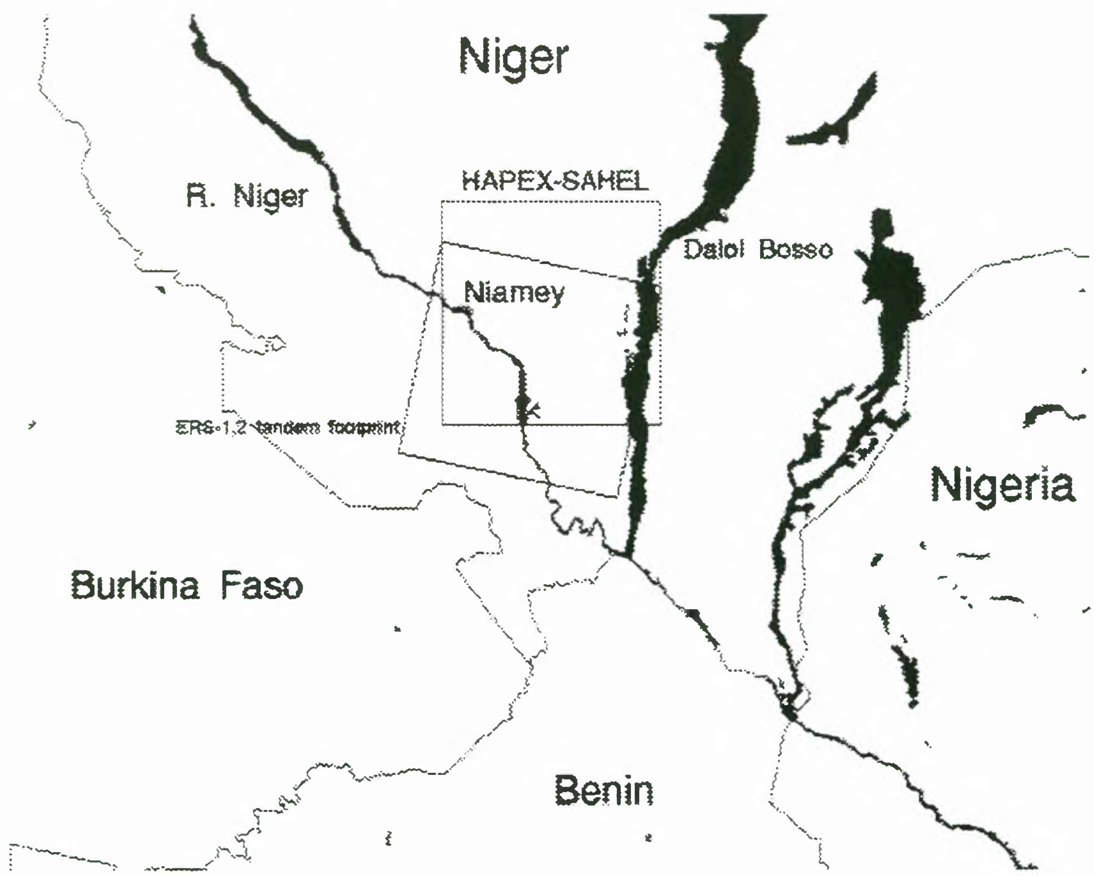

Figure 1. Overview map of the HAPEX-SAHEL study area using DCW map vectors

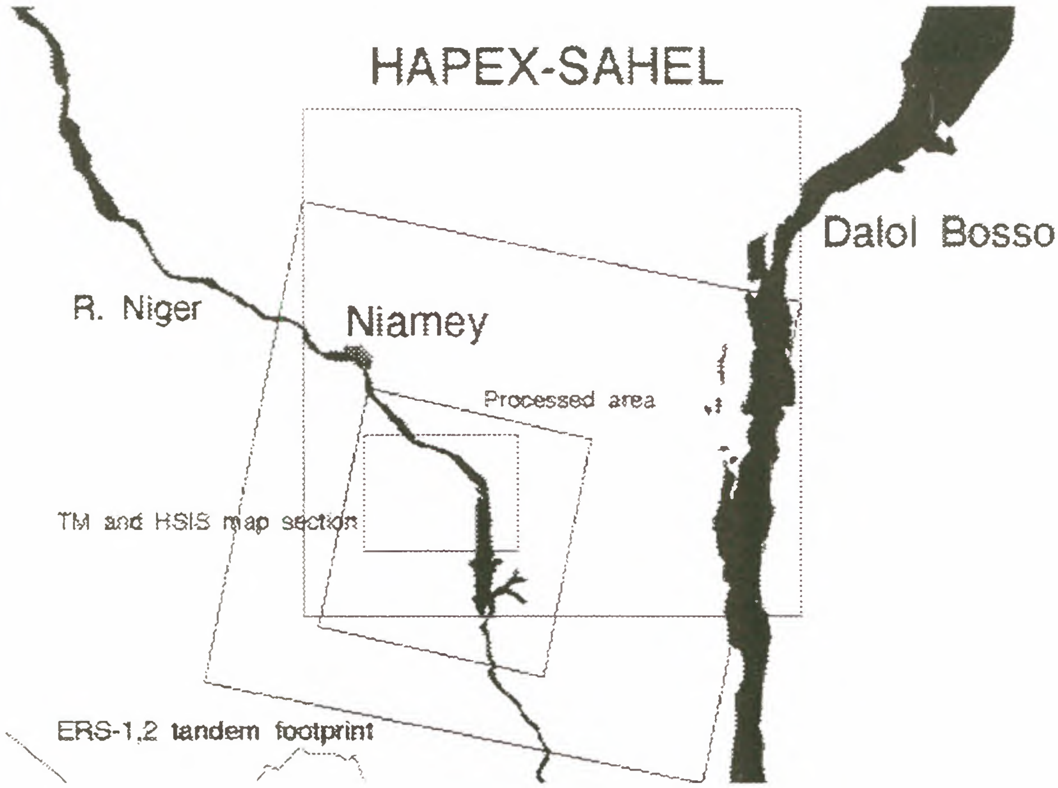

Figure 2. Close up of area in Figure 1 showing data sources used and test area

The details of the ERS tandem pair are given below in Table 1.

Area label	ERS	Orbit	Frame	Date	Latitude extent	Longitude extent	Bperp in m
HAPEX-SAHEL	ERS-1	24974	3339	24-April-96	12.67-13.82N	1.80-3.00E	102
HAPEX-SAHEL	ERS-2	5301	3339	25-April-96	12.67-13.82N	1.80-3.00E	102

Table 1. Characteristics of the ERS tandem pairs used for land cover mapping.

Method

An area of the full ERS-1,2 scene was selected for processing based upon the availablity of ground truth data from the HAPEX-SAHEL experiment. The commercial EDS-PulSAR system was used to focus the RAW data into an SLC product and further software was used to produce an interferogram and coherence image. In-house UCL software [*Muller et al.*, this proceedings] was used to flatten the interferogram and geocode to a (lat,lon) grid using a 30 arc-second (~1km) DEM together with the precision state orbital vectors from the D-PAF. The tandem pair had a perpendicular baseline seperation (Bperp) of 102m which meant the elevation difference implied by a whole phase cycle was 92m. This resulted in well spaced fringes which appeared easily unwrappable (see Figure 3).

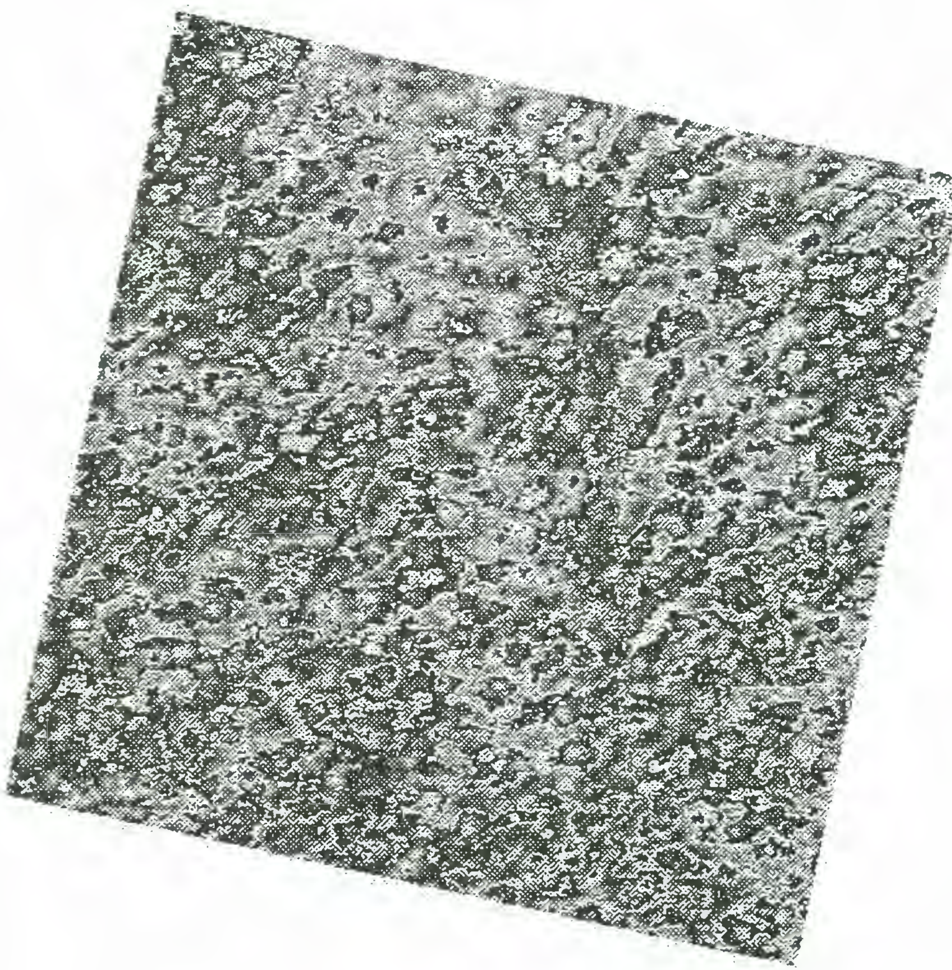

Figure 3. UCL-IfSAR geocoded flattened fringe pattern using 30 arc-second DEM (C) UCL/ESA 1996

The phase coherence image (Figure 4) and histogram (Figure 5) computed show that the phase coherence values are high enough for our application.

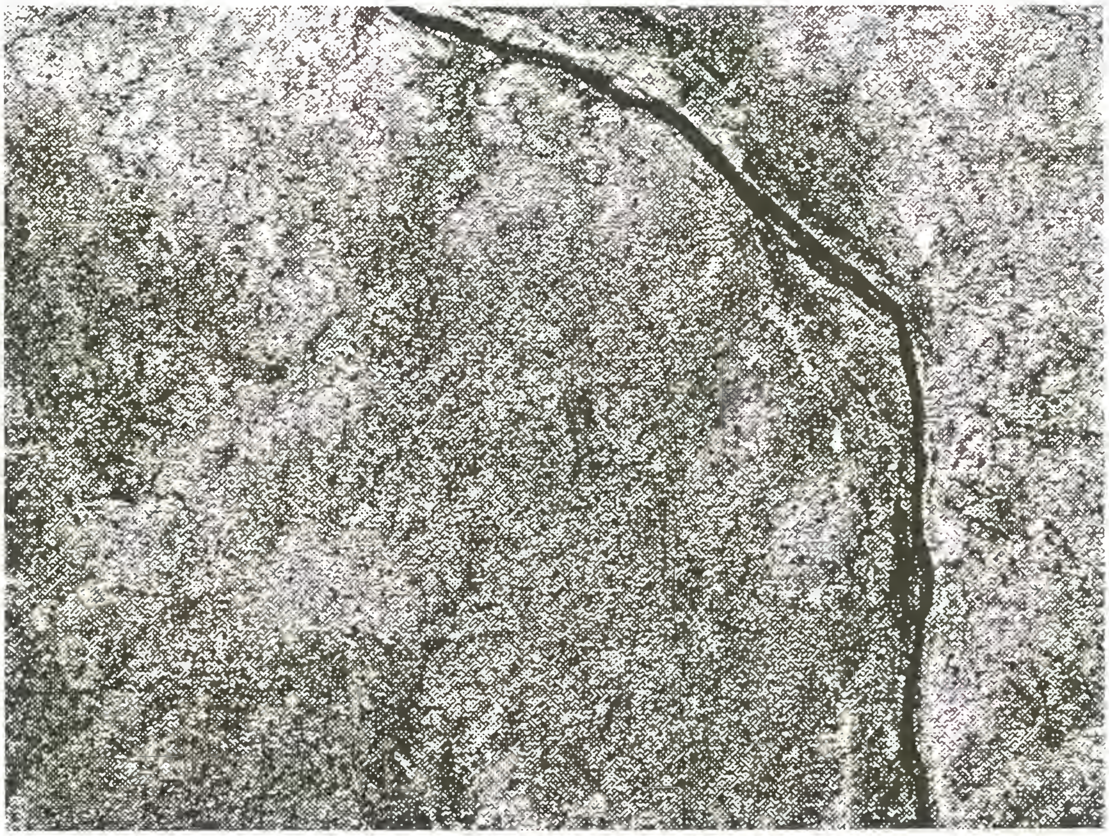

Figure 4. Phase coherence image for test area (C) UCL/ESA 1996

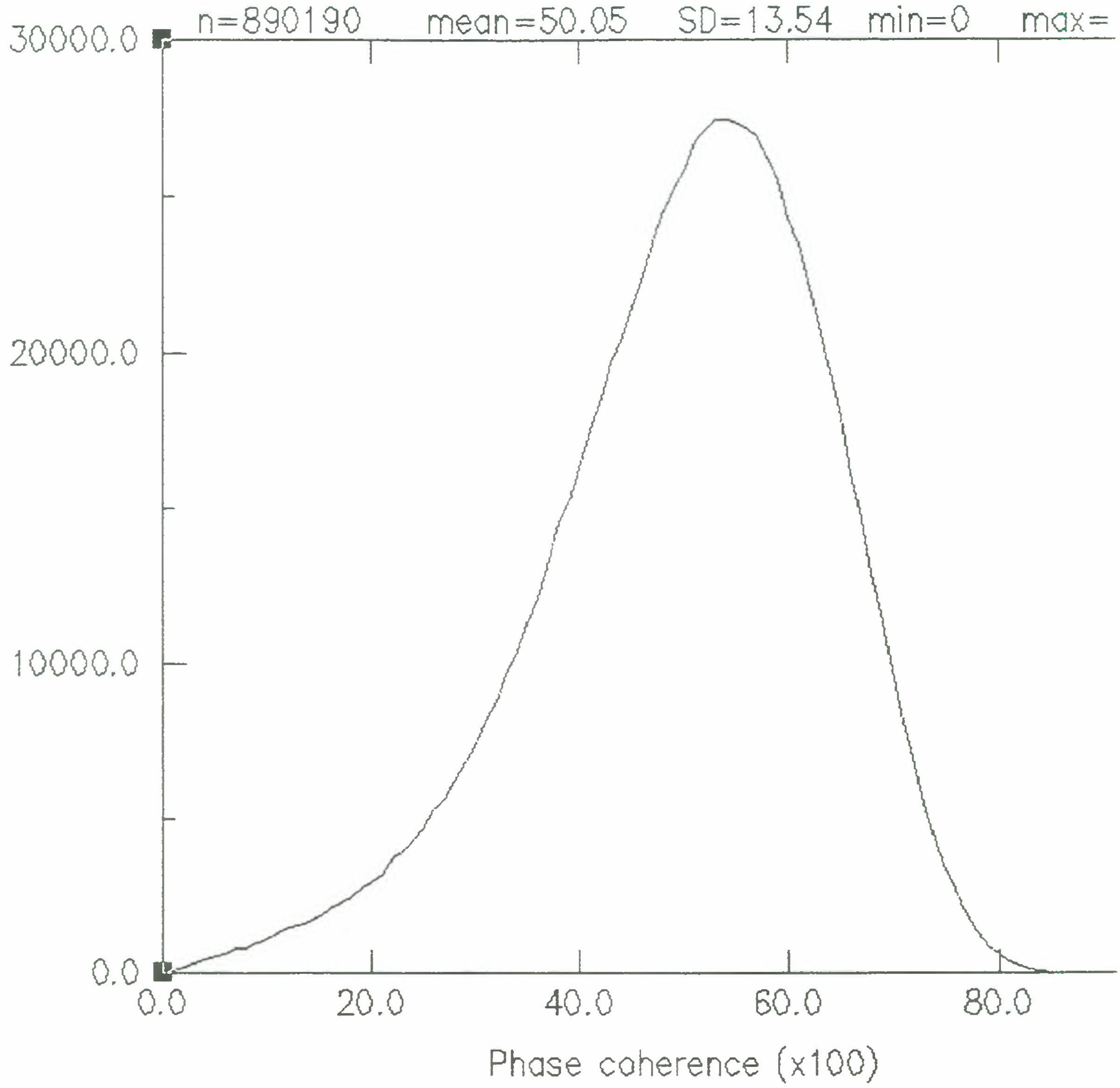

Figure 5. Phase coherence histogram for test area (C) UCL/ESA 1996

The UCL-IfSAR system for unwrapping is similar to that described by [*Goldstein et al.*, 1988] with the additional use of the coherence image to prevent unwrapping in areas of very low coherence. The residues were first calculated and then opposite-signed residues were linked to produce branch cuts which must not be crossed during unwrapping. Although it is possible to unwrap an interferogram using just a single phase seed point, some 25 seed points were chosen throughout the interferogram. These seeds were chosen by allocating a 'zeroth' fringe and then counting up or down the fringes depending on the grey scale gradient. Having joined the residues and produced a seed point file the algorithm was used to integrate the phase values throughout the interferogram and produce absolute values without the 2PI ambiguity inherent in the interferogram. The unwrapped interferogram was analysed visually in order to determine if any obvious blunders had occurred which would need further seed points to correct. Since there were no obvious blunders the unwrapped phase values were converted to heights using the coarse DEM and the orbital trajectory data and another UCL algorithm (see Figure 6).

Figure 6. UCL-IfSAR hill shaded DEM using 30 arc-second DEM for phase flattening (with overlay box showing test area) (C) UCL/ESA 1996

The ERS-1 and ERS-2 amplitude images were terrain geocoded to the same (lat,lon) coordinates of the coherence image (see Figures 7 and 8). A rectangular section enclosing all available data sources was selected for further analysis (see Figure 6 for location).

Figure 7. ERS1 amplitude image for test area (C) UCL/ESA 1996

Figure 8. ERS2 amplitude image for test area (C) UCL/ESA 1996

An amplitude difference image was then computed and is shown in Figure 9.

Figure 9. Amplitude difference image for test area (C) UCL/ESA 1996

The considerable speckle noise present in these images was considered potentially damaging to classification accuracies. *Pratt* (1978) suggested the use of a median filter in order to reduce speckle. A 5x5 kernel was selected after investigating the speckle-supression and edge-retention characteristics of a 3x3 and 7x7 kernel. *Wegmueller and Werner,* 1995 suggest the construction of a false colour composite using the coherence, a single data amplitude and amplitude difference images in order to facilitate visualisation of the thematic information contained within the various SAR products. A schematic diagram of this proposed method is shown in Figure 10.

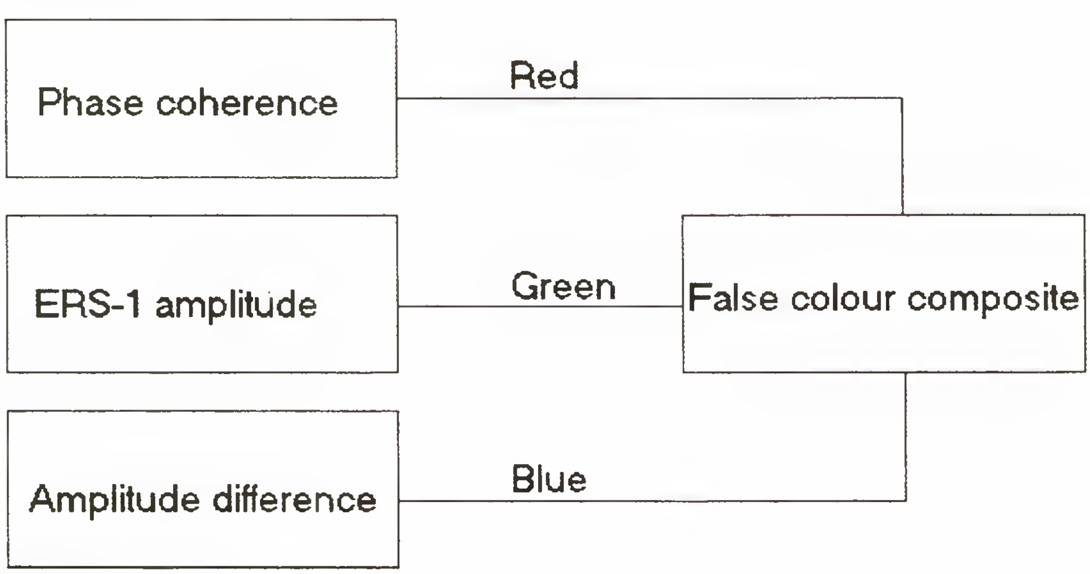

Figure 10. Wegmueller and Werner proposed false colour composite procedure

Such a composite was produced using the geocoded SAR products described above (see Figure 11).

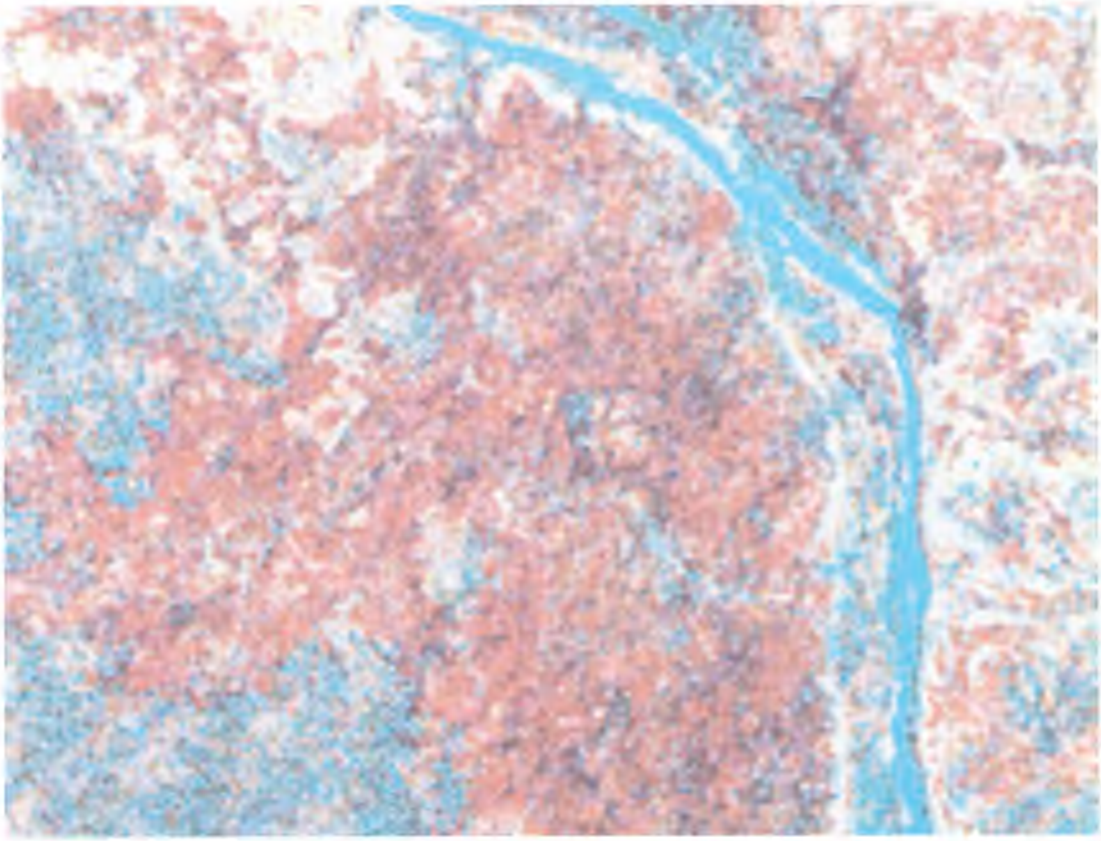

Figure 11. False colour composite using colour scheme shown in Figure 10. (C) UCL/ESA 1996

The false colour composite (Figure 11) showed several distinct classes and presented good evidence on its own of the land cover capabilities of IfSAR. A 50-class ISODATA unsupervised classification was then performed using ERDAS-IMAGINE on the dataset in order to enhance the class information present in the image in line with the classification procedure shown below in Figure 12.

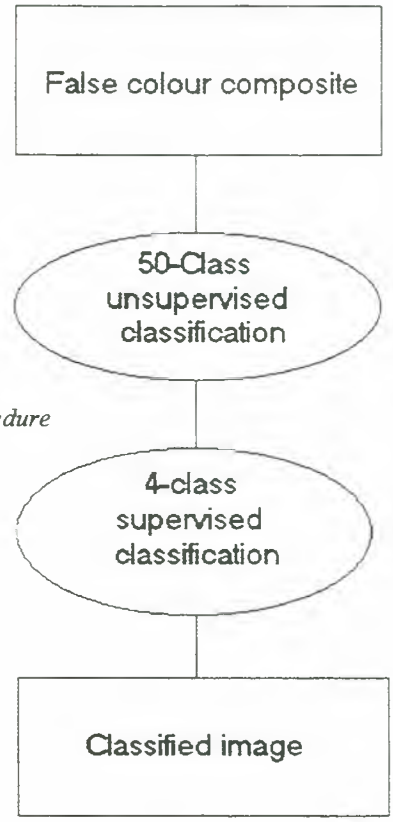

Figure 12. Overview of classification procedure

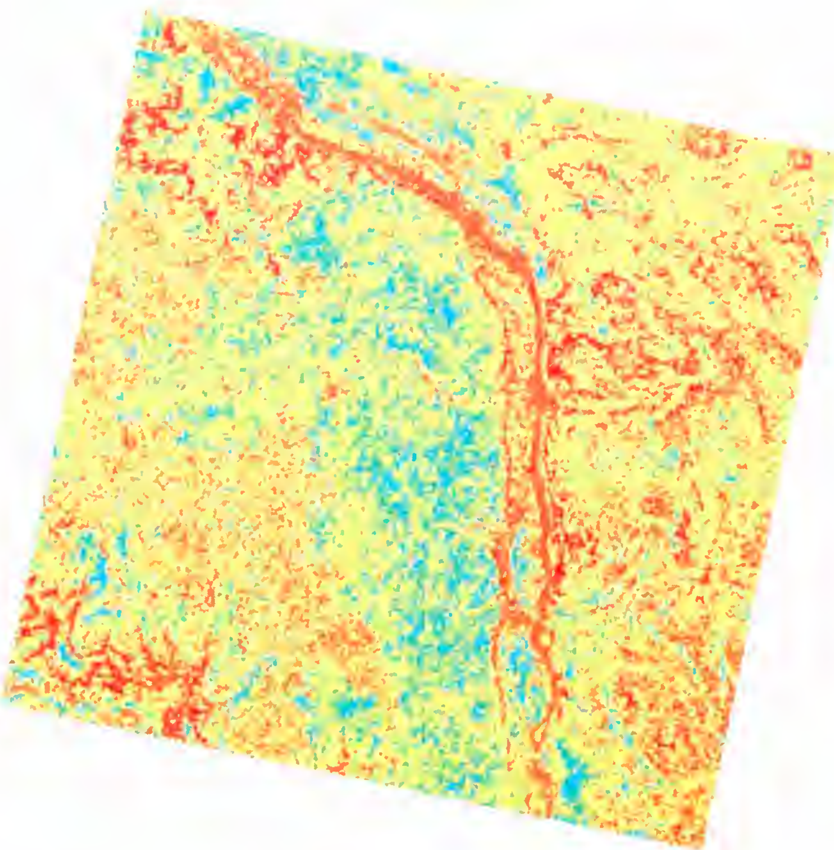

Figure 13. Unsupervised classification of SAR datasets (C) UCL/ESA 1996

The result of this classification helped in the selection of 4 training areas for a maximum likelihood supervised classification shown in Figure 14.

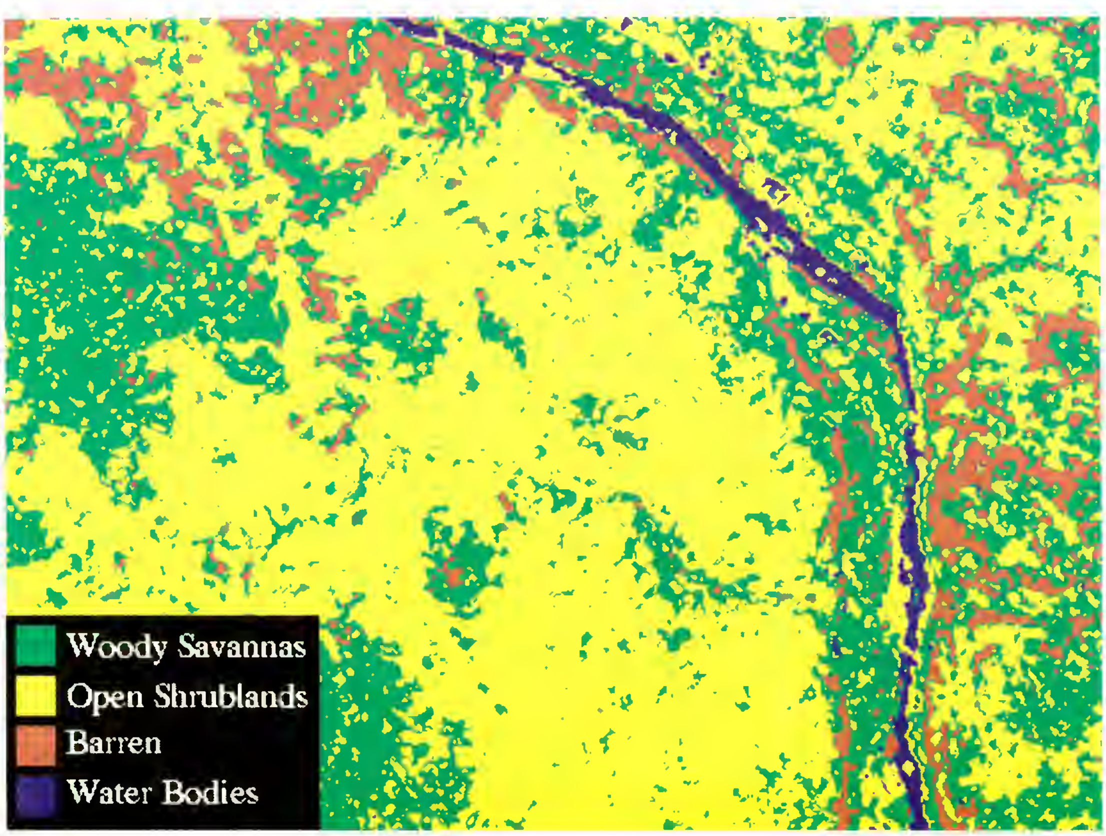

Figure 14. Supervised land cover classification map of SAR with colour key (C) UCL/ESA 1996

A land cover map produced in 1992 using SPOT-XS data acquired on September 25th 1992 as part of the HAPEX-SAHEL experiment [*Prince et al.*, 1994] was downloaded from the HSIS www site (http://www.orstom.fr/hapex/index.htm) (acknowledgement J.M d'Herbes, C. Valentin, B. Mougenot). The map which was derived using supervised classification was originally in 6 classes as shown in Table 2 below.

Class	Description	% woody	%grassy
1	Woody vegetation	25-75	10
2	Bare soil	0	0
3	Shrubby savanna	10-35	25-75
4	Grassy vegetation	<5	20-50
5	Light vegetation	<10	<10
6	Free water	N/A	N/A

Table 2. Original classes of the HSIS map

The 6-class map was reduced to 4 classes which correspond to the IGBP classification scheme [*Belward and Loveland*, 1995]. Classes 3, 4 and 5 were merged, producing the final classification scheme shown in Table 3 and in Figure 15.

Class	Description	%woody	%grassy
1	Woody savannas	25-75	10
2	Barren	0	0
3	Open shrublands	5-35	10-50
4	Water bodies	N/A	N/A

Table 3. HSIS classes after merging to 4-class IGBP scheme

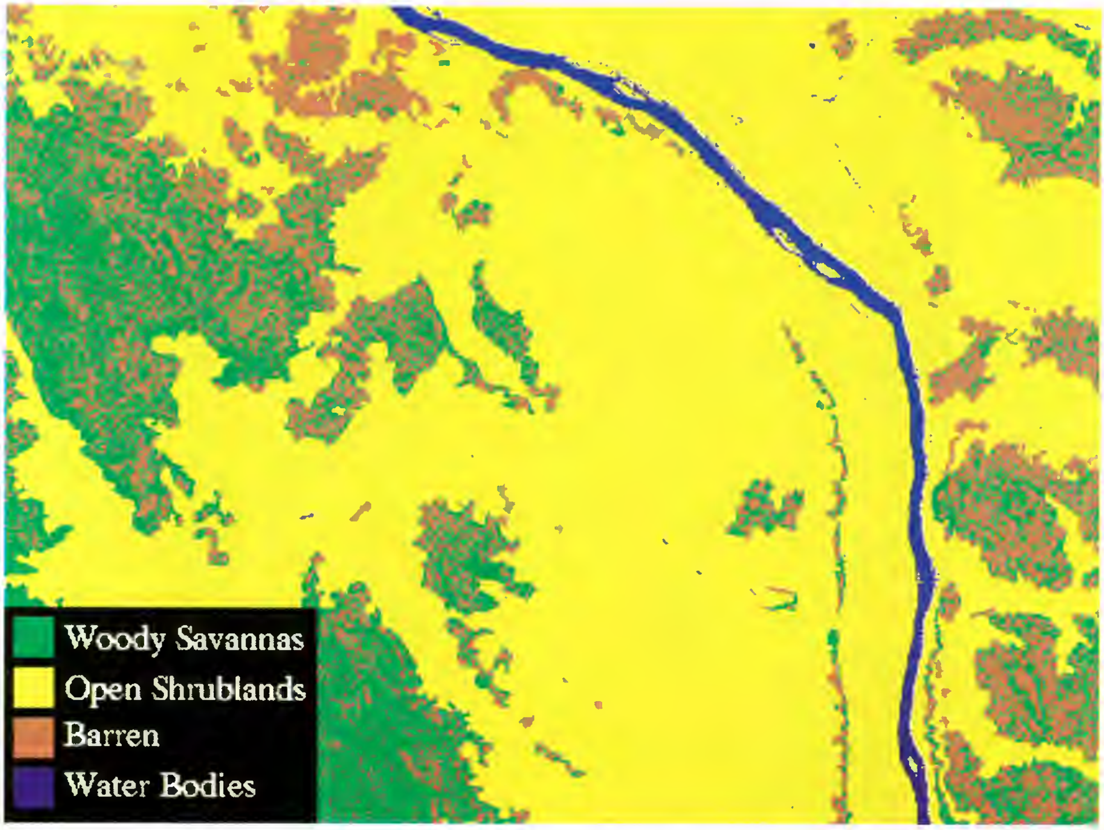

Figure 15. Supervised land cover classification map of HSIS with colour key

The map was registered to the radar imagery using a cubic transformation with some 10 ground control points. A section of a 7-band Thematic Mapper scene was available and this was registered to the same (lat,lon) coordinates as the IfSAR products in the same way as the HSIS map. A 50-class ISODATA unsupervised classification was performed on the 6 non-thermal bands in order to help select 4 training areas for a maximum likelihood supervised classification (Figure 16).

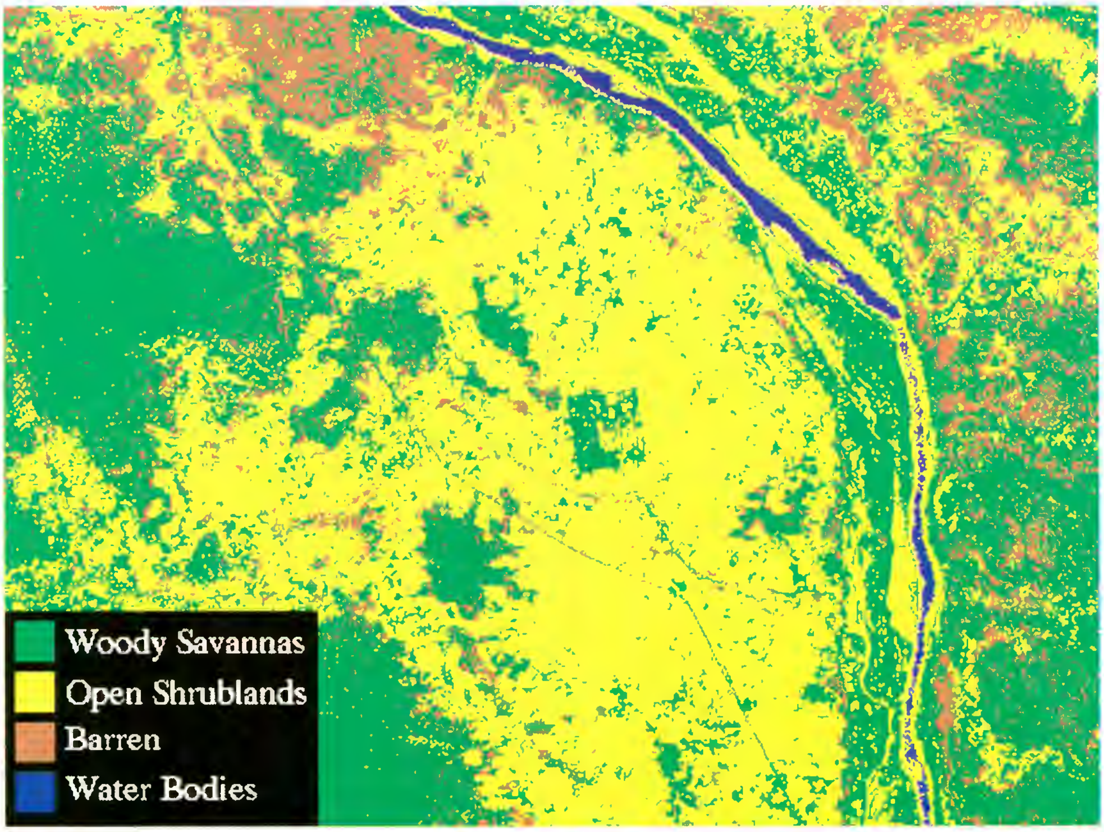

Figure 16. Supervised land cover classification map of LANDSAT-TM with colour key

The footprints of the three data sources were not identical which necessitated the selection of a rectangular area enclosing all three sources for further analysis. The HSIS map was treated as a reference source and the common areas in the radar and TM classifications were extracted.

Congalton, (1991) recommended random stratified sampling in order to fairly assess the accuracy of classifications based on remotely sensed data. 40,000 random stratified samples (representing approx. 5% of the pixels present in the area selected for quality assessment) were selected from the reference dataset. Error matrices were then produced using the radar and TM classifications (see next section). The correlation between the radar and TM classifications was also directly assessed. The construction of error matrices allowed a simple statistical analysis of the classification accuracies to take place.

Results

WS= woody savannas, BA= barren, OS=open shrublands, WB=water bodies.

Table 4 below shows the error matrix computed for the SAR classification using HSIS as the reference source. HSIS classes are along the top, SAR classes are down the side.

WS	BA	OS	WB	
6697	2724	4316	36	13773
343	1247	767	15	2372
2797	1623	18834	130	23384
3	1	143	365	512
9840	5595	24060	546	

Table 4. Error matrix for radar classification using HSIS as reference

PRODUCER'S ACCURACIES: 68%,22%,78%,67%
USER'S ACCURACIES : 49%,53%,81%,71%
OVERALL ACCURACY: 68%

The producer's accuracies show the proportion of reference pixels correctly identified by the radar classification. The user's accuracies show how many pixels labelled a particular class by the radar classification actually are that class in the reference data. The two measures together are extremely useful as they give the commision and omission errors. For example, a map could be produced where every single pixel was labelled as `barren'. A simple test of the producer's accuracy for `barren' would give a figure of 100% - no omissions. However, the user's accuracy would reveal the true nature of the classification by showing the huge commision errors.

The figures for the radar classification are reasonable with the exception of `barren' - with producer's and user's accuracies of 22% and 53% respectively. The overall accuracy of 68% is encouraging however despite being weighted considerably by the good results for the large `open shrublands' class. The HSIS map was produced using imagery acquired during September, when vegetation is at a maximum. The radar imagery was acquired at the height of the dry season and therefore the classification results are expected to differ considerably.

WS	B	OS	WB	
7078	3417	4053	8	14556
1920	1860	3530	3	7313
842	318	16471	130	17761
0	0	6	364	370
9840	5595	24060	505	

Table 5. Error matrix for TM classification using HSIS as reference

Producer's accuracies: 72%,33%,68%,72%
User's accuracies : 49%,25%,93%,98%
Overall accuracy: 64%

Table 5 above shows that the barren class is again very badly represented in both omission and comission errors. The user's accuracies for `open shrublands' and `water bodies' are extremely high indicating that these classes had a very distinct profile in the TM imagery.

Table 6 below shows the error matrix computed for the SAR classification using TM as the reference source.

WS	B	OS	WB	
8631	2589	2552	1	13773
1162	939	271	0	2372
4732	3775	14789	47	23343
31	10	149	322	512
14556	7313	17761	370	

Table 6. Error matrix for radar classification using TM as reference data

Producer's accuracies: 59%, 13%, 83%, 87%
User's accuracies : 63%, 40%, 63%, 63%
Overall accuracy : 62%

This error analysis indicates that there is virtually no correlation between the areas marked as barren in the TM and radar imagery. The other classes are well correlated and the overall accuracy is fair.

Discussion and conclusions

The land cover maps produced using SAR interferometry show high correlation with both the LANDSAT-TM and SPOT-XS results for the vegetated classes. The differences may partly be due to the different times of year (this is particularly true for the barren class which are much higher for the SAR than the other two satellite-produced maps) and partly due to the fact that the SAR senses the volume scattering from within the vegetation canopy [*Gatelli et al.*, 1994] as opposed to the response of the vegetation at different spectral wavelengths at optical/NIR wavelengths.

SAR interferometry has been shown to be an extremely effective method, from a single date of obtaining land cover information in a semi-arid environment. A quantitative assessment was made of SAR-derived land cover using the IGBP classification scheme using both SPOT-XS and LANDSAT-TM as "ground" truth. For vegetated and water classes the correlation was high whereas for barren the SAR consistently shows a greater coverage.

Further studies are underway to assess the land cover potential of IfSAR over other areas in Africa including wetlands (Morley & Muller, this proceedings), savannah and tropical forested areas as well as within Europe. Reports on these experiments will be made in upcoming Florence meeting.

Acknowledgements

Ben Mumford acknowledges receipt of a NERC Advanced Course studentship (GT3/95/140/E0) for a Master of Science programme in Remote Sensing. This work was supported by BNSC under the Application Development Programme with Logica Space Systems and by NERC under the framework of the TIGER-SVATS project. Finally, ERS raw data was supplied under the ESA data grant (AOL.UK201).

References

Barnsley, M.J., S.L. Barr, and T. Tsang. (1995). Producing large-area land cover maps from satellite sensor images: scaling issues and generalisation techniques., in *Environmental Remote Sensing from regional to global scales*, edited by G. Foody, and P. Curran, John Wiley & Sons.

Belward, A. and Loveland, T. (1995). The IGBP-DIS 1Km Land Cover Project. *Proc. 21st annual conference of the remote sensing society*, Southampton, UK. Remote sensing society, Nottingham. 1099-1106.

Congalton, R. (1991). A review of assessing the accuracy of classifications of remotely sensed data. *Rem. Sens. Env.*, Vol.37. 35-46.

Gatelli, F., A.M. Guarnieri, F. Parizzi, P. Pasquali, C. Prati, and F. Rocca. (1994). The wavenumber shift in SAR interferometry., *IEEE Trans. Geosci. Rem. Sensing, 32*, 855-865.

Goldstein, R. M., Zebker, H. A. & Werner, C. L. (1988). Satellite radar interferometry: Two dimensional phase unwrapping". *Radio Science*, Vol.23, No.4, 713-720.

Higgins, N.A. (1995). Potential of the ATSR-2 on ERS-2 for monitoring land cover change., in *21st Annual Conference of the UK Remote Sensing Society*, edited by P.J. Curran, and Y.C. Roberston, pp. 320-324, Remote Sensing Society, University of Southampton, 11-14 September.

Loveland, T.R., J.W. Merchant, D.O. Ohlen, and J.F. Brown (1991). Development of a Land Cover Characteristics Database for the Conterminous US, *Photogrammetric Engineering and Remote Sensing, 57* (11), 1453-1463.

Pratt, W. K. (1978). *Digital Image Processing*. Wiley, New York.

Prince, S. D., Kerr, Y. H., Goutorbe, J.-P., Lebel, T., Tinga, A., Bessemoulin, P., Brouwer, J., Dolman, A. J., Engman, E. T., Gash, J. H. C., Hoepffner, M., Kabat, P., Monteny, B., Said, F., Sellers, P., & Wallace, J. (1995). Geographical, biological and remote sensing aspects of the Hydrologic Atmospheric Pilot Experiment in the Sahel (HAPEX-SAHEL). *Rem. Sens. Env.*, 51(1), 215-234.

Wegmueller, U. and Werner, C. L. (1995). Land surface analysis using ERS-1 SAR interferometry. *ESA Bull.*, No.81, Feb. 1995. 30-37

Wetland monitoring in Mali using SAR interferometry

Jeremy Morley — University College London, Gower Street, London. WC1E 6BT U.K.
jmorley@ps.ucl.ac.uk
http://www.ps.ucl.ac.uk/~jmorley

Jan-Peter Muller — University College London, Gower Street, London. WC1E 6BT U.K.
jpmuller@ps.ucl.ac.uk
http://www.ps.ucl.ac.uk/

Sean Madden — University College London, Gower Street, London. WC1E 6BT U.K.
madden@mss.isunet.edu
http://www.ps.ucl.ac.uk/

Abstract

Wetland environments are found worldwide, from the Sudd Marshes in Africa to the Amazon river basin. Wetlands are important elements of continental hydrological networks, attenuating flood surges, forming sinks or stores for runoff and providing an important link in the hydrological cycle between river channels and the atmosphere.

The study area in this project is a region of wetlands in Mali on the River Niger ~(15degN, 5degW). These wetlands were chosen for environmental and pragmatic reasons. The wetlands lie in the Sahelian semi-arid zone and are therefore a major regional source of water to the atmosphere through evapotranspiration. The wetlands also lie in both Libreville and Maspalomas receiving station masks, increasing the available coverage by ERS SAR.

In this paper we examine the use of ERS phase coherence data in delineation of the flooded extents, comparing a pair of scenes from the dry season (January/February 1993) with scenes from the wet season (September/October 1993). Phase coherence is shown to provide greatly increased contrast between flooded and non-flooded regions. For the dry season pair, we demonstrate that usual image classification methods produce apparently acceptable land cover interpretations, although we currently have no land cover map to verify this.

Keywords: SAR Interferometry Monitoring Wetlands Africa Hydrology

1. INTRODUCTION

Wetland environments are found world-wide, from the Sudd Marshes in Africa, to the Amazon river basin, to salt marshes on the East Coast of the USA. They provide unique habitats for complex ecologies. The wetland habitat, according to the Worldwide Fund for Nature (WWF), is the second most threatened globally behind tropical forests. As an example, in the USA alone the extent of the wetland area has dropped from 87 million hectares to around 42 million ha in the 503 years since Columbus.

The wetland ecological systems are not only important for biodiversity but they also perform crucial roles in biogeochemical systems, acting as sinks from river networks of dissolved nitrates and phosphates, and exchanging greenhouse gases with the lower atmosphere.

Wetlands additionally are important elements of continental hydrological networks. Firstly, wetlands act as complex reservoirs, attenuating flood surges and forming sinks or stores for runoff. Secondly, wetlands provide an important link in the hydrological cycle between river channels and the atmosphere. Water is generally stored in wetlands over large areas at a relatively shallow depth. This favours evaporation of the water, providing an important link between the rivers and the atmosphere. For example, (UNEP, 1986) suggests that two thirds of all the water entering the Zambezi river system does not reach the Indian Ocean due to evaporative losses.

Remotely sensed imagery can be used to extract flooded extents for wetlands. This has been studied with both AVHRR and METEOSAT imagery (Mason et al. 1992). In addition, radar altimetry from the US Navy's GEOSAT mission was used to measure contemporaneous water levels with these measurements of flood extent. Between them, these data can be used to monitor variations in wetland water volume if the underlying surface topography is known to a high degree of accuracy. This previous study found the combination of AVHRR imagery and GEOSAT altimetry adequate, given certain assumptions, for monitoring wetland water volumes for large wetlands. However, the problem of cloudiness in the AVHRR images obscuring the wetlands and the cost of the large number of images needed, plus at that time the lack of on-going altimetric data acquisition prohibited development of an operational system.

Previous work using Synthetic Aperture Radar (SAR) data has focused on studies of tidal flooding (*e.g.* Imhoff and Gesch, 1990; Mason et al., 1994), or single-event flood monitoring (*e.g.* Matthews and Gaffney, 1994).

2. STUDY AIMS

This paper examines the potential of SAR systems for monitoring in-land, fresh-water wetland inundation extents. In the longer term we aim to use SAR interferometric methods (see for example, Massonnet and Rabaute, 1993) to provide Digital Elevation Models (DEMs) of the wetland basins for use in assessing water storage volumes. However, here we limit the aim to demonstrating that SAR data can be used to separate flooded and non-flooded regions of a seasonally flooded wetland, as a step towards development of an automated image segmentation scheme.

SAR has a much higher spatial resolution (~25m) than any of the instruments used to date for measuring flooded extents of these regions (~1km), albeit at a different wavelength, and has the advantages of day-and-night operations and the ability to sense through clouds. The principal SAR instruments we are using are the systems on the European Space Agency ERS satellites, although additional data is available from the NASA/DARA Shuttle Imaging Radar-C (SIR-C) and X-SAR missions of 1994. The ERS SAR is a C-band radar (5.6cm wavelength), SIR-C is a C- and L-band system (6cm and 23.5cm wavelengths) and X-SAR operates in the X-band (3.1cm wavelength). In addition, in some regions SIR-C provides multi-polarisation data. These sensors all provide data at ~25m planimetric resolution after processing.

3. THE INTERNAL DELTA OF THE NIGER

The study area is a region of wetlands in Mali on the River Niger (see figure 1 for orientation map) also known as the Internal Delta of the Niger. These wetlands were chosen for environmental and pragmatic reasons. The area feeding the Niger upstream of the wetlands has distinct dry and wet seasons (November-March and May-October respectively), producing well defined seasonal flow into the wetlands. While the catchment lies in the West African tropical Guinea zone, with rainfall of 800 to 1400mm per year (Grove, 1985), the wetlands themselves lie inland in Sahelian semi-arid conditions (less than 300mm per year (Grove, 1985)). The evaporation from the wetlands therefore also provides a strong atmospheric moisture contrast between the wetlands and the surroundings - the World Atlas of Desertification (UNEP, 1992) shows this region as having one of the highest evapotranspiration rates in the world (greater than 2400mm of water per annum).

The wetlands cover approximately 20 000 to 30 000 km^2. The structure and vegetation of this large wetland has a significant effect on the river flow, for example delaying the flood peak by 4 months, comparing incoming and outgoing flows (Whigham et al., 1993). An unusual feature of these wetlands is a zone of fossilised dunes towards the north of the wetlands. These dunes are each about a kilometer wide and 160km long (Grove, 1985). The dunes are sufficiently high to constrain the flooding to the troughs between dunes, the crests remaining relatively dry. This provides additional information in interpreting the SAR imagery.

The wetlands are relatively confined, however, relative to the 100km ERS SAR swath width, making data coverage manageable. Finally, the wetlands lie in both the Maspalomas and the Libreville groundstation coverages for ERS SAR data collection, increasing the possibilities for SAR coverage. ESA are supporting the work with a SAR data grant (AO-L.UK202) for imagery from the Libreville station.

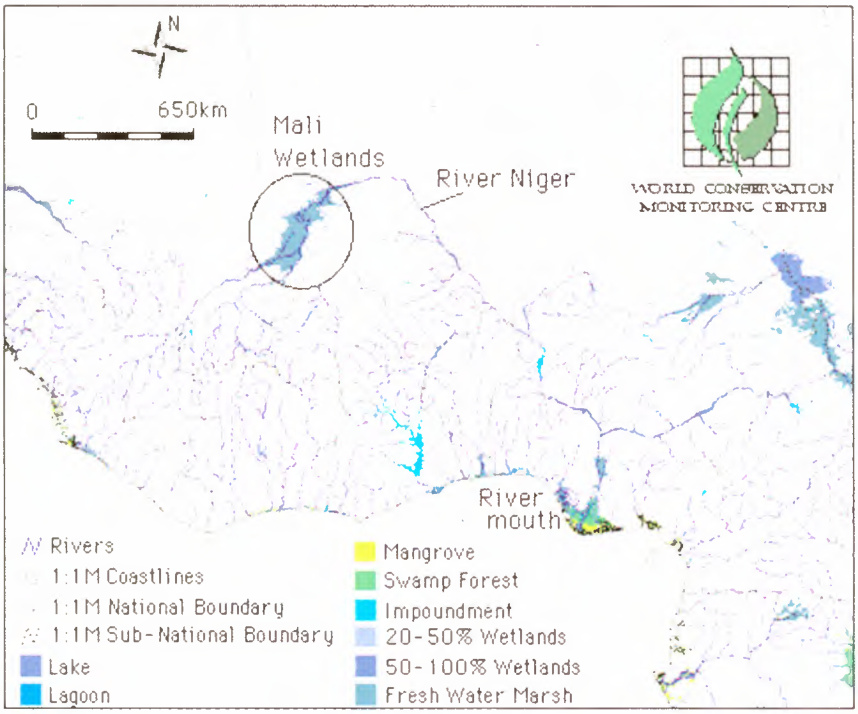

Figure 1 A map of southern West Africa, highlighting the wetlands of the Internal Delta of the River Niger. Original figure prepared by World Conservation Monitoring Centre, Cambridge, UK.

4. SAR DATASETS

A time series of ERS-1 SAR images from November 1992 to October 1993, with repeat images every 35-days in this orbital phase, have been collected by ESA. Here we focus on images from the dry and maximum-flood seasons - 7 January/11 February 1993 (dry season) and 5 August/9 September 1993 (high flood conditions). We also concentrate on a single frame (track 87, frame 315) in the North of the wetlands (in the area covered by the fossilised dune field) as an example. Figure 2 shows a map of the wetlands, highlighting the area covered by the example SAR frames.

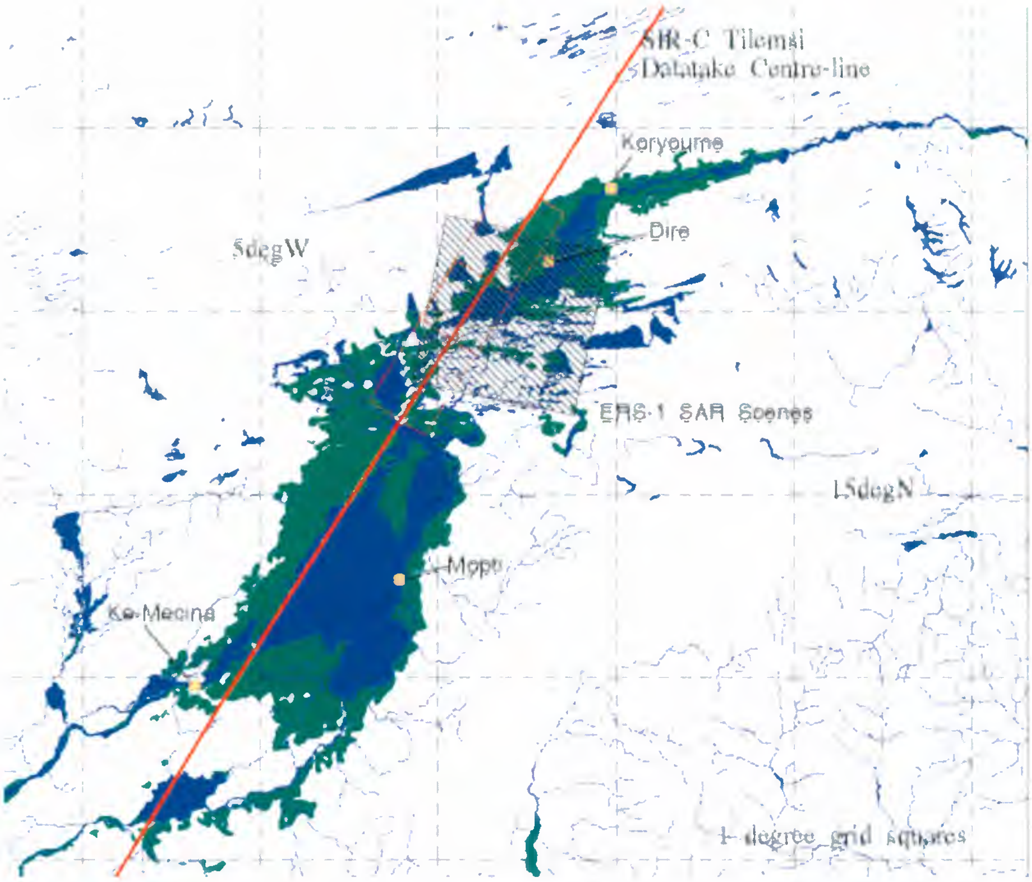

Figure 2 Map of the wetlands showing coverage of the ERS SAR imagery (track 87, frame 315 - dashed box). Green areas indicates seasonally flooded regions; blue areas indicates rivers, lakes, and permanently flooded regions. Red track and box indicate SIR-C acquisitions in this area (October '93). Point markers indicate river gauging stations. Map data source: Digital Chart of the World (Denko, 1992).

A mosaic of cloud-free AVHRR images (AVHRR bands 1, 2 and 3, various times), covering the area of figure 2, was available at UCL (Muller et al., 1993 and 1995). The majority of the scene was acquired at night when the principal radiance in band 3 is due to thermal emission - the water in the wetlands is warmer than the surrounding land as a result of its higher thermal inertia and hence is brighter in this band. As a result, open areas of water appear blue in this image, contrasting strongly with the surrounding areas. The linear features that can be seen towards the north of the wetlands indicate the approximately east-west lie of the fossilised dunes.

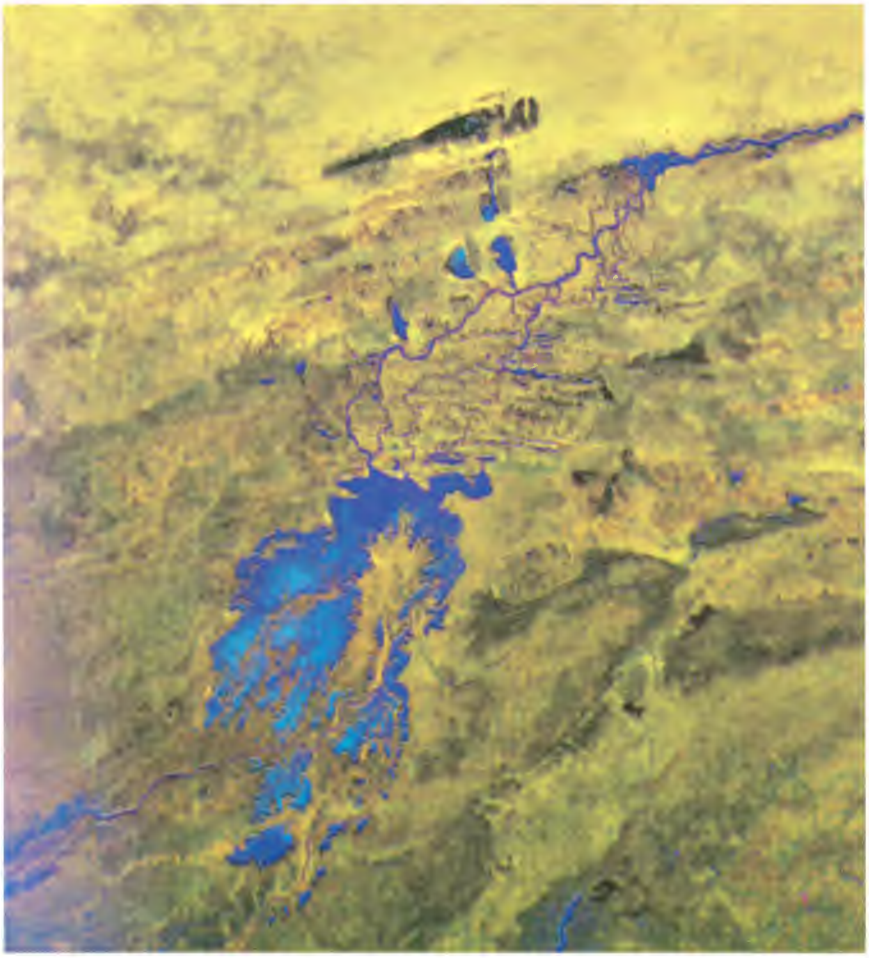

Figure 3 AVHRR mosaic image over the Mali wetlands - Red = band 1; green = band 2; blue = band 3). The saturation in the lower left corner is due to the mosaicing of two different season images. In the mosaicing, the image has been resampled onto a geographical grid. Part of the ImagingBase, (c) UCL 1991, courtesy of GlobalVisions.

Figures 4 and 5 show a pair of example scenes covering the area highlighted in figure 2. The scene in figure 4 was acquired during the dry season, on 7 January 1993. Figure 5 shows the same area acquired on 5 August 1993, close to the peak flooding of the wet season. These images have been processed to SLC level - the amplitudes are shown here. The DN values of each image have been linearly scaled through 2 standard deviations about the mean DN for the purposes of illustration. Additionally, the images have been firstly averaged by a factor of 4 in azimuth, and then subsampled for display by a factor of 11.25 in both dimensions. (All subsequent derived datasets are presented at the same resolution.)

Figure 4 ERS-1 SAR Amplitude Image of the wetlands. Acquisition date: 7 January 1993 (Dry season). (c) ESA/UCL 1996

Figure 5 Repeat ERS-1 SAR Amplitude Image. Acquisition date: 5 August 1993 (Wet season). (c) ESA/UCL 1996

There are several points to note from this pair of images. Firstly, open water courses, such as the River Niger itself (which flows from left to right across this scene) and the two lakes to the left of the image, show distinct contrast in both images from the surrounding areas. This is especially true in the dry season image where the backscatter from the water courses can be seen to dominate figure 4. The August image shows generally reduced contrast. Although the region is semi-arid, there is sufficient vegetation growth and rainfall to to reduce the radar backscatter from the non-flooded areas in the wet season. The linear features running roughly from left to right across the image are a result of the difference in surface properties between the dune crests and troughs, for example due to flooding in the troughs.

We have previously discussed [Morley and Muller 1995] interpretation of the signals visible in simple SAR image composites in this test area. Briefly, these composites show that the amplitude images show backscatter changes between seasons associated with the dune systems. These changes appear to be linked to flooding between dunes, a hypothesis that is supported by a comparison with AVHRR channel 3 data.

5. COHERENCE IMAGES

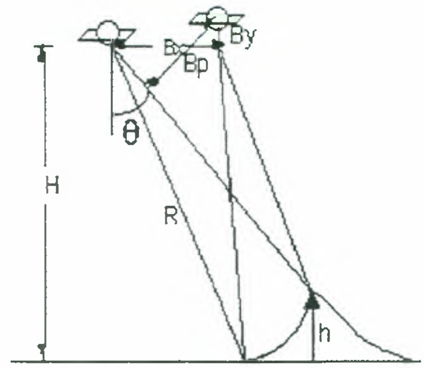

$$h = H - R\cos\theta$$
$$\phi = 2\pi/\lambda\,[Bx\sin\theta - By\cos\theta]$$

Figure 6 Basic Geometry for SAR Interferometry

Figure 6 shows the geometry which forms the basis of SAR interferometry. The indicated sensor positions might be a pair of SAR systems offset on the same platform, a pair of satellites, or the same satellite revisiting the scene after a time delay. In the time periods in 1993 for which we currently have data, the ERS-2 satellite had not yet been launched, so we are limited to the third case of using ERS-1 data from repeat orbits. The orbital repeat period at this point was 35 days - the suitability of this repeat for interferometric purposes is discussed further below.

In figure 6,

```
H        = Orbital altitude;
h        = Surface elevation at imaged point;
R        = Range from sensor to imaged point;
Bx, By   = Horizontal and vertical baseline separations of the satellites;
Bp       = Perpendicular baseline between satellites;
[theta]  = Off-nadir angle to imaged point;
[lamda]  = Radar wavelength;
[phi]    = Phase difference between image path lengths.
```

The phase difference is a measure of the difference in path length to the same point on the ground from each observation position. It is from the variation in phase difference across the area of overlap between a pair of images that the surface topography can be reconstructed, *e.g.* [Zebker & Goldstein, 1986]. A complicating factor is that the phase difference that is extracted from the images is `wrapped' into a modulo-2[pi] range, *e.g.* [Goldstein et al., 1988].

Between two satellite repeats, a number of factors can affect the radar returns from a given point. Using the terminology of [Zebker & Villasenor, 1992], these effects can be described as `thermal', `spatial' or `temporal' in nature. Thermal effects result from thermal noise in the radar system. Spatial effects result from differences in sensing geometry. Temporal effects result from changes in the actual surface point being imaged. This includes both physical movement of the surface, and changes in backscatter properties, for example due to vegetation growth.

A measure of the consistency in radar return between two images is the image coherence, [gamma], (also known as correlation - given the symbol [rho] in [Zebker & Villasenor, 1992]) defined by:

$$\gamma = \frac{\langle s_1 . s_2^* \rangle}{\sqrt{\langle s_1 s_1^* \rangle . \langle s_2 s_s^* \rangle}}$$ where

```
s1       = Complex pixel value in image 1;
s2       = Complex pixel value in image 2;
[gamma]  = Coherence.
```

[Zebker & Villasenor, 1992] shows that the total coherence of a scene is the product of the coherences associated with each of the thermal, spatial and temporal decorrelating effects. Temporal decorrelation results from any surface effects that change the scattering centres' returns or relative orientations. Spatial decorrelation results, for instance, from increasing baseline between the views (*i.e.* increasing Bp). The increasing difference in incidence angle at each pixel changes both the relative orientation of the scattering centres in the pixel and the backscatter response from the centres, changing the summed response from the pixel and hence reducing the correlation.

Decorrelating effects act to add noise to the radar echoes. This increases the standard deviation of not only the phases and phase differences inferred from the imagery, but hence also the final derived surface elevations. The coherence is therefore a useful tool in the quality assessment of interferometric products. However, here we are more interested in the information about surface conditions contained in the coherence.

[Zebker & Villasenor, 1992] examined changes in the behaviour of coherence with different surface types. Although the authors could not account for all the signatures visible, they observed distinct differences in temporal coherence with surface type. Other studies have also shown that temporal coherence is dependant on surface cover type. However, a number of other factors, such as surface moisture (which changes the surface backscatter properties, reducing coherence with increasing moisture) or wind (which disturbs the scattering centres, changing the summed response) can dominate the coherence response.

Here, we are examining the coherence and changes in coherence both for contrast due to cover type, and differences due to change in the inundation extent of the wetlands. We are therefore primarily interested in coherence signatures due to differences in temporal correlation - image pairs were therefore chosen not only to give pairs from the peaks of the wet and dry seasons, but also to give as small baselines as possible, reducing spatial baseline decorrelation. Between the January and February images, the perpendicular baseline, Bp, is 84m. Between the August and September images, Bp is 31m.

6. RESULTS

Figure 8 Phase coherence image generated for the dry-season pair (January and February 1993).

Figure 8 shows the coherence image generated between the dry-season (January / February) pair. Of most note here is the increased contrast between dune crests and troughs compared with the amplitude imagery (figures 4 and 5). On the crests, the surface is arid and especially at this time of year sparsely vegetated. Although this does not provide strong backscatter, the scattering elements are relatively stable, providing a strong coherence (typically 80%) between the 35-day repeat images. In the troughs, however, the surface is more moist, in some places possibly retaining flood water, and more vegetated. Here again, this does not provide strong backscatter. However, the moist surface and denser vegetation lowers the 35-day coherence to typically 40-60%.

We have previously compared (private paper, distributed at ISPRS Congress 1996, and in preparation for International Journal of Remote Sensing) phase coherence signatures for regions of the wetlands from the dry and wet seasons. The signatures indicate that flooded and non-flooded areas have distinctly different coherence statistics, especially in the dry season when the vegetation is at a minimum and the non-flooded areas are especially arid. Indeed, a broad classification into flooded, non-flooded, and open-water classes was possible based on a simple thresholding of wet- and dry-season coherences with one dry-season image.

Here we extend this previous work to look in more detail at the classification of the dry season imagery. Previously, (Wegmuller & Werner, 1995) have used SAR imagery and coherence to examine land cover variations in forested areas and here we use the same band composites to examine the cover types in the Inner Delta. (Wegmuller & Werner, 1995) introduce an "interferometric signature visualization image" which is an RGB composite of a backscatter image, phase coherence between a pair of images, and the difference between the two backscatter images.

Figure 9 shows the amplitude difference image of the January and February images. (The images were manually co-registered to the slant-range coherence image). Over the majority of the image, the differences are relatively small, despite the 35-day separation. This supports the deduction from the high coherence values that without rainfall in this area at this time of year, there is relatively little to affect the surface scattering conditions. The principal areas to show a change in amplitude are the water courses. In the rivers and part of the lake areas, the difference is strongly negative. However, certain areas within the lakes show an opposite, positive difference.

Figure 9 Amplitude difference image for January and February 1993 pair. (Mid-grey indicates zero difference; lighter shades are more positive differences; differences are (January-February)). Note that image mis-registration adds some texture to the image towards the top-right corner.

Figure 10 shows the RGB composite of the difference between the February and January images; the phase coherence between the same pair of images (figure 8); and the difference in amplitude between the images. A number of features can be noted in this composite. Firstly, the open water courses are again very distinct due to the strong backscatter in the January image (giving the blue colour). Both of the lakes feeding into the Niger show strong magenta areas, due to the strong positive difference between the January and February images. This is possibly due to changing lake levels during the 35-day period. This magenta colour occurs elsewhere in the image, generally close to watercourses and may reflect the final drying out of these regions towards the end of the dry season. A possible alternative is that this is due to vegetation growth on the lake surface during this time.

Away from the main water bodies and watercourses, the image is dominated by the contrast between dune crests (light green) and troughs (purple), due principally to the strong coherence on the dune crests. There is a general change in hue of the the trough regions from top-right to bottom-left across the image.

The area to the top-left of the image, above the lakes, lies above and outside the wetlands. This area, which we assume represents the standard semi-arid grassland with sparse trees of this region of Mali, is of uniformly high coherence. Certain areas here, especially to the right of the lakes, also show strong backscatter and may correspond to exposed rock on the slopes at the edge of the wetland.

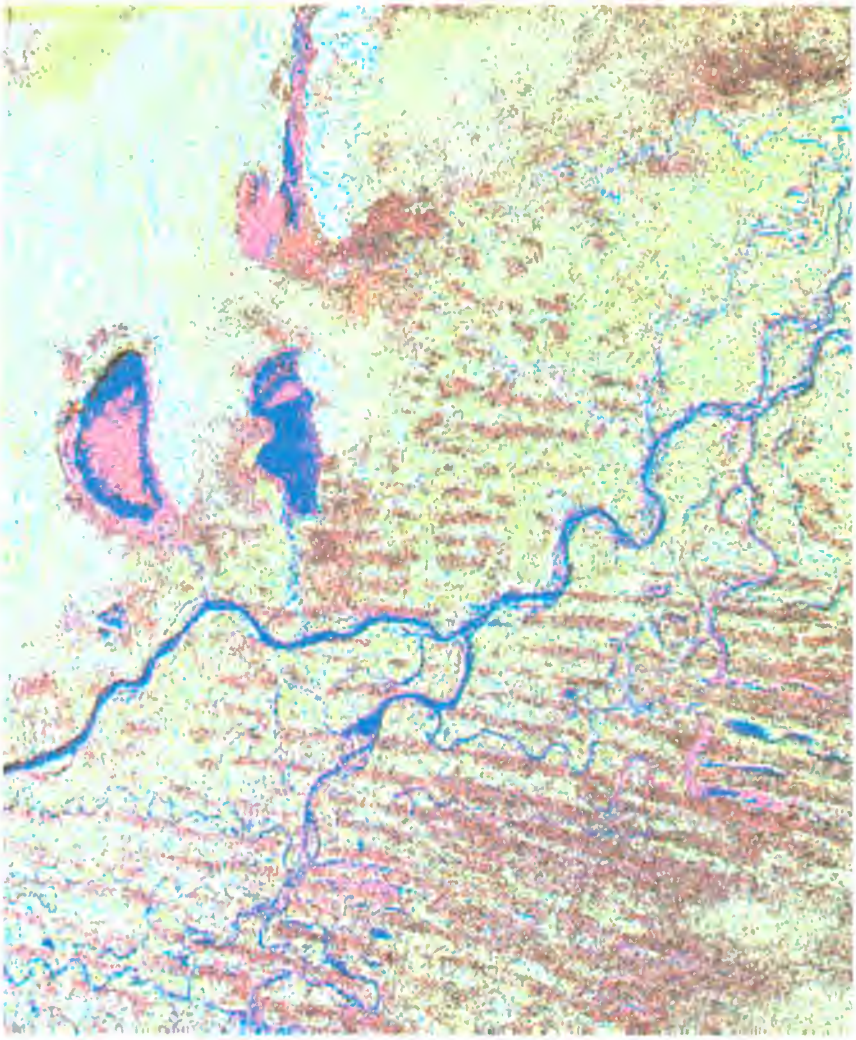

Figure 10 RGB Composite of amplitude difference; phase coherence; and the January amplitude.

An unsupervised classification of the Wegmuller and Werner composite was tested. This was performed using the ISODATA method within ERDAS IMAGINE using the file statistics to produce the initial clusters. The resulting 12-class classification is shown in figure 11. The classification separates two main arid-area classes (yellow and brown in figure 11) and three classes that can be associated with the water courses (dark blue). The other classes are associated with dune troughs and especially the apparently wetter areas of the wetlands within this scene (as indicated by the coherence in figure 8 and the drainage patterns in figure 4) - we nominally associate these classes with denser vegetation growth and possibly wetland inundation.

The classification was carried out on the full-size imagery (after averaging by a factor of 4 in azimuth to give even pixel resolution in range and azimuth).

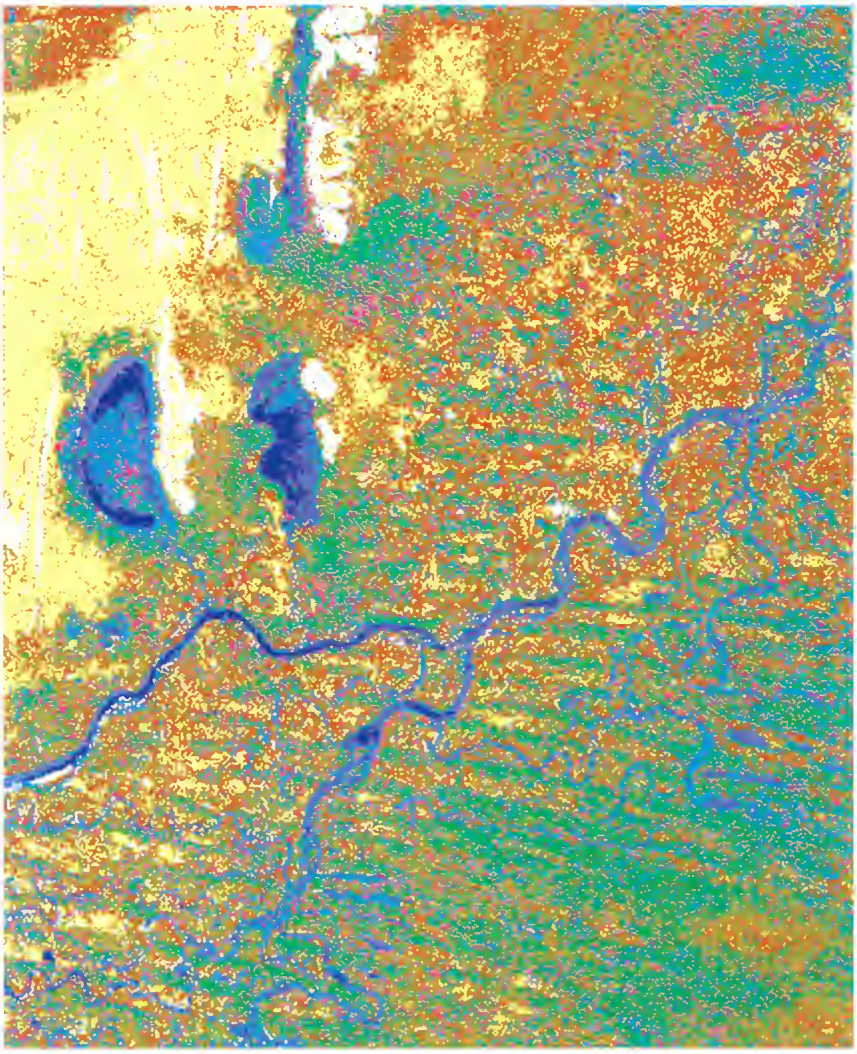

Figure 11 Unsupervised classification of composite in figure 10 (resulting in 12 classes).

A manual classification of the scene was then attempted, again within the ERDAS IMAGINE package.. Twelve classes were chosen, prompted by the results of the unsupervised method. The manual class training areas were chosen on the basis of the patterns observed in the unsupervised method (*i.e.* so that manual training areas were selected in areas of dense concentrations of each of the unsupervised classes), plus the hypotheses outlined in the discussion above of figure 10 concerning the nature of the various areas in the scene. Figure 12 shows the locations of the selected training areas, along with the class names.

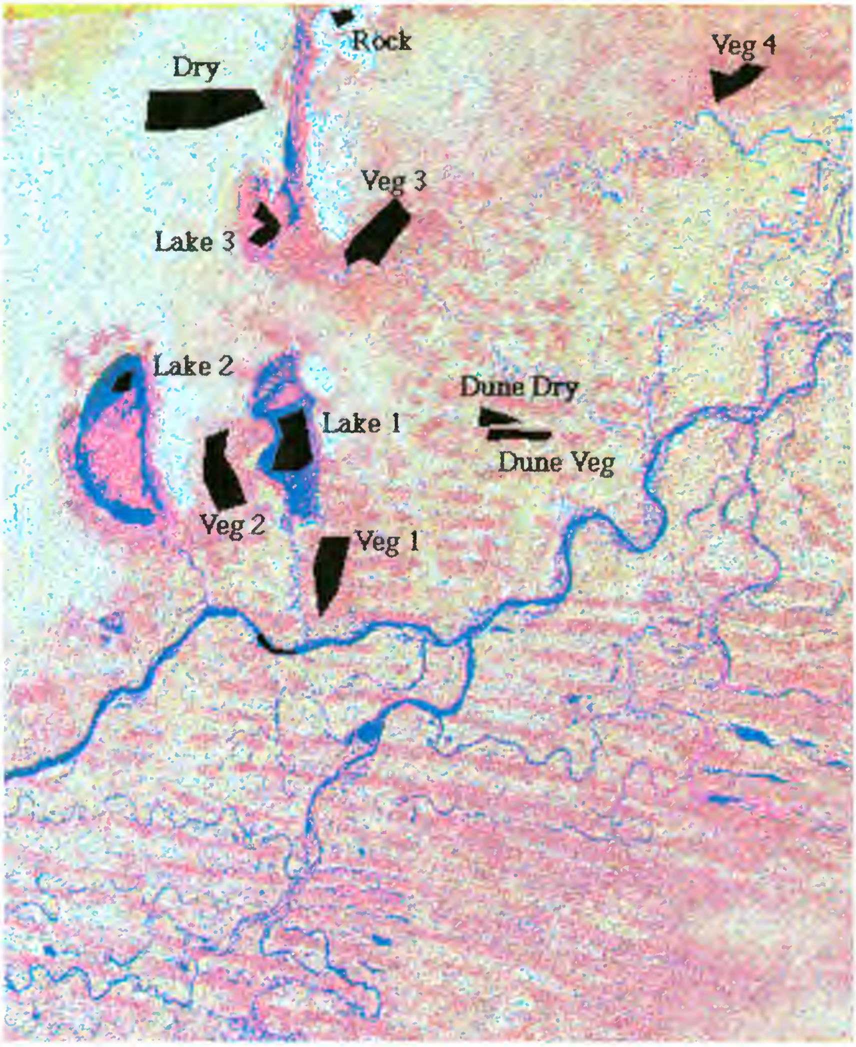

Figure 12 The 12 training areas used for supervised classification of the composite in figure 10.

Figure 13 shows the results of the supervised classification - note that the palette chosen here is the same as for the unsupervised results in figure 1, for equivalent classes. The manual classification improves the classification of the dry areas, producing more homogeneous classification of "Rock", "Dry" and "Dune Dry" areas. The classification of the open rivers is also improved, with the "River" class becoming dominant in these areas. The vegetation signatures remain confused, however, although generally limited to the dune trough areas.

Figure 13 Supervised classification of composite in figure 10 into 12 classes, with nominal class key. Same colour palette as figure 11.

We currently face the problem that we have no reliable surface cover map at this scale for this region which makes validation of these classifications difficult, especially given the temporal variability of the cover in this area. In lieu of such an absolute validation, we can examine the accuracy of classification of the original training areas by the final scheme. These results are presented in table 1.

These error statistics lead to similar conclusions to the visual inspection of the classification image, above. There are three main groups of classes: "Dry", "Water Course" and "Vegetation". Within the "Dry" group are the "Dry", "Rock" and "Dune Dry" classes; within the "Water Course" group are the "River" and "Lake" classes; with the other classes comprising the "Vegetation" group. While there is some mis-classification within the groups, the inter-group classifications (table 2) show accuracies of better than 90%.

		REFERENCE DATA--->>							
		RIVER	VEG 1	VEG 2	LAKE 1	LAKE 2	DUNE VEG	DUNE DRY	VEG 3
C	RIVER	17.33%	0.00%	0.07%	12.21%	11.59%	0.00%	0.11%	0.07%
L	VEG 1	0.00%	21.13%	8.83%	0.00%	0.00%	17.47%	1.01%	7.92%
A	VEG 2	1.49%	11.78%	62.18%	0.00%	0.00%	5.82%	5.62%	2.26%
S	LAKE 1	21.04%	0.00%	0.00%	61.11%	6.92%	0.00%	0.11%	0.07%
S	LAKE 2	58.66%	0.00%	0.00%	25.65%	81.50%	0.00%	0.00%	0.00%
I	DUNE VEG	0.00%	5.61%	3.28%	0.00%	0.00%	7.00%	3.60%	2.86%
F	DUNE DRY	0.74%	2.78%	8.49%	0.00%	0.00%	5.06%	58.27%	0.36%
I	VEG 3	0.00%	31.17%	9.88%	0.00%	0.00%	38.90%	0.00%	54.61%
E	LAKE 3	0.00%	3.45%	2.59%	1.03%	0.00%	3.12%	1.01%	3.80%
D	DRY	0.25%	0.00%	2.30%	0.00%	0.00%	0.08%	21.60%	0.00%
	VEG 4	0.00%	24.07%	2.32%	0.00%	0.00%	22.53%	3.49%	28.04%
D	ROCK	0.50%	0.00%	0.05%	0.00%	0.00%	0.00%	5.17%	0.00%
A									
T	Total	404	3564	4088	3399	535	1185	889	4155
A	Pixels								

Table 1 Error Matrix for classsification of reference training areas according to final manual classification scheme (cell values are percentages of reference classes).

CLASSIFIED DATA	REFERENCE DATA--->> WATER COURSE	DRY	VEG
WATER COURSE	98.67%	0.13%	2.89%
DRY	0.10%	96.85%	4.41%
VEG	1.22%	3.02%	92.70%
	5730	9152	15004

Table 2 Error Matrix for classsification of reference training *groups* according to final manual classification scheme (cell values are percentages of reference classes).

The full classification in table 1 indicates that it may be possible to produce a finer classification of this scene into different cover types within the three groups. At present we are limited in this respect by a poor understanding of the actual *in situ* mix of surface cover and its temporal variations. We aim to use optical imagery, especially Landsat TM or ATSR-2, to provide a further guide to the surface cover. The hope to use the optical data to develop and validate the segmentation, rather than as an intrinsic part of a new scheme.

7. CONCLUSIONS

These results represent a first test of the use of SAR data alone in image segmentation of a wetland region. They suggest that phase coherence will play an important part in segmentation of such semi-arid wetland regions, especially providing improved contrast between flooded and non-flooded areas. In addition, the classification results obtained here suggest that a clear separation can be made between dry areas, on dune crests and outside the wetlands; water courses; and a generic 'vegetated' class. It is this class which needs further study to separate vegetation types and especially to retieve an accurate flood extent. Future work will also explore classification of wet season imagery which is expected to be somewhat more complicated due to poorer phase coherence contrast, and added vegetation effects.

It is hoped that additional optical imagery will provide additional information on surface cover. This would ideally provide a guideline for a purely SAR-based segmentation scheme, rather than being an essential element in the segmentation itself. We hope to be able to use Landsat TM for cover mapping. Work carried out in the Sahelian HAPEX-SAHEL test area (Madden et al., 1996, these proceedings), comparing segmented Landat TM imagery with results from ERS SAR data, including phase coherence, produced a strong correlation between the TM IGBP vegetation classes and classes derived for the SAR data by a manual classification.

Additionally, ERS-2 includes the new ATSR-2 instrument which includes optical channels potentially useful for vegetation cover studies. Although ATSR-2 was off-line between January and May 1996, it is hoped that study of the vegetation signatures from the 1995 wet season and the earlier dry season at the end of 1995 will yield the information needed to better understand the variations in cover across the region. We are additionally pursuing contacts in Mali to provide *in-situ* data, as well as collaborations with groups working in similar wetlands in Nigeria and the Cameroons.

During the 1996 dry season, and into the wet season, ESA have acquiring SAR data over Mali for this project from both the ERS-1 and ERS-2 satellites. These form a dataset within the Tandem use of this pair of satellites. The SAR systems on each satellite are of identical design, while the satellite orbits are identically specified, except that ERS-2 follows ERS-1 such that ERS-2 can acquire images of the ground 25 hours after ERS-1. This means that images from ERS-1 and ERS-2 can not only be combined interferometrically but also that the temporal decorrelation is significantly reduced compared with the 35-day repeat data used in generating coherences here. This reduction in the repeat interval should produce coherence signatures associated more closely with the actual cover types since the cover types can be expected to change only minimally in 25 hours, especially compared with the changes in vegetation or flooding possible over 35-days.

A further line of future investigation is the use of L-band radar data, either instead or in combination with the ERS C-band data, for wetland cover type extraction, for instance using JERS-1 data. Work such as Hess et al. '95 (IEEE Trans. Geosci. Rem. Sens. 33 4 896-903) has explored the use of SIR-C data in delineating inundated areas, there within the Amazon floodplain. SIR-C is also a relatively high incidence-angle radar (loc. sit.: 31-35 degrees) and is capable of L-Band and multi-polarisation C-band imagery. The Hess et al. study concluded that HH-polarised L-band imagery was most suited to flooded/non-flooded delineation. Given the less dense vegetation in our study area, we conclude that the JERS-1 L-band data should prove effective at flooded/ non-flooded delineation for Mali.

8. ACKNOWLEDGEMENTS

ERS SAR imagery courtesy of the European Space Agency under data grant AO-L.UK202. ImagingBase AVHRR imagery courtesy of GlobalVisions, copyright UCL. This work was funded in part under UK NERC TIGER 3.3 grant GST/02/628.

REFERENCES

Denko, D. 1992.
The Digital Chart of the World. CD-ROM, GeoData.

Goldstein, R.M., Zebker, H.A., Werner, C.L. 1988.
Satellite radar interferometry: two-dimensional phase unwrapping. *Radio Sci.* **23.**

Grove, A.T. [Ed.] 1985.
The Niger and its neighbours: environmental history and hydrobiology, human use and health hazards of the major West African rivers. A.A. Balkema, Rotterdam.

Imhoff, M.L., Gesch, D.B. 1990.
The Derivation of a Sub-Canopy Digital Terrain Model of a Flooded Forest Using Synthetic Aperture Radar. *Photogrammetric Engineering and Remote Sensing,* **56** 8, pp 1155-1162

Mason, D., Davenport, I., Flather, R., McCartney, B., Robinson, G. 1994.
Development of an Inter-Tidal Digital Elevation Model for the UK Land-Ocean Interaction Study Using ERS-1 SAR Data. *Proceedings of the International Space Year Conference, Munich, 1992,* pp. 337-342

Mason, I.M., Harris, A.R., Moody, J.N., Birkett, C.M., Cudlip, W., Vlachogiannis, D. 1992.
Monitoring Wetland Hydrology by Remote Sensing: a Case Study of the Sudd Using Infra-Red Images and Radar Altimetry. *Proceedings of the International Space Year Conference, Munich, 1992,* pp. 1-6

Massonnet, D., Rabaute, T. 1993.
Radar Interferometry: Limits and Potential. *IEEE Transactions on Geoscience and Remote Sensing,* **31** 2, pp. 445-464

Mathews, J., Gaffney, S. 1994.
A Study of Flooding on Lough Corrib, Ireland, During Early 1994 Using ERS-1 SAR Data. *Proceedings of the First Workshop on ERS-1 Pilot Projects, Toledo, Spain,* 1994, pp. 125-128

Morley, J.G., Muller, J-P., 1995.
The Application of Spaceborne Techniques in the Monitoring of Wetlands. *Proceedings of the 21st Annual Conference of the Remote Sensing Society, RSS'96 "Remote Sensing in Action", Southampton, 1995,* p238

UNEP 1986.
Assessment of the Present and Future Activities Related to the Zambezi Action Plan, *"United Nations Environmental Program - Report by the UNEP Mission of Experts to the Zambezi Countries"* p. 115

UNEP 1992
Atlas of Desertification.

Wegmuller, U., Werner, C.L. 1995.
SAR Interferometric Signatures of Forest. *IEEE Transactions on Geoscience and Remote Sensing,* **33,** 5, pp. 1153-1161

Whigham, D., Dykjova, D., Dykjova, S. 1993.
Wetlands of the World: Inventory, Ecology and Management. Kluwer Academic Publishers, Dordrecht.

Zebker, H., Goldstein, R. 1986.
Topographic Mapping from Interferometric SAR Observation. *Journal of Geophysical Research,* **91** (B5), pp. 4993-4999

Zebker, H., Villasenor, J. 1992.
Decorrelation in Interferometric Experiments with ERS-1. *IEEE Transactions on Geoscience and Remote Sensing,* **30,** pp. 950-959.

Multiple Images SAR Interferometry

Dominique Derauw Centre Spatial de liège, Avenue du Pré Aily, B-4031, Angleur, Belgium
CSLULG@vm1.ulg.ac.be or dderauw@ulg.ac.be

Jean Moxhet Laboratoire de Géomorphologie et Télédétection, Université de Liège, Sart-Tilman, B-4000 Liège, Belgium
Jean.Moxhet@physun.geo.ulg.ac.be
phypc9.geo.ulg.ac.be

Abstract

The interferometry SAR (InSAR) processor and the differential interferometry SAR (DInSAR) processor developed at CSL are described. We show that the use of multiple Tandem interferometric pairs allow to increase or decrease artificially the ambiguity altitude and, thus, to decrease or increase the fringe rate. In particular, this allows to generate DEM in regions having a highly energetic relief but at the cost of a lost of altimetric resolution.

Four images DInSAR is described and an exemple using two Tandem interferometric pairs is presented. This exemple shows that even Tandem interferograms may contain fringes due to optical path variations. The correct interpretation of such fringes can only be performed with the help of ancillary data. This exemple shows that interferograms used as topographical reference must be chosen with care. A second exemple of "four images SAR interferometry" is presented on the well-known Landers earthquake.

Keywords: SAR Differential Interferometry

Introduction

Interferometric radar techniques have been widely used to produce highly accurate digital elevation models (DEM's)[1-7] and, to a less extend, to measure displacement field or terrain motions in an observed scene. Mainly, two groups have demonstrated the ability to use differential interferometry for the study of seismic phenomena: Massonet & al. (CNES)[10] and Zebker & al. (JPL)[8,9] . Each of them has used a different approach to solve the problem. They both start from an interferogram containing elevation information (topographic fringes) and motion information (displacement fringes), but the DEM's they use to remove the topography come from different sources. In the case of the study of the Landers earthquake (28 June 1992), the JPL team uses a DEM produced by SAR interferometry with another pair of images and the CNES team uses a DEM coming from the U.S. Geological Survey (USGS).

SAR images and interferometric products derived therefrom cover very large areas over which geological structures can be studied at a regional scale. The interest of these products, in particular digital terrain models (DTMs) is to allow the caracterization and tri-dimensional analysis of these structures. Figure 1 shows the relationship between geological structures clearly visible in amplitude SAR images and the known structures widely documented in the literature. However, the image also shows sub-rectilinear features or lineaments that are not documented. This illustrates the wealth of informations contained in SAR data. The study of these structures is generally performed using "classical" methods (geologic, geomorphologic, seismic or geodesic), having point-like or linear character. On the other hand, differential interferometry over a sufficiently long period and with appropriate time-frequency can provide a synoptic vue of the displacements under concern. Using SAR differential interferometry, LGT (Laboratoire de Géomorphologie et Télédétection, ULg) hopes to explain global movements as well as dislocations and, as a result, to determine possible fracture zones.

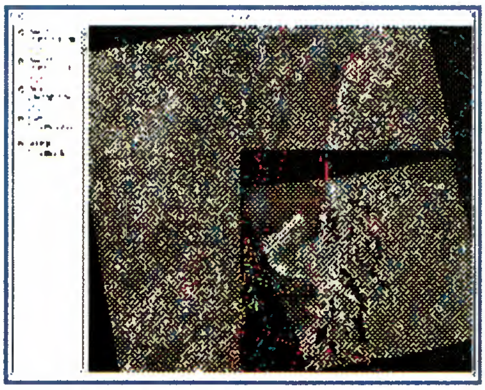

Figure 1
Death Sea area: geological structures superimposed to the SAR image
One quadrant is corrected using the interferometric DTM.

However, interpretation based on SAR imagery and derived products is not yet accurate enough to allow a complete three-dimensional understanding of the lineaments. The Death Sea area was selected because of the absence of vegetation cover, its climate stability, its geologically favourable relief and an interesting tectonic context, related to the presence of a strike slip fault area and to the forming of pull-apart bassins.

In the following, we shall rediscuss the theory of SAR Interferometry and SAR differential interferometry. Next, we shall present the approach we use to combine two Tandem interferometric pairs. Interferogram combination allows to increase the ambiguity altitude to ease the phase unwrapping in high fringe density regions but to the detriment of the altimetric resolution. An example is given; we produced a DEM of the south-west side of the Death Sea using two Tandem pairs having a too small ambiguity altitude to be solved independently.

Finally, we shall present four-images DInSAR results obtained from two Tandem interferometric pairs covering the Death sea area. We show that even Tandem pairs may contain optical path variations and that interferogram used as topographic reference to perform DInSAR must be chosen with care.

Results obtained using four-images DInSAR to study the Landers eartquake are also presented.

SUMMARY OF THEORY

Digital Elevation Models

In this section, we derive the equations needed to generate DEM's from interferometric pairs of SAR images and we discuss the processing steps needed to combine two or more interferograms.

Geometry

In spaceborne SAR interferometry, two images of the same scene are acquired by a single sensor or by two different antennas passing above the area of interest along two successive orbits next to each other. Figure 1 represents the geometry here used for SAR interferometry.

From Figure 2, we can deduce the relationship which allows us to calculate the altitude of a point above the spherical Earth[11]:

$$S^2 + z_1^2 - 2Sz_1\cos(\alpha - a_t) = (R_t + h)^2 \tag{1}$$

To calculate the altitude, we need to determine the angle (α - a_t). This one is obtained from the triangle (z_1 B z_2):

$$\begin{gathered} z_1^2 + B^2 - 2z_1B\cos(\gamma) = z_2^2 \\ \gamma - \theta + \alpha - a_t = \frac{\pi}{2} \end{gathered} \tag{2}$$

Interferometry takes place in the calculation of z_2:

$$z_2 = z_1 + \frac{\Delta\varphi}{k_{z_0}} \tag{3}$$

where $\Delta\varphi$ is the phase difference measured in the interferogram and k_{z0} is the Radar carrier wave number.

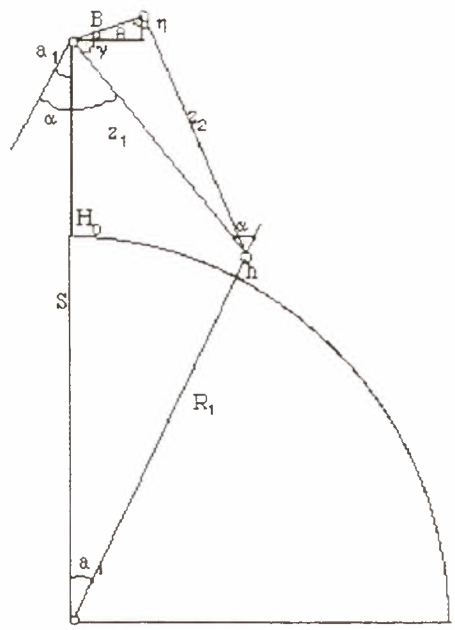

Figure 2
Viewing geometry in spaceborn SAR interferometry

Interferogram Combination

When generating a DEM from a single interferometric pair of SAR images, the processing steps are the following:

- First, we must coregistrate one image (the slave one) with respect to the other (the master one). As a result of the coregistration, we get the best bilinear transform that must be applied to the slave image to make it superimposable to the master one[12]
- Secondly, the slave image must be interpolated according to this bilinear transform in order to genarate the interferogram.
- Afterwards, the interferogram is unwrapped[13]
- Finally, from the unwrapped phase and with the use of relationships (1) to (3), we calculate the elevation of each point in the scene.

When combining several pairs, the procedure is slightly different mainly concerning the coregistration:

- One image is chosen as master image and all the others are considered as slave images. Within each interferometric pair, we coregistrate the first image of each pair with respect to the master one using maximisation of the correlation coefficient of the modulus of both images as criterion. This generally allows to coregistrate the images with an accuracy of one pixel or better.
- The first image of each interferometric pair is interpolated, using the bilinear transform obtained as a result of the coregistration.
- The second image of each interferometric pair is coregistrated with respect to the first one using maximisation of local coherence on numerous anchor points as criterion. This allows to coregistrate the images with an accuracy up to a tenth of a pixel.
- The second image of each interferometric pair is interpolated, using the bilinear transform obtained as a result of the coregistration to make it superimposable to the first one
- Afterwards, each interferogram is generated. But now, they are all in the same Slant range-Azimuth geometry, i.e. the one of the master image.

Altitude retrieval

To calculate a DEM from two or more combined interferograms, we must use the first order developement of (1):

$$\Delta\varphi_i \approx k_{z_0}\left(z_{i2}^p - z_{i1}\right) - k_{z_0}\frac{B_i\cos\left(\theta_i - (\alpha - a_t)_i^p\right)}{\sin(\alpha - a_t)_i^p}\frac{R_t}{S}\frac{h}{z_{i2}^p} \tag{4}$$

Where:

- i is the index of the i^{th} interferometric pair.
- the index p means values relative to a flat Earth

For convenience, (4) may be expressed as:

$$\Delta\varphi_i \approx \Delta\varphi_i^p + 2\pi\frac{h}{ha_i} \tag{5}$$

Where $\Delta\varphi^p$ is the flat Earth phase and ha is the ambiguity altitude.

If we remove the flat Earth phase from each interferogram and if we sum them, we get a combined interferogram with an ambiguity altitude given by:

$$\frac{1}{ha_{eq}} = \sum_{i=1}^{N}\frac{1}{ha_i} \tag{6}$$

It is thus possible to increase or decrease the ambiguity altitude by a convenient baseline combination. Moreover, since the phase noise from one interferogram to another may be considered as statistically independent, the summation of this term tends to zero with N. In particular, if we use two interferograms having each a good signal to noise ratio (SNR) to derive a combined one with a higher fringe rate, we will get an interferogram keeping a good SNR, even if this new ambiguity altitude corresponds to a single baseline wich theoretically generates a high decorrelation.

Increasing the ambiguity altitude, since it corresponds to a lowering of the fringe rate, may be useful to process areas having an highly energetic relief. On the contrary, lowering the ambiguity altitude and thus, increasing the fringe rate may be useful to get a better altimetric resolution on smooth reliefs.

Differential Interferometry

The interference pattern of two SAR images of the same region, acquired on two consecutivepasses depends on the topography.

If a movement occured between the two passes, or if there exists any local optical path variation between the two acquisitions, "displacement fringes" shall also be present.

To retreive only displacement fringes, one must substract the topographic component of the phase in the interferogram.

Differential SAR interferometry was first proposed by JPL[8] to measure small elevation changes or any other changes that induce optical path variations (called hereunder: "displacement"). They use three images to form two interferometric pairs; one containing only topographic fringes and used as a topographic reference, and the other containing topographic fringes and displacement fringes. But as we experienced it, it is often difficult to find such an interferometric triplet. Another solution is the one proposed by the CNES[10], where two SAR images are used to form an interferogram containing topographic fringes and displacement fringes and where topographic reference is taken from an other information source (map, DEM in ground range projection, ...). However, it may reveal difficult to obtain a good DEM for the region under concern.

Another solution consist in what we call here "four-images DInSAR". This method is a simple alternative to the three-images method used by JPL. It make use of two distinct interferometric pairs, one containing the displacements to be measured and another used as a topographic reference.

Three-Images Differential Interferometry

The priciple of SAR differential interferometry based on an image triplet is shematically described on Figure 3. It is supposed that no movements take place between the two first takes in order to generate a topographic reference. Displacements are supposed to occur between the second and the third image aquisitions. A small elevation change, or any optical path variation, induces an erroneous calculation of the view angle α_{13} and, in turn, of the altitude h_{13}, if the phase is interpreted as only due to the topography. From Figure 3, we deduce the relationship between the elevation angles α_{12}, α_{13} and β_{13}, which are measured by "classical" interferometry (eq. 2) and the optical path variation δz_1:

$$\delta z_1 \approx z_1(\alpha_{13} - \alpha_{12})\tan(\alpha_{13} - \beta_{13}) \tag{7}$$

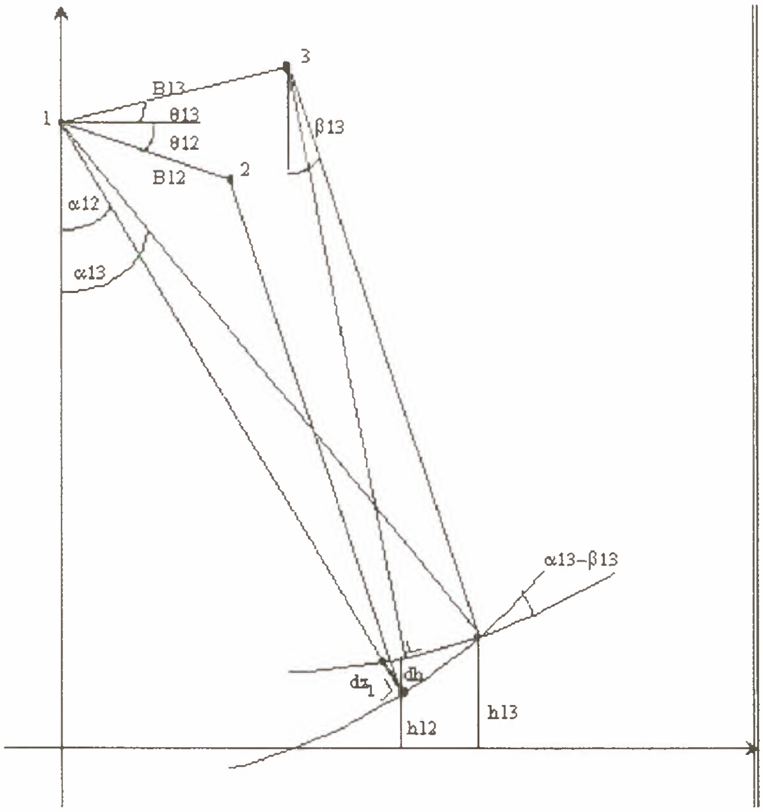

Figure 3
Shematic representation of the "three-images Differential SAR interferometry" method

Remarks

- The angle β is obtained from the following relationships:

$$B = z_1\cos(\gamma) + z_2\cos(\eta)$$

$$\eta = \frac{\pi}{2} + \beta - a_t - \theta$$

- Equation 7 is directly applicable to both unwrapped interferograms.
- h_{13} is the height that would be measured if displacement fringes were interpreted as topographical ones.

Four Images SAR Differential Interferometry

Four-images SAR interferometry makes use of two independent interferometric pairs: one containing a topographic phase as well as the displacement component that we want to measure, and a second interferometric pair which is supposed to contain only a topographic phase component in order to be used as reference.

Four images SAR interferometry is similar in its principle to the method developped by JPL since it uses a SAR interferogram to generate the phase component due to the topography. However it is often easier to find two coherent pairs than one coherent triplet.

All the images are coregistered with respect to a single one in order to generate a topographical reference interferogram which is directely in the same Slant Range - Azimuth geometry as the interferogram containing the displacement fringes. We thus obtain two interferograms; one containing the topography as well as the displacement information, and a second one containing only the topography:

The phase information in a SAR interferogram may be expressed as follow:

$$\Delta\varphi_i = k_{z_0}(z_{i2} - z_{i1}) \approx \Delta\varphi_i^p + 2\pi\frac{h}{ha_i} - k_{z_0}\delta z_{i1} \qquad (9)$$

- The first term corresponds to the "flat Earth" phase component.
- The second term is the topographic phase component.
- The third term is due to any local optical path variation.

Since the second interferogram is considered as a topographic reference, it is suposed that δz_{21} (10)

Remarks

- Displacement may also be present in the interferometric pair considered as reference. In that case, the topographical reference is considered as corrupted and the measured result corresponds to the cumulated and weighted displacements that occured during each of the interferometric aquisitions:

$$\varphi_{diff} = -k_{z_0}(\delta z_{11} - \kappa\delta z_{21})$$

$$\kappa = \frac{ha_2}{ha_1}$$

- It is preferable to choose $|\kappa| < 1$ in order to lower the phase error in the transposed reference interferogram.
- The former processing is also applicable to the classical three images DInSAR. In that case, the weihgting factor κ is simply [9]:

$$\kappa = \frac{B_{1\perp}}{B_{2\perp}}$$

EXAMPLES

DIGITAL ELEVATION MODEL CALCULATION

Increasing of the ambiguity altitude

When a scene shows a highly energetic relief its often difficult to use interferograms with low ambiguity altitude because the fringe rate may be too high to allow phase unwrapping even if the signal to noise ratio is good. It thus may be useful to artificially increase this ambiguity altitude using two or more interferograms in order to lower the fringe rate in the resulting interferogram. This eases the phase unwrapping and allows to connect regions that would have been separated using a single interferogram, but at the cost of a loss of accuracy. An example is given hereafter; we used two Tandem interferograms of the "Death Sea" area, each one having an ambiguity altitude around 30 m. The images characteristics are summarized in Table 1.

Dates	E1 Orbit Ndeg.	E2 Orbit	Frame	B_x	B_y	ha
10-11 November 1995	22604	2931	621	375 m	-21 m	-25m
16-15 December 1995	23105	3432	621	-333 m	12 m	28m

Table 1

Because of the highly energetic relief in that area and the very small ambiguity altitudes of both the Tandem pairs, each interferogram exhibits a very high fringe rate (Figure 4). Residues are numerous even if the signal to noise ratio is good because of the too high fringe rate. The image of the residue connections shows a lot of independent zones. Finally, both of the Tandem interferograms reveals to be nearly impossible to be unwrapped suitably.

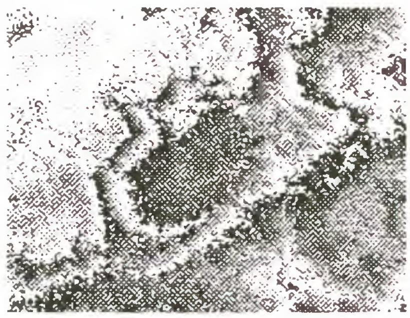

Figure 4
Tandem interferogram of the south-west side of the Death Sea.

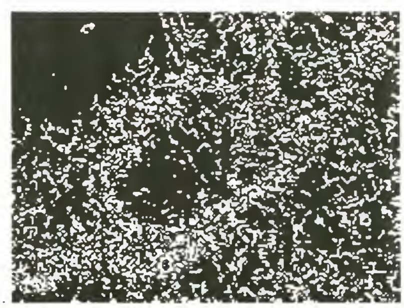

Figure 5
Residue connections

Combining the two interfergrams allows us to generate a new one having an ambiguity altitude of 234m (Figure 6). This new interferogram shows fewer residues and can be entirely unwrapped with ease. As a result, we can generate a D.E.M. over the whole combined interferogram (Figure 7).

Figure 6
Combined interferogram (ha_{eq} = 234m) obtained from two Tandem interferograms (ha_1 = -25m, ha_2 = 28m).

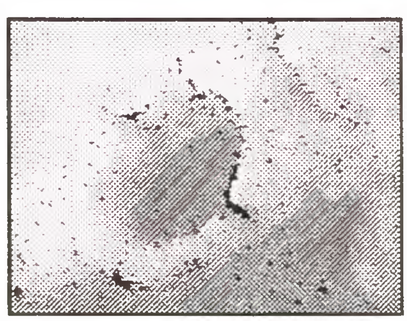

Figure 7
DTM issued from the combined interferogram.

FOUR IMAGES DINSAR EXAMPLE

The Landers Earthquake (June 28, 1992)

To validate our processor, we performed a study of the well-known Landers earthquake using four-images differential SAR interferometry. We thus used two interferometric pairs. The first one (figure 8) is the same as the one used by the CNES[9] and contains the displacement informations we want to detect (April 24, 1992 - August 7, 1992). The second interferometric pair is a Tandem pair acquired on 7th and 8th of January 1996 (figure 9). This Tandem pair is supposed to contain only topographic information and was considered as the topographic reference.

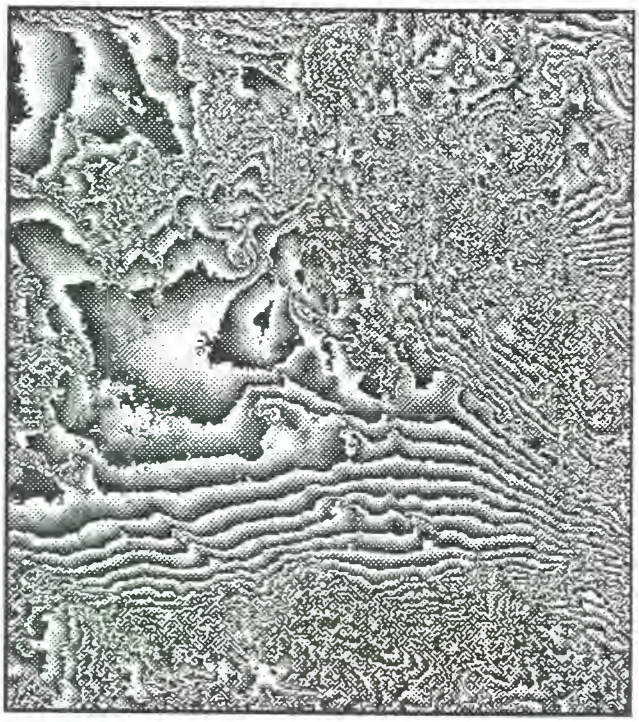

Figure 8
First interferogram of the Landers area:
April 24, 1992 / August 7, 1992
Interferogram containing displacement fringes

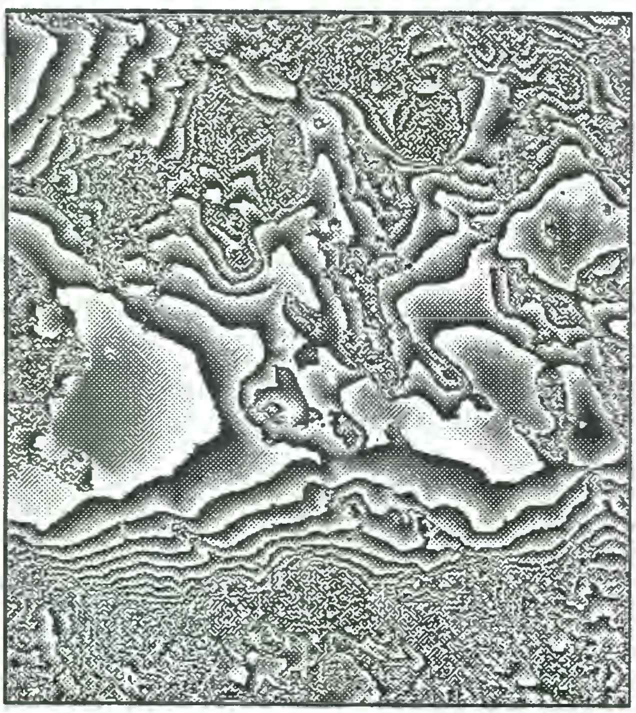

Figure 9
Tandem interferogram of the Landers area:
January 7 and 8, 1996
Interferogram considered as the topographic reference

The processing steps are the following:

- All the images are coregistered and interpolated with respect to the first one (April 24, 1992).
- Both interferograms are generated in the same Slant range - Azimuth geometry.
- The second interferogram is unwrapped and transposed in the viewing geometry of the first pair (i.e. multiplied by the ratio of the ambiguity altitudes).
- The " transposed " interferogram is retrieved from the first one to generate the differential interferogram (Figure 10).

Figure 10
Differential interferogram of the Landers earthquake

The Death Sea Area

We performed four-images differential interferometry using the two Tandem pairs covering the Death Sea area. The relative position of the satellites are represented on figure 11. The image acquired the 10th of November 1995 was chosen as the master one. The three other images were coregistrated as already described. The two quadrants of the scene covering the Jordanian part, east of the Death Sea, showed a sufficiently smooth relief to allow phase unwrapping on large areas in the second interferogram (16-15/12/95) (Figure 12). This one was thus considered as a topographic reference and transposed in the geometry of the first Tandem interferogram in order to flaten it. It was expected to get a completely flat interferogram since no seismic event occured during both the Tandem acquisitions even if an earthquake occured between the 11 of November and the 15 of December.

Figure 11
Relative positions of ERS1 and ERS2 for the acquisition under concern.
(dx = -674m, dy = 31m)

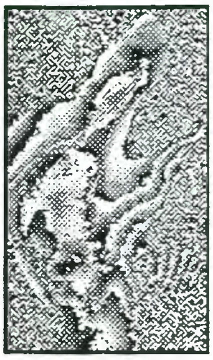

Figure 12
Tandem interferogram used as topographic reference.

Due to a to high fringe rate in some areas, the reference interferogram is difficult to unwrap. As a result, the four-images differential interferogram is is made of numerous independent zones.

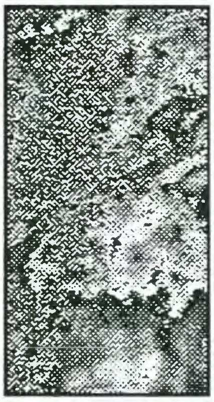

Figure 13
Four-images differential interferogram

The differential interferogram (Figure 13) is flattened in most of the areas even in regions which showed a very high fringe rate. But two residual fringes are clearly visible following the south-west to north-east direction.

An error in the calculation of the baselines is not sufficient to explain the presence of such remaining fringes. If those fringes were only due to a residual baseline component, fringes would have been also present elsewhere, particularily, on the summit located right to the east of the Lisan peninsula which shows a much more " energetic " relief.

It it thus supposed that these fringes contain information related to a local change in the optical path that occured in one or both of the Tandem acquisitions (eq. 11).

Determination of the Perturbed Image

Even if the baseline between the acquisition of the 10th of November and the one of the 16th of December is long, the coherence between these two takes is sufficiently preserved to generate an interferogram. This allowed us to generate two differential interferograms, each using one of the two Tandem pairs as topographic reference (Figure 14). We observe that the "displacement" fringes show a fringe rate twice higher when using the first Tandem pair (10-11/11/95) as a reference. If a reference interferogram is corrupted by "displacement" fringes, the corresponding phase shall appear twice in the differential interferogram; first from the interferogram covering the period 10/11/95 to 16/12/95 and secondly from the reference interferogram multiplied by the factor κ (eq. 11). Consequently, if the first Tandem pair is corrupted, the "displacement" fringes are approximately multiplied by 2 ($\kappa \approx 1,1$) in the first differential interferogram and must appear only once in the second one. From Figure 14, we can deduce that displacement fringes are mainly contained in the first Tandem pair and that the first image, the one of 10 November, is probably perturbed with respect to the others.

Figure 14
Three images differential interferogram of the Lisan peninsula
a) Tandem pair 10-11/11/95 taken as topographical reference
b) Tandem pair 16-15/12/95 taken as topographical reference

Fringes Interpretation

Two cases are possible. First, the Lisan peninsula and the north-east plateau underwent a one-day movement of approximately 3 cm between the 10th and the 11th of November. This hypothesis seems unprobable but is still under verification. Secondly, meteorological effects induced local optical path variations between the two takes. This hypothesis seems more probable because, even if there was no precipitation during the first Tandem aquisition, the cloud covering and the relative humidity were completely different for the two takes. The sky was nearly completely covered during the first acqisition and completely clear during the second (Figure 15).

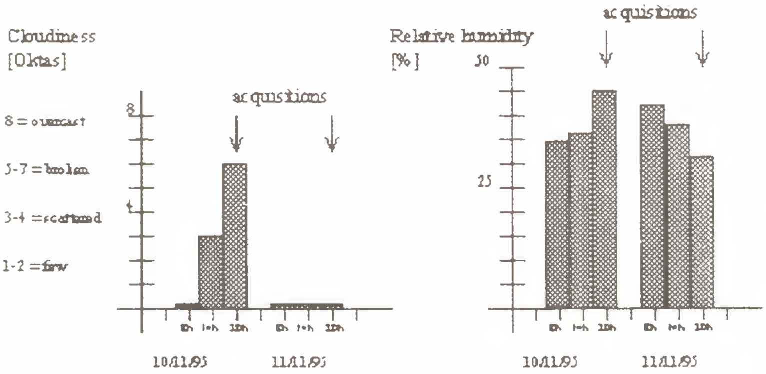

Figure 15
Cloudiness and relative humidity during the first Tandem acqisition
(Sources: Meteorological Services, Ministery of Transport, State of Israel)

Moreover, the orientation of the residual fringes corresponds to the main orientation of the cloud front observed on 10th November.

Knowing that a variation of 15% of relative humidity may induce up to two fringes via optical variation[14], the fringes observed might correspond to a local variation of approximately 11%. This is comparable to the 14% measured by the Meteorological Services of the State of Israel.

Conclusions

It has been shown that combining interferograms allows to increase or decrease artificially the ambiguity altitude. Increasing the ambiguity altitude and, thus, decreasing the fringe rate may be usefull to unwrap interferograms covering hilly regions or having a too long baseline, but at the cost of a loss of accuracy.

When using a SAR interferometric pair as a topographic reference to perform differential interferometry, one must carefully verify the validity of this reference. If the reference interferogram contains fringes due to any optical path variation, the differential interferogram shall be completely corrupted. To assess the validity of an interferogram used as topographic reference, ancillary data (e.g., meteorological data as in the present study) are mandatory.

Acknowledgements

This work was supported by the Belgian Federal Offices for Scientific, Technical an Cultural Affairs (O.S.T.C.) under contract Nr. T3/12/32 of the TELSAT-III National Remote Sensing Program.
DD. wishes to thank Prof. H.A. Zebker and Dr. D. Massonnet for helpfull discussions.

References

[1] A.K. Gabriel and R.M. Goldstein
"Crossed Orbit Interferometry: Theory and Experimental Results from SIR-B",
Int. J. Remote Sensing, **1988**, Vol 9, N°5, pp 857-872.
[2] H.A. Zebker and R.M. Goldstein
"Topographic Mapping from Interferometric SAR Observations",
J. Geophys. Res., **1986**, Vol 91, pp 4993-4999.
[3] R.M. Goldstein, H.A. Zebker and Ch.L. Werner
"Satellite Radar Interferometry: Two Dimensional Phase Unwrapping",
Radio Science, **1988**, Vol 23, N°4, pp 713-720.
[4] C. Prati, F. Rocca, A.M. Guarniere and E. Damonti
"Seismic Migration for SAR Focusing: Interferometrical Applications",
IEEE Trans. Geosci. Remote. Sensing, **1990**, Vol 28, pp 627-640.
[5] H.A. Zebker and J. Villasenor
"Decorrelation in Interferometric Radar Echoes",
IEEE Trans. Geosci. Remote. Sensing, **1992**, Vol 30, N°5, pp 950-959.
[6] F.K. Li and R.M. Goldstein
"Studies of Multibaseline Spaceborne Interferometric SAR",
IEEE Trans. Geosci. Remote. Sensing, **1990**, Vol 28, N°1, pp 88-97.
[7] D. Massonnet and Th. Rabaute
"Radar Interferometry: Limits and Potential",
IEEE Trans. Geosci. Remote. Sensing, **1993**, Vol 31, N°2, pp 455-464.
[8] A.K. Gabriel, R.M. Goldstein and H.A. Zebker
"Mapping Small Elevation Changes over Large Areas: Differential Radar Interferometry",
J. Geophys. Res., **1989**, Vol 94, N°B7, pp 9183-9191.
[9] H.A. Zebker, P.A. Rosen, R.M. Goldstein, A.K. Gabriel and Ch.L. Werner
"On the Derivation of Coseismic Displacement Field using Differential Radar interferometry: The Landers earthquake",
J. Geophys. Res., **1994**, Vol 99, N°B10, pp 19617-19634.
[10] D. Massonnet, M. Rossi, C. Carmona, F. Adragna, G. Peltzer, K. Feigl and Th. Rabaute.
"The Displacement Field of the Landers Earthquake mapped by Radar Interferometry",
Nature, **1993**, Vol 364, pp 138-142.
[11] Derauw
"Developement of an Interferometric SAR Processor"
Proc. SPIE 2584, **1995**, pp 319-324.
[12] Derauw and S. Rose
"Coregistration and Complex Interpolation"
Proc. SPIE 2584, **1995**, pp 320-331.
[13] Derauw
"Phase Unwrapping using Coherence Measurement"
Proc. SPIE 2584, **1995**, pp 376-383.
[14] H.A. Zebker and P.A. Rosen
"Atmospheric Artefacts in Interferometric SAR Surface Deformation and Topographic Maps",
submitted to: J. Geophys. Res.- Solid Earth.

Weather Effects on SAR Backscatter for Agricultural Surfaces

Stephen Hobbs College of Aeronautics,
Cranfield University, Cranfield,
Bedford, MK43 0AL, GB
s.e.hobbs@cranfield.ac.uk
http://www.cranfield.ac.uk/coa

Abstract

Weather is a significant perturbing factor on radar backscatter from natural surfaces but one whose effects have not been carefully studied. We are working to quantify these effects on the backscatter intensity and phase correlation of SAR images. The objectives of the project are to (1) create a dataset with the required ground truth and SAR image data, (2) derive statistical relationships between weather conditions and the observed backscatter variation and phase (de) correlations, and (3) use electromagnetic scattering models to interpret the observations.

Observations of crop growth for typical UK agricultural crops (wheat, beans, oil-seed rape) are made regularly using local test sites (within 5 km of Cranfield University's airfield). Local weather conditions are also being recorded, and these data will be compared with the observed variations in radar backscatter intensity and phase correlation for ERS SAR images. Electromagnetic scattering models will be used to interpret the observations.

Results from a phase coherence simulator and two simple analytical models are presented. These help quantify weather effects on phase correlation and show the importance of weather-independent scatterers on coherence.

The expected outcomes of the project are (1) statistical relationships between backscatter or phase correlation and weather, and (2) models (new or adapted) to help understand the underlying physics. The results may have application in agricultural monitoring, meteorology, and SAR interferometry.

Keywords: SAR, backscatter, phase correlation, coherence, weather, agriculture

Introduction

Radar backscatter from natural surfaces is determined primarily by the moisture content and structure of the scatterers. Both these factors are influenced by weather, and thus a relationship of some sort between weather and radar backscatter is expected. A few observations are reported in the literature of the influence of weather on ^{0} (e.g. Ulaby *et al.* 1986, quote a variation of 3 dB due to surface moisture on vegetation) but the author is not aware of any systematic study in this area. Recent developments in the use of backscatter phase as well as intensity highlight the power of the SAR technique. If the relationship between weather and backscatter can be understood for typical surfaces then it should be possible to make even better use of SAR data.

For the last year work has been underway at Cranfield to study the influence of weather on radar backscatter intensity for typical UK agricultural crops. This entails making observations of (1) local weather conditions and (2) crop growth for three test sites, and recording ERS SAR images (the data available are ^{0,} have approximately 25 m resolution, and are accessed using RAIDS (RApid Information Dissemination System, operated by Matra-Marconi, Space, National Remote Sensing Centre Ltd., Defence Research Agency and Logica)). The ERS Tandem Mission gives the opportunity to extend this work to the effect of weather on phase correlation, which is a valuable addition in view of the wide range of applications being developed based on SAR phase measurements.

The next section describes the observations being made and the test sites. The modelling approaches being followed are described, together with some preliminary results from a phase correlation simulation. The final section is a discussion including an outline of the next stages of the project.

Project Database

A key element of this project is the construction of a database on which our models can be developed. The database has three components: (1) observations of crop growth for three test sites, (2) local weather data to allow us to quantify the surface moisture history and general weather conditions, and (3) ERS SAR images of the test sites.

The test sites were chosen to be representative of important agricultural crops in Eastern England and also to sample a variety of plant geometries. A third constraint was that only limited resources were available to undertake the fieldwork. Three test sites are used, all within 5 km of the University (52 04' N, 0 37' W), with crops (1995/96 season) of winter wheat, oil-seed rape and beans. The sampling strategy is relatively rudimentary: plant height and number per unit area are recorded, and a few "representative" plants are brought back to the laboratory for drying to measure their moisture content and dry mass. Photographs of the fields and of individual plants *in situ* are taken as an additional record. Observations are taken at one or two week intervals through the growing season to harvest. Qualitative observations of the soil condition (moist / dry / cracked / etc.) are also made. The intention of this project is to study the *relative* effect of weather rather than to provide a high quality *absolute* database and for this goal it is currently felt that the above sampling regime is adequate, although it is of course possible that later stages of the analysis may point to the need for additional information.

Weather data are recorded using an automatic weather station installed on the airfield at Cranfield University. Variables recorded are air temperature and humidity, incident and net radiation, wind speed and direction, rainfall and soil temperature profile. Data from other stations within about 20 km are available for times when the data quality from the local station is poor.

ERS SAR data have been recorded from RAIDS over the period May 1995 to date. These data are all at approximately 25 m resolution and are related to backscatter intensity. The relative calibration is constant although the absolute calibration is unknown. Participation in the ERS Tandem Mission gives us access to ERS Interferometric SAR image pairs (SLC) over the period June 1995 to July 1996.

Backscatter Modelling

Parallel to the observational work, modelling studies are being carried out to attempt to simulate the effect of weather on SAR backscatter for agricultural crops. Two approaches have been used so far: (1) MIMICS (the backscatter model originally developed at the University of Michigan for forest applications) is being used for studies of backscatter intensity, and (2) a simple phase correlation simulation has been developed. Results from MIMICS are not yet available, but some preliminary results from the phase correlation simulator are presented below.

Phase Correlation Models

Three models have been developed for a preliminary exploration of SAR phase correlation. The first is a Monte Carlo simulator to allow simple weather parameterizations to be applied and the others are simple analytical model to help interpret the results of the simulator.

Monte Carlo Simulator

A simple model to simulate phase correlation dependence on weather has been developed. The model assumes that scatterers within the scattering volume have different responses to weather, e.g. the soil surface may have constant properties, while plant stalks and leaves are moderately or highly sensitive to weather conditions. The model identifies targets within the scattering volume (called pixel hereinafter) as belonging to one of two basic classes: static or weather-dependent. All the static targets are represented by a single equivalent scatterer. The weather-dependent scatterers are represented by one or two equivalent scatterers (to allow for the possibility that more than one type of weather dependence may need to be described). A user of the model specifies the relative strengths of the equivalent scatterers (by defining a $|^0|$ value for each). The other parameters chosen by the user represent the effect of weather on the scatterer classes.

Weather effects are modelled by specifying the mean and standard deviation for the changes in phase and magnitude of ^{0} for each component relative to a "zero weather" case. The signal for zero weather for each pixel is obtained by phasor addition of the electric field vectors for each of the equivalent scatterers, allowing a random phase for the field of each scatterer. Two different weather cases are applied to the zero weather state for each pixel, and the resultant electric field phase for each case is calculated (Figure 1). From the resultant electric field phasors it is possible to calculate the *coherence* between the two images. The phase for the second weather case is adjusted (by adding 2 radians) to ensure it is within radians of the phase of the first case (this allows a *linear correlation* between the phases to be calculated).

The model is implemented using a standard spreadsheet (Microsoft Excel v7.0), taking advantage of the built-in random number generator and inverse Normal distribution functions in particular. The model's behaviour has been checked carefully to ensure that it has been implemented correctly using a variety of qualitative and quantitative tests.

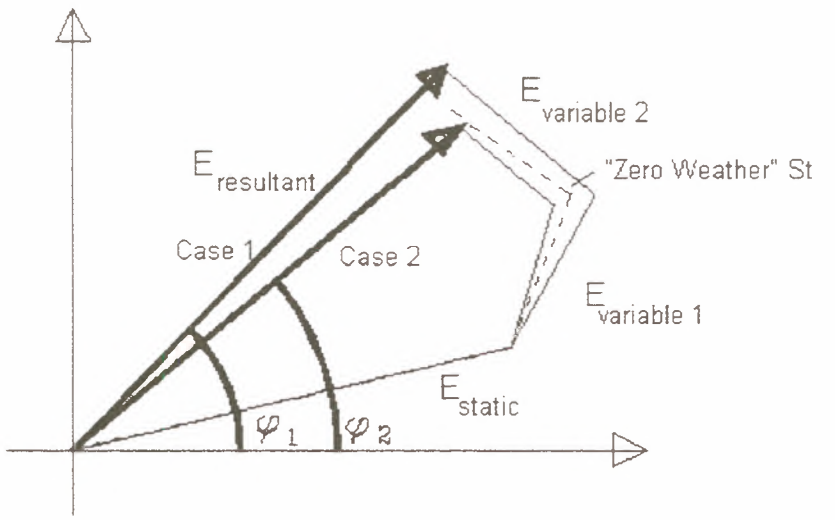

Figure 1: Phasor diagram showing the reference ("zero weather") case (dashed line), the two weather cases based on this (Case 1, Case 2), and the resultant phase angles ($_1$, $_2$) for a single pixel. Note that the static component is common to both weather cases and that the model can be run with one or two variable components.

The current model uses the Monte Carlo method to simulate signals for 100 independent pixels. Figure 2 shows an example of the model's output with only one weather-dependent component for the following parameters:

	Static	Weather-Dependent	
		Weather 1	Weather 2
$\|^0\|$	0.7	0.3	
^{0} magnitude shift	n.a.	0	0
standard deviation	n.a.	0	0
^{0} phase shift	n.a.	5	45
standard deviation	n.a.	5	45

Table 1: Simulation parameters used to produce Figure 2.

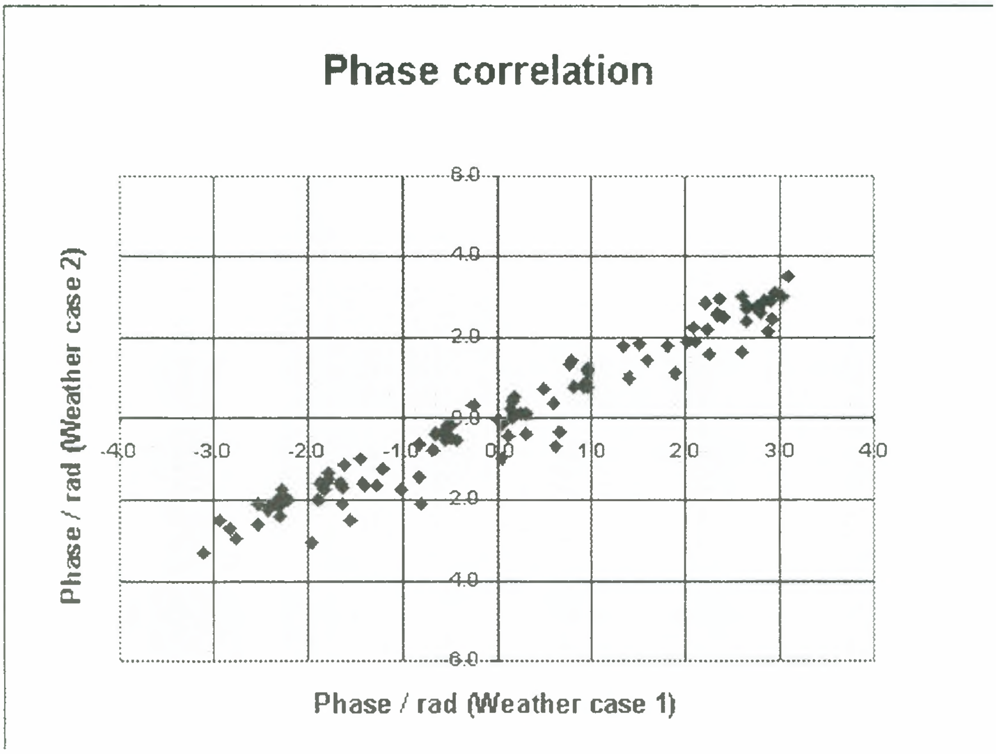

Figure 2: Example model output for 100 independent pixels (linear correlation coefficient = 0.974); the simulation parameters are given in Table 1.

A linear correlation coefficient was calculated using the 100 independent pixels simulated. In addition, a check on the mean backscatter intensity for each weather case was also calculated to ensure that it was close to the nominal (user specified) value.

Analytical Models

Two simple analytical models have been developed to interpret the results of the simulator. The first model relates the linear correlation coefficient to the relative phases for the two weather cases, and the second relates the image pair's coherence to the relative strengths of the different scatterer types.

Linear Phase Correlation

A simple analytical model suggested by the general form of the results shown in Figure 2 was developed. This model assumes that the phase of weather case 2 ($_2$) is linearly dependent on the phase of weather case 1 ($_1$) except for being randomly dispersed in a range b about the line $_2 = _1$, and that $_1$ is uniformly distributed over the range a (a = for the Monte Carlo simulation). Figure 3 shows the model assumed.

For two variables x_i and y_i (i = 1 to N), the standard linear correlation coefficient () definition used is:

$$\rho = \frac{\sum_{i=1}^{N} (x_i - \bar{x})(y_i - \bar{y})}{\sqrt{\sum_{i=1}^{N} (x_i - \bar{x})^2 \sum_{i=1}^{N} (y_i - \bar{y})^2}}$$

For the uniform random distribution shown in Figure 3, this expression (in the limit of large N) evaluates to:

$$\rho = \left[1 + \left(\frac{b}{a} \right)^2 \right]^{-1/2}$$

For the phase correlation simulator a = , and the maximum size of b is also . This sets a lower limit on of 1/2 (corresponding to a completely random scatter of phases).

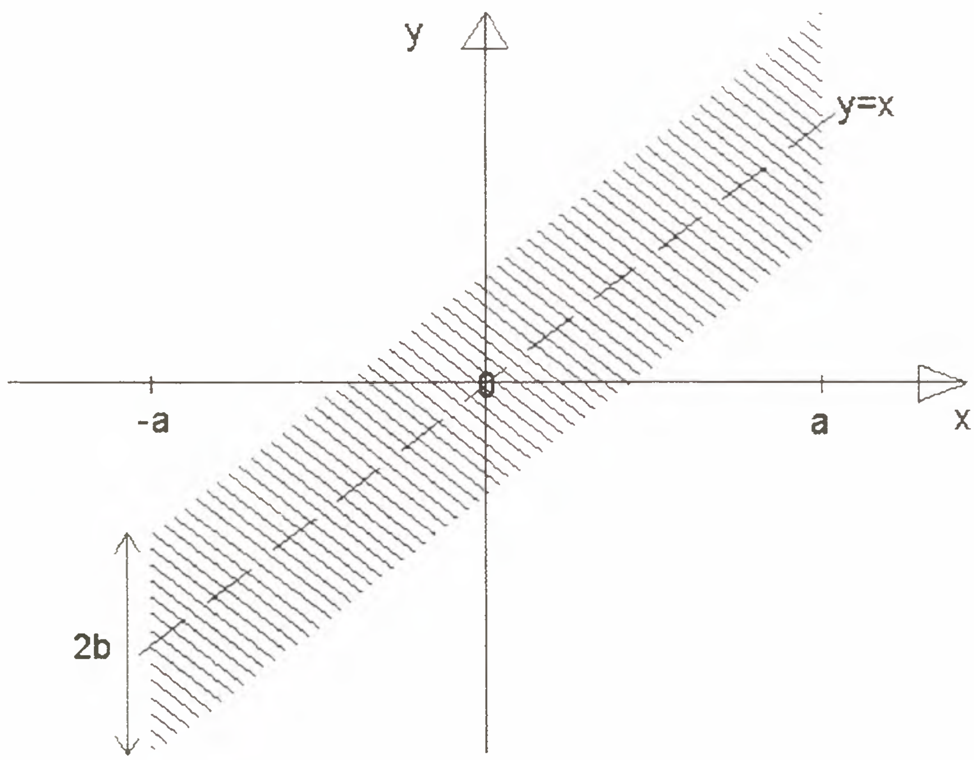

Figure 3: The phase correlation distribution on which the analytical model is based. $_1$ (x-axis) is uniformly distributed between -a and +a; $_2$ (y-axis) is uniformly distributed between x-b and x+b.

The analytical model is clearly a simplification in that the scatter is not completely uniform in practice. However, a characteristic width corresponding to b can usually be identified. It should be noted that the correlation coefficient is not affected if there is an offset between $_1$ and $_2$ (e.g. $_2 = {}_1 + c$). Figure 4 shows the dependence of the correlation coefficient on the width of the phase scatter (b) predicted using the analytical model.

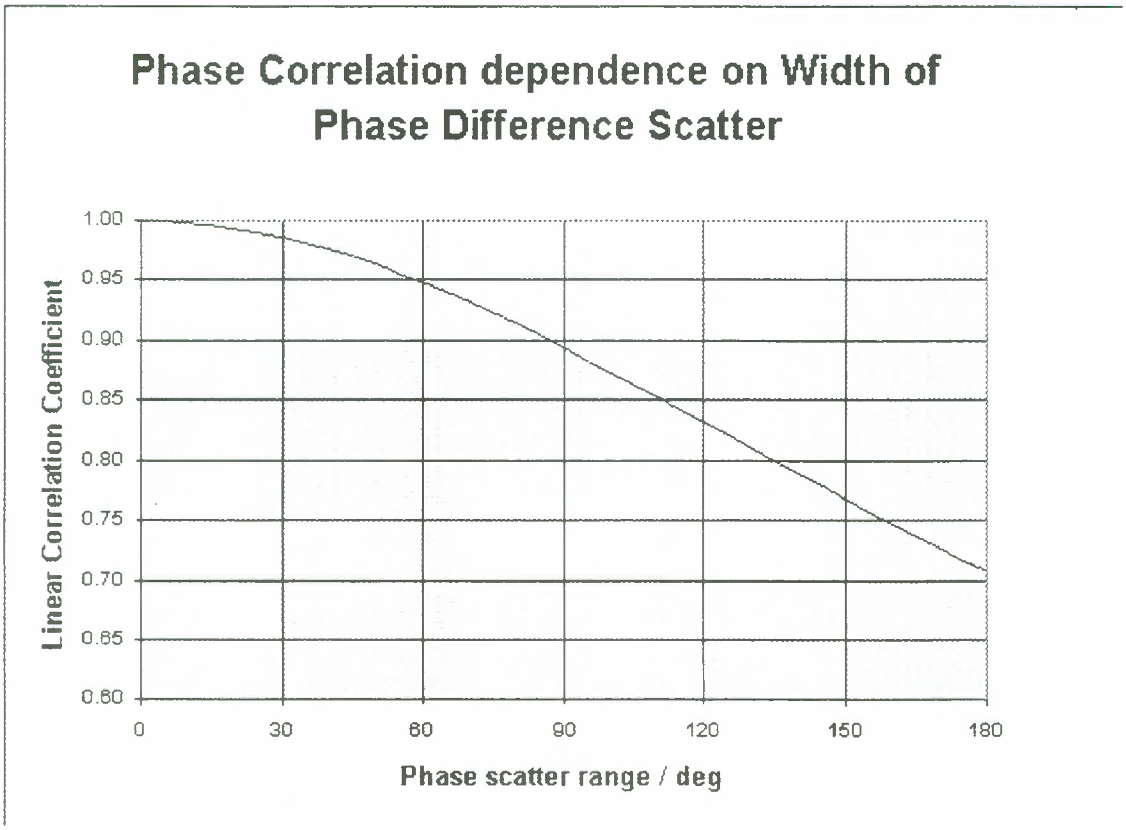

Figure 4: Correlation coefficient dependence on the width of the phase scatter predicted by the analytical model.

Coherence

Coherence is easily calculated from the simulation results since there are no unknown systematic corrections which need to be applied. The definition of coherence () is based on the electric field phasors for the two weather cases for each pixel and generated by averaging over the simulated pixels.

$$\gamma = \frac{\langle E_1 E_2^* \rangle}{\sqrt{\langle |E_1|^2 \rangle \langle |E_2|^2 \rangle}}$$

The Monte Carlo model developed above assumes that the electric field consists of a static (E_{i0}, weather independent) component and one or two variable (weather dependent) components. For pixel i (i = 1,2),

$$E_i = E_{i0} + E_{i1} + E_{i2}$$

where E_{i0} is common to both weather cases:

$$E_{i0} = a\, e^{j\theta}$$

The weather dependent fields are described by

$$E_{i1} = \left(b + \delta b_i\right) e^{j(\phi + \delta\phi_i)}$$
$$E_{i2} = \left(c + \delta c_i\right) e^{j(\psi + \delta\psi_i)}$$

For any pixel, a, b, c, , . are fixed and define the "zero weather" case. a, b, c are given by the square root of the average power scattered by that component (chosen by the simulation's user). The phases . . are uniformly distributed over [-, +). Weather dependence is described by the parameters b_i, $_i$, c_i, $_i$, each of which is normally distributed with a mean and standard deviation specified by the user (i.e. eight parameters are needed for two weather-dependent components).

In the case of (1) the different field components being independent (implicit in the model's approach), (2) only the scattering *phases* varying with the weather (i.e. $b_i = c_i = 0$), and (3) the scatter being broad (i.e. > 1 cycle), the expression for the coherence averaged over N pixels can be evaluated to a relatively simple result:

$$\left\langle |E_i|^2 \right\rangle = a^2 + b^2 + c^2$$

$$\left\langle E_1 E_2^* \right\rangle = a^2 + b^2 \frac{e^{j\alpha}}{\sqrt{N}} + c^2 \frac{e^{j\beta}}{\sqrt{N}}$$

where , are random phase angles. This expression shows the importance of the static component (a^2) and the number of independent pixels (N) in determining the coherence in the case of large scatter due to weather effects. Physically, "large" scatter corresponds to displacement spreads of the order of half a wavelength or less; such scatter is not unreasonable in windy conditions with many types of vegetation.

Initial Simulation Runs and Preliminary Results

The Monte Carlo model described in the section above was used to study the situation in which the relative strength of the static and variable components varies and in which the backscatter phase shift and standard deviation vary from 0 to 360. The two-component version of the model was used. The strength of the static component was varied from 1 to 0. The weather-dependent component's strength was adjusted to keep the total backscatter intensity equal to 1. The *magnitude* of the variable component was not weather dependent, and its backscatter phase shift and standard deviation were kept equal to each other as they varied from 0 to 360.

Five runs (using different samples of random numbers) were carried out for each set of parameters to simulate 100 independent pixels per run. The coherence and linear correlation coefficient values obtained for the five runs were used to calculate a mean and standard deviation. The results are shown in Figure 5 (linear *correlation coefficient* for the phases for six different relative strengths of the static and variable components, static component backscatter intensity = 0.95, 0.80, 0.70, 0.50, 0.25, 0.05) and Figure 6 (*coherence* for 7 different relative strengths of the static component).

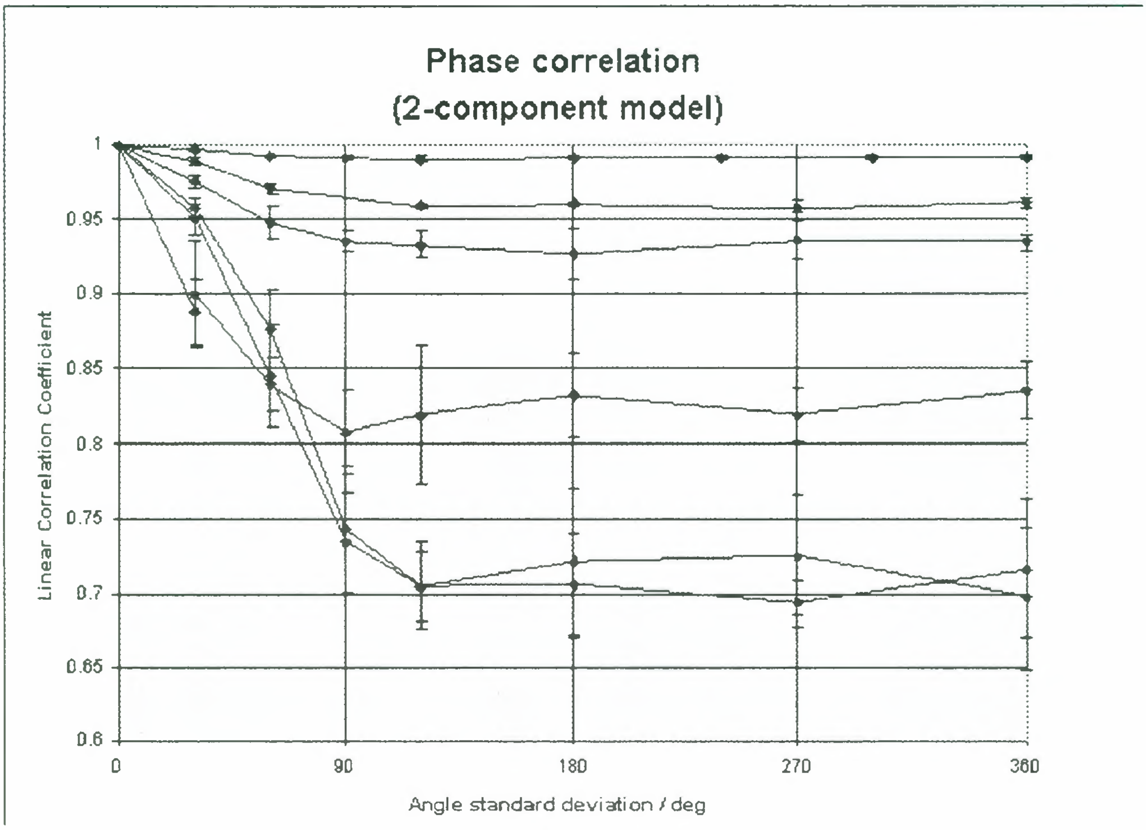

Figure 5: Linear phase correlation as a function of the backscatter phase standard deviation for six different sizes of the static component (0.95, 0.80, 0.70, 0.50, 0.25, 0.05 - in order from top to bottom of the figure for phase standard deviation = 180). The weather-dependent component was set to give a total backscatter intensity of 1. Each point plotted represents the mean (with 1- error bars) of 5 values, where each value is based on 100 independent pixels.

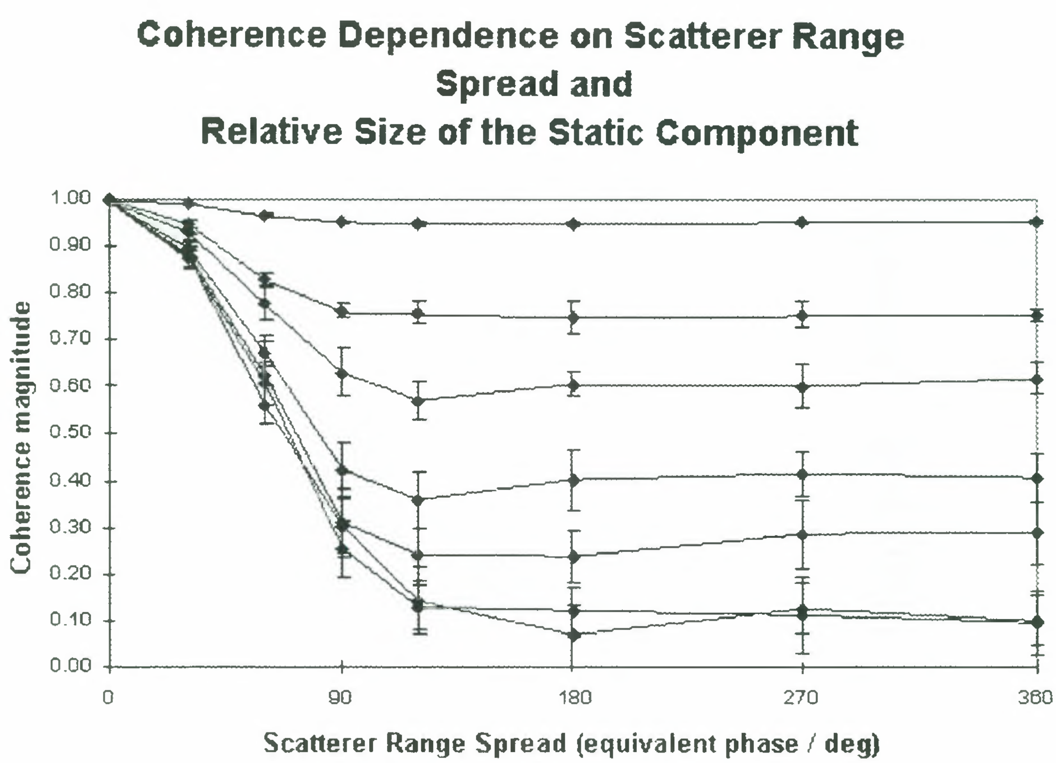

Figure 6: Coherence dependence on scatterer range spread and relative size of the static component. Reading from top to bottom the sizes of the static component are 0.95, 0.75, 0.60, 0.40, 0.25. 0.05, 0.00 (the total backscatter intensity is always 1). Each point plotted represents the mean (with 1- error bars) of 6 values, where each value is based on 100 independent pixels.

Discussion

The main feature of the results in Figures 5 and 6 is the decrease in correlation or coherence from 1 to an asymptotic value as the angle standard deviation increases. The asymptotic value is reached once the angle standard deviation reaches 90 - 120. The scale of this decorrelation phase angle standard deviation can be converted into a standard deviation of the equivalent scatterer's displacement in the slant direction. For ERS SAR, this corresponds to a distance of about 7 mm (/8), i.e. if the *variation* from pixel to pixel of the slant range to the equivalent scatterer exceeds approximately 7 mm then correlation due to that component is lost. Individual scattering elements in vegetation taller than about 20 cm can easily be displaced by this amount. This raises the question of how well such individual displacements relate to the position of the equivalent scatterer for the whole pixel. The following discussions show that the *value* of the asymptote can be predicted quantitatively using the analytical models presented above.

Correlation Coefficient

The correlation is small for cases in which the static component is small relative to the variable component. The cases with the static component intensity equal to 25% and 5% of the total overlap significantly while there is a clearer distinction at higher proportions.

The case with the static and variable components equal in size leads to anomalously low correlations for small phase standard deviations since it is possible for the variable component to "fold back" on the static component leaving a resultant with small magnitude. The two different weather cases can then be almost exactly 180 apart in phase and the distribution of phase differences becomes significantly non-Gaussian. Such behaviour is not found for other relative sizes of the components.

The analytical model's results (Figure 4) agree well with the levels of correlation found. For example, the cases with a dominant variable component and high phase standard deviation would expect to show almost completely random behaviour. The analytical model predicts a correlation of $2^{-0.5} = 0.707$ in this case, which is as observed. (Lower correlations can be measured in practice if the phase difference scatter is biassed towards the extremes of the permitted range.)

Coherence

Two aspects of the asymptotic coherence value are predicted well by the analytical model above. The model predicts the mean value of the coherence magnitude to be equal to the fraction of the total power from the static component in the broad scatter case, and also that in the limit of a static component equal to zero and one weather-dependent component the coherence magnitude should be 1/N.

Conclusions

The work presented above provides a framework for the rest of our investigation of the weather dependence of SAR phase correlation. Several specific conclusions can be drawn from the simulations:

- The relative strength of the static component is important. This implies that weather sensitivity is likely to vary through the growing season.
- A small spread (/8) due to weather in the position of the equivalent scatterers' slant range is enough to destroy phase correlation due to that component.
- There is possible synergy between the effects of different types of weather, e.g. precipitation may emphasise scattering from a class of scatterers (e.g. leaves) which is also more susceptible to disturbance by wind.
- The concept of the "equivalent scatterer" is central to the modelling presented here and should be investigated to understand its applicability. Its variability may be scale-dependent, which implies that there may be different optimum measurement scales for different applications.
- Coherence is a more useful general measure than the linear correlation coefficient because of its more natural range (0 to 1) and the fact that it uses phase and magnitude information. It may be appropriate to investigate the use of measures of correlation derived specifically for directional data (Batschelet, 1981; Mardia, 1972).

The next stages in the project are to (1) start analysis of ERS SAR data for our test sites, (2) attempt to quantify the physical effects of weather on SAR backscatter using a combination of models and field observations, and (3) use the models above (and MIMICS) to analyse the data.

The expected outcomes of the project are (1) statistical relationships between backscatter or phase correlation and suitable weather parameters, and (2) models (which may be applications of existing models such as MIMICS) to help understand the underlying physics. The results may have application in agricultural monitoring, meteorology, and SAR interferometry (by identifying image pairs likely to exhibit good phase correlation).

Acknowledgements

The work described here has been sponsored by the following organisations: European Space Agency, the Royal Society, AEA Technology plc, the RAIDS consortium, the Engineering and Physical Science Research Council and Cranfield University. The author is grateful for the support of all these organisations.

References

Batschelet, E., 1981:
Circular statistics in biology. Academic Press, London, 371 pages.
Mardia, K.V., 1972:
Statistics of directional data. Academic Press, London, 357 pages.
Ulaby, F.T., Moore, R.K., and Fung, A.K., 1986:
Microwave remote sensing, Active and Passive, Volume 3, From theory to applications. Artech House, Norwood, MA, 2162 pages (Vols. 1 to 3).

On the accuracy of differential SAR interferometry over Mt Etna

J.-P. Muller, M. Upton, J. G. Morley University College London, Gower Street, London. WC1E 6BT, U.K.

G. Wadge, N. Stevens NERC-ESSC, Reading

J.B. Murray Open University

Abstract

The NERC project on "Volcano monitoring using SAR interferometry" led by Prof. Geoff Wadge (Reading, NERC-ESSC) is concerned with the quantitative evaluation of the accuracy of differential interferometry for volcano monitoring using ERS data.

The UCL 3D Image Maker System for differential SAR interferometry (described by Upton, Muller, Smith; this workshop) has been employed to produce a variety of differential interferograms using the 2-pass + DEM method pioneered by Massonnett and co-workers.

Firstly the ERS-1 pairs analysed by Massonnet have been subject to an independent assessment using precision state vectors obtained from the D-PAF. Three different DEMs have been employed in the 2-pasds method to assess the impact of DEM accuracy on any possible artifacts which may appear in the differential interferogram. A 10m DEM grid-point interpolated from 1:10 000 10m contours kindly provided by CNR together with a SPOT-DEM generated using a specially commissioned overpass in August 1995 together with the 100m EURODEM (derived from FDTYED level 1) have all been used. Results will be presented of the impact of these DEMs on the differential interferogram at the Workshop.

Keywords:

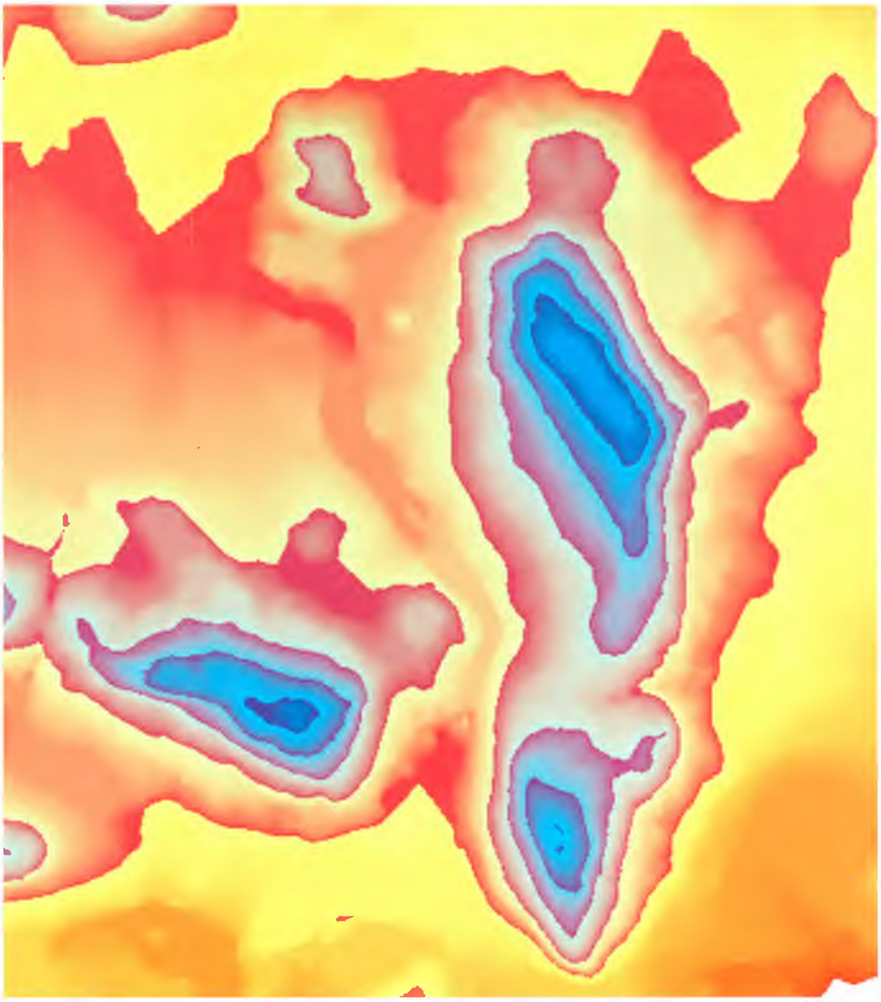

Figure 6: Existing height model.

Conclusions

Methods have been developed for utilization of SAR interferometry for DEM generation and land use mapping. These include the necessary rectification procedures for using the results together with existing maps. A project is currently being planned where the DEM of Northern Finland will be updated by means of SAR interferometry. This will make it possible to do the same for other areas or generate DEMs for areas where such information is not available.

Acknowledgment

The work reported here has been partly funded by the Technology Development Center of Finland. The Finnish Board of Survey provided the digital terrain model and land use maps for the area investigated.

Figure 7: Coherence for a 10 km by 6 km area.

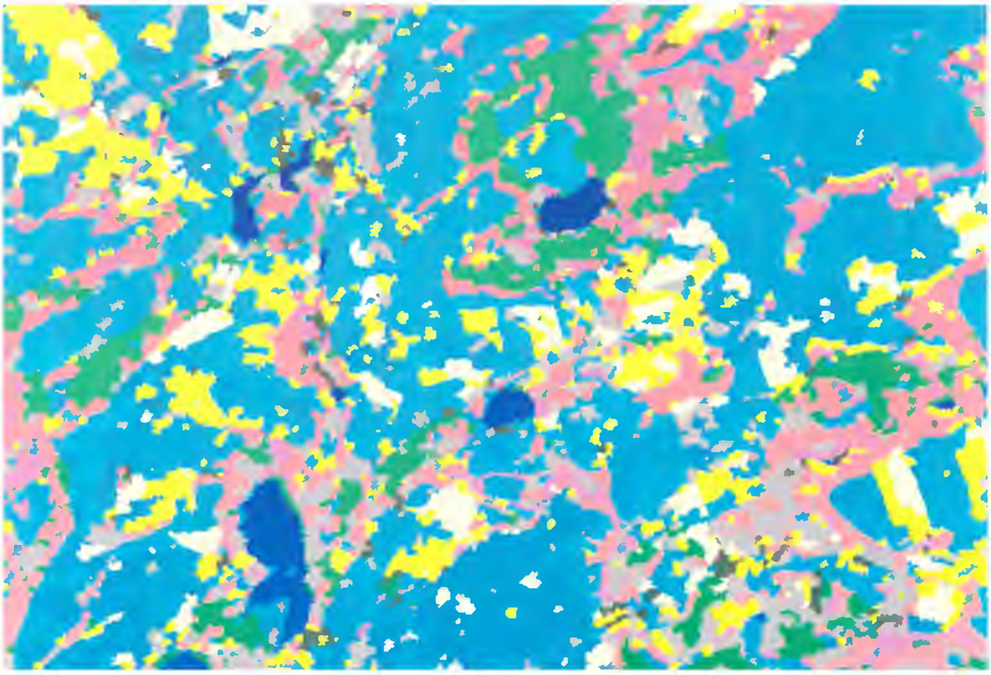

Figure 8: Land use map for the area in figure 7.

References

Gens, R. and J.L. van Genderen, 1996:
SAR interferometry-issues, techniques, applications. *International Journal of Remote Sensing*, Vol. 17, No. 10, 1996, pp. 1803-1835.

Engdahl, M., 1996:
Phase Unwrapping in SAR Interferometry Using Instantaneous Frequency Estimation, Master's Thesis.

Pritt, M.D., and J.S.Shipman, 1994:
Least-Squares Two-Dimensional Phase Unwrapping Using FFT's. *IEEE Trans. Geoscience and Remote Sensing*, Vol.32, no.3, pp.706-708.

Wegmüller et.al, 1995:
Land surface analysis using ERS-1 SAR interferometry. *ESA Bulletin*, No. 81,, pp. 30-37.

Herland, Einar-Arne, 1995:
SAR interferometry with ERS-1 in forested areas. *IGARSS'95*, Florence, Italy, pp. 202-204.

An Interferometric Quick-Look Processor

F. Gatelli, A. Monti Guarnieri, C. Prati and F. Rocca
Dipartimento di Elettronica - Politecnico di Milano
Piazza L. da Vinci, 32 - 20133 Milano - Italy
Fax: +39-2-23993585

Abstract

A real time technique to get strip-map SAR interferograms and coherence maps with common Unix Workstations / PC is presented. For the ERS mission, the ``real time'' throughput corresponds to approximately 1/8 of PRF: e.g. approximately 3 min for processing a 100 x 100 km image pair. The proposed algorithm computes a multi-look averaged interferogram + coherence map (at a resolution 50 x 50 m) in 18 minutes by means of a low cost PC (Pentium Pro). This goal is achieved, at a price of some data loss, by exploiting fast techniques for presumming, focusing, image coregistration and coherence estimate.

Introduction

With the huge amount of interferometric SAR data that are now and potentially will be available from satellite SAR missions (ERS-1, ERS-2, RADARSAT, SIR-C/X-SAR III), the computing time to obtain interferograms and coherence maps in a semi-operative scenario should be kept as short as possible. Thus, to select SAR pairs that actually can be exploited for interferometric applications the generation of fast, low-resolution surveys (e.g. fringes and coherence maps) should be carried out routinely on those pairs that show a suitable perpendicular baseline.

A ``quick-look`` processor is presented in this paper. The processor computes *interferogram and coherence maps* in blocks of 33 x 100 km, at a geometric resolution *45* x *45 m* on the ground (for flat earth). A good altimetric accuracy has been achieved by averaging the interferograms of *5 azimuth looks*. Several adjacent ``blocks`` are then mosaicked to get a continuous azimuth strip.

The processor performs near to real time on common low-cost machine: approximately *6 min* are requested to compute a single block (*32 x 100 km*, 5 looks averaged) interferogram & coherence map, by using a *PC PENTIUM PRO 200* running under Unix. Real time processing, i.e. 8 x the survey time (including some margin for data ingestion from HDDT), would require a machine 5 times faster.

Efficiency has been obtained, at a cost of some quality loss, by designing fast techniques for:

- range and azimuth focusing,
- images co-registration,
- estimate of coherence maps.

Raw data presumming

The look formation is performed, before range and azimuth focusing, by bandpass filtering and subsampling raw data. This approach gives the following advantages:

(a) the data rate is reduced by discarding less correlated (and noisy) contributions both in azimuth and in range. For range presumming, the central frequency is tuned according to the spectral shift predicted by the baseline [1].

(b) 2D wave-number domain focusing can be performed on smaller kernels and with ``approximate'' references. These kernels fit better in the processor cache. Moreover the cost of the Fourier Transforms is reduced.

(c) The processor can be easily implemented on multi-processor machines.

The cost of presumming stage is minimized by using polyphase filters and implementing an ``integer" format that handles one complex (I+Q) sample as a single integer word (16 bits) [2].

The processing time is thus reduced by a factor of 2.2 times due to range presumming (half band is dropped), 2 times due azimuth presumming (3 of the possible 8 looks are discarded) and 1.3 due to approximate focusing. These improvements are achieved at the cost of some information loss: nominally 50 % of the signal (for very low baselines) is lost due to range presumming and almost nothing for azimuth baseline in the tandem case due to the 300 Hz Doppler shift.

Coherence estimate

A *fast algorithm* has been designed (named *quick & dirty*) to compute coherence maps. The estimator achieves a computational time gain greater than 100, with respect of the conventional estimator, at the cost of a reduced statistical confidence (its accuracy being 3 to 5 times worse for coherence values > 0.4).

The proposed estimator exploits the images amplitudes, and it is based upon the relation between the absolute value of the complex coherence,

$$\gamma = \frac{\left|E\left[v_1 \cdot v_2^* \exp(j\phi(x,y))\right]\right|}{\sqrt{E\left[|v_1|^2\right] E\left[|v_2|^2\right]}}$$

(being $\phi(x,y)$ the averaged interferometric phase), and the normalized cross-correlation r of the detected SAR images:

$$r = \frac{E\left[\left(|v_1|^2\right) \cdot \left(|v_2|^2\right)\right]}{\sqrt{E\left[|v_1|^4\right] E\left[|v_2|^4\right]}}$$

The following expression [3]

$$r = \frac{\gamma^2 + 1}{2}$$

can be exploited to compute the complex coherence, given an estimate of the normalized cross-correlation of the amplitude image, r. The amplitude based coherence estimator is more efficient, since it does not require the knowledge of the interferometric phase (or local frequency). Moreover, it is not affected by possible local frequency estimation errors being insensitive to the interferometric phase.

It can be shown that the proposed estimator is strongly biased by amplitude non stationarities, however this bias can be effectively reduced by applying a sort of automatic gain control (AGC) to both detected images before computing the coherence estimate [3].

The proposed estimator can be efficiently implemented to compute a coherence map by exploiting overlapped Bartlett or Boxcar windows at a cost of 50 flops for each image pixel, independently of the window size.

Image coregistering & oversampling

The estimate of co-registering parameters has been improved by means of the ``*quick & dirty*" coherence estimator. Large windows can be explored since the estimator is independent of fringes & phases non-stationarities. Image co-registration is performed by two 1D resampling, since, for ERS, image rotation is well approximated by means of two 1-D skews.

Short space domain kernels are used for resampling & oversampling at the same time. Kernels are optimized for minimal phase noise and tabulated in steps of 1/100 pixel. A 6-7 samples kernel gives a coherence loss less than 2%. This approach is faster than frequency domain processing.

Interferogram generation

The looks image are aligned in phase (to recover the effect of approximate resampling) and then coherently averaged. The multiple look interferogram is performed as usual by conjugate cross-multiplication. Finally the low-resolution interferogram (fringes) is generated by filtering and subsampling. Here again short kernels (6 samples) are used. After mosaicking the blocks to get a large strip, a residual range flattening is given to compensate for flat earth. Notice that these steps are not requested if the generation of coherence maps is the sole requirement.

Computational complexity

The computing time achieved by the interferometric quick-look (for a 33 x 100 Km image block) is summarized in table 1.

Processing Step	**Quick-look**			**Polimi-ESA**
	CPU time [min:sec]		Mflops	CPU Time [min:sec]
	1 look	5 looks		
Doppler Centroid Estimate	0:01	0:01	-	
Baseline Estimation	0:01	0:01	-	
Filtering and Subsampling	*1:10*	*1:10*	31	
Focusing	*0:36*	*3:00*	27	
Registration params. estimate	0:03	0:03	-	0:30 - 15:00
Image #1 Resampling	*0:20*	*1:40*	27	0:41
Image #2 Oversampling	*0:05*	*0:25*	30	0:11
Interferogram Generation	0:06	0:07	31	
TOTAL	2:22	6:27		
Coherence Estimate	*0:14*	*0:30*		48:28

Table 1: Computing times (first two columns) and computational complexity (third column) for getting a 33 x 100 km interferogram and coherence map by means of the proposed quick-look processor. Last column: computing time requested to process the same amount of data with the standard processor (POLIMI-ESA). Time measures have been made by means of a 30 Mflops/s Unix Workstation, e.g. equivalent to a PENTIUM PRO 200.

The most time-consuming steps have been highlighted in italics. Note the advantage achieved with respect to the standard - public domain interferometric processor, due to a much more efficient way to compute coherence.

Conclusions

An algorithm for generating interferograms & coherence strips has been presented. It is intended for data screening / browsing. All the processing steps requested for generating the interferogram have been revisited - efficiency has been achieved by keeping coherence loss due to processing less then 5%. A ``*quick-and-dirty*", phase-independent coherence estimator has been introduced. It requires 14" to compute a 33 x 100 km, 5 looks averaged coherence map.

A 5 looks averaged, 33 x 100 km ERS interferogram can be computed in 6' with a 30 Mflops/s Workstation. A prototype processor, installed at ESRIN, has produced several interferograms and coherence strip-maps more than thousand km long.

Acknowledgments

The authors would like to thank the European Space Agency and Advanced Computer Systems (ACS) for sponsoring the work.

Figure 1: Low resolution interferogram from ERS-1/ERS-2 tandem mission (jan '96), Greenland. Images' size is approximately 300 x 100 km. Left: absolute value; center: coherence map; and right: fringes.

Figure 2: Enlargement of the previous image: an area of approximately 7 x 15 km has been shown. Note the fast fringes due to the movement of ice near the coast (iceberg ?).

References

1 A. Monti-Guarnieri, C. Prati, F. Rocca, ``SAR interferometric quick-look`` in *Proc. IGARSS '93, (Tokyo, Japan)*, Aug. 93. Vol. 3, pp. 988-990.

2 A. Monti Guarnieri, C. Prati, F. Rocca `` Development and Implementation of an ERS-1 Quick-Look Algorithm," *ESA contract* report N. 8658/90/HGE-I. Jan. 1991.

3 A. Monti Guarnieri, C. Prati ``SAR Interferometry: a "Quick and Dirty" Coherence Estimator for Data Browsing`` accepted for publication on *IEEE Trans. on Geosci. and Remote Sensing.*

4 F. Gatelli, A. Monti Guarnieri, C. Prati, F. Rocca, ``Medium Resolution Efficient Phase Preserving Focusing for Interferometry,`` in *Proc. IGARSS' 96*, (Lincoln, Nebraska,) 27-31 May, 1996.

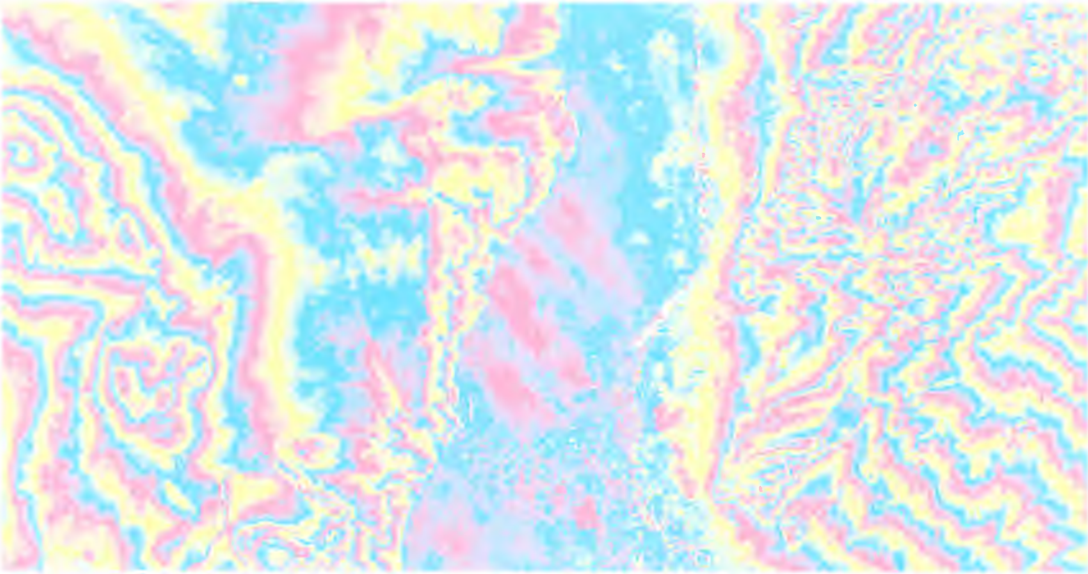

Figure 6: Flattened interferometric phase of ERS-1/ERS-2 for Cairo. CPRF. processing was used for both SLC.

on the other hand, the Bern interferogram appears noisy even in the one-day repeat tandem configuration and the rather short baseline. The production of a DEM would require numerous user interactions during the unwrapping task.

Coherence Maps

The coherence histograms and statistics are an indicator for the quality of the various processors. The processing of image pairs from the same raw data in particular reveals the relative phase differences introduced by the different processors.

Singletrack

Figure 7 shows the coherence that can be achieved when combining products from different SAR processors in the singletrack case. Notice how a difference, even if small, is present in the phase information provided by different focusing programs starting from the same raw data. The level of phase noise is directly related to the correlation coefficient (Bamler R. and Just D., 1993): the results presented in Figure 7 concerning the coherence distribution confirm the results seen in Table 1 in terms of phase noise.

In this case no systematic phase trends need to be considered as a source of coherence loss, since the estimation of the correlation coefficient is performed on relatively small subwindows. No temporal decorrelation effects are present in this combination: only image misregistration, differential defocusing and different processor noise levels are possible sources for this small loss of coherence.

Comparison of several multi-look processing procedures in INSAR processing for ERS-1&2 tandem mode

Yonghong Huang International Institute for Aerospace Survey and Earth Science (ITC),

P.O.Box 6, 7500 AA Enschede, The Netherlands. huang@itc.nl

J.L.van Genderen International Institute for Aerospace Survey and Earth Science (ITC),

P.O.Box 6, 7500 AA Enschede, The Netherlands. genderen@itc.nl

Abstract

Multi-look processing, as a traditional method to reduce phase noise in SAR processing, has been used in INSAR processing since the INSAR techniques developed in the late 1970's. In INSAR processing, there are several possibilities to insert multi-look processing into the processing chain. The first method is to form an interferogram after two multi-look images have been obtained from two single-look images. The second method is to obtain an interferogram by summing several multi-look processed interferograms. A third method is to produce an interferogram by filtering single-look interferometric image in the complex image domain. In this paper, we are aim to compare these multi-look processing procedures for ERS-1 and ERS-2 tandem mode data. The results will be evaluated by judging noise reduction in the interferogram and by the accuracy improvement in the 2-D phase unwrapping in INSAR processing.

Keywords: Multi-look processing, Phase noise.

Introduction

Topographic maps and DEM's over the global land obtained by interferometric SAR(INSAR) techniques have gained increasing interesting from scientists in a variety of research areas, such as geology, hydrology, geophysics, and so on, due to the fact that topographic maps produced by SAR interferometry have the advantages of all weather condition, high accuracy and automatic processing. INSAR techniques, which concentrate on the phase information included in two SAR complex images obtained from two antennas simultaneously or from repeat pass, have developed rapidly since the first concept proposed by Graham in 1974. General INSAR processing procedures, consisting of registration, baseline estimation, forming interferogram, filtering, flat area phase removal, 2-D phase unwrapping, etc., have been well investigated(Gens and Genderen, 1996). However, some technical details still remain controversial. Phase noise reduction is one of the troublesome topics needing to be solved in the near future since it directly influences the accuracy of DEM's produced by INSAR processing. Some papers have addressed this problem briefly and proposed some methods to solve it. In 1988, Goldstein indicated that multi-look processing can reduce speckle noise of interferograms and improve the accuracy of 2-D phase unwrapping. Since then, multi-look processing for interferometry has been included in INSAR processing. In 1990, Li established a complete model for INSAR, in which speckle noise and thermal noise are considered. He proposed an *ad hoc* method to simply sum up the interferometric images over the multiply looks in the complex vector domain so as to obtain a complex vector with interferometric phase information. The expected height uncertainties due to phase errors caused by speckle noise was estimated by his simulation results. Afterwards, Lee(1994) presented his results on a statistical model of interferometric and polarization SAR images. He also demonstrated the results of the relationship between phase standard deviation and the number of looks. From another point of view, Lin(1992) pointed out that the median filter was helpful for speckle reduction of interferograms.

In order to make further research on the influence of phase noise in INSAR imagery, our approach has been to investigate, as a first step, several multi-look processing procedures and analyze the test results. In the following sections, we first summarize the sources of noise in INSAR. The second part presents three noise reduction procedures used in INSAR processing. Part three compares the results obtained with these three procedures and evaluates the results by visualization procedures.

Summary of Phase Sources

Phase noise forms an obstacle to interpret interferogram or to generate DEM from an interferogram. If the phase noise is too strong, some fringes will be completely lost which will result in errors in the DEM. Phase noise(Zebker, 1992 and 1994; Huang, 1996) is mainly caused by radar thermal noise, speckle noise due to coherent SAR processing, decorrelation, sampling, processing artifacts, interpolation noise, defocusing, registration noise, etc. There are briefly explained below:

Thermal noise, regarded as an additive noise, is caused by the radar system itself. Increasing the signal-to-noise ratio(SNR) of the radar system can reduce thermal noise to the quality requirement of a SAR image. It is not a crucial noise source in a normal SAR image since the SNR of the radar receiver and coherent SAR processing ensues that the final image possessed a large enough SNR to omit the effect of thermal noise. However, it is an important noise source in INSAR due to the combination of two SAR images enhancing the intensity of the thermal noise to a certain extent. Especially, in the dark areas, the SNR is quite low in an INSAR image.

Registration noise, caused by not properly registering two SAR images, will lead to the fringe pattern of the interferogram being smeared and sometimes even completely lost. The interferogram generated from misregistration becomes drastically noisier. This noise cannot be remedied by post processing such as filtering. It can only be reduced by a fine registration operation. Thus, image co-registration is a crucial step in INSAR processing.

Speckle noise, regarded as a multiplicative noise, is generated from coherent processing formation of a SAR image. It is a dominate noise source in a SAR image. Eventually, it exists in an INSAR product due to the speckle characteristics of two SAR images used to form an interferometric image being not entirely identical. Incoherent summation helpful to reduce speckle noise has been proven by many research reports (Huang, 1996).

Decorrelation noise, regarded as a complicated noise, is caused by two SAR images which are used to form an interferometric image being not exactly the same, since they are observed from a slightly different antenna viewing angle, at a different time and during varying terrain condition. It is dependent on the antenna separation, antenna rotation, bandwidth of the radar, time interval between the two images obtained, variation of terrain, etc.

Processing artifact noise , such as quantization noise, interpolation noise, sidelobe noise, defocusing noise, Doppler Certroid estimating error, etc., lead to an unexpected random noise added in an interferometric image. To minmize these noise sources, a highly precise processing algorithm is required to improve the quality of SAR processing and increase the creditability of INSAR processing.

Description of Several Multi-look Processing Procedures

Multi-look processing in INSAR processing, introduced from original SAR processing, is used as an efficient algorithm to reduce phase noise in an interferometric image since it is the optimal estimator in a maximum likelihood sense for an interferometric image. There are three main methods to insert multi-look processing in a normal INSAR processing chain. Fig.1 shows three processing chains including multi-look processing.

1. *Method I*

Mutli-look processing is performed in both SAR images. Several multi-look processed image pairs are used to form several interferometric images. Then, these interferometric images can be summed to achieve a final interferometric image. The interferogram is extracted from the phase of the interferometric image.

1. *Method II*

Multi-look processing is performed after the single-look interferometric image has been generated. Then, the averaging operation is implemented in this single-look interferometric image to form the multi-look interferogram.

1. *Method III*

After the single-look interferometric image is formed, a weighted low pass filter is used in the interferometric image. The filtered interferometric image can form the final interferogram. Window size determination is a crucial step in the filtering process. Actually, Method II is similar to Method III. But, Method III is more flexible to filter the interferometric images.

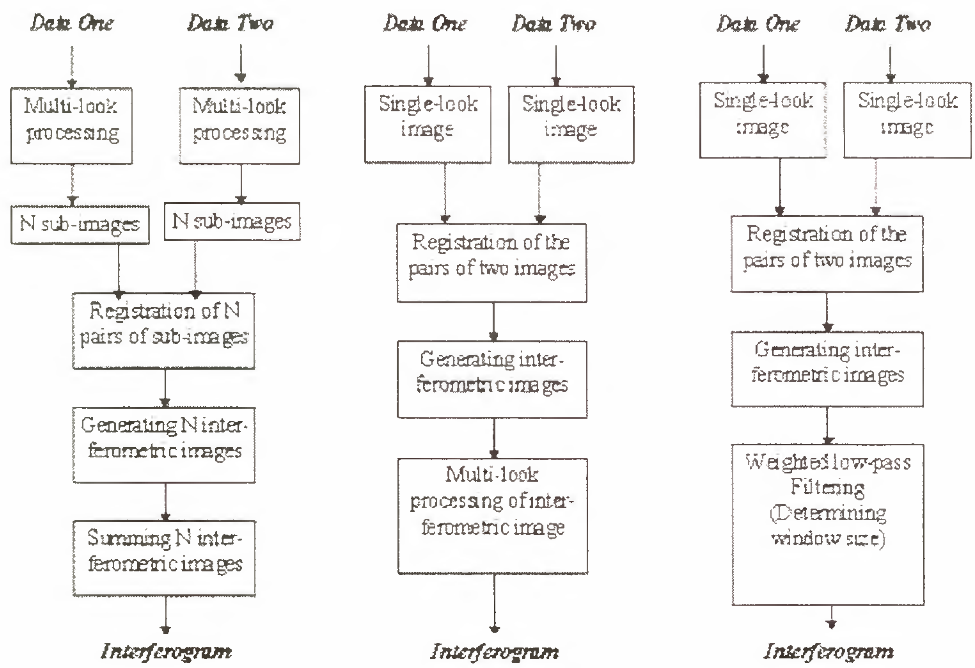

Method I Method II M ethod III

Fig.1 Three processing chains for multi-look processing

Comparison of Three Multi-look processing Methods with ERS-1 and ERS-2 Tandem Data

The area selected for testing the three methods described above is a subset of an Italian test site, using ERS-1 and ERS-2 single-look complex imagery consisting of 512 slant range pixels and 2048 azimuth pixels.The image covering this area is shown in Fig.2. In order to match the size of azimuth to the range, the image has been averaged four times in azimuth. The data set obtained from ERS-2 is one day delay to ERS-1 on Sept.5, 1995. The baseline of data set is estimated about 50m in cross-track.

Fig.4 Interferogram with flat phase removal.

Fig.3 Interferogram of test area

The first step of INSARprocessing is registration. Registration of two SAR images consists of two steps. The first step is called coarse registration, by which two images can be registered to the accuracy of one pixel space in both directions.The second step is called fine registrat-ion, by which two images will be registered to the accuracy of sub-pixel space. The registration criteria we used in our processing is to searchthe maxi-mum of value of the coherence co-efficient proposed by Li in 1990.After the step of fine registration, the interferogram is generated by multiplying the first image with the conjugate of the second image. The result of the single-look interferogram is shown in Fig.3. Due to the size in azimuth being four times in range, the result is decimated by four times.Fig.4 shows the interferogram after we roughly remove the phase term of a spherical earth at a constant terrain height by shifting the spectrum of the interferometric image in range. The fine removal is not implemented due to lack of enough accurate satellite data as required. However, the fringe pattern image in Fig.4 is sufficient to illustrate the noise reduction by multi-look processing in the following part.

Fig.5 Multi-look processed Interferogram(Method two)

Both Fig.3 and Fig.4 appear to contain too much noisier to recognize the fringe pattern. Hence, we use multi-look processing(Method II) to reduce the phase noise. The result is shown in Fig.5. In Fig.5, the interferometric image is averaged by four times in azimuth and then the phase difference is extract from the interferometric image to form interferogram. Compared with single-look interferogram in Fig.4, the multi-look processed interferogram looks much better and the fringe pattern is clearer in Fig.5.

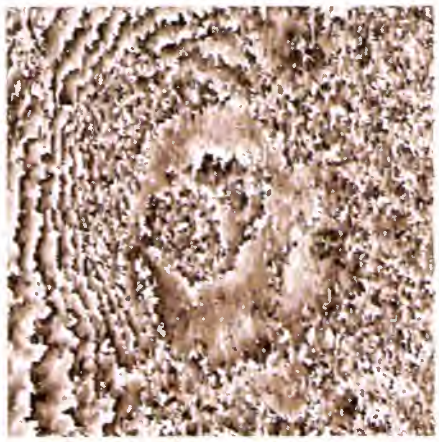

Fig.6 Multi-look processed Interferogram(Method one)

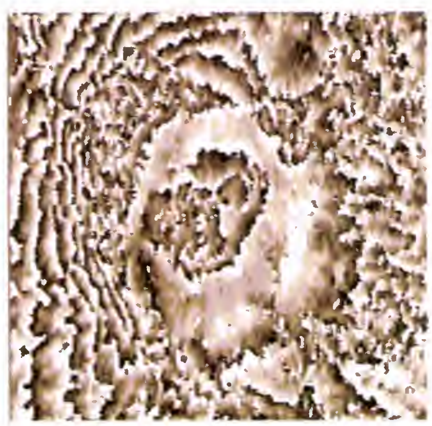

Fig.7 Multi-look processed Interferogram(Method three)

We also tested Method I and Method III with the same data set according to the diagram of multi-look processing illustrated in Fig.1. There are several key points which need to be mentioned here: In Method I, the two SAR single-look images ought to be processed into multi-look images of 512 by 512 pixels with the same Doppler certroid frequency so as not to lose coherence in every pair of multi-look processed images. Each pair forms an interferometric image with amplitude and phase. Then, a complex summation operation is performed to obtain a final interferometric image. The interferogram is shown in Fig.6. Due to registration errors existing on the registration of each pair, the result obtained from Method I is not as good as that from Method II. In Method III, two single-look images are registered first and the complex interferometric image is formed based on the registered images. We can design different low-pass filters to filter it and reduce phase noise as less as possible. Filtering can be implemented in the frequency domain by FFT operation or in the time domain by convoluting a filter kernel with the interfermetric images in range and azimuth dimensions. Different weighting functions can be used in the filter design. Here we tested various ones,such as the rectangular function, exponential weighting function, Sinc weighting function, etc. One crucial point in filter design is to know how to select bandwidths of range and azimuth in two dimensions or to determine the window size of range and azimuth in the time domain. For cross-track interferometric SAR, the fringe pattern is oriented along-track so that the bandwidth in azimuth can be much smaller than that in range. That means the fringe pattern in range is more sensitive to the filter bandwidth than that in azimuth. In addition to these above reasons, the choice of the filter bandwidth is influenced by terrain slope, coherence coefficient, baseline,etc. If the bandwidth of the filter is too large, the filter is less efficient to remove phase noise. If it is too small, it will smooth the fringe and demage the subtle details of the interferogram.

After several tests, the quasi-optimal filter window size we selected for our test image is 5 in range by 35 in azimuth. The filtered result is shown in Fig.7. We also tested the Sinc weighting filter and the Exponential weighting function filter. These results are shown in Fig.8 and Fig.9. Test results indicate that the Method III is more flexible to reduce noise as well as preserving the fringe pattern by adjusting filter bandwidth. Fig.8 and Fig.9 show that weighting filters are more efficient to remove phase noise whilst keeping the subtle details of the fringe pattern. The Sinc weighting filter appears slightly better than Exponential one.

Fig.9 Filtered Interferogram with Sinc Weighting Filter

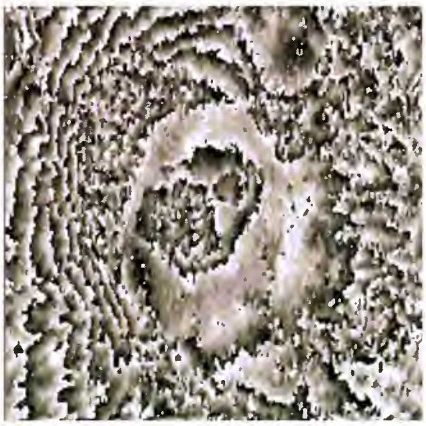

Fig.8 Filtered Interferogram with Exponential Weighting Filter

Conclusions

In this paper, three multi-look processing methods have been investigated both in terms of theory, and in practice by experiments. The test results show that Method III is the best one to filter phase noise as well as preserving fringe patterns of the interferogram. Our further research will focus on designing an adaptive filter dependent on the characteristics of phase noise to make further improvement to the interferogram.

Acknowledgements

The authors wish to acknowledge the support of the European Space Agency in provision of data(Tandem Mode Principal Investigator Project No.AO-T.NL.301), and for the provision of a Post Doctor Fellowship. The authors also acknowledge the financial support of the European Commision, as part of contract No.CHRX-CT93-0310.

References

Gatelli F., Guarnieri A.M., Parizzi F., Pasquali P., Prati C.and Rocca F., 1994:

"The Wavenumber Shift in SAR Interferometry", *IEEE Transac. on Geosci. and Remote Sensing,* Vol.32, No.4, pp855-864.

Gens R., Genderen J.L.van, 1996:

"Review Article: SAR interferometry- issue,techniques, applications", *Int. J. Remote Sensing,* Vol.17, no.10, pp.1803-1835.

Goldstein R.M., Zebker H.A. and Werner C.L., 1988:

"Satellite Radar Interferometric: Two-dimensional phase unwrapping", *Radio Sci.*, Vol.23, No.4, pp.713-720.

Huang Y. , Genderen J.L.van, 1996:

"SAR Speckle Reduction: A Review of Filtering Techniques and An Evaluation of Filter Performance", *ITC Internal Report*.

Huang Y., Genderen J.L.van, 1996:

"Speckle and Thermal Noise Reduction Techniques for SAR Interferogram", *Proceedings of the Second International Airborne Remote Sensing Conference and Exhibition,* San Francisco, California, Vol.3, pp.278-287.

Lee Jong-sen, Hoppel K.W., Mango S.A. and Miller A.R., 1994:

"Intersity and Phase Statistics of Multilook Polarimetric SAR Imagery", *IEEE Transac. on Geosci. and Remote Sensing,* Vol. GE-32,No.5, pp.1017-1027.

Li F.K., Goldstein R.M., 1990:

"Studies of Multibaseline Spaceborne Interferometric SAR", *IEEE Transac. on Geosci. and Remote Sensing,* Vol.28, No.1, pp88-97.

Lin Qian, Vesecky J.F., and Zebker H.A., 1992:

"New Approaches in Interferometric SAR Data Processing", *IEEE Transac. on Geosci. and Remote Sensing,* Vol.30, No.3, pp.560-567.

Zebker H.A. and Villasenor J., 1992:

" Decorrelation in Interferometric Radar Echoes", *IEEE Transac. on Geosci. and Remote Sensing,* Vol.30, No.5, pp.950-959.

Zebker H.A., Werner C.L., Rosen P.A.and Hensley S.,1994:

"Accuracy of Topographic Maps Derived from ERS-1 Interferometric Radar", *IEEE Transac. on Geosci. and Remote Sensing,* Vol.32, No.4, pp.823-836.

Impact of Precise Orbits on SAR Interferometry

Christoph Reigber	GeoForschungsZentrum Potsdam Telegrafenberg A17, D-14473 Potsdam reigber@gfz-potsdam.de
Ye Xia	GeoForschungsZentrum Potsdam Telegrafenberg A17, D-14473 Potsdam xiaye@gfz-potsdam.de
Hermann Kaufmann	GeoForschungsZentrum Potsdam Telegrafenberg A17, D-14473 Potsdam
Franz-Heinrich Massmann	GeoForschungsZentrum Potsdam, GFZ/D-PAF c/o DLR, D-82230 Oberpfaffenhofen fhm@dfd.dlr.de
Ludger Timmen	GeoForschungsZentrum Potsdam Telegrafenberg A17, D-14473 Potsdam timmen@gfz-potsdam.de
Johann Bodechtel	Institute for General and Applied Geology University of Munich Luisenstr. 37, D-803333 München
Michaela Frei	Institute for General and Applied Geology University of Munich Luisenstr. 37, D-803333 München

*

Abstract

For repeat pass SAR interferometry, two precision orbit products from ESA (processed at GFZ/D-PAF, Oberpfaffenhofen) are available: ERS-1/2.ORB.PRC's and ERS-1/2.ORB.PRL's. The conversion of interferogram phases to absolute surface heights require a relative baseline accuracy of 5 cm or even better. In a case study, the preliminary (PRL) and precise (PRC) orbits are used to derive DEMs. The results are compared with existing DTMs. In the test area in Thuringia (Germany), corner reflectors allow an additional accuracy assessment. The impact of orbit uncertainties on D-INSAR deformation analysis is less critical and the PRC's already fulfil the accuracy demands. This is demonstrated by an example from the Dead Sea transform zone in Israel.

Keywords: Precise Orbits, DEM accuracy, corner reflectors

Introduction

Repeat-pass interferometric techniques are employed for generation of topography models (DEMs) and, as a related application, for monitoring temporal surface changes (deformations connected with earthquakes or vulcanism, land sliding, soil erosion). The "state of the art" radar sensors, such as those established on ERS-2 and RADARSAT, acquire SAR image pairs from seperated orbit positions at different epochs. Their accurate knowledge allows a fringe pattern estimation of a reference surface and a conversion from phase differences to surface heights or displacements. Actually, there are uncertainties in the available orbit ephemerides which may distort the imaging geometry significantly. This problem can partly be overcome by using flat areas or sea shores as references. After "flat earth" correction (reduction of ellipsoid fringes), the interferogram fringe pattern must not show any height changes in this parts of the image. The interferogram may be adjusted and a conclusion for the relative orbit positions can be drawn. A more sophisticated approach for baseline assessment is to deploy a radar corner reflector array over the scene, e.g. one line of reflectors in slant range and one in azimuth direction. Unfortunately this can only be done in very few study areas because of the logistical, financial and timing limitations. The most straightforward way to solve the baseline problem is the determination of precision orbits using geodetic satellite tracking techniques like laser ranging and PRARE range and doppler observations. In this paper, the accuracy of the ESA orbit products ERS-1/2.ORB.PRC and ERS-1/2.ORB.PRL is investigated and compared with the SAR interferometry (INSAR) requirements.

ERS orbit accuracy demands

In order to obtain an analytical estimation of the required orbit accuracy for INSAR applications, the mathematical dependency of the interferogram phase from the SAR sensor and the object position have to be understood. In Fig. 1, the across track interferometer geometry is shown with a plain reference surface (for simplification), the sensor positions S_1 and S_2 at altitude H, the object P with elevation h, the baseline components B_x and B_y, the slange ranges R_1 and R_2, and the off-nadir angle (look direction). Because the height h as well as the baseline length B are small compared with H or R, the following equation is valid (Hartl and Xia 1993):

$$\phi = \frac{4\pi}{\lambda}(R_1 - R_2) = \frac{4\pi}{\lambda}\left(B_x\sqrt{1-\frac{H^2}{R_1^2}} - B_y\frac{H}{R_1}\right). \tag{1}$$

By differentiating with respect to B_x, B_y and H, we obtain:

$$\frac{\partial\phi}{\partial B_x} = \frac{4\pi}{\lambda}\sqrt{1-\frac{H^2}{R_1^2}}, \quad \frac{\partial\phi}{\partial B_y} = \frac{-4\pi}{\lambda}\cdot\frac{H}{R_1}, \quad \frac{\partial\phi}{\partial H} = \frac{-4\pi}{\lambda}\left(\frac{B_x H}{\sqrt{1-(H^2/R_1^2)}\cdot R_1^2} + \frac{B_y}{R_1}\right). \tag{2}$$

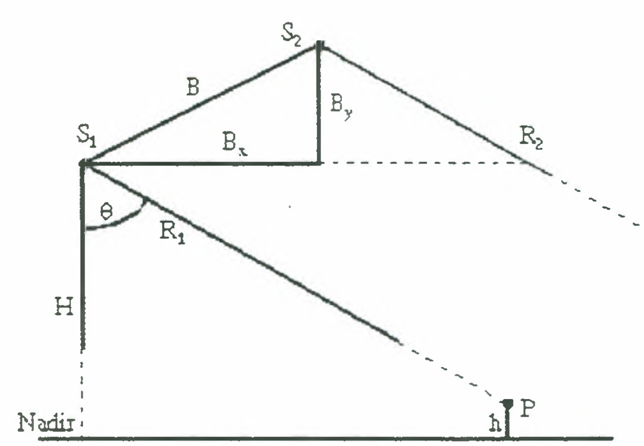

Fig. 1: Imaging geometry of a SAR SLC image pair (S_1, S_2: sensor position at epoch 1 and 2; R_1, R_2: slant ranges to object P; B_x, B_y: baseline components; h: topographic height)

For INSAR the impact of orbit uncertainties on areas with limited extension in ground range are of interest. Therefore, the maximum relative error d = d_{far} - d_{near} has been calculated. The extension of the test areas are assumed to be 5 km (local) and 50 km (regional), and the baseline seperation is considered with 50 m (differential INSAR applications) and 200 m (DEM generation). Approximate parameters of ERS-1 SAR system (= 0.057 m, H = 785000 m, $R_{mid\ swath}$ = 853000 m) are introduced in the error equations.

The interferogram phase shows a very low sensitivity to errors in sensor altitude. With dH = 10 m, the effect on topography or displacement is in the order of 1 m or 1 mm. For baseline errors of 0.05 m and 1.00 m, systematic phase errors will be obtained as compiled in Tab. 1. They are converted to surface displacement or topography errors using the equations:

$$d\rho = \frac{\Delta\, d\Phi}{4\pi}\lambda\ , \quad dh = \frac{\Delta\, d\Phi}{4\pi}\cdot\frac{R_1\,\lambda\ \tan 23^\circ}{B_x}$$

To assess the results in Tab. 1, they have to be related to the phase noise which is typically inherent in an interferogram of ERS-1/2 SAR data. The noise is caused by temporal decorrelation (e.g. vegetation, moisture), atmospheric perturbations, geometric baseline decorrelation, as well as data acquisition and processing defects. The validation of radar topography maps yielded errors of 5 to 10 m rms, (e.g. Prati et al. 1993, Small et al. 1993, Schwäbisch 1995, Zebker et al. 1994). This corresponds to a phase uncertainty of about one tenth of the wavelength or 0.6 rad. The phase noise acts mainly locally on a DEM and not systematically over the whole image. The effect of local noise may be a few times larger than the rms values. Therefore, the impact of orbit uncertainties is allowed to be in the order of 0.6 rad or even larger for local displacement analyses.

Tab. 1: Systematic errors for surface heights and displacements due to baseline errors of 0.05 m and 1.00 m. The derived values are related to areas with 5 km (local) or 50 km (regional) spartial extension, and to baseline length of 50 m (for change detection) or 200 m (for topography modelling).

	dB_x=0.05 m	dB_y=0.05 m	dB_x=1.00 m	dB_y=1.00 m
Interferogram Phase Error				
d(5 km) [rad]	0.06	0.02	1.1	0.5
d (50 km) [rad]	0.5	0.2	10.2	4.6
Displacement Error (Slant Range)				
d(5 km) [mm]	0.3	0.1	4.9	2.2
d (50 km) [mm]	2.2	0.9	45.5	20.5
Topography Error, B_x=50 m				
dh(5 km) [m]	2.0	0.7	36.4	16.6
dh(50 km) [m]	16.6	6.6	337.8	152.3
Topography Error, B_x=200 m				
dh(5 km) [m]	0.5	0.2	9.1	4.1
dh(50 km) [m]	4.1	1.7	84.4	38.1

From Tab. 1 the following conclusions can be drawn:

- as expected, the across track baseline component B_x is dominant, but the radial component must not be neglected;
- to avoid significant systematic errors in topography mapping (e.g. a tilt in ground range direction) a baseline precision of 5 cm has to be striven for;
- for the detection of surface uplift or subsidence in areas with local extension, the baseline precision should be better than 1 m; for areas with larger extensions, the baseline should be accurate up to 0.1 m.

At GFZ/D-PAF, the quality of the generated orbit products ERS-1/2.ORB.PRC and ERS-1/2.ORB.PRL is controlled internally by examining the fits of the laser ranges and the altimeter crossovers to the adjusted orbits and by comparing overlapping arc segments (Massmann et al. 1994, Gruber et al. 1996). Results (mean differences) of orbit investigations over a time interval of 6 month are given in Tab. 2.

Tab. 2: Accuracy of ESA orbit products ERS-1/2.ORB.PRC and ERS-1/2.ORB.PRL, derived form internal quality checks (fit of tracking observations to adjusted orbit, comparison of overlapping arc segments)

Orbit Product	radial	across	along
.PRC	7 cm	33 cm	31 cm
.PRL	8 cm	35 cm	35 cm

As shown in Tab. 2 the accuracy of .PRC and .PRL products is very similar. The demanded accuracy of 5 cm for DEM generation is not achieved, which makes a baseline estimation during the interferometric SAR processing still necessary. Such an estimation can serve as an external test of the orbit quality and will help to find out, whether there are advantages of .PRC orbits compared to .PRL orbits.

Application of ESA ERS-1/2 orbit products

In this section we provide two INSAR products generated with the ESA orbit products (humid climate in Germany, arid climate along the Dead Sea Rift). It is demonstrated how the orbit is used to generate the fringe pattern of a reference flat surface and what the orbit accuracy is.

In the first example a digital elevation model (DEM) is generated for the test area Ronneburg in Thuringia/Germany (50.8° N and 12.2° E). The single look image data pair was acquired during a tandem operation on the 8th of Feb. 1996 by ERS-1 and on the 9th. of Feb. 1996 by ERS-2. Fig. 2 shows the intensity of the SAR image over an area of 30 km in azimuth and 40 km in ground range. As reference the ellipsoid surface of WGS84 is applied. The following equation models the fringe pattern of the ellipsoid surface for a slant range line in the interferogram:

$$\varphi_{(i)} = 2\pi(c_0 + \frac{1}{2}c_1 i + \frac{1}{3}c_2 i^2)i + \varphi_0$$

Here, is the phase of the pixel i (i is normalized by image pixel number $N-1$ from 0 to 1), $_0$ is the initial phase of the considered line, c_0, c_1, and c_2 are the polynomial coefficients. The instantaneous fringe frequency derived from Eq. 4 is:

$$f_{(i)} = c_0 + c_1 i + c_2 i^2$$

In order to calculate the polynomial coefficients c_0, c_1, and c_2 the following linear equation system has to be solved:

$$\begin{bmatrix} f_0 \\ f_{1/2} \\ f_1 \end{bmatrix} = \begin{bmatrix} 1 & 0 & 0 \\ 1 & 0.5 & 0.25 \\ 1 & 1 & 1 \end{bmatrix} \begin{bmatrix} c_0 \\ c_1 \\ c_2 \end{bmatrix}$$

Here f_0, $f_{1/2}$ and f_1 are the instantaneous fringe frequencies by $i=0$, $1/2$ and 1, respectively.

The mathematical representation of the orbit (position and velocity) for the primary and the secondary satellite is identical, but with different coefficients:

$$\begin{cases} x_{(t)} = \sum_{n=0}^{4} a_n t^n \\ y_{(t)} = \sum_{n=0}^{4} b_n t^n \\ z_{(t)} = \sum_{n=0}^{4} c_n t^n \end{cases}$$

The coefficients are derived from the precision orbit ephemerides as determined by GFZ /D-PAF in accordance with the image acquisition time. By means of the orbital state (position vector $\vec{S}$ and velocity vector $\vec{V}_s$) and using equations from Curlander (1982), the pixel coordinate $P_{(Xp,\ Yp,\ Zp)}$ for $i=0,\ 1/2$, and 1 can be determined for each slant range line:

$$\begin{cases} \dfrac{\left(x_p^2 + y_p^2\right)}{R_A^2} + \dfrac{z_p^2}{R_p^2} = 1 & \textit{ellipsoid equation} \\ \dfrac{2}{\lambda R_s}(\vec{V}_s - \vec{V}_p) \cdot (\vec{S} - \vec{P}) = f_d & \textit{doppler equation} \\ \sqrt{(\vec{S} - \vec{P}) \cdot (\vec{S} - \vec{P})} = R_s & \textit{distance equation} \end{cases}$$

The position of the secondary satellite according to object P is obtained by solving the following equation:

$$\left(x_{(t)} - x_p\right)\frac{dx_{(t)}}{dt} + \left(y_{(t)} - y_p\right)\frac{dy_{(t)}}{dt} + \left(z_{(t)} - z_p\right)\frac{dz_{(t)}}{dt} = 0$$

As soon as the satellite positions and pixel position for $i=0,\ 1/2$, and 1 are known, the instantaneous fringe frequency is obtained from equation

$$f_{(i)} = \frac{\varphi_{i+1/N} - \varphi_i}{2\pi} N.$$

Removing the fringe pattern of the reference surface, the residual phase (or so-called relative phase) remains, which is shown in Fig. 3. After phase unwrapping and conversion from phase to height (Fig. 4), a comparison between the INSAR elevation model using .PRC orbits and the DEM derived from aerial photogrammetry (Fig. 5) can be carried out. Fig. 6 shows a systematic slope error of 65 m in across direction from near range to far range (40 km). In this case (baseline=142 m) the systematic slope error of 65 m is equivalent to a fringe frequency error of 0.89 or a baseline error of 62 cm. Fig. 7 compares the corrected height model derived from INSAR with the DGM. In the test area of 30 km * 40 km the standard deviation is 8.5 m (or in phase 40°) and the mean difference is -0.06 m. The maximum differences occur in the area of the open-cast mining where large mass movements (depositing of slagheap material in the open pit) are taking place since several years.

To compare the accuracy of the ESA orbit products ERS-1/2.ORB.PRC and ERS-1/2.ORB.PRL, the Ronneburg data set is evaluated with each of them. In Tab. 3, the fringe frequencies are calculated for the first slant range line as an example, the baseline is estimated in the middle of this line. The improvement of fringe frequency and baseline estimation by using of the .PRC orbit instead of the .PRL orbit is only 0.05 and 4 cm, respectively. This result confirms the assessment from the internal quality checks of the GFZ/D-PAF [Tab. 2].

Tab. 3: Comparison of the fringe frequencies and the corresponding baseline after applying the ESA orbit products ERS-1/2.ORB.PRC and ERS-1/2.ORB.PRL: the improvement for fringe frequency and baseline is 0.05 and 4 cm, respectively

	fringe f_0	fringe $f_{1/2}$	fringe f_1	baseline (m)
derived from PRC	223.09	204.06	188.03	141.92
derived from PRL	223.04	204.01	188.98	141.88

During the SAR data acquisition in Feb. 1996, 5 passive corner reflectors (CRs) were available in the test area, all positioned by GPS (5 mm accuracy). Tab. 4 compares the heights derived from INSAR and GPS for all CRs.

Tab. 4: Comparison of CR heights derived from INSAR and from GPS: CR 2 was chosen as reference point, as level ellipsoid the parameters of WGS84 are used .

Corner No.	Height (GPS)	Height (INSAR)	Height Difference
1	306.25m	305.42m	0.83m
2	295.50m	295.50m	0.00m
3	335.75m	333.45m	2.30m
4	328.32m	324.96m	3.36m
9	379.67m	369.40m	10.27m

The CR 2 was chosen as the reference point. The maximum difference occurs for CR 9 and amounts to 10.27 m. A big metaled light, fixed to a wooden post in about 5 m altitude, and not removed at that time was just in the direction from CR 9 to the satellite. This would explain the large discrepancy. Considering the first 4 CRs, the result is very good. The differences correspond to a radar wave resolution of 1 mm.

In order to check the impact of the ERS PRC orbits on geocoding of INSAR images, a positioning procedure for all CRs were accomplished by use of the Eq. (7), (8) and the CR heights as derived from GPS. The result is shown in Tab. 5, the global geocentric coordinate system of ITRF is used and the all differences were transformed into a local astronomical coordinate system. The positioning accuracy for all CRs is in the order of several meters. It must be noted that the resolution of the sampling in slant range is 7.9 m, in azimuth direction about 4 m, or the pixel spacing of ERS-1 and ERS-2 is 20 m*4 m related to the Earth's surface.

Tab. 5: Comparison of the positioning results: the global coordinate system of ITRF is used and all differences are transformed into a local astronomical coordinate system

Corner	X (m)		x (m)	Y (m)		y (m)	Z (m)		z (m)
Number	GPS	INSAR		GPS	INSAR		GPS	INSAR	
1	3939304.5	3939312.5	6.1	855789.4	855793.3	-0.5	4926507.9	4926509.5	6.8
2	3939234.6	3939243.2	2.9	856216.2	856213.7	-6.0	4926476.4	4926478.5	6.8
3	3940137.9	3940145.2	3.1	854230.7	854234.1	0.1	4926152.6	4926155.0	7.0
4	3940583.2	3940590.5	4.0	855904.6	855905.3	-2.6	4925500.6	4925503.5	6.9
9	3945132.2	3945147.0	-1.3	851565.0	851564.5	-6.3	4922695.9	4922693.0	7.0

The second example concerns the detection of subtle surface changes along the Dead Sea Rift, the natural border between Israel and Jordan. The zone is well known as an active plate boundary, marked by e.g. 32 earthquakes with magnitude > Ms. 4.5 in 1993. Using the differential SAR interferometry technique the area has been investigated because an earthquake occured on November 22, 1995, near the transform zone in the Gulf of Elat/Aqaba to the south. In 1995 three single look complex image sets were acquired: on August 16 (21373/585) and on November 29 (22878/585) by ERS-1, and on

September 21 (2201/585) by ERS-2, respectively. Fig. 8 shows the intensity image of the test area (29.24° N / 34.55 ° E. 40 km*40 km). First we have calculated two interferograms from the three data sets. The one pair (21373/585 and 2201/585) with a baseline of 308 m spans 35 days. the other one (21373/585 and 22878/585) with a baseline of 76 m spans 105 days. In each case the fringe pattern of the reference surface was removed using the precise orbits. After phase unwrapping the first interferogram was normalized with the baseline rate, and was subtracted from the corresponding second interferogram. The result focussing on the transform zone is shown in Fig. 9, where no distinct changes due to coseismic displacements can be observed. This is mainly due to the fact that the epicenter of the earthquake is located about 100 km to the south in the Gulf of Aqaba/Elat. Nevertheless, observable subtle changes in the data are various. There is an increasing level (blue) of a surface mud-dump to the north caused by mining activities at the Timma Complex to the southwest. Decreasing values (red) are displayed by partly harvested vegetation areas (south) covering the northern rim of the Gulf, and by pediments and alluvial fans at the western part of the rift. Most of the phenomena can also be attributed to heavy rains within the given recording frame. Assuming that the accuracy of the baseline estimation by use of the precise orbits is in the range of 1 m, and that the standard deviation of the relative phase is not more than 40°, the accuracy of the detected mass movements is approximate 0.3 cm.

Conclusions

The accuracy requirement of the satellite orbits for SAR interferometry is discussed in this paper. To avoid significant systematic errors, a baseline accuracy of 5 cm for DGM generation and of better than 1 m for subtle change or mass movement detection has to be striven for. The comparison of an elevation model derived from INSAR by use of ESA precise orbits with the existing DEM demonstrates that ESA precise orbits provides a baseline accuracy of better than one meter. This satisfies the D-INSAR needs in most cases. A positioning example of CRs shows that an accuracy of 1 resolution cell may be achievable. For the goal of DEM generation, the employment of CRs and their GPS survey is still essential.

Fig. 2 Intensity image of the test area Ronneburg

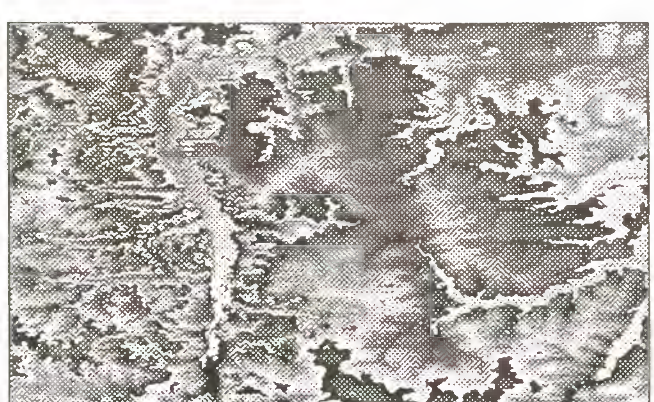

Fig. 3 Relative phase image by use of .PRC orbits

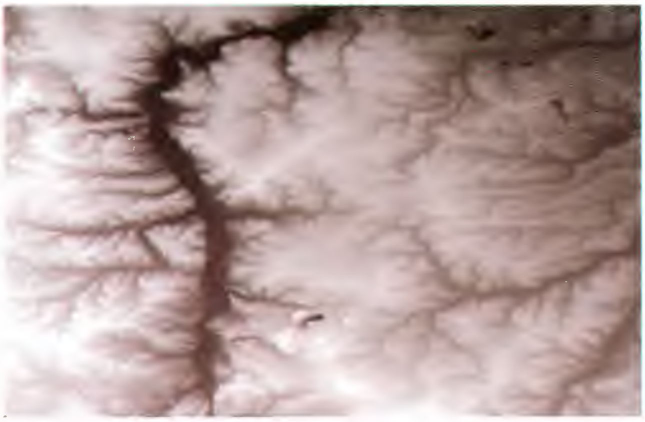

Fig 4. Elevation model derived from INSAR

105 m 393 m

Fig. 5 Existing DEM derived from photogrammetry

148 m 386 m

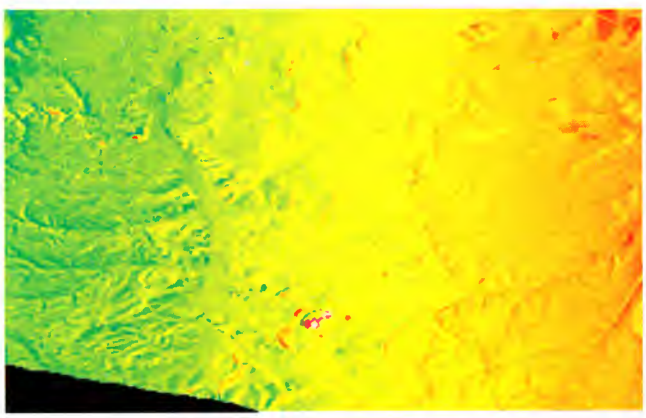

Fig. 6 Height difference between DEM derived from INSAR and existing DEM: a systematic slope error of 65 m in across direction (40 km) corresponds to a fringe frequency error of 0.89 or to a baseline error of 62 cm.

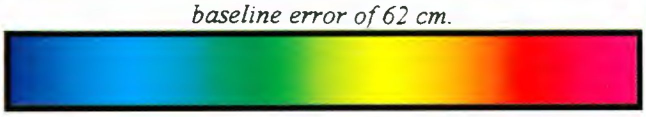

-45 m 40 m

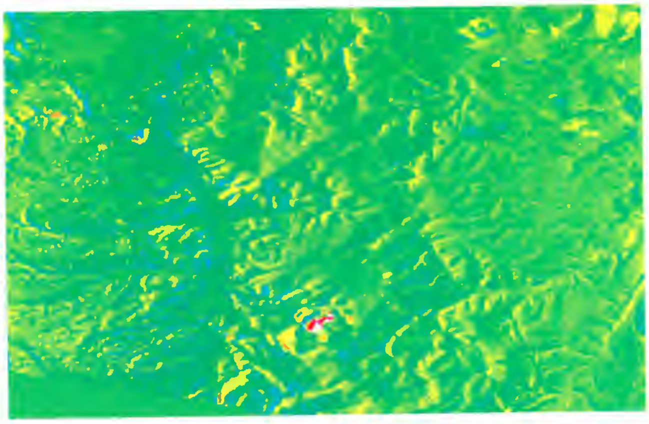

Fig. 7 Height difference between corrected DEM derived from INSAR and existing DEM: mean=-0.06 m, standard deviation=8.5 m, the maximum differences occur in the area of the open-cast mining.

-112 m 106 m

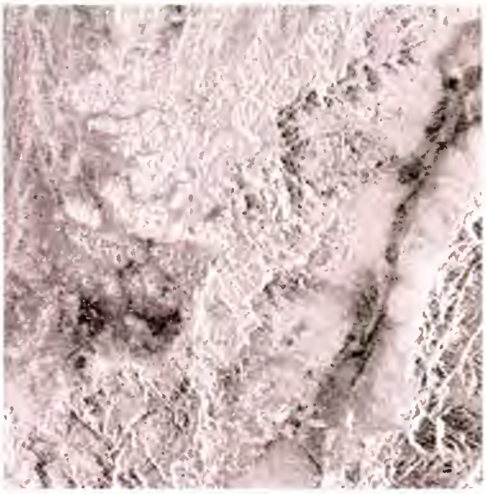

Fig. 8 Intensity image of an area north of the Gulf of Elat/Aqaba (Israel/Jordan): the scene site is *29.24° N / 34.55° E*, the area is 40 km * 40 km.

References

Curlander, J. C. 1982:
Location of Spaceborne SAR Imagery, *IEEE transaction on Geoscience and Remote Sensing*, Vol. 20, N0. 3, pp. 359-364

Gruber, Th., Massmann, F.-H., Reigber, Ch., 1996:
The German PAF for ERS, ERS D-PAF altimeter and global products manual, ERS-D-GPM-31200.

Hartl, Ph., Xia Ye 1993:
Datenverarbeitung bei der SAR-Interferometrie, *Zeitschrift für Photogrammetrie und Fernerkundung*, 6/93, pp. 214-222

Massmann, F.-H., Reigber, Ch., König, R., Ralmondo J. C., Rajasenan, C., 1994:
ERS-1 orbit information provided by D-PAF. Proceedings Second ERS-1 Symposium - Space at the Service of our Environment, Hamburg, Germany, 11-14 October 1993, ESA SP-361, pp. 765-770.

Prati, C., Rocca, F., Monti Guarnieri, A., 1993:
SAR interferometry experiments with ERS-1. Proceedings First ERS-1 Symposium - Space at the Service of our Environment, Cannes, France, 4-8 November 1992, ESA SP-359, pp. 211-218.

Schwäbisch, M. ,1995:
Die SAR-Interferometrie zur Erzeugung digitaler Geländemodelle. DLR-Forschungsbericht 95-25, Deutsche Forschungsanstalt für Luft und Raumfahrt e.V. (German Aerospace Research Establishment), Köln, 125 pages.

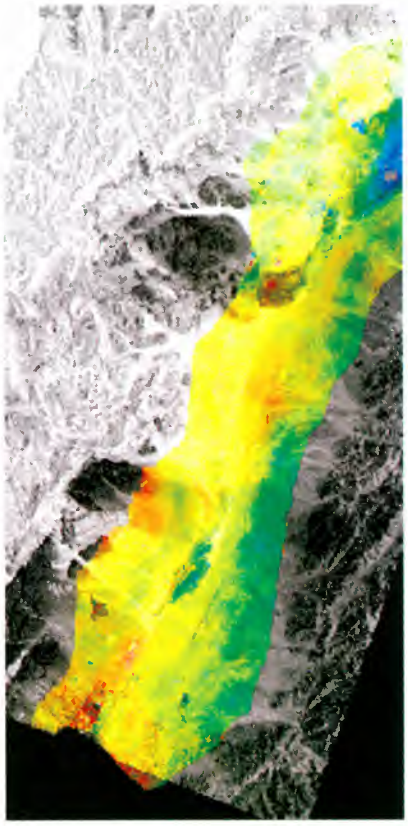

Fig. 9 Result of D-INSAR for the Dead Sea Rift area in the transform zone near Elat/Aqaba: the data sets were acquired at 16.08.95, 21.09.95 and 29.11.95. IHS-color merge of optical (Landsat TM band 4) and differential INSAR result (I=TM, H,S =D-INSAR).

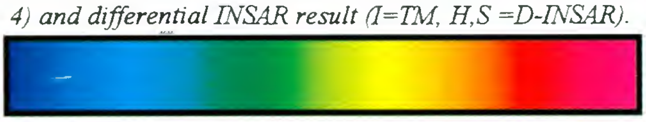

1.4 cm 0 -1.4 cm

Small, D., Werner, C., Nüesch, D., 1993:
Baseline modelling for ERS-1 SAR Interferometry. Proceedings of IGARSS´93, Tokyo, pp. 1204-1206.

Zebker, H., Werner, C., Rosen, P., Hensley, S., 1994:
Accuracy of topographic maps derived from ERS-1 interferometric radar. IEEE Transactions on Geoscience and Remote Sensing, Vol. 32, No. 4, pp. 823-836.

ERS Interferometric Products Development at ASI-Space Geodesy Center

Ettore Lopinto — Nuova Telespazio, Matera (Italy)
lopinto@ipaf.mt.asi.it

Cosimo Marzo — Agenzia Spaziale Italiana - Centro di Geodesia Spaziale, Matera (Italy)
marzo@ipaf.mt.asi.it

Abstract

The scope of this work is to describe the two ERS Interferometric Products developed at ASI-Space Geodesy Center. These products will be available to the users as "application independent interferometric raw data" that will simplify the processing activities. The first product "SRI" (Single look complex Registered Image) is a multiband image obtained registering one or more slaves SLC to a master SLC. The final data consists of a set of annotated complex images. The second product "WFI" Wavenumber shift Filtered Image is a multiband product, derived by the SRI, containing the following layers: complex and filtered interferogram, coherence map and Interferogram Flattened on the earth ellipsoid.
Keywords: Interferometry, Coherence, Interferometric processing, Wavenumber Shift Filtering

Introduction

A lot of work has been done in the Research and Validation of the SAR Interferometry. Although the technique is well proven, to develop an applications, the users often has to start from the standard SLC products and has to properly process these data. Due to the presence at CGS of the Italian Processing and Archiving Facility, an effort has been done to define and develop a set of interferometric products which will make possible the use of the SAR Interferometry in an operational way.

An extensive papers review has been carried out to define a products set which could be useful for a wide spectrum of applications and the best processing algorithms available.

Data processing has been structured in a pipeline fashion, which permits to obtain all the intermediate products and simplify both the SW test and product validation. Furthermore the absence of manual operator intervention results in a well stable product quality.

In this paper a overview of the products characteristics and of the processing algorithms is presented. The first product is called SRI (Single look complex Registered Images) and contains a couple of registered complex images with some annotations like the baseline value for every image line. The second called WFI (Wavenumber shift Filtered Interferogram) is composed by a set of image layers: wavenumber effect filtered images, complex interferogram (optionally flattened on the earth ellipsoid) and coherence map.

SRI (Single look complex Registered Images)

The input data for the Image Registration step is a couple of complex products (e.g. ERS.SAR.SLC), in slant range/azimuth coordinate system, given as a IQ data sequence with each channel quantized in signed 16 bit format. The key point in the SLC registration is the derivation of the distortion function (hereinafter called the warp function WF). The WF sets up a corrispondence between the pixels of the master image and those of the slave image.

The WF is derived using: orbital & geographic informations, image morphology, phase information. From the master and slave image geographic location and the orbit, a Very Coarse Registration is derived. The precision of this first estimate of the warp is poor (10-20 pixels) but has the great advantage of a completly automatic processing. No tie points and no image visualization is necessary during this step.

The next operation (the Coarse Registration) refines this registration extracting and correlating a set of master-slave cells. The cell extraction is done using the corrispondence obtained from the previous step and the cross correlation is interpolated to reach a 0.1 - 0.5 pixel precision. Because the correlation is done between the cells amplitude, no phase information is used.

The last step in the warp evaluation is called Fine Registration and uses the APF (Average Phase Fluctuation) algorithm to find a high precision shift between the master-slave cell couple. The slave cell is shifted using the FFT properties and the cell interferogram is then derived. A two dimensional minimization is used to find the shifts which produce the minimum phase noise. Knowing the precise shifts parameters in every cell, a best fit polynomial WF is obtained. Three degrees are available spanning from the first to the third. The next operation consists in the slave interpolation on a new grid defined by the WF. Due to the dimensions of the images, first of all the slave SLC is segmented in small blocks (e.g. 200x200 pix) and then each tile is registered onto the master. The interpolator function has to be carefully selected because: in the azimuth direction the warp function shows small variation but the spectra is not zero centered and so no "simple" low pass interpolator can be used; in the range direction the spectra are zero centered but the variation of the warp function are high. For these reasons we have chosen the following interpolation type: a FFT in azimuth, evalued for every line and a cubic convolution in range computed for every pixel. The master image is resized to contain only the portion common to both the images.

As last step, a coarse baseline computation is done, based on the propagated orbits and the WF knowledge. Using the WF it is possible to sincronize the time of the two orbits and to evaluate the baseline as vector function of the range line. The coefficients of the polinomial which give the baseline are annotated in the output product.

WFI (Wavenumber shift Filtered Interferogram)

The presence of a terrain slope seen in slight different way by the master and the slave sensors produce a shift in the range spectra of the interferometric couple [1] [2]. This effect, called wavenumber shift has to be properly handled if we want to avoid the interferogram decorrelation associated to the geometry. To correct this decorrelation effect, a filtering of both the images must be done, with a couple of "wavenumber" filters. These filters must be generated starting from the knowledge of the local interferogram fringe frequency (related to the local terrain slope).

In the first step, a subdivision of the SRI data is done, selecting a set of cells equally spatially in the image. The sampling is done with a somewhat high spatial frequency because the frequency shift has a strict dependency from the slope change in the imaged terrain zone. For each cell, the relative frequency shift is estimated deriving a local range fringe frequency map. The "wavenumber" filters (distinct for the master and slave image) are then generated as range and azimuth dependent functions and a standard method (like Overlap & Save) is used to filter the entire SRI data. It is worth to say that, before the filtering, the images are interpolated in range by two, using a FFT and zero pad, to avoid the aliasing effect during the interferogram formation step. The resulting output product is called WFI - (Wavenumber effect Filtered Images) and is constituted by a wavenumber effect filtered master-slave couple.

From the previous WFI couple the complex interferogram is simply obtained multiplying the master WFI with the coniugate of the slave WFI. This leads to a complex image which has as amplitude the product of the master and slave amplitude, and as phase the phase difference between the two images. The coherence map can be evalued as usual but correcting the topographic factor (as given from the local 2D fringe frequency) and using "non biased" coherence estimation algorithms [3][4]. In such way the coherence map is derived and given as a further layer of the WFI data.

Given a certain geometry of a couple of side looking SAR sensors, only one half of the fringe frequencies has a physical meaning. The other half comes from the noise and the layover effect. The geometry determines which is the right half spectrum and so the sign of the layover filter. Once this filter is evalued, the complex interferogram can be filtered giving in output another layer of the WFI product, the complex filtered interferogram.

Using the baseline, the orbital data and the earth ellipsoid shape the phase contribution which depends by the presence of a "mean terrain", can be computed. The subtraction of this effect from the interferogram is called "flat terrain removal". After this step, the interferogram fringes depends only by the elevation above the ellipsoid.

The last step is the phase unwrapping of the interferogram, which recovers the true phase from its residual modulus 2 PI. At present many algorithms exists, each with advantages and drawbacks [5]. For this reason we are actually analyzing the various approaches, to find the best solution to the unwrapping problem into a operational context.

Conclusions

A first descripription of the I-PAF Interferometric products has been given. The product SRI is under validation and will be soon available to the users. The WFI product, without the unwrapped layer, is in advanced development phase and will be released in the early 1997.

References

[1] C.Prati, F. Rocca
Use of the spectral shift in sar interferometry - Proceedings Second Ers-1 Simposium 1993

[2] F.Gatelli A.M.Guarnieri F.Parizzi P.Pasquali C.Prati F.Rocca
The Wavenumber Shift in SAR Interferometry - IEEE Transaction on GEOSCIENCE and REMOTE SENSING Jul. VOL.32 n.4 1994

[3] R.Touzi A.Lopes J.Bruniquel P.Vachon
Unbiased estimation of the coherence from multi-look SAR data - Proceedings of IGARSS 96 Nebraska Lincoln. 1996

[4] M.Cattabeni A.Monti-Guarnieri F.Rocca
Estimation and Improvement of Coherence in SAR Interferograms - IEEE 1994

[5] D.Just N.Adam M.Schwabisch R.Bamler
Comparison of Phase unwrapping algorithms for SAR interferograms - IEEE 1995

A Novel Interferometric Processor based on Chirp Scaling

D. Fernandes, K. Papathanassiou, A. Reigber, G. Riegler
Deutsche Forschungsanstalt für Luft- und Raumfahrt (DLR) Institut für Hochfrequenztechnik D-82230 Wessling, Germany
fernandes@ohf015.hf.op.dlr.de

Abstract

Generating an interferogram from a pair of complex SAR images requires a very accurate co-registration of the data. In order to avoid this time consuming processing step we investigated the possibility of including the co-registration in the generation of the complex images.

The Extended Chirp Scaling Algorithm allows to generate co-registered SAR images. We are developing such a 2D-processor, which uses precise orbit information together with radar parameters to simultaneously generate and co-register two SAR images. The scaling which is not only applied in range but also in azimuth allows to correct for the different viewing geometry and for different sampling distance in range and azimuth (e.g. different PRF). The processor also includes spectral filtering in order to reject the non-overlapping parts of the two image spectra.

The performance was tested with simulated data as well as with data from ERS-1/2. Results from ERS-1 and from the tandem mission will be presented at the workshop.

INSAR Products of the JENA-SAR Software System

Fiksel T   Daimler Benz Aerospace, Jena Optronik, Prussingstrasse 41, Jena 7745, Germany

Hartmann R   Daimler Benz Aerospace, Jena Optronik, Prussingstrasse 41, Jena 7745, Germany
hart@djo-jena.de

Winzer W   Daimler Benz Aerospace, Jena Optronik, Prussingstrasse 41, Jena 7745, Germany

Abstract

**JENA-SAR is a new modular software package which is being developed at Jena-Optronik for a large field of spaceborne interferometric SAR (INSAR) researches and applications.
On the one hand intensity images, coherence images and interferograms are generated from SLC data. Especially for GIS applications various geocoding procedures (map projections, slant range - azimuth projection) for SLC data as well as for INSAR products are available.
JENA-SAR can generate the interferometric phase of the 'flat' earth and of digital elevation models (DEM) in the form of synthetic interferograms using the true geometry of the orbit pair, the earth ellipsoid and several DEM coordinate systems. These products can be used for DEM generation or differential interferometric SAR (INSAR) applications.
A main goal of the software system is on the other hand the detection of small motions especially with the use of corner reflectors (CR). There for procedures for the accurate determination of the interferometric base line, the fringe period, the height per fringe etc. at exactly measured tie points and for known orbits are an important part of JENA-SAR. It is possible to create and manipulate orbits for an interactive varying of the interferometric base in order to generate for instance special artificial interferograms. By means of terestrical measured CR positions the relative location of an orbit pair can be calculated with high precision.
Some results of SAR interferometric processing with JENA-SAR are presented here. JENA-SAR is an open system and further moduls will be added in progress.**

Towards an Operational INSAR Processor for Topographic Radar Mapping

Harald Eichenherr, Nikolaus P. Faller, Michael Voelker
Dornier Satellitensysteme GmbH, D-88039 Friedrichshafen

Abstract

DSS (Dornier Satellitensysteme) are developing an INSAR processor for operational application with airborne as well as spaceborne sensor systems. A basic requirement is that the data acquired by the airborne single-pass DO-SAR sensor during one flight day can in quasi real time be processed to a level allowing data quality control with respect to full INSAR evaluation.

The throughput requirements imply a block processing system and an overall data and parameter handling philosophy which allows to keep track of the large number of signal input and output and auxiliary data files involved.

The processor design is to some extent based on experience with the previous development, under ESA contract, of the IAB INSAR workstation installed at ESTEC.

Vexcel/Gamma 3D Satellite SAR Ground Processing System

John C. Curlander Vexcel Corporation

Urs Wegmuller Gamma Remote Sensing

Abstract

The Vexcel/Gamma 3D Satellite SAR Ground Processing System is a low-cost system for reception, capture and processing of spaceborne SAR data. The system produces map registered image and topographic data products. It features a programmable Level 0 processor for data capture of the raw downlink from any of the spaceborne SAR satellites (i.e., Radarsat, ERS, JERS) and output to a disk array. This Level 0 processor will plug into existing X-band ground stations for SPOT and Landsat or any ERS and JERS stations. The Level 0 processor output is a frame syncronized product in the RAW CEOS format. The SAR processor has the capability for image formation, stereo and interferometric SAR digital terrainn model production and orthorectification of the image to a variety of map projections. It will operate on any UNIX workstation and handles data from all spaceborne SAR satellites. The system is operated from high level graphical user interfaces. It is the first operational SAR ground station to produce GIS compatable products from spaceborne SAR data.

Proceedings of the 'Fringe 96' Workshop on ERS SAR Interferometry, *Zurich, 30 September - 2 October 1996* (ESA SP-406, March 1997)

Scalable SAR Processing

Dave Curkendall Jet Propulsion Laboratory, 4800 Oak Grove Drive, Pasadena, California, USA 91109

Abstract

A new NASA program in High Performance Grand Challenge Computing will be discussed. The investigation seeks to capitalize on work started at the Jet Propulsion Laboratory and develop a core suite of SAR software in portable, scalable code targeted for MPP machines.

Performance results for SIR-C data processing will be discussed. The intent of the new three year program is to focus both on distributed network processing for high throughput situations that need to use several machines to balance the processing load and to develop access to interactive SAR processing initiated at the scientific workstation but executed on the large parallel machines. While current versions of the code extend through image formation only, interferometric extensions are being designed and will be added.

Proceedings of the 'Fringe 96' Workshop on ERS SAR Interferometry, *Zurich, 30 September - 2 October 1996* (ESA SP-406, March 1997)

Session 5

Algorithms & Techniques

Chairman: E. Attema

Multi Baseline Interferometric Techniques and Applications

A.Ferretti, A. Monti Guarnieri, C.Prati and F.Rocca
Dipartimento di Elettronica e Informazione (DEI) Politecnico di Milano (POLIMI), Piazza Leonardo da Vinci 32, 20133 Milano, Italy
aferre@elet.polimi.it monti@elet.polimi.it
http://www.elet.polimi.it

Abstract

Multi baseline interferometric data can be exploited for generating DEM, to estimate volumetric scattering and to get resolution on areas affected by foreshortening and layover. Moreover, multi baseline data allow to increase the elevation ambiguity interval, to detect and reduce atmospheric artifacts and to get high resolution coherence maps (i.e. an ensemble average is used instead of a space average). Results of the improvements achievable from multi baseline ERS-1 and Tandem data will be presented for the area of Bonn (ERS-1 images taken at 3 days interval during March 92) and Naples (4 Tandem pairs on Mt. Vesuvius, 1995-1996, have been used).

Keywords: SAR-Interferometry, Phase Unwrapping, DEM reconstruction, Atmospheric Effects, Coherence Estimation

Introduction

The aim of this paper is to present some results that can be achieved in SAR interferometry using multi baseline techniques, i.e. when more than one interferogram is available.

The difficulties related to this kind of approach are essentially due to the lack of precise satellite ephemerides and good estimation of the phase noise power superimposed on each interferogram. The former issue can be overcome by using optimization algorithms and good reference ephemerides (e.g. German PAF precise orbits), the latter using a local coherence estimation.

Precise location of the flight paths together with a good estimation of the standard deviation of the phase noise allow, in fact, the use of powerful statistics techniques, such as Maximum Likelihood (ML) and Maximum A Posteriori (MAP), to accurately estimate the height difference of each pixel with respect to a reference one with known elevation.

The same concept can be exploited to estimate the coherence using an ensemble average instead of a space one. The achieved coherence map highlights what remains unchanged during the time interval between the first and the last acquisition and could be exploited for image segmentation and classification.

Moreover, multi baseline techniques can be usefully exploited to get a DEM that is less affected by artifacts by averaging the uncorrelated atmospheric contributions coming from the single interferograms. When the ML DEM is generated it is possible to get the phase difference with respect to each interferogram. These phase residues are proportional to targets motion and/or atmospheric changes. In conclusion, the proposed technique can provide:

- a multiple interferograms averaged DEM
- an "atmospheric" noise map for each interferogram
- a multiple interferograms averaged coherence map, that gives a measure of SNR on a fine spatial resolution.

Maximum Likelihood Unwrapping and Mapping Algorithm

The image is divided in small patches (or blocks) such that:

1. The orbits can be considered linear.
2. The phase to height conversion function can be well approximated, for each interferogram, by a linear function:

dh = A * dr + B * dy + C * dphi (1)

where:

dh is the height variation
dr is the range variation
dy is the azimuth variation
dphi is the interferometric phase variation.

All these variations are defined with respect to a reference point chosen inside the block. The reference point will be a pixel having high coherence value in all the interferograms.

The parameters A, B and C are iteratively optimized as more and more points are unwrapped. A LMS optimization algorithm is used to minimize the error between the elevation values obtained from the interferograms and a reference DEM. If no *a priori* information is available (i.e. a rough DEM or GCPs) the baselines are optimized relative to one of the input interferograms, considered the reference for the other ones: the phase to height conversion function is considered fixed and known for this interferogram and at the end of the processing the final (combined) DEM will be affected by a systematic error due to the inaccurate estimates of the acquisition system geometry and a low frequency distortion due to atmospheric effects (the impact of this kind of distortion on the final DEM depends upon the mean value of the normal baseline of the reference interferogram: the higher the baseline, the lower the DEM distortion).

The patching of the unwrapped regions inside each block is operated only when all the blocks are processed. The algorithm starts from the reference point, as in a region growing algorithm (Hock et al., 1995), and it looks among the neighbor pixels for the most "reliable" point to be unwrapped. The unwrapping operation is reliable if all the interferograms estimate the same height variation for the running pixel with respect to the reference point. The dispersion "r" of the probability density function (p.d.f.) of the random variable dh(i,j) around the maximum is an indication of the "reliability" of the pixel P(i,j). The narrower the p.d.f. the more reliable the unwrapping.

In order to compute the p.d.f. of this random variable we use the coherence maps associated to each interferogram. From the absolute value of the coherence it is possible to achieved the expression of the p.d.f. of the interferometric phase (Lee J.S. et al., 1994) (Bamler R. and Just D., 1993) and thus of the elevation. The data from the "N" interferograms are "N" independent measures of the same physical variable (elevation), and we can compute its "a posteriori" p.d.f.(f), i.e. the p.d.f. of dh conditioned to the data:

f(dh/dphi1,dphi2,..,dphiN) = K* g(dphi1,dphi2,..,dphiN/dh)*ap(dh)
= g(dphi1/dh) * g(dphi2/dh) * .. * g(dphiN/dh) * ap(dh) (2)

where:

K is a normalization constant
g(dphin/dh) is p.d.f. to observe the value dphin for the interferometric phase of the interferogram "n" when the actual height variation is dh.
ap(dh) is the *a priori* information (this function is a constant if no reference DEM of the region is available).

The estimated value of dh (dh_est) maximizes the likelihood function f. When the value of dh_est is determined it is easy to choose the value of 2pi to be added to each interferogram: the correct value of the phase will correspond, in fact, to the height value nearest to the estimated one. In this way is then possible to compute the reliability (r) associated to each transition from the edge of the already unwrapped region to the neighbor pixels.

Many different measures of confidence can be considered for the "a posteriori" p.d.f. ; we have chosen a very simple one:

r = integral[dh_est-M,dh_est+M] f(dh) d(dh) (3) being M a parameter that fixes the range of allowed altitude variation (e.g. to avoid aliasing, as will be discussed below). The reliability is then the probability that the correct value of the height variation lies inside the interval [dh_est-M,dh_est+M]. It is a positive value less than 1 and can be considered a measure of the multi image "topographic" coherence.

The algorithm will unwrap a point only if

1. This reliability is the maximum value among all the points around the edge of the region already unwrapped.
2. The reliability is greater than a threshold: r(i,j) > THR_REL

When a new point is unwrapped we can carry on the optimization of the geometric parameters and we can compute the reliability values for the neighborhood of this new point. Again the algorithm will look for the more reliable pixel to be unwrapped and so on.

When all the image blocks are processed, the reference point with the highest value of coherence is chosen has the reference point for all the image and the block of this seed point is considered the reference block. The algorithm proceeds unwrapping the blocks exactly in the same way it had unwrapped the points inside each block.

The benefits of this algorithm are twofold. In the first place the coherence information is properly exploited: the coherence maps highlight the best path for the unwrapping algorithm and give an estimation of the standard deviation of the error on the final DEM. In the second place there is less risk of aliasing with respect of conventional single interferogram phase unwrapping (Goldstein R.M et al., 1988) (Prati C. et al., 1990). Theoretically it would be enough to have three interferograms with baselines that are prime with respect to each other to remove ambiguities (Chinese remainder theorem). In a practical case, where data are noisy and baselines random, the use of multiple interferograms increases significantly the elevation ambiguity level.

Atmospheric Effects and Multi-Image Coherence Estimation

Once the Digital Elevation Model is available (ML DEM) it is possible to compute N differential interferograms between the original data and the synthetic version obtained from the ML DEM and the optimized baselines values. These phase difference maps can highlight interesting changes in the phase of some targets and/or atmospheric effects due to the change in the refraction index from one acquisition to another. Both effects are clearly visible in the phase error maps we got from the region around Bonn and Mt. Vesuvius (see next paragraph).

When a good DEM is available with the same resolution of the original SAR images, it is also possible to compute a multi image coherence map. In this case the increased number of freedom degrees (due to the multiple interferograms) allows to get high resolution coherence maps (say 40 x 40 m). These maps are actually computed by compensating for the estimated interferogram phases, and then averaging all the interferograms. The final result highlights what actually remains unchanged in all the images.

Experiments

The multi baseline approach to phase unwrapping and DEM reconstruction was tested with two different data sets. During March 1992, ERS-1 surveyed ten times (i.e. every three day) the region around Bonn. One image was chosen as the "master" image and 4 different interferograms were produced using 4 other images of this data set. The baselines values are 93, 110, 150 and 162 meters (the altitudes of ambiguity about 97, 82, 60 and 55 meters).

The topography presents no particular difficulty, but the presence of the river and low coherence forested areas make this area suitable for testing the feasibility of automatic phase unwrapping of not connected blocks (Figure 1).

Figure 1: Bonn area: Amplitude Image - Dimensions: 600 (range) x 2000 (azimuth).

The ML DEM we obtained at the end of the processing (Figure 2) is smooth and presents no relevant phase unwrapping error.

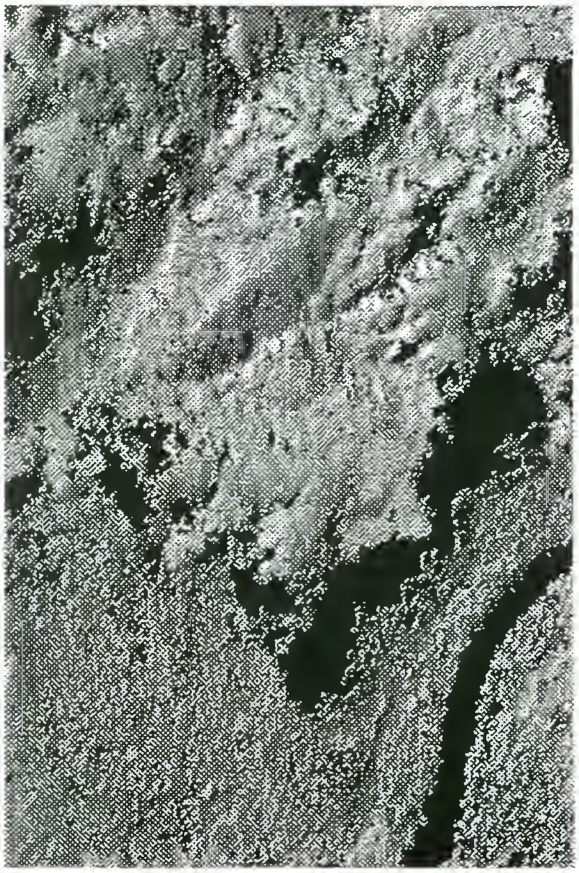

Figure 2: Bonn area: Maximum Likelihood DEM.

The black areas are not unwrapped areas: the reliability was under threshold in these regions. The two banks of the river have been correctly unwrapped even if there is no path between them. It is interesting to compare the ML DEM with that obtained using only a single interferogram: the former looks smoother and less noisy because of the optimum combination of all the information available. It is then possible to compare one of the coherence map associated to one of the input interferogram with the "reliability map" obtained at the end of the processing (Figure 3) again it is clear that combining multi baseline interferograms we can improve the resolution of the final product.

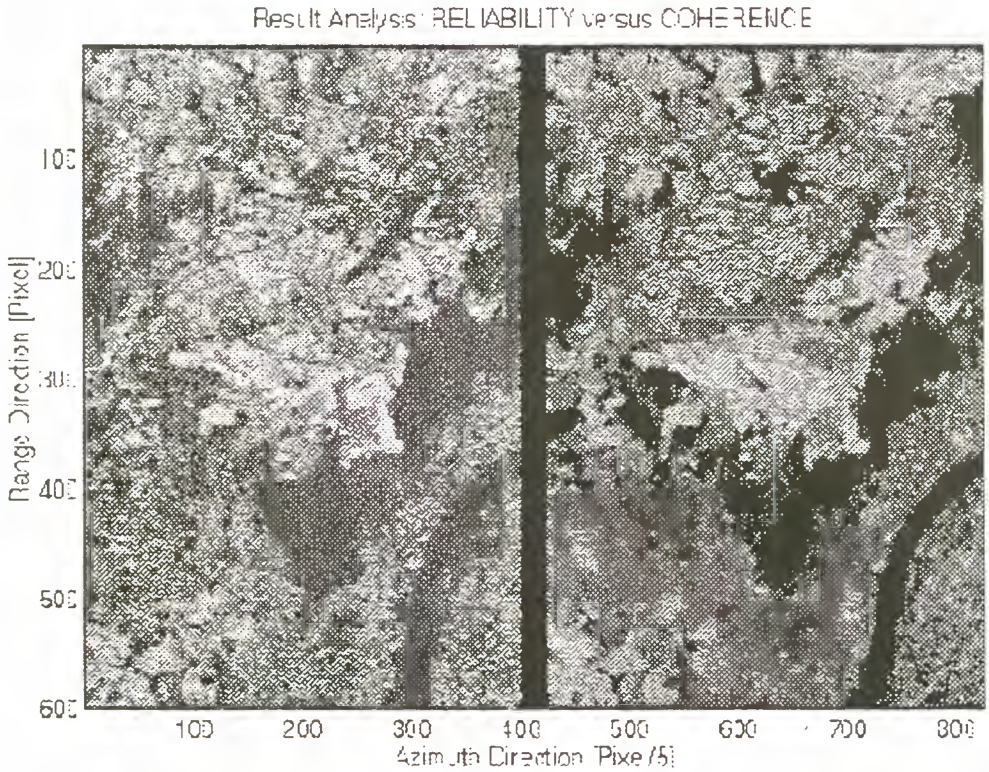

Figure 3: On the left hand side one of the input coherence maps, on the right hand side the final reliability map.

The differential interferograms (Figure 4) between the data used for the processing and the synthetic interferogram obtained using the optimized baseline values show interesting features in the image and highlight the regions where the reflectivity changed from one image to another due to atmospheric effects (low frequency effects) and antropogenics causes (single fields).

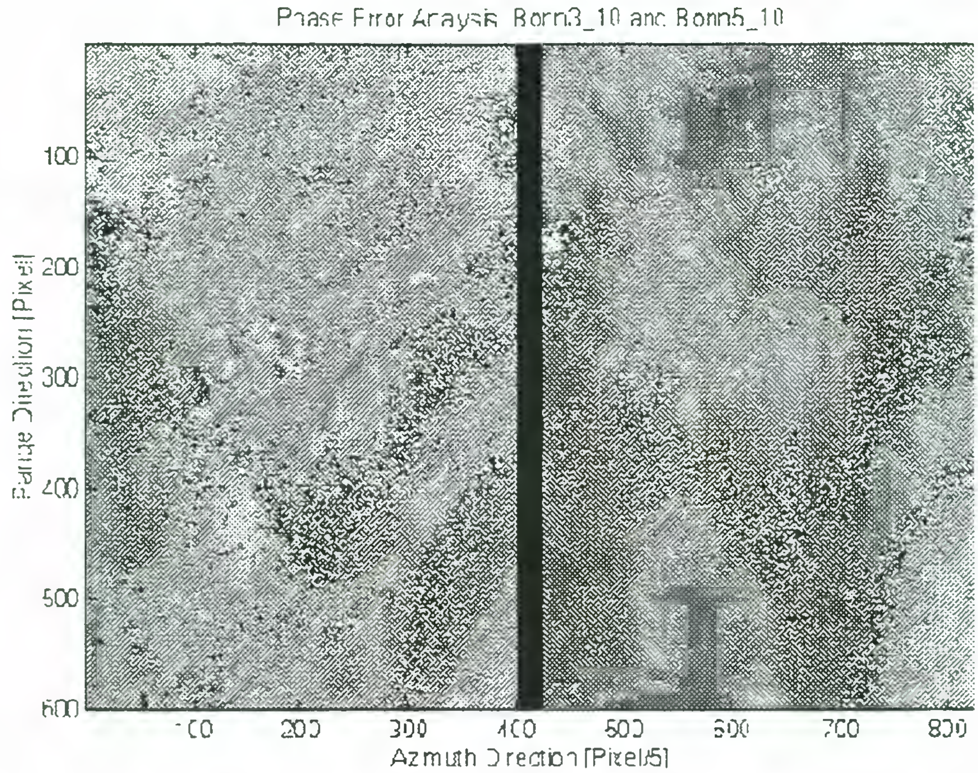

Figure 4: Two phase error maps (in radians [0..2pi]). The baselines values of the two input interferograms used to produce these images are 150 (on the left hand side) and 110 meters (on the right hand side).

In Figure 5, we can see another interesting comparison. On the left hand side we have a multi-image coherence maps obtained using 6 different images and the ML DEM to compensate the phase of each pair. The coherence is estimated using an ensemble average instead of a space one.

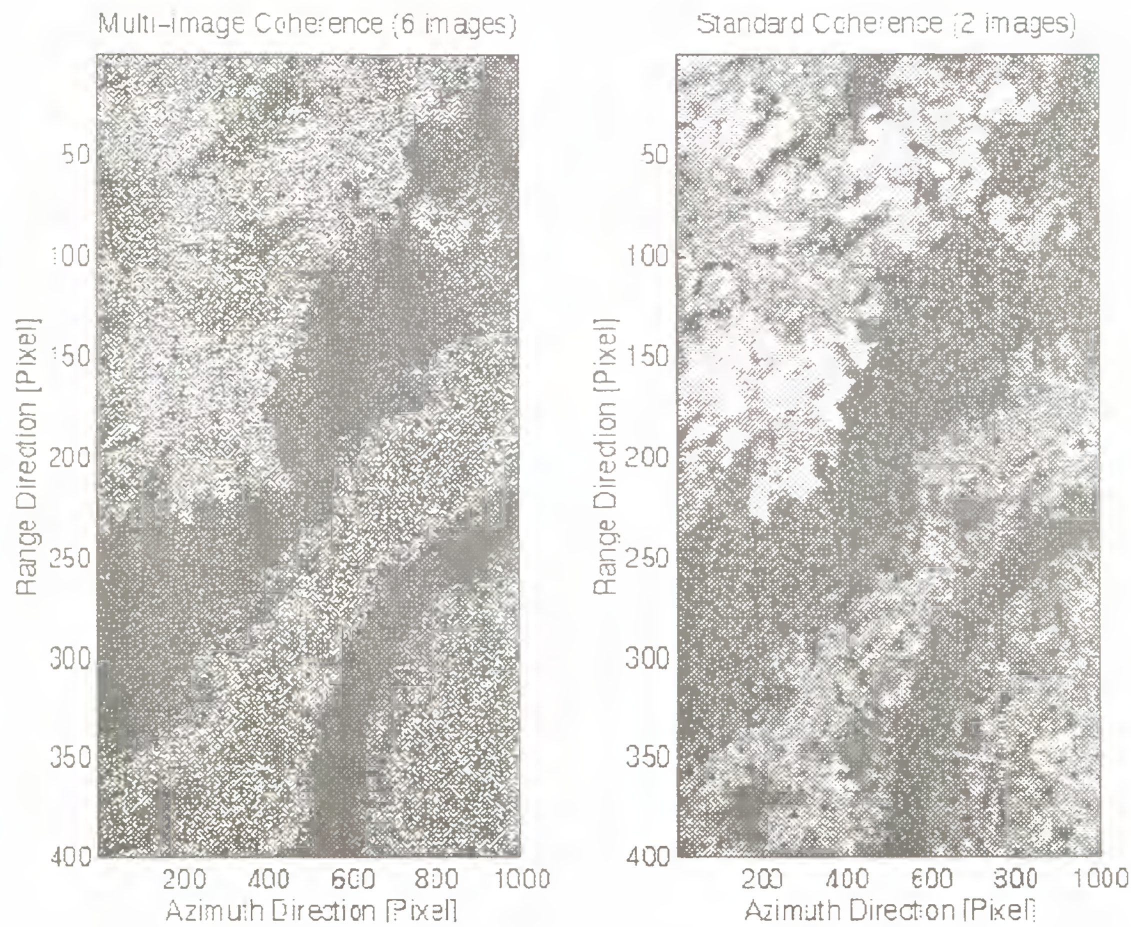

Figure 5: Bonn: Multi-image and standard coherence maps.

The same algorithm was tested using a different data set: 4 Tandem pairs on Mt. Vesuvius, the Italian volcano near Naples, (Figure 6).

Figure 6: Vesuvius: Amplitude Image - Dimensions: 600 (range) x 2700 (azimuth).

The baselines values are 106, 146, 220 and 253 meters (the altitudes of ambiguity about 85, 62, 41 and 35 meters). No *a priori* information was exploited during the processing, the final result is presented in Figure 7.

Figure 7: Vesuvius: Maximum Likelihood DEM.

The estimated error standard deviation map is reported in Figure 8.

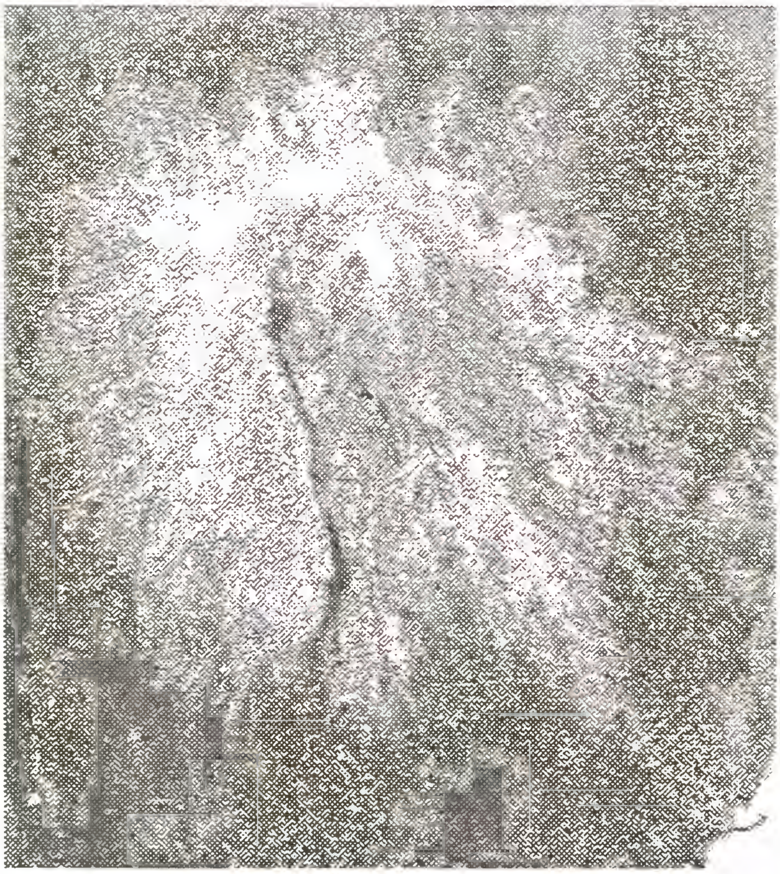

Figure 8: Vesuvius: Estimated Error Standard Deviation (for unwrapped areas the range of values is 1..7.5 meters - white corresponds to not unwrapped pixels).

Again, the reliability map highlights new features not visible in any of the coherence maps used (Figure 9).

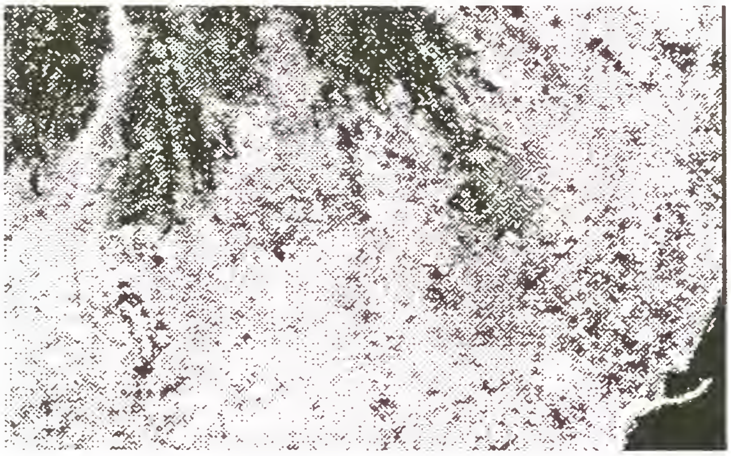

Figure 9: Vesuvius: Reliability Map (region around Torre del Greco).

The "residues" between the data and the synthetic interferograms have been obtained and no evidence of unwrapping errors is visible (Figure 10).

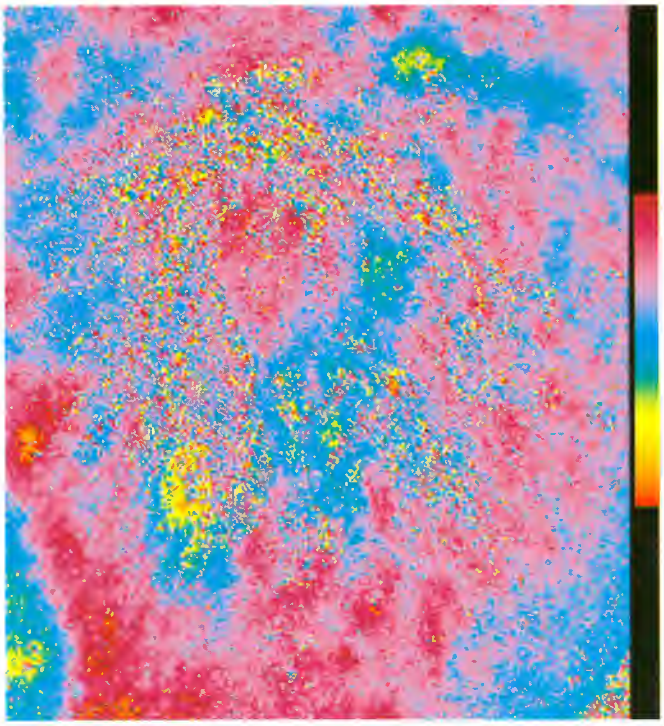

Figure 10: Vesuvius: one of the error maps (in radians [0..2pi]). Normal baseline value: 106 meters. Low frequency atmospheric effects are visible.

Conclusions

This paper describes a multi-baseline phase unwrapping technique for DEM generation. It is shown that the combination of more than two SAR images allows to get a robust technique and that coherence maps quality can be substantially improved. Moreover, the combination of many uncorrelated phase artifacts (mainly due to atmospheric changes) strongly reduces their impact on DEM accuracy. Even if some aspects of the processing chain must be still improved and optimized, the first results on real data are encouraging. The computational burden is not as high as it can appear (both the 12 by 10 km maps shown in the paper have been obtained in less than 90 minutes, using a medium workstation). The next step will be to integrate this software with a geocoding algorithm to obtain a ML DEM on the UTM grid.

Acknowledgements

We'd like to thank Marcello Caramma for the processing of image of the multi image coherence map and Prof.J.P.Muller of University College of London for some helpful discussions.

References

Bamler R. and Just D., 1993
Phase Statistics and Decorrelation in SAR Interferograms. *Proc. IGARSS '93*, pp. 980-984.

Richard M. Goldstein, Howard A. Zebker, 1988
Satellite Radar Interferometry: Twodimensional Phase Unwrapping. *Radio Science*, July 1988, **23**, pp.713-720.

Prati C.,Giani M. and Leuratti N., 1990
SAR interferometry: a 2D Phase Unwrapping Technique Based on Phase and Absolute Value Informations. *Proc. IGARSS 90*, 1990, Washigton D.C., USA, pp. 2043-2046.

Hock Lim, Wei Xu, Xiaojing Huang, 1995
Two New Practical Methods for Phase Unwrapping. *Proc. IGARSS 95*, Florence - Vol. I, pp.196-198.

Lee J.S., Hoppel K.W., Mango S.A., Miller A.R., 1994
Intensity and Phase Statistics of Multilook Polarimetric and Interferometric SAR Imagery. *IEEE Trans. Geosci. Remore Sens.*, 1994, **32**, (5).

Presentation of an improved Phase Unwrapping Algorithm based on Kalman filters combined with local slope estimation

Rainer Krämer
Zentrum für Sensorsysteme (ZESS), Universität-GH-Siegen,
Paul-Bonatz-Str. 9-11, D-57068 Siegen, Germany
kraemer@nv.et-inf..uni-siegen.de
www.nv.et-inf.uni-siegen.de/pb2/www_pb2

Otmar Loffeld
Zentrum für Sensorsysteme (ZESS), Universität-GH-Siegen,
Paul-Bonatz-Str. 9-11, D-57068 Siegen, Germany
loffeld@wiener.zess.uni-siegen.de
www.nv.et-inf.uni-siegen.de/pb2/www_pb2

Abstract

The paper presents a phase unwrapping algorithm based on an Extended Kalman filter. The Kalman filter exploits a so called „Basic - Slope Model" enabling the filter to incorporate additional local slope information obtained from the sample frequency spectrum of the interferogram by a local slope estimator. The local slope information is then optimally fused with the information directly obtained from real and imaginary part of the interferogram. The paper outlines the principle operation of the phase unwrapping algorithm and explains the cooperation of the Extended Kalman filter with the local slope estimator. At last the efficiency of this phase unwrapping algorithm will be shown by simulations and real InSAR images.
Keywords: Phase unwrapping techniques, phase slope estimation, SAR - interferometry

Introduction

The main problem in calculating digital terrain elevation maps from a SAR interferogram is the unwrapping of the phases. The "measured" phases, calculated directly with the arctan-function from the complex interferogram, are all mapped into the same „baseband" interval (e.g. -,), while any absolute phase offset (an integer multiple of 2) is lost. The searched unambiguous "height" phase, which is a geometrical function of the height, must be generated from the measured phase by phase unwrapping.

In the year 1994 we firstly demonstrated the basic possibility of doing phase unwrapping with Extended Kalman filters. Since then we are working on the improvement of this kind of phase unwrapping algorithms. Based on a new optimised model we were able to remarkably improve the performance of the Kalman filter. The main idea of the new model is to apply a "Basic - Slope - Model", incorporating information which is obtained with an algorithm we would call "Local - Slope - Estimator". With this model, being inexact and partly incorrect, the Kalman filter 'fuses' two kinds of information - the local slope information obtained from a local slope estimator - and the information directly gained from exploiting inphase and quadrature components of the complex interferogram.

The phase unwrapping algorithm

The concept of our phase unwrapping algorithm is shown in figure 1. Starting points are the two coregistered SAR images from which the interferogram, a coherence map and the measured (interferometric) phase is calculated.

Proceedings of the 'Fringe 96' Workshop on ERS SAR Interferometry, *Zurich, 30 September - 2 October 1996* (ESA SP-406, March 1997)

In the next step the algorithm computes the necessary parameters for the Kalman filter. The measurement noise variance is calculated from the data of the interferometric amplitude and the coherence map. The measurement noise variance is needed in the observation model of the Kalman filter. Running in parallel the Local - Slope Estimation, which will be described later, calculates the local phase slopes as well as their error variances. With these parameters a very robust and efficient state space model can be built.

In the next step the two dimensional extended linearized Kalman filter optimally combines the information from the local slope estimation given in the state space model, with the interferometric phase observations. The principle operation of a two dimensional Kalman filter for phase unwrapping has been published in (Krämer et. al.,1996a), (Loffeld et. al.,1996) and (Loffeld et. al.,1994) and will not be described in this paper. The state space model will be outlined in the next chapter.

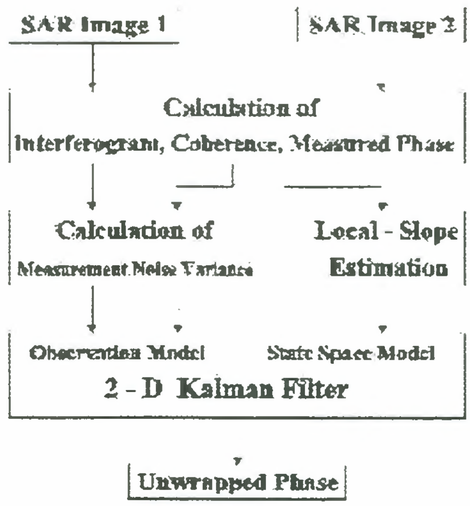

Figure 1: Concept of the phase unwrapping algorithm

The state space model utilised by the Kalman Filter

Due to the Local - Slope Estimation the state vector of the state space model can be simplified to only one dimension and we get following state space model:

$$x(n,m) = \frac{1}{2}\left[x(n-1,m) + s_h(n-1,m) + x(n,m-1) + s_v(n,m-1)\right]$$

where x(n,m) is the searched unwrapped phase and $s_h(n,m)$ and $s_v(n,m)$ are the local phase slopes in horizontal and vertical direction calculated by the local slope estimator. The phase x(n,m) is calculated as the mean of the preceding phase value plus the local phase slope in horizontal direction and the preceding phase value plus the phase slope in vertical direction. (See figure 2)

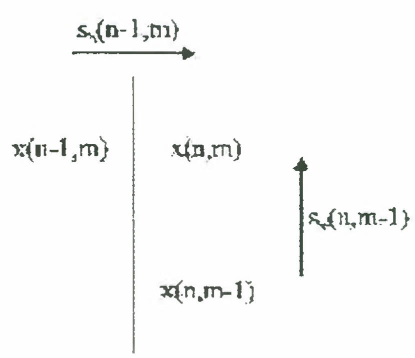

Figure 2: Calculation of a new phase value x(n,m)

The Local - Slope Estimator

The local slope estimation

In the following the local slope estimator will be described in the one dimensional case. The two dimensional case is straight forward.

The searched unwrapped phase can be written as follows:

$$\varphi(t) = \varphi(t_0) + \int_{t_0}^{t} \dot{\varphi}(\tau)d\tau = \varphi(t_0) + 2\pi \cdot \int_{t_0}^{t} (f_0 + f_i(\tau))d\tau$$

$$= \varphi(t_0) + \underbrace{2\pi \cdot f_0 \cdot (t - t_0)}_{\text{mean phase variation}} + \underbrace{2\pi \cdot \int_{t_0}^{t} f_i(\tau)d\tau}_{\text{dynamic phase variation}}$$

where

$\varphi(t)$: momentary phase
$\dot{\varphi}(t)$: phase derivative
f_0 : mean ins tantaneous frequency in some i nterval $[t_0, t_x)$
$f_i(\tau)$: time vary ing instan taneous fr equency

In the discrete case with t=(k+1)T and t_0=kT we obtain

$$\varphi(k+1) = \varphi(k) + \underbrace{2\pi \cdot f_0 \cdot T}_{\text{mean phase variation}} + w(k)$$

where $w(k) = \underbrace{2\pi \cdot \int_{t_0}^{t} f_i(\tau)d\tau}_{\text{dynamic phase variation}}$ is the unknown phase variation.

As we can see the phase variation can be decomposed into two parts the mean and dynamic phase variation. The goal of the local slope estimator is to calculate the mean variation of the phase, respectively the frequency f_0, and also the variance of the dynamic phase variation $Ew(k)^2$.

The estimation of the unknown mean phase variation:

The complex interferogram can be written as:

$$y(t) = a(t) \cdot e^{j\varphi(t)} + n(t)$$

$$= a(t) \cdot \exp j\left(\varphi(t_0) + \underbrace{2\pi \cdot f_0 \cdot (t - t_0)}_{\text{mean phase variation}} + \underbrace{2\pi \cdot \int_{t_0}^{t} f_i(\tau)d\tau}_{\text{dynamic phase variation}} \right) + n(t)$$

$$= a(t) \cdot e^{j\varphi(t_0)} \cdot \underbrace{\exp j\left[2\pi \cdot \int_{t_0}^{t} f_i(\tau)d\tau \right]}_{\text{dynamic phase variation}} \cdot \exp\left[j2\pi \cdot f_0 \cdot t \right] + n(t)$$

$$= \underbrace{s(t)}_{\substack{\text{phase and amplitude modulated signal} \\ \text{yielding spectral broadening}}} \cdot \underbrace{\exp\left[j2\pi \cdot f_0 \cdot t \right]}_{\text{complex harmonic phasor yielding a frequency shift}} + n(t)$$

We notice that the mean phase variation $2\pi f_0 T$ can be observed as a spectral shift f_0 in the interferogram. The complex autocorrelation can be written as:

$$\begin{aligned}
\varphi_{yy}(\tau) &= E\{y(t)\cdot y(t+\tau)\} \\
&= E\left\{\left[s(t)\cdot e^{j2\pi f_0 t} + n(t)\right]\cdot\left[s(t+\tau)^{*}\cdot e^{-j2\pi f_0 (t+\tau)} + n(t+\tau)^{*}\right]\right\} \\
&= E\left\{s(t)\cdot s(t+\tau)\cdot e^{j2\pi f_0 \tau}\right\} + \varphi_{nn}(\tau) \\
&= \varphi_{ss}(\tau)\cdot e^{j2\pi f_0 \tau} + \varphi_{nn}(\tau)
\end{aligned}$$

With this equation the power spectral density is:

$$\begin{aligned}
\Phi_{yy}(f) &= \Phi_{ss}(f) * \delta(f - f_0) + \Phi_{nn}(f) \\
&= \Phi_{ss}(f - f_0) + \Phi_{nn}(f)
\end{aligned}$$

If the power spectral density is unimodal and approximately symmetric around the mode, then

$$\Phi_{yy}(f)\big|_{f=f_0} \approx \max\{\Phi_{yy}(f)\}$$

and the spectral shift f_0 can be estimated with the relation

$$\hat{f}_0 = \arg_{\max}\{\Phi_{yy}(f)\}$$

which means, that the spectral shift can be found by seeking the spectral mode of the power spectral density.

Estimating of the variance of the dynamic phase variation

The variance $E\{w(k)^2\}$, where $w(k)$ denotes the difference between nominal (mean) phase variation and total phase variation, is identical with the driving noise covariance $Q(k)$ which is needed by the Kalman filter.

The variance ${}_{f0}{}^2(k)$ of the variation between the estimated mean slope variation and the true mean slope variation can be obtained from the spectral bandwidth of the interferogram, by calculating the squared spectral bandwidth as the second central moment

$$\hat{E}\{f_0(k)\} = \int_{-\infty}^{\infty} f \cdot \tilde{\Phi}_{yy}(f,k)\,df$$

$$\hat{E}\{f_0^2(k)\} = \int_{-\infty}^{\infty} f^2 \cdot \tilde{\Phi}_{yy}(f,k)\,df$$

and

$$\sigma_{f0}^2(k) = E\{f_0^2(k)\} - E\{f_0(k)\}^2$$

$$\tilde{\Phi}yy(f,k) = \frac{\Phi_{yy}(f,k)}{\int\limits_{f=-\infty}^{\infty} \Phi_{yy}(f,k)df}$$

where is the normalised power spectral density from a section of y(k) bounded by the interval [k-N/2,k+N/2].

We are now able to calculate the driving noise variance. Starting with

$$\sigma_{f0}^2(k) = E\left\{\left[f_0(k) - \hat{f}_0(k)\right]^2\right\} = E\left\{\left[\frac{1}{N+1}\sum_{i=k-\frac{N}{2}}^{k+\frac{N}{2}} f(i) - \hat{f}_0(k)\right]^2\right\}$$

where $\hat{f}_0(k)$ is the estimated mean frequency in the interval [k-N/2,k+N/2] we get under the assumption of $E\{f(i)\cdot f(j)\} = \sigma_f^2(i)\cdot \delta(i,j) + E\{f(i)\}\cdot E\{f(j)\}$ the following solution for the error variance of the spectral shift:

$$\sigma_{f0}^2(k) = \frac{\overline{\sigma_f^2}(k)}{N+1}$$

where $\overline{\sigma_f^2}(k)$ is the ensemble average of all individual variances within the interval [k-N/2,k+N/2]. Finally we get the desired driving noise variance:

$$\begin{aligned} Q(k) &= (2\pi T)^2 \cdot \overline{\sigma_f^2}(k) \\ &= (2\pi T)^2 \cdot (N+1)\cdot \sigma_{f0}^2(k) \end{aligned}$$

Results

The capability of the filter will be shown by a fractally simulated phase image and an ERS1/2 scene from Egypt.

We will begin with the fractally simulated phase image, which is shown in figure 3. Starting with this phase a measured phase is generated by superimposing white Gaussian noise onto the complex image and wrapping the result. The measured phase, which we got for a signal to noise ratio of -7.2dB corresponding to a coherence value of 0.4, is shown in figure 4. The result of the phase unwrapping is depicted in figure 5. If we rewrap this result again (figure 6), we can compare the result with the measured phase. We see that the noise has been cancelled completely and that neither additional fringelines occur nor any fringelines are missing, which is an important requirement for error free phase unwrapping.

 

Figure 3: Original phase Figure 4: Measured phase

 

Figure 5: Unwrapped phase Figure 6: Unwrapped phase

In the following pictures we see the phase unwrapping result of a real ERS1/2 interferogram of a part of Egypt. Figure 7 shows the measured phase and the images 8 and 9 the coherence of the interferogram. As we can see there are large regions of very low coherences in that interferogram.

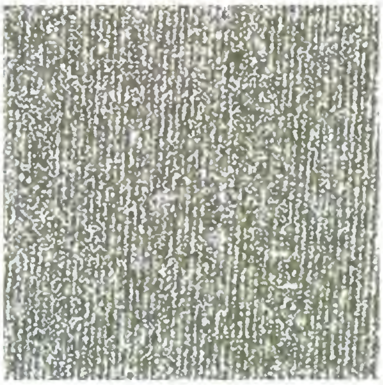

Figure 7: Measured phase


Figure 8: Places with coherence Figure 9: Places with coherence lower than 0 4 lower than 0.1

Figure 10 presents the result we got from the phase unwrapping algorithm. To examine the errors we have rewrapped this result again (fig. 11). We see that some little error propagations occurr, but only in very large regions of low coherence and even there the errors do not always occur. As we can see this kind of phase unwrapping algorithm works very well even there are regions of coherences near zero if this regions are not to large.


Figure 10: Unwrapped phase Figure 11: Unwrapped phase

Conclusions

A method to calculate local slope variations has been presented. The results of this local slope estimation was used to improve the state space model of a phase unwrapping algorithm based on an extended Kalman filter. The results show that this combination yields a very robust phase unwrapping algorithm which works down to a coherence value of 0.4 without error propagation, but also it is able to cross limited regions of coherence down to zero, if these regions are not too large.

Further work will be concentrated to improve this phase unwrapper in a way, that should the occasion of a error propagation arise, this error propagation should be limited on a small area in the image.

The work herein has been motivated and funded by the DARA (project „Rapid", grand number 50 EE 9431) which is greatly appreciated.

References

Krämer, Rainer, Loffeld, Otmar, 1996a:
Phase Unwrapping for SAR Interferometry with Kalman Filters. In: *Proceedings of the EUSAR'96 Conference*, pp. 165-169.
Krämer, Rainer, Loffeld, Otmar, 1996b:
A Novel Procedure for Cutline Detection. In: *Proceedings of the EUSAR'96 Conference*, pp. 253-256.
Krämer, Rainer, Loffeld, Otmar, 1996c:
A Novel Procedure for Cutline Detection. In: *International Journal of Electronics and*

References

Krämer, Rainer, Loffeld, Otmar, 1996a:
Phase Unwrapping for SAR Interferometry with Kalman Filters. In: *Proceedings of the EUSAR'96 Conference*, pp. 165-169.

Krämer, Rainer, Loffeld, Otmar, 1996b:
A Novel Procedure for Cutline Detection. In: *Proceedings of the EUSAR'96 Conference*, pp. 253-256.

Krämer, Rainer, Loffeld, Otmar, 1996c:
A Novel Procedure for Cutline Detection. In: *International Journal of Electronics and Communications*, Vol. 50, No. 2, Hirzel Verlag, Stuttgart, pp. 112-116.

Loffeld, Otmar, Krämer, Rainer, 1996:
Local Slope Estimation and Kalman Filtering. *PIERS'96, Innsbruck.*

Loffeld, Otmar, Krämer, Rainer, 1994:
Phase Unwrapping for SAR Interferometry. In: *Proceedings of the IGARSS'94 Conference*, pp. 2282-2284.

A Phase Unwrapping Method Based on Network Programming

Mario Costantini ESA ESRIN
Via G. Galilei, c.p. 64
00044 Frascati, Roma, Italy
Phone/Fax: +39-6-94180516/280
E-mail: marioc@mail.esrin.esa.it

Abstract

Phase unwrapping is the reconstruction of a function on a grid given its values modulo 2π. A new phase unwrapping method, which is a significant advance from existing techniques, is described and tested. The method starts from the fact that the neighboring pixel phase differences can be estimated with possibly an error which is an integer multiple of 2π.This suggest the formulation of the phase unwrapping problem as a minimization problem with integer variables. In fact, it is possible to equate this to the problem of finding the minimum cost flow on a network, for the solution of which there exist very efficient techniques. The tests performed confirm the validity of this approach.
Keywords: Phase Unwrapping, Network Programming, SAR Interferometry

Introduction

Phase unwrapping is the reconstruction of a function on a grid given the value modulo 2π of the function on the grid. We refer to these two quantities as the unwrapped and the wrapped phase respectively. In the last few years an increasing interest has been devoted to phase unwrapping, mainly due to the developing of SAR (Synthetic Aperture Radar) interferometry (Zebker and Godstein, 1986), although there are applications of phase unwrapping in several other fields.

Basically all the existing phase unwrapping techniques start from the fact that it is possible to estimate the neighboring pixel differences of the unwrapped phase when these differences are less than π. From these, the unwrapped phase can be reconstructed up to an additive constant. The methods differ in the way they overcome the difficulty posed by the fact that this hypothesis may be somewhere false, which cause the estimated unwrapped phase differences to be inconsistent, that is their "integral" depends on the integration path.

Branch cuts methods (Goldstein *et al.*,1988; Prati *et al.*, 1990) unwrap by integrating the estimated neighboring pixel differences of the unwrapped phase along paths avoiding the regions where these estimated differences are inconsistent. The problem of building cuts delimiting these regions is very difficult and the resulting phase unwrapping algorithm is very expensive computationally.

In least squares methods (Fried, 1977; Hudgin, 1977; Hunt, 1979), unwrapping is achieved by minimizing the mean square deviation between the estimated and the unknown neighboring pixel differences of the unwrapped phase. Least squares methods are very efficient computationally when they make use of fast Fourier transform techniques (Takajo and Takahashi, 1988; Ghiglia and Romero, 1994). But the resulting unwrapping is not very accurate, because least squares procedures tend to spread the errors that are instead concentrated on a limited set of points. To overcome this problem a weighting of the wrapped phase can be useful. However, the weighted least squares algorithms proposed (Ghiglia and Romero, 1994; Pritt, M. D., 1996) are iterative and not as efficient as the unweighted ones. Moreover, the accuracy of the results depends on the weighting mask used.

Proceedings of the 'Fringe 96' Workshop on ERS SAR Interferometry, *Zurich, 30 September - 2 October 1996* (ESA SP-406, March 1997)

Here we propose a new method for phase unwrapping. We exploit the fact that the neighboring pixel differences of the unwrapped phase are estimated with possibly an error which is an integer multiple of 2π. This leads to formulate the phase unwrapping model as the problem of minimizing the deviations between the estimated and the unknown neighboring pixel differences of the unwrapped phase with the constraint that the deviations must be integer multiple of 2π. This constraint prevents the errors from spreading; so that a weighting of the data is not necessary. In any case, weighting is allowed in our formulation (without loss of efficiency), and can be useful when there are large regions of noisy data. Minimization problem with integer variables are usually very complex computationally. However, recognizing the network structure underlying our problem makes available very efficient strategies for its solution. In fact, our problem can be equated to the problem of finding the minimum cost flow on a network, for the solution of which there exist very efficient algorithms.

Finally, we present tests of our method performed on simulated data and on the real wrapped phase obtained from the interferometry of a pair of ERS-1 and ERS-2 Tandem SAR images. The results are really satisfactory: they demonstrate the consistency and efficiency of the method, which seems to be accurate. Comparative tests using a least squares method are presented too.

The Method

Let Φ be a real valued function defined on a rectangular grid, and let

$$\Psi(i,j) = \left[\Phi(i,j)\right]_{2\pi} \tag{1}$$

where, for a generic real x, $[x]_{2\pi} = x + 2\pi n$, with n the integer such that $[x]_{2\pi} \in [-\pi, \pi)$. For simplicity of notation, in (1) as in the following, we adopt the convention that in any formula the indices run over the grid where the formula is defined. We refer to Φ and Ψ as the unwrapped and the wrapped phase functions respectively. The inversion of (1), that is the reconstruction of Φ from Ψ is the phase unwrapping process.

Let us define:

$$\Psi_1(i,j) = \left[\Psi(i+1,j) - \Psi(i,j)\right]_{2\pi} \tag{2}$$

$$\Psi_2(i,j) = \left[\Psi(i,j+1) - \Psi(i,j)\right]_{2\pi} \tag{3}$$

When $\Phi(i+1,j) - \Phi(i,j) \in [-\pi,\pi)$ and $\Phi(i,j+1) - \Phi(i,j) \in [-\pi,\pi)$, we have that $\Psi_1(i,j) = \Phi(i+1,j) - \Phi(i,j)$ and $\Psi_2(i,j) = \Phi(i,j+1) - \Phi(i,j)$. We assume that these relations hold in the majority of cases. In general we can restate the phase unwrapping problem of inverting (1) as the problem of finding the following residuals:

$$K_1(i,j) = \frac{1}{2\pi}\left[\Phi(i+1,j) - \Phi(i,j) - \Psi_1(i,j)\right] \tag{4}$$

$$K_2(i,j) = \frac{1}{2\pi}\left[\Phi(i,j+1) - \Phi(i,j) - \Psi_2(i,j)\right] \tag{5}$$

from which the neighboring pixel differences of the unwrapped phase can be calculated; then, through their integration, the unwrapped phase is reconstructed up to an additive constant which is an integer multiple of 2π

Let $c_1(i,j)$ and $c_2(i,j)$ be given non-negative real numbers weighting the a priori confidence that the residuals $k_1(i,j)$ and $k_2(i,j)$ must be small; when such an priori knowledge is not available, all the weights $c_1(i,j)$ and $c_2(i,j)$ are chosen equal to 1. We can estimate the residuals $k_1(i,j)$ and $k_2(i,j)$ as the solution of the following minimization problem:

$$\min_{\{k_1,k_2\}}\left\{\sum_{i,j} c_1(i,j)\left|k_1(i,j)\right| + \sum_{i,j} c_2(i,j)\left|k_2(i,j)\right|\right\} \tag{6}$$

subject to the constraints

$$\begin{aligned} &k_1(i,j+1) - k_1(i,j) - k_2(i+1,j) + k_2(i,j) = \\ &= -\frac{1}{2\pi}\left[\Psi_1(i,j+1) - \Psi_1(i,j) - \Psi_2(i+1,j) + \Psi_2(i,j)\right] \end{aligned} \tag{7}$$

$$k_1(i,j) \text{ integer} \tag{8}$$

$$k_2(i,j) \text{ integer} \tag{9}$$

The objective function to be minimized in (6) comes from the assumption that the residuals $K_1(i,j)$ and $K_2(i,j)$ are zero almost always; the absolute value function is chosen as the error criterion because it allows an efficient solution of the minimization problem, through the transformation shown below. The constraints in (7) express the property that $\Psi_1 + 2\pi K_1$ and $\Psi_2 + 2\pi K_2$ represent the neighboring pixel differences of a function (the unknown function Φ), as it results from (4) and (5); these constraints ensure that the unwrapped phase reconstructed from the solution of the minimization problem does not depend on the integration path. The constraints in (8) and (9) are a consequence of the fact that K_1 and K_2 take integer values, as it can be seen from (1), (2), (3), (4) and (5); as a consequence, the unwrapped phase achievable from the solution of the problem above is identical to the original wrapped phase when re-wrapped.

The problem given in (6), (7), (8) and (9) is a non-linear minimization problem with integer variables. Consider the following change of variables:

$$x_1^+(i,j) = \max\left(0, k_1(i,j)\right), \quad x_1^-(i,j) = \min\left(0, k_1(i,j)\right) \tag{10}$$

$$x_2^+(i,j) = \max\left(0, k_2(i,j)\right), \quad x_2^-(i,j) = \min\left(0, k_2(i,j)\right) \tag{11}$$

It can be seen that, through (10) and (11), the problem stated in (6), (7), (8) and (9) can be transformed so that it defines a minimum cost flow problem on a network, with the new variables representing the flow along the arcs of the network. In Figure 1 it is shown the network associated with the phase unwrapping problem.

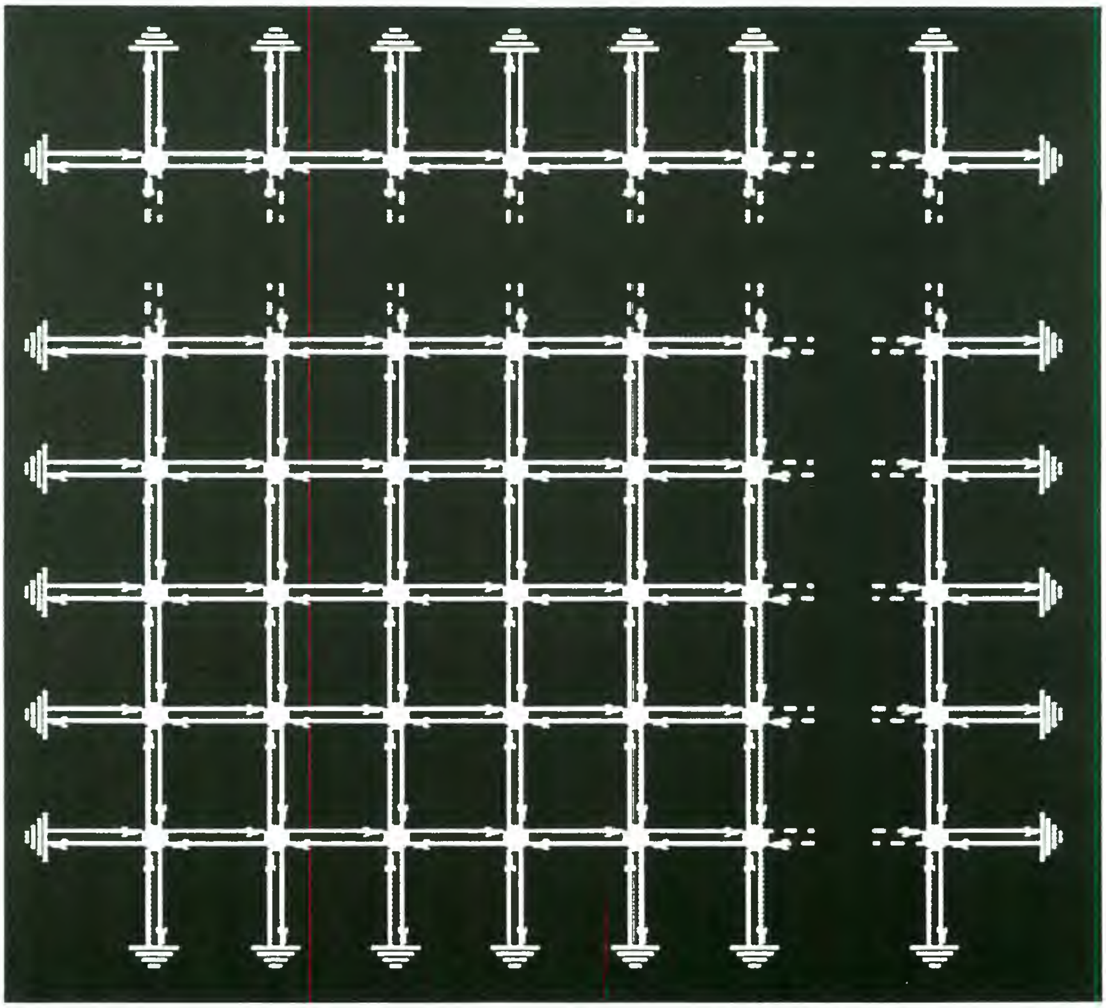

Figure 1: The network associated with the phase unwrapping problem: the circles and the arrows represent the nodes and the arcs of the network respectively, while the boundary arcs are connected to the "earth" (by analogy with electrical networks) node

In the transformed problem the objective function in (6) becomes the total cost of the flow; the constraints corresponding to those given in (7) express the conservation of flow at the nodes; finally, the constraints in (8) and (9) are replaced by constraints defining the capacities of the arcs.

The transformation of the problem defined in (6), (7), (8) and (9) into a minimum cost flow problem on a network makes for an efficient solution, both as regards the memory and the computation required. An exhaustive review of algorithms for the solution of minimum cost network flow problems can be found for example in (Ahuja *et al.*, 1993).

Experimental Results

The examples chosen to test our algorithm come from SAR interferometry, which provides one of the most difficult and interesting application of phase unwrapping. The first data set is a simulation of the wrapped phase obtained from SAR interferometric images relative to a scene consisting of a cone on a flat surface. The parameters of this experiment are chosen to simulate a real experiment with the ERS-1 SAR; for clarity, we have not introduced noise in the data. The simulated wrapped interferometric phase relative to the cone scene is shown in Figure 2. The neighboring pixel differences of the unwrapped phase estimated from the wrapped phase are somewhere inconsistent because the unwrapped phase is discontinuous (due to the simulation of the SAR phenomenon of layover). In Figure 3 it is shown where these inconsistencies are located. The unwrapped phase reconstructed with our algorithm (without weighting) is shown in Figure 4. It is perfectly identical to the "true" unwrapped phase resulting from the simulation. For a comparison, in Figure 5 we show the results of the unwrapping obtained using an unweighted least squares algorithm. Note the propagation of errors from the regions where the estimated neighboring pixel differences of the unwrapped phase are inconsistent.

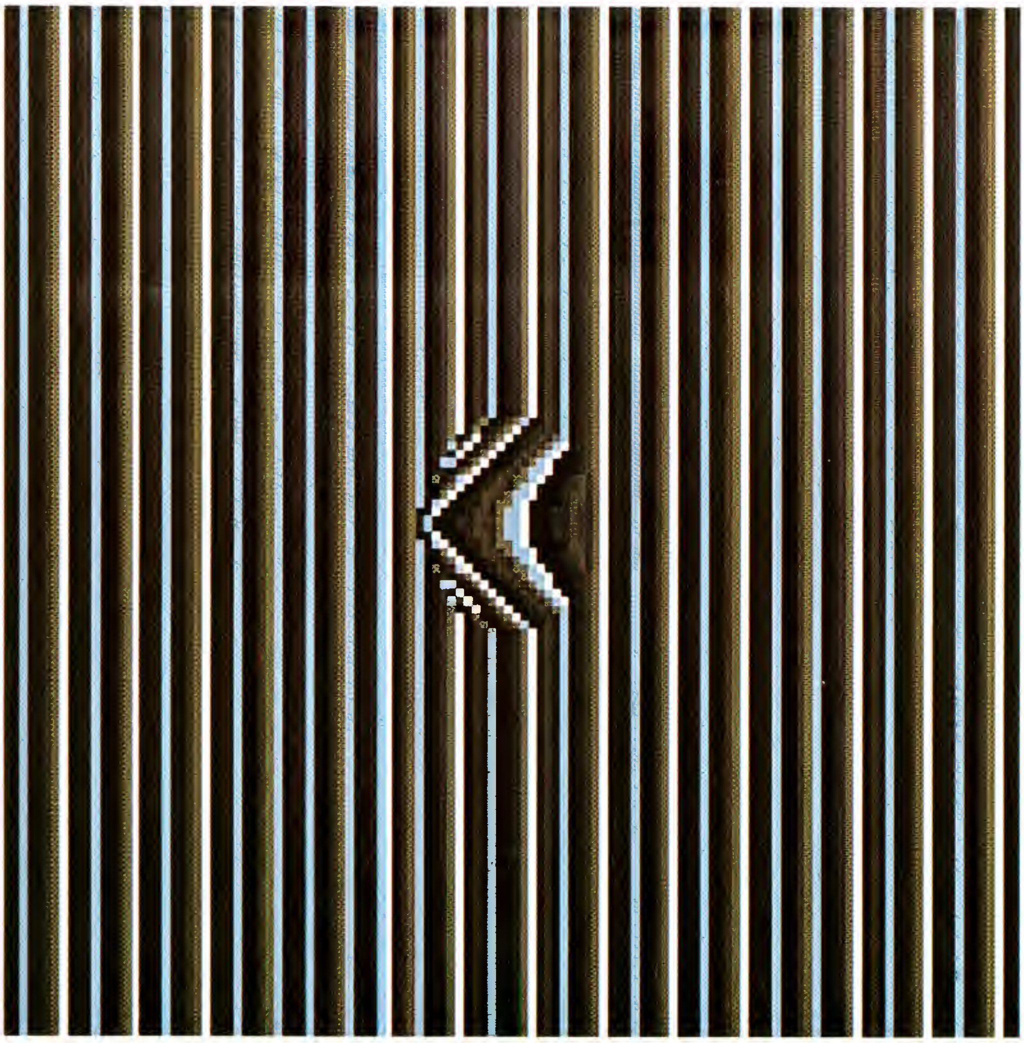

Figure 2: The wrapped phase obtained from a simulated interferometric experiment (gray levels representation)

Figure 3: The regions where the neighboring pixel differences of the unwrapped phase estimated from the data of Figure 2 are inconsistent (in white)

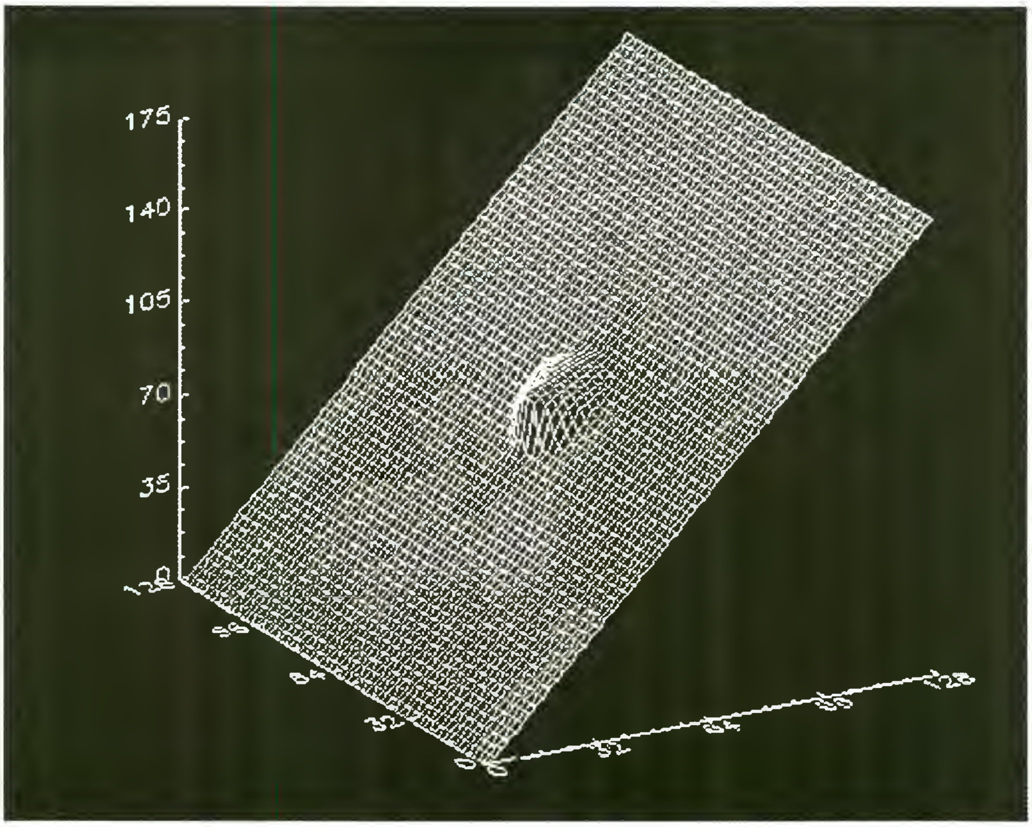

Figure 4: The unwrapped phase reconstructed from the data of Figure 2 with our algorithm (perspective view); as the reconstruction is perfect, this is the "true" unwrapped phase obtained from the simulation

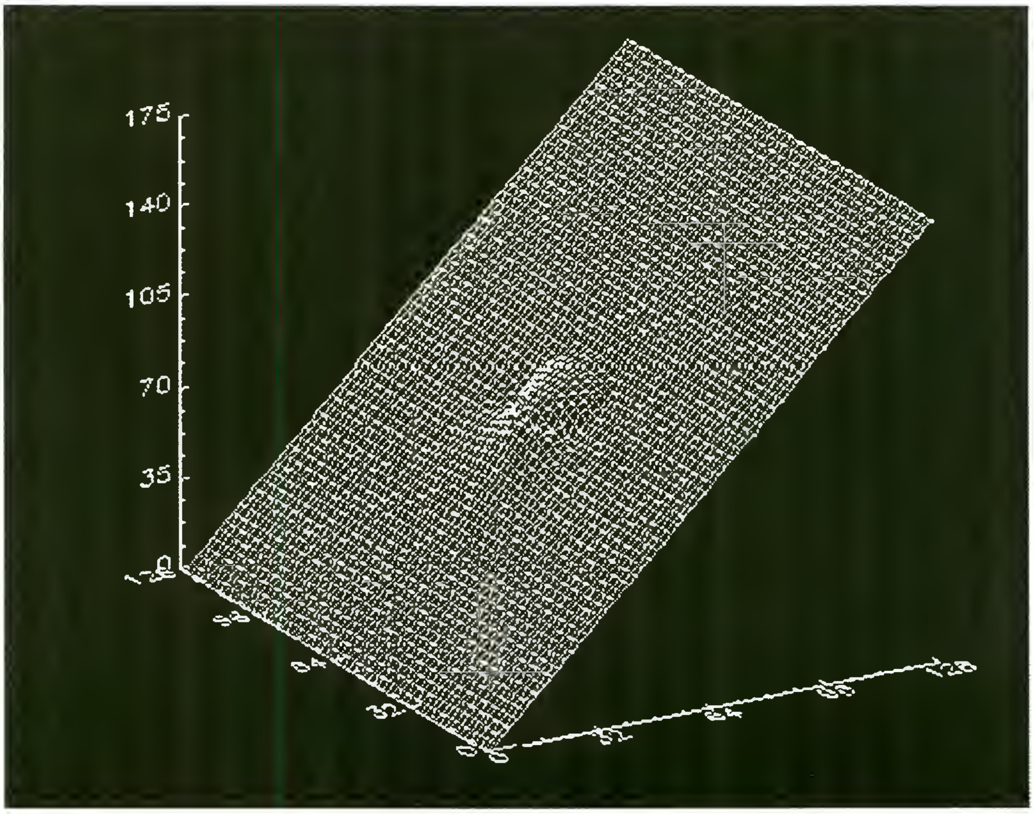

Figure 5: The unwrapped phase reconstructed from the data in Figure 2 with a least squares algorithm (perspective view)

The second data set is the wrapped phase obtained from the interferometry of two real images taken during the tandem campaign by the ERS-1 SAR and the ERS-2 SAR over the region of Etna volcano, Sicily, Italy. The wrapped phase is shown in Figure 6. Although the quality of the data is quite good, there are many inconsistencies in the neighboring pixel differences of the unwrapped phase estimated from the wrapped phase. The inconsistencies are due to phenomena well known in SAR interferometry: in particular can be recognized low coherence corresponding to the sea region at the right bottom of the image, layover in correspondence of the peak of the volcano, and maybe both of these phenomena corresponding to the mountainous region at the top of the figure. The location of the inconsistencies is shown in Figure 7. In Figure 8 we show the unwrapped phase reconstructed with our algorithm (without weighting). The result is visibly good: in particular, very sharp details can be appreciated. Finally, in Figure 9 we show the results of re-wrapping the unwrapped phase reconstructed using an unweighted least squares algorithm. By comparison with Figure 6, it can be noted that this wrapped phase is significantly different from the original one, for example in correspondence of the peak of the mountain. On the contrary, remember that the unwrapped phase obtained with the method proposed in this paper is identical to the original wrapped phase when re-wrapped.

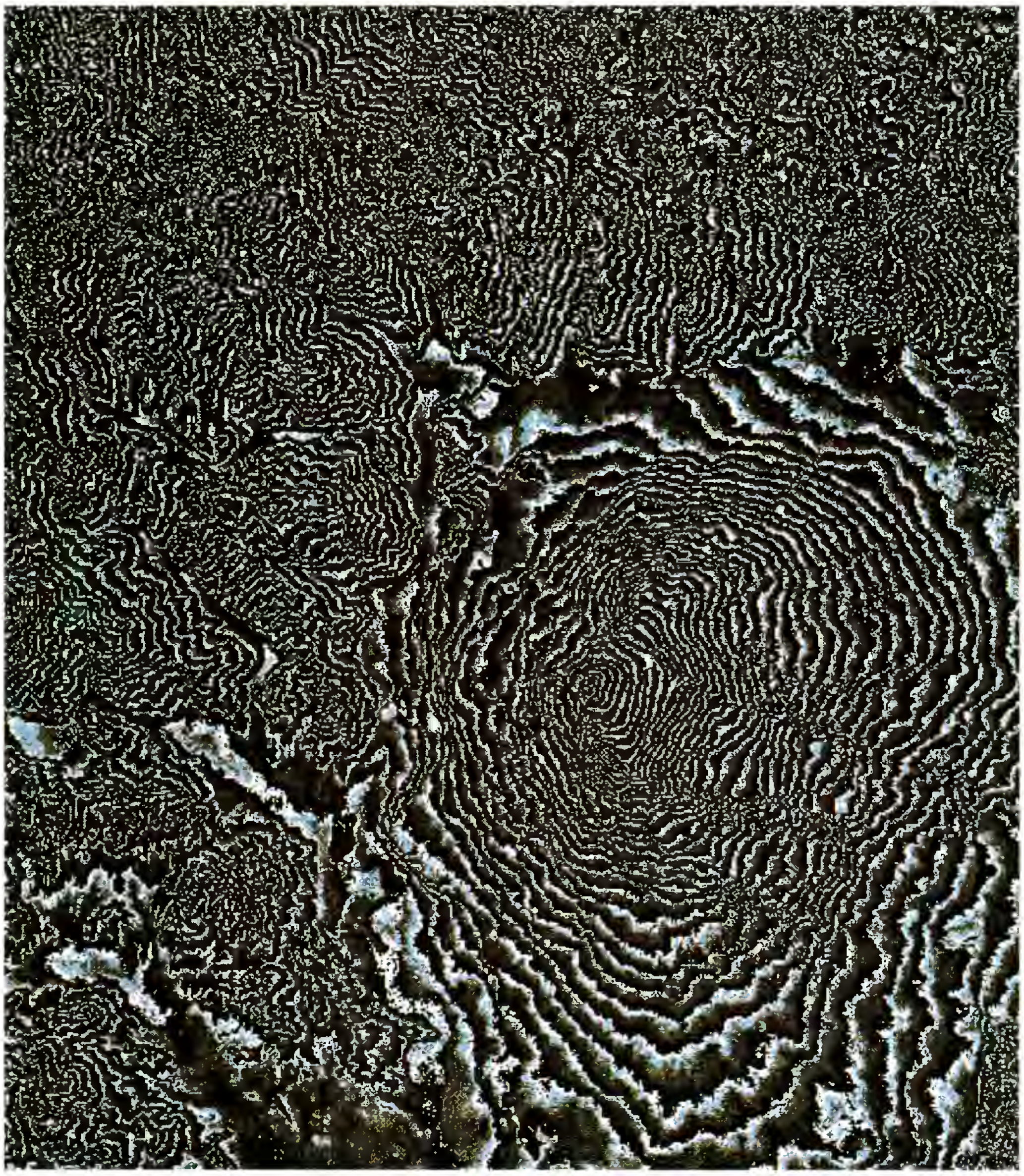

Figure 6: The wrapped phase obtained from the interferometry of a pair of SAR images of the Etna volcano region, Sicily, Italy (gray levels representation)

Figure 7: The regions where the neighboring pixel differences of the unwrapped phase estimated from the data of Figure 6 are inconsistent (in white)

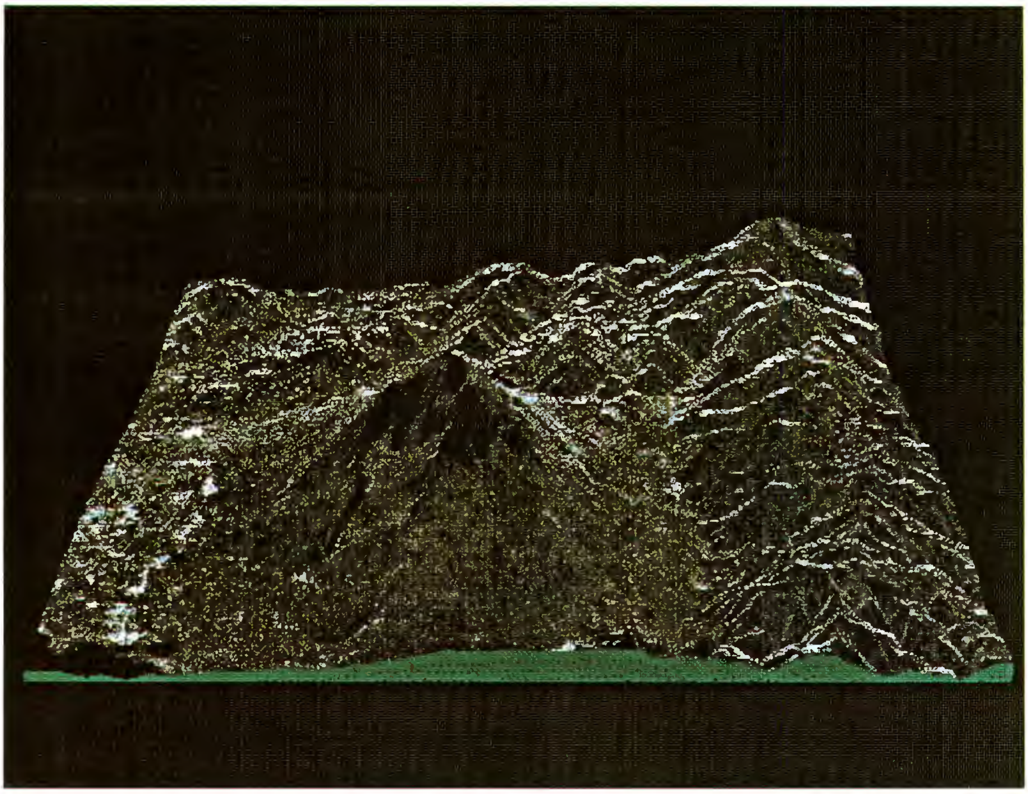

Figure 8: The unwrapped phase reconstructed from the data of Figure 6 with our algorithm (perspective view; the gray level is given by the ERS-1 SAR image intensity)

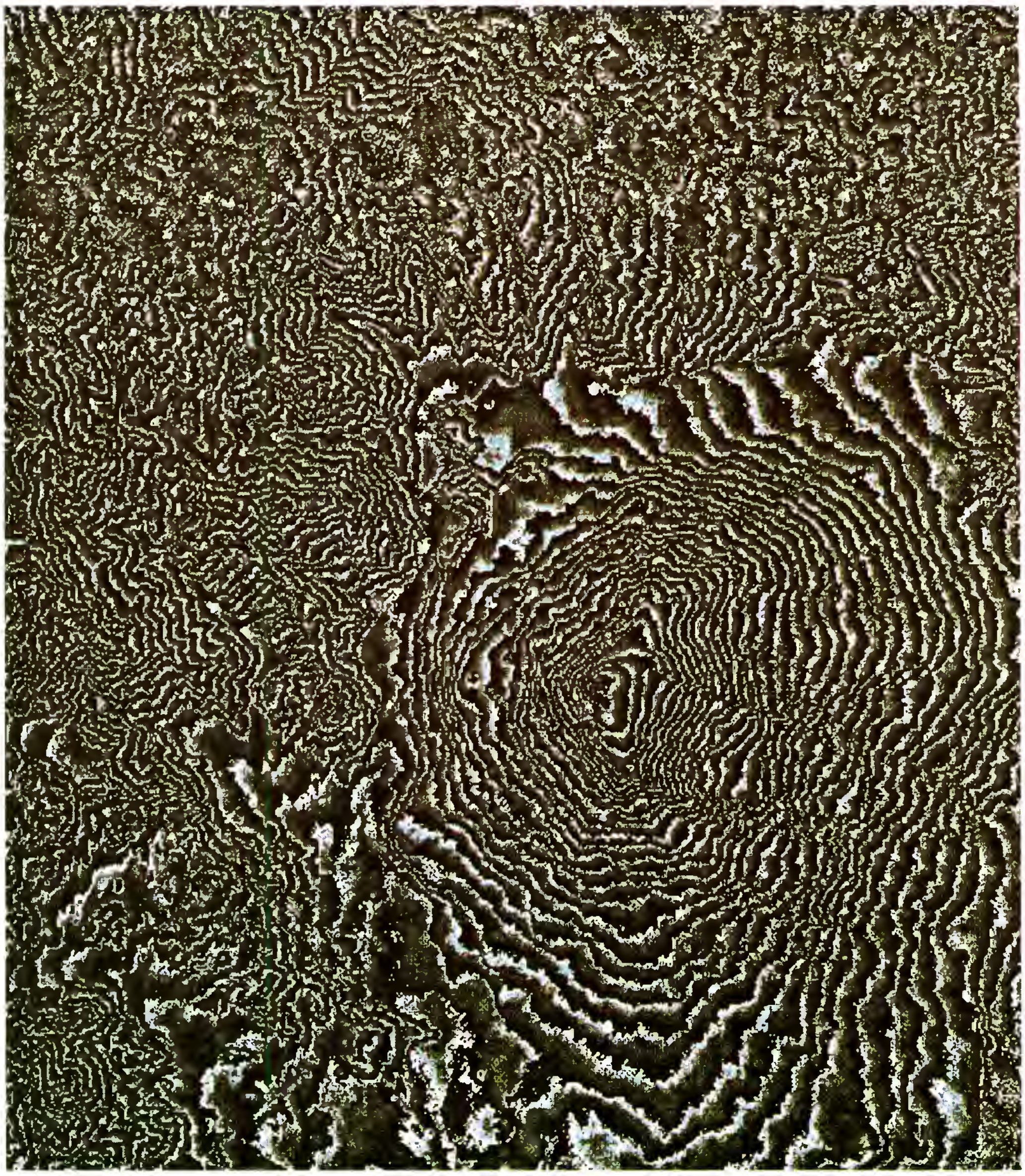

Figure 9: The wrapped phase obtained re-wrapping the phase unwrapped from the data in Figure 6 with a least squares algorithm (gray levels representation)

The computation efficiency of our phase unwrapping technique depends on the minimum cost flow algorithm used. In fact, many different strategies are possible to solve minimum cost problems on a network. The algorithm employed in the above examples requires about 10 seconds for the 128×128 pixels simulated data and about 2 hours for the 1240×1400 pixels Etna data on a Silicon Graphics Power Onyx RE2 (using 1 cpu R8000 at 75 Mhz). Probably, the efficiency of our method can be improved using a technique optimized for the particular network resulting from the phase unwrapping problem.

Conclusions

We propose a new method for phase unwrapping which appears to be accurate and efficient. The key points are: to formulate the phase unwrapping problem exploiting globally its integer qualities, which ensures accurate results; and to recognize the network structure underlying our formulation of the phase unwrapping problem, which makes for an efficient solution. The tests performed demonstrate the validity of this approach.

Details on the technique proposed will be reported in a more complete paper in preparation. Further validation tests are in progress and possible efficiency improvements are under investigation.

Acknowledgments

We would like to acknowledge Karl Heinz Theil and Xiaoqing Wu, of the University of Stuttgart (Germany) Institute of Navigation, for providing the wrapped phase of Figure 6, and Fabrizio Rossi, of the Università dell'Aquila (Italy) Dipartimento of Matematica Pura e Applicata, for useful discussions on network programming algorithms. We also would like to thank Alfonso Farina, of the Alenia Area Sistemi, Roma, and Francesco Zirilli, of the Università di Roma Dipartimento di Matematica, for their advice and encouragement. Finally, we wish to thank Steve Coulson and the staff of ESA ESRIN, Frascati (Italy), for support during the research reported on this paper.

References

Ahuja, R. K.,Magnanti, T. L., Orlin, J. B., 1993:
Network Flows: Theory, Algorithms, and Applications. Prentice-Hall, Englewood Cliffs, New Jersey, USA.

Fried, D. L., 1977:
Least-Squares Fitting a Wave-Front Distortion Estimate to an Array of Phase-Difference Measurements. *Journal of the Optical Society of America*, **67**, pp.370-375.

Ghiglia, D. C., and Romero, L. A., 1994:
Robust Two-Dimensional Weighted and Unweighted Phase Unwrapping Using Fast Transforms and Iterative Methods. *Journal of the Optical Society of America A*, **11**, pp. 107-117.

Goldstein, R. M., Zebker, H. A., and Werner, C. L., 1988:
Satellite Radar Interferometry: Two-Dimensional Phase Unwrapping. *Radio Science*, **23**, pp. 713-720.

Hudgin, R. H., 1977:
Wave-Front Reconstruction for Compensated Imaging. *Journal of the Optical Society of America*, **67**, pp. 375-378.

Hunt, B. R., 1979:
Matrix Formulation of the Reconstruction of Phase Values from Phase Differences. *Journal of the Optical Society of America*, **69**., pp. 393-399.

Prati, C., Giani, M., Leuratti, N., 1990:
SAR Interferometry: a 2D Phase Unwrapping Technique Based on Phase and Absolute Value Informations. *IGARSS '90*, pp. 2043-2046.

Pritt, M. D., 1996:
Phase Unwrapping by Means of Multigrid Techniques for Interferometric SAR. *IEEE Transactions on Geoscience and Remote Sensing*, **34**, pp. 728-738.

Takajo, H. and Takahashi, T, 1988:
Noniterative Method for Obtaining the Exact Solution for the Normal Equation in Least-Squares Phase Estimation from the Phase Difference. *Journal of the Optical Society of America A*, **5**., pp. 1818-1827.

Zebker, H. A., Goldstein, R. M., 1986:
Topographic Mapping from Interferometric Synthetic Aperture Radar Observations. *Journal of Geophysical Research*, **91**, pp. 4993-4999.

The multiresolution approach in SAR interferometry

Mihai Datcu Deutsche Forschungsanstalt für Luft und Raumfahrt e.V., Deutsches Fernerkundungsdatenzentrum, D-82234 Wessling, Germany
datcu@dfd.dlr.de
http://www.dfd.dlr.de/

Abstract

The high interest to derive digital elevation models from interferometric SAR data stimulated the research to optimally and numerically efficient solve the phase unwrapping problem. Several solutions have been proposed. We address the solution of the phase unwrapping stated as a least squares problem and its multiresolution solutions. The multiresolution algorithms are computationaly efficient implementations of the phase unwrapping solution, the wavelet implementation is systematic and allows to deal with the noise in the data.

Keywords: SAR Interferometry, multiresolution analysis, partial differential equations

Introduction

The paper is a short presentation and theoretical comparison of multigrid, finite element, and wavelet methods to solve the partial differential equation problem for applications in Interferometric SAR phase unwrapping.

The phase unwrapping: problem statement

The phase unwrapping is the key step in recovering the terrain elevations from Interferometric SAR data. The problem is to find an estimate of the phase values known the wrapped noisy phase observations. The problem is ill-posed and the solution requires regularization .

Several solutions have been proposed. We refer only the ones based on the minimization of the mean square error between the desired phase gradient and the observations of the wrapped phase gradient. The problem is equivalent to solve a Poisson equation [Ghiglia].

The multigrid algorithms

[Pritt] proposed as a solution for phase unwrapping the weighted least squares method implemented as a multigrid Gauss-Seidel relaxation. The multigrid algorithms are iteratively renewing the solution of the partial differential equation in finer grids using the results from a coarser grid. The multigrid algorithms relies on transforming, by transferring the problem to coarser grids, the low frequency components of the errors into high frequency components which can be removed by the Gauss-Seidel relaxation. The transfer to coarser grids is implemented trough a restriction operator, and the transfer to finer grids with a prolongation operator. These are scale operators similar to wavelet bases of functions but non-systematic mixing the hierarchical decomposition and the resolution steps.

[Fornaro] introduced a finite element method for the phase unwrapping method. The finite element method is computationally efficient in a multigrid implementation, but taking into account the weighting the efficiency is reduced.

The advantage of the multigrid algorithm is the fast convergence and the way to accommodate the weighted least square solution.

The wavelet solution

The wavelet method assumes to decompose the differential operators in a wavelet basis.

[Daubechies] introduced a parameterized family of orthonormal system of functions: the compactly supported wavelets. They are generated from a scaling function and its dual, the wavelet, by dilatations and translations. The elements of the system of functions have compact support and are continuous, the support of the basis functions, due to the rescaling, becomes smaller for larger scaling index. The coefficients of the expansion can be computed with an O(N) algorithm.

[Mallat] demonstrated the multiresolution representation of a given function. Using the scaling and wavelet functions one can represent a function in a system of coarser-finer scales. The Mallat transform consists of convolutions with the filters defining the scaling and wavelet function and downsampling.

[Wells] and [Glowinski] proposed to use the scaling functions at a given scale as finite elements.

[Beylkin] and [Glowinski] introduced a method to solve elliptic differential operators with Dirichlet boundary conditions in the wavelet system of coordinates, by constructing the Green function in O(N) operations. Once the Green function is obtained the solution reduces to a matrix-vector multiplication.

Comparison of the methods

The solution of the partial differential equation using wavelet transforms have several advantages. In the wavelet system of coordinates the differential equations with boundary conditions are characterized by diagonal preconditioner leading to operations with sparse matrices having the condition number O(1), resulting in O(N) algorithms. The condition number is very good, as consequence avoids instabilities, minimizes the errors, and speed up the convergence.

The orthogonality of the wavelet systems allows a systematic and simple mapping in between adjacent scales and also encapsulation of prior knowledge in the solution by disregarding certain wavelet coefficients.

However the wavelets systems are not so easy to compute as finite elements, but the transform is done only once, the number of further iterations compensate this drawback.

Both multigrid and wavelet are using hierarchical decompositions and resolution steps. The wavelet methods for solving the Poisson equation are similar to the multigrid methods, but are using more information: the orthogonal basis of the wavelet decomposition.

The difference of the two methods is in the utilization of the hierarchical decomposition: the multigrid methods mix the hierarchical decomposition and the resolution steps, while the wavelet based method are clearly separated.

Conclusions

The numerical solution of partial differential equation using wavelet decompositions is a new promising field. The emerged methods show a faster convergence, a better accuracy of the solutions and, important for our problem - the SAR interferometry - enable us to deal in a systematic way with the noise of the process.

References

Beylkin G.,
On the representation of operators in bases of compactly supported wavelets, *SIAM J. on Numerical Analysis*, Vol. 6, No. 6, pp 1716-1740, 1992.

Beylkin G.,
On wavelet-based algorithms for solving differential equations, *preprint, CRC Press, University of Colorado at Boudler*, 1993.

Daubechies I.,
Orthonormal bases of compactly supported wavelets, *Comm. Pure Appl. Math.* 41, pp. 906-966.
Fornaro G., Franceschetti G., Lanari R., Rossi D., Tesauro M.,
Interferometric SAR Phase Unwrapping via Finite Elements Method, *submitted to IEE Proc. Radar, Sonar, Navigation,* 1996.
Ghiglia D. C., Romero. L.A.,
Direct phase estimation from phase differences using fast elliptic partial differential equation solver, *Optics Letters,* vol.14, pp. 1107-1109, 1989.
Glowinski R., Rieder A., Wells R.O., Zhou X.,
A wavelet multigrid preconditioner for Dirichlet boundary value problems in general domains, *preprint, Computational Mathematics Laboratory TR93-06*, Rice university, 1993.
Mallat S.,
Multiresolution approximation and wavelet orthonormal bases of L2(R), *Trans. Amer. Math. Soc.*315, pp. 69-87, 1989.
Pritt M. ,
Phase Unwrapping by means of Multigrid techniques for Interferometric SAR, *IEEE Tr. on GSRS,* Vol. 34, No.3, pp. 728-738, 1996.
Wells R.O.,
Multiscale Applications of Wavelets to Solutions of Partial Difference Equations, *preprint, Dept. of Mathematics*, Rice University, 1993.

The potential of ERS tandem for global 100m topography by the year 2000

J.-P. Muller Department of Photogrammetry & Surveying, University College London, Gower Street, London. WC1E 6BT, U.K.

Abstract

The recent ERS tandem mission from ESA offers the potential to create large area DEMs over a variety of different land cover regions at unprecedented resolutions and accuracy. Studies at UCL reported elsewhere at this meeting indicate that accuracies which exceed the specification of the DMA DTED level 1 (3 arc-second grid-spacing and 25m Zrms) can be provided by the automated generation of DEMs from tandem pairs if surface wind conditions are not too severe and night-time data is available.

An analysis of the potential of ERS tandem will be made using data from ESRIN and presented at the workshop as well as a comparison with the recently announced SRTM mission particularly for areas northwards of 58N and 58S.

A first quantitative evaluation of atmospheric effects on SAR interferometry

Ramon Hanssen Delft Institute for Earth Oriented Space Research, Delft University of Technology, Thijsseweg 11, 2629 JA Delft, The Netherlands
hanssen@geo.tudelft.nl
http://www.geo.tudelft.nl/fmr/

Arnout Feijt Royal Netherlands Meteorological Institute (KNMI), PO Box 201, 3730 AE, De Bilt, The Netherlands
feijt@knmi.nl
http://www.knmi.nl/

Abstract

Considerable interest has been generated recently in the use of SAR interferometry for monitoring slow deformation processes. Previous studies have shown that atmospheric inhomogeneities can form a major error source in these measurements. Since these inhomogeneities are distributed with a significant temporal and spatial variance, the corresponding phase delay can be observed within a single interferometric SAR pair. Especially in sea-bordering countries as the Netherlands, interferometric pairs are influenced considerably by the rapidly changing tropospheric conditions. In this study it will be tried to give a first quantitative evaluation of observed effects in SAR interferograms of the Netherlands. Using additional measurements and standard meteorological information, the plausibility of the effects to be atmospherical of origin is examined.

Keywords: insar, atmosphere, deformation

Introduction

Since the state-of-the-art in SAR interferometry is strongly progressing towards a more quantitative and localized approach, the influence of error budgets is becoming more important. The influence of atmospheric inhomogeneities on SAR interferometry has been studied by several authors (see e.g. (Tarayre and Massonnet, 1994/1996), (Goldstein, 1995) and (Zebker and Rosen, 1996)). In this study, special attention is paid to the influence of tropospheric inhomogeneities for small baseline tandem interferograms of an area with no significant variation in elevation. The purpose of these interferograms is to estimate the feasibility of the detection of very slow subsidence rates over a long time span. Although the main problem for this type of measurements seems to be the temporal decorrelation, atmospheric effects can be easily misinterpreted as subsidence. Therefore, it is tried to estimate what the magnitude of the phase shifts due to atmospheric effects can be, and to suggest some possibilities to tackle these problems. The area of interest, Groningen, is situated in the North-East of the Netherlands and is slowly subsiding due to the extraction of natural gas.
This work is confined by emphasizing on tropospheric effects, especially the partial water vapour density, and the restriction to two-pass interferometry. Furhermore small baselines were used on a very flat area, so no Digital Elevation Model was necessary, and ERS1/2 tandem data with their one day time interval to avoid strong temporal decorrelation.
The two main topics we address in this paper are the following. In first instance we want to get some feeling for the relationship between tropospheric parameters as temperature, relative humidity and pressure with respect to relative interferometric phase changes. Secundary, it is tried to give a meteorological interpretation of these relationship in terms of feasibility.
After a short introduction on the subject, some aspects of the nature of the atmospheric effects are mentioned with emphasis on their behaviour in SAR imagery. The following paragraph focusses more on the quantitative aspect, in which we will evaluate the sensibility of the interferometric phase against some important parameters. A small casestudy is performed next, where different data sources are combined to evaluate a SAR interferogram of the Groningen area. Some ideas on the way to approach the atmospheric problem for slow subsidence studies are discussed, after which we will make some concluding remarks.

Characteristics of atmospheric disturbances on INSAR

For two-pass, short baseline interferometry, the influence of elevation on the interferometric phase is small due to the large height ambiguity. Therefore,assuming sufficiently correlated imagery, an interferometric phase change can only be due to surface deformations and inhomogeneities in the propagating medium. Whereas SAR interferometry for the estimation of Digital Elevation Models (DEM's) is strongly dependent on the length of the baseline, its use for deformation studies is not. The phase shift due to atmospheric inhomogeneities is equal for both DEM applications and deformation studies. However, the magnitude of these errors in the final products, DEM's and deformation maps, is different. For DEM's, the magnitude of the error is directly proportional to the height ambiguity, and therefore inversely proportional to the baseline. For deformation maps, the magnitude of the error is not related to the baseline.
Important properties of SAR interferograms are the relatively high resolution in an image of approximately 100 by 100 kilometers, and the fact that we use two semi-instantaneous observations. Translated to the atmosphere, this is related to the high spatial variability in the atmosphere's parameters, and the fact that there is no correlation between the state of the atmosphere at the two observation times.
Ionospheric disturbances have been reported by Tarayre and Massonet(1996) and Massonnet et al (1994). Travelling Ionospheric Disturbances (TID) are defined as areas in which the total electron content is significantly different from its surroundings. The influence of the electron content on the propagation of electromagnetic waves is dependent of the frequency of the signal and have been observed up to 2.8 cm for C-band radar (Massonnet and Feigl, 1995). The spatial extension of TID's are mostly larger than 30 km, which is an important characteristic for recognizing and identifying the effects. Due to this relatively long extension, we expect the effect of ionospheric disturbances to be almost linear for ERS quarter scenes.
Tropospheric disturbances are more common to occur, even on sub kilometer scale. The often turbulent behaviour of masses of air causes a constant mixture of temperature, pressure and relative humidity. Cloud forming processes are an example for the temporal and spatial scale of the inhomogeneity of this part of the atmosphere. A more quantitative evaluation of tropospheric disturbances will be given in the following paragraph.

Magnitude of the tropospheric inhomogeneities

Theory

The phase shift of a radio signal that propagates two-way in a medium with a refractive index equal to 1 (free space) can be expressed as:

$$\varphi = \frac{4\pi}{\lambda}\rho$$

where rho is the one-way propagation path length. For a signal propagating in a medium with a refractive index unequal to 1, an incremental path length will be observed due to the signal delay in the medium, hence

$$\varphi = \frac{4\pi}{\lambda}(\rho + \Delta\rho)$$

If we compare the phases of two SAR images, to calculate the interferometric phase, we obtain

$$\varphi_{12} = \varphi_1 - \varphi_2 = \frac{4\pi}{\lambda}(\rho_1 - \rho_2 + \Delta\rho_1 - \Delta\rho_2)$$

Assuming that we are dealing with a very short baseline (< 50 m) and a flat, horizontal area with no deformations, the only coherent phase fluctuations will be caused by the difference in incremental path length:

$$\varphi_{12} = \frac{4\pi}{\lambda}\Delta\rho_{12}.$$

From the latter equation we see that we cannot differ between the tropospheric states of the two acquisitions. Experimental measurements of the influence of atmospheric pressure, temperature and the partial pressure of water vapour (Smith and Weintraub, 1953)(Zebker and Rosen,1996), have shown that the incremental path length can be approximated by integrating these parameters over the total path length in the troposphere:

$$\Delta\rho = 7.76 \cdot 10^{-5} \int_0^{atm} \frac{P}{T} dx + 3.73 \cdot 10^{-1} \int_0^{atm} \frac{e}{T^2} dx$$

In practice, however, the vertical profiles of the three parameters, needed for the calculation of the delay, cannot be calculated for every pixel. Fortunately, the incremental path length caused by the tropospheric delay can be estimated using e.g. a Saastamoinen tropospherical model. This model expresses the incremental path length as a function of *pressure*, *relative humidity*, *temperature* and *inclination*.

The Saastamoinen model

The height integral over the refractive index $\int (n-1)\,dr$ of the atmospheric refractivity for electromagnetic waves, taken from the earth's surface up to the top of the atmosphere, is direcly proportional to the ground pressure. This follows from the law of Gladstone and Dale, and the fact that the barometer measures the weight of the overlying atmosphere.
Therefore the refraction formulas can be simplified and improved by determining the refractivity integral without a detailed knowledge of the height distribution of the refractive index (Saastamoinen,1972).
For the latitude of the Netherlands, a simplified form of the Saastamoinen model is

$$\Delta\rho = 2.277 \cdot 10^{-3} \frac{P + (\frac{1225}{t+273.15} + 0.05)e - 1.156 \tan^2\theta}{\cos\theta}$$

in which P is the total atmospheric pressure in HPa, t is the temperature in degrees Celcius, theta is the inclination angle and e is the partial water vapour pressure. The latter can be derived from the relative humidity rh[%] using:

$$e = \frac{rh}{100} e^{(-37.2465+0.213166(t+273.15)-0.000256908(t+273.15)^2)}$$

The important consequence of this model is that an estimation of the phase delay can be determined without having to know all the parameters a

A quantitative evaluation of the parameters

The Saastamoinen model can be used to perform a first quantitative evaluation of the sensibility of phase changes due to the three major parameters; *relative humidity* ,*temperature* and *pressure*. What we assume here, is that the atmosphere is divided spatially into columns with a certain average value of the three variables. In the horizontal direction, differences can occur between the columns, resulting in a relative phase shift in the interferogram.
Figure 1 shows the influence of pressure changes (HPa) on the interferometric phase. We can see that e.g. a difference of 5 HPa represents a corresponding phase shift of 0.4 phase cycle. Note that the pressure is not correlated with temperature or relative humidity. Pressure changes of 5 HPa over 50 kilometers are possible to occur in a meteorological front zone, and will be visible as a linear trend in the interferogram.

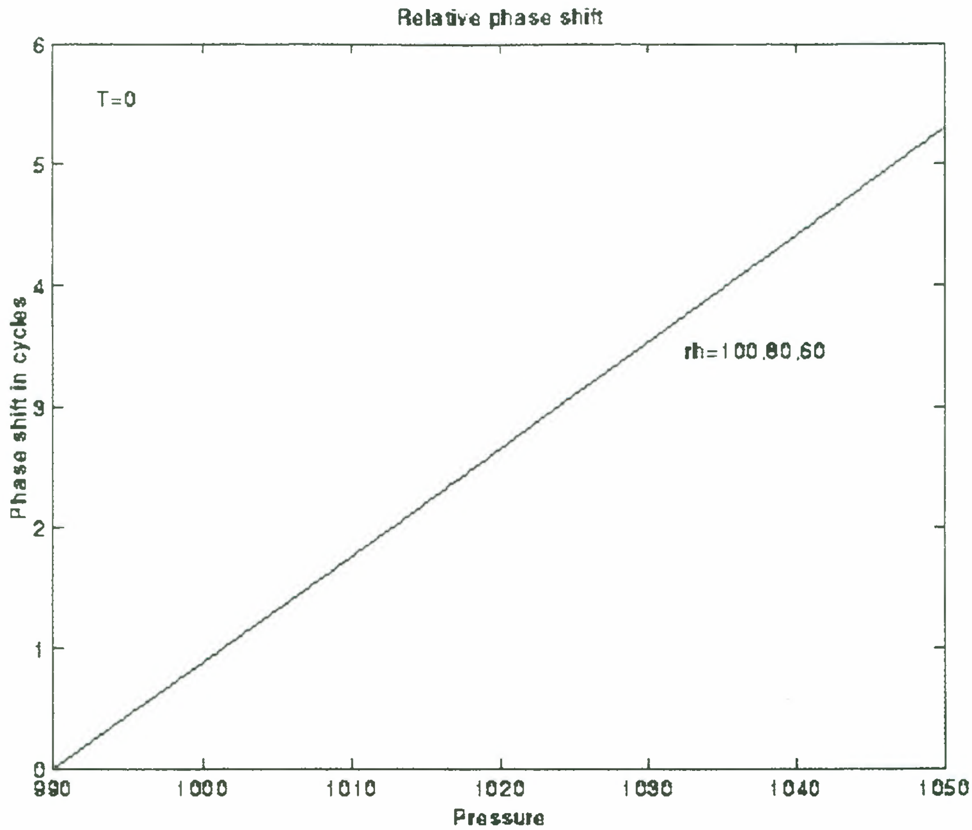

Figure 1: Relative phase shift as a function of pressure in the Saastamoinen model. Pressure is expressed in HPa.

In figure 2 the connection between temperature and relative phase change is shown for three values of the relative humidity and a fixed pressure of 1010 HPa. Here we see that a (horizontal) temperature gradient of 5 degrees can have considerable influence on the corresponding phase shift, depending on the absolute temperature and the relative humidity. If we keep in mind that in a standard atmosphere the temperature drops with 6.5 degrees every kilometer, the influence of the lower layers will be significantly more important than higher layers.

In the horizontal direction the first 40 meters above ground level can have strong variations in temperature, depending on the nature of the surface. Above this layer, at fixed altitudes, the horizontal differences in temperature will be limited to large scale trends. Due to the limited extend of this lower layer, it can be doubted if it will have enough influence to alter the interferometric phase.

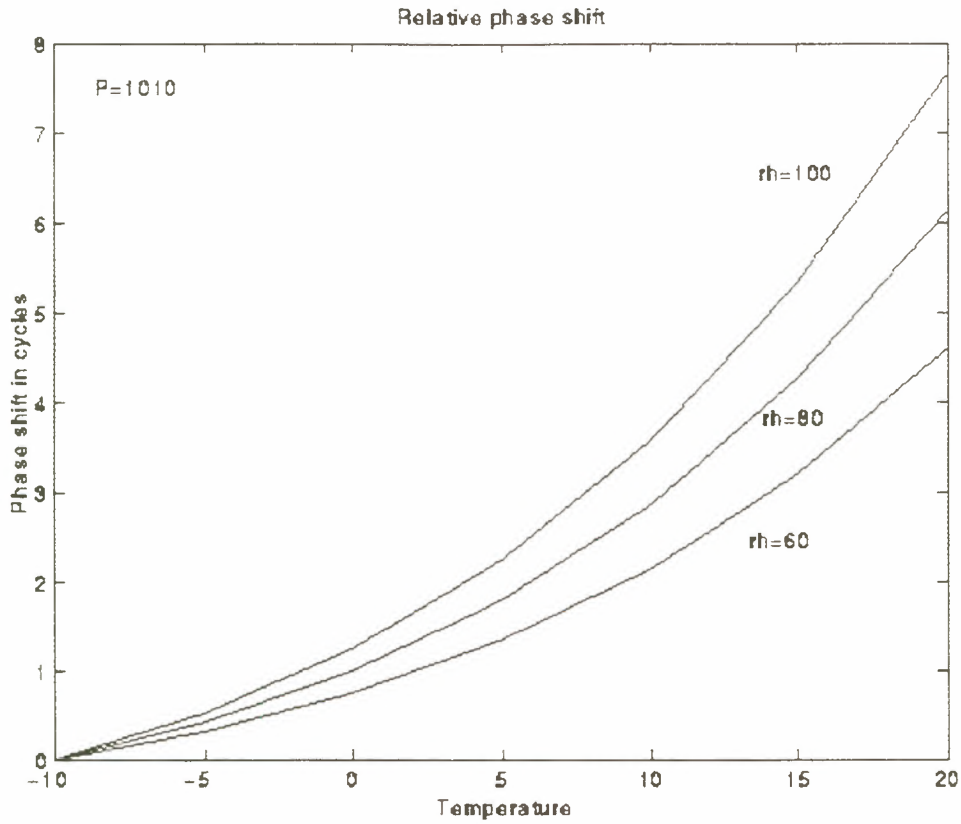

Figure 2: Relative phase shift as a function of temperature in the Saastamoinen model. Temperature is expressed in degrees Celsius.

Finally, figure 3 shows the influence of the relative humidity on the relative phase change, for three different temperatures. These temperatures can be coupled directly to altitude, and due to the decrease in temperature with height, the influence of a humidity change at low temperatures becomes significantly more important than at higher temperatures. For a temperature of 0 degrees Celsius, a 20% change in relative humidity horizontally would count for a half cycle phase difference in the interferogram.

Strong variations in relative humidity are to be expected e.g. near cumulus clouds, where dry and warm air is moving upwards, cools down, and condensates (increase in relative humidity). The consequence of this movement is a downward movement at some distance from the upward one. In this downward movement, cold and humid air is warmed up, hereby decreasing in humidity. As a consequence we might expect changes in relative humidity of tens of percents, even on a kilometer scale.

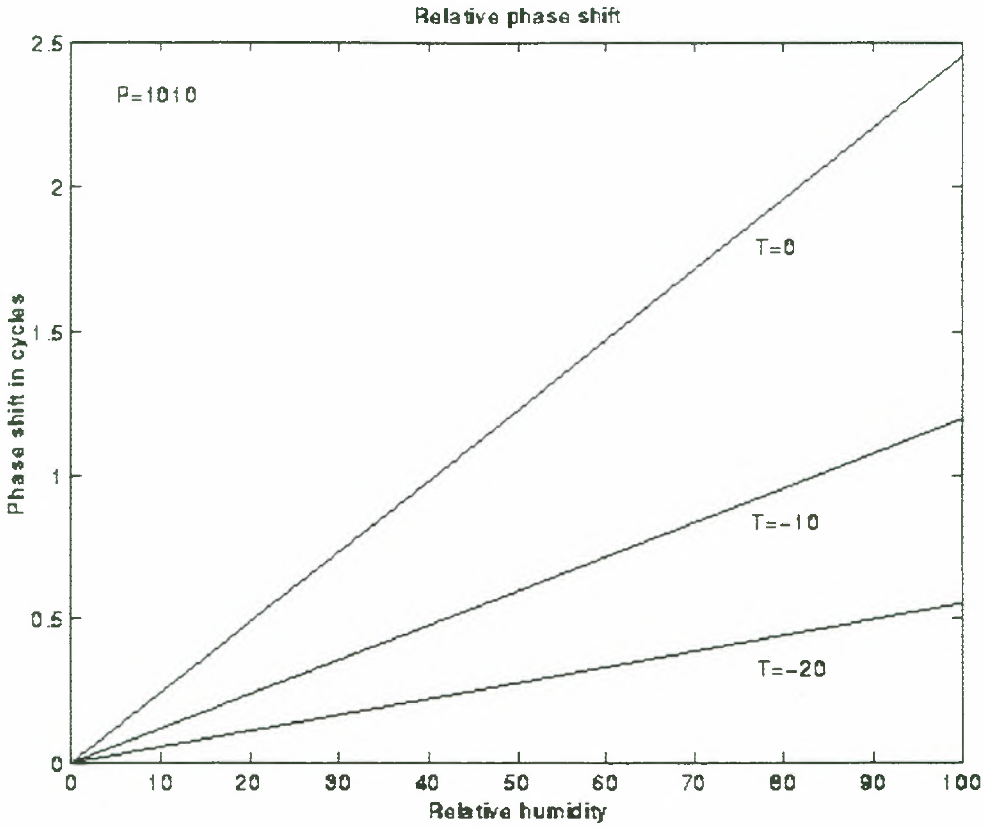

Figure 3: Relative phase shift as a function of the relative humidity in the Saastamoinen model.

Casestudy: Groningen Interferometric SAR experiment

Interferometric observations

In the Groningen Interferometric SAR Experiment (GISARE), an interferogram was obtained using the ERS images of february 26 and 27, 1996 at 10:29 UTC (see figure 4). The elevation differences in this area do not exceed 5 meters, which corresponds to a phase cycle of 0.02 for this baseline. Therefore, topography can be neglected as a source of phase changes in the interferogram.
The remaining phase differences are not influenced by the baseline, so only phase delay or surface deformation will be visible in the interferogram. However, large scale deformations are unlikely within a time period of one day. Over the land areas we see changes in interferometric phase of about 0.4 phase cycle, corresponding with approximately 1 cm excess path length in the direction of the satellite. Furthermore, there appear to be patterns in these disturbances in North-East South-West direction. The inclination of the image for this descending orbit is approximately 13 degrees.

Estimating the derivative of modulo-mapped phases

Otmar Loffeld Zentrum für Sensorsysteme (ZESS), Universität-GH-Siegen, Paul-Bonatz-Str. 9-11
57068 Siegen, Germany
loffeld@wiener.zess.uni-siegen.de
http://www.zess.uni-siegen.de

Christoph Arndt Zentrum für Sensorsysteme (ZESS), Universität-GH-Siegen, Paul-Bonatz-Str. 9-11
57068 Siegen, Germany
arndt@nv.et-inf.uni-siegen.de
http://www.nv.et-inf.uni-siegen.de/pb2/www_pb2

Achim Hein Zentrum für Sensorsysteme (ZESS), Universität-GH-Siegen, Paul-Bonatz-Str. 9-11
57068 Siegen, Germany
hein@nv.et-inf.uni-siegen.de
http://www.nv.et-inf.uni-siegen.de/pb2/www_pb2

Abstract

Nearly all known phase unwrapping techniques try to unwrap the mapped phases by a sequence of differentiating, taking the principal value of the discrete derivative and integrating again. This procedure, conceptually appealing as it may appear, however, yields strongly biased phase derivatives and thus strongly biased phase estimates as the paper will show. This bias is a serious drawback of any differentiation of modulo mapped noise contaminated functions. The problem lies in the methodology rather than in the wrap around effect, as no sequence of linear and nonlinear operations may be altered without seriously affecting the result. It can be shown mathematically, that computing the discrete derivative of noisy modulo-2 mapped phase yields estimates of the unambiguous discrete derivative, which are always biased towards lower absolute values. Thus phase slopes are always underestimated. It can be shown further that the bias clearly depends on the phase slope itself as well as on the coherence. The paper will present the theoretical analysis, and give some hints of how to circumvent the problem.
Keywords: Phase unwrapping techniques, phase slope estimation, biased phase estimates

Introduction

The determination of the unambiguous phase from noisy observations of complex angularly modulated signals is an unsolved problem in general, especially if phase and amplitude are mutually uncorrelated or even independent. This is clearly the case for a complex SAR interferogram. In terms of signal theory a SAR interferogram can be considered as a complex, simultaneously amplitude and phase modulated 2D signal with non Gaussian error statistics. Usually the wanted interferometric phase is obtained by a simple $\tan^{-1}$ operation delivering phase values within the principal interval (e.g. -, , depending on the kind of inverse function). These phases contain all the information needed for the generation of digital terrain elevation maps of observed areas but they do not contain that information in an unambiguous way as any absolute phase offset (an integer multiple of 2) is lost. Furthermore they are subject to phase noise coming from the superimposed amplitude noise in real and imaginary part of the InSAR image. The process of resolving these phase ambiguities is usually called phase unwrapping which in terms of signal theory is *simply* a two dimensional phase demodulation problem. Nearly all classical approaches to phase unwrapping, known from optical interferometry apply a sequence of differentiating, taking the principal value of the discrete derivative and integrating again along specified paths. The paper will show that such a sequence of operations always yields more or less badly biased estimates of the wanted derivative of the unambiguous phase. This especially applies to a combination with Linear Least Squares techniques which are commonly used to reduce stochastic phase errors. The paper will present the analysis, the numerical, and the analytical evaluation of the phase bias depending on the phase slope and on the signal to noise ratio. Finally some hints to circumvent the problem will be given.

1. Theory and Concepts

1.1 1D Stochastic Analysis

Let the observed phase obtained from a $\tan^{-1}$-operation form real and imaginary part of the interferogram, be related to the unambiguous phase by the following mapping:

$$y_{\varphi}(k)=\left[\varphi(k)+\tilde{e}_{\varphi}(k)\right]_{|2\pi} \tag{1}$$

where (k) is the true unambiguous phase at time or point k, $\tilde{e}_{\varphi}(k)$ is the phase error and the bracket indicates the operation of taking the principal value of the argument phase term in a way that:

$$\tilde{\varphi}=\left[\varphi\right]_{|2\pi}=\varphi\pm n\cdot 2\pi\in(-\pi,\pi] \quad and: \quad |\tilde{\varphi}|\leq\pi \tag{2}$$

As a result of equations 1 and 2 the observed phase always lies within the base interval (-,. This effect, arising anytime when the interferometric phase is computed by a $\tan^{-1}()$ operation from quadrature and inphase component of an interferogram, is well known as the wrap around effect.

Nearly all known phase unwrapping techniques with the exception of /LoKr1, LoKr2/ try to unwrap the mapped phases by a sequence of differentiating, taking the principal value of the discrete derivative and integrating again.

The operation of forming the discrete derivative yields:

$$\begin{aligned}\Delta_{p}(k)&=\left[y_{p}(k+1)-y_{p}(k)\right]_{|2\pi}=\left[\left[\varphi(k+1)+\tilde{e}_{p}(k+1)\right]_{|2\pi}-\left[\varphi(k)+\tilde{e}_{p}(k)\right]_{|2\pi}\right]_{|2\pi}\\&=\left[\left[\left[\varphi(k+1)\right]_{|2\pi}+\left[\tilde{e}_{p}(k+1)\right]_{|2\pi}\right]_{|2\pi}-\left[\left[\varphi(k)\right]_{|2\pi}+\left[\tilde{e}_{p}(k)\right]_{|2\pi}\right]_{|2\pi}\right]_{|2\pi}\\&=\left[\left[\varphi(k+1)\right]_{|2\pi}-\left[\varphi(k)\right]_{|2\pi}+e_{p}(k+1)-e_{p}(k)\right]_{|2\pi}\end{aligned} \tag{3}$$

In the sequence of operations in equation 3 we have only used the fact that adding any integer multiple of 2 does not change the result of a modulo-2 operation. $e_{\varphi}(k+1),\ e_{\varphi}(k)$ are the phase errors at points k and k+1, respectively, mapped into the base interval (-,. The stochastic properties of these errors, namely distribution density and second order moments are known. Now again using the same identities in equation 3 as before we can further write:

$$\begin{aligned}\Delta_{p}(k)&=\left[\left[\varphi(k+1)-\varphi(k)\right]_{|2\pi}+\left[e_{p}(k+1)-e_{p}(k)\right]_{|2\pi}\right]_{|2\pi}\\&=\left[\left[\delta_{p}(k)\right]_{|2\pi}+\left[e_{p}(k+1)-e_{p}(k)\right]_{|2\pi}\right]_{|2\pi}=\left[\delta_{p}(k)+\left[e_{p}(k+1)-e_{p}(k)\right]_{|2\pi}\right]_{|2\pi}\end{aligned} \tag{4}$$

where the last equality has exploited that along normal integration paths the true phase variation's modulus is always smaller than . Normal refers to those integration paths which do not cross a cutline. $\delta_{\varphi}(k)$ is the true discrete phase derivative.

Equation 4 clearly expresses the error which we commit when forming the discrete derivative from modulo-2 mapped noisy data. If there were no phase error present the result would be totally correct, but since phase errors always occur in normal interferograms, we commit a systematic error when 'differentiating' modulo-2 mapped data. The phase derivative will be - depending on the noise - more or less badly biased and so will be the unwrapped phase if the biased derivative is integrated again.

The further investigation of the bias error will be organized as follows. In a first step we will investigate the stochastic features of the phase error difference in the second term of equation 4. Then we will evaluate, how a modulo operation, which occurs twice, changes the known distribution density of random variable. Let us introduce the non-mapped phase error difference variable by:

$$\tilde{\delta}_e(k) = e_p(k+1) - e_p(k) \tag{5}$$

Obviously the numerical values can vary between 2, as any of the terms in the difference can vary between . Assuming that the phase errors of two subsequent phase samples are independent random variables with identical and symmetric distributions the resulting distribution density of the phase difference is the correlation product of the individual phase distribution densities. Thus we have:

$$f_{\tilde{\delta}_e(k)}(\xi) = f_{e_p(k+1)}(-\xi) * f_{e_p(k)}(\xi) = \int_{-\infty}^{\infty} f_{e_p(k+1)}(u) \cdot f_{e_p(k)}(\xi+u)du \tag{6}$$

Later on we will need the distribution function rather than the density. This function is simply obtained by:

$$\begin{aligned} F_{\tilde{\delta}_e(k)}(\xi) &= \int_{-\infty}^{\xi} f_{\tilde{\delta}_e(k)}(z)dz = \int_{-\infty}^{\xi}\int_{-\infty}^{\infty} f_{e_p(k+1)}(u) \cdot f_{e_p(k)}(z+u)dudz \\ &= \int_{-\infty}^{\infty} f_{e_p(k+1)}(u) \cdot \int_{-\infty}^{\xi} f_{e_p(k)}(z+u)dzdu = \int_{-\infty}^{\infty} f_{e_p(k+1)}(u) \cdot F_{e_p(k)}(\xi+u)du \\ &= \int_{-\infty}^{\infty} F_{e_p(k)}(u) \cdot f_{e_p(k+1)}(u-\xi)du \end{aligned} \tag{7}$$

Conceptually equation 7 can be solved since the individual terms are known from /Mid1, LoKr1/. The phase error distribution density, given there, is:

$$\begin{aligned} f_{e_p(k)}(\varepsilon) &= \frac{1}{2\pi}\cdot\frac{1-|\gamma|^2}{1-|\gamma|^2\cdot\cos^2(\varepsilon)}\cdot\left[1+\frac{|\gamma|\cdot\cos(\varepsilon)\cdot\left[\pi-\arccos(|\gamma|\cdot\cos(\varepsilon))\right]}{\sqrt{1-|\gamma|^2\cdot\cos^2(\varepsilon)}}\right] \\ &= \frac{1-|\gamma|^2}{2\pi\cdot\left(1-|\gamma|^2\cdot\cos^2(\varepsilon)\right)}\cdot\left[1+\frac{|\gamma|\cdot\cos(\varepsilon)}{\sqrt{1-|\gamma|^2\cdot\cos^2(\varepsilon)}}\cdot\left[\frac{\pi}{2}+\arctan\left(\frac{|\gamma|\cdot\cos(\varepsilon)}{\sqrt{1-|\gamma|^2\cdot\cos^2(\varepsilon)}}\right)\right]\right] \end{aligned} \tag{8}$$

where $|\gamma| = |\gamma(k)|$ is the coherence at point k. The corresponding distribution function which we also need in equation 7, obtained from /Mid1/ is given by:

$$\begin{aligned} F_{e_p(k)}(\varepsilon) &= \frac{1}{2}\cdot\left[1+\frac{\varepsilon}{\pi}+\frac{1}{\pi}\frac{|\gamma|\cdot\sin(\varepsilon)}{\sqrt{1-|\gamma|^2\cdot\cos^2(\varepsilon)}}\cdot\arccos\left(-|\gamma|\cdot\cos(\varepsilon)\right)\right] \quad \text{if } |\varepsilon|\le\pi \\ &= 1 \quad \text{if } \varepsilon>\pi \\ &= 0 \quad \text{if } \varepsilon<-\pi \end{aligned} \tag{9}$$

As indicated earlier the phase difference $\tilde{\delta}_e(k)$ given in equation 5 and showing values between 2 is now mapped into the base interval between . The functional mapping is:

$$\delta_e(k) = \begin{cases} \tilde{\delta}_e(k) + 2\pi & \tilde{\delta}_e(k) \in (-2\pi, -\pi] \\ \tilde{\delta}_e(k) & \text{if} \quad \tilde{\delta}_e(k) \in (-\pi, \ \pi] \\ \tilde{\delta}_e(k) - 2\pi & \tilde{\delta}_e(k) \in (\pi, \ 2\pi] \end{cases} \tag{10}$$

The distribution density of the -mapped phase error difference $\delta_e(k)$ can be obtained by letting:

$$f_{\delta_e(k)}(\xi) = \int_{-2\pi}^{2\pi} f_{\delta_e(k)\tilde{\delta}_e(k)}(\xi, u)du = \int_{-2\pi}^{2\pi} f_{\delta_e(k)/\tilde{\delta}_e(k)}(\xi / u) \cdot f_{\tilde{\delta}_e(k)}(u)du$$

$$= \int_{-2\pi}^{-\pi} f_{\delta_e(k)/\tilde{\delta}_e(k)}(\xi / u) \cdot f_{\tilde{\delta}_e(k)}(u)du + \int_{-\pi}^{\pi} f_{\delta_e(k)/\tilde{\delta}_e(k)}(\xi / u) \cdot f_{\tilde{\delta}_e(k)}(u)du + \int_{\pi}^{2\pi} f_{\delta_e(k)/\tilde{\delta}_e(k)}(\xi / u) \cdot f_{\tilde{\delta}_e(k)}(u)du \tag{11}$$

Using the correct functional mapping in each of the intervals and exploiting the fact the conditional probability density of a functionally mapped variable only consists of a Dirac impulse we have:

$$f_{\delta_e(k)}(\xi) = \int_{-2\pi}^{-\pi} \delta(\xi - (u + 2\pi)) \cdot f_{\tilde{\delta}_e(k)}(u)du + \int_{-\pi}^{\pi} \delta(\xi - u) f_{\tilde{\delta}_e(k)}(u)du + \int_{\pi}^{2\pi} \delta(\xi - (u - 2\pi)) f_{\tilde{\delta}_e(k)}(u)du$$

$$= \begin{cases} f_{\tilde{\delta}_e(k)}(\xi - 2\pi) + f_{\tilde{\delta}_e(k)}(\xi) + f_{\tilde{\delta}_e(k)}(\xi + 2\pi) & \text{if} \quad \xi \in (-\pi, \pi] \\ 0 & \text{else} \end{cases} \tag{12}$$

$$= \left[f_{\tilde{\delta}_e(k)}(\xi - 2\pi) + f_{\tilde{\delta}_e(k)}(\xi) + f_{\tilde{\delta}_e(k)}(\xi + 2\pi) \right] \cdot rect\left[\frac{\xi}{2\pi} \right]$$

Now we return to the sum in equation 4 and introduce the non-mapped discrete difference by:

$$\tilde{\Delta}(k) = \delta_p(k) + \left[e_p(k+1) - e_p(k) \right]_{|2\pi} = \delta_p(k) + \delta_e(k) \tag{13}$$

Further introducing the conditional density of $\tilde{\Delta}(k)$ conditioned on the fact that the true phase derivative takes on the value δ_0 we may write:

$$f_{\tilde{\Delta}(k)/\delta_\varphi(k)}(\xi/\delta_0) = f_{\bar{\delta}_\epsilon(k)/\delta_\varphi(k)}(\xi-\delta_0/\delta_0) = f_{\bar{\delta}_\epsilon(k)}(\xi-\delta_0) \qquad (14)$$

In the last equality we have used the fact that the -mapped phase error difference $\delta_\epsilon(k)$ is independent of the true phase derivative $\delta_\varphi(k)$. Substituting equation 12 into 14 we obtain:

$$\begin{aligned} f_{\tilde{\Delta}(k)/\delta_\varphi(k)}(\xi/\delta_0) = & \left[f_{\bar{\delta}_\epsilon(k)}(\xi-\delta_0-2\pi) + f_{\bar{\delta}_\epsilon(k)}(\xi-\delta_0) + f_{\bar{\delta}_\epsilon(k)}(\xi-\delta_0+2\pi) \right] \\ & \cdot rect\left[\frac{\xi-\delta_0}{2\pi}\right] \end{aligned} \qquad (15)$$

This is the conditional distribution density of $\tilde{\Delta}(k)$ conditioned on the fact that the true phase derivative takes on the value δ_0. This variable is -mapped again to yield $\Delta_\varphi(k)$ (Equ. 4). Now utilizing the same arguments and reasoning as before, we get the final result for the conditional density of the 'mapped' phase derivative, conditioned on the fact that the true phase derivative takes on the value δ_0:

$$\begin{aligned} & f_{\Delta_\varphi(k)/\delta_\varphi(k)}(\xi/\delta_0) \\ & = \left[f_{\tilde{\Delta}_\varphi(k)/\delta_\varphi(k)}(\xi-2\pi/\delta_0) + f_{\Delta_\varphi(k)/\delta_\varphi(k)}(\xi/\delta_0) + f_{\Delta_\varphi(k)/\delta_\varphi(k)}(\xi+2\pi/\delta_0) \right] \cdot rect\left[\frac{\xi}{2\pi}\right] \\ & = \left[f_0(\xi-\delta_0-2\pi) + f_0(\xi-\delta_0) + f_0(\xi-\delta_0+2\pi) \right] \cdot rect\left[\frac{\xi}{2\pi}\right] \end{aligned}$$

where the short hand expression $f_0(\xi)$ has been utilized for convenience. This expression is the 2-cutout of the sum of three shifted replicas of the distribution density $f_{\bar{\delta}_\epsilon(k)}(\xi)$ (cf. Equ. 15):

$$f_0(\xi) = \left[f_{\bar{\delta}_\epsilon(k)}(\xi-2\pi) + f_{\bar{\delta}_\epsilon(k)}(\xi) + f_{\bar{\delta}_\epsilon(k)}(\xi+2\pi) \right] \cdot rect\left[\frac{\xi}{2\pi}\right] \qquad (17)$$

Figure 1 demonstrates the generation of $f_0(\xi)$ for an arbitrary density $f_{\bar{\delta}_\epsilon(k)}(\xi)$:

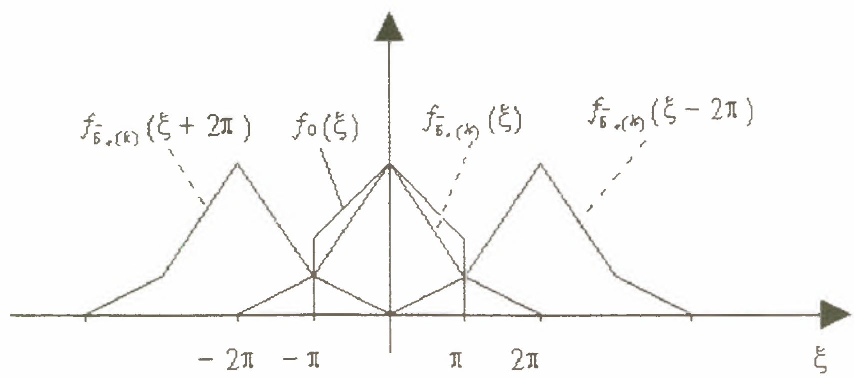

Figure 1: The generation of $f_0(\xi)$ as a cutout of three superimposed densities

To simplify the further derivation we introduce the bias error of the 'mapped' derivative:

$$e(k) = \Delta_{\varphi}(k) - \delta_{\varphi}(k) \tag{18}$$

If we now evaluate the conditional density of this error conditioned on $\delta_p(k) = \delta_0$, we can evaluate any stochastic measure of the bias conditioned on any value of the derivative, which we seek, e.g. the conditional mean of the bias. From probability theory we know that:

$$\begin{aligned} f_{e(k)/\delta_{\varphi}(k)}(\xi / \delta_0) \cdot d\xi &= P\left\{\omega : e(k,\omega) \in (\xi, \xi + d\xi] \,/\, \delta_p(k,\omega) = \delta_0\right\} \\ &= P\left\{\omega : \Delta_p(k,\omega) - \delta_p(k,\omega) \in (\xi, \xi + d\xi] \,/\, \delta_p(k,\omega) = \delta_0\right\} \\ &= P\left\{\omega : \Delta_p(k,\omega) \in (\xi + \delta_0, \xi + \delta_0 + d\xi] \,/\, \delta_p(k,\omega) = \delta_0\right\} \\ &= f_{\Delta_{\varphi}(k)/\delta_{\varphi}(k)}(\xi + \delta_0 / \delta_0) \cdot d\xi \end{aligned} \tag{19}$$

Substituting the identity of equ. 19 into equation 16 we obtain the wanted conditional density:

$$f_{e(k)/\delta_{\varphi}(k)}(\xi / \delta_0) = \left[f_0(\xi - 2\pi) + f_0(\xi) + f_0(\xi + 2\pi) \right] \cdot rect\left[\frac{\xi + \delta_0}{2\pi} \right] \tag{20}$$

with $f_0(\xi)$ given in equation 17. Figure 2 demonstrates the meaning of equation 20 graphically:

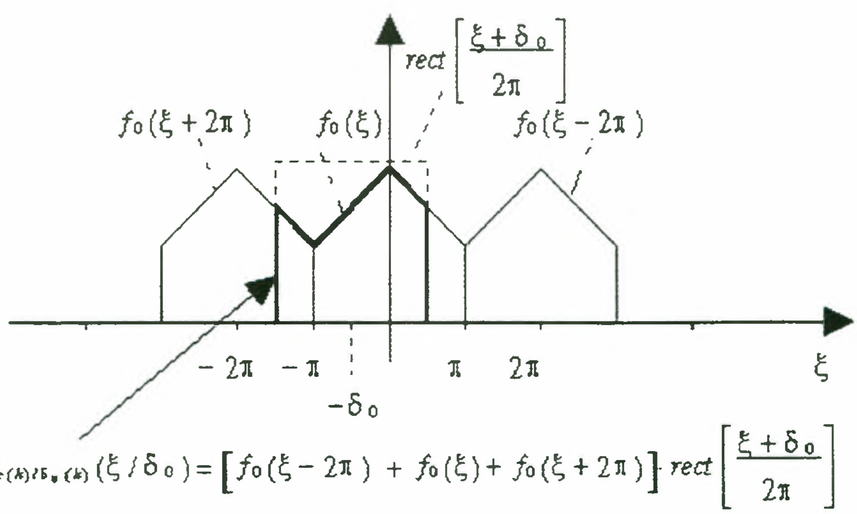

Figure 2: The generation of the conditional error distribution

With the help of figure 2 the conditional expectation of the bias error is readily calculated:

$$E\left\{e(k) / \delta_p(k) = \delta_0\right\} = \int_{-\delta_0 - \pi}^{-\delta_0 + \pi} \xi \cdot f_{e(k)/\delta_{\varphi}(k)}(\xi / \delta_0) \cdot d\xi \tag{21}$$

1. As our first case we will consider the interval $-\pi < \delta_0 \leq 0$. For this case we can subdivide the integral into the following two parts:

$$
\begin{aligned}
E\{e(k) / \delta_p(k)=\delta_0\} &= \int_{-\delta_0-\pi}^{\pi} \xi \cdot f_0(\xi) \cdot d\xi + \int_{\pi}^{-\delta_0+\pi} \xi \cdot f_0(\xi-2\pi) \cdot d\xi \\
&= \int_{-\delta_0-\pi}^{\pi} \xi \cdot f_0(\xi) \cdot d\xi + \int_{-\pi}^{-\delta_0-\pi} (u+2\pi) \cdot f_0(u) \cdot du \\
&= \int_{-\pi}^{\pi} \xi \cdot f_0(\xi) \cdot d\xi + 2\pi \cdot \int_{-\pi}^{-\delta_0-\pi} f_0(u) \cdot du \\
&= 2\pi \cdot (F_0(-\delta_0-\pi) - F_0(-\pi)) = 2\pi \cdot F_0(-\delta_0-\pi) \\
&= 2\pi \cdot F_0(|\delta_0| - \pi)
\end{aligned}
\tag{22}
$$

2. The second case is given by: $0 < \delta_0 \leq \pi$. Here the following sequence of operations is valid:

$$
\begin{aligned}
E\{e(k) / \delta_p(k)=\delta_0\} &= \int_{-\delta_0-\pi}^{-\pi} \xi \cdot f_0(\xi+2\pi) \cdot d\xi + \int_{-\pi}^{-\delta_0+\pi} \xi \cdot f_0(\xi) \cdot d\xi \\
&= \int_{-\delta_0+\pi}^{\pi} (u-2\pi) \cdot f_0(u) \cdot du + \int_{-\pi}^{-\delta_0+\pi} \xi \cdot f_0(\xi) \cdot d\xi \\
&= \int_{-\pi}^{\pi} \xi \cdot f_0(\xi) \cdot d\xi - 2\pi \cdot \int_{-\delta_0+\pi}^{\pi} f_0(u) \cdot du \\
&= -2\pi \cdot (F_0(\pi) - F_0(\pi-\delta_0)) = -2\pi \cdot F_0(\delta_0-\pi)
\end{aligned}
\tag{23}
$$

Since $f_0(\xi) = f_0(-\xi)$ is an even density function symmetric around zero, the corresponding distribution $F_0(\xi)$ will show the following symmetry:

$$
F_0(-\xi) = 1 - F_0(\xi) \tag{24}
$$

From inspecting equations 22 and 23, respectively, we conclude that the conditional mean of the bias error is an odd function with respect to the nominal value δ_0:

$$
E\{e(k) / \delta_p(k) = -\delta_0\} = -E\{e(k) / \delta_p(k) = \delta_0\} \tag{25}
$$

1.2 Preliminary Observations

General observations:

Summarizing equations 22-25 we note that:

- The bias error and true value have opposite signs
- The bias is an odd function with respect to the true value
- Thus the estimate of the phase derivative computed from modulo-mapped phases will always be biased towards lower absolute values. The phase slope is always underestimated.

Limiting cases:

a) Maximum Phase Slope

Inspecting equations 22 and 23 we note that the bias error clearly depends on the value of the true phase slope. Knowing that:

$$\begin{aligned} F_0(\pi) &= 1 \\ F_0(0) &= 0.5 \\ F_0(-\pi) &= 0 \end{aligned} \tag{26}$$

we conclude from equations 23 and 25 that:

$$\begin{aligned} &E\{e(k) / \delta_p(k) = \pi\} = -2\pi \cdot (1 - F_0(0)) = -\pi \\ &and: \\ &E\{e(k) / \delta_p(k) = -\pi\} = \pi \end{aligned} \tag{27}$$

Thus phase slopes of $\delta_\varphi(k)$ = will always - even for good coherence - be estimated with the maximum possible bias error of -sign($\delta_\varphi(k)$)!

b) Ideal Case: Perfect Correlation

In this case we have:

$$f_0(\xi) = \delta(\xi) \qquad F_0(\xi) = \begin{cases} 1 & \xi > 0 \\ 0.5 \text{ if } & \xi = 0 \\ 0 & \xi < 0 \end{cases} \tag{28}$$

and using equations 22 and 23 we note that:

$$E\{e(k) / \delta_p(k) \in (-\pi, \pi)\} = 0 \tag{29}$$

c) Worst Case: No Correlation

In the zero correlation case we get a uniform distribution density $f_0(\xi) = \frac{1}{2\pi} \cdot rect\left[\frac{\xi}{2\pi}\right]$ and a ramp distribution:

$$F_0(\xi) = \begin{cases} 1 & \xi \geq \pi \\ \dfrac{\xi + \pi}{2\pi} \text{ if } & |\xi| < \pi \\ 0 & \xi \leq -\pi \end{cases} \tag{30}$$

and from equations 22 and 23 we get the final result:

$$E\{e(k) / \delta_p(k) = \delta_0\} = -\delta_0 \tag{31}$$

so that in this case the estimated phase slope will always be zero, which is quite remarkable.

1.3 The General Case - Numerical Results

From equations 22, 23 we conclude that knowing $F_0()$ is completely sufficient for determining the bias error. If we furthermore restrict us to the case of phase slopes between , we can utilize equation 17 and write:

$$\begin{aligned} F_0(\xi) &= \int_{-\pi}^{\xi} f_0(u)du = \int_{-\pi}^{\xi} f_{\bar{\delta}_e(k)}(u+2\pi)du + \int_{-\pi}^{\xi} f_{\bar{\delta}_e(k)}(u)du + \int_{-\pi}^{\xi} f_{\bar{\delta}_e(k)}(u-2\pi)du \\ &= \int_{+\pi}^{\xi+2\pi} f_{\bar{\delta}_e(k)}(u)du + \int_{-\pi}^{\xi} f_{\bar{\delta}_e(k)}(u)du + \int_{-3\pi}^{\xi-2\pi} f_{\bar{\delta}_e(k)}(u)du \\ &= F_{\bar{\delta}_e(k)}(\xi+2\pi) - F_{\bar{\delta}_e(k)}(\pi) + F_{\bar{\delta}_e(k)}(\xi) - F_{\bar{\delta}_e(k)}(-\pi) \\ &\quad + F_{\bar{\delta}_e(k)}(\xi-2\pi) - F_{\bar{\delta}_e(k)}(-3\pi) \\ &= F_{\bar{\delta}_e(k)}(\xi+2\pi) + F_{\bar{\delta}_e(k)}(\xi) + F_{\bar{\delta}_e(k)}(\xi-2\pi) - 1 \end{aligned} \tag{32}$$

where in the last equality we have only used the usual symmetry properties (cf. equ. 24). For convenience we will furtheron restrict ourselves to the case of positive slopes so that we can substitute equation 32 into equation 23 and write:

$$\begin{aligned} E\{e(k)/\delta_p(k)=\delta_0\} &= -2\pi \cdot F_0(\delta_0-\pi) \\ &= -2\pi \cdot \left[F_{\bar{\delta}_e(k)}(\delta_0+\pi) + F_{\bar{\delta}_e(k)}(\delta_0-\pi) + \underbrace{F_{\bar{\delta}_e(k)}(\delta_0-3\pi)}_{=0} - 1 \right] \\ &= -2\pi \cdot \left[F_{\bar{\delta}_e(k)}(\delta_0+\pi) - F_{\bar{\delta}_e(k)}(\pi-\delta_0) \right] = -2\pi \cdot \int_{\pi-\delta_0}^{\delta_0+\pi} f_{\bar{\delta}_e(k)}(\xi)d\xi \end{aligned} \tag{33}$$

The distribution density is periodic with respect to 4. This means that we can expand it in a Fourier series:

$$f_{\bar{\delta}_e(k)}(\xi) = \sum_{m=-\infty}^{\infty} d_m \exp\left[j\frac{m\cdot\xi}{2} \right] \tag{34}$$

Substituting equation 34 into 33 we readily obtain:

$$\begin{aligned} E\{e(k)/\delta_p(k)=\delta_0\} &= -2\pi \cdot \int_{\pi-\delta_0}^{\delta_0+\pi} \sum_{m=-\infty}^{\infty} d_m \exp\left[j\frac{m\cdot\xi}{2} \right] d\xi \\ &= -2\pi \cdot \sum_{m=-\infty}^{\infty} d_m \int_{\pi-\delta_0}^{\delta_0+\pi} \exp\left[j\frac{m\cdot\xi}{2} \right] d\xi \\ &= -4\pi \cdot \sum_{m=-\infty}^{\infty} d_m \frac{1}{m} \cdot \exp\left[j\frac{m\cdot\pi}{2} \right] 2\sin\left(\frac{m\cdot\delta_0}{2} \right) \\ &= -4\pi\delta_0 \cdot \sum_{m=-\infty}^{\infty} d_m \cdot j^m \cdot si\left(\frac{m\cdot\delta_0}{2} \right) \\ &= -4\pi\delta_0 \cdot \sum_{m=-\infty}^{\infty} d_{2m} \cdot (-1)^m \cdot si(m\cdot\delta_0) \end{aligned} \tag{35}$$

where the Fourier coefficients are given by:

$$d_m = \frac{1}{4\pi} \cdot \int_{-2\pi}^{2\pi} f_{\bar{\delta}_e(k)}(v) \cdot \exp\left[-j\frac{mv}{2}\right] dv \tag{36}$$

Since we do not want to solve the integral analytically we approximately calculate d_m by FFT-techniques by:

$$d_m \cong \frac{1}{N} \cdot \begin{cases} \Phi_{\bar{\delta}_e(k)}(m) & \text{for} \quad 0 \le m < \frac{N}{2} \\ \Phi_{\bar{\delta}_e(k)}(N-m) & \quad -\frac{N}{2} \le m \le -1 \end{cases}$$
$$\text{where:} \quad \Phi_{\bar{\delta}_e(k)}(m) = \sum_{n=0}^{N-1} f_{\bar{\delta}_e(k)}(n) \cdot \exp\left[-j2\pi\frac{nm}{N}\right] \tag{37}$$

$f_{\bar{\delta}_e(k)}(n)$ is the sampled continuous density $f_{\bar{\delta}_e(k)}(\xi)$ where:

$$f_{\bar{\delta}_e(k)}(n) = f_{\bar{\delta}_e(k)}(\xi_n = n \cdot \varphi_0)$$
$$\text{where:} \quad \varphi_0 = \frac{4\pi}{N} \text{ is the sampling interval} \tag{38}$$

The continuous density $f_{\bar{\delta}_e(k)}(\xi)$ is, as indicated by equation 6, the continuous correlation:

$$f_{\bar{\delta}_e(k)}(\xi) = f_{\epsilon_\varphi(k+1)}(-\xi) * f_{\epsilon_\varphi(k)}(\xi) \tag{39}$$

The discrete equivalent employing the sampled versions of the individual densities is given by:

$$f_{\bar{\delta}_e(k)}(n) = \frac{4\pi}{N} \cdot f_{\epsilon_\varphi(k+1)}(-n) * f_{\epsilon_\varphi(k)}(n) \tag{40}$$

Realizing this discrete convolution as a cyclic convolution we carry over to FFT-techniques by writing:

$$f_{\bar{\delta}_e(k)}(n) = \frac{4\pi}{N} \cdot \sum_{l=0}^{N-1} f_{\epsilon_\varphi(k+1)}(l) \cdot f_{\epsilon_\varphi(k)}(l+n) \tag{41}$$

The result of equation 41 can be easily obtained in the frequency domain by letting:

$$\Phi_{\bar{\delta}_e(k)}(m) = \frac{4\pi}{N} \cdot \Phi_{\epsilon_\varphi(k+1)}(m)^* \cdot \Phi_{\epsilon_\varphi(k)}(m) \tag{42}$$

where the Fourier transforms are calulated by::

$$\Phi_{\varepsilon_\varphi(k+1)}(m) = \sum_{n=0}^{N-1} f_{\varepsilon_\varphi(k+1)}(n) \cdot \exp\left[-j2\pi \frac{nm}{N}\right]$$
$$and:\tag{43}$$
$$\Phi_{\varepsilon_\varphi(k)}(m) = \sum_{n=0}^{N-1} f_{\varepsilon_\varphi(k)}(n) \cdot \exp\left[-j2\pi \frac{nm}{N}\right]$$

Then the rule for approximately evaluating the bias is:

$$E\left\{ e(k) / \delta_p(k) = \delta_0 \right\} \cong -4\pi\delta_0 \cdot \sum_{m=-\frac{N}{2}}^{\frac{N}{2}} \tilde{d}_m \cdot j^m \cdot si\left(\frac{m \cdot \delta_0}{2}\right)$$

$$\tilde{d}_m = 4\pi \cdot \begin{cases} \tilde{\Phi}_{\varepsilon_\varphi(k+1)}(m)^* \cdot \tilde{\Phi}_{\varepsilon_\varphi(k)}(m) & \text{for } 0 \le m < \frac{N}{2} \\ \tilde{\Phi}_{\varepsilon_\varphi(k+1)}(N-m)^* \cdot \tilde{\Phi}_{\varepsilon_\varphi(k)}(N-m) & -\frac{N}{2} \le m \le -1 \end{cases}$$

$$\tilde{\Phi}_{\varepsilon_\varphi(k+1)}(m) = \frac{1}{N} \cdot \sum_{n=0}^{N-1} f_{\varepsilon_\varphi(k+1)}(n) \cdot \exp\left[-j2\pi \frac{nm}{N}\right] \tag{44}$$
$$and:$$
$$\tilde{\Phi}_{\varepsilon_\varphi(k)}(m) = \frac{1}{N} \sum_{n=0}^{N-1} f_{\varepsilon_\varphi(k)}(n) \cdot \exp\left[-j2\pi \frac{nm}{N}\right]$$

$$0 \le \delta_0 \le \pi$$

Finally we obtain the solution for negative phase slopes by (equation 25):

$$E\left\{ e(k) / \delta_p(k) = -\delta_0 \right\} = -E\left\{ e(k) / \delta_p(k) = \delta_0 \right\} \tag{45}$$

Equations 44 and 45 provide the final result and form the basic framework for evaluating the bias error depending on the phase slope itself as well as on the form of the densities. These densities depend on the degree of coherence or on the SNR of the interferogram (the quality of the fringes). In the following we will give some quantitative results. We will assume identical distribution densities for two successive points. Figure 3 shows the wrapped phase error density for different coherence values.

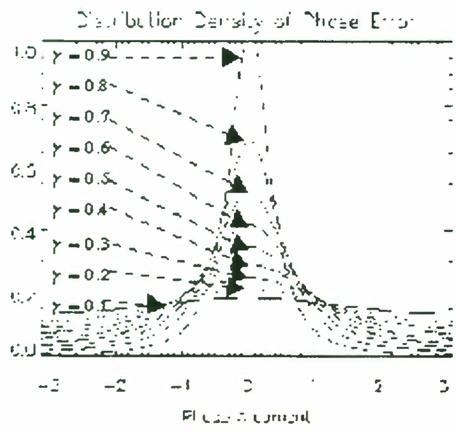

Figure 3: Distribution Density of the Phase Error

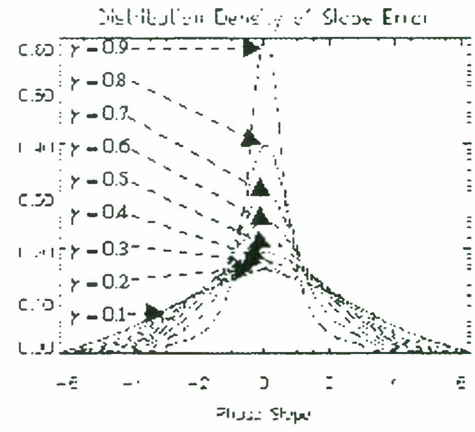

Figure 4: Distribution Density of the unwrapped Phase Slope Error

Figure 4 shows the distribution density of the unwrapped phase slope error for different degrees of coherence. Figure 5 shows the outcoming bias over the true phase slope evaluated for different degrees of coherence.

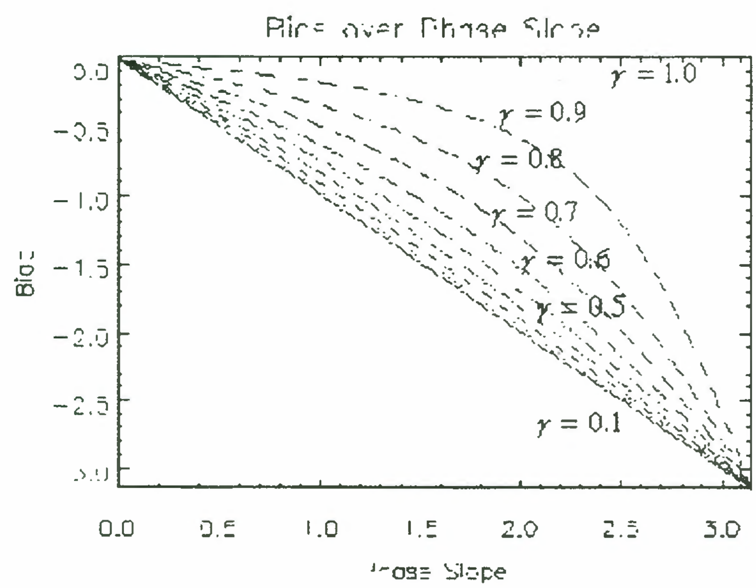

It is completely obvious that the maximum allowed phase slope that may be estimated with negligible bias strongly depends on the coherence. If the coherence is one, there is no phase slope bias as long as the phase slope is less than . The other extreme is a coherence of 0.1. In this case the slope bias is considerable even for small slopes.

Figure 5: Bias Error over Phase Slope

2.0 Approaches to solve or circumvent the problem

The following chapter will give a short overview about how to avoid or circumvent the problem of biased phase derivative estimates.

1. *Do not apply any filtering or averaging techniques to the phase slope!*

Any filter operation to remove the stochastic influences from the phase derivative will produce an estimate which is 'nearer' to the conditional mean, which is not identical with the true phase slope. On the other hand the simple branch/cut methods which do not apply any filtering to the phase slope estimates provide noisy but unbiased phase estimates. If any filtering is to be applied it should be applied to complex data rather than to the phases or phase slopes.

1. *Keep the phase slopes as small as possible by successive flattening techniques!*

Since the bias of the slope estimation clearly depends on the slope itself, one method to keep the bias small might be to keep the phase slope small. This can be achieved by successive flattening. The biased phase estimates obtained in the first run are utilized to 'demodulate' the complex interferogram. Then the residual phase slope is estimated again, this time with a smaller bias. The unambiguous phase is generated and used again to demodulate the interferogram. The whole loop is repeated until the bias has been reduced satisfactorily. Such a procedure (as reported in /For1 / clearly yields asymptotically unbiased phase estimates.

1. *Correct the systematic error by subtracting the phase slope bias!*

With the results given in equations 44 and 45 it should be possible to further utilize the phase slope estimator based on finite differences of wrapped phases and to eliminate the bias by simply subtracting it. This method would be advantageously applicable to homogeneous scenes with a sufficiently smooth coherence distribution, since then the densities would not have to be calculated and Fourier transformed for any individual pixel. In this case the additional computational burden would be moderate. The bias estimation of equations 44 and 45 would be the key to maintain Linear Least Squares phase unwrapping approaches.

1. *Do not calculate phase slopes by finite differences from modulo mapped phases!*

Clearly the best solution to a problem is an approach which prevents the problem from arising. This can be achieved by applying unbiased phase slope estimators. All these estimators share the common property that they operate on complex data rather than on the phases. Either they use real and imaginary part of the interferogram and exploit the argument of a complex correlation kernel (known from Madsen's Correlation Doppler Estimator, as proposed by /Bam1/) or they operate in the power spectral density domain (such as the Local Spectral Mode Estimator, proposed by /KrLo2, LoKr2/). Another approach would be to use a nonlinear estimator in form of an Extended Kalman Filter which does not explicitly differentiate any mapped phases (as proposed in /LoKr1, KrLo1/). Recently a combination of local slope estimation and Kalman filtering techniques has been proposed in /KrLo2, LoKr2/. This combination seems to be the most powerful approach to phase unwrapping, yielding unbiased and nearly perfectly noisefree unwrapped phases down to coherence values of 0.3 without any prefiltering!

Conclusions

The paper has presented the analysis, the derivation and evaluation of the estimation bias if the phase slope is determined form modulo-2 mapped phases. A finite series representation for the phase slope bias has been given, where the coefficients can be easily determined from the FFT spectrum of the distribution density of the wrapped phase error. This kind of distribution density is known for a lot of special cases even if 'multi-look' prefiltering is applied. Thus the technique is widely applicable. The numerical results calculated with the approach are in perfect agreement with the expectation. Finally some hints to circumvent or solve the problem were presented.

Acknowledgment

The work reported in the paper is an integral part of our activities on phase unwrapping in cooperation with DLR and has been funded by the DARA (project „Rapid", grant number 50 EE 9431) which is greatly appreciated.

References

Middleton, D., 1987:
Introduction to Statistical Communication Theory, Peninsula Publishing, Los Altos, pp. 396-410. (Mid1)

Loffeld, O., Krämer, R., 1994
'Phase Unwrapping for SAR Interferometry', Proc. IGARSS'94, Pasadena,, pp. 2282-2284, (LoKr1)

Krämer, R., Loffeld, O., 1996
'Phase Unwrapping for SAR Interferometry with Kalman Filters ', Proc. EUSAR'96, Königswinter, pp. 199-202, (KrLo1)

Krämer, R., Loffeld, O., 1996
'Local Slope Estimation in cooperation with Kalman Filtering Techniques', DLR Workshop on Phase Unwrapping, (KrLo2)

Loffeld, O., Krämer, R., 1996
'Local Slope Estimation and Kalman Filtering', PIERS'96 Symposium, Innsbruck, 1996 (LoKr2).

Bamler, R., Davidson, G., 1996
'The mystery of lost fringes in 2D-Least-Squares Phase Unwrapping', Piers'96, Symposium, Innsbruck, 1996. (Bam1)

Fornaro, G., Franceschetti, G. Lanari, R., Rossi,D., Tesauro, M., 1996
'Phase Unwrapping by using the Finite Element Method (FEM)', Piers'96, Symposium, Innsbruck, 1996. (For1)

An efficient time-frequency hybrid method for Phase Unwrapping

Gianfranco Fornaro,	Dipartimento di Ingegneria Elettronica,
Giorgio Franceschetti,	Universita' degli Studi di Napoli "Federico II",
Eugenio Sansosti,	via Claudio 21, I-80125 Napoli, Italy
Manlio Tesauro	francesc@irece1.irece.na.cnr.it
	http://diesun.die.unina.it/
Riccardo Lanari	IRECE-CNR, via Diocleziano 328, I-80124 Napoli, Italy
	lanari@irece1.irece.na.cnr.it
	http://www.area.na.cnr.it/istituti/franceschetti.html

Abstract

We present a weighted least-squares solution for phase unwrapping based on the combination of a time-domain and a frequency-domain approach. The former is applied to estimate the original phase gradient only in the unreliable (weighted) areas. The latter, based on the First Green's identity algorithm, is used for robust integration of the overall phase gradient. Presented experiments on real and simulated data validate the proposed algorithm.

Keywords: SAR Interferometry, phase unwrapping

Introduction

Synthetic Aperture Radar Interferometry (IFSAR) is a technique for the generation of high resolution digital elevation models (DEMs) (Q. Lin *et al.*, 1994). This result is achieved by exploiting the phase difference (*unwrapped phase*) of two SAR images of the same area related to two slightly different look angles. Unfortunately, it is only possible to evaluate the restriction of this phase difference to the base interval (*wrapped phase*). Since the altimetry of the observed scene is related to the unwrapped phase it is necessary an operation, usually referred to as phase unwrapping, that allows to retrieve the original phase starting from the wrapped one.

Phase unwrapping (PhU) techniques are usually based on two steps:

1. 1. estimation of the gradient of the unwrapped phase from wrapped data;

   2. integration of the computed gradient.

First step is generally carried out by computing the gradient of the unwrapped phase taking the principal value of the gradient of the measured data (Fornaro *et al.*, 1996a). However, in *critical areas* (i.e. layover and large noisy regions), this evaluation is incorrect (Lanari *et al.*, 1996).

A "global integration" operation can be carried out on the estimated gradient in order to limit the propagation of the errors due to the presence of the *critical areas*. This result is achieved by minimizing the distance between the estimated gradient and the desired true gradient of the unwrapped phase (Ghiglia *et al.*, 1994). Equivalent results can be obtained by applying the First Green's identity as discussed in (Fornaro *et al.*, 1996a) and in (Fornaro *et al.*, 1996c). This global integration operation can be implemented in the two-dimensional Fourier domain and achieve high computational efficiency by using Fast Fourier Transform (FFT) codes.

However, in the presence of large noisy zones or very critical layover situations even the use of global integration procedures can cause excessive errors. Therefore these critical areas must be excluded by introducing weighting functions (Ghiglia *et al.*, 1994).

This option needs iterations, thus increasing the required number of FFTs (Ghiglia *et al.*, 1994) if compared to the unweighted case. This shortcoming can be alleviated by implementing the iterative solutions via the Finite Difference (FD) method (Pritt, 1995) or the Finite Elements Method (FEM) (Fornaro *et al.*, 1996b) directly in time domain.

We present in this paper a new method for efficient weighted phase unwrapping based on the combination of a time-domain and frequency-domain approach.

The Algorithm

Iterative time-domain unweighted PhU procedures carry out the unwrapping operation by solving a sistem of linear equations. These approaches can be easly extended to the weighted case because this option simply requires to modify and/or exclude some equations (Ghiglia *et al.*, 1994) and (Fornaro *et al.*, 1996b).

Non-iterative frequency-domain algorithms are, for the unweighted case, more efficient than the iterative procedures because unwrapping operation is carried out via deconvolution implemented by using FFTs codes.

However the extention to the weighted case is, for the frequency-domain approaches, not trivial. In fact these algorithms need the knowledge of the unwrapped phase gradients everywhere, including the unreliable zones excluded by weights. This problem is solved by estimating the missing gradient components via iterations (on the overall domain), thus reducing the computational performance of the procedure (Ghiglia *et al.*, 1994).

We present a new PhU method particularly efficient if the weighted areas are relatively small and sufficiently sparse. The proposed algorithm is hybrid in the sense that combines an iterative time-domain approach with a noniterative frequency-domain one. In particular, we first apply the time-domain weighted FEM algorithm (Fornaro *et al.*, 1996b) to estimate the gradients in the unreliable regions (by solving the phase unwrapping problem only in a small area around the weighted regions) and then carry out the overall integration via First Green's identity based method (Fornaro *et al.*, 1996a).

A block scheme of the algorithm is sketched in Fig. 1.

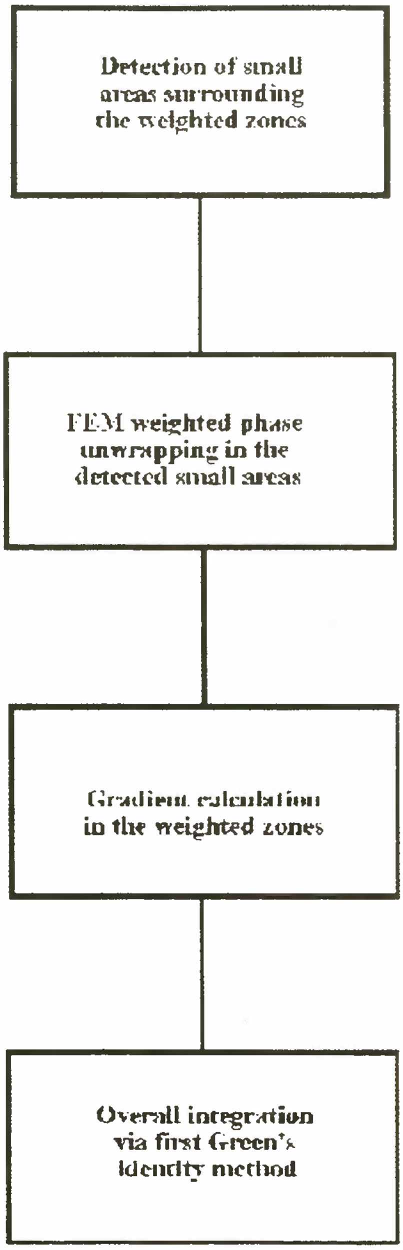

Figure 1: Block scheme of the proposed method

The first step is represented by the individuation of the small areas surrounding the weighted regions. A pictorial example of such localization is shown in Fig. 2 where the continuous lines represent the weighted regions.

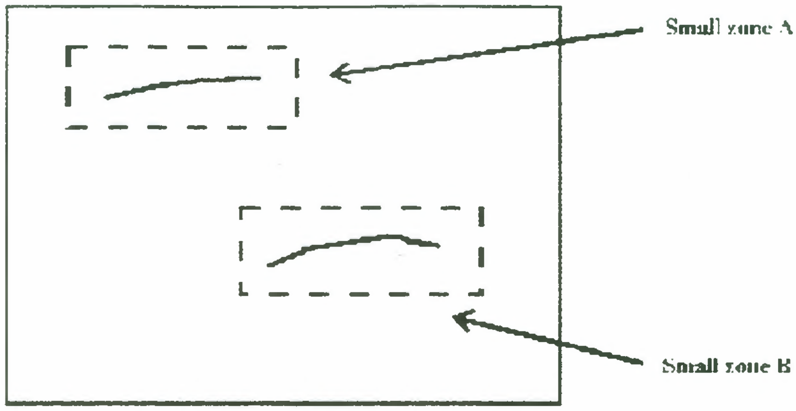

Figure 2: An example of individuation of small zones

Subsequently, a weighted unwrapping (via FEM) operation is carried out in the detected zones (Fornaro *et al.*, 1996b) and then the phase gradient components in the weighted areas are computed. Note that, since we need to compute only gradients, the different constants resulting from the unwrapping procedures applied in the different zones do not play any role.

Once we have evaluated the unknown gradient components in weighted areas, the overall unwrapped phase pattern is computed by applying the direct method discussed in (Fornaro *et al.*, 1996a).

As a final remark we want to stress that the algorithm performance is strongly dependent on two factors:

1. 1. the percentage of the weighted zones with respect to the overall area must be small;

   2. a proper selection of the shape of the zones surrounding the weighted areas is necessary in order to avoid an excessive increase of their dimensions.

With respect to the second point we underlines the capability of the FEM to be applied to non-rectangular data grids.

Experimental Results

In order to validate the proposed method, we present in this section experimental results carried out on simulated and real data.

The simulated phase pattern is shown in Figure 3. It represents a piramid of 128 by 128 pixels, with two ledges.

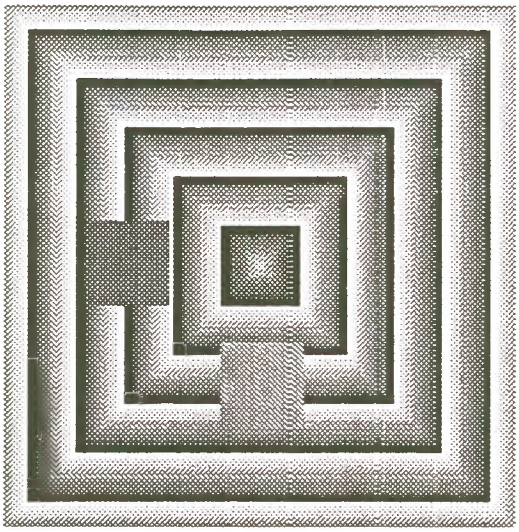

Figure 3: Interferogram of the simulated phase pattern

The weighting function used to unwrap the phase pattern of Figure 3 is shown in Figure 4 (weighted regions are in black).

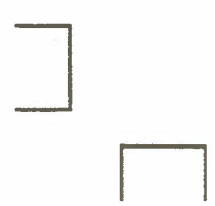

Figure 4: Weighting function for the simulated phase pattern

We present in Figure 5 a selected small zone wherein the gradient estimation operation via FEM procedure is carried out.

Figure 5: Small zone processed by FEM algorithm

The overall unwrapped phase is shown in Figure 6. The reconstruction operation required about 1:30 minutes of CPU on a IBM Risc machine.

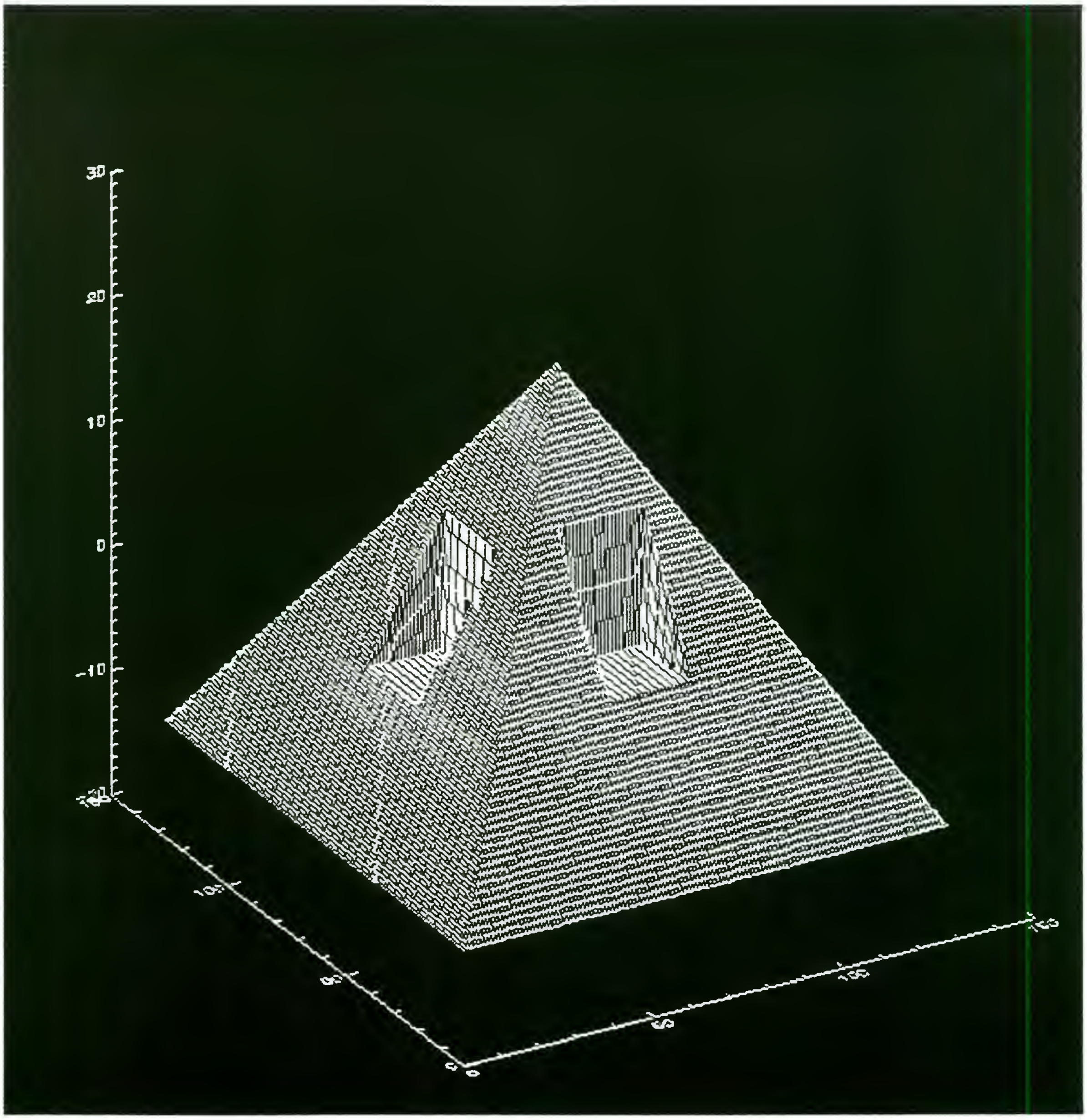

Figure 6: Unwrapped phase pattern

Let us consider the real interferogram relative to the Mt. Etna (Sicilia, Italia) test site (see Figure 7) illuminated by the sensors ERS-1 and ERS-2. Data dimensions are: 800 by 820 pixels.

Figure 7: Interferogram of Mt. Etna ERS1-ERS2 tandem mission

Figure 8 shows the wheighting function applied for the unwrapping operation.

Figure 8: Weighting function for the interferogram of Figure 7

Figure 9 is dedicated to the achieved uwwrapped phase pattern. This result was obtained in about 35 minutes of CPU.

Conclusions

A new method for weighted phase unwrapping, particularly efficient in the case of relatively small and sparse weighted areas, has been presented. It combines a time-domain FEM appproach used to estimate the unknown gradient components in the unrealiable (weighted) areas to a frequency-domain algorithm for robust integration of the overall phase gradient.

A number of experiments have been presented in order to validate the proposed method.

References

G. Fornaro, G. Franceschetti and R. Lanari, 1996a:
Interferometric SAR phase unwrapping using Green's formulation. *IEEE Trans. Geosci. Remote Sensing*, **34**, pp. 720-727.

G. Fornaro, G. Franceschetti, R. Lanari, D. Rossi and M. Tesauro, 1996b:
Interferometric SAR phase unwrapping via FEM method. *Proc. SPIE*, Taormina (Italy), 1996.

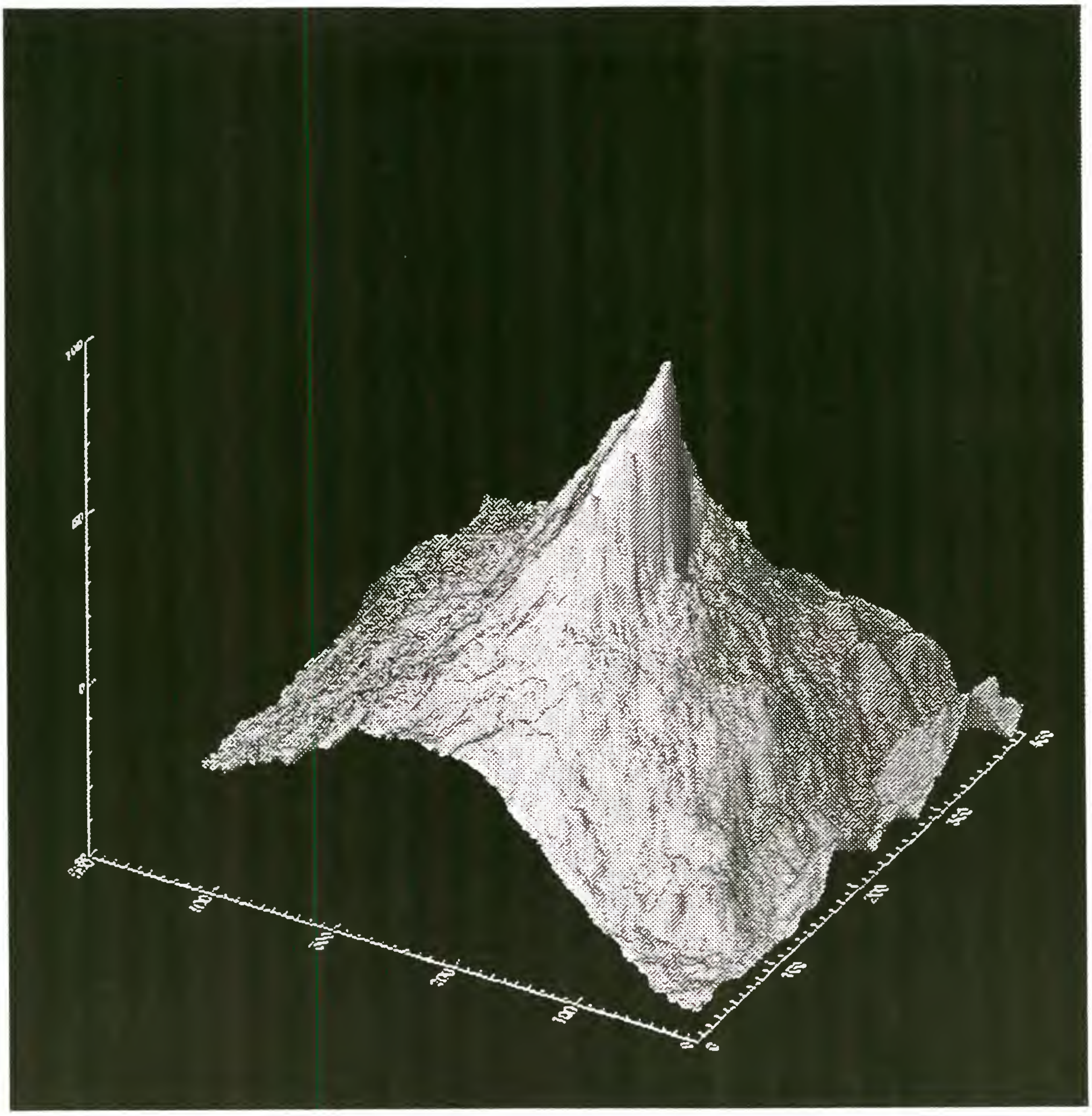

Figure 9: 3-D view of the unwrapped phase

G. Fornaro, G. Franceschetti, R. Lanari and E. Sansosti, 1996c:
A theoretical analysis on the robust phase unwrapping techniques. *Proc. IGARSS '96*, Lincoln, NE, pp. 2047-2049.

D.C. Ghiglia and L. R. Romero, 1994:
Robust two-dimensional weighted and unweighted phase unwrapping that uses fast transform and iterative methods. *J. Opt. Soc. Am. A*, **11**, pp. 107-117.

R. Lanari *et al.*, 1996:
Generation of Digital Elevation Models by using SIR-C/X-SAR multifrequency two-pass interferometry: the Etna case study. *IEEE Trans. Geosci. Remote Sensing*, **34**, September special issue.

Q. Lin, F. Vesecky and H.A. Zebker, 1994:
Comparison of elevation derived from INSAR data with DEM over large relief terrain. *Int. J. Remote Sensing*, **15**, pp. 1775-1990.

M. D. Pritt, 1995:
Weighted least squares phase unwrapping by means of multigrid techniques. *Proc. SPIE*, Vol. 2584, pp. 278-288.

Linear feature extraction from ERS SAR scenes using INSAR coherence maps

Olaf Hellwich Technical University Munich, Chair for Photogrammetry and Remote Sensing, 80290 Munich, Germany
olaf@photo.verm.tu-muenchen.de
http://www.photo.verm.tu-muenchen.de/staff/olaf

Abstract

A Bayesian approach to the extraction of linear features from SAR scenes is proposed. The SAR data evaluated are the intensity and the coherence from interferometric processing. Both are analysed using a rotating template. The results are combined in the likelihood function of Bayes' theorem. Prior knowledge about the continuity of thin curvilinear structures is formulated as a Markov random field. The object parameters are determined by an approximate maximum a posteriori estimate using simulated annealing or by local highest confidence first estimation.

Keywords: line extraction, Markov random fields, SAR, coherence data

Session 6

Validation

Chairman: G. Solaas

Cross-Compatibility of ERS-SLC Products

A. Barmettler, P. Pasquali, D. Small and D. Nüesch
Remote Sensing Laboratories (RSL)
University of Zürich, Winterthurerstrasse 190, CH-8057 Zürich, Switzerland
barmettler@rsl.geo.unizh.ch
http://www.geo.unizh.ch/rsl/

Abstract

The SAR image products (ERS-SLC) from the ERS AMI sensor are produced and distributed by various PAFs, such as CPRF, I-PAF and D-PAF. For high end applications that fully exploit the phase information of the coherent recording system (i.e. interferometric applications / DEM generation) the feasibility of combining products from different processing facilities is important. During this study, the level of cross-compatibility of SLCs was assessed by comparing interferograms and coherence maps which exploit combinations of pairs of SLCs. This included auto-interferograms from different processors. The conclusions is that the tested SLC products can be exchanged without a significant increase of the phase noise. Nevertheless, high precision measurements must take into account the systematic errors - phase offset and trend - introduced into the data.

Keywords - *SAR-Interferometry, Phase Noise, Image Quality, SLC, PAF*

Introduction

The user community has an interest in performing SAR Interferometry by using existing SLC (Single Look Complex) images, without having to take into account which PAF (Processing and Archiving Facility) produced them. The requirements for SLC images are described in the *ERS.SAR.SLC-I Product Specifications* (ESA Pub., 1995), where a number of tests are defined, e.g. to confirm the phase preservation during the processing. However, these tests do not ensure the cross-compatibility of the images processed by different SAR processors for high quality SAR interferometry, since they check mainly the quality of the azimuth compression algorithm rather than the overall performance of the processor.

The interferometric phase depends heavily on the surface structure. To be representative of as many applications as possible, the chosen test scenes included areas with a large variety of coherences. We used two different tandem scenes, acquired over Bern (Switzerland) and Cairo (Egypt), respectively. The Bern tandem data from 13/14 August 1995 covers agricultural, forest and urban areas as well as lakes: a mid to low level of coherence was observed in this area.

The Cairo scene comprises larger regions with rocks and dry areas to provide a completely different coherence distribution. The desert area south-west of Cairo showed high temporal coherence on the tandem 1-day repeat data from 19/20 November 1995.

The SLC images received from SAR processors used at CPRF (Central Processing Reference Facility, ESRIN) - ESA VMP (Verification Mode Processor) - and I-PAF (ASI) were analysed and their CEOS parameters and Doppler spectra compared. This was important for the interpretation of the interferograms and its statistics, which were processed subsequently from each pair of the SLC products. The InSAR processing was performed using our in-house developed interferometric SAR processor ISP and Zürich InSAR Processor (ZIP).

Doppler Centroid

The azimuth spectrum contains information about the Doppler shift, and its bandwidth is related to the spatial resolution in the azimuth direction. For the interpretation of the coherence map statistics the knowledge of the relative resolution between the SLC images is required.

Figure 1 presents the averaged total azimuth power spectra for the Cairo SLC. It is evident that ERS-1 and ERS-2 spectra have their maxima at a different Doppler frequency (i.e. the Doppler centroid frequency) due to different squint angles. In interferometric processing, one has to avoid relating the not common spectral parts by filtering. However, the systems have the same spectral shape and the same processed and even a corresponding half-power bandwidth of about 605 Hz (both, Cairo and Bern, 36% of the PRF of 1679.9 Hz). On the other hand, the values indicated for the processed Doppler bandwidth in the CEOS header differ significantly, probably using different definitions of the term "bandwidth".

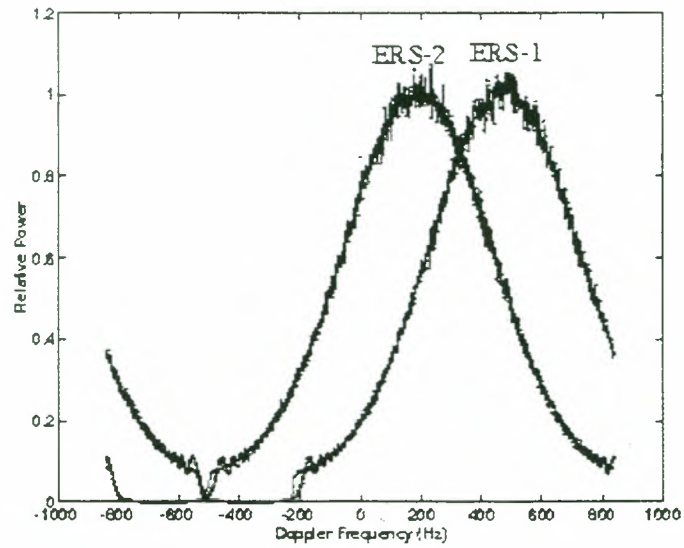

Figure 1: Relative azimuth power spectrum of ERS-1 (right) and ERS-2 for CPRF (solid line) and I-PAF (dot ted). Bern test site.

The Doppler centroid frequency (the frequency of the spectra's maximum) is a main driver for accurate azimuth focusing. Since it depends on the Earth's rotation and satellite yaw steering, it varies in slant range. This dependency is usually approximated by a polynomial of small degree. In Figure 2 the polynomials given in the header files are plotted and compared with the calculated average of the Doppler Centroid frequency for the ERS-2 SLC processed by RSL. All PAFs use polynomials of small degree to represent the range dependency of the Doppler Centroid frequency. The CEOS third order polynomials used by the CPRF and D-PAF show inconsistencies compared to our own estimation from raw data, whereas I-PAF represents an acceptable linear fit.

The Centroid shows a high dependence on the mean altitude above sea level. For ERS the azimuthal displacement is in the order of 100 m per 1000 m change in altitude, which corresponds to -30 Hz. Therefore it is important to use an algorithm that takes as many azimuth samples as possible into account to mitigate this topographic influence. If this is not the case, the Doppler Centroid is expected to show a significant dependence on azimuth position, and thus shows a high variability compared to the mean value of the Doppler Centroid over the whole scene.

If one estimates the Doppler Centroid by exploiting the final SLC product one finds a good representation of the polynomial used during focusing, as expected since the Doppler Centroid is projected into the data.

However, the polynomials used at CPRF and D-PAF show significantly different coefficients and the I-PAF even a different polynomial degree, hence the parameters or the software to estimate the Doppler centroid frequency must be different among these PAFs.

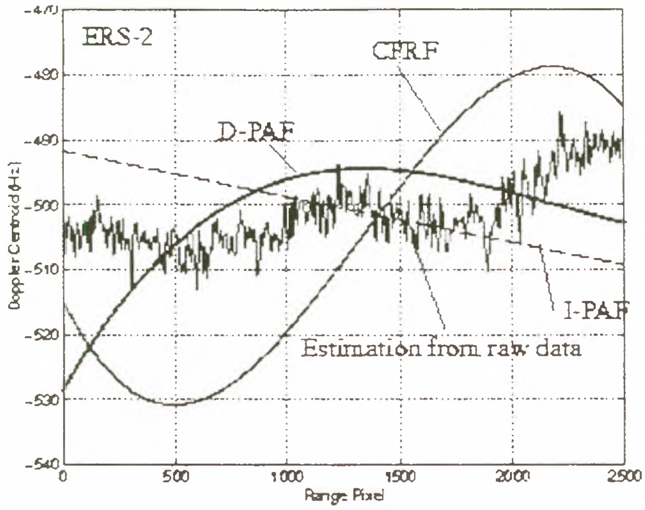

Figure 2: Doppler Centroid variation along slant range for ERS-2 from Cairo processed at the various PAFs. The polynomial coefficients are taken from the SLC CEOS leader files. Estimation is the 10 point average with an FFT size of 8192 samples.

Interferograms

More than a dozen interferograms were computed and analysed. To distinguish auto-interferograms and tandem interferograms, the terms *Singletrack* and *Multitrack* are introduced. *Singletrack* means that the identical original raw data from the sensor is processed at different PAFs and that these products are compared. *Multitrack* is the common tandem configuration of ERS-1 and ERS-2. ERS-1 is considered the master track within this report.

Singletrack

Singletrack interferograms provide a useful way to compare the SAR processors. To calculate the phase difference of the two images, a coregistration had to be performed. This resulted in a shift in range of none to several pixels, whereas the azimuth offset additionally showed a subpixel offset. The observed range offset must be explained by inaccurate time-referencing of the SAR processors. The azimuth shift of up to thousands of pixels is originated by the non-standardized starting time of the frames and differences in the sensor velocities used for focusing, together with inaccurate azimuth time-referencing.

The phase statistics of the coregistered auto-interferograms are compiled in Table 1. The value of the interferometric phase between SLC from the various PAF was almost constant but non-zero. According to the requirement of Phase Preservation of the SLC (ESA Pub., 1995), the zero phase of the azimuth filters are designated to the zero Doppler point in the time domain. Since the auto-interferograms act similar to the interferometric offset processing test proposed in (ESA Pub., 1995), we expected a mean phase of less than 0.1 degrees. The observed phase bias leads to the assumption that at least one of the tested SAR processors has problems with phase preservation. Most likely this is due to differences in the Doppler centroid estimation.

Cairo	Interferogram	Mean Phase Value (deg)	Std Dev Phase (deg)
ERS-1	CPRF / I-PAF	306.5	3.50
ERS-1	CPRF / D-PAF	189.1	3.04
ERS-2	CPRF / I-PAF	155.8	2.98
ERS-2	CPRF / D-PAF	10.3	3.21

Table 1: Singletrack interferogram of SLC products. Cairo site.

This observed variability of the mean interferometric phase implies that absolute phase measurement (besides the 2π ambiguity) is still not possible. However, each processor passes the requirement on the standard deviation of the interferometric phase. It lies below the limit of 5 degrees.

It was a surprise to observe that the CPRF and D-PAF processors do not show a smaller standard deviation, since both are assumed to use identical source code. Though, if the start time in azimuth is different between CPRF and D-PAF, the final products are not identical, and could show the observed variation on the same level as two different processors do. Therefore it is still possible that the processors have the same source code.

This random phase offset could be a problem when mosaicing full frame or quarter scene images: the phase continuity at the border would not be guaranteed.

In the following we tested for a systematic error in the phase, i.e. a dependency on range or azimuth position. Figure 3 reveals no phase trend in azimuth for the auto-interferograms. Moreover, the mean phase stays in the interval of 0.1 degrees.

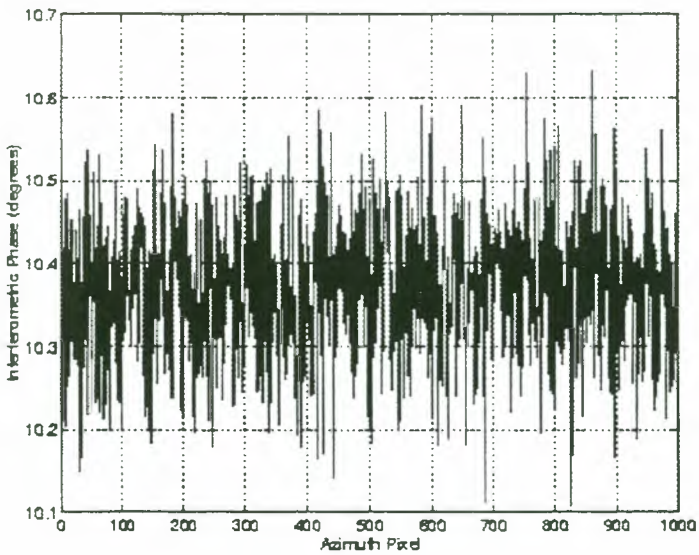

Figure 3: Interferometric phase variation along azimuth direction for the CPRF / D-PAF interferogram. ERS-2, Cairo area.

On the other hand, Figure 4 reveals a systematic phase trend in the range direction on the order of 0.6 degrees. This phase trend in range is most probably due to differences in the polynomial used to approximate the Doppler Centroid frequency as a function of range, and hence the Doppler Centroid estimation software.

We believe that it is less important that the Doppler Centroid estimation is a perfect representation of the physical Doppler Centroid frequency than that the various PAFs calculate the data using the same algorithm and polynomial order.

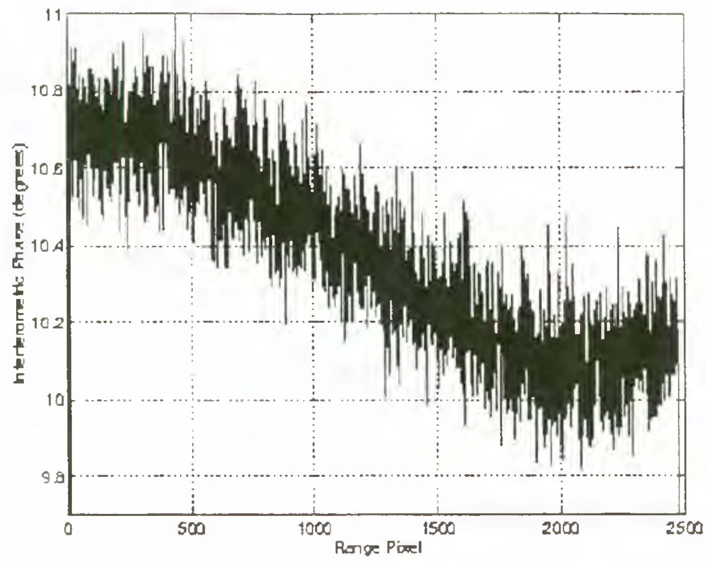

Figure 4: Interferometric phase variation along range direction for the CPRF / D-PAF interferogram. ERS-2, Cairo area.

Multitrack

The generation of the multitrack interferogram is the conventional task of producing a tandem interferogram. Figure 5 and 6 show the 2π fringes of the flattened interferogram. The resulting phase fringes have a periodicity equivalent to a change in height of about 150 m for the Bern interferogram and of about 40 m for Cairo.

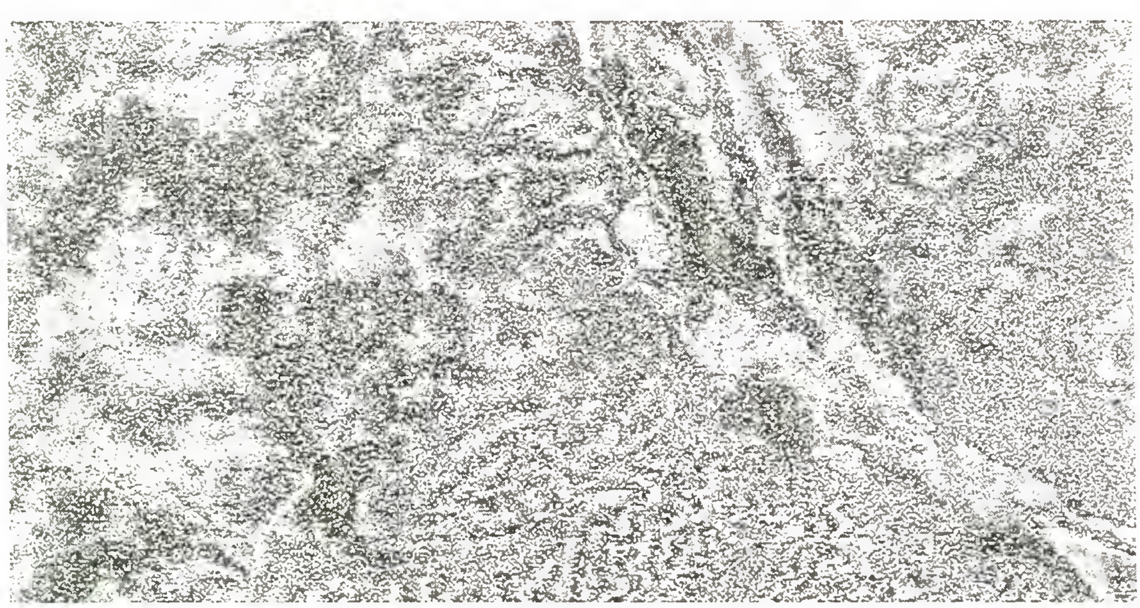

Figure 5: Flattened interferometric phase of ERS-1/ERS-2 for Bern. CPRF processing was used for both SLC.

The two interferograms confirm the choice of the two test sites: on the one hand there is the accurate and high-resolution interferogram from the flat and dry area around Cairo, which could be used for direct phase unwrapping without any further processing steps;

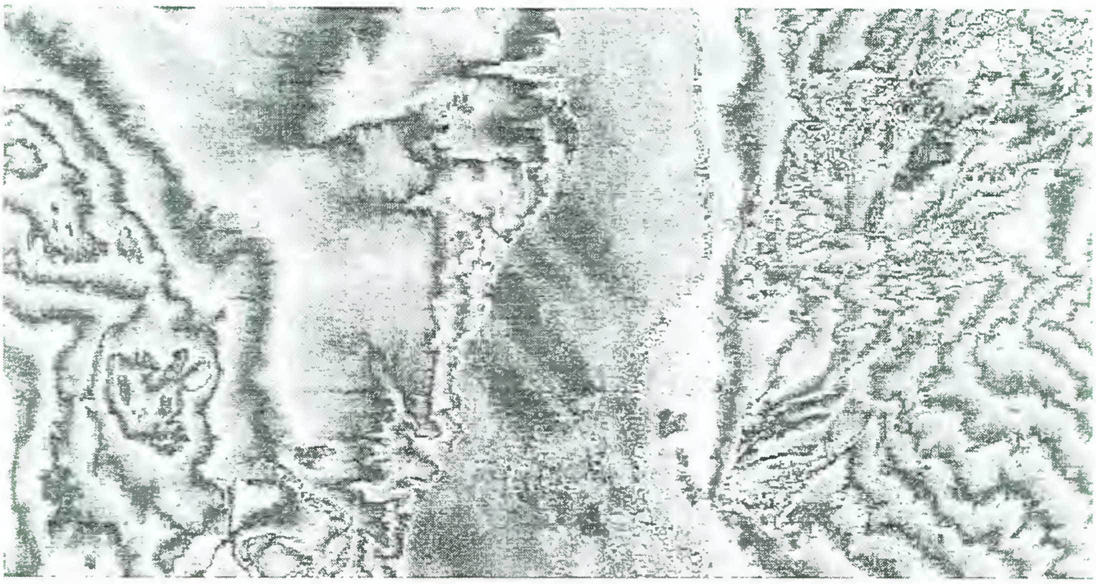

Figure 6: Flattened interferometric phase of ERS-1/ERS-2 for Cairo. CPRF. processing was used for both SLC.

on the other hand, the Bern interferogram appears noisy even in the one-day repeat tandem configuration and the rather short baseline. The production of a DEM would require numerous user interactions during the unwrapping task.

Coherence Maps

The coherence histograms and statistics are an indicator for the quality of the various processors. The processing of image pairs from the same raw data in particular reveals the relative phase differences introduced by the different processors.

Singletrack

Figure 7 shows the coherence that can be achieved when combining products from different SAR processors in the singletrack case. Notice how a difference, even if small, is present in the phase information provided by different focusing programs starting from the same raw data. The level of phase noise is directly related to the correlation coefficient (Bamler R. and Just D., 1993): the results presented in Figure 7 concerning the coherence distribution confirm the results seen in Table 1 in terms of phase noise.

In this case no systematic phase trends need to be considered as a source of coherence loss, since the estimation of the correlation coefficient is performed on relatively small subwindows. No temporal decorrelation effects are present in this combination: only image misregistration, differential defocusing and different processor noise levels are possible sources for this small loss of coherence.

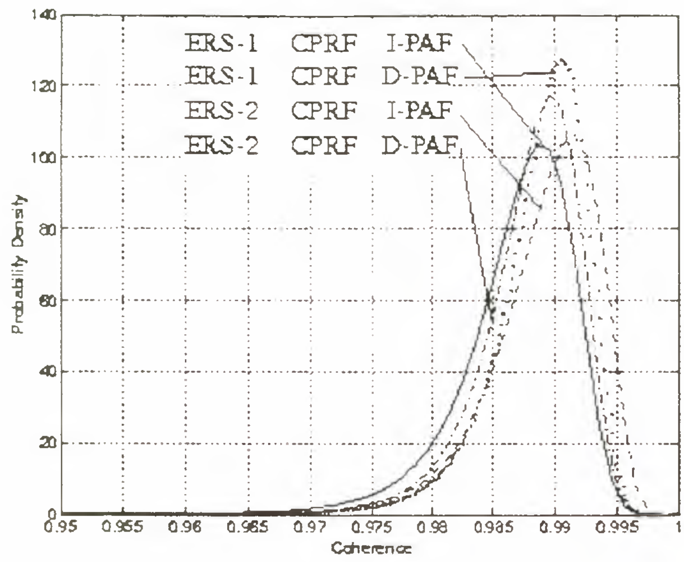

Figure 7: Coherence for Cairo images: solid ERS-1 CPRF / I-PAF; dotted ERS1 CPRF / D-PAF; dashed ERS-2 CPRF / I-PAF; dashdot ERS-2 CPRF / D-PAF.

Multitrack

The multitrack tandem coherence maps are also affected by the temporal decorrelation. The histograms in Figure 10 and 11 confirm again the choice of two completely different sites, by showing distinct distribution and maxima values.

Figure 8: Coherence map of the Bern test site. SLCs processed at CPRF. White represents high coherence

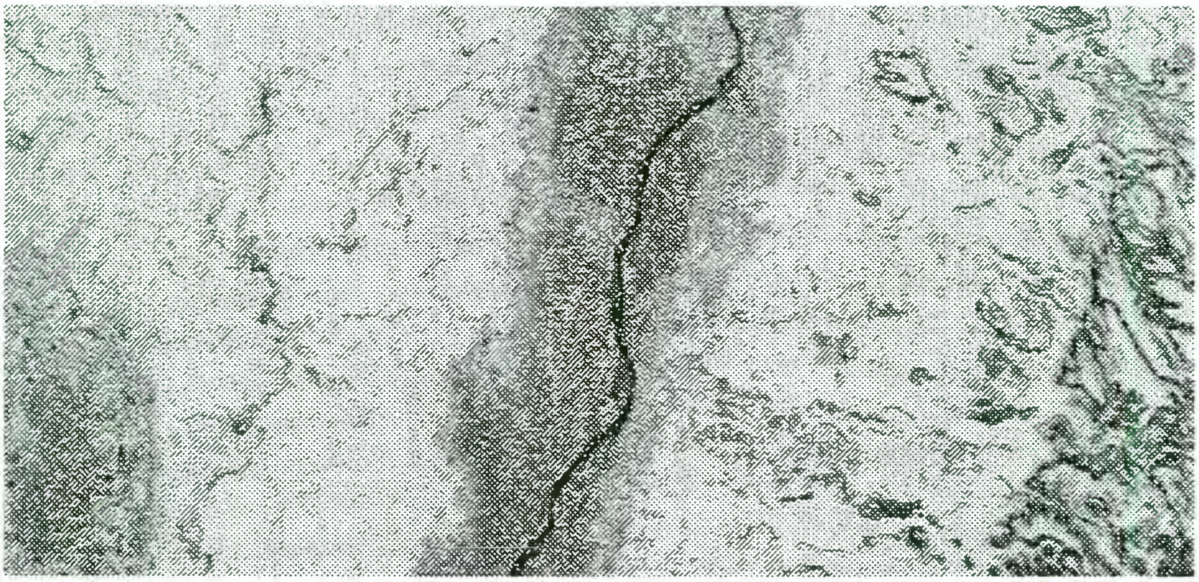

Figure 9: Coherence map of the Cairo test site. SLCs processed at CPRF. White represents high coherence

For the Bern site (Figure 10), all calculated interferograms show about the same probability distribution function. Very small differences in the estimated coherence values are noticeable only when analysing the numerical results. No reasons appear from this test to suggest that one must necessarily use SLC pairs focused by the same processor to produce interferometric images.

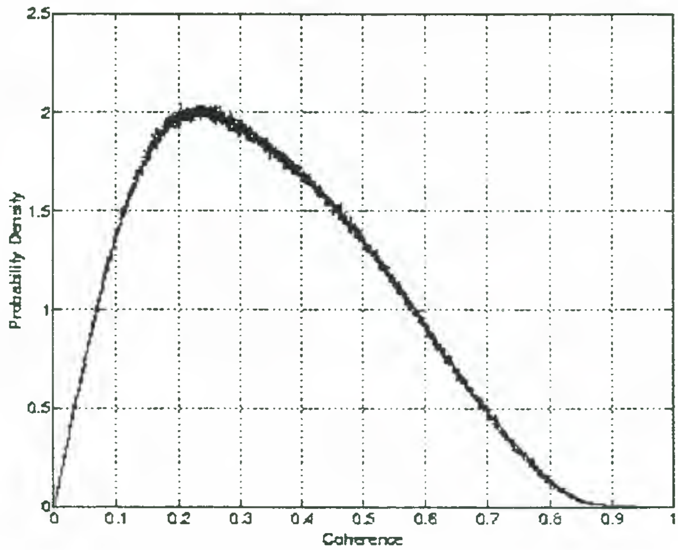

Figure 10: Coherence for ERS-1/ERS-2 Tandem images over Bern. Following combinations are used: I-PAF/CPRF, I-PAF/I-PAF, CPRF/CPRF, CPRF/I-PAF.

For the Cairo site (Figure 9) some differences can be noticed between the different coherence maps obtained from the various SLC combinations. Table 2 compiles the figures of statistics. The mean coherence of an interferogram produced using SLCs from different processors is not necessarily lower than that obtained from SLC produced by the same processor: on the contrary, the maximum value of coherence for this site was obtained by exploiting two data sets focused by different processors.

Cairo		Mean Coherence	Std Dev of Coherence
ERS-1	ERS-2		
CPRF	CPRF	0.6961	0.1526
CPRF	I-PAF	0.7025	0.1549
I-PAF	CPRF	0.6599	0.1445
I-PAF	I-PAF	0.6757	0.1476

Table 2: Coherence statistics for the tandem interferograms. Cairo site.

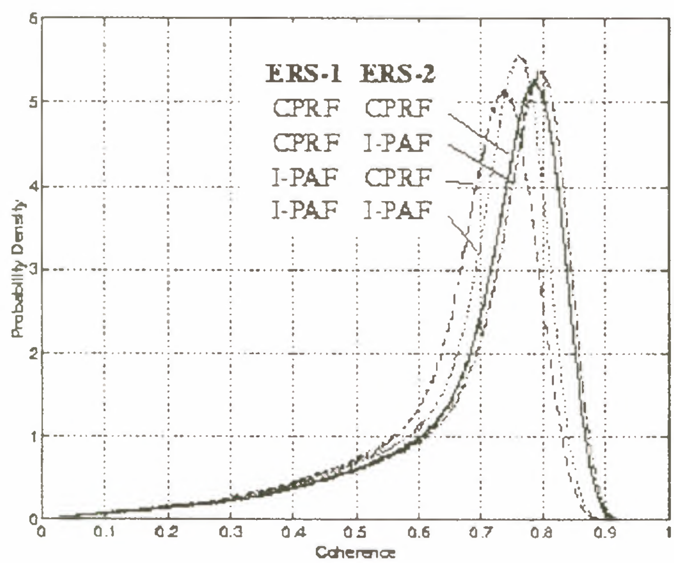

Figure 11: The coherence for ERS-1/ERS-2 Tandem images over Cairo. Starting from left: I-PAF/C-PAF (dashed), I-PAF/I-PAF (dotted), CPRF/CPRF (solid), CPRF/I-PAF (dash-dotted).

The observed coherence differences can be explained in terms of residual defocusing effects (Monti Guarnieri A., 1996), differences in the focusing algorithms and considering the normal variability of the phase noise introduced by every processor.

Conclusions

Although this study revealed some remarkable qualitative results, we could not perform further tests to get better statistics for quantitative data extraction. It should be kept in mind that only a small data set has been used within this analysis.

The investigated SLC image did not show any anomalies, i.e. sidelobe artefacts or saturated areas. However, the tested processors are not compatible with respect to the Doppler Centroid estimation. The values for this frequency deviates by as much as 50 Hz compared at one specific range distance. The Doppler Centroid frequency dependency on range is represented by polynomials of a degree not consistent among all PAFs. This uncertainty may be the source for a random phase offset introduced into the SLCs. In turn, this may lead to a phase inconsistency when stepping quarter scenes to full frames (or full frame images to larger mosaics), and makes reconstruction of the absolute phase of the interferometric products without the use of ground control points impossible.

Auto- and differential interferograms showed a phase trend in the range direction over a quarter scene swath, whereas the mean interferometric phase in the azimuth direction was observed to be constant. This phase trend is probably introduced by the SAR processors and leads to systematic errors in the reconstructed DEMs.

The influence of this trend is larger in interferometric applications with small baselines.

The product specifications (ESA Pub., 1995) point out that SLC-I products consist of a full frame. To date, most of the operational SAR processors (suitable for SAR interferometry) have only been capable of processing single quarter scenes at a time. Thus, for larger-scale interferometry, a full scene is assembled from four independently processed parts, with the possibility of introducing a phase inconsistency at the borders. Hence, the phase trends and discontinuity will become more severe when considering full frames.

Most important, the InSAR processing of SLC data from different PAFs did not increase phase noise. The user can combine SLCs from various PAFs for producing interferograms without a loss of the overall quality.

However, there are some secondary restrictions to the cross-compatibility: e.g. areas covered by the SLC are not standardized, especially the azimuth times. This may lead to a shift of up to 25% of the length of corresponding quarter scenes. The parameters included within the CEOS header are defined differently for each PAF (i.e. I-PAF and CPRF even indicate different wavelengths, pulse repetition frequencies, and spatial resolutions). Some of these data seem to be in disagreement with the image positions. ESA has announced its intention to harmonize the time-referencing of the processors and CEOS header format used at ESA PAFs.

Acknowledgement

This work emerged from an ESA contract study addressed to ESRIN, Rome. We like to thank ESA for the generous provision of the required ERS images.

References

Bamler R. and Just D., 1993
Phase Statistics and Decorrelation in SAR Interferograms, Proc. IGARSS `93, pp. 980-984.
Barmettler A., *et. al.*, 1996
Cross-Compatibility of ERS-SLC-I Products, Report to the ESA/ESRIN, RSL Zürich.
Cattabeni M., *et. al.*, 1994
Estimation and Improvement of Coherence in SAR Interferometry, Proc. IGARSS '94, pp. 720-722.
ESA Pub., 1995
ERS.SAR.SLC-I Product Specifications, ESA Doc., Issue 1.
Goodman N.R., 1963
Statistical Analysis Based on a Certain Multivariate Complex Gaussian Distribution, Ann. Math. Statist., Vol. 34, No. 152, pp. 152-180.
Monti Guarnieri A., 1996
Residual SAR Focusing: An Application to Coherence Improvement, in IEEE Trans. GRS, Vol. 34, No. 1, pp. 201-211.

On the Interferometric Coherence: A Multifrequency and Multitemporal Analysis

K.P. Papathanassiou DLR Oberpfaffenhofen, P.O. Box 1116, D-82230 Wessling, Germany
papathanassiou@dlr.de

A. Reigber DLR Oberpfaffenhofen, P.O. Box 1116, D-82230 Wessling, Germany
reigber@ohffo1.hf.op.dlr.de

M. Coltelli Instituto Internazionale di Vulcanologia, Piazza Roma 2, I-95123 Catania, Italy
colt@iiv.ct.cnr.it

Abstract

The potential of satellite repeat-pass SAR interferometry for mapping and monitoring of different natural surfaces is discussed here. The presented approaches are based on analysis of the interferometric coherence using SIR-C/X-SAR and ERS-1/ERS-2 tandem data from the Mt. Etna test site in Sicily, Italy. The evaluation of the frequency dependent coherence of several volcanic terrain types is used as a first order approach for classification. Parallel a second classification algorithm based on the temporal decorrelation behavior of different surfaces in only one frequency is addressed. The results of the algorithms are compared and discussed.
Keywords: SAR interferometry, coherence analysis, multitemporal classification, multifrequency classification

1. Introduction

The illumination of the same area with two antennas with slightly different look angles leads to the assumption that the statistical phase contribution due to the different speckle characteristic in the two received signals is about the same. Their phase difference is therefore deterministic and corresponds to the path difference of both signals. The interferometric coherence is defined as the normalized complex cross-correlation of both complex signals s_1 and s_2:

$$\boxed{\gamma = \frac{< s_1 s_2^* >}{\sqrt{< s_1 s_1^* >< s_2 s_2^* >}}}$$

where <...> means the expectation value and * is the complex conjugation operator. The absolute value of the interferometric coherence varies between 0 and 1. The coherence is a maximum if both signals are identical, and vanish if the signals do not correlate. Interferometric coherence depends primarily on:

- Baseline: the spatial separation of the two antennas has to be smaller than the critical effective baseline. The loss of coherence due to the non-overlapping parts of the range spectra can be avoided by applying range spectral filtering. [1] [2]
- Doppler centroid: the azimuth doppler spectra of the two passes must have sufficient overlap, i.e. the two surveys must see the scene under the same squint angle. Also here, the decorrelation due to the only partial overlap of the azimuth spectra can be filtered. [3] [4]
- Additive noise in either signal, processing artifacts and defocusing.

If the two signals are not received simultaneously (one-pass interferometry) but at different times during two repeating passes over the same area (repeat-pass interferometry) the following additional temporal decorrelation effects decrease the coherence:

- changing of the scattering geometry within the resolution cell during the time between the two aquisitions,
- changing of the physical properties of the scattering mechanisms during the time between the two aquisitions,
- changing of the behaviour of the propagation medium (atmospheric effects).

The amount of temporal decorrelation describes processes occurring on size scales of the signal wavelength with a time resolution defined by the repeat time interval (temporal baseline). The sensitivity of the coherence to changes in the characteristics of the scattering mechanisms in time can be used for the detection of a wide variety of surface processes and the corresponding surface types.

2. Data description and processing

For the presented investigations data aquired during the second SIR-C/X-SAR mission and ERS-1/ERS-2 tandem data of the Mt. Etna Sicily/Italy test site were used. This test site has been choosen because of the availability of good geological and topographic maps as well as an interferometric and photogrammetric DEM. The multifrequent SIR-C/X-SAR data sets were acquired on October 9 and 10, 1994 (data takes 141.1 and 157.1). The C- and L-band image pairs were processed by NASA/JPL in Pasadena, and the X-band image pair was processed by DLR/D-PAF in Oberpfaffenhofen. The multitemporal ERS-1/ERS-2 data sets were aquired on September 5-6 and on November 14-15, 1995 (frame 0747) and processed by DLR/NE-HF in Oberpfaffenhofen [5].

After spectral filtering in range and azimuth of the SLC images and coregistration we form the interferogram by multiplying the first image with the complex conjugate of the second image. The coherence images are evaluated using an average window with a size of 4 (range) by 5 (azimuth) pixels for the SIR-C/X-SAR data and of 4 by 12 pixels for the ERS-1/ERS-2 data. Because of this big average window the bias in the coherence estimation is small and has been neglected [6].. To avoid the influence of topography in the coherence estimation, we have extracted the topography related phase-gradient from the interferogram before the coherence estimation.

3. Multifrequency coherence analysis

Figure 3 shows the slant-range coherence maps of the Etna test site in the three frequencies, aquired with a time difference of one day between the pictures. White corresponds to a coherence of 1, and black corresponds to a coherence of 0.

3.1. Interpretation of the coherence maps

Lava flows around the volcano, where no or only pioneer vegetation is present, show a high temporal stability and have high coherence in all three frequencies. Very young lava on the eastern side of the volcano has a higher coherence in X-band than in C- and L-band. The reason for this effect could be the high scattering sensitivity of the short wavelength for the small scale roughness component, characteristic for young lava surfaces [7]. The high backscattered intensity in X-band increases the signal-to-noise ratio of the received signal and the resulting coherence values are therefore higher compared with the corresponding values in the C- and L- band coherence maps.

On the eastern side of the volcano a triangular feature having a very low coherence can be seen in the L-band coherence map below the three craters. This feature corresponds to an area covered with fresh volcanic fallout. The fact of volume scattering alone is not enough to justify such a high decorrelation, so it can be assumed that a change in the volume-scattering properties has occurred during the time between the two passes, e.g. a change in the volume moisture content. Unfortunately, it was not possible to get detailed information about weather conditions during the mission to verify this assumption.

We can also see that the forested areas around the volcano are dark in X- and C-bands and bright in L-band. The reason for this is that short wavelengths like X-band and C-band do not penetrate into the forest volume, and the backscattering from branches and leaves on the top of the trees is dominant. The movement of the tree branches produces a change in the scatterer geometry inside a resolution cell and therefore, a degradation in the coherence between the two interferometric images. In L-band the waves penetrate into the forest volume, and the backscattering is mainly due to double bounce and surface scattering. Therefore, the influence of the scatterer movement in the upper part of the trees is neglectible, and the coherence is high. The same is valid for agricultural areas around settlements. The settlements, however, have a high coherence in all three frequencies as expected.

3.2. Multifrequency classification

Based on the interpretation of the frequency dependent behavior of the interferometric coherence mentioned in the previous section a first-order classification algorithm is addressed. A schematic representation of this algorithm is shown in Figure 1. The starting frequency for the classification is X-band because this frequency shows a higher sensitivity in its interaction with different surface textures. Four different classes of surface, each having different coherence values and characterized by homogeneous geological and/or morphological properties, were detected:

- **Class A: Surfaces with a coherence below 0.40.** This class contains surfaces of high and dense vegetation such as the pine and oak forests and tree plantations around the volcano, but also a part of the fresh ash and scoria mantle that covers the upper region of Etna, in particular the scoria fallout deposit from the 1990's eruptions. In Figure 4a this class is indicated with dark green.
- **Class B: Surfaces with a coherence between 0.40 and 0.55.** This class represents surfaces with lower vegetation as bushes, meadows, grasses, and agricultural growings, and also the ash and scoria mantle with pioneer vegetation, most of the ash and scoria mantle without vegetation, and the summit craters of Etna with fumaroles, lateral scoria cones, and very old lava (>15.000 years) with intermittent ash cover. In Figure 4a this class is indicated with dark grey.
- **Class C: Surfaces with a coherence between 0.55 and 0.65.** This class includes historical lava flows with alterated surface, historical lava flows with pioneer vegetation, historical lava with ash cover, a few prehistorical lava, and buildings and other man-made structures. In Figure 4a this class is indicated with yellow.
- **Class D: Surfaces with a coherence between 0.65 and 1.0.** This class consists off historical lava flow with fresh surfaces (most of these are less than three centuries old) and a few prehistorical lava with fresh surfaces (less than 3000 years). In Figure 4a this class is indicated with orange.

A very good discrimination can be made in X-band between lava surfaces and the other surface types. Also the discrimination between high and low vegetation is very successful. However, the coherence behaviour of surfaces covered with fresh ash or fresh scoria and high vegetation, and the coherence behaviour of the older ash or scoria mantle and lower vegetation are too similar for discrimination with only one frequency. Further ambiguities are present in the differentiation of prehistorical and historical lava covered with ash and/or pioneer vegetation. For the elimination of these ambiguities it is necessary to extract information from the other two frequencies:

- The coherence difference between X- and C-band can be used for evaluation of the ambiguities of the different lava surface types. Lava surfaces covered with pioneer vegetation have a higher coherence in C-band than in X-band. On the other hand, lava without vegetation or ash cover and with very fresh surface has a higher coherence in X-band than in C-band. In this way it is possible to split the last two classes into new, thematic more restricted and homogeneous classes.
- The coherence difference between C- and L-band reaches a maximum for surfaces with vegetation due to the different scattering mechanisms of these two frequencies. Using the coherence difference between C- and L-band, a separation of surfaces with vegetation from surfaces covered with ash and scoria can be made.

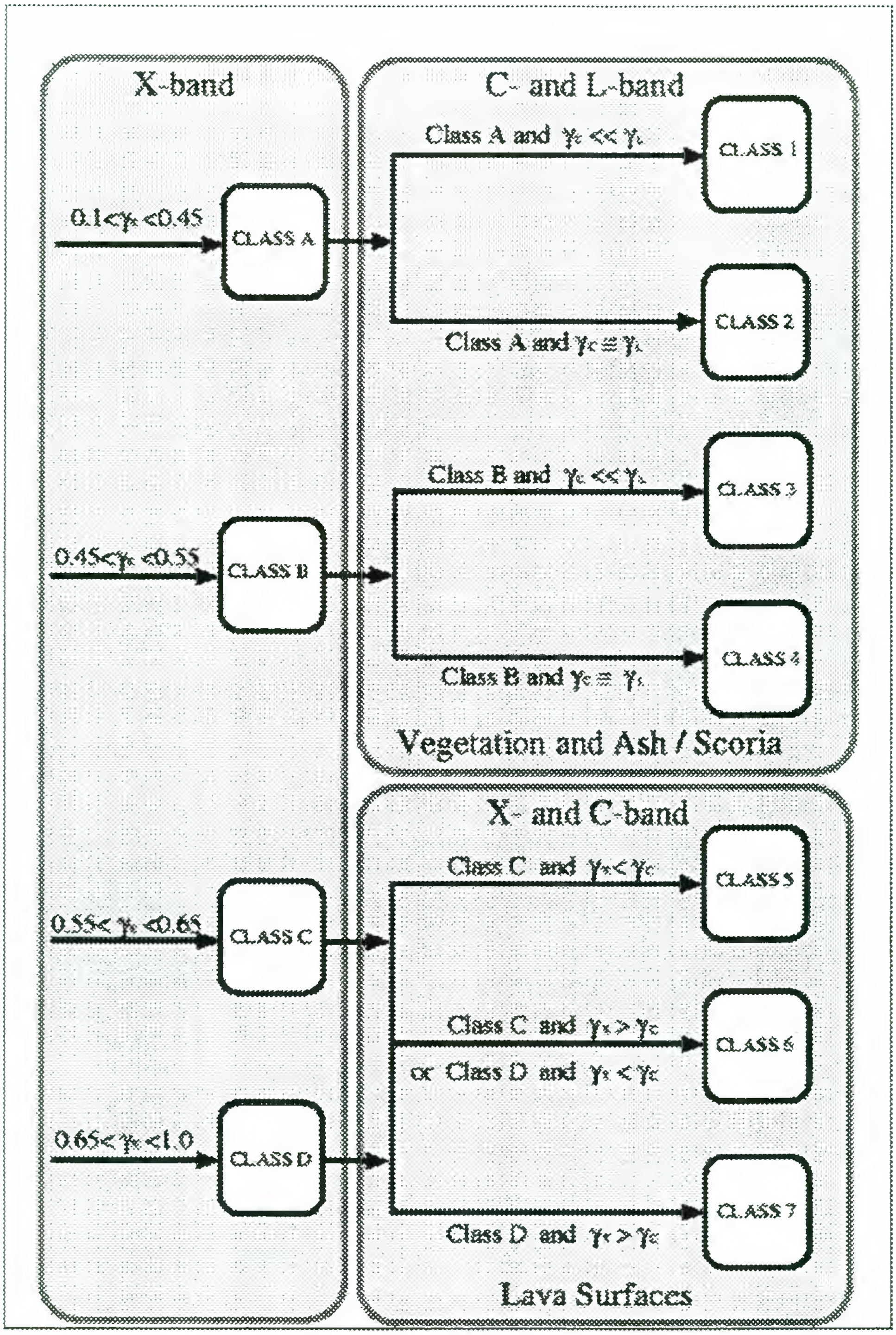

Figure 1: Multifrequency coherence classification algorithm scheme.

The result of classifying the coherence differences in the three frequencies is given in the following seven classes:

- **Class 1: Surfaces with a coherence below 0.40 in X-band and with a high coherence difference between C- and L-band.** This class contains now mainly surfaces of high and dense vegetation. The small part of the ash and scoria fallout deposit of the 1990's eruptions of Etna that is included in this class can by considered as an error due to the low coherence of L-band in this region. In Figure 4b this class is indicated with dark green.
- **Class 2: Surfaces with a coherence between 0.10 and 0.40 in X-band and with a low coherence difference between C- and L-band.** This class consists off the majority of the ash and scoria fallout of the 1990's eruptions, and a part of the summit craters with fumaroles. In Figure 4b this class is indicated with pale grey.

- **Class 3:Surfaces with a coherence between 0.40 and 0.55 in X-band and with a high coherence difference between C- and L-band.** This class includes mainly surfaces with lower vegetation, and agricultural areas, as well as parts of the old ash and scoria mantle covered with pioneer vegetation. This class is indicated with pale green.
- **Class 4: Surfaces with a coherence between 0.40 and 0.55 in X-band and with a low coherence difference between C- and L-band.** This class contains the majority of the ash and scoria mantle without vegetation, lateral scoria cones, and very old lava with intermittend ash cover. In Figure 4b this class is indicated with dark grey.
- **Class 5: Surfaces with a coherence between 0.55 and 0.65 in X-band and with a lower coherence in X-band than in C-band.** This class includes historical lava flow with alterated surface and historical lava flow with ash and/or pioneer vegetation cover. This class is indicated with yellow.
- **Class 6: Surfaces with a coherence between 0.55 and 0.65 in X-band and a higher coherence in X-band than in C-band, or with a coherence between 0.65 and 1.0 in X-band and a lower coherence in X-band than in C-band.** In this class are mainly historical lava flows and a few prehistorical lava with fresh surfaces. In Figure 4b this class is indicated with orange.
- **Class 7: Surfaces with a coherence between 0.65 and 1.0 in X-band and with a higher coherence in X-band than in C-band.** In this class we find only very young lava flows. In Figure 4b this class is indicated with red.

3.3. Error analysis

In order to provide a quality assessment of the classification algorithm it is appropriate to measure quantitatively how good the classification results matches the volcanic terrain. A way to accomplish this is to compare the classification results to the available geological maps. This caused some problems due to the different scales and thematic contents in coherence and geological maps.

Class 2 falls within the 5 January 1990 scoria fall deposit typology, and the classification error is about 10% mainly due to the large dark green triangle in Fig. 3 located SW of the summit craters, which, due to the presence of sparse vegetation, coming out from the scoria deposit, belongs to class 1.

With regard to class 4, we note that the expected typologies are the summit and adventive pyroclastics cones and the older lava, depending on the amount of ageing of the different areas. The classification error is about 12%, because in the lower regions this kind of typology is covered by vegetation and frequently falls into classes 1 and 3.

Since classes 5 and 6 corresponds to the same typology of historical lava flows, only a overall performance analysis can be accomplished. The classification error is around 10%. Several historical lava flows, expected in class 5, are classified in the class 4 due to growth of the vegetation (in particular on the lower flanks of the volcano).

For the classes 1 and 3, including the vegetated areas, it was not possible to find accurate and actual botanic maps of the area to check the accuracy of the separation. Analysis based on selected areas show that the classification error between high and dense and sparce vegetation is around 20%. On the other hand the separation between vegetated and unvegetated surfaces is very high (>95%).

4. Multitemporal coherence analysis

In order to reduce the statistical errors in the coherence estimation and the influence of occasionally local effects we have calculated a mean value between the two one-day maps from the September and November data, and also from the ERS-1/ERS-1 and the ERS-2/ERS-2 constellation with 70 days time difference. Figure 5 shows the resulting two slant-range coherence maps.

Due to the very montainous region with terrain heights between 0 and 3400 meters and the very steep sensor look angle of 22 degrees the coherence maps show strong geometrical deformations, especially on the western side of the volcano. Locally very high slopes are causing either layover areas or are distorting the picture so strong that it is not possible to recognize the features of the coherence map. It is very complicated to make any prediction there. In the following we therefore concentrate only on the eastern side of the volcano.

4.1 Interpretation of the coherence maps

In an elliptic region around the top the coherence is very low in the tandem pair from November and also in both 70-days pairs. The snow line on Etna at the november, 15th 1995 was around 2400m, which corresponds very well with the observed low coherent area. The low coherence in this area does not allow a further classification.

The young and uncovered lava flows around the volcano show a very high coherence in the 1-day and also in the 70-days map. As it could be expected, the temporal stability is very high on this rocky ground. All other surfaces show an essentially higher decorrelation in time. Older lava fields, which are already covered with pioneer vegetation or with some sporadic bushes, show a decrease in the coherence, but even after 70 days they are clearly visible in the coherence map. The highly correlated backscattering from the bare lava surfaces between the vegetation causes this high long-time coherence. Also the settlements and other man-made structures show this kind of stability. The denser vegetation of various height which grows on old, earthy ground, is totally uncorrelated after 70 days and appears black in the correspondig map. But in this regions the short-time coherence allows a separation of the different land covers. High and dense vegetation like forests show a very low coherence even in the 1-day map, mostly because of the movements of the leaves and branches. Lower vegetation is more correlated, especially meadows and harvested agricultural fields have a very high coherence which produces ambiguities with lava surfaces if one only looks at the 1-day coherence.

4.2. Multitemporal classification

Based on the interpretation of the time dependent decay of the coherence in only one band as mentioned in the previous section, a first order classification algorithm has been developed. The snow-covered area around the top has been masked out by hand. A schematic representation of this algorithm is shown in Figure 2. We started with the 70-days coherence map with the intention to extract all lava and man-made surfaces. We are able to detect the following homogenous surfaces:

- **Class A: Surfaces with a long-time coherence over 0.70.** This class contains all the historical and some of the prehistorical lava flows with fresh surfaces.
- **Class B: Surfaces with a long-time coherence between 0.40 and 0.70.** This class contains mainly old lavaflows in lower regions which are again sporadic vegetated with bushes and other low vegetation. We also find settlements and other man-made structures in this class.
- **Class C: Surfaces with a long-time coherence below 0.40.** In this class we find all surfaces which are completly covered with vegetation of different height.

With the long-time coherence a very good discrimination can be made between mostly uncovered areas with rocky ground and surfaces with vegetation. Also the discrimination between fresh lava surfaces and older, slightly vegetated lava is sucessfull. All the completely vegetated surfaces appear decorrelated in the long-time coherence. To classify these areas it is possible to use the short-time coherence. The lava surfaces are already separated so no ambiguities between lava and other high coherent areas can occur. The result of this classification is shown in Figure 6

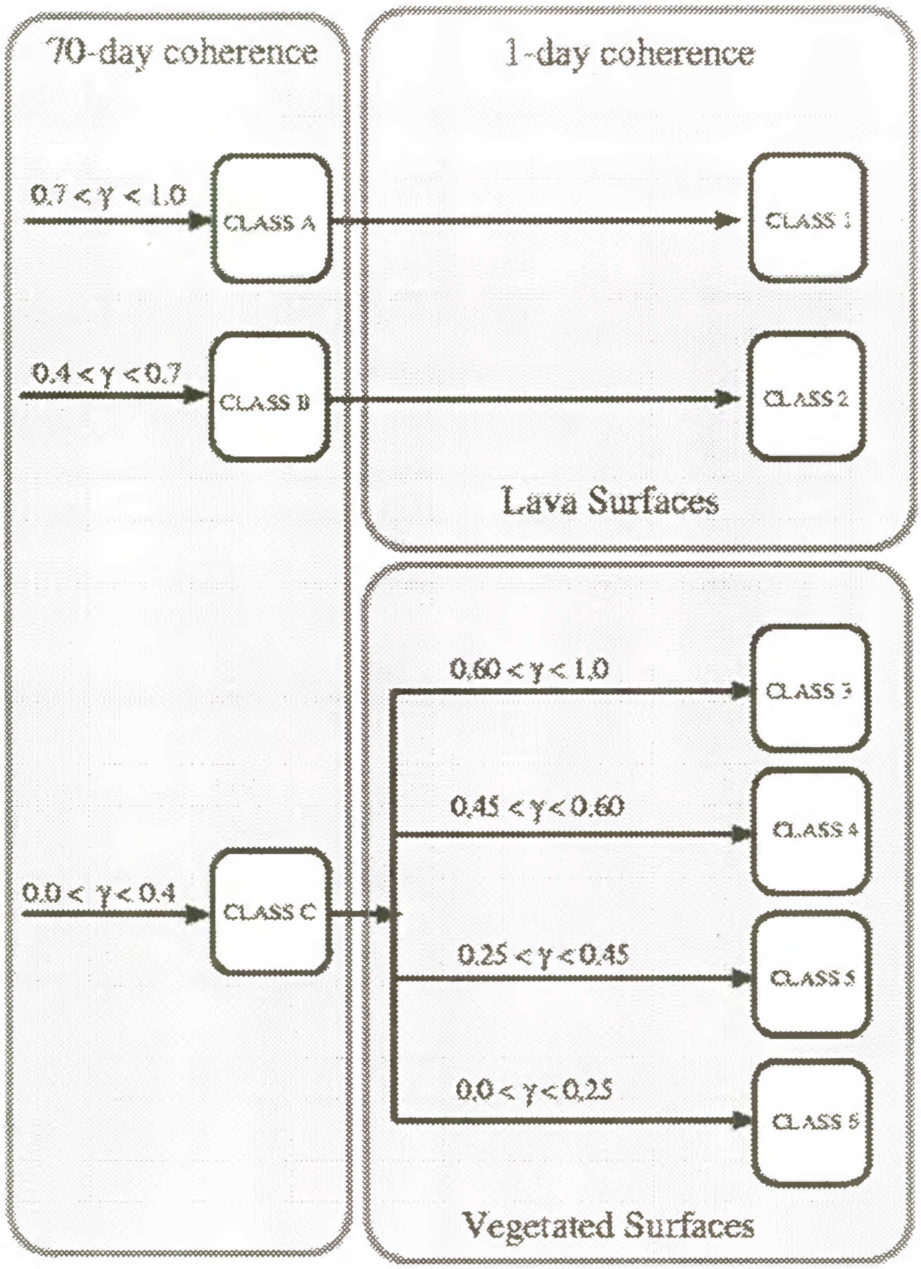

Figure 2: Multitemporal coherence classification algorithm scheme.

With this method we were able to detect following six different classes:

- **Class 1: Surfaces with a 70-days coherence over 0.70.** This class, in Figure 6 shown in yellow, remains the same as before. It contains all the historical and some of the prehistorical lava flows with fresh surfaces.
- **Class 2: Surfaces with a 70-days coherence between 0.40 and 0.70.** Also this class remains the same as before and contains mainly old lavaflows which are sporadically vegetated and man-made structures. This class is indicated with purple.
- **Class 3: Surfaces with low long-time coherence and a 1-day coherence over 0.60.** In this class we find low meadows, actually unvegetated cultivated areas and other surfaces with very low vegetation and is indicated with pale green in figure 6.
- **Class 4: Surfaces with low long-time coherence and a 1-day coherence between 0.45 and 0.60.** This class shown in green consists of lower vegetation like bushes and vineyards as well as ash and scoria mantle without vegetation. This class is indicated with green

- **Class 5: Surfaces with low long-time coherence and a 1-day coherence between 0.25 and 0.45.** This class contains mainly surfaces with high and dense vegetation, like pine and oak forest and is shown in dark green in figure 6
- **Class 6: Surfaces with low long-time coherence and a 1-day coherence below 0.25.** This class contains only the water of the mediterraniean sea, which appears fully decorrelated. In the case of presence of very dense forest a misclassification of the forest into this class could happen. This class is indicated with blue

4.2. Error analysis

Like in section 3.3 we compared the obtained results with the geological and also with the topographic map. Geometrical errors in the coherence maps and the low information about the vegetation complicated the error analysis in some cases.

Class 1 corresponds very well to the historical lava flows around the volcano. The classification error is about 15%, mainly due to high regions which are partly covered with fresh ash or pyroclastic material. In this case a misclassification into class 2 could happen. Except for this case, the recognition of lava with sporadic vegetation is very successful. The error in the separation of this kind of vegetation from other vegetated surfaces is around 7%. The completely ash covered lava in the higher regions which also appear in class 4 show an error of about 10%, mostly because partly covered lava sometimes shows also a fast decorrelation.

For the classes 3,4 and 5, which include the dense vegetation on earthy ground, it was not possible to find actual and accurate enough botanic maps of the area to check the accuracy of the separation. Analysis based on selected areas show that the classification error between high and dense and lower vegetation is around 15%. The error in the separation of lower vegetation and meadows and bare soil is around 20%. In any case it is not easy to divide some vegetation types into a special class.

5. Conclusions

As the obtained results show, the INSAR coherence can be used as a potential tool for the classification of different natural surfaces. The advantage of the coherence classification is the high sensitivity in the detection of temporal changes. The main problem is to relate the detected changes with a certain surface type or scattering mechanism. This relation is not in any case unambiguous because the same amount of change can be the result of different change processes. From this point of view a priori information can increase drastically the accuracy of the classification results.

The separation of vegetated areas from non-vegetated areas could be done very accurate with a short wavelength like X- or C- band and a temporal offset of one day. For further information it is very useful to use either several frequencies or multiple temporal offsets.

The multifrequency classification shows a high sensibility on unvegetated surfaces, because the different wavelengths offer the possibility to detect changing processes occuring on different orders of magnitude. Also the different penetration capabilities of the frequencies allow a better localisation and interpretation of the changing mechanisms.

In contrast the multitemporal approach is more successful in the separation of different vegetated surfaces. It takes advantage of the different time scales in the change processes of the vegetation, which can be well obsereved with a short wavelenght. To get more instructive informations it would be helpful to observe better distributed temporal offsets than the tandem data could provide.

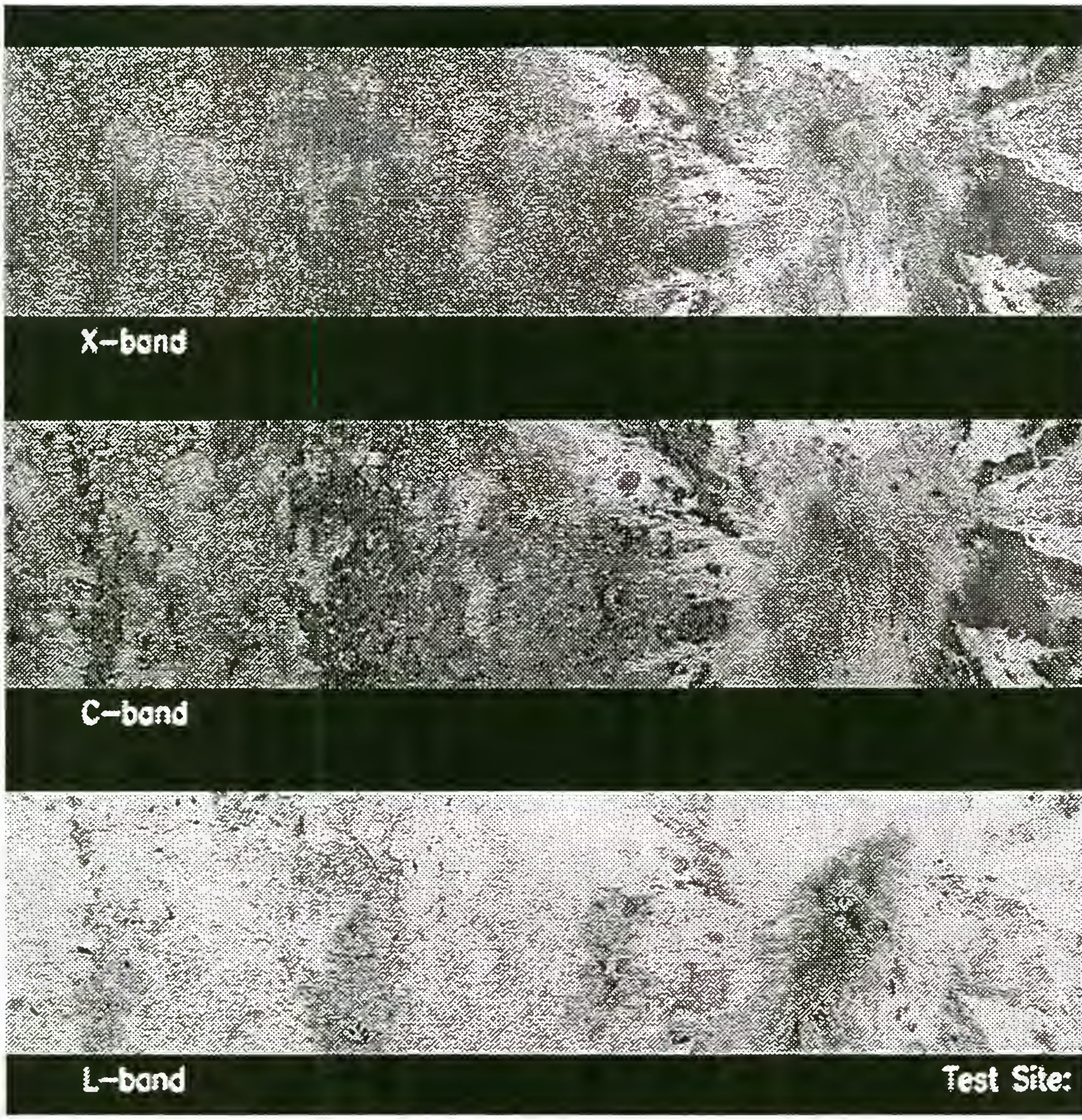

Figure 3: Coherence maps of the Mt. Etna area in the three frequencies: X- (left), C- (middle

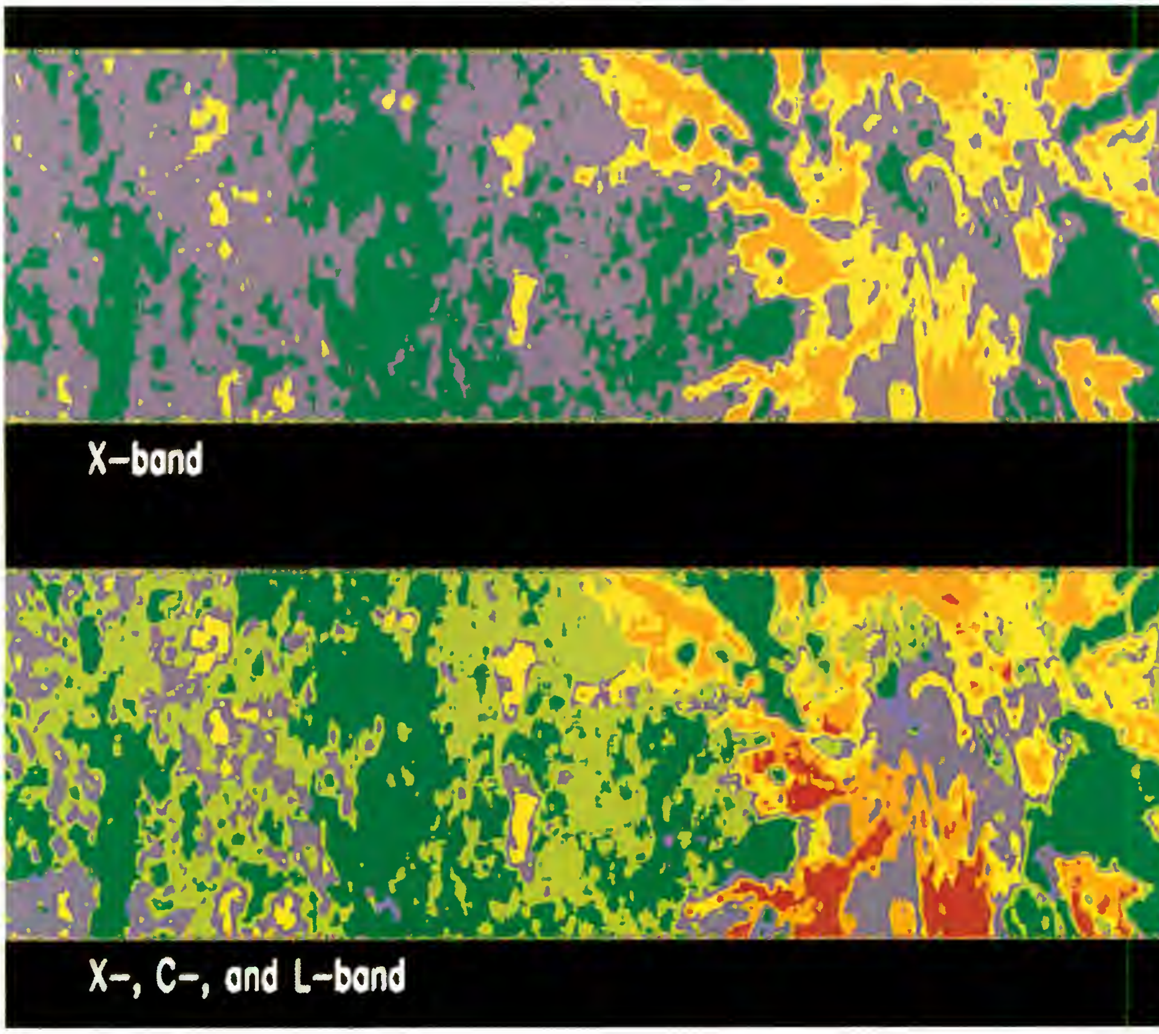

Figure 4: Coherence interpretation maps. Left: 4 classes interpretation based only on X-band. Right: 7 class[illegible] L-band

References

[1] C. Prati, F. Rocca,
"Use of the Spectral Shift in SAR Interferometry", Proc. of the First ERS-1 Symposium, Cannes, pp. 691-696, November 1993.

[2] F. Gatelli, A. Monti-Guarnieri, F. Pasquali, C. Prati, F. Rocca,
"The Wavenumber Shift in SAR Interferometry", *IEEE Trans. on Geoscience and Remote Sensing, Vol. 32, No. 4, pp. 855-863, Juli 1994.*

[3] C. Prati, F. Rocca,
"Focusing SAR Data with Time-Varying Doppler Centroid", *IEEE Trans. on Geoscience and Remote Sensing, Vol. 30, No. 3, pp. 550-559, May 1992.*

[4] M. Schwäbisch, D. Geudtner,
"Improvement of Phase and coherence Map Quality Using Azimuth Prefiltering: Examples from ERS-1 and X-SAR", *Proc. of IGARSS'95}, Firence, pp. 205-207, 1995.*

[5] D. Fernandez, G. Waller, J.R. Moreira,
"Registration of SAR images using the chirp scaling algorithm", *Proc. of IGARSS'96, Lincoln, pp. 799-801, 1996.*

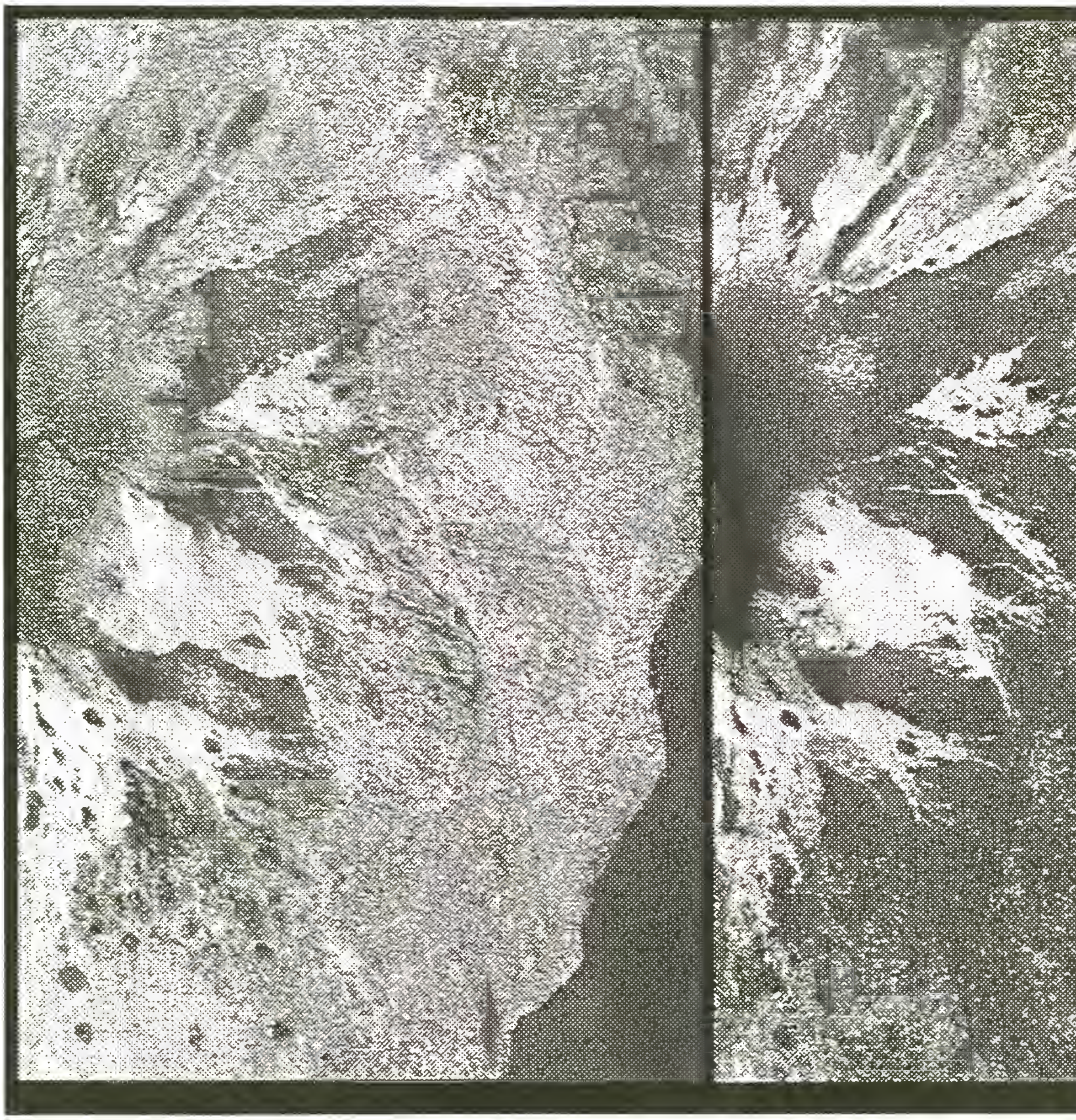

Figure 5: Coherence maps of the Mt. Etna area: 1-day coherence (left) and 70-days cohe

[6] **R. Touzi, A. Lopes, J. Bruniquel, P. Vachon,**
"Unbiased estimation of the coherence from multi-look SAR data", *IEEE Trans. on Geoscience and Remote Sensing, Vol. 68, No. 4, pp. 662-664, 1996.*

[7] **S.G. Wells, J.C. Dohrenwend, L.D. McFadden, B.D. Turrin and K.D. Mahrer**
"Late Cenozoid Landscape Evolution on Lava Flow Surfaces of the Clima Volcanic Field, Mojave Desert, California", *Geological Soc. Amer. Bulletin}, vol. 96, pp. 1518-1529, 1985.*

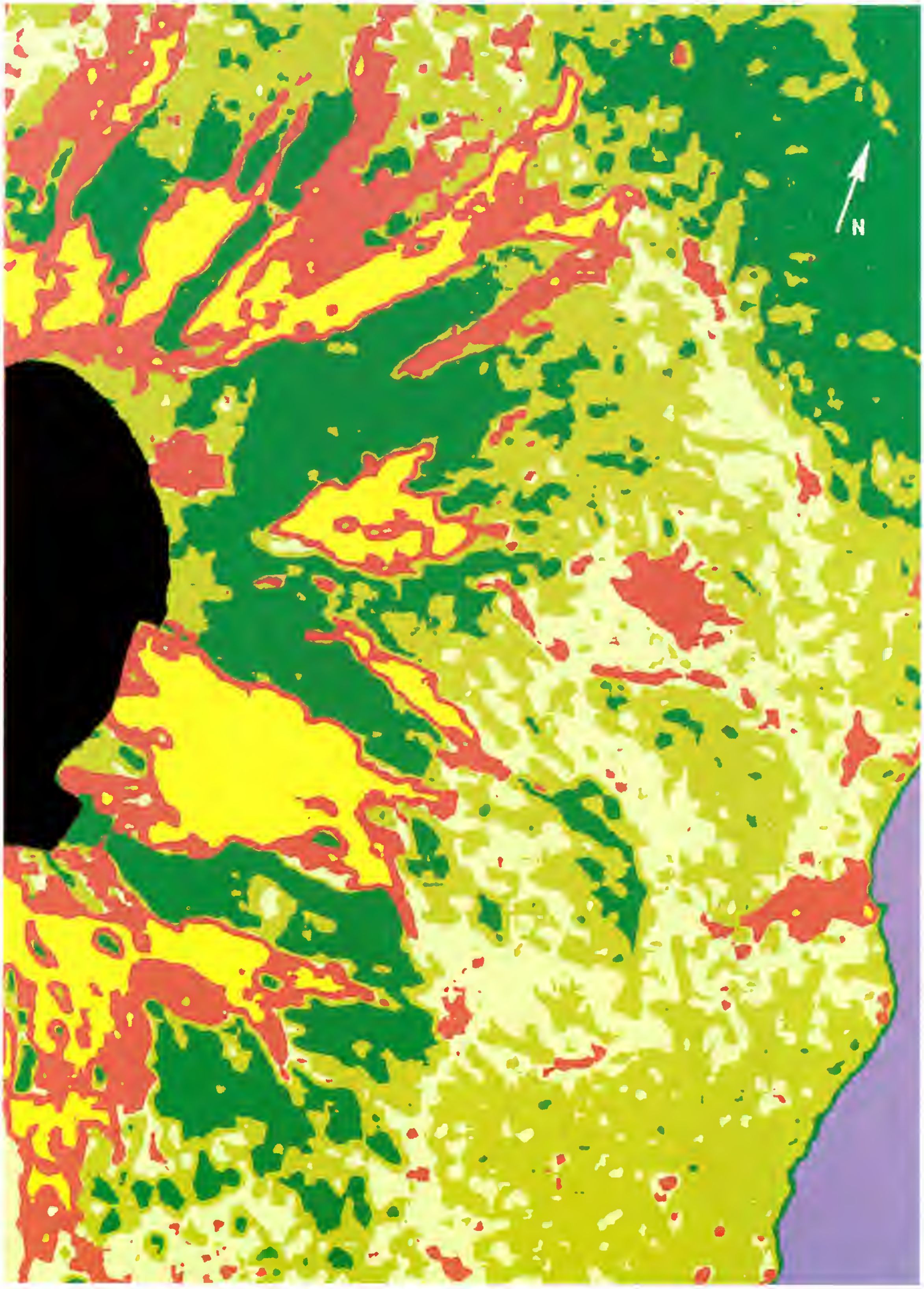

Figure 6: Multitemporal coherence interpretation map

An Approach of Error Propagation Modelling of SAR Interferometric Data

Rüdiger Gens — International Institute for Aerospace Survey and Earth Sciences (ITC), P.O. Box 6, 7500 AA Enschede, The Netherlands
gens@itc.nl
http://www.itc.nl/~gens/

John L. van Genderen — International Institute for Aerospace Survey and Earth Sciences (ITC), P.O. Box 6, 7500 AA Enschede, The Netherlands
genderen@itc.nl

Abstract

SAR interferometry has proved to be a promising technique for a number of geoscientific applications by providing height information. The theoretical aspects are basically understood and the current research focuses on the potentials investigating the limitations of the technique. In order to reach an operational status, it is necessary to have a good quality assessment of the results. One possible way to assess the accuracy and reliability of SAR interferometric products is the development of an error propagation model. This can provide information about the sensitivity of each single input parameter or processing step as well as a quantitative quality measure for the output, which is independent from additional information introduced as reference data. The development and implementation of this error propagation model is addressed in this paper.

Keywords: Error propagation model, quality assessment

Introduction

As user of any products based on a certain processing scheme it is essential to have information on the reliability of the data sets. Often the details of the different processing steps are not available. This makes it even more difficult to estimate the quality of the data set. A common approach for assessing the quality of interferometric products is the comparison with a reference data set. We will focus in this paper on the quality assessment of digital elevation models (DEMs).

In order to be able to compare an interferometrically derived DEM with a reference model, such a reference model needs to be accessable. This can be a problem in remote areas where no additional information is available. The use of a reference model for a comparison is done assuming that this model is reliable and without any distortions. From the statistical point of view, a reference DEM with an accuary, which is one order better than the InSAR DEM, is required. The result of the comparison of the DEMs gives a quantitative measure how well the two elevation models fit together. Any systematic errors remain undetected.

To overcome these problems, we estimate the quality of an InSAR DEM using an error propagation model based on an empirical approach. The theoretical background and the implementation of this error propagation model is described in the following chapters.

Error propagation model

The error propagation model is implemented in an empirical way because this needs only a limited knowledge about the software used for the processing. The values of all input parameters as well as their accuracies are needed in the model. A list of all output parameters is also required. Each single processing step needs to be estimated separately. On the other hand, it is possible to perform the error propagation in a flexible way to different stages of the processing.

The accuracy of the input parameters is sometimes difficult to estimate. There are studies undertaken to assess the quality of some parameters, e.g. baseline (Solaas, 1994). Using precise orbit information for the processing also quality estimates are provided (Massmann, 1995). Other values such as wavelength, bandwidth, etc. vary slightly in the data sets and are difficult to calibrate.

The use of an error propagation model has also its limitations. Errors caused by atmospheric effects (described by Tarayre and Massonnet, 1994) or backscatter related influences are not considered unless there are included in any of the processing steps.

Another aspect of discussion is the question how the final result of the quality assessment is required. There are three different levels for which the quality measure could be defined: the pixel level, the feature level, and the whole image. The user might be most interested in certain features.

Implementation

In order to keep the approach as flexible as possible, the implementation of the error propagation model is performed in an empirical way. There is no information necessary how the software is actually implemented. Figure 1 shows a general scheme of the error propagation.

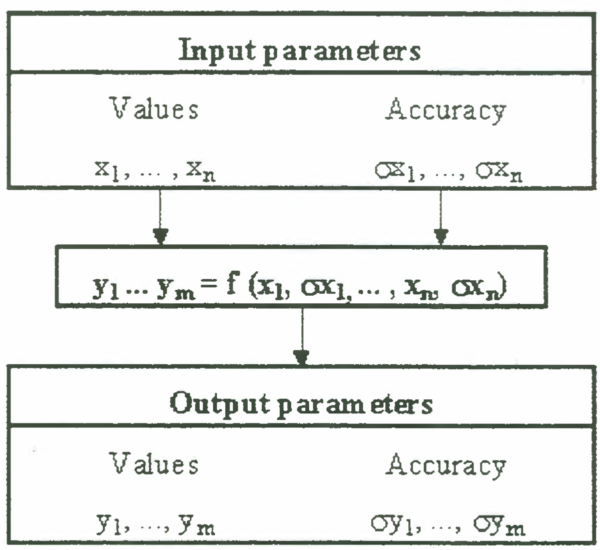

Figure 1: General scheme of the error propagation

For each single processing step the values and the accuracies of all input parameters as well as a list of output parameters have to be known. The data set is then processed once with the original values and afterwards each time with one slightly changed input parameter. The accuracy of the output parameters is then derived from the changes of the adapted and the original calculation.

This empirical approach also allows to estimate the sensitivity of the different parameters on the processing step. In this early stage of the implementation, the processing is performed with full quarter scenes in order to investigate the influence of input parameters on characteristics such as the terrain height, slope direction, etc. Another aspect is to setup rules for choosing areas for the quality assessment. The data processing can be performed using the full scenes but the quality assessment should be limited to a small representative area. As mentioned before, this also depends on the final result of the quality assessment. The user could choose an area, which is representative and where also features of interest are included.

Conclusions

The development of the error propagation provides the opportunity to assess the quality of interferometric data independently from any reference data. It can be adapted to different software realisations because it is independent from the actual calculation. This is an advantage due to the fact that there is no standard method in the processing of SAR interferometric data sets. It can also be used for optimising the interferometric processing in terms of accuracy. It is a promising tool but for a final evaluation of the usefulness of this approach it needs to be further investigated.

Acknowledgements

The ITC research on SAR interferometry forms part of the CEC's Human Capital and Mobility Programme Research Network "Synergy of Remotely Sensed Data". Contract No. CHRX-CT93-0310. It is also supported by the European Space Agency (AOT.NL 303).

References

Massmann, F.-H., 1995:
Information for ERS PRL/PRC Users, Technical Note, German Processing and Archiving Facility (D-PAF).

Solaas, G.A., 1994:
ERS-1 Interferometric Baseline Algorithm Verification, ESA report ES-TN-DPE-OM-GS02.

Tarayre, H. and Massonnet, D., 1994:
Effects of a Refractive Atmosphere on Interferometric Processing. *Proceedings of IGARSS '94*, Pasadena, California, pp. 717-719.

Session 7
Ice & Glaciers
Chairman: Y-L. Desnos

First results from ERS tandem INSAR processing on Svalbard

Knut Eldhuset	Forsvarets Forskningsinstitutt (Norwegian Defence Research Establishment) Knut.Eldhuset@ffi.no http://wwwspace.ffi.no
Frank Aanvik	Universitetet i Oslo (University of Oslo)
Kaare Aksnes	Universitetet i Oslo (University of Oslo)
Jostein Amlien	Norsk Polarinstitutt (Norwegian Polar Institute)
Per Helge Andersen	Forsvarets Forskningsinstitutt (Norwegian Defence Research Establishment)
Svein Hauge	Forsvarets Forskningsinstitutt (Norwegian Defence Research Establishment)
Elisabeth Isaksson	Norsk Polarinstitutt (Norwegian Polar Institute)
Terje Wahl	Forsvarets Forskningsinstitutt (Norwegian Defence Research Establishment)
Dan Johan Weydahl	Forsvarets Forskningsinstitutt (Norwegian Defence Research Establishment)

Abstract

This paper describes some results from a work on how INSAR tandem data can be utilized with the EETF SAR processor combined with the GEOSAT orbit determination program. It is demonstrated how an interferogram simulator can be used to detect errors in existing DEM's and how fringes caused by the terrain can be subtracted from the real interferogram. For the first time it has been possible to monitor motion of the lower part of the fast moving glacier Kronebreen with INSAR due to 1 day interval between the two SAR images. A DEM computed from interferograms (INSAR DEM) over Svalbard is assessed using the existing NP DEM. The precise orbit determination makes the fringes follow the coastline very well over parts of the scene, however, uncertainties in the baseline estimation may cause systematic errors in the INSAR DEM over larger areas in the azimuth direction.

Keywords: SAR processing, orbit determination, interferogram, glacier motion, DEM

1. Introduction

FFI, NP and UiO have recently started an ESA announcement of opportunity project for the scientific exploitation of the ERS Tandem Mission (*Eldhuset et. al., 1996a*). The ERS Tandem Mission gives unique possibility for testing the limitations of multi-pass INSAR and demonstration of possible applications. Svalbard (79 deg. N, 18 deg. E) has been selected by FFI as test area for that purpose and is one of the most northern populated areas in the world. The low atmospheric humidity, mountain terrain, sparse vegetation and active glaciers make this area very interesting for SAR Interferometry. The paper gives examples of interferograms processed at FFI and a brief description of the processing methods is provided. The importance of precise orbit determination in interferometry is demonstrated.

Proceedings of the 'Fringe 96' Workshop on ERS SAR Interferometry, *Zurich, 30 September - 2 October 1996* (ESA SP-406, March 1997)

2. Interferogram generation

All processing steps from raw data to interferogram including precise orbit determination were performed at FFI. The different steps are briefly described below.

2.1 Precise orbit determination and baseline estimation

At FFI a high precision orbit determination software has been developed, called GEOSAT (*Andersen, 1995a*), (*Andersen et. al. , 1995b*) and (*Andersen , 1995c*). It is unique in the sense that it copes with several types of measurements (e.g. VLBI, SLR, GPS, PRARE, DORIS and WVR). The ERS-1 and ERS-2 orbits were computed for the interferometric pair from 27/28 September 1995 on Svalbard. A geodetic VLBI and PRARE station is located in Ny-Aalesund which is within the test area. The GEOSAT orbit determination yielded rms errors between computed and measured ranges of about 6 cm. Both orbits were transformed to an earth-fixed system to allow estimation of the interferometric baseline components, Bx and By. The baseline components were: Bx=139.44 m, By= -9.16 m at the start of the scenes t1=0 and Bx= 147.55 m ,By= -9.28 at t2=t1+17.1 s. This means that the orbits are non-parallell which would introduce dominating phase ramps if not compensated when generating the interferogram.

2.2 SAR processing

A SAR processor developed at FFI, called second-order Extended Exact Transfer Function (EETF2) (*Eldhuset, 1995a*) and (*Eldhuset, 1996b*), was used to process single look complex images. The EETF2 processor is phase preserving. The interferometric offset test with offset 100 pixels in both azimuth and range yields a mean less than 0.001 degrees and standard deviation less than 2.4 degrees. Figure 1 shows an SAR image around the Woodfjorddalen on Svalbard. The valley to the left in the image is very flat and only few meters above the sea level. The highest peak is around 1300 m. Three distinct glaciers move into this valley from the right.

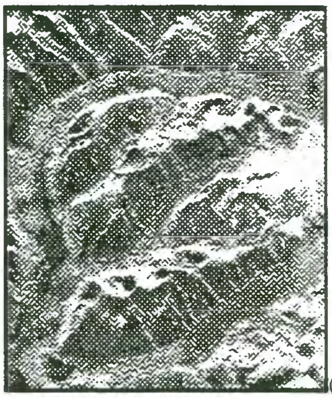
(Size: 377x447,8-bit)

Figure 1: SAR image around the Woodfjorddalen. Size: 18.1 km in azimuth, 26.8 km in range. The azimuth direction is horizontal. ©ESA/FFI.

2.3 Interferogram generation

Prior to interferogram generation the two tandem scenes are registrated on sub-pixel accuracy. The pixel offsets in both azimuth and range are updated for every new block (Size 690 x 1020 pixels) in both directions when the phase difference from the tandem pair is computed. The compensation of the phase caused by non-parallell orbits and slant range variation is updated for each pixel in both range and azimuth to obtain high interferogram quality.This avoids phase discontinuities at the block boundaries. An ellipsoid was used as earth model. Also, the altitude variation of the satellite above the earth was taken into account. Figure 2 shows an interferogram around the Woodfjorddalen which is almost flat up to the end of the upper glacier in the image. The three glaciers seem to have negligible differential motion since the fringes look like ordinary elevation curves.

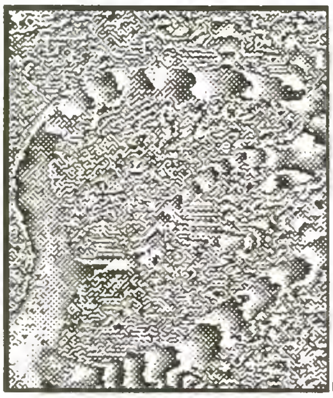

(Size: 377x447,8-bit)

Figure 2: Interferogram around the Woodfjorddalen (same region as in Figure 1). Size: 18.1 km in azimuth, 26.8 km in range. ©ESA/FFI.

2.4 Interferogram simulation

The simulator first performs a registration of the SAR image with the DEM and is nearly identical to the registration part of the FFI ship detector (*Eldhuset*, 1996d) and (*Eldhuset*, 1995b). Then an interferogram simulator computes phase differences using the same two orbits for ERS-1 and ERS-2 as the interferogram generator described in section 2.3. A simulated interferogram covering the same region as in figure 2 is shown in figure 3. It is interesting to note that the river from the upper glacier can be seen in the real interferogram in figure 2, while the simulated interferogram does not show the river. There is a striking similarity between the interferograms in figures 2 and 3.

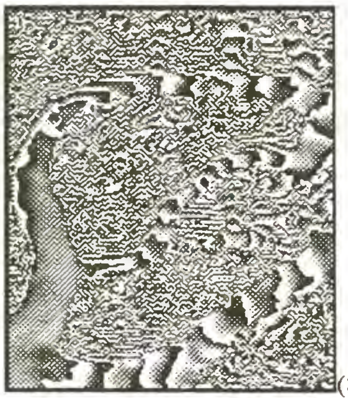

(Size: 377x447,8-bit)

Figure 3: Simulated interferogram around the Woodfjorddalen (same region as in Figure 1). Note that the interferograms in Figures 2 and 3 are not scaled to the same reference phase. Size: 18.1 km in azimuth, 26.8 km in range. ©ESA/NP/FFI.

3. DEM generation

The elevation of ambiguity was estimated using the precise orbits (baseline components) and an ellipsoid as earth model. The elevation of ambiguity was updated for each pixel in the image. The unwrapping was performed using the NP DEM. Over a test region which was 65 km x 42 km , the rms between the NP DEM and the INSAR DEM varied from 12 m to 22 m if the height reference was updated for each processed block. Each processed block was 16.3 km x 14 km. If the height reference was fixed for all of the test region, the rms varied between 15 m to 60 m.

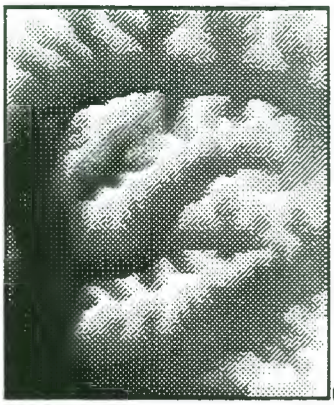
(Size: 377x447,8-bit)

Figure 4: INSAR DEM around the Woodfjorddalen (same region as in Figure 1). Size: 18.1 km in azimuth, 26.8 km in range. ©ESA/NP/FFI.

4. Assessment of interferogram quality

We now show two methods to assess the interferogram quality. The interferogram can be very easily checked by an investigation of how well the fringes follows the coast line. A more complicated way is to compare an existing DEM with a DEM computed from the real tandem interferogram.

4.1 Assessment of fringe alignment with the shoreline

On Svalbard there are several fiords where it is easy to see whether fringes are parallell with the shoreline. Here we have one example from Dicksonfjorden and Ekmanfjorden (the noisy regions) shown in Figure 5. The GEOSAT program was as mentioned used to compute the ERS-1 and ERS-2 orbits. We see that the fringes follow quite well the shoreline, but not perfectly. When the AO-data have been received and processed we shall investigate the fringes along the 100 km long Widjefjorden.


((Size: 654x404,8-bit)

Figure 5: Interferogram around the Dicksonfjorden and Ekmanfjorden. Size: 41.4 km in azimuth, 32.2 km in range. ©ESA/FFI.

4.2 Comparison of INSAR DEM and existing DEM

When the INSAR DEM was computed we selected a reference height in the existing DEM. We processed blocks of size 690 range x 1020 azimuth pixels. We estimated the mean difference of the heights in the existing NP DEM and the INSAR DEM in each block. An image consisting of 4 azimuth blocks (65 km) and 3 range blocks (42 km) was processed. In figure 6 is shown the mean difference when a block has its own height reference. In figure 7 all blocks have a common height reference. We see that when the height reference is updated for each block, the mean differences oscillate around 0 m. In some cases the difference is very close to 0 m while the worst case is about 22 m. It should be noted that this terrain is rugged with heights from 0 m to 1300 m. In addition some parts of the INSAR DEM has motion fringes where the unwrapping fails. If only one reference heigth was used, there was an obvious drift in the height differences in azimuth direction (see figure 7). The height differences in range direction varied only a few meters. The rms error of 6 cm of the GEOSAT orbits may explain the drift in azimuth direction.

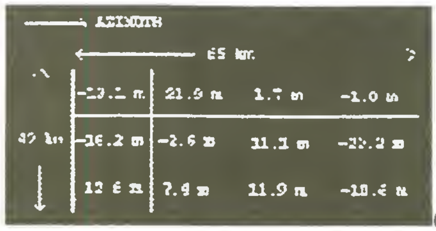

((Size: 496x246,8-bit)

Figure 6: Assessment of INSAR DEM with updated reference ©FFI.

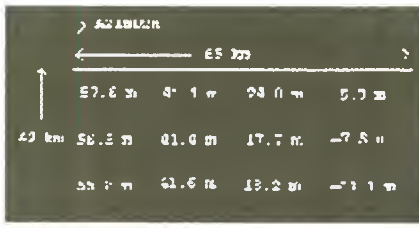

(Size: 496x246,8-bit)

Figure 7: Assessment of INSAR DEM with fixed reference ©FFI.

5. Detection of errors in existing DEM's

It has been demonstarted at FFI that simulation of interferograms from existing DEM's can be used to reveal errors. This can be done by a direct comparison of the real and simulated interferograms. An example in the northern part of Norway can be found in (*Eldhuset*, 1996c). Another example is shown in figures 8 and 9. Figure 8 is real and figure 9 is a simulated interferogram. The interferogram covers part of a glacier with some mountains. Over the mountain areas the interferograms are very similar. An obvious feature in the simulated interferogram is in the middle of the image. This correspond to a hole in the NP DEM. The elevation of ambiguity is around 75 m, so the hole may be 100 m on a rather flat glacier. A corresponding hole is not seen in the real interferogram. In a new version of the DEM at NP the hole is not observed. This version shall be used at FFI in the future.

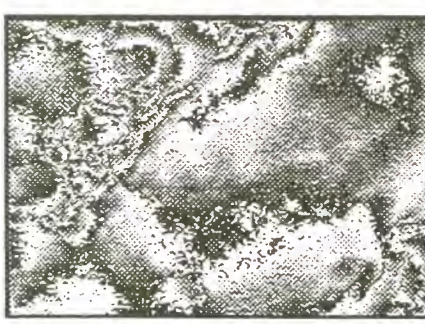

(Size: 543x387,8-bit)

Figure 8: Real interferogram over a glacier with some mountains. Pixel size is 16 m in azimuth and 20 m in ground range. ©ESA/FFI.

(Size: 543x387,8-bit)

Figure 9: Simulated interferogram over a glacier with some mountains. Pixel size is 16 m in azimuth and 20 m in ground range. ©ESA/NP/FFI.

6. Motion fringes on glaciers

It has already be demonstrated that the ERS-1 can be used to monitor motion of ice sheets with interferometric SAR (INSAR) e.g., see (Goldstein et. al. , 1993) and (Kwock et. al., 1996). The ERS-1 had both 3 days and 35 days repeat cycle. The repeat cycle of ERS tandem (ERS-1/ERS-2) is only 1 day and provides the opportunity to monitor faster glaciers than with ERS-1 alone. Tandem data were used in (Mohr et. al., 1996) to study a glacier on Greenland, but they did not have a DEM available.

6.1 Kronebreen and Kongsvegen

Figure 10 shows the SAR image over the two merging glaciers Kronebreen and Kongsvegen. Figure 11 shows an interferogram where fringes caused by slant range variation and non-parallell orbits have been removed using an ellipsoid as earth model. Figure 12 shows the interferogram in Figure 11 when the fringes caused by the terrain have been removed using the NP DEM. It has not been possible to extract motion fringes from ERS-1/ERS-1 interferograms in this part of Kronebreen (Lefauconnier, 1996). In our further work we shall monitor the motion fringes throughout the tandem period.

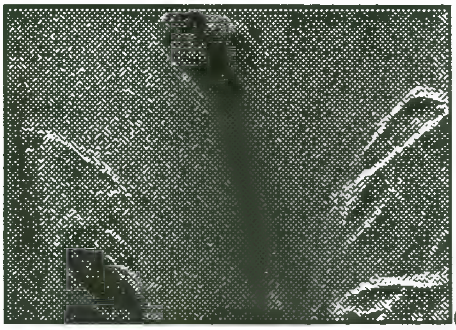
(Size: 636x443,8-bit)

Figure 10: ERS-1 SAR image over Kronebreen (left) and Kongsvegen(right), 27th September 1995. Pixel size is 16 m in azimuth and 20 m in ground range. ©ESA/FFI.

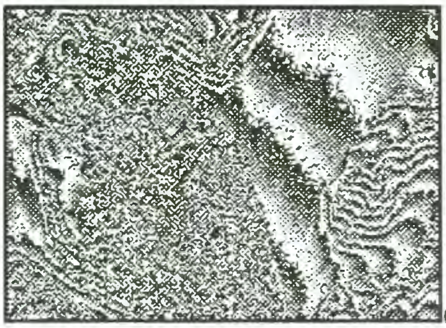
(Size: 636x443,8-bit)

Figure 11: ERS-1/ERS-2 interferogram over the lower parts of the glaciers Kronebreen and Kongsvegen, 27/28 September 1995. ©ESA/FFI.

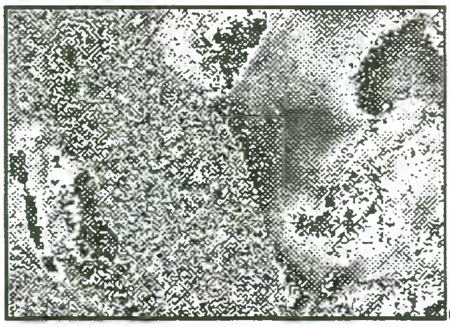
(Size: 636x443,8-bit)

Figure 12: Interferogram in Figure 2 where terrain fringes have been removed using the NP DEM. ©ESA/NP/FFI.

6.2 Preliminary analysis

In figure 11 we can see that even with tandem the interferogram is noisy at the fast moving front of Kronebreen and in the contact zone with Kongsvegen. The most likely explanation for this is probably to be found in the very complicated crevasse pattern, due to high shear stresses, in these parts of the glacier. One can see from Figure 11 that Kronebreen has typical motion fringes while Kongsvegen has mostly terrain fringes. In Figure 12 one can see that when terrain fringes have been subtracted, the remaining fringes on Kongsvegen indicates very small differential motion while on Kronebreen there is a quite complicated motion pattern which is due to differential motion. Field measurements done in 1990 suggests ice velocities of more than 2 m/day in the central part of Kronebreen while velocities on Kongsvegen are in the order of 1-2 cm/day (*Melvold, 1992*) A photogrammetric study using SPOT images confirmed these velocities for Kronebreen (Lefauconnier et al., 1994). ((*Lefauconnier et al*., 1994)) On both glaciers the ice velocity rapidly decrease towards the margins. The difference in velocity magnitude between these two glaciers is clearly visible in the interferogram. A detailed analysis of the motion pattern is presently being performed at NP. Preliminary results suggests that velocity magnitudes obtained from the interferograms agree with previous studies. It seems like in order to obtain velocity information on glaciers like Kronebreen, where parts of the glacier are heavily crevassed, a combination of field measurements, photogrammetic methods and interferometry are most likely to be successful.

7. Conclusions

We have demonstrated how the EETF SAR processor has been combined with the GEOSAT precise orbit determination software to process a tandem interferogram with high quality. The fringes follows the coast line very good in parts of the scene. An INSAR DEM was generated and compared with an existing DEM. The height differences of the two DEM's are especially dependent of the size of the DEM in azimuth direction if the height reference is fixed. This may be explained by uncertainties in the baseline estimation. It was shown how an interferogram simulator can be used to reveal errors in an existing DEM. For the first time ice velocity on the fast moving glacier Kronebreen has been estimated using SAR interferometry. Velocity magnitudes extracted from the interferogram agree well with ground measurements and estimation from SPOT images.

8. Acknowledgement

The FFI EETF SAR processor has been industrialized by the Norwegian company Kongsberg Informasjonskontroll (KIK) and has been delivered to th National University of Singapore for ERS-1 processing. It is currently installed at Tromsoe Satellite Station for RADARSAT processing. The work described in this paper is partly supported by the Norwegian Space Center.

References

Andersen P.H., 1995a:

High-precision station positioning and satellite orbit determination. *NDRE/PUBLICATION-95/01094*, Norwegian Defence Research Establishment, P.O. Box 25, 2007 Kjeller, Norway.

Andersen P.H., Hauge S., Kristiansen O., 1995b:
Precise ERS-1 orbit calculation. *Bulletin Geodesique*, vol 69, pp. 192-199.

Andersen P.H., 1995c:
http://wwwspace.ffi.no/SpaceWeb/RSGroup/Orbit_analysis.html.

Eldhuset K., 1995a:
FFI EETF Algorithm 2nd Order . *http://wwwspace.ffi.no/SpaceWeb/RSGroup/FFI_EETF_Alg.html* .

Eldhuset K., 1995b:
Automatic Detection . *http://wwwspace.ffi.no/SpaceWeb/RSGroup/Automatic_detection.html* .

Eldhuset K. (P.I.), Aanvik F., Aksnes K., Andersen K., Hauge S., Isaksson E., Wahl T., Weydahl D.J., 1996a:
ERS tandem interferometric SAR studies on Svalbard . *ESA AOT.N301 project* , 1996-1998.

Eldhuset K., 1996b:
Accurate attitude estimation using ERS-1 SAR raw data . *International Journal of Remote Sensing*, vol. 17,no. 14, pp. 2827-2844.

Eldhuset K. and Wahl T., 1996c:
SAR interferometry for detecting errors in old DEM's .
http://wwwspace.ffi.no/SpaceWeb/RSGroup/HIPSAR/HIPSARNews/News96/ErrorsInOldDEMs.html

Eldhuset K., 1996d:
An automatic Ship and Ship Wake Detection System for Spaceborne SAR Images in Coastal Regions. *IEEE Trans. On Geosc. and Remote Sensing*, vol. 34, no. 4, pp. 1010-1019.

Goldstein R.M., Engelhardt H., Kamb B., Frolich R.M., 1993:
Satellite Radar Interferometry for Monitoring Ice Sheet Motion: Application to an Antarctic Ice Stream. *Science* , vol. 262, pp. 1525-1529.

Kwok R., Fahnestock M.A., 1996:
Ice Sheet Motion and Topography from Radar Interferometry. *IEEE Trans. on Geosc. and Remote Sensing*, vol GRS-34, No 1, pp. 189-200.

Lefauconnier B., Hagen J.O., Rudant J.P., 1994:
Flow speed and calving rate of Kronebreen glacier, Svalbard, using SPOT images. *Polar Research*, vol. 13, no. 1, pp. 59-65.

Lefauconnier B., 1996:
Personal communication.

Melvold K., 1992:
Study of glacier motion on Kongsvegen and Kronebreen, Svalbard. *Technical Report*, Department of Geography, University of Oslo.

Mohr J.J., Madsen S.N., 1996:
Application of Interferometry to Studies of Glacier Dynamics. In: *Proc. IGARSS'96 Symp.*, pp. 972-974.

Multi-pass interferometry for studies of glacier dynamics

Johan Jacob Mohr — Danish Center for Remote Sensing, Dept. of Electromagnetic Systems, Technical University of Denmark, B-348, DK-2800 Lyngby, Denmark
jm@emi.dtu.dk
http://www.dcrs.dtu.dk

Søren Nørvang Madsen — Danish Center for Remote Sensing, Dept. of Electromagnetic Systems, Technical University of Denmark, B-348, DK-2800 Lyngby, Denmark
snm@emi.dtu.dk
http://www.dcrs.dtu.dk

Abstract

This paper presents recent results from the ESA Tandem Announcement of Opportunity study 'An Investigation of the Utility of ERS SAR Data for Studies of Glacier Dynamics.' The study is conducted by the Danish Center for Remote Sensing in collaboration with the Danish Polar Center.
A key element in the study is multi-baseline repeat track interferometry (RTI), which potentially can be used to measure both velocities and the micro topography of glaciers. A primary test site has been established on the Storstrømmen Glacier in North-East Greenland. Tandem ERS data acquired in August - December 1995 covering the glacier have been investigated. DCRS has acquired complementary airborne RTI data over the glacier in August of 1994 and RTI as well as single-pass interferometry (XTI) data in August of 1995. In-situ measurements including repeated positioning of poles as well as deployments of corner reflectors were performed by the Danish Polar Center.

Keywords: SAR, Interferometry, Glacier, ERS, EMISAR

Introduction

This article describes work performed in connection with the ERS Announcement of Opportunity study 'An investigation of the utility of ERS SAR data for studies of glaciers dynamics.' The focus is on glaciers in north-east Greenland which are important as the dynamics and mass balance of glaciers in that region is not well understood. Recent studies indicates that the major outlet glacier Storstrømmen has a surge like behavior with a 70 years period (Reeh, *et al.*, 1994), and thus extrapolations of observations performed within a short period of time should be interpreted with care as the natural variability of the extend and thickness of some glaciers might be large. Also the mass balance of the north-eastern region of Greenland has great interest as 20 km3/y of ice cannot be accounted for in present models. Possible explanations are that the ice-sheet is growing thicker, or the ice is removed by some unmodelled drain such as melting at bottom of large floating glaciers, (Reeh, 1993).

The AO study augments on-going experiments with the airborne polarimetric and interferometric EMISAR (Christensen *et. al.* , 1996), (Madsen *et. al.*, 1996), operated by the Danish Center for Remote Sensing (DCRS) and intensive field work in north east Greenland conducted by the Danish Polar Center (DPC) and the Alfred Wegener Institute. Questions addressed includes

1. Can multi-baseline interferometric SAR data provide useful measurements of glacier dynamics?
2. Can satellite SAR data (interferometric or not) be utilized to spatially and temporally interpolate results from localized studies involving high resolution airborne SAR and extensive ground truth programmes?

This paper describes the on-going work at Storstrommen, recent results from the decomposition of ERS tandem interferograms into displacement and topography, and discuss the limitations of the products generated with interferometric techniques.

Experiments on Storstrømmen

The Danish Polar Center in collaboration with the Alfred Wegener Institute has performed field work on Storstrømmen in the field seasons 1989ñ1995, (Reeh *et al.*, 1994). The work included collection of surface velocity and height data by repeated GPS positioning of stakes. Mean velocities during time periods spanning from 2 to 30 years have also been measured by surveys of lake ridges. Between 700 and 1000 m a.s.l. a large number of lakes are located in stationary surface depressions. Each year a ridge is formed, and thus the velocity can be estimated by measuring the distance between the ridges. Velocities and ice margins have also been derived from aerial photographs taken in 1963 and 1978. In all seasons meteorological data were collected.

In 1994 and 1995 DCRS acquired EMISAR radar data from a 10 km (N-S) by 30 km (E-W) test field on the lower part of the glacier. In 1994 C-band repeat track interferometric (RTI) and C-band polarimetric data were collected on a one day mission. In 1995 L-band RTI data, C-band topographic across track interferometric (XTI) data and L-band polarimetric data were acquired on two consecutive days. Compared to the one day mission in 1994 where the maximum temporal baseline achieved was on the order of two hours, the one day baseline of the 1995 data greatly enhance the chance of getting useful velocities from the RTI data.

In 1994 corner reflectors were deployed by DPC. Two on the bedrock to the West of Storstrømmen on Dronning Louise Land and two on the semi-nunatak near the Eastern ice margin. The positions of the reflectors, serving as reference points for the radar observations, were surveyed by GPS in 1994 as well as in 1995.

Other data such as surface elevations along profiles collected in collaboration with the Greenland Ice Core Programme (GRIP) are also available.

Importance of interferometric measurements of topography and velocity of glaciers

Topography and velocities can potentially be derived from multi pass interferometric SAR, (Massonnet *et. al.*, 1993), (Goldstein *et. al.*, 1993), (Kwok and Fahnestock, 1996). On a point by point basis, the accuracy of field measurements is generally much better than the corresponding interferometric SAR measurement. However, the interferometric measurement has a lot of advantages, the most important being:

1. Imaging capability, - providing spatial measurements on a dense regular net.
2. Global availability, - since satellites usually covers most of the Earth. This makes regional or even global studies feasible.
3. Temporal availability, - as the measurements are usually repeated within a short time interval (days to months). However, the life time of a satellite is short (some years), but occasionally a series of similar satellites is launched.

The imaging capability enables studies not possible solely with the sparse amount of in-situ measurements usually available. Valuable input for further studies is a DEM and a velocity map, enabling a direct modeling of the dynamics and mass balance of a glacier. It is important to note that for glaciers and ice-sheets a velocity map is an unavoidable product when generating a DEM, since glaciers in general is moving or deforming. The required accuracy of DEMís for different applications is summarized by Zebker *et. al.* (1994).

Recent results from ERS Tandem Data

We have presently received five descending ERS tandem data sets covering the glacier Storstrømmen from ESA. Two pairs from late October and early December 1995, with good coherence and favorable spatial baselines, were selected for further investigation. The data cover a 100 km by 200 km region around Storstrømmen as two frames were merged before processing. The basic processing includes:

- CEOS header reading.
- Cleaning (missing lines, SWST changes etc.) and merging of raw data.
- Doppler estimation.
- Processing to single look complex imagery, (common reference line).
- Estimation of interferometric baseline by cross correlation of small image patches.
- Interferogram formation and multi-looking.
- Unwrapping.

At present a simple decomposition procedure is utilized. First the baseline in each interferogram is tuned separately using tie-points. Secondly the phase is decomposed into displacement and topography. The displacement is converted from a slant range displacement to an equivalent horizontal velocity towards the radar, see figure 1. In figure 2, the corresponding topography map is shown. Note that both images are in slant range projection and have been spatially averaged in order to ease the electronically publishing. Note that north is up to the left and that the satellites were flying down the right side of the figures as they are shown here.

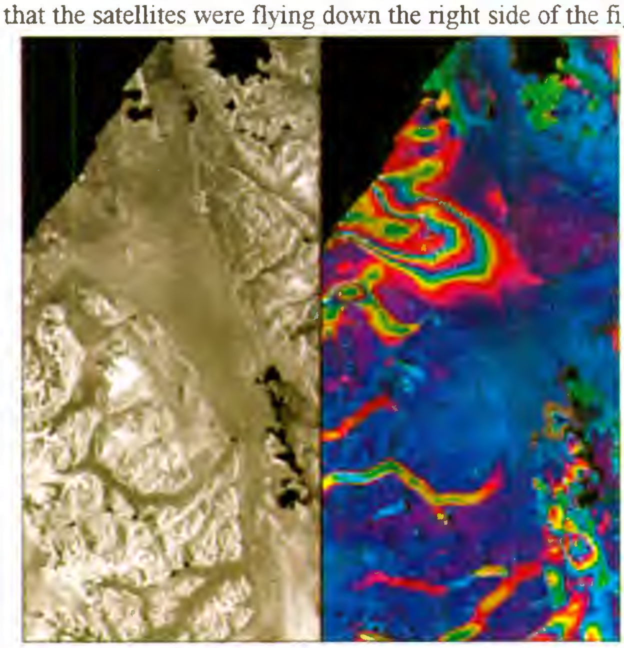

Figure 1. Equivalent horizontal velocity towards the radar of Storstrømmen, North-East Greenland (right) magnitude image (left). One color cycle is 100 m/y, blue is 0 m/y, red is +30 m/y, green +60 m/y etc. Data: ERS-1/2.SAR.RAW. Acquired: 951028 - 951203. Processed: 960906. Track: 382. Frame: 2025+2043. Number of looks: 20.

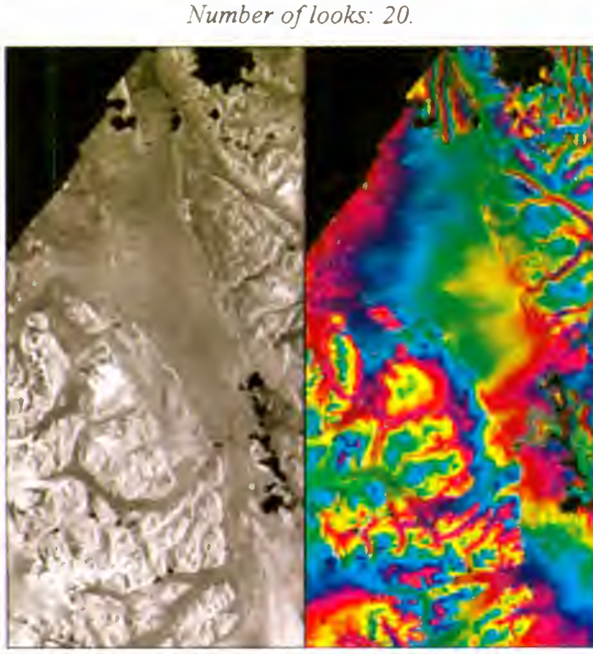

Figure 2. Surface height of Storstrømmen, North-East Greenland (right), magnitude image (left). One color cycle is 1000 m, red is 0, green is +300 m, blue +600 m etc. Data: ERS-1/2.SAR.RAW. Acquired: 951028 - 951203. Processed: 960906. Track: 382. Frame: 2025+2043. Number of looks: 20.

The accuracy of the velocity map shown in Figure 1 is easily evaluated, as rocks are present throughout the image. The worst case velocity error is 10 m/y of which at most half can be linked to residual topography. The remaining uncertainty seems to be caused by some low frequency undulations of the phase in one of the interferograms. Those undulations corresponds to 0.5 cm variation in the path length which might be caused by changes in the delay in the troposphere.

In the upper right corner of the velocity map some regular shaped artifacts are seen in the mountains. Those are caused by unwrapping errors. Fortunately unwrapping errors are most unlikely to appear on the ice (at least in areas with good coherence). On the other hand unwrapping errors also cause errors in the topographic products. In areas with steep mountains, those errors will require operator interaction to be identified and corrected.

The quality of the topographic map is not sufficient for most applications. The reason is the short spatial baselines of approximately 20 m and 2 m. This implies that baseline uncertainties and path length changes due to tropospheric delays scale the errors to much more than with a baseline of some hundreds of meters optimal for topographic mapping.

A second reason for the large uncertainties in the topographic data is the quality of the tie-points. A major limitation with the present method is the identification of tie-points on a map. The exact horizontal position of stationary points (mountains) is difficult to identify in the interferograms and since the mountains typically are steep, this translates into a height error on the tie-point.

A possible improvement is to enhance the tie-pointing method, or probably better, to develop software for utilization of the coarse DEMís available for the area. On-going work is also to utilize the Precision Orbit Data (PRC) from the D-PAF. This will ease the generation of interferograms as the processor (originally developed for airborne SAR) allows focusing of the raw data to a common reference line. This will also simplify the geocoding since the PRC data are in a common earth body fixed reference system.

Limitations on ERS Interferometry

Space borne SAR interferometry is a promising technique, that has already proven useful for generation of input to models of glacier dynamics. However, some limitations apply depending on the application. In the following the most important limitations are addressed.

Temporal decorrelation and phase unwrapping

As reported in virtually all previous work on satellite interferometry, temporal decorrelation pose a significant problem as it corrupts the phase measurement and eventually prevents phase unwrapping. For arctic regions the most likely causes are surface melting when the temperature exceeds 0 C, and changes in the surface caused by precipitation. The five tandem pairs analyzed in this study have exhibited correlations reaching from zero to nearly one, see table 1.

Date	Track	Bper[m]	Corr.ñIce	Corr.ñRock	Orbits [E1/E2]
July 31, 1995	110	-14	0.20-0.50	0.95	21140/01467
Sep. 4, 1995	110	55	0.40-0.70	0.95	21641/01968
Sep. 24, 1995	382	-112	0.10-0.60	0.85	21913/02240
Oct. 29, 1995	382	-21	0.90	0.95	22414/02741
Dec. 3, 1995	382	1	0.65-0.95	0.70-0.95	22915/03242

Table 1. Baselines and correlations for processed images. Baselines are estimated from the data. Correlations are typical values. All data sets are 1-day repeat ERS-1/2 tandem pairs, frame 2025+2043 (100 km x 200 km).

We have only been able to unwrap a reasonable large area in two (Oct. and Dec.) of those five interferograms.

The solution to the decorrelation problem seems to be to avoid data from periods with significant surface melting. and to acquire/process more than one data set of each area of interest. in order to maximize the chance of getting data from a period without excessive precipitation (or other processes changing the surface such as strong winds).

Baseline estimation

Even with multiple baseline interferometry the full set of baseline parameters can not be estimated directly from the data. The relative distances between the satellite tracks can in principle be estimated, but there is no mean for distinguishing a common mode rotation of the baseline angles from a tilt in the landscape.

In areas with mountains or other stationary features the remaining baseline parameters can be estimated by means of a DEM (available for most of Greenland) or by some other reference points for instance obtained with altimetry. If no tie-points are available it might be considered to utilize ascending and descending orbit data of the same area to remove the tilt as described by (Malliot, 1996).

Another uncertainty almost indistinguishable from baseline uncertainties is drift in the carrier. Massonet (1995) observed that a frequency drift caused several fringes in the azimuth direction over a few frames of ERS-1 data. This implies that not only the modulo 2*pi uncertainty from the phase unwrapping need to be estimated, but also the fractional value of the absolute phase.

Tropospheric effects

Path length changes caused by changes in the troposphere have previously been reported, (Goldstein, 1995:) and (Massonet, 1995). Such path length changes of up to some wavelengths create artifacts in the interferograms only distinguishable from real features if multiple interferograms from the same area are available. This implies that for generation of reliable products of unknown regions, multiple interferograms (and data acquisitions) are necessary.

In one of the two interferograms used above some artifacts are observed which we believe are due to tropospheric changes. A magnitude image, an interferogram and a correlation image of a window of the Oct. 29, 1995 data set are shown in figures 3, 4 and 5 respectively. The images cover approximately 40 km by 30 km of the lower part of Storstrømmen and Bistrup Bræ.

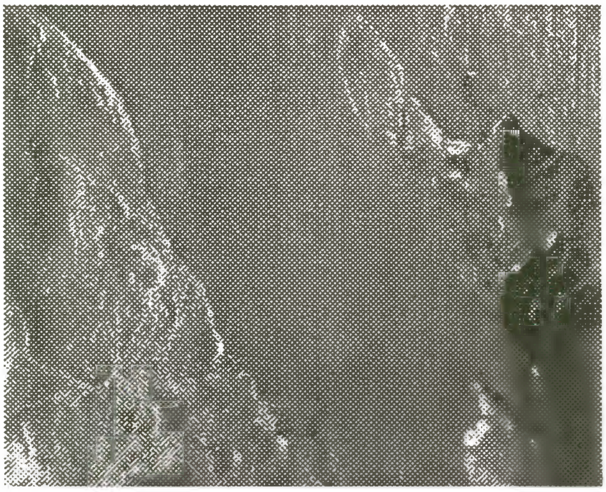

Figure 3. Magnitude of a 40 km by 30 km window in the Oct. 29, 1995 interferogram.

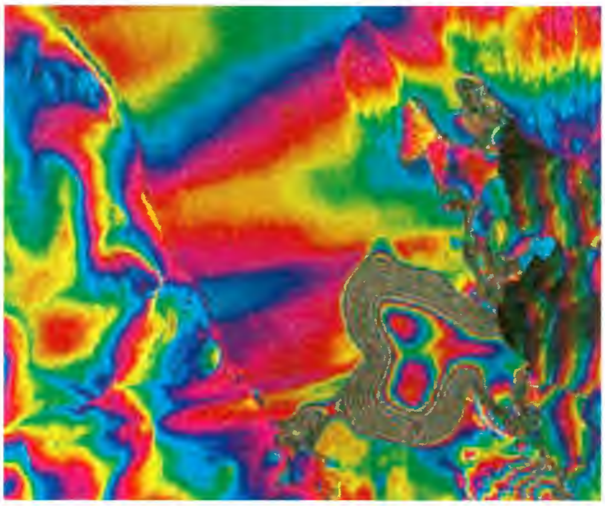

Figure 4. A 40 km by 30 km window in the Oct. 29, 1995 interferogram.

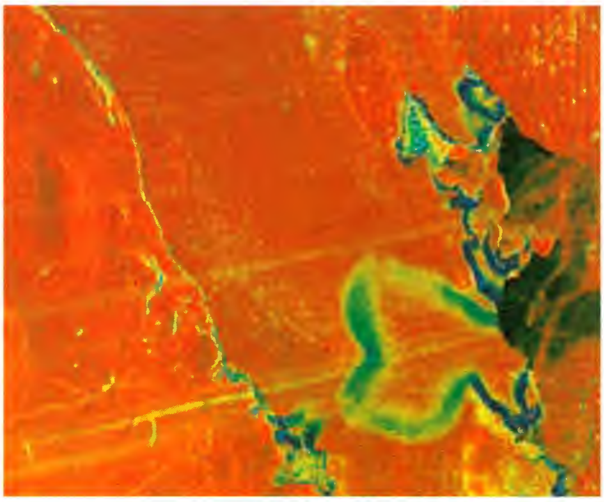

Figure 5. Coherence of a 40 km by 30 km window in the Oct. 29, 1995 interferogram.

A phenomenon which we have not been able to explain is observed on the flat part of the glacier just south of the semi-nunatak. As the ambiguity height is approximately 500 m, the one fringe deep pattern cannot be caused by topography as the topographic changes on that part of the glacier are much smaller. Neither can it be due to motion as the pattern extends into the stationary mountains. Note also that the in-situ measurements in 1995 have shown that the actual glacier motion presently is a few meters per year.

In the same region of the image some streaks are observed in the correlation image. A closer examination of the streaks will show that they are not exactly aligned with the above mentioned phenomenon observed in the phase image. The cause of the streaks in the correlation image is presently not understood, and we do not even know whether they are caused by sensor effects or a geophysical phenomenon.

Ascending orbit data

Only the line of sight motion can be determined by interferometric measurements, thus descending orbit data alone can at most give a 1-D velocity measurement. The line of sight motion can simply be projected onto the glacier surface, taking the local slope (also available from multi-pass interferometry) into account. This approach will leave a minor bias (which can be modeled), as the velocity vectors in general points into the glacier in the accumulation zone and out of the glacier in the ablation zone. This is, however, a tiny effect.

An intrinsic limitation on interferometric measurements is that no information can be derived on the displacements parallel to the flight direction. In large parts of the central ice sheet the 2-D pattern might be modeled utilizing the local slope. However, the behavior of glaciers in the marginal zones is much more complicated. It is not a valid assumption that the flow direction can be derived from the direction of the local slope. As demonstrated on Storstrømmen it is neither valid to assume that the flow is stationary, as the glacier might grow thicker in some areas and thin in others. In general, mass-balance studies are difficult without a

2-D pattern, as it is impossible to extract bottom melting, runoff, ice build up etc. if the flow divergence is unknown.

Another important issue is validation of the developed models of ice dynamics. Multi pass interferometry from different angles giving 2-D velocity maps clearly has the potential for improving present modeling techniques.

An obvious solution is to acquire data from different track headings such as for instance descending and ascending orbits.

Tidal effects

A significant problem related to the extraction of the 2-D velocity pattern is that tidal uplift of the floating parts of glaciers corrupts the decomposition of the displacement into two horizontal components. Furthermore, the decomposition of the interferometric phase into displacement and topography is corrupted if the uplift is not exactly the same in the two interferograms.

An example of the effect of tidal uplift is shown on Figure 4, in the area with the dense fringe pattern. In the derived topography map on figure 2, this feature comes out with a height of 8000 m below sea level. Also note that the correlation drop significantly in the deformation zone, see Figure 5. In this image the problem is small, but other glaciers such as Nioghalvfjerds Bræ is floating over large areas.

There is no easy way to handle this problem with multi pass interferometry. Useful measurements might be extracted, but the uplift need to be modeled accurate and/or the observation must be acquired with the glacier in a near stationary position at high or low tide. Basicly the only reliable solution is to use a single pass interferometer either from an airplane or in the future from a satellite to generate the topographic component with a zero temporal baseline.

Discrimination

For regional studies a discrimination between glacier ice, shorefast ice, rock, lakes, etc. is of significant interest but automatic methods are much needed to do this job. In the winter images processed until now, different types of terrain exhibit similar backscatter and coherence. Solutions to this task might involve using interferograms from different times of the year, and/or using interferograms with a 35-day repeat or longer.

Conclusions

A displacement map has been generated for the glacier Storstrømmen in North-East Greenland from two descending pass ERS tandem interferograms. Only one component of the displacements has been extracted, but if ascending orbit data have sufficient coherence, a 2-D pattern can be generated. In combination with a data set with a larger spatial baseline which would enable the generation of a useful topographic map, this would allow us to solve for the 3-dimensional velocity vector. Only some of the ERS data sets exhibited sufficient correlation to allow phase unwrapping and in general it seems most desirable to acquire multiple data sets of each area to increase the chance of acquiring data with good correlation. Multiple data sets also allows for identification of artifacts caused by tropospheric path delays, and ease the delineation of different terrain classes.

Acknowledgments

We thank Niels Reeh (formerly DPC, now DCRS) for reviewing the manuscript and for providing information on the DPC field work.

The Danish Center for Remote Sensing (DCRS) is established and funded by the Danish National Research Foundation.

Development of the EMISAR was sponsored by the Thomas B. Thriges Foundation, the Danish Technical Research Council (STVF), the Royal Danish Air Force (RDAF), the Technical University of Denmark and the Joint Research Centre (JRC).

References

Christensen *et. al.*, 1996:
EMISAR: C- and L-band Polarimetric and Interferometric SAR. *Proceedings of IGARSSi96*, Lincoln, Nebraska, 27-31 May 1996, pp. 1629-1632.

Goldstein, Engelhardt, Kamb, Frolich, 1993:
Satellite Radar Interferometry for Monitoring Ice Sheet Motion: Application to an Arctic Ice Stream. *Science*, **262**, pp. 1282-1285.

Goldstein, Richard, 1995:
Atmospheric limitations to repeat-track radar interferometry. Geophysical Research Letters, Vol. 22, No. 18, pages 2517-2520.

Kwok, Fahnestock, 1996:
Ice Sheet Motion and Topography from Radar Interferometry. *IEEE trans. Geosci. Remote Sensing*, **34**, pp. 189-200.

Madsen *et. al.*, 1996:
A System for Airborne SAR Interferometry. *AEÜ International Journal of Electronics and Communications*, **50**, pp. 106-111.

Malliot, 1996:
ER-2 IFSAR Digital Terrain Matrix Collection System. *Proceedings of IGARSSi96*, Lincoln, Nebraska, 27-31 May 1996, pp. 2349-2354.

Massonnet *et. al.*, 1993:
The Displacement Field of the Landers Earthquake Mapped by Radar Interferometry. *Nature*, **364**, pp. 138-142.

Massonnet, 1995:
Limitations to SAR Interferometry due to Instrument, Climate or Target Geometry Instabilities. *EARSeL Advances in Remote Sensing, Topography from Space*, Vol. 4, no. 2, October 1995, pp. 19-25.

Reeh, Bøggild, Oerter, 1994:
Surge of Storstrømmen, a Large Outlet Glacier from the Inland Ice of North-East Greenland. *Rapp. Grønlands Geol. Unders.*, **162**, pp. 201-209.

Reeh, 1993:
Calving from Greenland Glaciers: Observations, Balance Estimates of Calving Rates, Calving Laws. *Report on the Workshop on the Calving Rate of West Greenland Glaciers in Response to Climate Change, 13-15 September 1993, Copenhagen Denmark*, Danish Polar Center 1994, Denmark, pp. 85-102. (ISBN: 87-601-4387-8).

Zebker, Farr, Salazar, Dixon, 1994:
Mapping the Worldís Topography Using Radar Interferometry: The TOPSAT Mission. *Proceedings of the IEEE*, **56**, pp. 1774-1786.

Glacier Flow Measurements with ERS Tandem Mission Data

Ian Cumming and Juan-Luis Valero

Radar Remote Sensing Group,
Dept. of Electrical Engineering,
The University of British Columbia,
2356 Main Mall,
Vancouver, BC, Canada V6T 1Z4.

E-mail address: ianc@ee.ubc.ca
http://www.ee.ubc.ca/sar/

Paris Vachon, Karim Mattar,
Dirk Geudtner and Laurence Gray

Canada Centre for Remote Sensing,
588 Booth Street,
Ottawa, Ontario, Canada K1A 0Y7

E-mail address: vachon@ccrs.emr.ca
http://www.ccrs.nrcan.gc.ca/

Abstract

Glacier flow measurements have provided one of the more striking applications of differential satellite SAR interferometry. In this paper, we summarize some results we have obtained on the Saskatchewan Glacier in the Columbia Icefield in the Rocky Mountains of western Canada. Glacier measurements are important for hydrological studies, but are difficult to measure from the ground. We show that dense, wide-area flow measurements can be made from ERS Tandem Mission data, as long as the surface of the glacier is stable. The necessary stability conditions occur when the temperature is below freezing and no precipitation or strong winds occur during the observation interval.

Differential interferometry requires that the phase due to topography be removed from the phase due to motion in the interferogram. We do this by using an accurate DEM obtained from the CCRS Convair-580 across-track interferometer, then using the ERS satellite geometry to derive the phase due to the topography and the viewing parallax (baseline). When this phase is subtracted, the motion fringes can be processed to obtain line-of-sight glacier flow. Then, by assuming a given glacier flow direction, the LOS motion can be projected to the proper flow direction.

We show results obtained from the Saskatchewan Glacier on November 2/3 1995. The measured flows range up to 30 cm/day. They have been verified to be accurate to within 10% by ground measurements, and later SAR observations taken in November 1995, March 1996 and April 1996 reveal that the fine-scale structure of the glacier flow patterns are very repeatable. Glaciological studies are now underway to understand the physics behind the detailed observed flows.

Keywords: Differential interferometry, Glacier flow measurements

Table of Contents

1. Introduction

In this paper, we show how differential interferometry from the ERS satellites operating in Tandem Mode can yield excellent measurements of the flow rates of Alpine Glaciers. As long as the surface conditions are stable during the observation interval, accuracies of a few cm/day can be obtained from the ERS data.

In the interferometric processing, a means must be available to separate the phase differences in the interferogram due to topography from those due to motion. In this work, we use a DEM and a model of the satellite geometry to subtract the topographic phase, leaving a clear picture of glacier surface motion.

Our main results are taken over the Saskatchewan Glacier in western Canada in November 1995. We show the topographically-corrected interferogram, and the velocity map derived from it.

2. Glacier Measurements

Glaciers have been studied for a long time, including measuring their area, depth, accumulation, water runoff, snow line position and terminus extent. They are an important indicator of historical and present global climate, as their parameters are an integral of climate and environmental effects such as temperature, precipitation and pollution. By taking core samples and dimensional measurements, glaciologists can infer climate and make models of glacier dynamics. Now that water resources are in scarce supply in many parts of the world, it is all the more important to make accurate measurements and models of glacier mass balance to forecast the water available for future consumption and to predict floods and droughts.

Measurements have traditionally be made on glaciers by ground-based crews, and sometimes by helicopters. These measurements are difficult and expensive to make, with the result that few glaciers are monitored, and even then, only a sparse set of readings can be taken. Many glaciers are relatively inaccessible and weather conditions often prevent operation by field crews.

3. The Columbia Icefield

The Columbia Icefield in the Rocky Mountains of Western Canada was chosen as our study area because:

1. There are 7 glaciers flowing in all directions, so we can find one that is best for the ERS viewing directions, and can see the effects of other viewing directions.
2.
3. The glaciers are relatively accessible for taking ground truth measurements, as a major highway and government interpretation centre are located there.
4.
5. These glaciers have been studied for many years, go good-quality historical flow data is available.
6.
7. These glaciers are typical of many inaccessible Alpine glaciers.

We will focus our attention on the Saskatchewan Glacier, located at 52°8'N, 117°11'W. It is the largest glacier in the Columbia Icefield, and has a favourable orientation for imaging with ERS ascending passes. The descending pass view direction is also reasonably good. The tongue of the glacier flows from west to east and is approximately 10 Km long and 1 Km wide. A 1:50,000 topographic map of the glacier is shown in Figure 1.

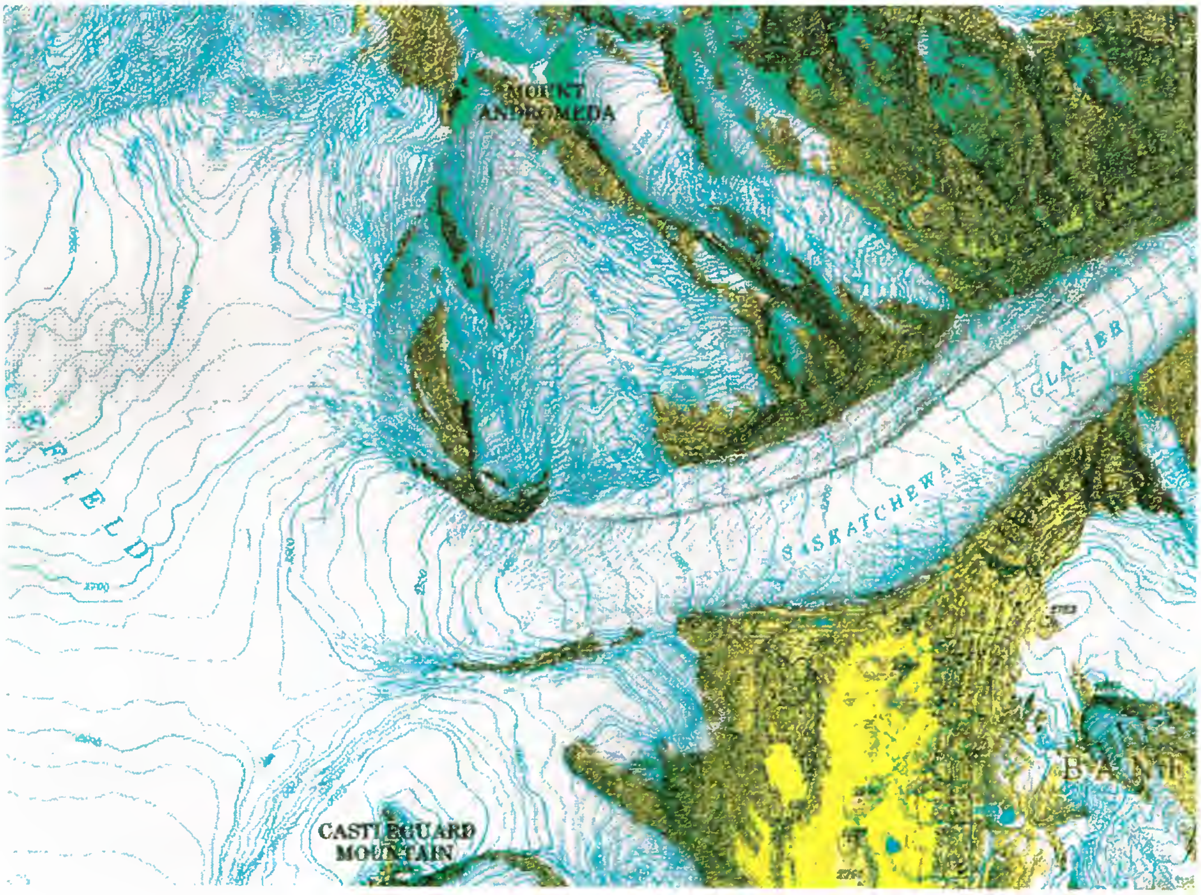

Figure 1: Topographic map of Saskatchewan Glacier.

4. InSAR Processing

We will apply repeat-pass satellite interferometry processing to the 1-day repeat coverage ERS Tandem Mission data. Our data comes from frame 1035, with ERS-1 orbit 22481 on November 2, 1995 and ERS-2 orbit 2808 on November 3, 1995. The data is processed into SLC images with the MacDonald Dettwiler SAR processor, registered and an interferogram formed.

The magnitude and phase of the interferogram is given in Figure 2 and Figure 3 respectively, showing a 16 Km (range) by 5 Km (azimuth) portion of the scene. The left hand 1/5 of the scene shows the Columbia Icefield, which is the accumulation area of the glacier.The 10 Km long tongue of the Saskatchewan Glacier runs from left to right through the middle of the scene, ending in a terminal moraine at the right of the image. Note than the SAR images are rotated about 12° with respect to the map, as they are in the slant range alignment given by the ascending pass viewing direction.

The interferogram shows reasonably good coherence on the ice surface (average coherence about 0.8). The areas where the phase noise is high are mountainous areas above and below the glacier, where layover is significant.

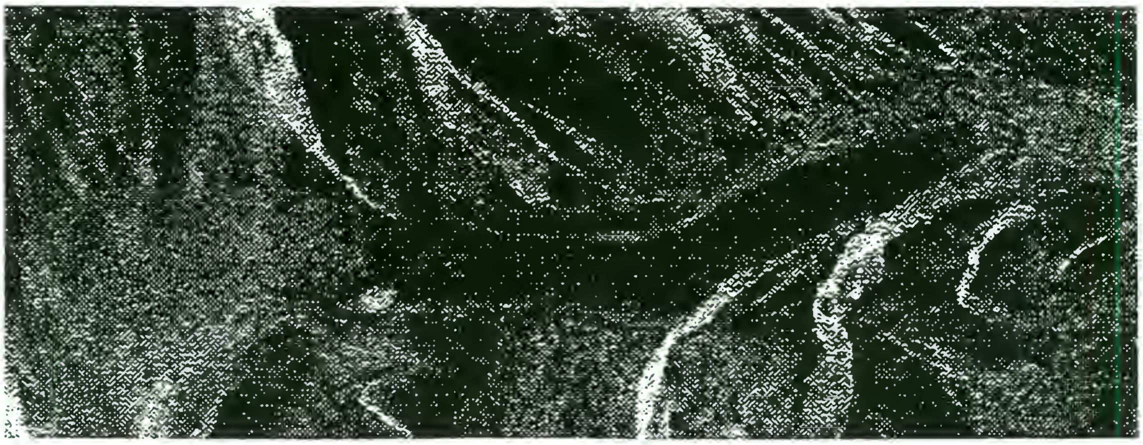

Figure 2: Magnitude of interferogram of Saskatchewan Glacier

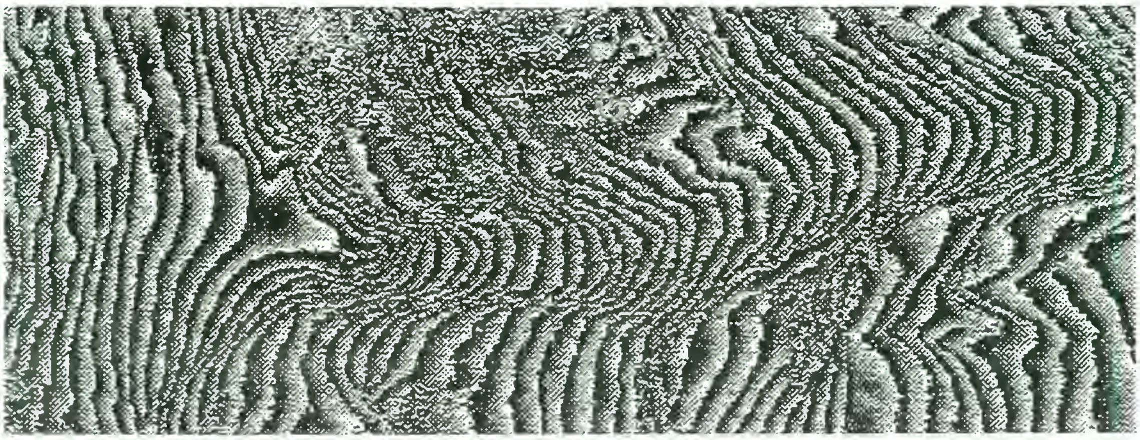

Figure 3: Phase of interferogram of Saskatchewan Glacier.

4.1 Processing the Glacier Interferogram

In the interferogram, the differential phase is due to:

1. topographic effects, because of the different satellite beam incidence angles (cross-track parallax),
2.
3. displacement effects, due to surface motion between the data takes, and
4.
5. noise effects, from sources such as receiver noise and random scatterer motion.

As we are interested in extracting glacier motion, the topography phase must be removed from the interferogram. This can be done in at least two ways:

1. Predict the phase due to topography/parallax, and subtract it from the interferogram. If a DEM is available, it can be used with a satellite geometry model (knowing the baseline) to compute the topography phase.
2.
3. If two interferograms are available with different baselines and/or different data take intervals, the interferogram phase can be solved using two independent equations for the two unknowns (topo and displacement phases). This requires the assumption that the glacier velocity is constant between the two pairs of data takes.

The second approach has been used successfully by Joughin on the Greenland Ice Sheet [Joughin, 1995]. In our case, an accurate DEM has been obtained by the CCRS Convair-580, and will be used with the first method above.

4.2 The Convair-580 DEM

The Convair-580 SAR was flown over the test area in March and August 1995, with a viewing direction from the north-east (looking up the glacier). Figure 4 shows a SAR image taken from the August flight. Compared to the ERS images, the Convair image has a higher resolution, larger incidence angle and a higher SNR.

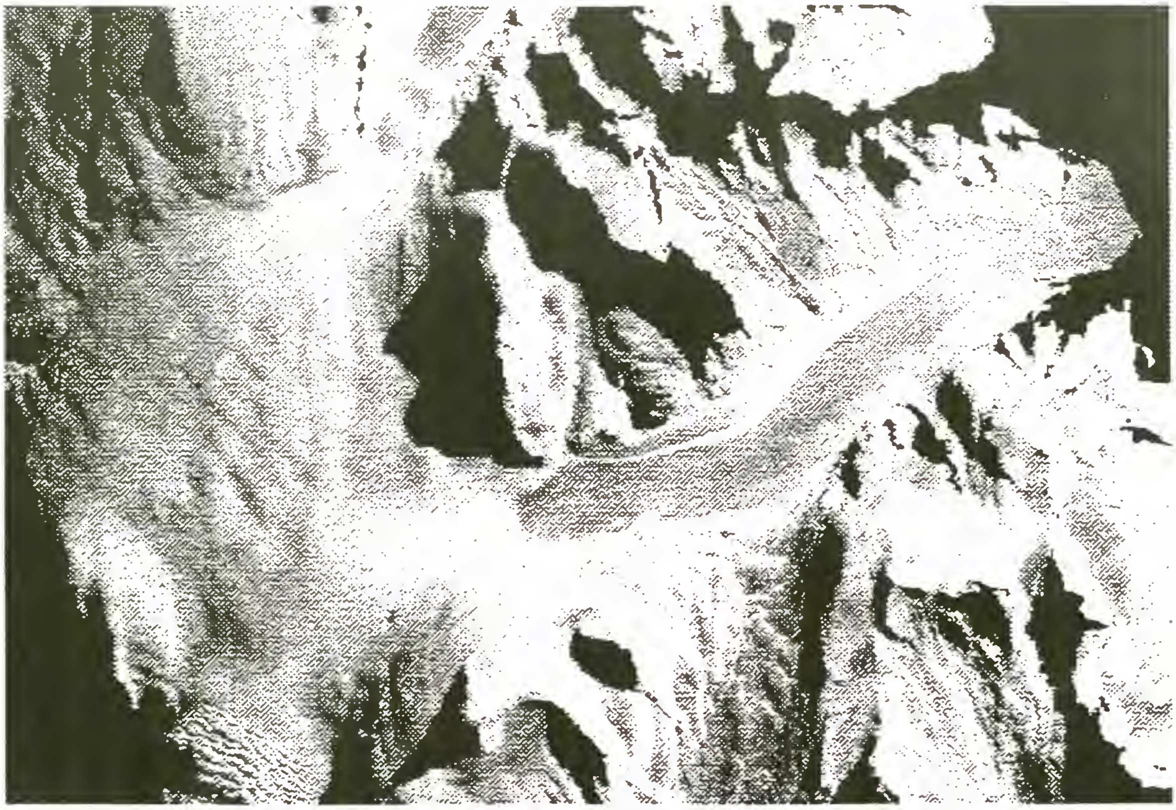

Figure 4: SAR magnitude image obtained by CCRS Convair-580

The Convair cross-track interferometric data was processed to a DEM using both the April and August data. They agreed to within 5 meters in most areas. The DEM is quite accurate because of the high SNR and resolution, and because the two interferometric channels are collected simultaneously. The DEM was produced in UTM coordinates, and can be used to create a perspective view of the SAR image, as shown in Figure 5.

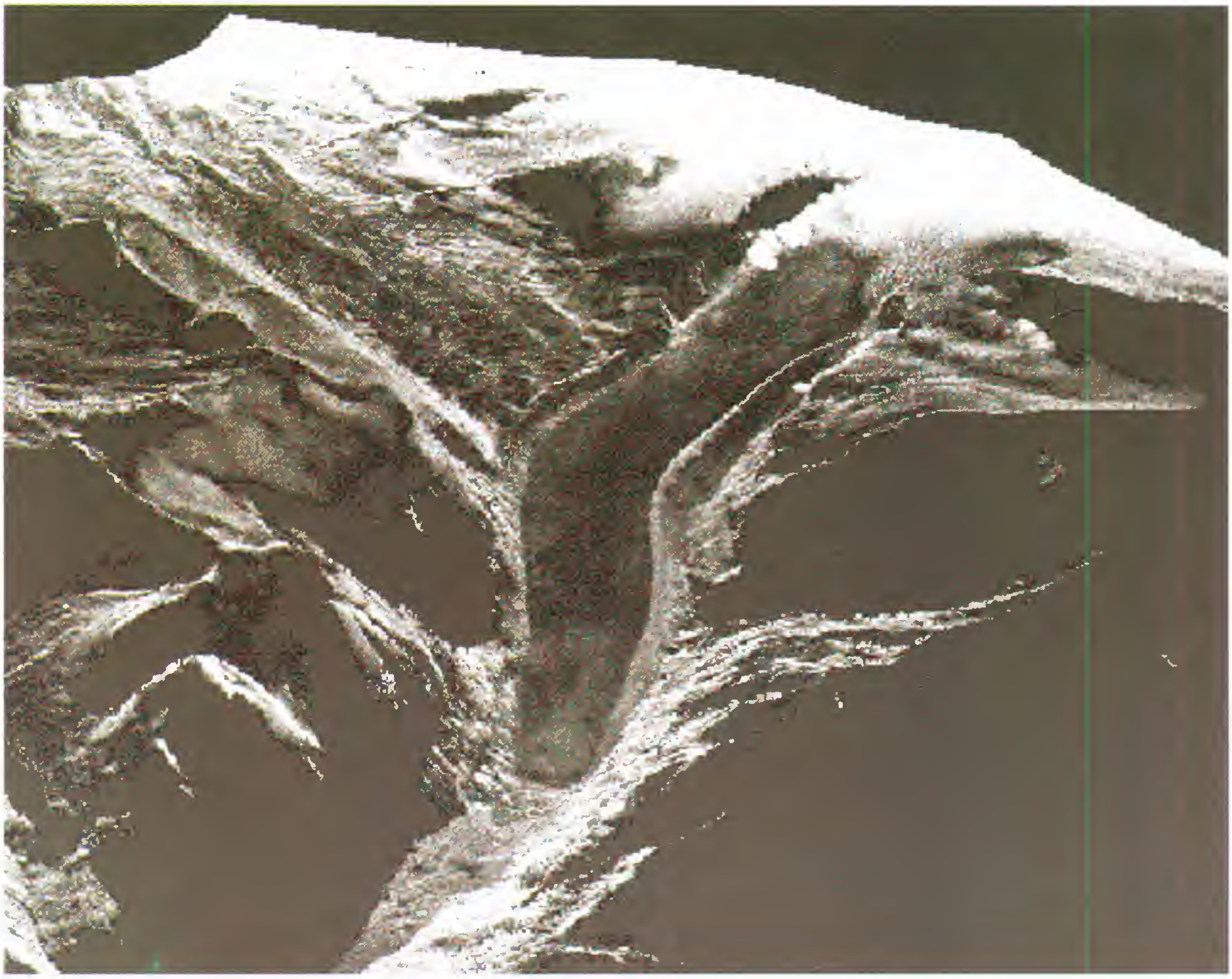

Figure 5: Perspective view of Saskatchewan Glacier from Convair DEM.

The DEM is mainly used to remove the topographic phase from the ERS interferogram. However, other parameters can be extracted from the DEM, which are subsequently used to project the ERS measured displacement along the glacier flow direction. These parameters include the height of the glacier, the surface slope and down-slope direction, all measured along the centreline. These parameters are shown in Figure 6.

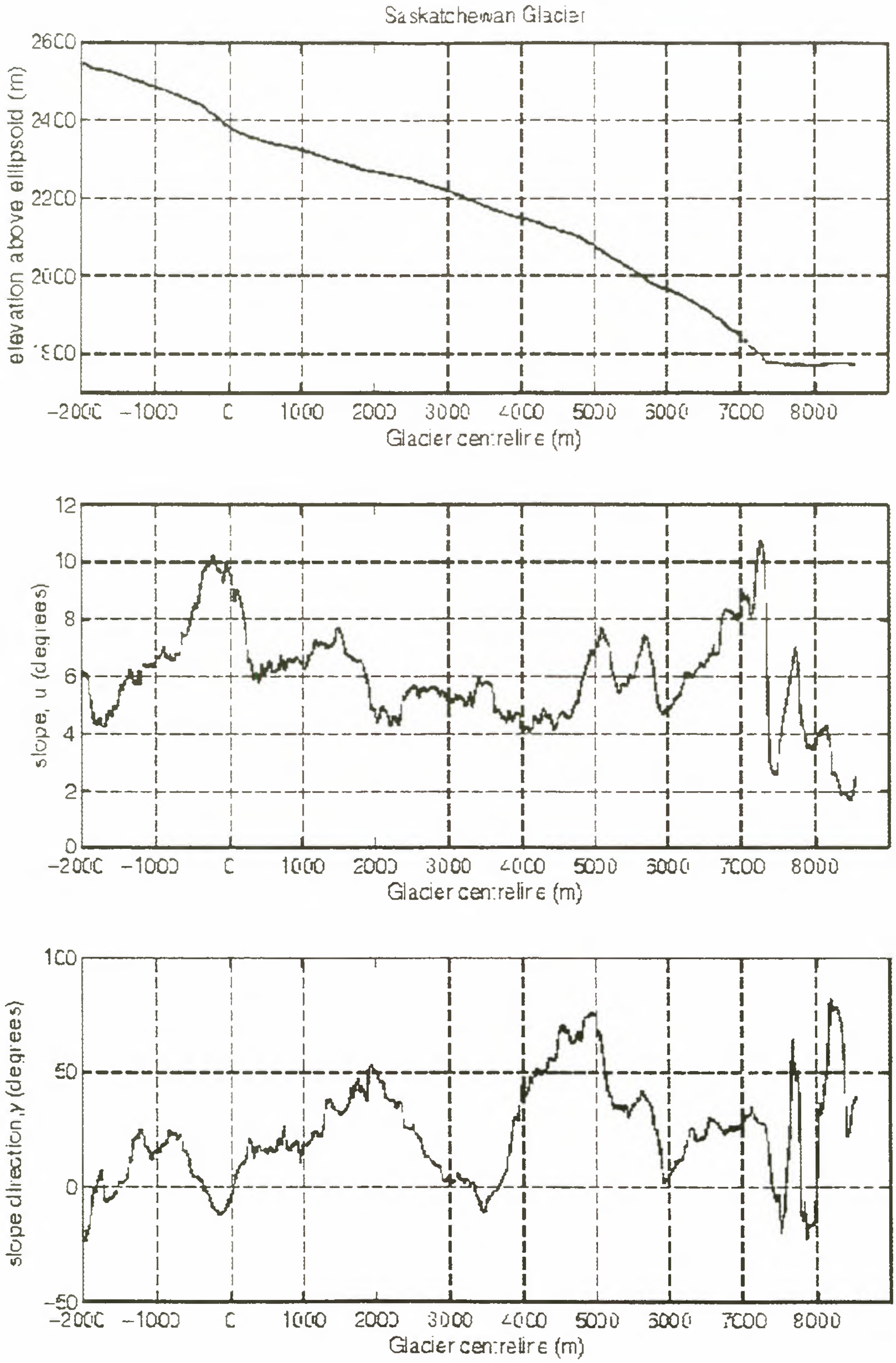

Figure 6: Glacier height, slope and flow direction from Convair data.

4.3 Removing Topographic Phase from the Interferogram

The Convair-580 DEM was resampled to the ERS slant range/azimuth grid, and used to compute the topographic phase that would be expected with the 94 meter baseline. The result is shown in Figure 7, where fringes due to the change in line-of-sight velocity are clearly seen. Most of the rocky areas adjacent to the glacier have the same phase, which can be assigned a zero motion value.

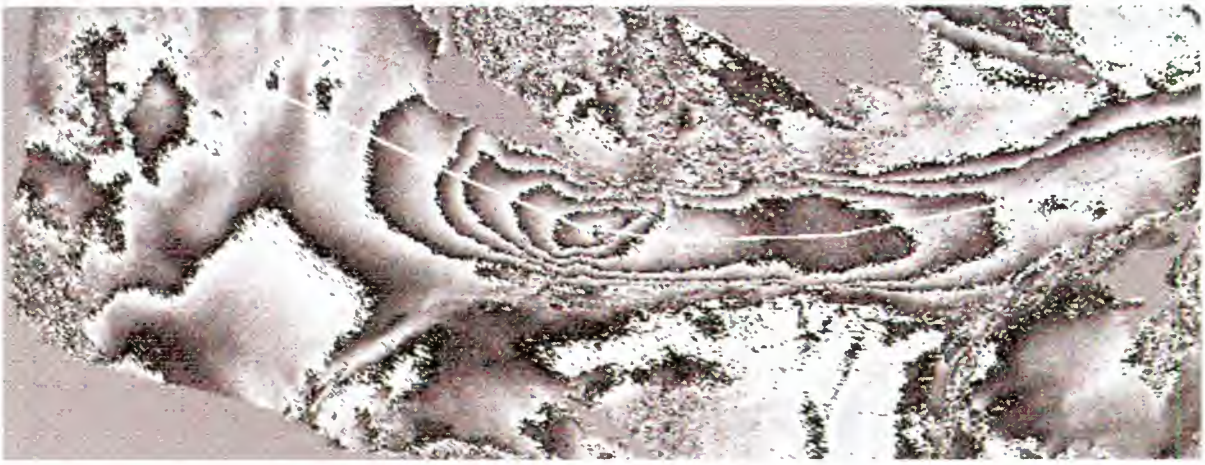

Figure 7: Interferogram phase after topographic phase removed.

5. Glacier Flow Measurements

In this section, we extract the glacier flow from the ERS SAR data, and compare it to flow measurements taken from surface readings.

5.1 InSAR Flow Measurements

A 200 meter strip of the ERS SAR data was chosen around the glacier centerline (the white line in Figure 7). The phase was smoothed in this region, then unwrapped. As each phase fringe represents 2.85 cm of motion parallel to the radar beam vector over the 1-day interval, a curve of line-of-sight (LOS) displacement could be plotted vs. the distance along the centreline.

However, our interest lies in measuring the surface velocity, so we must determine what surface velocity creates the measured LOS velocity. To do this, we make the assumption that the surface flow is parallel to the surface, in the direction of the maximum slope. Then, using a reverse projection, the LOS displacement values are converted into surface displacements.

To date, five Tandem Mission data pairs taken between November 1995 and April 1996 have been analyzed in this fashion, and the surface displacements in cm/day are plotted in Figure 8. Six other Tandem Mission data pairs taken during this interval had too low a coherence to give useful results [Vachon, 1996].

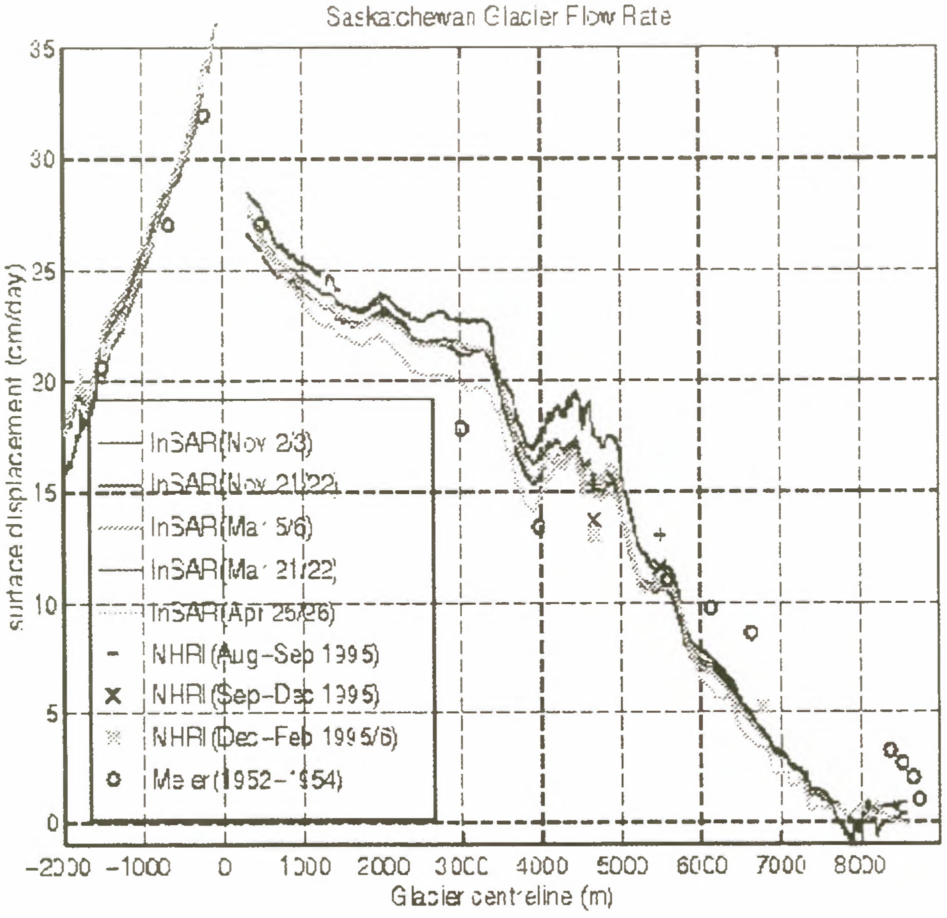

Figure 8: Glacier flow velocities from SAR data and ground measurements.

5.2 Ground Truth Measurements

Four sets of measurements were taken by NHRI between August 1995 and February 1996, yielding 3 sets of relative displacements drawn in Figure 8. These were done by drilling 3 poles into the ice, and using theodolites to measure their position accurately every month or two. The poles were insulated to minimize their melting into the ice.

Also shown in Figure 8 are measurement taken by Meier in the 1950s. They cover a larger area of the glacier, and are the average over a whole year of observations. Both these and the NHRI measurements included 3-dimensional displacement measurements, and confirmed that our assumption of flow direction was accurate to within a few degrees.

Weather readings logged every hour confirmed that the temperatures were always below freezing and no precipitation occurred on the 5 days that the high-coherence InSAR measurements were taken. Typical temperatures of the air and of the ice were between -1°C and -10°C for these 5 days [Vachon, 1996].

5.3 Discussion

First note that there is a remarkable consistency between the 5 sets of SAR measurements. The fine-scale structure is almost the same, and there is a gradual slowing down of the surface velocity, as would be expected as the ice cools down from the beginning to the end of the winter. This consistency leads us to believe that the SAR measurements are accurate to 1 or 2 cm/day, although some of the similarity of the fine-scale structure comes from the fact that the same projection direction was used in each of the 5 cases.

Second note that the agreement between the SAR and the ground measurements is very good -- in the order of 2 cm/day.

There are a number of errors in the SAR and the ground measurements, and in how they are compared, such as:

1.
2. Relative registration between the SAR and ground readings with respect to the horizontal axis of Figure 8.
3.
4. Different location and averaging methods between the readings.
5.
6. Time differences between the SAR and ground measurements.
7.
8. Assumption of glacier flow direction used in the SAR data projection.
9.
10. InSAR calibration and the choice of the zero velocity datum.
11.
12. Difference between the pole velocities (buried in the ice) and the ice surface from which the radar beam scatters.

We cannot fully quantify all these errors, but given the uncertainty caused by each of them, we are pleasantly surprised by the agreement between the SAR and ground readings.

6. Conclusions

We have obtained glacier surface motion measurements using differential interferometry analysis of ERS Tandem Mission data over an Alpine glacier in the Canadian Rocky Mountains. The 5 sets of SAR measurements show a remarkable consistency with each other, and there is good agreement with several sets of ground measurements taken around the same time.

Compared to the limited measurements taken by a ground survey crew, the SAR measurements cover the whole glacier surface (with roughly a 30 meter spacing), and can be obtained with modest incremental cost whenever the surface of the glacier is stable. Our limited experience suggest that winter conditions provide the best SAR observation conditions.

From this we can conclude that differential SAR interferometry is a useful tool for monitoring the surface motion of Alpine glaciers. We hope that glaciologists can make good use of this new instrument, and that it will improve the accuracy of their glacier modeling work.

7. Acknowledgements

The authors would like thank Dr. Mindy Brugman and her crew for taking the surface measurements on the glacier. The authors are also grateful to Mike Seymour of UBC's Radar Remote Sensing Group for providing the programs and advice for the interferometric processing.

Funding for this work was provided by the NSERC/MDA Industrial Research Chair in Radar Remote Sensing.

References

Vachon, P., D. Geudtner, K. Mattar, A. L. Gray, M. Brugman and I. G.Cumming
Differential SAR Interferometry Measurements of Athabasca and Saskatchewan Glacier Flow Rates, Canadian J.~of Remote Sensing, Accepted for publication, September 1996.

Joughin, Ian, 1995:
Estimation of Ice-Sheet Topography and Motion Using Interferometric Synthetic Aperture Radar. PhD thesis, University of Washington.

Solaas, G. A., 1994:
ERS-1 Interferometric Baseline Algorithm Verification. *Technical Report ES-TN-DPE-OM-GS02* Version 1.0, ESA. *http://gds.esrin.esa.it:80/CEFB565F/CORBITS.*

INSAR at ASF: Analysis of the 1993 Bering Glacier Surge

Dennis R. Fatland
Alaska SAR Facility, Geophysical Institute, University of Alaska, PO Box 757320, AK99775 7320 Fairbanks, USA
Rob.Fatland.fatland@arsc.edu

Abstract

This talk will begin with a brief discussion of the development of SAR interferometry at the Alaska SAR Facility (ASF) and will proceed to an analysis of interferometrically derived data on the Bering Glacier. The Bering Glacier and its associated accumulation area, the Bagley Ice Field, are located in South Central Alaska in the Chugach-St.Elias Mountains. Together they comprise the largest temperate valley glacier in North America.

Differential SAR interferometry is applied to the Bagley Ice Field prior to and after the onset of a major surge event in the spring of 1993 using data from the two ERS-1 Ice Phases (early in 1992 and 1994). Variations in surface elevation and surface ice velocity in the quiescent accumulation area upstream of the catastrophically disrupted surging region are discussed in the context of surge mass balance estimation. The flow directions in the region of interest tend to run roughly in the cross-track direction but conversion of line-of- sight displacement over three day repeat-pass intervals to surface velocity vector fields is neverthe less problematical.

Attention is also given to the difficulties in analyzing low-coherence signals from temperate-climate glacier surface ice near the Gulf Coast of Alaska. Despite these obstacles, interferometry is providing high-resolution data input to the general problem of understanding the dynamic nature of this glacier system.

SAR interferometry over Rutford Ice Stream and Carlson Inlet, Antarctica

R. Frolich British Antarctic Survey, Madingley Road, Cambridge, CB3 0ET, UK
r.frolich@bas.ac.uk

Ch. Doake British Antarctic Survey, Madingley Road, Cambridge, CB3 0ET, UK
c.doake@bas.ac.uk

Abstract

An interferogram is formed from two sets of ERS-1 SAR SLC images acquired six days apart over Rutford Ice Stream, Antarctica. Ground surveys carried out in the area over the last 15 years provide more than 100 tie-points with which to optimise the interferometric baseline. Where flow is approximately along levelled lines between tie-points, the vertical component of ice movement is estimated by assuming that flow is parallel to appropriately averaged surface slopes. Non-independent tie-point errors are dealt with by constructing a variance-covariance matrix for the expected values of the unwrapped interferometric phases at the tie-points. When the weighted residual variance is minimised, RMS tie-point residuals of less than 1 cm are obtained. These can be attributed to a combination of interferometric phase noise, movement survey errors and inadequate slope information.
The pattern and size of the residuals suggest no changes in ice movement between 1978 and 1992. The upper 50 km of Carlson Inlet are confirmed to flow at less than a tenth of the speed of the neighbouring Rutford Ice Stream. The entry of faster moving ice into the lower reaches of Carlson Inlet and the position of part of the Carlson Inlet grounding line are confirmed.

Keywords: Glaciology, Rutford Ice Stream, Antarctica, slope, tie-points, residuals

Glacier flow measurements in Spitsbergen, Svalbard, from differential interferometry

Bernard Lefauconnier Norsk Polarinstitutt, Oslo
Laboratoire de Glaciologie, Grenoble

Geir Anker Norsk Polarinstitutt, Oslo

Marc Rossi CNES, Toulouse

Abstract

The work was supported by the ESA under a contract with Matra CS.

Interferometric pairs have been obtained at CNES from a combination of 3 ERS-1 scenes recorded over the alpine relief of the north eastern Spitsbergen at the end of the ablation period in September and October 1991. The Norwegian Polar Institute provided a DEM based on maps at a scale of 1/100 000 and constructed from air photographs. Two differential interferogrammes have then been obtained by removing the fringes due to elevation and orbital trajectories. The residual fringes are due to ice movements over 6 and 9 days respectively and a third interferogramme over 3 days was obtained by difference of the two previous one. The result provides number of glaciological information and the possibility to determine the ice flow velocity over a number of glaciers.

I: Exemple of general information obtained from fringe morphology: a) precise determination of ice-divides and information about the relief of the subglacial bedrock; b) in many case, deduction of the main flow line; c) detection of stagnant or near stagnant ice; d) concentric and elongated fringes indicate an increasing then a decreasing ice velocity along the glacier basin. The phenomena occurred when a tributary join a glacier with a lesser ice velocity and may also be linked to the topography. On valley glaciers ending on land such fringes reflect also the subpolar nature of the glacier with a cold and near stagnant ice overlying the permafrost at the front, leading the decrease in velocity; c1) the altitude of the higher velocity (and of the center of the concentric fringes) is a relevant information about the glacier. As an exemple, the altitude of this point on two neighbouring glaciers, the "D'arod" glacier and the "Quatorze juillet" glacier is 350 and 500 m a.s.l. respectively; c2) the relative wideness of the fringes indicate that there are various velocity transverse profiles among glaciers as well as along a given glacier.

II: Ice velocities over number of glaciers: a) as exemples, the two above mentioned "D'arod" and "Quatorze juillet" glaciers flowing almost facing the satellite track, reach a maximum velocity of 56 mm and 66 mm per day. Such velocities are within the range of velocities expected from similar Svalbard glaciers; b) a differential velocity equivalent to 150 per year over 8 kilometers on the Monaco glacier seems to confirm the detection (from a previous work on coherence) of the early phase of a surge which was actually observed one year later. c) clear fringes are present all over the Holtedahlfonna, one plateau feeding the Kronebreen, the most active and calving glacier in Svalbard. These fringes allow to monitor the ice flow over the main part of the basin. Along the main flow line, the velocity increase from 15,6 cm per day at 29 km to the front in the main accumulation plateau to 28,5 cm per day at 22 km to the front and to 55,7 cm per day at 15 km to the front. Then, there are no visible fringes and lack of coherence (from there to the front are large crevasses and high velocity). Previous work indicates a mean annual velocity of 2 m per day at the front, the obtained velocity is then coherent with the ice velocity at the front and provides essential information about the ice dynamics and the balance of the glacier. In order to validate the result, three stakes were settled in the basin in May 1996, the coordinates were recorded by GPS technique. The positions will be recorded again this autumn and during the next spring season.

Achache J
B.R.G.M.
B.P. 6009
Orleans Cedex
45060 France

Adragna F
CNES
Image Processing
18 Av Edouard Belin
Toulouse Cedex
31055 France

Ahmed S
Canadian Space Agency
6767 Route de L'Aéroport
St Hubert
Quebec
J3Y 8Y9 Canada

Amelung F
Inst. de Physique du
Globe
5 Rue Descartes
Strasbourg
67084 France

Archambault F
Aerospatiale SE/TNA
BP 99
Cannes La Bocca Cedex
6322 France

Arndt C
University Siegen
Centre for Sensor Systems
Paul Bonatz Strasse 9-11
Siegen
57068 Germany

Askne J.
Chalmers Univ.Technology
Radio & Space Science
Rannvagen 6
Goteborg
S-412 96 Sweden

Attema E
ESA/ESTEC
Keplerlaan 1
Noordwijk
2200 AG Netherlands

Baker J
BNSC
Monks Wood
Abbots Ripton
Huntington, Cambridgeshire
PE17 2ls UK

Bally P
Spot Image
5, Rue des Satellites
BP 4359
Toulouse
31030 France

Baltuck M
NASA, Code YSG
Oceans, Solid Earth &
Natural Hazards
Washington D.C.
20546 USA

Bamber J L
University of Bristol
Centre for Remote Sensing
University Road
Bristol
BS8 1SS UK

Bamler R
DLR-DFD
Postfach 1116
Oberpfaffenhofen
82234 Germany

Barbier C
CSL
Universite De Liege
Parc Scientifique Sart
Tilman
Av. Du Pre Aily
B4031 Angleur-Liege
Belgium

Bartmettler A
University Of Zurich
Inst. Geographique
Winterthurerststs. 190
Zurich
8057 Switzerland

Beaudoin A
LCT
CEMAGREF/ENGREF
500 Rue J-F. Breton
Montpellier
34093 France

Boalch C
BNSC
Bridge Place
88/89 Eccleston Square
London
SW1V 1PT UK

Boerner T
DLR Oberpfaffenhoffen
Institut fur
Hochfrequenztechnik
Wessling
82230 Germany

Borgeaud M
ESA/ESTEC
Keperlaan 1
Noordwijk
2200 AG Netherlands

Bruzzi S
ESA
8-10 Rue Mario Nikis
Paris Cedex 15
75738 France

Buck C
ESA/ESTEC
Keplerlaan 1
Noordwijk
2200 AG Netherlands

Buhrke T
Wittelsbacher Allee 19
Leimen
69181 Germany

Capes R
The NPA Group
1, Fircroft Way
Edenbridge
Kent
TN8 6MS UK

Carballo G
Facultad De Ingenieria -
Centro De Calculo
Julio Herrera Y Reissig 565
Montevideo
11300 Uruguay

Carnec C
BRGM
Geophysics and Geological
Imagery
3, Avenue C Guillemin
Orleans Cedex 2
45060 France

Carrasco D
UPC, Signal Theory and
Communications dpt.
EEF Group
Gran Capitan sn - Campus
Nord UPC D3, Barcelona
08034 Spain

Carron B
Matra CAP Systemes
Lab. de Traitement des
Images et du Signal
6, Rue Dewoitine
Velizy Villacoublay
78142 France

Castillo M
Institut Cartografic de
Catalunya
Parc de Montjuic s.n.
Barcelona
08037 Spain

Chen D.K.S
National Central University
Centre for Space and
Remote Sensing Research
Chung-Li
32054 Taiwan, R.O.C.

Coelho C
Elsag Bailey
Via G Puccini 2
Genova
016154 Italy

Coren F
Osservatorio Geofisico
Sperimentale Ogs
PO Box 2011
Trieste
034016 Italy

Corr D
DRA, Space Dept, Remote
Sensing
Room 107A, R16 Bldg
DRA Farnborough
Hampshire
GU14 6TD UK

Costantini M
ESA/ESRIN
Via Galileo Galilei
CP 64
Frascati
I-00044 Italy

Coulson S
ESA/ESRIN
Via Galileo Galilei
CP 64
Frascati
I-00044 Italy

Crosetto M
DIIAR
Politecnico di Milano
Sez. Rilevamento
P. Leonardo da Vinci 32
Milano
20133 Italy

Cross A
European Commission
200, Rue de la Loi
Brussels
1047 Belgium

Curkendall D
JPL
4800 oak Grove Drive
Pasadena
California
91109 USA

Curlander J
Vexcel Corporation
Image Information
Engineering
2477 55th Street
Suite 201
Boulder, CO
80301-5703 USA

Dammert P
Chalmers Univ.Technology
Radio & Space Science
Rannvagen 6
Goteborg
S-412 96 Sweden

Datcu M
DLR-DFD
Algorithms and Methods
Wessling/Obb
D 82234 Germany

Dautrebande S
Unite D'Hydroulique
Agricole
Passage Des Deportes, 2
Gembloux
5030 Belgium

De Chabalier J-B
Institut De Physique Du
Globe De Paris
Equipe de Simotectonique
4 Place Jussieu
Paris Cedex 05
75252 France

De Groof H
Joint Research Centre
Remote Sensing
Ispra
21020 Italy

Delacourt C
Institut de Physique du
Globe de Paris
CEA
4 Place Jussieu
Paris Cedex 05
75252 France

Derauw D
Centre Spatial De Liege
Parc Scientifique Sart
Tilman
Av. Du Pre Aily
Angleur-Liege
4031 Belgium

Desnos Y-L
ESA/ESTEC
Envisat Project
Keplerlaan 1
Noordwijk
2200 AG Netherlands

Doake C
British Antarctic Survey
Madingley Road
Cambridge
CB3 0ET UK

Duchossois G
ESA
8-13 rue Mario Nikis
Paris Cedex 15
75738 France

Eichenherr H
Dornier Gmbh
RSX(M)233
1420 Friedrichshafen
88039 Germany

Eineder M
DLR
Wessling
82234 Germany

Ekholm S
National Survey and
Cadastre
Rentemestervej 8
Copenhagen Nv
2400 Denmark

Eldhuset K
FFI
PO Box 25
Kjeller
2007 Norway

Emiliani L
ESA
8-13 rue Mario Nikis
Paris Cedex 15
75738 France

Evans D
JPL
180-703 Pasadena
California
91109 USA

Faller Nick
Dornier Gmbh
RSX(M)233
1420
Friedrichshafen
88039 Germany

Fanelli A
Univ. degli Studi di Napoli
Dip di Scienza e Ingegneria
dello Spazio
P.le V Tecchio 80
Naples
80125 Italy

Farr T
JPL
MS 300-232
Pasadena, CA
91108 USA

Fatland R
Alaska Sar Facility
Geophysical Institute
University Of Alaska
PO Box 757320
Fairbanks, Alaska
99775-7320 USA

Fellah K
SERTIT
Bld. Sebastien Brandt
Illkirch
67400 France

Fernandes D
DLR, Inst. fur
Hochfrequenztechnik
Postfach 1116
Wessling
D82230 Germany

Ferretti A
Politecnico/DEI
Piazza L da Vinci, 32
Milano
20133 Italy

Floury N
CESB, CNES-CNRS
Universite Paul Sabatier
18 Ave. E Belin
Toulouse Cedex 4
31401 France

Franceschetti G
Universita' degli Studi Di
Napoli Federico II
D. di Ingegneria elettronica
Via Claudio 21
Napoli
80125 Italy

Friehl M
Institut fur Photogrammetrie
und Kartographie
Petersenstrasse 13
Darmstadt
61287 Germany

Frolich R
British Antarctic Survey
Madingley Road
Cambridge
CB3 0ET UK

Fruneau B
Inst. de Physique du Globe
Dept. Etudes Spatiales
4 Place Jussieu
Paris Cedex 05
75252 France

Fueglistaler S
University of Zurich
RSL
Winterthurerstrasse 190
Zurich
8057 Swizterland

Gens R
ITC
350 Boulevard 1945
Enschede
NL7500 Netherlands

Goze S
Alcatel Espace
26 Ave. JF Champollion
Toulouse Cedex
31037 France

Guerre L F
SPOT IMAGE
5, Rue des Satellies
Toulouse Cedex
31030 France

Guignard JP
ESA/ESRIN
Via Galileo Galilei
CP 64
Frascati
00044 Italy

Guo H
Institute of Remote Sensing
Applicaitons
Chinese Academy of
Sciences
PO Box 9718
Beijing
100101 China

Haefner H
University of Zurich
Dept. of Geography
Winterthurerstrasse 190
Zurich
8057 Swizterland

Hagedorn J
Dept. Physical Geography
University of Gottingen
Goldschmidtstr 5
Gottingen
37077 Germany

Hagg W
Inst. of Photogrammetry and
Remote Sensing
Karlsruhe University
Englerstr. 7
Karlsruhe
D 76128 Germany

Hall J
Geological Survey of Israel
Marine Geology, Mapping
and Tectonics Division
30 Malchei Israel Street
Jerusalem
95501 Israel

Hallikainen M
Helsinki University of
Technology
Lab. of Space Technology
Otakaari 5 A
Espoo
SF-02150 Finland

Hamazaki T
NASDA
1-29-6, Hamamasucho
Minato-ku
Tokyo
105 Japan

Hanssen R
D.U.T., Faculty Of
Geodetic Engineering
Thijsseweg 11
Delft
2629 JA Netherlands

Hartmann R
Daimler Benz Aerospace
Prussingstrasse 41
Jena
7745 Germany

Hellmann M
DLR, Institute for Radio
Frequency
PO Box 1116
Wessling
82230 Germany

Hellwich O
Technical Univ. Munich
Photogrammetry and
Remote Sensing
Arcisstr. 21
Munich
80290 Germany

Herland E
Tech. Research Centre of
Finland, VTT Automation
Space Technology
P.O.Box 13031
02044 Finland

Herrmann J
Dornier Satellitensysteme
Friedrichshafen 1420
88039 Germany

Hirtz P
University of Zurich, RSL
Winterthurerstrasse 190
Zurich
8057 Swizterland

Hobbs S
Cranfield University
College Of Aeronautics
Cranfield, Bedford
MK43 OAL UK

Hochschild V
Lehrstuhl Geoinformatik,
Geohydrologie und
Modellierung
Friedrich-Schiller Univ.
Lobderraben 32
Jena, 7743 Germany

Hoekman D
Dept Of Water Resources
Nieuwe Kanaal 11
Wageningen
6709 PA Netherlands

Holcomb D
ERDAS
2801 Buford Hwy
Atlanta, GA
30329 USA

Holecz F
University of Zurich, RSL
Winterthurerstrasse 190
Zurich
8057 Swizterland

Howes S
ESYS
Berkeley House
London Square Cross Lanes
Guildford, Surrey
GU1 1UE UK

Huang Y
ITC
350 Boulevard 1945
Enschede
7500 Netherlands

Hurlemann P
Dept. Physica Geography
University Of Gottingen
Goldschmidtstr 5
Gottingen
37077 Germany

Husxy P O
Kongsberg
Informasjonskontroll
Hvamstubben 17
Skjetten
2013 Norway

Hyyppa J
Helsinki University Of
Technology
Lab Of Space Technology
Otakaari 5a
02150 Espoo Finland

Isola L
Elsag Bailey
Via G Puccini 2
Genova
16154 Italy

Isono K
Remote Sensing Tech.
Roppongi First Bldg. 8F
1-9-9 Roppongi
Minatok-Ku, Tokyo
106 Japan

Itten K
University of Zurich
RSL
Winterthurerstrasse 190
Zurich
8057 Swizterland

Kenyi L
Inst. For Digital Image
Processing
Wastiangasse 6
Graz
8010 Austria

Kervyn F
Musee Royal de l'Afrique
Centrale
13 Leuvensesteenweg
Tervuren
3080 Belgium

Khokhlachov V
Centre of Aerospace
Research of the Earth
National Aerospace Agency
55-6 Chekalov str.
Kiev GSP
252601 Ukraine

King C
BRGM
Dept. Geophysique et
Imagerie Geologique
BP6009
Orleans Cedex 2
45060 France

Klees R
DUT
Geodetic Engineering
Thesseweg 11
Delft
2629 TT Netherlands

Koethe R
Dept. Physica Geography
University Of Gottingen
Goldschmidtstr 5
Gottingen
37077 Germany

Kohlhammer G
ESA/ESRIN
Via Galileo Galieli
Frascati
00044 Italy

Kosmann D
DLR DFD
Muenchenerstr. 20
Wessling
82230 Germany

Kraemer R
University Siegen
Center for Sensor Systems
Paul Bonatz Strasse 9-11
Siegen
57068 Germany

Langham E
Canadian Space Agnecy
RADARSAT I Programme
6767 Toute de l'Airopor
St Hubert, Quebec
J3Y 8Y9 Canada

Laur H
ESA/ESRIN
Via Galileo Galieli
Frascati
00044 Italy

Lawrence G
Treic
46 Pondcroft Rd
Knebworkth
SG2 6DB UK

Lefauconnier B
Norsk Polarinstitut
Middelthuns gate 29
P O Box 5072,
Majorstua, Oslo
N-0301 Norway

LeToan T
CESB-CNES-CNRS
Université Paul Sabatier
18 Ave. E Belin
Toulouse Cedex 4
31401 France

Li H
Institute of Geodesy and
Photogrammetry, ETH
Zurich
8093 Switzerland

Lichtenegger J
ESA/ESRIN
Via Galileo Galieli
Frascati
00044 Italy

Loffeld O
University Siegen
Center for Sensor Systems
Paul Bonatz Strasse 9-11
Siegen
57068 Germany

Lopinto E
Nuova Telespazio
PO Box 155
Matera
Italy

Luca D
ETH Zuerich
Comm. Technology Lab
Gloriastr. 35
Zurich
8092 Switzerland

Luckman A
BNSC
Monks Wood
Abbots Ripton
Huntington, Cambridgeshire
PE17 2LS UK

Mandanayake A
University College London
Dept. of Photogrammetry
and Surveying
Gower Street
London
WC1E 6BT UK

Marinelli L
GEOIMAGE
Les Espaces de Sophia
80, Route des Lucioles
Sophia Antipolis
6560 France

Martin P
ESA
8-10 Rue Mario Nikis
Paris Cedex 15
75738 France

Martinez A
Indra Espacio
C/Mar Egeo S/N
S Fernando De Hanares
Madrid
28830 Spain

Marzo C
Agenzia Spaziale Italiana
Centro de Geodesia
Spaziale 'G Colombo'
Matera
75100 Italy

Massonet D
CNES
Image Processing
18 Av Edouard Belin
Toulouse Cedex
31055 France

Meier E
University of Zurich
RSL
Winterthurerstrasse 190
Zurich
8057 Swizterland

Meuret P
University of Zurich
RSL
Winterthurerstrasse 190
Zurich
8057 Switzerland

Mica S
Advanced Computer
Systems
Via Belli 23
Frascati
00044 Italy

Moccia A
Universita Di Napoli
Facolta Di Ingegneria
P.Le Le Tecchio 80
Napoli
80125 Italy

Mohr J
Dept of Electromagnetic
Systems
Technical University of
Denmark
Lyngby
2800 Denmark

Molander S
SSc Satellitbild
Product Development Dept
PO box 816
Kiruna
S 981 28 Sweden

Monson R
NASA, Code YF
Washington DC
20546-0001 USA

Monti Guarnieri A
Politechnico di Milano
Pzza. L. Da Vinci 32
Milano
20133 Italy

Morley J
University College London
Dept. of Photogrammetry
and Surveying
Gower Street
London
WC1E 6BT UK

Mouchot M-C
Dept Image et Traitement
de l'Information
ENSTB
BP 832, Brest Cedex
29285 France

Muller J-P
University College London
Dept. of Photogrammetry
and Surveying
Gower Street
London
WC1E 6BT UK

Noack W
DLR-DFD
Postfach 1116
Oberpfaffenhofen
82234 Germany

Nonin P
ISTAR, E. Beethoven Bat 2
Route des Lucioles
Sophia Antipolis
6560 France

Nuesch D
University Of Zurich
Inst. Geographique
Winterthurersts. 190
Zurich
8057 Switzerland

Ostir K
Scientific Research Centre
Slovenian Academy Of
Sciences & Arts
Gosposka 13
Ljubljana
61000 Slovenia

Papathanassiou K
DLR Oberpfaffenhofen
Institut fur
Hochfrequenztechnik
Postfach 1116
Wessling
82230 Germany

Parcharidis I
Earthquake Planning and
Protection Org.
32 Xanthou
N. Psychiko
Athens
15451 Greece

Pasquali P
University of Zurich
RSL
Winterthurerstrasse 190
Zurich
8057 Swizterland

Pattyn F
Department of Geography
Vrije Universiteit Brussel
Pleinlaan 2
Brussels
1050 Belgium

Peltzer G
JPL
MS 183
4800 Oak Grove Drive
Pasadena, CA
91109 USA

Perlant
Matra CAP Systemes
Lab. de Traitement des
Images et du Signal
6, Rue Dewoitine
Velizy Villacoublay
78142 France

Piau P
Alcatel Espace
26 Ave. JF Champollion
Toulouse
31037 France

Piesbergen J
University of Zurich
RSL
Winterthurerstrasse 190
Zurich
8057 Switzerland

Pirchl P
University of Zurich
RSL
Winterthurerstrasse 190
Zurich
8057 Switzerland

Poehler P
SAIC
700 S. Babcock St
Suite 300
Melbourne, FL
USA

Polidori L
Aerospatiale SE/TNA
BP 99
Cannes La Bocca Cedex
6322 France

Prati C
Politecnico/DEI
Piazza L da Vinci, 32
Milano
20133 Italy

Press N
NPA Group
Edenbridge
Kent
TN8 65R UK

Raggam H
Inst. For Digital Image
Processing
Wastiangasse 6
Graz
8010 Austria

Ramella P
Elsag Bailey
Via G Puccini 2
Genova
16154 Italy

Raymond D
Universite M & P Curie
Dept. De Geotectonique
Tour 26-16 Etage 1
4 Place Jussieu
Paris
75005 France

Reich M
University Of Stuttgart
Institut For Navigation
Keplerstrasse 11
Stuttgart
70174 Germany

Reigber A
DLR Oberpfaffenhofen
Institut fur
Hochfrequenztechnik
Postfach 1116
Wessling
82230 Germany

Reigber Ch.
Geoforschungs Zentrum
GFZ
Telegrafenberg 17a
60 07 51
Postdam
14473 Germany

Rignot E
JPL
4800 Oak Grove Drive
Pasadena, CA
91109 USA

Ritter P
DARA
Koenigswinterer Str. 524
Bonn
53227 Germany

Rocca F
Politecnico/DEI
Piazza L da Vinci, 32
Milano
20133 Italy

Rogers C
Matra Marconi Space UK
Ltd
Anchorage Road
Portsmouth
PO3 5PU UK

Rosich B
ESA/ESRIN
Via Galileo Galieli
Frascati
00044 Italy

Roth A
DLR-DFD
Postfach 1116
Oberpfaffenhofen
82234 Germany

Rott H
University Of Innsbruck
I.Fuer Meteo. Und Geoph.
Innrain 52
Innsbruck
6020 Austria

Rouze M
CNES
18, Ave Edouard Belin
Toulouse Cedex
31055 France

Rowan E
University Of Dundee
Dundee
DD1 4HN UK

Rudant J-P
Université P&M Curie
Dept. De Geotectonique
Tour 26-16 Etage 1
4 Place Jussieu
Paris
75005 France

Rufini G
Univ. degli Studi di Napoli
Scienza e Ingegneria dello
Spazio
Piazzale Tecchio, 80
Naples
80125 Italy

Runge H
DLR-DFD
Postfach 1116
Oberpfaffenhofen
82234 Germany

Salamonowicz P
Defence Mapping Agency
8613 Lee Highway
Fairfax, VA
22031-2197 USA

Schepp H
Dept. Physical Geography
University Of Gottingen
Goldschmidtstr 5
Gottingen
37077 Germany

Scheuchl B
University of Innsbruck
I.Fuer Meteo. und Geoph.
Innrain 52,
Innsbruck
6020 Austria

Schieche B
University of Gottingen
Dept. Physica Geography
Goldschmidtstr 5
Gottingen
37077 Germany

Schmid H
University Of Zurich
Winterthurersts. 190
Zurich
8057 Switzerland

Schmidt J
University of Stuttgart
Keplerstrasse 11
Stuttgart
70174 Germany

Schreiber B
Oerlikon Contraves Space
Schafhauserstrass 580
Zurich
8052 Switzerland

Schumann R
Asian Institute of
Technology
STAR Programme
GPO Box 2754
Bangkok
10501 Thailand

Schwaebisch M
DLR-DFD
Oberpfaffenhofen
82230 Germany

Seidel K
Bildwissenschaft ETHZ
Gloriastr. 35
Zurich
8092 Switzerland

Seifert F M
DLR Oberpfaffenhofen
Institut fur
Hochfrequenztechnik
PO Box 1116
Wessling
82230 Germany

Seymour M
Univ. of British Columbia
Department of Electrical
Engineering
2356 Main Mall
Vancouver
V6T 1Z4 Canada

Siegel A
University of Innsbruck
I.Fuer Meteo. und Geoph.
Innrain 52
Innsbruck
6020 Austria

Sievers J
IFAG
Rich.-Strauss-Allee 11
Frankfurt Am Main 70
6000 Germany

Singh K
Centre for Remote Imaging,
Sensing and Processing
National Univ. of Singapore
Lower Kent Ridge Road
119260 Singapore

Slater J
ADAS Cambridge
Brookalnds Ave
Cambridge
CB2 2BL UK

Small D
University of Zurich
Inst. Geographique
Winterthurersts. 190
Zurich
8057 Switzerland

Smits P
DIBE
University Of Genoa
11a, Via All'Opera Pia
Genova
16145 Italy

Solaas G
ESA/ESRIN
Via Galileo Galilei
Frascati
I-00044 Italy

Spoerri S
University of Zurich
RSL
Winterthurerstrasse 190
Zurich
8057 Swizterland

Sponemann J
Dept. Physica Geography
University Of Gottingen
Goldschmidtstr 5
Gottingen
Germany

Stebler O
University Of Zurich
Inst. Geographique
Winterthurersts. 190
Zurich
8057 Switzerland

Stow R
Doncaster College
Waterdale
Doncaster
DN1 3EX UK

Streck C
Kayser-Threse Gmbh
Environmental Monitoring
Wolfratshouser Str. 48
Munich
81379 Germany

Stroobants W
ETCA/CTME/GIS/CEGN
16 bis Ave. Prieur de la
Code d'Or
Arcueil
94114 France

Stussi N
Centre for Remote Imaging,
Sensing and Processing
Univ. of Singapore
Lower Kent Ridge Road
119260 Singapore

Suter M
RSL
University of Zurich
Winterthurerstr. 190
Zurich
8057 Switzerland

Sutherland D
Adas Cambridge
Brooklands Ave
Cambridge
CB2 2BL UK

Sylos Labini G
Planetek Italia srl
c/o Tecnopolis
Valenzano, Bari
7010 Italy

Tannous I
SYSECA
66 Ave P Brossolette
Malakoff Cedex
92247 France

Tarayre H
ONERA
DES/STD/IM
29 Ave De La Division
Leclerc
Chatillon
92322 France

Tarchi M
JRC European Commission
Via E Fermi
Ispra
Varese
20120 Italy

Theilen-Willige B
University of Harlsiuhe
Birkenweg 2
Stockach
78333 Germany

Thiel K-H
Universitat Stuttgart
Inst. Fur Navigation
Keplerstr. 11
Stuttgart
70174 Germany

Timmen L
Geoforschungs Zentrum
Kinematics and Dynamics
of the Earth, Section 1.5
Telegrafenberg 17a
Postdam
14473 Germany

Trouve E
E.N.S.T.
Dep Images
46 rue Barrault
Paris
75013 France

Ulander L
Defense Research
Establishment
CARABAS Laboratory
P.O. Box 1165
Linkvping
581 11 Sweden

Unggul Prakoso K
Wageningen Agricultural
University
Department of Water
Resources
Nieuwe Kanaal 11
Wageningen
6709 PA Netherlands

Unwin B
Mullard Space Science Lab
University College London
Holmbury St Mary
Dorking, Surrey
RH5 6NT UK

Upton M
University College London
Dept. of Photogrammetry
and Surveying
Gower Street
London
WC1E 6BT UK

Usai S
DUT, Faculty of Geodetic
Engineering
Thijsseweg 11
Delft
2629 JA Netherlands

Valero JL
Western European Union
Satellite Centre
Apd. Correos 511
Madrid
28850 Spain

Van Der Kooij M
Atlantis Scientific Systems
1827 Woodward Drive
Ottawa, Ontario
K2C OP9 Canada

Van Genderen J
Dept of Earth Resources
Surveys, ITC
PO Box 6, Enschede
7400 AA Netherlands

van Halsema E
TNO, Physics and
Electronics Laboratory
PO Box 96864
The Hague
2509 JG Netherlands

Van Zyl J
JPL
180-703
Pasadena, CA
91109 USA

Varekamp C
Dept. of Water Resources
Nieuwe Kanaal 11
Wageningen
6709 PA Netherlands

Verbauwhede M
SSTC/DWTC
Spatial Ruimtevaart
8 Rue De La Science
Wetenschapsstraat, 8
Brussels
1000 Belgium

Vernazza G.
DIBE
University Of Genoa
11a, Via All'Opera Pia
Genova
16145 Italy

Vita-Finzi C
University College London
Geological Sciences
Gower Street
London
WC1E 6BT UK

Voelker M
Dornier Gmbh
RSX(M)233
1420
Friedrichshafen
88039 Germany

Voulfson L
Natl. Academy of Sciences
Centre of Aerospace
Research of the Earth
National Aerospace Agency
55-6 Chekalov str.
Kiev GSP
252601 Ukraine

Wahl M
DARA
Koenigswinterer Str. 524
Bonn
Germany

Wakabayachi H
NASDA
Earth Ob. Satellite Group
1-29-6 Hamamatsu-cho
Minato-ku
Tokyo
105 Japan

Wang C-T
National Central University
Centre for Space and
Remote Sensing Research
Chung-Li
32054 Taiwan, R.O.C.

Wegmuller U
Gamma Remote Sensing
Thunstrasse 120
Muri B
Bern
3074 Switzerland

Wehr A
Universitat Stuttgart
Inst. Fur Navigation
Keplerstr. 11
Stuttgart
70174 Germany

Wensink G.J.
ARGOSS
P.O. 61
Vollenhove
8325 Netherlands

Werner C.
JPL 300-323
4800 Oak Grove Drive
Pasadena, CA
91109 USA

Wettstein-Gloor R
University of Zurich, RSL
Winterthurerstrasse 190
Zurich
8057 Swizterland

Wienholz K
Geoforschungszentrum
Potsdam GFZ
Telegraphenberg A17
Potsdam
14473 Germany

Wilson J
ESA/ESTEC
RF Systems Division
Keplerlaan 1
Noordwijk
2200 AG Netherlands

Winzer W
Daimler Benz Aerospace
Prussingstrasse 41
Jena
7745 Germany

Wismann V
Institute for Applied
Remote Sensing
Bahnhofstrasse 54
Wedel
22880 Germany

Woodhouse I
Dept. of Water Resources
Nieuwe Kanaal 11
Wageningen
6709 PA Netherlands

Wright T
GEC Marconi
West Hanningfield Road
Great Baddow
Chelmsford, Essex
CM2 8HN UK

Wu X
University Of Stuttgart
Institut For Navigation
Keplerstrasse 11
Stuttgart
D-70174 Germany

Wunderle S
Inst. fur Physische Geo.
Albert Ludwigs Universitat
Werderring 4
Freiburg
79085 Germany

Xia Ye
Geoforschungs Zentrum
Telegrafenberg 17a
60 07 51, Postdam
14473 Germany

Zakharov A
Inst. of Radioengineering
and Electronics, RAS
Vvendensky aq.1
Fryazino
141120 Russia

Zink M
DLR Oberpfaffenhofen
Institut fur
Hochfrequenztechnik
Postfach 1116
Wessling
2230 Germany

Zmuda A
Remote Sensing
Applications consultants Ltd
4 Mansfield Park
Medstead, Alton
Hants
GU34 5PZ UK

European Space Agency
Agence spatiale européenne

Contact: ESA Publications Division
c/o ESTEC, PO Box 299, 2200 AG Noordwijk, The Netherlands
Tel (31) 71 565 3400 - Fax (31) 71 565 5433